

# Concrete behaviour in multiaxial compression : numerical modelling

**Citation for published version (APA):**

Bongers, J. P. W. (2006). *Concrete behaviour in multiaxial compression : numerical modelling*. [Phd Thesis 1 (Research TU/e / Graduation TU/e), Built Environment]. Technische Universiteit Eindhoven.  
<https://doi.org/10.6100/IR616457>

**DOI:**

[10.6100/IR616457](https://doi.org/10.6100/IR616457)

**Document status and date:**

Published: 01/01/2006

**Document Version:**

Publisher's PDF, also known as Version of Record (includes final page, issue and volume numbers)

**Please check the document version of this publication:**

- A submitted manuscript is the version of the article upon submission and before peer-review. There can be important differences between the submitted version and the official published version of record. People interested in the research are advised to contact the author for the final version of the publication, or visit the DOI to the publisher's website.
- The final author version and the galley proof are versions of the publication after peer review.
- The final published version features the final layout of the paper including the volume, issue and page numbers.

[Link to publication](#)

**General rights**

Copyright and moral rights for the publications made accessible in the public portal are retained by the authors and/or other copyright owners and it is a condition of accessing publications that users recognise and abide by the legal requirements associated with these rights.

- Users may download and print one copy of any publication from the public portal for the purpose of private study or research.
- You may not further distribute the material or use it for any profit-making activity or commercial gain
- You may freely distribute the URL identifying the publication in the public portal.

If the publication is distributed under the terms of Article 25fa of the Dutch Copyright Act, indicated by the "Taverne" license above, please follow below link for the End User Agreement:

[www.tue.nl/taverne](http://www.tue.nl/taverne)

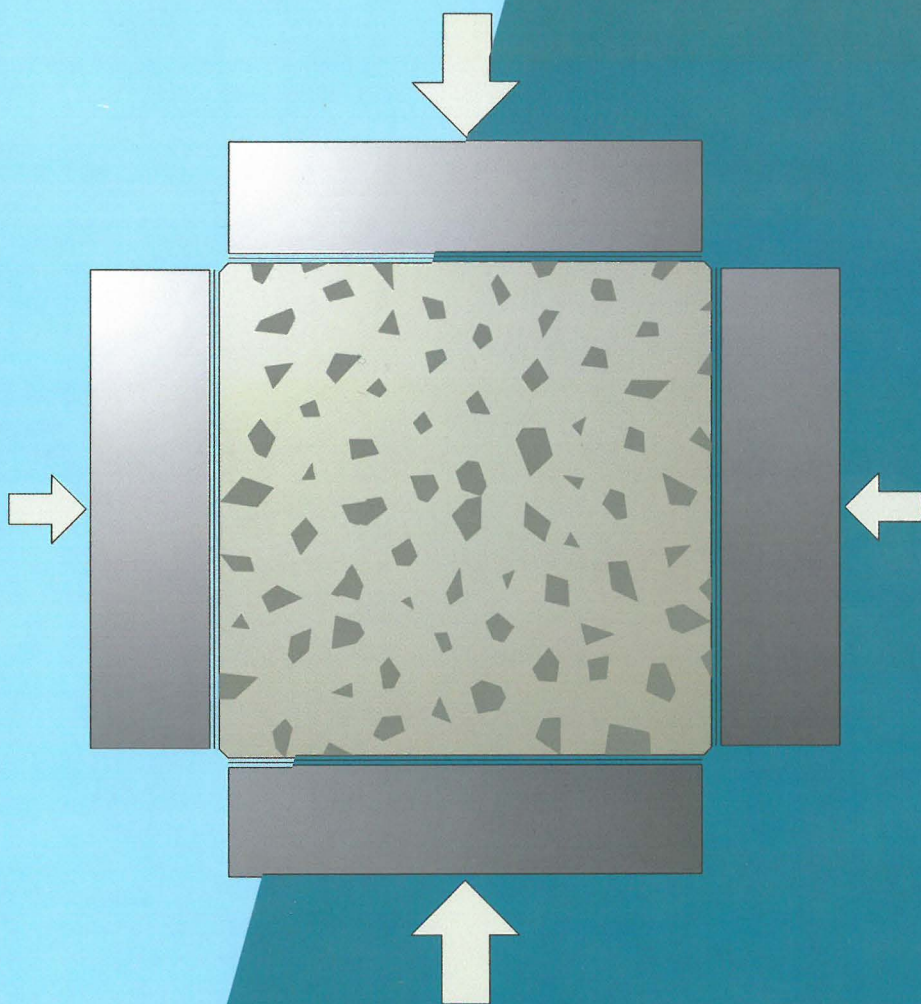
**Take down policy**

If you believe that this document breaches copyright please contact us at:

[openaccess@tue.nl](mailto:openaccess@tue.nl)

providing details and we will investigate your claim.

# bouwstenen



J.P.W. Bongers

## Concrete behaviour in multi-axial compression

Numerical modelling

/ faculteit bouwkunde

117

**CONCRETE BEHAVIOUR IN  
MULTIAXIAL COMPRESSION**

**NUMERICAL MODELLING**

# CONCRETE BEHAVIOUR IN MULTIAXIAL COMPRESSION

NUMERICAL MODELLING

**Proefschrift**

ter verkrijging van de graad van doctor aan de  
Technische Universiteit Eindhoven op gezag van de  
Rector Magnificus, prof.dr.ir. C.J. van Duijn, voor een  
commissie aangewezen door het College voor  
Promoties in het openbaar te verdedigen  
op dinsdag 12 december 2006 om 16.00 uur

door

**Johannes Peter Wilhelmus Bongers**

geboren te Valkenswaard

CIP-GEGEVENS KONINKLIJKE BIBLIOTHEEK, DEN HAAG

Bongers, J.P.W.

Concrete behaviour in multiaxial compression – Numerical modelling

Bouwstenen 117

ISBN 90-6814-605-X

NUR 955

Subject headings: concrete – mechanical properties / constitutive modelling  
concrete structures – multiaxial loading

Trefwoorden: beton – mechanische eigenschappen / materiaalmodellen  
betonconstructies – multi-axiale belastingen

© 2006 by J.P.W. Bongers

Cover design by J. de Kok / J.P.W. Bongers

Printed in the Netherlands by University Press Facilities, Eindhoven University of  
Technology

Dit proefschrift is goedgekeurd door de promotoren:

prof.dr.ir. H.S. Rutten  
en  
prof.Dr.-Ing. K. Willam

## ACKNOWLEDGEMENTS

First of all, I wish to express my gratitude to Prof. Rutten and to Henk Fijneman (B.Sc.) for their scientific and moral support during this research project. Secondly, I would like to thank Prof. Willam, Prof. van Mier and Prof. Rots for their contributions towards completion of this thesis.

Special thanks are for Dr. Erik van Geel, with whom I enjoyed working very much during this cooperative research project. Also, the valuable assistance of Johan van de Oever and Jac van Ishoven is appreciated. Furthermore, I would like to thank all my former colleagues of the Department of Structural Design for the pleasant working atmosphere during the time I was employed at Eindhoven University of Technology.

The financial support provided by the Dutch Technology Foundation (STW) is gratefully acknowledged.

The company of Betonson – and especially Gerrit Bruin (B.Eng.) – is highly appreciated for giving me the opportunity to finally complete this thesis.

My appreciation also goes to my dear wife Yvonne, who still managed to support me in spite of the turbulence crossing our course of life. Also, I owe much gratitude to my parents and parents-in-law for their unremitting support. Without their help I could not have managed to complete this thesis.

Finally, I would like to thank my children Femke and Lucas, just for being there ...

Hans Bongers  
Eindhoven, September 2006

### Constitution of the doctoral committee:

prof.ir. J. Westra (chair)  
prof.dr.ir. H.S. Rutten  
prof.Dr.-Ing. K. Willam  
prof.dr.ir. J.G.M. van Mier  
prof.dr.ir. J.G. Rots  
prof.dr.ir. J.C. Walraven  
prof.dr.ir. J. Carmeliet  
dr.ir. P.E. Roelfstra  
ir. H.J. Fijneman  
ing. G.P. Bruin

## TABLE OF CONTENTS

Abstract .....	v
Samenvatting .....	vii
Symbols, Notation and Abbreviations .....	ix
1. INTRODUCTION .....	1
1.1 <i>Scope and objectives</i> .....	1
1.2 <i>Terminology and symbols</i> .....	3
1.2.1 Coordinate systems and stress-strain states .....	3
1.2.2 Fracture of concrete .....	7
1.2.3 Theory of elasto-plasticity .....	9
1.2.4 Concept of a stress-state bounding surface .....	12
2. REVIEW OF LITERATURE .....	17
2.1 <i>Experiments</i> .....	17
2.1.1 Multiaxial compressive stress state .....	17
2.1.1.1 Influence on strength .....	17
2.1.1.1.1 Biaxial strength .....	17
2.1.1.1.2 Triaxial strength .....	19
2.1.1.2 Stress-displacement curves .....	22
2.1.2 Cracking in concrete .....	24
2.1.2.1 Uniaxial compression .....	24
2.1.2.2 Triaxial compression .....	26
2.1.2.3 Crack patterns at failure .....	26
2.1.2.4 Localisation of deformations .....	28
2.2 <i>Modelling</i> .....	29
2.2.1 Discrete crack modelling .....	29
2.2.1.1 Discrete crack modelling in a homogeneous brittle solid: Linear Elastic Fracture Mechanics (LEFM) .....	29
2.2.1.2 Influence of heterogeneity .....	31
2.2.2 Non-continuum modelling .....	33
2.2.2.1 Lattice modelling .....	33
2.2.2.2 Assemblages of spheres or disks .....	35
2.2.3 Continuum solid mechanics .....	36
2.2.3.1 Diffuse cracking in continuum solid mechanics .....	36
2.2.3.1.1 Elasto-plasticity .....	36
2.2.3.1.2 Continuum damage mechanics .....	37
2.2.3.1.3 Coupling of elasto-plasticity and continuum damage mechanics .....	38
2.2.3.1.4 Heterogeneity .....	39
2.2.3.1.5 Isotropy/anisotropy .....	39
2.2.3.2 Localisation of deformations in continuum solid mechanics .....	40

3. FUNDAMENTALS OF CONCRETE LOADED IN MULTIAXIAL COMPRESSION.....	43
3.1 <i>Scale levels</i> .....	44
3.1.1 Micro level.....	44
3.1.2 Meso level.....	47
3.1.2.1 Mechanical properties of the constituents.....	47
3.1.2.2 Mechanical behaviour of the composite.....	48
3.1.3 Macro level.....	53
3.2 <i>Stages in crack formation</i> .....	55
3.2.1 Linear elastic stage (I).....	55
3.2.2 Non-linear strengthening stage (II).....	56
3.2.3 Around peak stress (III).....	60
3.2.4 Softening stage (IV).....	64
4. NUMERICAL MODELLING AT THE MESO LEVEL.....	69
4.1 <i>Computational environment</i> .....	70
4.1.1 Division into blocks and contacts.....	70
4.1.2 Explicit finite difference solution scheme.....	70
4.2 <i>Mesh generation</i> .....	72
4.3 <i>Constitutive theory (Stage I &amp; II)</i> .....	75
4.3.1 The concept of a Representative Volume Element (RVE).....	75
4.3.2 RVE calculation scheme.....	77
4.3.3 Effective elastic moduli for the RVE.....	79
4.3.4 Elastic stress distribution in the ITZ.....	81
4.3.5 Treatment of non-linear behaviour in the ITZ.....	88
4.3.5.1 Elementary state I - Stress/displacement field.....	91
4.3.5.2 Elementary state II - Stress/displacement field.....	94
4.3.5.3 Stress/displacement fields for arbitrary ITZ stress correction vectors.....	97
4.3.6 Constitutive model for ITZ non-linear behaviour.....	98
4.3.6.1 Mesoscopic mode I and mode II cracking along the ITZ.....	99
4.3.6.2 Pore collapse.....	101
4.3.6.3 Mesoscopic cracking along the ITZ or microscopic pore collapse?.....	107
4.3.6.4 Crack closure.....	110
4.3.7 Crack interaction effects.....	111
4.3.8 Correction of trial macro stress state.....	113
4.4 <i>Performance of the numerical model</i> .....	115
5. NUMERICAL MODELLING OF STAGE III AND IV BEHAVIOUR.....	129
5.1 <i>RVE for meso- and macro-cracking</i> .....	129
5.2 <i>Incorporation in main calculation scheme</i> .....	130
5.3 <i>Crack initiation criterion</i> .....	132
5.3.1 Straight crack running through cement paste or aggregate grains.....	133
5.3.2 Curved crack running through cement paste.....	134
5.3.3 Overall bounding surface.....	138

5.3.4 Potential crack directions.....	141
5.3.5 Material parameters.....	142
5.4 <i>Mechanical behaviour of a crack after initiation</i> .....	146
5.4.1 Rotation of the stress state after crack initiation.....	146
5.4.2 Plastic crack deformations and return mapping of trial stress state.....	149
5.4.3 Mode I crack closure.....	153
5.4.4 Implications due to redistribution of local stresses around the crack after initial (mode II) sliding.....	154
5.4.4.1 Bounding surface of a curved crack through cement paste after initial sliding and after de-bonding between the opposite crack faces.....	154
5.4.4.2 Plastic deformations during initial crack sliding.....	160
5.4.4.3 Extension to combined curved and straight cracking.....	164
5.4.4.4 Decoupling ‘material strengthening during initial crack sliding’ and ‘material softening as a result of de-bonding’.....	168
5.4.5 Introduction of softening behaviour.....	173
5.4.5.1 Tensile softening.....	174
5.4.5.2 Cohesive and frictional softening.....	176
5.5 <i>Localisation of deformations and smeared crack analysis</i> .....	186
5.5.1 Alignment of macroscopic cracks.....	187
5.6 <i>Overview of computational procedure</i> .....	191
5.7 <i>Performance of the numerical model</i> .....	195
5.7.1 Mesh design.....	195
5.7.2 Discussion of material properties.....	196
5.7.3 Simulations of proportional tests.....	197
5.7.4 Influence of loading path in stress space.....	203
5.7.5 Influence of boundary conditions.....	207
5.7.6 Parameter study.....	212
5.7.7 Discussion of results.....	216
6. TOWARDS NUMERICAL MODELLING AT THE MACRO LEVEL.....	219
6.1 <i>Implicit modelling of the coarse aggregate grains</i> .....	219
6.1.1 Dimensions of the RVE <sub>1</sub> .....	220
6.1.2 Alternative way of introducing heterogeneity.....	220
6.2 <i>Performance of the model</i> .....	223
6.2.1 Simulations of proportional tests.....	225
7. CONCLUSIONS AND RECOMMENDATIONS.....	229
7.1 <i>General conclusions</i> .....	229
7.2 <i>General recommendations</i> .....	229
7.3 <i>Conclusions/recommendations regarding stage I/II</i> .....	230
7.4 <i>Conclusions/recommendations regarding stage III/IV</i> .....	231
REFERENCES.....	233

APPENDIX A. ELASTIC PROPERTIES OF THE RVE.....	245
A.1 General equations in cylindrical coordinates.....	245
A.2 Elementary state I: Uniform radial boundary stress (or displacement).....	246
A.2.1 Homogeneous solid.....	248
A.2.2 Heterogeneous RVE.....	249
A.2.3 Determination of effective elastic moduli.....	251
A.3 Elementary state II: Sine curved radial boundary stress.....	252
A.3.1 Macrostress prescribed approach.....	252
A.3.1.1 Homogeneous solid.....	254
A.3.1.2 Heterogeneous RVE.....	254
A.3.1.3 Determination of effective elastic moduli.....	258
A.3.2 Macrostrain prescribed approach.....	260
A.3.2.1 Heterogeneous RVE.....	261
A.3.2.2 Determination of effective elastic moduli.....	263
A.3.3 Comparison of results from the macrostress and macrostrain approach.....	265
APPENDIX B. EQUILIBRIUM OF THE RVE.....	267

## ABSTRACT

The research presented comprises the development of a two-dimensional (2D) numerical model, which is capable of providing predictions of the mechanical response of multiaxial compressive tests on concrete specimens in a 2D test lay-out of sufficient accuracy (from the point of view of the Building Codes for the design of structures). As the model aims at predicting realistically the mechanical response of an arbitrary 2D concrete structure subjected to an arbitrary loading path, the model has been based on sound physical/mechanical interpretation and explanation – rather than empirical formulations – of the mechanical behaviour of concrete loaded in multiaxial compression as observed in experimental tests.

The (numerical) research presented is the prolongation of a long history of concrete research at Eindhoven University of Technology – initiated in the early eighties of the 20<sup>th</sup> century – and was carried out in close cooperation with the (experimental) research done by Van Geel<sup>1998</sup>. As a result of the close interaction between laboratory experiments and numerical modelling, the numerical model has firmly been based on the results of the extensive test program of Van Geel and vice versa, changes and additions to the experimental test program were specified as a result of new insights gained from the numerical modelling.

To establish sound physical/mechanical explanations of the complex mechanical behaviour of concrete loaded in multiaxial compression, this behaviour is subdivided in two ways. On the one side, three scale levels of perception/observation are distinguished. On the other side, a distinction is made between four typical behavioural stages in multiaxial compression tests. This subdivision is chosen because the macroscopically observed mechanical behaviour is very characteristic for each of these four stages. Furthermore, the consideration of multiple scale levels of observation at each of these stages is essential, as the complex macroscopic mechanical behaviour at each of those stages proves to be directly related to the physical conditions and basic mechanisms prevailing at the lower scale levels.

The subdivision of the mechanical behaviour of concrete with respect to scale levels of observation and typical behavioural stages in a multiaxial compression test has provided a solid basis for constitutive modelling. Herewith, the concept of a Representative Volume Element (RVE) has been adopted to account for the specific heterogeneity of concrete at the lower scale levels of observation. Such an RVE at a material point of a continuum is defined as a material volume statistically representative of a small material neighbourhood of that point.

The great differences in scale of heterogeneity of the concrete material between the *pre-peak* and the *post-peak* region of a multiaxial compression test could be



captured well by the subdivision chosen. These differences in scale of heterogeneity, however, could not be captured by a single RVE. Consequently, two different RVEs have been conceived. The first one, RVE<sub>1</sub>, captures the most dominant features having first-order influence on the *pre-peak* mechanical behaviour of concrete loaded in multiaxial compression. The second one, RVE<sub>2</sub>, captures the most dominant features with first-order influence on the *post-peak* mechanical behaviour of concrete.

By choosing the geometrical shape of the RVEs rationally and with a thorough analysis of basic (crack) mechanics, straightforward ‘low-scale’ constitutive laws could be efficiently combined with sophisticated – physically appealing – ‘high-scale’ constitutive laws, applicable both in the pre-peak and post-peak region. For linear elastic material behaviour, in this way general analytic solutions of the stress/displacement fields have been derived for both RVEs. Non-linear material behaviour within the RVEs has been effectively introduced through the development of sophisticated ‘high-scale’ elasto-plastic laws, derived exclusively from straightforward Mohr-Coulomb stress-state bounding surfaces in 3D stress space.

The numerical model, which consists of the above RVE-formulations incorporating linear elastic as well as the whole range of non-linear material behaviour in multiaxial compression, has been entitled as ‘mesoscopic model’. This model – as outlined in chapters 4 and 5 – is well suited for *small-scale* analyses of concrete structures subjected to multiaxial compression. For *large-scale* analyses, the mesoscopic model is less practical. To enhance the practicality and speed up computations, chapter 6 presents an adjusted approach, entitled as ‘macroscopic model’.

The performance of both the mesoscopic and the macroscopic model is illustrated by a wide range of accurate numerical simulations of multiaxial compressive tests from the extensive experimental test program performed by Van Geel<sup>1998</sup>. The experimental data is reproduced well, not only in terms of overall monotonic (and cyclic) loading curves in all (axial and lateral) directions, but also in terms of crack patterns, influence of loading path and boundary conditions.

## SAMENVATTING

Het onderhavige onderzoek omvat de ontwikkeling van een tweedimensionaal (2D) numeriek model, dat in staat is om het mechanische gedrag uit meerassige drukproeven op betonnen proefstukken in een 2D proefopstelling voldoende nauwkeurig (uit het oogpunt van de Bouwvoorschriften voor het constructieve ontwerp) te voorspellen. Aangezien het model zich ten doel stelt om het constructieve gedrag van een willekeurige 2D betonconstructie realistisch te voorspellen bij een willekeurig belastingspad, is het model gebaseerd op solide fysische/mechanische interpretatie en verklaring – en niet op empirische formules – van het constructieve betongedrag onder meerassige druk zoals bekend en voorhanden uit laboratoriumproeven.

Dit (numerieke) onderzoek is het vervolg op een lange historie van betononderzoek aan de Technische Universiteit Eindhoven, geïnitieerd in het begin van de jaren tachtig van de 20<sup>e</sup> eeuw. Het is uitgevoerd in nauwe samenwerking met het (experimentele) onderzoek van Van Geel<sup>1998</sup>. Door de sterke wisselwerking tussen het laboratorium onderzoek en het numeriek modelleren, werd het ontwikkelde numerieke model deugdelijk ondersteund door de resultaten van het uitgebreide proevenprogramma van Van Geel enerzijds en anderzijds werd het proevenprogramma ook aangepast en uitgebreid als gevolg van het voortschrijdend inzicht verkregen uit de resultaten van het numerieke onderzoek.

Om te komen tot een solide fysische/mechanische onderbouwing van het (complexe) betongedrag onder meerassige druk, is dit betongedrag onderverdeeld op twee verschillende manieren. Enerzijds worden drie verschillende schaalniveaus van observatie/schematisatie onderscheiden. Anderzijds wordt er een onderscheid gemaakt tussen vier gedragsstadia in geval van meerassige drukproeven. Dit onderscheid is gemaakt omdat de karakteristieken van het macroscopisch waargenomen betongedrag duidelijk verschillen in elk van deze vier stadia. Bovendien is het beschouwen van meerdere schaalniveaus van observatie/schematisatie binnen elk van de gedragsstadia essentieel. Het complexe macroscopische betongedrag blijkt namelijk direct verband te houden met de fysische condities en fundamentele mechanismen zoals deze zich voordoen en werken op de lagere schaalniveaus.

De onderverdeling van het gedrag van beton onder meerassige druk met betrekking tot schaalniveaus van observatie en karakteristieke gedragsstadia heeft een solide basis opgeleverd voor de ontwikkeling van constitutieve materiaalmodellen. Om de invloed van de specifieke heterogeniteit van beton – zoals deze bestaat op de lagere schaalniveaus – in rekening te brengen, is daarbij in de modellering het concept van een ‘Representatief Volume Element’ (RVE) gebruikt. Een RVE in een punt van

een materiaalcontinuüm is gedefinieerd als een materiaal volume dat statistisch representatief is voor de materiaalstructuur in de directe omgeving van dat punt.

De grote verschillen in mate van heterogeniteit van het betonmateriaal *voor* en *na* het bereiken van de maximale sterkte in een meerassige drukproef kunnen goed in de gekozen onderverdeling worden ondergebracht. Deze verschillen kunnen echter niet worden verenigd in één RVE, daarom zijn twee verschillende RVE's ontwikkeld. In de eerste, RVE<sub>1</sub>, worden de overheersende kenmerken verdisconteerd die een 1<sup>e</sup> orde invloed hebben op het constructieve betongedrag *voor* het bereiken van de maximale sterkte in een meerassige drukproef. De tweede, RVE<sub>2</sub>, bevat de overheersende kenmerken die een 1<sup>e</sup> orde invloed hebben op het constructieve betongedrag *na* het bereiken van de maximale sterkte.

Op basis van een rationele keuze van de geometrische vorm van de RVE's en een grondige analyse van de fundamentele (scheur) mechanismen kunnen eenvoudige constitutieve formuleringen op een 'laag schaalniveau' effectief gecombineerd worden tot verfijnde – fysisch onderbouwde – constitutieve materiaalmodellen op een 'hoog schaalniveau', toepasbaar voor het constructieve betongedrag zowel *voor* als *na* het bereiken van de maximale sterkte.

Op deze wijze zijn – voor lineair elastisch materiaalgedrag – algemene analytische oplossingen afgeleid voor de spannings- en verplaatsingsvelden van beide RVE's. Niet-lineair materiaalgedrag in de RVE's is effectief geïntroduceerd door de ontwikkeling van verfijnde elasto-plastische constitutieve materiaalmodellen op een 'hoog schaalniveau', gebaseerd op uitsluitend eenvoudige constitutieve formuleringen in de vorm van Mohr-Coulomb plasticiteit in de 3D spanningsruimte.

Het numerieke model, bestaande uit bovenstaande RVE modelleringen die zowel het lineair elastische alsmede de hele reeks van niet-lineair materiaalgedrag van beton onder een meerassige drukbelasting beschrijven, wordt het 'mesoscopisch model' genoemd. Dit model – zoals beschreven in de hoofdstukken 4 en 5 – is zeer geschikt voor de analyse van *kleinschalige* betonconstructies onder een meerassige drukbelasting. Voor de analyse van *grootschalige* betonconstructies is het model minder geschikt. Teneinde deze toepasbaarheid te vergroten en de berekeningen te versnellen, wordt in hoofdstuk 6 een aangepaste methode gepresenteerd, het 'macroscopisch model'.

De 'performance' van zowel het mesoscopisch als het macroscopisch model wordt geïllustreerd aan de hand van de resultaten van een groot aantal numerieke simulaties van meerassige drukproeven uit het uitgebreide proevenprogramma van Van Geel<sup>1998</sup>. De experimentele resultaten worden goed benaderd, niet alleen met betrekking tot de globale (monotone en cyclische) last-verplaatsingskrommen in alle richtingen (axiaal en lateraal), maar ook met betrekking tot scheurpatronen, de invloed van het belastingspad en de proefstuk randvoorwaarden.

## SYMBOLS, NOTATION AND ABBREVIATIONS

### LATIN CAPITALS

$A$	cross-sectional area
$A_{agg}$	cross-sectional area of aggregate grain(s)
$A_{bulk}$	cross-sectional area of the bulk cement paste
$A_{ITZ}$	cross-sectional area of the ITZ
$C_M$	centre of Mohr's stress circle
$D$	diameter
$D_{agg}$	diameter of aggregate grain
$D_{max}$	diameter of the largest aggregate grain in the concrete mix
$Det$	determinant
$E$	Young's Modulus
$E_{agg}$	Young's Modulus of the aggregate grains
$E_{bulk}$	Young's Modulus of the bulk cement paste
$E_{ITZ}$	Young's Modulus of the ITZ
$F$	force
$O$	order of magnitude function
$R_0$	radius at centre of ITZ-layer in RVE <sub>1</sub> representation
$R_1$	radius of aggregate grain in RVE <sub>1</sub> representation
$R_2$	outer radius of ITZ-layer in RVE <sub>1</sub> representation
$R_3$	outer radius of bulk cement paste layer in RVE <sub>1</sub> representation
$V$	volume
$W$	work (done by a force)

### LATIN LOWER CASE

$c$	cohesion
$c_{agg}$	cohesion for aggregate fracture / cement paste crushing
$c_{ini}$	cohesion at (macro)crack initiation (before redistribution of local stresses along the crack)
$c_{pc,ini}$	cohesion at zero pore closure (compressive pore collapse)
$c_{pc,end}$	cohesion at maximum pore closure (compressive pore collapse)
$d$	width of the unit cell (RVE <sub>2</sub> )
$f(r,\theta)$	stress function in cylindrical coordinates
$f, f_1, f_2$	mathematic functions of stress-state bounding surfaces
$f_{c,agg}$	uniaxial compressive strength of the aggregate

$f_{c,pc}$	compressive strength for compressive pore collapse
$f_t$	tensile strength
$f_{t,bulk}$	tensile strength of the bulk cement paste
$f_{t,bulk}^{eq}$	equivalent tensile strength for <i>local</i> mode II cracking through bulk cement paste along a <i>global</i> mode I crack
$f_{t,cp}$	tensile strength of the cement paste (ITZ + bulk cement paste)
$f_{t,cp}^{mode I}$	tensile strength for global mode I cracking
$f_{t,fc}$	<i>fictitious</i> tensile strength, introduced in the transformation process of the stress-state bounding surface during local stress redistribution
$f_{t,ini}$	initial <i>local</i> tensile strength of the ITZ (stage I/II)
$f_{t,ITZ}$	<i>average</i> tensile strength of the ITZ along a curved crack
$f_{t,ITZ}^{eq}$	equivalent tensile strength for <i>local</i> mode II cracking through the ITZ along a <i>global</i> mode I crack
$f_{t,pc}$	tensile strength for compressive pore collapse
$l$	length or width
$m$	mass
$r$	radius
$r_M$	radius of Mohr's stress circle
$t$	(point in) time
$u$	displacement in radial direction (cylindrical $(r,\theta)$ – coordinate system)
$u_1, u_2, u_3$	displacements in principal directions ( $u_1$ = maximum displacement, $u_3$ = minimum displacement)
$u^{cr}$	crack opening displacement
$w$	displacement in tangential direction (cylindrical $(r,\theta)$ – coordinate system)
$w^{cr}$	crack sliding displacement
$w_{max}^{cr}$	material parameter defining the crack sliding displacement for which softening ends (during aggregate fracture/cement paste crushing)

## GREEK

$\alpha$	(global) angle of crack plane with respect to the direction of the minimum (most compressive) principal stress
$\beta$	ratio between the maximum and the minimum principal stress
$\gamma_{max}$	maximum shear strain
$\gamma_{nt}$	(in-plane) shear strain (rotated Cartesian $(n,t,z)$ – coordinate system)
$\gamma_{r\theta}$	(in-plane) shear strain (cylindrical $(r,\theta)$ – coordinate system)
$\gamma_{xy}, \gamma_{xz}, \gamma_{yz}$	shear strains (global Cartesian $(x,y,z)$ – coordinate system)
$\epsilon_1, \epsilon_2, \epsilon_3$	principal strains ( $\epsilon_1$ = maximum strain, $\epsilon_3$ = minimum strain)
$\epsilon_n, \epsilon_t, \epsilon_z$	normal strains (rotated Cartesian $(n,t,z)$ – coordinate system)
$\epsilon_r, \epsilon_\theta$	normal strains (cylindrical $(r,\theta)$ – coordinate system)

$\epsilon_{vol}$	volumetric strain
$\epsilon_x, \epsilon_y, \epsilon_z$	normal strains (global Cartesian $(x,y,z)$ – coordinate system)
$\eta$	heterogeneity (material) parameter
$\theta$	angle of the $n$ -axis (of rotated $(n,t,z)$ – coordinate system) with respect to the orientation of the normal to the plane of maximum shear stress
$\theta^*$	angle of the $n$ -axis (of rotated $(n,t,z)$ – coordinate system) with respect to the global $y$ -axis
$\theta^{**}$	angle of the $n$ -axis (of rotated $(n,t,z)$ – coordinate system) with respect to the global $x$ -axis
$\vartheta_\epsilon$	plastic multiplier (plastic flow formulated in terms of <i>strains</i> )
$\vartheta_u$	plastic multiplier (plastic flow formulated in terms of <i>displacements</i> )
$\kappa$	internal state parameter
$\kappa_1$	internal state parameter governing tensile softening
$\kappa_{1,max}$	material parameter defining the end of tensile softening
$\kappa_2$	plastic volumetric compaction (internal state parameter)
$\kappa_{2,max}$	material parameter defining the plastic volumetric compaction at maximum pore closure
$\lambda_{mech1}$	<i>momentary</i> value of relative crack length with crack sliding displacement according to the 'overriding' mechanism
$\bar{\lambda}_{mech1}$	<i>average</i> value of $\lambda_{mech1}$ throughout the formation history of a macrocrack
$\lambda_{rel}$	(model) parameter affecting the shape of the stress-state bounding surface at stage III/IV
$\mu$	mean value of normally distributed quantity
$\nu$	Poisson's ratio
$\rho$	overlap Mohr's stress circle with respect to the stress-state bounding surface of a straight crack
$\sigma$	standard deviation of normally distributed quantity
$\sigma_1, \sigma_2, \sigma_3$	principal stresses ( $\sigma_1$ = maximum stress, $\sigma_3$ = minimum stress)
$\sigma_n, \sigma_t$	normal stresses (rotated Cartesian $(n,t,z)$ – coordinate system)
$\sigma_r, \sigma_\theta$	normal stresses (cylindrical $(r,\theta)$ – coordinate system)
$\sigma_x, \sigma_y, \sigma_z$	normal stresses (global Cartesian $(x,y,z)$ – coordinate system)
$\tau_{max}$	maximum shear stress
$\tau_{nt}$	(in-plane) shear stress (rotated Cartesian $(n,t,z)$ – coordinate system)
$\tau_{r\theta}$	(in-plane) shear stress (cylindrical $(r,\theta)$ – coordinate system)
$\tau_{xy}, \tau_{xz}, \tau_{yz}$	shear stresses (global Cartesian $(x,y,z)$ – coordinate system)
$\phi$	friction angle
$\phi_{agg}$	friction angle for aggregate fracture / cement paste crushing
$\phi_{cp}$	friction angle for (straight) cracking through cement paste
$\phi_{pc}$	friction angle for compressive pore collapse
$\psi$	dilatancy angle
$\psi_{pc}$	dilatancy angle for compressive pore collapse

$\Delta\alpha$	maximum deviation angle of a curved crack
$\Delta\alpha_0$	maximum deviation angle of a curved crack in the virgin concrete
$\Delta\alpha_i$	local deviation angle of an irregularly curved crack
$\Delta\alpha_\psi$	maximum local deviation angle at which overriding still occurs
$\Delta\phi$	increase of friction angle due to the mesoscopic curvature of a crack
$\Delta\phi_{cp}$	increase of friction angle due to the mesoscopic curvature of a crack ( <i>before</i> redistribution of local stresses along the crack)
$\Delta\phi_{fic}$	increase of friction angle of ‘an equivalent fictitious regularly curved crack through cement paste’ (with equivalent crack dilatancy)
$\Delta\phi^m$	increase of friction angle due to the mesoscopic curvature of a crack ( <i>after</i> redistribution of local stresses along the crack)

### SUPERSCRIPTS

0	initial state
1	final state
I	elementary state I
II	elementary state II
<i>coarse</i>	coarse fraction of the aggregate grains
<i>cr</i>	crack quantity
<i>e</i>	elastic (strain, displacement)
<i>fine</i>	fine fraction of the aggregate grains
<i>ITZ</i>	material point is located within the ITZ
<i>loc</i>	local quantity
<i>m</i>	macroscopic quantity
<i>mode I</i>	mode I crack quantity
<i>mode II</i>	mode II crack quantity
<i>p</i>	plastic (strain, displacement)
<i>t</i>	trial state

### MISCELLANEOUS

$\dot{u}_x, \dot{\sigma}_x, \dot{\epsilon}_x$	dot above a quantity indicates a first order <i>derivative</i> with respect to time (e.g. <i>velocity</i> instead of displacement)
$\ddot{u}_x$	two dots above a quantity indicates a second order <i>derivative</i> with respect to time (e.g. acceleration instead of displacement)
$\bar{u}_x, \bar{\sigma}_x, \bar{\epsilon}_x$	narrow line above a quantity indicates an averaged or effective value
$\underline{u}, \underline{\sigma}, \underline{\epsilon}$	underlined quantity indicates a <i>vector</i> instead of a scalar
$\Delta u, \Delta \sigma, \Delta \epsilon$	<i>increments</i> or <i>corrections</i> of displacements, stresses and strains
$\Delta t$	<i>increment</i> of time (time step)

<b>D</b>	<b>bold</b> latin capital indicates a matrix
$[\cdot], [\cdot]$	matrix, vector
$[\cdot]^T, [\cdot]^T$	<i>transpose</i> of a matrix, vector
$[a; b]_{\min}$	<i>minimum value</i> of scalar <i>a</i> or <i>b</i>
$ a $	<i>absolute value</i> of scalar <i>a</i>
$ \underline{a} $	<i>length</i> of vector <i>a</i>
$\overrightarrow{AB}$	vector pointing from <i>A</i> to <i>B</i>
$\wedge$	<i>AND</i> operator
$\equiv$	<i>equivalent</i> symbol

### ABBREVIATIONS

2D	two-dimensional
3D	three-dimensional
<i>COD</i>	Crack Opening Displacement
<i>EUT</i>	Eindhoven University of Technology
<i>FEM</i>	Finite Element Method
<i>ITZ</i>	Interfacial Transition Zone
<i>LEFM</i>	Linear Elastic Fracture Mechanics
<i>LVDT</i>	Linear Variable Displacement Transducer
<i>ROT</i>	Rotation of finite element
<i>RVE</i>	Representative Volume Element
<i>UDEC</i>	Universal Distinct Element Code

## CHAPTER 1

### INTRODUCTION

#### 1.1 Scope and objectives

In the field of structural engineering, the considerable increase of load-bearing capacity due to confinement of a concrete element is common knowledge. A large increase of deformations accompanies this increase in load-bearing capacity.

The advantageous influence of a multiaxial compressive stress state, which arises due to a confinement of a concrete element, may be employed in many cases. With respect to service-state analysis of structures, multiaxial compressive stress states arise, for example, in many junctions of (possibly prestressed) concrete elements, in spirally reinforced concrete columns or in-filled concrete steel tube columns and in the introduction zones of concentrated loads (e.g. pre- and posttensioning).

In limit-state analysis, safety concepts such as structural integrity and absorption of energy during impact loading become increasingly important. In this respect, taking into account the advantageous effects of the large deformations generally accompanying multiaxial compressive stress states, looks promising (remember the large lateral bending deflections of the spirally reinforced concrete columns on ground level of the Pentagon – of the order of magnitude of three to four times the lateral dimensions – after the attack of 11 September 2001 [Harris<sup>2002</sup>]). Depending on the loading path of a potential multiaxial compressive stress state, carefully designed structural elements may well display large deformational capacity before reaching the ultimate strength and a high residual strength after reaching the ultimate strength [Van Geel<sup>1998</sup>].

In spite of this, the advantageous influence of multiaxial compressive stress states is scarcely found in building codes. General rules are not available. The existing rules on multiaxial compressive stress states are empirical formulations based on findings in extensive laboratory testing, valid only for the specific structural specimens tested.

This fundamental lack of knowledge triggered a research project at Eindhoven University of Technology (EUT) in the early eighties. Van Mier<sup>1984</sup> carried out an extensive laboratory test program on uniaxially and multiaxially loaded plain concrete specimens (cubes and prisms). Vonk<sup>1992</sup> focussed on the mechanical analysis and modelling of the structural behaviour (including failure) of concrete loaded in uniaxial compression. The term ‘structural behaviour’ was introduced to distinguish the failure process of a concrete specimen after reaching the ultimate load-bearing capacity. The behaviour before reaching the ultimate load-bearing capacity might be referred to as ‘material behaviour’, as the deformations upon loading at this stage are *grosso modo* still continuously distributed over the concrete volume. Consequently, neither the boundary conditions (test set-up), nor the

geometry and dimensions of the specimen dominantly influence the mechanical response of the specimen at this stage of loading.

Unlike the ‘continuum’ material behaviour as displayed at the loading stage before reaching the ultimate load-bearing capacity, the mechanical response of a concrete specimen at and after reaching the ultimate load-bearing capacity is governed by local fracture processes which dominate the behaviour of the surrounding continuum. These fracture processes prove to be highly dependent on the boundary conditions and the geometry/dimensions of the specimen, i.e. the entire structural system of the test set-up.

The present *numerical* research is carried out in close cooperation with the experimental research done by Van Geel<sup>1998</sup>. At EUT Van Geel carried out a large number of uniaxial and multiaxial compressive tests on plain concrete cubes and prisms. This research provided most of the experimental data needed for the development of a numerical model, such as:

- Overall data: stress-strain/displacement curves and failure patterns,
- Data on the development of cracks during loading,
- Data on the influence of the ‘loading path’,
- Data on the test set-up.

The main objective of the present research is to develop a two-dimensional (2D) numerical model, which is capable of providing accurate predictions of the mechanical response of multiaxial compressive tests in a 2D test lay-out. In a similar investigation later on, the 3D version of the numerical model is to be defined and accomplished.

As a result of close interaction between laboratory experiments and numerical modelling, a numerical model could be developed based on an extensive test program. Otherwise, the insight obtained from the numerical modelling also has been used to specify changes or additions to the experimental test program executed (by van Geel). The influence of the test set-up on the mechanical response of the concrete specimens upon loading could be allowed for by performing both the experiments and the numerical simulations on specimens matching geometry and boundary conditions as close as possible.

The numerical model developed aimed from the beginning at simulating the experimental test program as close as possible, but also at predicting the true mechanical response of an arbitrary 2D structure subjected to an arbitrary loading path. From this point of view, it was essential that convincing physical explanations – versus empirical formulations – should be found for the observed phenomena.

Empirical formulations should strictly be used within the limits of the test series upon which they are formulated. They are not likely to provide proper results for other geometries, boundary conditions and/or loading histories. The Eindhoven research project from the beginning followed the research track of interaction of alternate laboratory experiments and physical/numerical modelling, in order to circumvent a.o. the laming restrictions of the ‘empirical approach’.

The present research concentrated on the investigation of the influence of multiaxial stress states on the static, mechanical response of normal-strength concrete with aggregates of relatively high stiffness and strength. No influence of time effects, like drying shrinkage, creep or loading rate has been taken into account<sup>1</sup>.

The insight gained from this research, however, may be adopted for other concrete mixes. In this way, possibly new insight might be gained for material improvement by e.g. adaptation of the concrete mix.

## 1.2 Terminology and symbols

### 1.2.1 Coordinate systems and stress-strain states

Throughout this thesis a Cartesian  $(x,y,z)$  - coordinate system is used to indicate the *global* coordinates of a material point. Stresses and strains according to this global coordinate system are indexed according to figure 1.1.a. The sign convention of stresses and strains is also indicated in this figure: (ex)tension is positive while compression is negative. To satisfy the condition of moment equilibrium and according to the definition of shear strain the following conditions apply

$$\begin{array}{l|l} \tau_{xy} = \tau_{yx} & \gamma_{xy} = \gamma_{yx} \\ \tau_{yz} = \tau_{zy} & \gamma_{yz} = \gamma_{zy} \\ \tau_{zx} = \tau_{xz} & \gamma_{zx} = \gamma_{xz} \end{array}$$

A Cartesian  $(1,2,3)$  - coordinate system is used to indicate the *local* axes of principal stresses (or strains) in a certain material point (see figure 1.1.b).

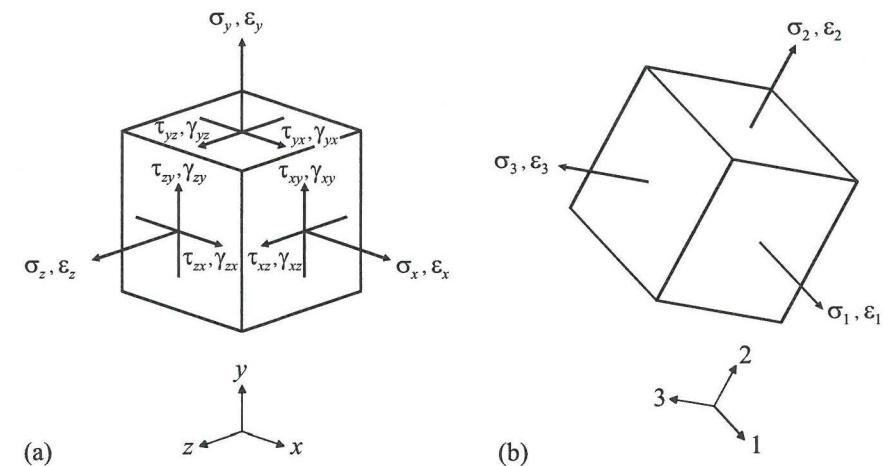


Figure 1.1. Coordinate systems for (a) a global (primary) stress/strain state and (b) for a principal stress/strain state.

<sup>1</sup> The concrete specimens used in the experimental test program [Van Geel<sup>1998</sup>] were stored under water during 28 days and sealed in plastic bags afterwards. Testing occurred at moderate loading rates. Ergo, the potential influence of drying shrinkage, creep and loading rate on the test results may be neglected.

A useful graphical method of analysing the state of stress and converting primary stresses into principal stresses has been developed by Mohr. In this method, the normal and shear stresses on any plane (e.g. the  $x,y$ -plane) are represented by a point on a plane orthogonal diagram of which the horizontal ‘coordinate’ is the normal stress (e.g.  $\sigma_x$  and  $\sigma_y$ ) and the vertical ‘coordinate’ is the shear stress (e.g.  $\tau_{xy}$  and  $\tau_{yx}$ ).

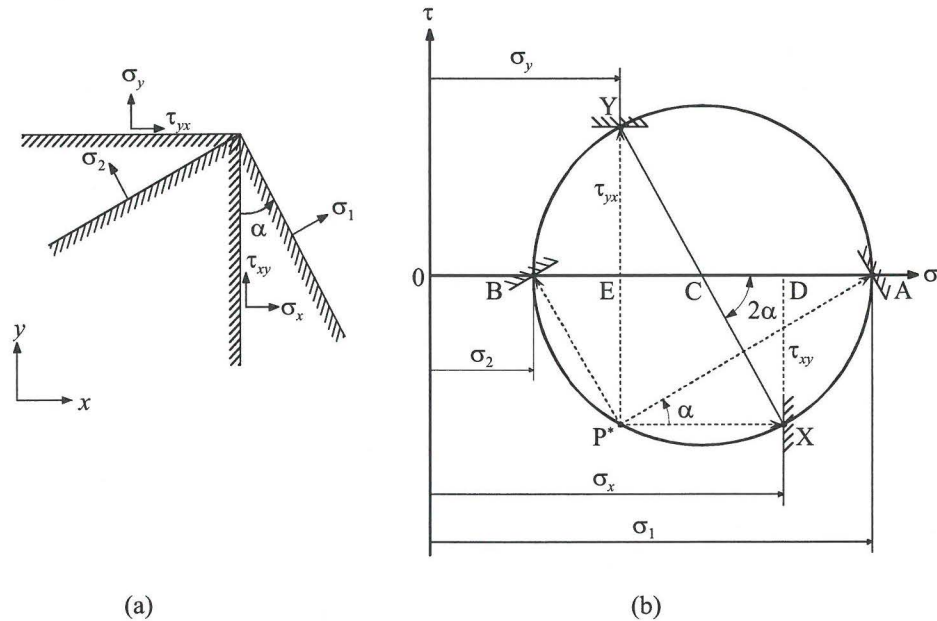


Figure 1.2. Mohr's construction for a two-dimensional state of stress. (a) Physical plane; (b) Mohr's plane.

For the present purpose, it is necessary only to regard the shear stress as positive if it has a clockwise moment about a point within the element. In figure 1.2, the points X and Y on the  $(\sigma,\tau)$  plane represent the stresses acting on planes perpendicular to the  $x$ - and  $y$ -axis. The circle drawn through X and Y and having its centre C on the  $\sigma$ -axis, is called Mohr's circle for the considered state of stress. The circle graphical represents the normal stress and shear stress on all planes through the  $z$ -axis (i.e.  $0 \leq \alpha \leq 2\pi$ ). The points A and B, where the circle intersects the  $\sigma$ -axis, define the principal stresses. The angle made by CA with CX is twice the angle the direction of  $\sigma_1$  makes with the  $x$ -axis in the physical plane.

Another point of interest is  $P^*$ , called the pole of a Mohr's circle. The stresses acting on and the direction of the normal to any plane can be graphically determined by drawing a line from  $P^*$  to any point on the circle. The angle between this line and  $P^*X$  is equal to the angle the normal to the plane makes with the  $x$ -axis.

For a three-dimensional stress state, three Mohr's circles for three orthogonal planes can be constructed. Likewise, a three-dimensional strain state is represented by three Mohr's circles in a plane diagram of which the horizontal ‘coordinate’ is the

normal strain (e.g.  $\epsilon_x$  and  $\epsilon_y$ ) and the vertical ‘coordinate’ is half the shear strain (e.g.  $\frac{1}{2}\gamma_{xy}$  and  $\frac{1}{2}\gamma_{yx}$ ). In order to denominate typical stress or strain states, a classification is made according to the potential presence of zero principal stress or strain in one or two directions (see figure 1.3 and 1.4).

<i>uniaxial stress state</i> (2 principal stresses are zero)	<i>uniaxial strain state</i> (2 principal strains are zero)
■ uniaxial tensile stress state 	■ uniaxial extensional strain state 
■ uniaxial compressive stress state 	■ uniaxial compressive strain state 
<i>biaxial/plane stress state</i> (1 principal stress is zero)	<i>biaxial/plane strain state</i> (1 principal strain is zero)
■ plane stress - tensile stress state 	■ plane strain - extensional strain state 
■ plane stress - tensile/compressive stress state 	■ plane strain - extensional/compressive strain state 
■ plane stress - compressive stress state 	■ plane strain - compressive strain state 

Figure 1.3. Uniaxial and biaxial stress/strain states.

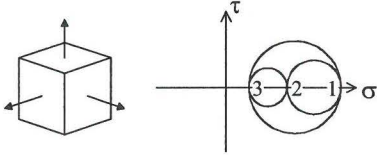
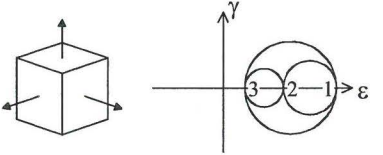
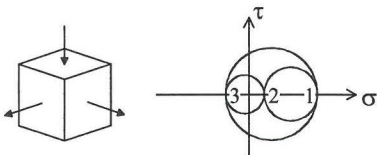
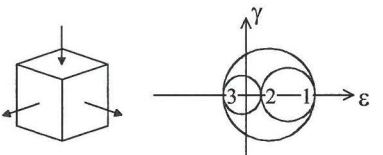
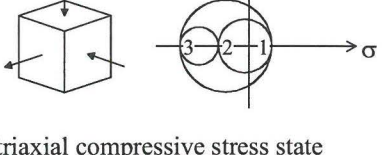
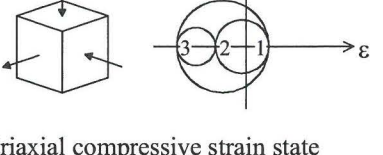
triaxial stress state (no principal stresses are zero)	triaxial strain state (no principal strains are zero)
<ul style="list-style-type: none"> <li>triaxial tensile stress state</li> </ul> 	<ul style="list-style-type: none"> <li>triaxial extensional strain state</li> </ul> 
<ul style="list-style-type: none"> <li>triaxial tensile/compressive stress state</li> </ul> 	<ul style="list-style-type: none"> <li>triaxial extensional/compressive strain state</li> </ul> 
<ul style="list-style-type: none"> <li>triaxial compressive stress state</li> </ul> 	<ul style="list-style-type: none"> <li>triaxial compressive strain state</li> </ul> 

Figure 1.4. Triaxial stress/strain states.

The material model for concrete mechanical behaviour, presented in this thesis, is limited to two dimensions. The global  $z$ -axis is in the following the (principal) out-of-plane direction. To describe in this 2D configuration stresses and displacements at a straight discontinuity (crack), it is convenient to define a local Cartesian  $(n, t, z)$ -coordinate system in which the  $n$ -axis runs perpendicular to the crack direction and the  $t$ -axis runs parallel to the in-plane crack direction (see figure 1.5).

To describe, in a 2D configuration, a stress/strain state at the circumference of a certain material point  $O$ , a cylindrical  $(r, \theta)$ -coordinate system is defined according to figure 1.6. Within this coordinate system the angle  $\theta$  is zero in the direction of maximum shear stress, or, the radius at  $\theta = 0$  makes an angle of  $\pi/4$  radians with the axes of maximum and minimum principal stress (1- and 3-axes).

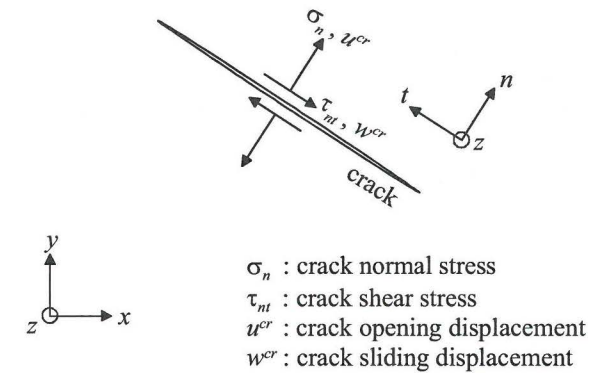


Figure 1.5. Denomination of crack stresses and displacements.

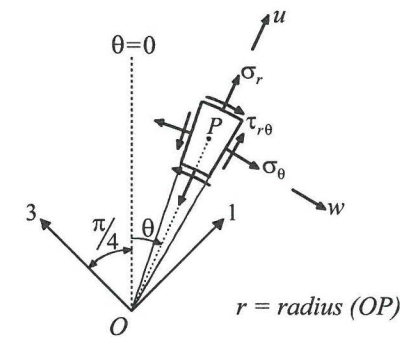


Figure 1.6. Stresses and displacements in a cylindrical  $(r, \theta)$ -coordinate system.

### 1.2.2 Fracture of concrete

A crack in a solid can be loaded in three different basic modes, as indicated in figure 1.7. Normal stresses give rise to the *opening mode* or mode I loading. In-plane shear loading results in the *sliding mode* or mode II loading, whereas out-of-plane shear loading leads to the *tearing mode* or mode III loading. A general case of loading can be described by a superposition of these three basic modes.

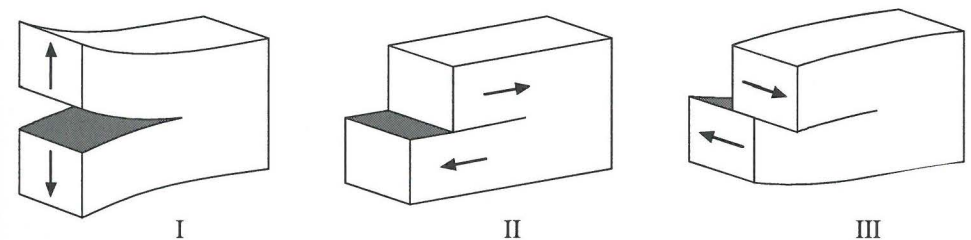


Figure 1.7. Three basic modes of loading [Broek<sup>1986</sup>].



If the solid consists of a heterogeneous material with strong inclusions (such as normal strength concrete), tortuous cracks will be formed, meandering around the strong inclusions (see figure 1.8). Although globally a mode II loading is applied, the local crack displacements along such cracks are a combination of opening and sliding crack displacements. When such a tortuous crack is considered on the global level, the crack is referred to as a mode II crack with crack dilatancy<sup>2</sup>.

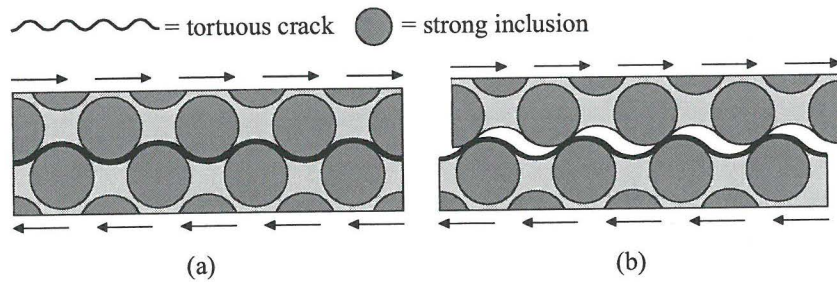


Figure 1.8. (a) Formation of a tortuous crack in mode II loading and (b) sliding and dilation of a tortuous mode II crack.

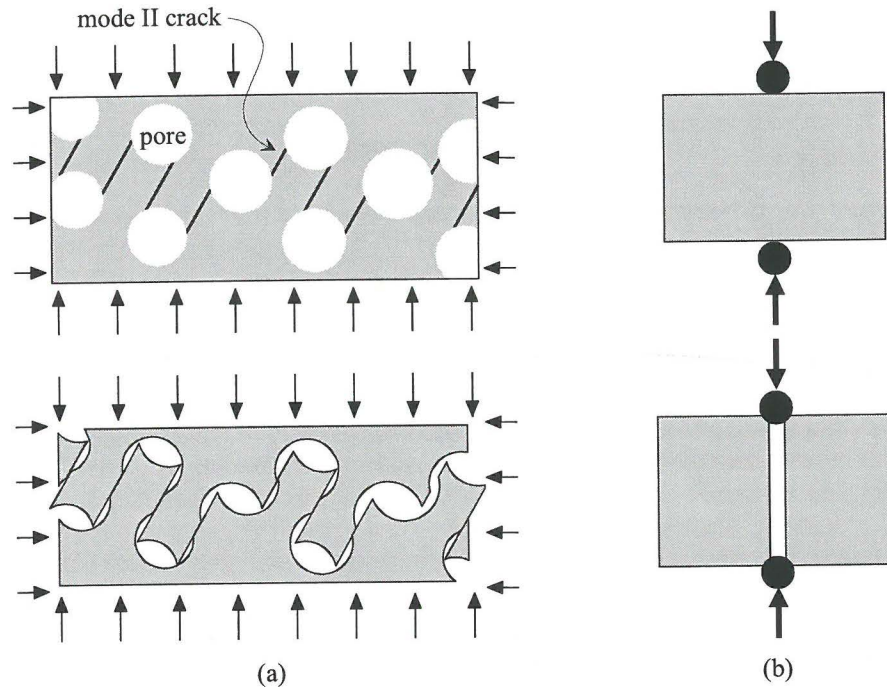


Figure 1.9. (a) Pore collapse and (b) tensile splitting.

<sup>2</sup> Originally, the basic crack modes concern potential *local* crack growth at the crack tip of an existing crack. In the present research, the same terminology is used also to specify the *global* loading condition along the length of the potential or existing crack.

In this research, two other terms regarding crack formation are discussed here: pore collapse and tensile splitting. When – in a highly porous material loaded in compression – the pore structure collapses due to largely distributed mode II cracking, the term pore collapse is used. When mode I cracking occurs in lateral direction due to axial splitting forces, the term tensile splitting is used (figure 1.9).

### 1.2.3 Theory of elasto-plasticity

The numerical model presented in chapter 4 and 5, is developed within the framework of elasto-plasticity. Therefore, the basics and terminology of this theory are discussed cursorily in this section.

According to the classical theory of elasto-plasticity, the strain vector  $\underline{\varepsilon}$  is decomposed in an elastic and a plastic component.

$$\underline{\varepsilon} = \underline{\varepsilon}^e + \underline{\varepsilon}^p$$

The constitutive relationship between the stress vector  $\underline{\sigma}$  and the strain vector  $\underline{\varepsilon}$  is given by

$$\underline{\sigma} = \mathbf{D}^e (\underline{\varepsilon} - \underline{\varepsilon}^p) \quad (1.1)$$

where  $\mathbf{D}^e$  is the matrix of the moduli of elasticity. The presented numerical model is developed in a 2D plane strain configuration. For plane strain analysis of an isotropic material, equation (1.1) yields for the in-plane global stress components

$$\begin{bmatrix} \sigma_x \\ \sigma_y \\ \tau_{xy} \end{bmatrix} = \frac{E}{(1+\nu)(1-2\nu)} \begin{bmatrix} 1-\nu & \nu & 0 \\ \nu & 1-\nu & 0 \\ 0 & 0 & \frac{1}{2}-\nu \end{bmatrix} \begin{bmatrix} \varepsilon_x - \varepsilon_x^p \\ \varepsilon_y - \varepsilon_y^p \\ \gamma_{xy} - \gamma_{xy}^p \end{bmatrix}$$

in which the isotropic elastic material behaviour is characterised by Young's modulus  $E$  and Poisson's ratio  $\nu$ .

The same theory may also be applied for describing the constitutive behaviour of a discontinuity (crack). In this case, the crack relative displacement vector  $\underline{u}$  is decomposed in an elastic and a plastic (crack) component  $\underline{u}^p = [u^{cr}, w^{cr}]^T$ .

$$\underline{u} = \underline{u}^e + \underline{u}^p$$

The constitutive relationship between the crack stresses  $\underline{\sigma} = [\sigma_n, \tau_{nt}]^T$  and the crack displacements is then given by

$$\underline{\sigma} = \mathbf{K}^e (\underline{u} - \underline{u}^p) \quad (1.2)$$

with  $\mathbf{K}^e$  being the matrix of the moduli of elasticity of the crack<sup>3</sup>.

<sup>3</sup> In reality, the elastic deformations of an interfacial (potential) crack are zero. Generally, this is accounted for by taking the elastic stiffness  $\mathbf{K}^e$  so high that the elastic deformations of the crack may be neglected with respect to the elastic deformations of the continuum.

For mode II cracking, the crack opening and crack sliding velocities are interrelated by the so-called dilatancy angle  $\psi$  (see figure 1.10)

$$\tan \psi = \frac{\dot{u}^{cr}}{\dot{w}^{cr}} \quad (1.3)$$

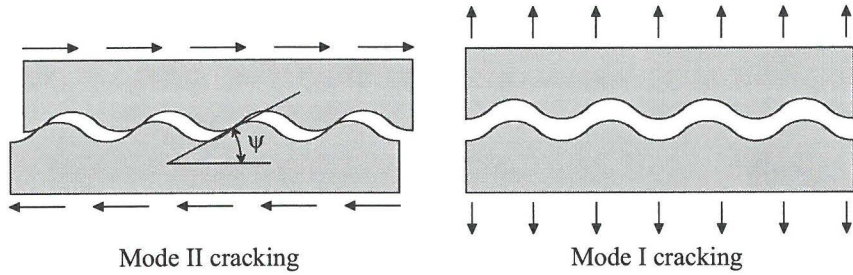


Figure 1.10. Direction of plastic flow for mode I and mode II cracking.

For mode I cracking the crack sliding velocity is zero, so for both crack modes the direction of plastic flow is fully determined.

$$\underline{\dot{u}}^p = \dot{\vartheta}_u^{mode II} \begin{bmatrix} \tan \psi \\ 1 \end{bmatrix} \quad (\text{Mode II cracking})$$

$$\underline{\dot{u}}^p = \dot{\vartheta}_u^{mode I} \begin{bmatrix} 1 \\ 0 \end{bmatrix} \quad (\text{Mode I cracking})$$

Where the plastic multipliers  $\dot{\vartheta}_u^{mode II}$  and  $\dot{\vartheta}_u^{mode I}$  are positive scalars, which are nonzero only when plastic deformations occur. They can be determined from the condition that during plastic flow the stresses remain bounded (see section 1.2.4).

Differentiation of equation (1.2) and inserting the expressions for the direction of plastic flow finally yields:

$$\begin{bmatrix} \dot{\sigma}_n \\ \dot{\tau}_{nt} \end{bmatrix} = \mathbf{K}^e \left[ \underline{\dot{u}} - \dot{\vartheta}_u^{mode II} \begin{bmatrix} \tan \psi \\ 1 \end{bmatrix} \right] \quad (\text{Mode II cracking}) \quad (1.4)$$

$$\begin{bmatrix} \dot{\sigma}_n \\ \dot{\tau}_{nt} \end{bmatrix} = \mathbf{K}^e \left[ \underline{\dot{u}} - \dot{\vartheta}_u^{mode I} \begin{bmatrix} 1 \\ 0 \end{bmatrix} \right] \quad (\text{Mode I cracking}) \quad (1.5)$$

In some cases, it is convenient to smear discrete crack displacements over a certain width  $\ell$  of the continuum. Plastic strain rates and crack velocities are in that case coupled according to figure 1.11.

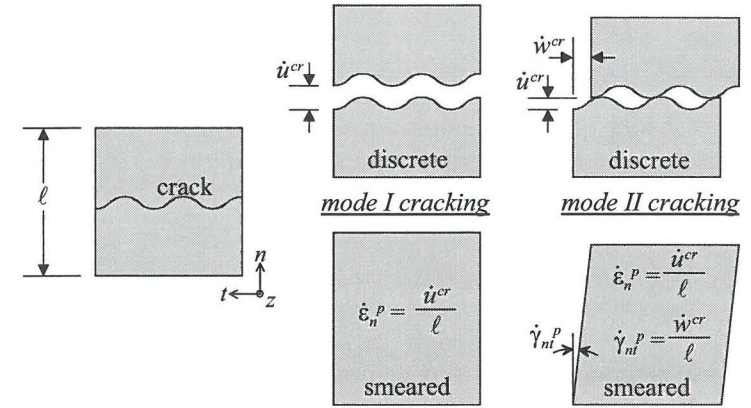


Figure 1.11. Smeared and discrete relative crack velocities.

According to figure 1.11, application of equation (1.3) results in – for smeared mode II cracking – the following relationship

$$\dot{\epsilon}_n^p = \dot{\gamma}_{nt}^p \tan \psi$$

The rate of plastic normal strain in  $t$ - and  $z$ -direction is zero, so the plastic volumetric strain rate  $\dot{\epsilon}_{vol}^p = \dot{\epsilon}_n^p + \dot{\epsilon}_t^p + \dot{\epsilon}_z^p$  and the rate of maximum plastic shear deformation  $\dot{\gamma}_{max}^p$  are expressed by

$$\dot{\epsilon}_{vol}^p = \dot{\epsilon}_n^p = \dot{\gamma}_{nt}^p \tan \psi \quad (1.6)$$

$$\begin{aligned} \dot{\gamma}_{max}^p &= \sqrt{(\dot{\epsilon}_n^p - \dot{\epsilon}_t^p)^2 + (\dot{\gamma}_{nt}^p)^2} \\ &= \dot{\gamma}_{nt}^p \sqrt{1 + \tan^2 \psi} \\ &= \frac{\dot{\gamma}_{nt}^p}{\cos \psi} \end{aligned} \quad (1.7)$$

Comparison of the expressions above gives the classical interrelation between the plastic volumetric strain rate and the rate of maximum plastic shear deformation.

$$\dot{\epsilon}_{vol}^p = \dot{\gamma}_{max}^p \sin \psi$$

As the maximum and minimum plastic principal strain rates are related to the plastic volumetric strain rate and the rate of maximum plastic shear deformation according to (out-of-plane plastic strain rate  $\dot{\epsilon}_2^p = \dot{\epsilon}_z^p = 0$ )

$$\dot{\epsilon}_{vol}^p = \dot{\epsilon}_1^p + \dot{\epsilon}_3^p$$

$$\dot{\gamma}_{max}^p = \dot{\epsilon}_1^p - \dot{\epsilon}_3^p$$

the following expression for the direction of plastic flow – for smeared mode II cracking – is found

$$\begin{bmatrix} \dot{\epsilon}_1 \\ \dot{\epsilon}_3 \end{bmatrix}^p = \dot{\vartheta}_\epsilon^{mode II} \begin{bmatrix} \frac{1}{2}(1 + \sin \psi) \\ -\frac{1}{2}(1 - \sin \psi) \end{bmatrix} \quad (\text{Mode II cracking})$$

For mode I cracking, the  $n$ -direction equals the maximum principal strain rate direction and the  $t$ -direction equals the direction of the minimum principal strain rate. As the rate of plastic normal strain in  $t$ -direction equals zero, the direction of plastic flow for smeared mode I cracking becomes

$$\begin{bmatrix} \dot{\epsilon}_1 \\ \dot{\epsilon}_3 \end{bmatrix}^p = \dot{\vartheta}_\epsilon^{mode I} \begin{bmatrix} 1 \\ 0 \end{bmatrix} \quad (\text{Mode I cracking})$$

Inserting the expressions for the direction of plastic flow in equation (1.1) finally gives after differentiation:

$$\begin{bmatrix} \dot{\sigma}_1 \\ \dot{\sigma}_3 \end{bmatrix} = \mathbf{D}^e \begin{bmatrix} \dot{\epsilon}_1 \\ \dot{\epsilon}_3 \end{bmatrix} - \dot{\vartheta}_\epsilon^{mode II} \begin{bmatrix} \frac{1}{2}(1 + \sin \psi) \\ -\frac{1}{2}(1 - \sin \psi) \end{bmatrix} \quad (\text{Mode II cracking}) \quad (1.8)$$

$$\begin{bmatrix} \dot{\sigma}_1 \\ \dot{\sigma}_3 \end{bmatrix} = \mathbf{D}^e \begin{bmatrix} \dot{\epsilon}_1 \\ \dot{\epsilon}_3 \end{bmatrix} - \dot{\vartheta}_\epsilon^{mode I} \begin{bmatrix} 1 \\ 0 \end{bmatrix} \quad (\text{Mode I cracking}) \quad (1.9)$$

#### 1.2.4 Concept of a stress-state bounding surface

The magnitude of plastic deformations – characterized by the plastic multiplier  $\vartheta_{\epsilon(u)}$  – is determined by introducing the concept of a stress-state bounding surface, formulated in stress space, which separates permissible from non-permissible stress states. If the stress state is inside the bounding surface the deformations are purely elastic, whereas plastic deformations can occur if the stress state is on the bounding surface. In this concept stress states outside the bounding surface are not allowed.

For application to concrete, the most known and simple examples of such surfaces are, for mode II cracking, the Mohr-Coulomb bounding surface and the Rankine bounding surface for mode I cracking. These bounding surfaces are governed by the following equations:

$$f_1(\underline{\sigma}) = |\tau_m| - c + \sigma_n \tan \phi = 0 \quad (\text{Mohr-Coulomb})$$

$$f_2(\underline{\sigma}) = \sigma_n - f_t = 0 \quad (\text{Rankine})$$

in which the cohesion  $c$ , the friction angle  $\phi$  and the tensile strength  $f_t$  are material properties.

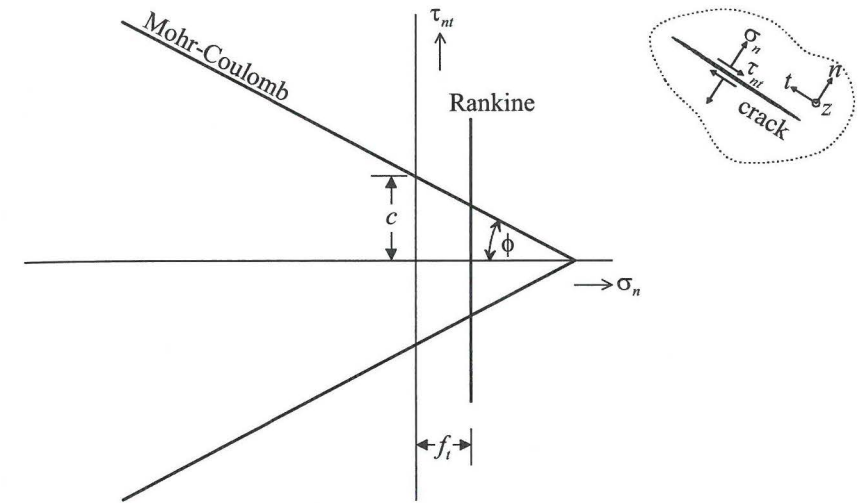


Figure 1.12. Mohr-Coulomb and Rankine stress-state bounding surfaces.

To trigger the initiation of a crack in a continuum, Mohr's stress circle for a certain state of stress may be applied in the  $(\sigma, \tau)$  plane. When the stress circle touches the bounding surface, a crack is initiated along a plane making an angle  $\alpha$  with the direction of the minimum (most compressive) principal stress (see figure 1.13).

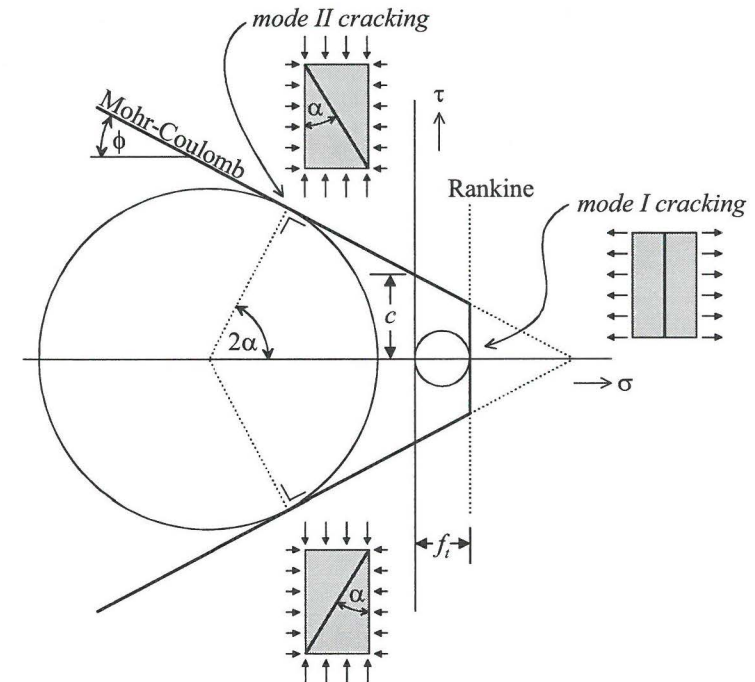


Figure 1.13. Mode I and mode II crack initiation.

So far, the stress-state bounding surface has been considered as a static surface in stress space. However, for a more detailed description of the inelastic behaviour of cracks, a dependency upon the previous loading history may be introduced. The simplest and most common extension to the theory as adopted above, is to make the expression for the bounding surface also dependent on a scalar measure  $\kappa$  of the plastic strain (or relative displacement) vector. This scalar  $\kappa$  is often referred to as an internal state parameter.

$$f = f(\underline{\sigma}, \kappa)$$

For increasing  $\kappa$  the bounding surface may either shrink or expand. In case the bounding surface expands, the term strengthening is used and if the bounding surface shrinks, the term softening is used.

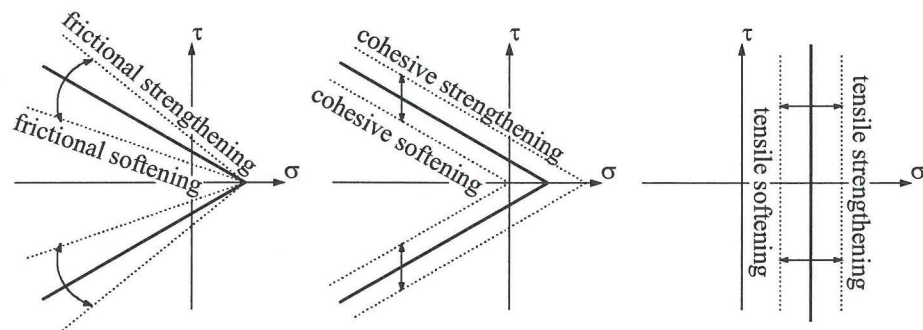


Figure 1.14. Terminology for expansion/shrinkage of Mohr-Coulomb and Rankine stress-state bounding surfaces.

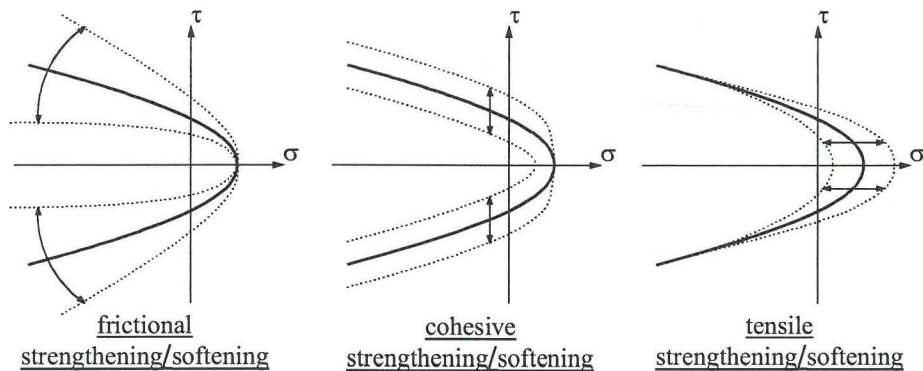


Figure 1.15. Terminology for expansion/shrinkage of a non-linear stress-state bounding surface.

For a Mohr-Coulomb bounding surface, both the cohesion  $c$  and the friction angle  $\phi$  may depend on  $\kappa$ . If the cohesion depends on  $\kappa$ , the term cohesive strengthening (or softening) is used. In case the friction angle depends on  $\kappa$ , the term frictional

strengthening/softening is used. Unlike the Mohr-Coulomb bounding surface, the Rankine bounding surface is characterized by just one parameter, the tensile strength  $f_t$ . In this case shrinkage or expansion of the bounding surface are denominated as tensile softening or strengthening (figure 1.14).

The same terminology not only applies for Mohr-Coulomb or Rankine plasticity, but also for non-linear bounding surfaces that account for both mode I and II cracking (see figure 1.15).

The concept of a stress-state bounding surface, as explained above, can be used to determine the magnitude of plastic flow. In section 1.2.3, a linear relation between the stress-rate vector  $\dot{\underline{\sigma}}$  and the strain-rate vector  $\dot{\underline{\epsilon}}$  is set. To obtain total stresses and strains at an arbitrary loading stage, the equations must hence be integrated along the loading path. To this end, it is assumed that the loading steps are very small. Under this condition, the material properties ( $\psi, \phi, c, f_t$ ) may be considered to remain constant during one small loading step and the stress/strain rate vectors in section 1.2.3 may be replaced by stress/strain increments. These considerations also apply for stresses and crack displacements in the case of discrete cracking.

Starting from an initial stress state  $\underline{\sigma}^0$ , a trial stress state  $\underline{\sigma}^t$  can be computed by adding an elastic trial stress increment.

$$\underline{\sigma}^t = \underline{\sigma}^0 + \mathbf{K}^e \Delta \underline{u} \quad \text{(discrete cracking)}$$

$$\underline{\sigma}^t = \underline{\sigma}^0 + \mathbf{D}^e \Delta \underline{\epsilon} \quad \text{(smeared cracking)}$$

If the trial stress state falls outside the bounding surface ( $f(\underline{\sigma}^t, \kappa^0) > 0$ ), cracking occurs and a correction must be applied, i.e. the trial stress state must be mapped back to the bounding surface. The direction of this correction  $\Delta \underline{\sigma}$  is given by the direction of plastic flow (see equations (1.4), (1.5), (1.8) and (1.9)). The magnitude is given by the condition that the final – corrected – stress state  $\underline{\sigma}^1$  is located on the bounding surface, i.e.  $f(\underline{\sigma}^1, \kappa^0) = 0$ .

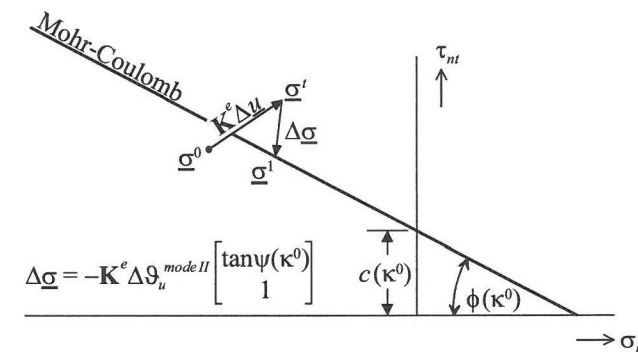


Figure 1.16. Return-mapping of crack stresses in case of Mohr-Coulomb plasticity.

## CHAPTER 2

### REVIEW OF LITERATURE

The review of literature presented here comprises two parts. First of all a review is given on the specific characteristics of the mechanical behaviour of concrete loaded in multiaxial compression as observed in experiments. In addition, more extensive reviews on this subject can be found in Newman<sup>1979</sup>, Van Mier<sup>1984</sup>, Vonk<sup>1992</sup> and Van Geel<sup>1995a, 1995b, 1998</sup>.

Secondly, an overview is given of existing modelling approaches for concrete that take into account the effects of mode I and mode II cracking in concrete.

### 2.1 Experiments

#### 2.1.1 *Multiaxial compressive stress state*

Multiaxial compression tests on concrete have been performed using two essentially different test setups. In the first setup, referred to as *triaxial cell*, the cylindrical shaped concrete test specimen is mounted between steel end blocks and placed in a pressure vessel. In radial direction, fluid pressure loads the specimen. In axial direction, the specimen is loaded independently by means of a hydraulic jack. Application of a flexible, impermeable membrane between the specimen and the hydraulic fluid prevents the fluid from entering the specimen. This test setup has the limitation that the two confining principal stresses are always equal.

The second test setup, the “true” *triaxial loading apparatus*, consists of a construction of three orthogonal loading frames permitting the concrete test specimen (cube or prism) to be loaded in three orthogonal directions independently.

#### 2.1.1.1 Influence on strength

The compressive strength of concrete in the main (axial) loading direction is highly sensitive to the presence of lateral confinement. The axial compressive strength decreases in the presence of lateral tensile stresses, while the strength increases in the presence of lateral compressive stresses. This sensitivity to the presence of lateral confinement is governed by the roughness of (potential) mode II cracks. As the roughness is characterized by the friction angle in the classic Mohr-Coulomb bounding surface, concrete is called a frictional material.

#### 2.1.1.1.1 Biaxial strength

Basically, the biaxial strength can be measured in a triaxial cell without axial load [Richart et al<sup>1928</sup>]. This technique has the limitation that  $\sigma_2$  always equals  $\sigma_3$  ( $\sigma_1 = 0$ ). To study the whole biaxial loading range, other techniques have been developed. Bellamy<sup>1961</sup> induced (approximate states of) biaxial compression by loading hollow mortar cylinders in a triaxial cell with an external fluid pressure. This technique, however, gives only satisfactory results for thin-walled mortar tubes (radial stresses

are nearly zero). Concretes with larger aggregates require thicker specimens and therefore cannot be tested in this way.

The aforementioned drawbacks do not exist when concrete cubes are loaded biaxially between two sets of load bearing platens and by independently controlled hydraulic jacks (similar to a ‘true’ triaxial loading apparatus without the third loading axis). Performing this kind of test Iyengar et al<sup>1965</sup> reproduced similar test results as Bellamy. In these tests rigid bearing platens were used. When the load is applied by these platens, significant frictional stresses along the ‘concrete – steel platen’ interfaces are introduced (i.e. a triaxial state of stress). Reduction of this platen restraint reduces the biaxial compressive strength of concrete considerably as can be found in the work of Robinson<sup>1967</sup>, Kupfer et al<sup>1969,1973</sup>, Liu<sup>1972</sup> and Nelissen<sup>1972</sup>.

Figure 2.1 shows biaxial strength data of Kupfer and Liu, with reduction of platen restraint, in addition to tests done at Eindhoven University of Technology, Technical University in Munich (TUM), Bundesanstalt für Materialprüfung in Berlin (BAM) [Schickert & Winkler<sup>1977</sup>] and the University of Colorado (CU).

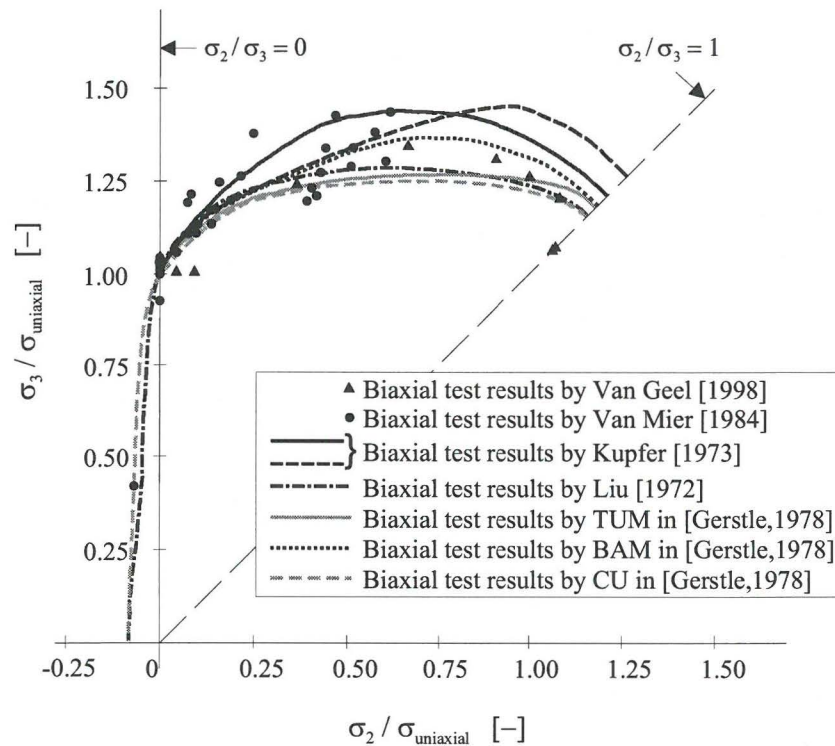


Figure 2.1. Plane stress (biaxial) strength envelope [Van Geel<sup>1998</sup>].

### 2.1.1.1.2 Triaxial strength

The strength of concrete is highly sensitive to the presence of lateral confinement. However, the biaxial strength envelope (see figure 2.1) shows the effect of the latter only poorly. The effect increases drastically when – moreover – confinement in the third principal direction is applied.

The essence of this kind of material behaviour is incorporated in the Mohr-Coulomb strength criterion based on the maximum and minimum principal stress and internal friction. This criterion is widely used because of its appealing physical background and its simplicity.

Triaxial strength data of concrete tested in a triaxial cell were first given by Richart et al<sup>1928</sup>. Afterwards, much testing has been done in the sixties and the seventies of the 20<sup>th</sup> century. Examples can be found in Hobbs<sup>1971</sup> of tests performed in a triaxial cell and in Mills et al<sup>1970</sup>, Launay et al<sup>1970</sup> and Bertacchi et al<sup>1972</sup> of tests performed in a ‘true’ triaxial loading apparatus. Test results of loading techniques, including extensive research on the influence of boundary conditions, are given in the cooperative research of Gerstle et al<sup>1978</sup>.

Ahmad et al<sup>1982</sup> gathered triaxial strength data by performing experiments on concrete confined by steel tubes of varying wall thickness. These results compared favourably with the test data above.

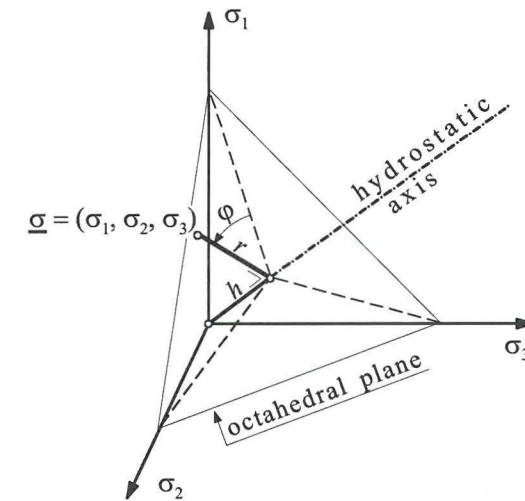


Figure 2.2. Haigh-Westergaard coordinate system in space of principal stresses.

Test data on triaxial strength are often visualised by adopting the Haigh-Westergaard cylindrical coordinate system (figure 2.2). This coordinate system is related to the Cartesian coordinate system of principal stresses by the following equations:

$$h = \sigma_o \sqrt{3}$$

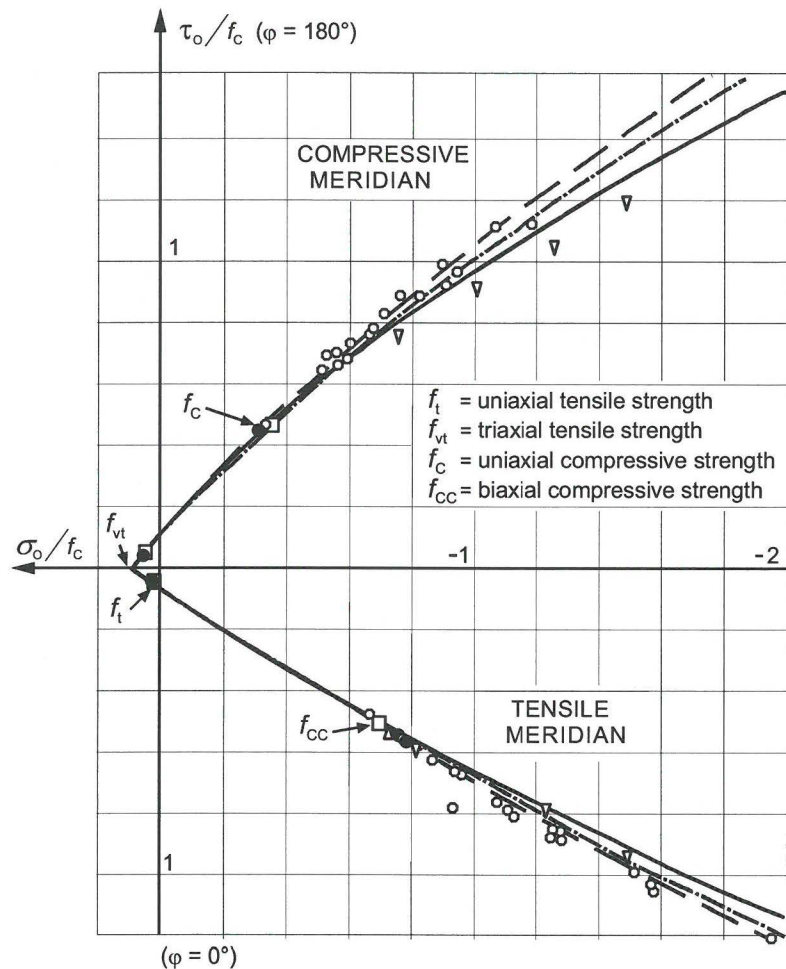
$$r = \tau_o \sqrt{3}$$

$$\cos \varphi = \frac{2\sigma_1 - \sigma_2 - \sigma_3}{3\tau_o \sqrt{2}}$$

$$\sigma_o = \frac{1}{3}(\sigma_1 + \sigma_2 + \sigma_3)$$

$$\tau_o = \frac{1}{3}\sqrt{(\sigma_1 - \sigma_2)^2 + (\sigma_2 - \sigma_3)^2 + (\sigma_3 - \sigma_1)^2}$$

in which  $\sigma_o$  is the octahedral normal stress and  $\tau_o$  is the octahedral shear stress.



Solid Line - Podgorski Criterion; Dashed Line - Ottosen Criterion; Dot Lin - Lade Criterion; Test Results of Mills and Zimmerman  $\circ$ ; Kupfer  $\bullet$ ; Tasuji et al.  $\square$ ; Andenaes et al.  $\Delta$ ; Schickert and Winkler  $\nabla$

Figure 2.3. Cross section of triaxial strength envelope in  $\tau_o$ - $\sigma_o$  plane [Podgorski<sup>1985</sup>].

Figure 2.3 shows the triaxial strength envelope in the Rendulic plane ( $\sigma_2 = \sigma_3$ ). All results from tests carried out in a triaxial cell are located in this plane. The compressive meridian comprises the ultimate stress states when one major compressive principal stress goes together with two equal minor confining principal stresses. The tensile meridian comprises the ultimate stress states when two equal major confining principal stresses go together with one minor compressive principal stress.

The shape of the strength envelope in the octahedral (or deviatoric) planes at various hydrostatic stress levels is depicted in figure 2.4. As tests carried out in a triaxial cell only provide data on the compressive and tensile meridians, more data from tests carried out in a "true" triaxial loading apparatus ( $\sigma_1 \neq \sigma_2 \neq \sigma_3$ ) are needed to construct the shape of the triaxial strength envelope in this plane.

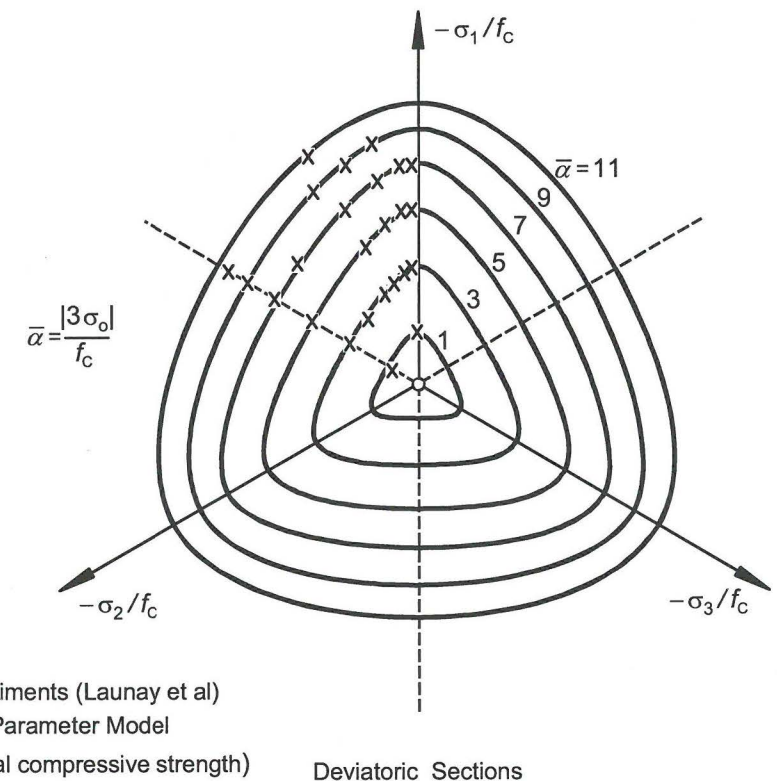


Figure 2.4. Cross section of triaxial strength envelope in octahedral (deviatoric) plane [Willam<sup>1975</sup>].

The basic characteristics of the Mohr-Coulomb strength criterion are indeed confirmed by experimental data as depicted in figure 2.3 and 2.4: the triaxial strength envelope is convex, highly sensitive to lateral confinement and open ended, i.e. no failure is found for high hydrostatic compression [Bažant et al<sup>1986</sup>].

The today's interpretation of the Mohr-Coulomb triaxial strength criterion is the first-order approximation of the triaxial strength envelope obtained by triaxial test data. The linear shaped compressive and tensile meridians and a linear interpolation between the meridians in the octahedral plane (i.e. no influence of the intermediate stress level), inherent to the Mohr-Coulomb criterion, do not permit an accurate estimation of the triaxial strength. Also, the experimentally observed change of shape of the deviatoric section, from triangular to more circular with increasing hydrostatic compression [Hannant<sup>1974</sup>], is not represented by the Mohr-Coulomb criterion.

Many researchers have proposed adjusted strength criteria for better agreement with experimental data. Empirical models with meridians as quadratic functions of the hydrostatic stress have been proposed [Hoek & Brown<sup>1980</sup>], possibly extended with a smooth elliptic interpolation in the deviatoric sections [Willam & Warnke<sup>1975</sup>; Menétrey & Willam<sup>1995</sup>]. Fan & Wang<sup>2002</sup> combined an empirical approach for the derivation of quadratic functions of the hydrostatic stress with a more theoretical approach of adjusting the shape of deviatoric sections by entering the intermediate principal stress level directly into the shape functions.

Other – more phenomenological models – try to capture the global shape of the experimentally observed strength envelope in a mathematical format with the assumption that the triaxial strength of concrete is a function of independent stress variables, such as the stress invariants [Lade<sup>1982</sup>; Hsieh et al<sup>1982</sup>; Podgorski<sup>1985</sup>].

### 2.1.1.2 Stress-displacement curves

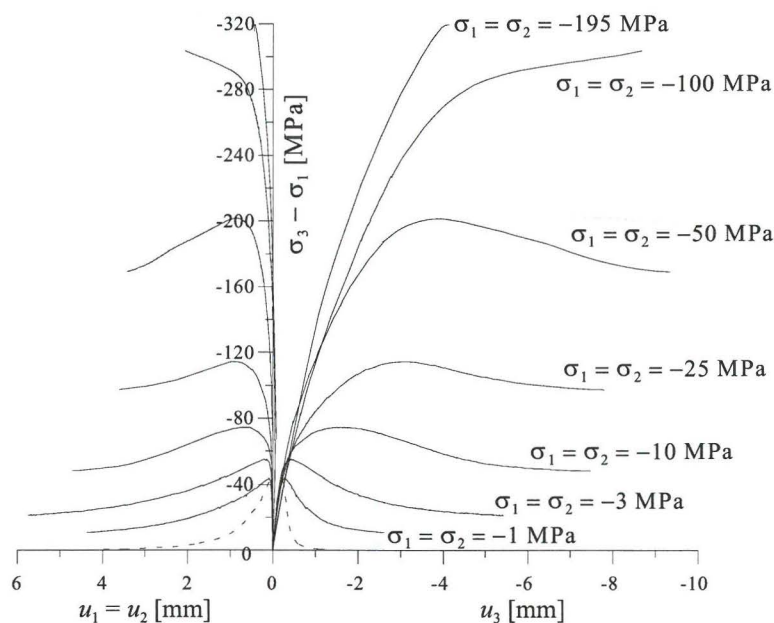


Figure 2.5. Stress-displacement curves in triaxial compression tests (dashed lines represent uniaxial test) [Van Geel<sup>1998</sup>].

Figure 2.5 shows typical test results of normal strength concrete cubes ( $100 \times 100 \times 100 \text{ mm}^3$ ) loaded in triaxial compression towards the compressive meridian ( $\sigma_3 < \sigma_1 = \sigma_2$ ). Apart from the major increase of strength with increasing confining pressure, also a considerable increase in ductility is observed. The post-peak response changes drastically from highly brittle in uniaxial compression to highly ductile for high confinement levels. This phenomenon, often referred to as brittle-ductile transition, is investigated by many experimentalists [Jamet<sup>1984</sup>; Smith et al<sup>1989</sup>; Sfer et al<sup>2002</sup>].

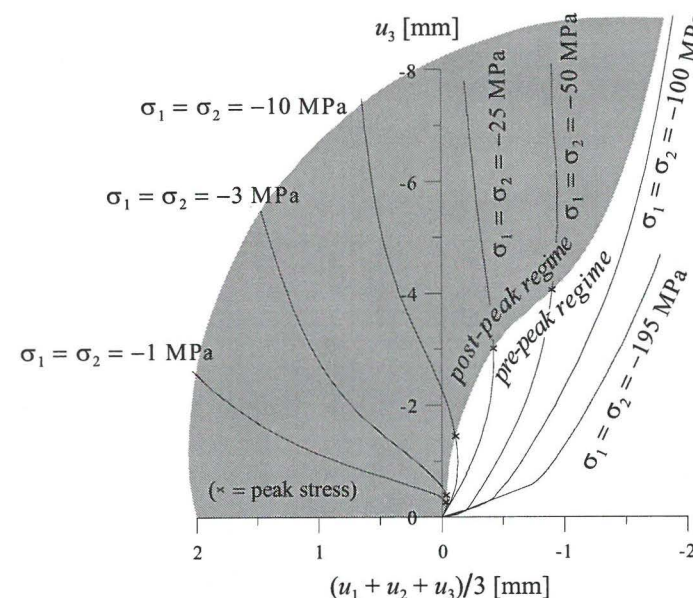


Figure 2.6. Axial displacement versus mean 'volumetric displacement' in triaxial tests on normal strength concrete [Van Geel<sup>1998</sup>].

Figure 2.6 shows another distinctive property of concrete loaded in triaxial compression, i.e. the development of volumetric strain (or displacement) during testing. Kotsovos & Newman<sup>1977</sup> pointed out that three notable points might be indicated in the curve of volumetric strain. The first point indicates a change in the rate of volumetric strain towards more contraction and exhibits distinct non-linear material behaviour. The second point indicates a change in the rate of volumetric strain towards more dilation. While the first two points can only be determined upon close examination of the deformational behaviour, and consequently, not from figure 2.6 only, the third point (around peak stress in figure 2.5) is easily defined since it coincides with the level at which the overall volume of the material becomes a minimum. These points indicate a distinctive change in the fracture process of the specimen [Kotsovos & Newman<sup>1977</sup>; Imran & Pantazopoulou<sup>1996</sup>]. Another topic of interest is the potential loading path dependency of triaxial test results. Based upon loading path variations in the pre-peak regime, Gerstle et al<sup>1978</sup>,



Smith et al<sup>1989</sup> and Imran & Pantazopoulou<sup>1996</sup> concluded that the triaxial strength of concrete was basically path-independent. Kotsovos<sup>1979</sup> confirmed this for low levels of confinement, but found the strength results in the ‘high confinement’ region somewhat dependent on the maximum achieved hydrostatic stress level during different loading paths. Although the observed path-dependency is only small regarding the strength of concrete, the pre-peak volumetric deformational behaviour is influenced much more by the chosen loading path [Kotsovos<sup>1979</sup>; Imran & Pantazopoulou<sup>1996</sup>].

By carrying out ‘rotation experiments’, i.e. tests in which the most compressive principal stress direction is rotated *after* reaching peak stress, Van Mier<sup>1984, 1986</sup> showed that the strength after rotation in some cases was dependent on the loading history. The existence of path dependency upon post-peak preloading was found to depend mainly on the direction of macrocracks formed in the post-peak stage *before* rotation.

## 2.1.2 Cracking in concrete

### 2.1.2.1 Uniaxial compression

The fracture process of normal strength concrete in uniaxial compression has been studied extensively in the early sixties of the 20<sup>th</sup> century at Cornell University. An extensive review of this research is given in Slate & Hover<sup>1984</sup>. Based on direct microscopic observations and x-ray photographs Hsu et al<sup>1963</sup> related the process of internal microcracking to the shape of the stress-strain curve. To comprehend the fracture process it is essential to consider the heterogeneous nature of the concrete material. To this end, the highly heterogeneous system of concrete was simplified to a two-phase composite structure of coarse aggregate grains embedded in a mortar matrix. A subdivision into three crack types was made:

- Aggregate cracks through coarse aggregate grains
- Mortar cracks through the mortar matrix
- Cracks occurring at the so-called interfacial transition zone (ITZ)<sup>1</sup>, providing bond between the mortar matrix and the surface of the aggregate grains.

It was observed that a significant number of cracks or crack-like voids exist prior to the application of external loads. These cracks are primarily ITZ cracks caused by micro bleeding at the coarse aggregate grains and non-homogeneous volume changes during setting and hydration. The existence of these cracks shows that the ITZ is the weakest link in the heterogeneous concrete system [Hsu & Slate<sup>1963</sup>; Alexander et al<sup>1968</sup>]. Above about 30% of the ultimate load, new ITZ cracks are formed and the existing ITZ cracks start to grow around the aggregate grains. The stress-strain curve starts to deviate from a straight line (see figure 2.7). As the load reaches 70 to 90% of the ultimate load, cracks through the mortar start to grow noticeably. These mortar cracks form bridges between adjacent ITZ cracks. The curvature of the stress-strain curve becomes more pronounced. This loading range

<sup>1</sup> The existence and specific structure of the ITZ is further explained in chapter 3.

coincides with the occurrence of a ‘critical stress’ level, i.e. the stress level at which the volume of the concrete starts to increase rather than continuing to decrease [Shah & Chandra<sup>1968</sup>].

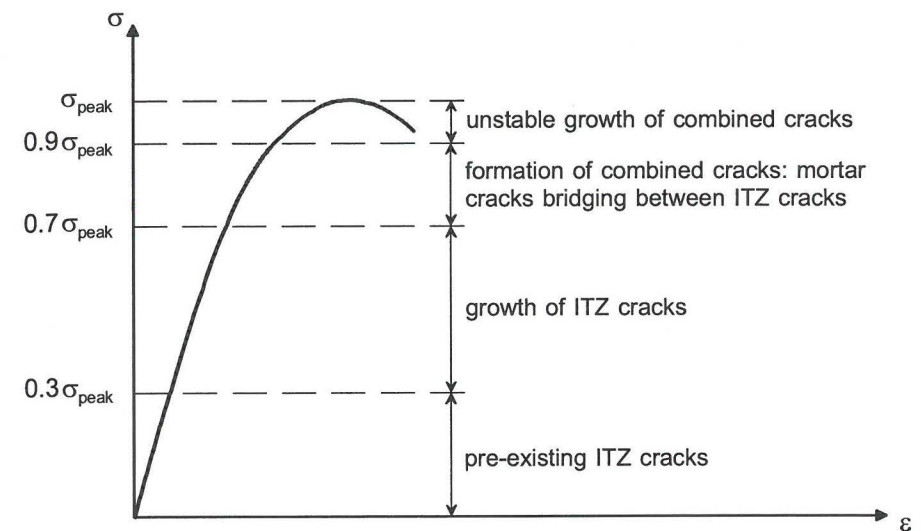


Figure 2.7. Crack formation and the compressive  $\sigma$ - $\epsilon$  curve according to Hsu et al<sup>1963</sup> (redrawn from Vonk<sup>1992</sup>).

At further increase of loading, crack growth becomes unstable resulting in the formation of a continuous crack pattern at failure.

More recently, much more research has been carried out on measurement of crack growth in concrete specimens loaded in uniaxial compression [amongst others: Suaris & Fernando<sup>1987</sup>; Darwin & Dewey<sup>1989</sup>; Nemat et al<sup>1998</sup>]. Although improved crack survey techniques permitted more cracks to be ‘visualised’, the process of crack growth as described by Hsu et al was generally confirmed.

Regarding the crack pattern at failure, much controversy exists about the relative degrees of mode I (axial splitting) versus mode II (inclined shear) cracking. In this respect, Torrenti et al<sup>1989</sup> reported clear mode II cracking while Rutland & Wang<sup>1997</sup> reported predominantly mode I cracking. Evidently, the mode of failure is much influenced by the boundary conditions, i.e. frictional restraint at the specimen-loading platen interface [Kotsovos<sup>1983</sup>]. With reduction of the frictional restraint at the loading surface, combined mode I and mode II crack planes were observed - in two orthogonal directions - dividing the specimen in slender conical pieces [Van Mier<sup>1984</sup>; Vonk<sup>1992</sup>; Van Geel<sup>1998</sup>].

The observation of combined mode I and mode II cracking does not necessarily imply the *initiation* of mode II cracks *during* loading. As stated before, isolated inclined (ITZ) cracks are already present in concrete prior to loading. Horii & Nemat-Nasser<sup>1985</sup> showed by analysing an idealized brittle material with pre-existing inclined flaws, that the formation of inclined macrocracks may occur solely

through the initiation of tensile splitting (mode I) cracks bridging between the *pre-existing* inclined flaws. Nevertheless, complete failure of the specimen occurs still by sliding along the pre-existing inclined cracks, implying that internal friction still remains a determinative factor in uniaxial compressive failure.

### 2.1.2.2 Triaxial compression

The fracture process of concrete loaded in triaxial compression is conceptually identical to fracture in uniaxial compression. It was observed by Krishnaswamy<sup>1968</sup> that the presence of lateral confinement only decreases the rate of development of internal cracks. As stated in section 2.1.1.2, Kotsovos & Newman<sup>1977</sup> pointed out three characteristic points on the curve of volumetric strain that were strongly related to the fracture process. The first point – indicating a tendency towards more contraction – is defined by “local fracture initiation”. Kotsovos postulated that the observed change in deformational behaviour was caused by strain redistribution due to limited crack branching at the tips of existing isolated cracks. The second point – indicating a tendency towards more dilation – is defined by the “onset of stable fracture propagation”, i.e. like in uniaxial compression pre-existing ITZ cracks start to grow continuously. The third point, indicating the level at which the overall volume of the material becomes a minimum, is defined by the “onset of unstable fracture propagation”, i.e. combined cracks have grown to such extent that the crack system becomes unstable. Acoustic emission measurements during triaxial compressive loading of model concrete specimens made with 5 mm glass balls and cement paste confirmed the existence of the transition points as indicated above [Bergues<sup>1982</sup>]. A clear difference in the fracture process between uniaxial and triaxial compression is that the change in the rate of volumetric strain towards more contraction practically does not exist in uniaxial compression.

More recently, Nemati et al<sup>1998</sup> reported that the crack *density* at 80 to 85% of the ultimate load decreased considerably with increasing confinement. Confinement also decreased the percentage of ITZ cracks. The recordings were made after impregnating the specimens with an alloy – called Wood’s metal – in the liquid phase, while the specimen was under load. The specimens were not unloaded until the metal was solidified to preserve the microstructure in the specimens under load. These observations indicate that the occurrence of interconnected open cracks under load, i.e. mode I cracks, decreases with increasing confinement. Isolated cracks and closed (mode II) cracks are not filled with the metal, and consequently, remained undetected.

### 2.1.2.3 Crack patterns at failure

Within the triaxial loading regime, Van Mier<sup>1984</sup> distinguished three distinct failure modes (figure 2.8):

- Planar failure mode. This mode is observed in triaxial tests allowing for only one tensile deformation (plane strain tests, triaxial tests with two clearly different confining pressures). These specimens show very pronounced inclined shear-bands with the normal oriented perpendicular to the intermediate compressive direction (one directional mode II failure).

- Cylindrical failure mode. This mode is observed in triaxial tests allowing for two large tensile (positive) deformations. This mode occurs in triaxial tests with equal confining pressures (compressive meridian) with the uniaxial compression test as a special case. These specimens show a more distributed failure mode, which is the result of interfering shear planes in two directions (two directional mode II failure).
- Tensile failure mode. This mode is displayed in specimens loaded in tension with one or two confining pressures. At failure, these specimens displayed a single tensile crack, perpendicular to the tensile stress direction (mode I failure).

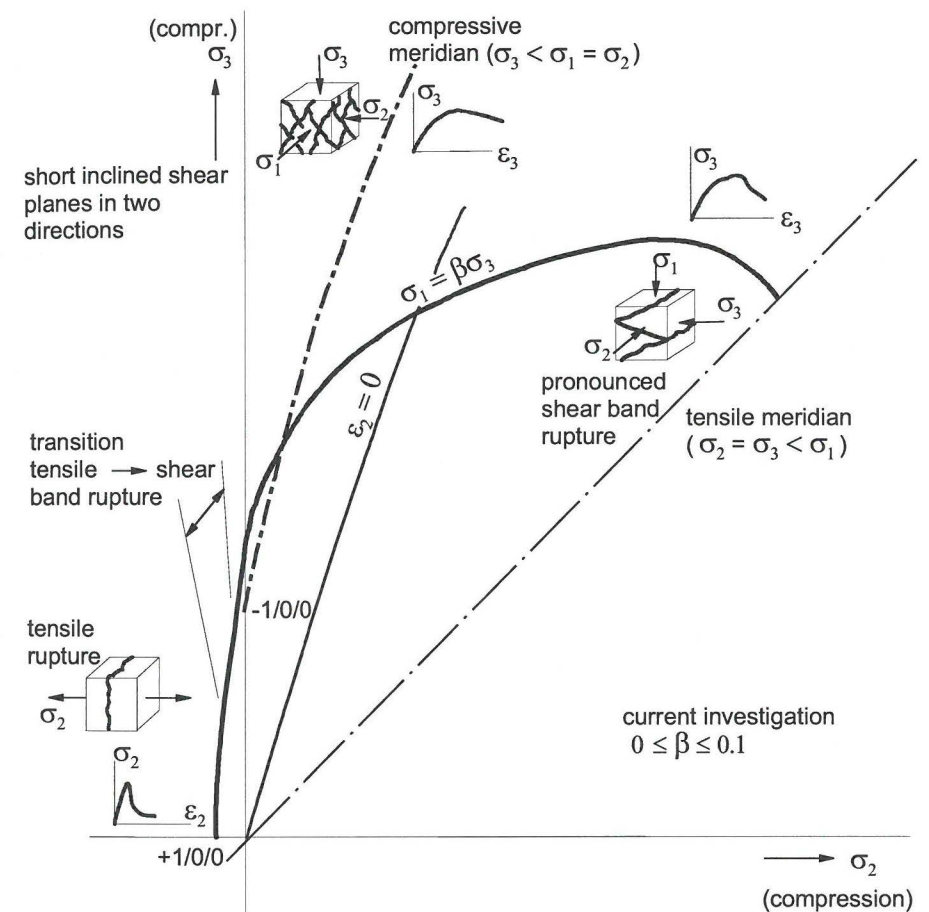


Figure 2.8. Classification of failure modes [Van Mier<sup>1984</sup>].

The observations of Van Mier were limited to a lateral level of confinement of 10% ( $\sigma_1 = \sigma_2 = 0,1\sigma_3$ ). Observations on specimens loaded in triaxial compression with a level of confinement of more than 25% revealed hardly any macroscopic (localised) fracture in the work of Jamet<sup>1984</sup> and Van Geel<sup>1998</sup>, although extensive deformation

is reported. Yet, such absence of localised fracture – at these high levels of confinement – is somewhat controversial, since also localised fracture is reported [Rutland & Wang<sup>1997</sup>; Sfer et al<sup>2002</sup>].

Considering the case of uniaxial compression within the triaxial loading regime of figure 2.8, it appears that this loading case is located in the transition regime between the tensile failure mode and the cylindrical failure mode. Therefore, it is not surprising that the failure mode in uniaxial compression is highly influenced by a small amount of lateral compression or tension, caused – for instance – by the boundary conditions.

#### 2.1.2.4 Localisation of deformations

The most salient aspect of post-peak concrete behaviour is the formation of large macrocracks forming a failure mechanism. All further deformations concentrate in these macrocracks while the surrounding continuum is unloaded, i.e. the deformations *localise* in a few macrocracks. Consequently, the geometry, dimensions and the boundary conditions dominantly influence the mechanical response of the concrete specimen/element. For this reason, often the term ‘structural’ behaviour is used as opposed to ‘material’ behaviour that marks a continuously well-distributed deformation pattern upon loading, for which the continuum theory is valid and the mechanical behaviour can be characterised by a unique stress-strain relationship. In this sense, pre-peak concrete behaviour macroscopically is material behaviour.

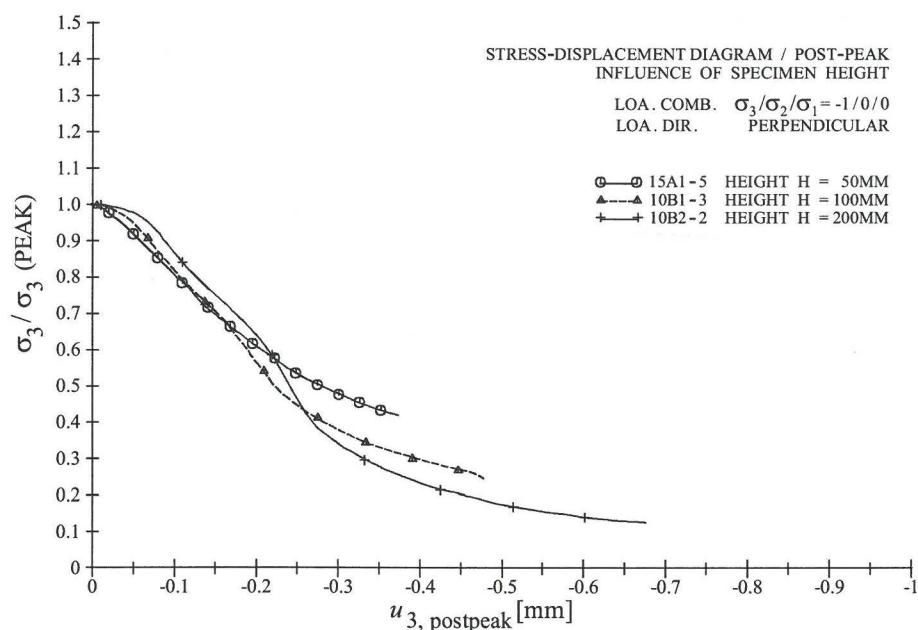


Figure 2.9. Measured post-peak response in uniaxial compression tests on three specimens with varying height (redrawn from Van Mier<sup>1984</sup>).

The occurrence of localised deformations is best demonstrated by comparing the stress-displacement curves of specimens of different size. After all, continuum ‘material’ behaviour incorporates a unique stress-strain relationship, while fully localised behaviour is governed by crack displacement and so incorporates a unique stress-displacement relationship [Van Mier<sup>1984</sup>]. In this way, Van Mier<sup>1984</sup> first demonstrated localisation of deformations in *uniaxial* compression in the post-peak loading regime (see figure 2.9). Later on, many experimentalists confirmed this finding [Vonk<sup>1992</sup>; Van Vliet<sup>1996</sup>; Van Mier et al<sup>1997</sup>]. Apart from the behaviour around peak stress, Van Geel<sup>1998</sup> found similar descending stress-displacement curves for concrete loaded in *multiaxial* compression. As already expected from the observed crack patterns at failure in these tests (pronounced shear band rupture, see figure 2.8), this confirms the existence of localisation of deformations also in the presence of confinement.

In the work of Van Geel<sup>1998</sup>, the presumption was further made that around peak stress the mechanical response is neither uniquely characterised by a stress-displacement curve, nor by a stress-strain curve. By performing extensive strain gauge measurements at the surface of the specimens under triaxial loading, Van Geel indeed demonstrated that the mechanical response at and just after peak strength was governed by continuum material behaviour as well as localised macrocrack growth. In such cases, also the strength of the structure is influenced by localisation of deformations. This effect, known as size effect for strength, has been observed for many concrete structures failing due to mode I cracking [Bažant<sup>1984, 1994</sup>].

## 2.2 Modelling

In this section, a global overview is given of existent modelling approaches dealing with the specific structural behaviour of concrete under loading as partially outlined in the preceding sections. A global distinction is made between models regarding cracks as true spatial discontinuities in a continuous solid (section 2.2.1), models that allow the formation of spatial discontinuities (cracks) at an arbitrary location and orientation by simplifying the geometric representation of the continuous solid (section 2.2.2) and models that account for the effects of cracking by distributing the crack *displacements* over a certain volume in order to produce crack *strains* and preserve the original continuity of the problem formulation (section 2.2.3).

### 2.2.1 Discrete crack modelling

#### 2.2.1.1 Discrete crack modelling in a homogeneous brittle solid: Linear Elastic Fracture Mechanics (LEFM)

Fundamental work on fracturing of brittle homogeneous materials was done by Griffith<sup>1924</sup>. He investigated the influence of a flaw on the strength of a homogeneous material in a uniformly loaded two-dimensional body by simulating such a flaw with an elliptical hole, for which Inglis<sup>1913</sup> gave previously the solution

of the elastic stress field. Griffith concluded that ‘maximum stress’ at the tip of the flaw was not an appropriate strength criterion and suggested an alternative theory based on an energy concept. This concept was that solids, similar to liquids, possess surface energy and, in order to propagate a crack (or increase its surface area), the corresponding surface energy must be compensated through externally added or internally released (strain) energy. For a linear elastic solid, the release of strain energy upon crack extension may be calculated from the solution of the elastic stress field of the crack problem.

In the early 1950’s, researchers who were primarily interested in catastrophic failure of large metallic structures reconsidered the energy balance theory. It was then concluded that for metals considerable plastic deformations are present at the crack front and that this plastic work should be included in the energy balance. Under the condition that the plastic zone around the crack tip is very small compared to the crack size, it was observed that the rate of strain energy available for fracture could still be calculated from the purely elastic solution of the crack problem. In addition, Irwin<sup>1957, 1958</sup> developed a universal method for calculating the rate of strain energy available for fracture of a solid. He recognized that stress and displacement fields around the crack front in a linear elastic solid under most general loading conditions may be expressed in terms of three sets of universal angular functions, multiplied by three ‘stress intensity factors’ for mode I, II and III cracking (see figure 1.7). These ‘stress intensity factors’ are the only quantities dependent on the loading and geometry of the solid. Based upon the stress intensity factors for a specific crack growth problem, the corresponding strain energy release rates  $G_I$ ,  $G_{II}$  and  $G_{III}$  (energy available to create a unit fracture surface) can be evaluated.

To complete the energy balance, a realistic single-parameter characterization of the material’s resistance to fracture is also needed. For brittle solids it is assumed that the size and the shape of the fracture process (or energy dissipation) zone remain essentially constant during crack propagation, which implies that the energy needed to create a unit fracture surface is a material constant (for each crack mode). Irwin designated this fracture resistance energy as *fracture toughness*  $G_C$  ( $G_{IC}$  for mode I cracking).

In later years, much effort has been put in solving stress and displacement fields of various linear elastic crack problems (mainly mode I) in order to calculate the stress intensity factors. For rather complicated geometries/loading this can only be done using numerical methods, like the Finite Element Method (FEM). An overview of such methods is given by Petit et al<sup>1996</sup>.

An important issue involving fracture mechanics is the *direction* of crack growth. In a pure mode I loading situation it is evident that the crack extension takes place in the direction of the original crack. Yet, in practical engineering problems, mode I loading is generally accompanied by a certain amount of mode II loading. In such *mixed-mode* loading conditions, crack extension usually takes place under an angle with respect to the direction of the original crack. Two criteria have been formulated to determine the angle of crack extension in mixed-mode loading conditions, the Maximum Stress Criterion [Erdogan & Sih<sup>1963</sup>] and the Strain Energy Density Criterion [Sih<sup>1974</sup>].

### 2.2.1.2 Influence of heterogeneity

LEFM may be applied for fracture of homogeneous solids where potential inelastic behaviour is limited to a small region around the crack tip compared to the crack size and the size of the solid. A highly heterogeneous material like concrete generally does not satisfy this condition. It is widely accepted that in concrete fracture a rather large *fracture process zone* exists ahead of the crack tip, displaying distinct non-linear material behaviour.

There exist consensus among researchers that LEFM may be applied to study large-scale crack growth in large-scale concrete structures, like concrete dams. In such massive structures, the influence of the small-scale heterogeneity of concrete disappears. The structure can be considered macroscopically homogeneous and the size of the fracture process zone becomes small compared to the crack size and the size of the structure [Ingraffea & Saouma<sup>1985</sup>].

The scale of most concrete structures, however, is too small to justify the application of LEFM. As the same deficiency existed in the case of fracture of ductile metals, the concrete fracture mechanics community reviewed various techniques developed for these metals, utilizing elasto-plastic fracture mechanics (with emphasis on mode I fracture). Worth mentioning in this respect is the J-integral technique [Rice<sup>1968</sup>], which was found to be applicable for *elastic* (linear and non-linear) material behaviour in the fracture process zone. Since non-linear elasticity is equivalent to the deformation theory of plasticity (provided there is no unloading), the J-integral technique performed well for fracture of ductile metals. Mode I cracking in concrete, however, displays a considerable amount of unloading within the fracture process zone. Hence, the J-integral technique is not applicable for the analysis of concrete mode I fracture [Hillerborg<sup>1983</sup>].

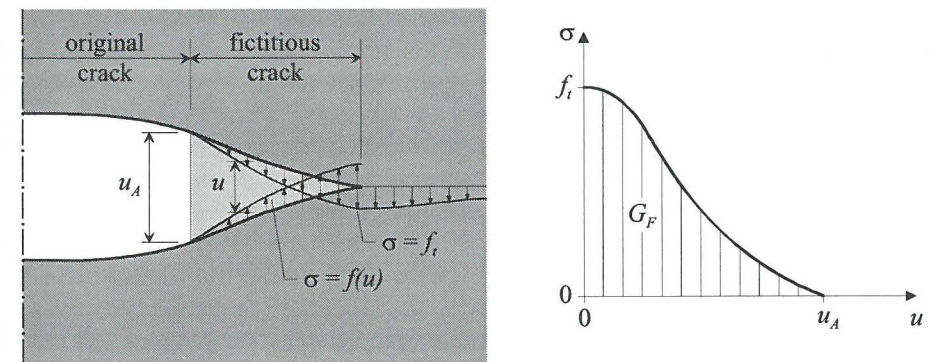


Figure 2.10. Representation of fracture process zone in ‘Fictitious Crack Model’ [Hillerborg et al<sup>1976</sup>].

Based on the plastic crack models of Dugdale<sup>1960</sup> and Barenblatt<sup>1962</sup> for metallic fracture, Hillerborg et al<sup>1976</sup> proposed a concept named ‘Fictitious Crack Model’, which has since been used extensively for modelling mode I cracking in concrete. In this model, the crack is assumed to propagate when the normal stress at the crack

tip reaches the tensile strength  $f_t$ . When the crack opens, the stress is not assumed to fall to zero at once, but to decrease with increasing crack opening  $u$ . At the crack opening  $u_A$  the stress has fallen to zero. For that part of the crack ( $u < u_A$ ), the 'fictitious' crack in reality corresponds to a microcracked zone (fracture process zone) with some ligaments for stress transfer. The amount of energy  $G_F$  absorbed per unit crack area in opening the crack from zero to or beyond  $u_A$  is

$$G_F = \int_0^{u_A} \sigma du$$

and corresponds to the area under the stress-displacement curve  $\sigma = f(u)$  as depicted in figure 2.10. The fracture energy  $G_F$  and the shape of the stress-displacement curve (figure 2.10) are regarded in this model as material properties.

Using either LEFM or Hillerborg type fracture mechanics, the discrete crack approach may be applied within FEM computations. However, this has some serious implications. A priori, it is generally not known in what direction potential cracks will propagate. This information comes only available during the FEM analysis, implying that during the analysis the geometry of the structure (including the cracks) constantly changes and remeshing of the structure is inevitable. This procedure might be very time-consuming unless the process is highly automated and the remeshing technique is made computationally very efficient. Using LEFM, this kind of analysis has been reported by Ingraffea & Saouma<sup>1985</sup>, Sousa et al<sup>1989</sup>, Reich et al<sup>1994</sup> and Bittencourt et al<sup>1996</sup>.

Above difficulties can be avoided when the crack path is known in advance. In such cases the continuum elements are aligned along the assumed crack path and interface fracture may occur along the aligned element edges. Crack problems being not very sensitive to the true direction of cracking might also be dealt with by inserting interface elements along all conceivable paths in the beginning of the analysis [Tran et al<sup>1998</sup>; Pearce et al<sup>2000</sup>].

Analyses incorporating non-linear mode I fracture models (e.g. Fictitious Crack Model) may be performed with pre-assumed crack paths [Rots<sup>1988</sup>; Reich et al<sup>1994</sup>]. Extension of the Fictitious Crack Model to include also mode II cracking is also reported. With a crack path obtained from previous LEFM analysis, Gálvez et al<sup>2002</sup> investigated the potential influence of mixed-mode cracking by supplementing the scalar-valued tensile strength criterion with a non-linear (Mohr-Coulomb type) stress-state bounding surface, incorporating tensile and cohesive softening.

Another approach to allow for the heterogeneity of the concrete material is to model the heterogeneous structure of concrete explicitly, for instance, by a stochastic approach in which material properties (e.g. ultimate strength, Young's modulus) are randomly distributed throughout the structure. Such an approach requires the size of the mesh elements to be sufficiently small with respect to the size of the structure to be modelled, so that the probabilistic analysis performed on the scale of the mesh elements is representative of the structure as a whole. Such analyses indicate that, despite the application of a local brittle failure criterion, stochastic modelling

introduces (ductile) softening behaviour on the global (structural) level caused by crack arrest effects at stronger adjacent mesh elements [Rossi et al<sup>1987, 1992</sup>].

The heterogeneous structure of concrete might also be modelled explicitly by considering the micro/mesostructure of concrete, for instance, by modelling concrete as a two-phase composite of large aggregate grains embedded in a mortar matrix with pre-existing cracks present at the ITZ between hardened cement paste and aggregate grains [Zaitsev & Wittmann<sup>1981</sup>; Wang & Huet<sup>1993</sup>]. Assuming that each of the phases is homogeneous and behaves in a linear elastic and brittle way, LEFM may be applied in such systems. Classical crack path criteria for elastically homogeneous materials, however, are not valid when the crack advances at a bimaterial interface, because – in this case – the relative magnitudes of the fracture toughnesses between the constituent materials and the interface are also involved [Büyükoztürk & Lee<sup>1993</sup>].

The assumption of linear elastic brittle material behaviour in each phase of a two-phase characterization of concrete (with inherent stress singularity at the crack tip), however, is still debatable. Finite element computations, using a two-phase characterization of concrete and non-linear Hillerborg type material behaviour for mode I cracking, show that for obtaining a close match between simulation and experimental test results, the introduction of – though more brittle – tensile softening laws is still required [Vonk<sup>1992</sup>; Roelfstra<sup>1989</sup>; Stankowski<sup>1990, 1992</sup>; Kwan et al<sup>1999</sup>]. To allow for realistic concrete behaviour in uniaxial compression, the material laws in these modelling approaches were supplemented with a Mohr-Coulomb type slip criterion, allowing for the effects of cohesion and internal friction between crack faces loaded in shear/compression (mode II).

## 2.2.2 Non-continuum modelling

A major drawback of the discrete crack approach is that, unless the crack path is known in advance, extensive remeshing has to be performed during the crack analyses. This problem is avoided in the approaches presented in this section. These approaches assume a discretization of the continuum solid, i.e. a non-'space filling' structure is generated that could resemble the porosity of concrete. For such structures it is possible to allow for potential cracking (displacement discontinuity) anywhere throughout the structure.

### 2.2.2.1 Lattice modelling

In a lattice type model the material is schematised as a network of (small) truss or beam elements. Crack growth is obtained by removing elements that exceed a certain fracture criterion, most often their tensile strength.

Concrete fracture in mode I was simulated in this way by Burt & Dougill<sup>1977</sup>, adopting geometrically random lattices (2D) with overlapping truss elements. The truss elements were taken to be linear elastic and brittle, the heterogeneity was introduced by assigning a random distribution of the material properties (Young's modulus and tensile strength) throughout the structure.

Another way of introducing the heterogeneity of concrete is projecting a lattice on top of a generated structure of aggregate grains embedded in a mortar matrix and

assigning a different strength and stiffness to the beam (or truss) elements depending on their location in the two-phase material (see figure 2.11). Using truss elements and introducing tensile softening, this kind of modelling is adopted by Schorn & Rode<sup>1991</sup>, Bažant et al<sup>1990</sup>. Realistic mode I crack patterns and load-deformation curves are obtained. However, a geometrically random lattice of truss elements, as used by Bažant, is not capable of reproducing a correct value of Poisson's ratio because the *truss* elements only allow axial force transfer. In the work of Van Mier & Schlangen [Schlangen & Van Mier<sup>1992a,b</sup>, Schlangen<sup>1993</sup>], triangular regular and random lattices of non-overlapping *beam* elements<sup>2</sup> are used in order to predict correct values of Poisson's ratio. Simulated (mode I) crack patterns match very well those observed in experiments. Although brittle fracture is assigned to the individual beams, the load-deformation curves still show some ductility as a result of the heterogeneity introduced. Yet – compared to experiments – the simulated structural response is too brittle.

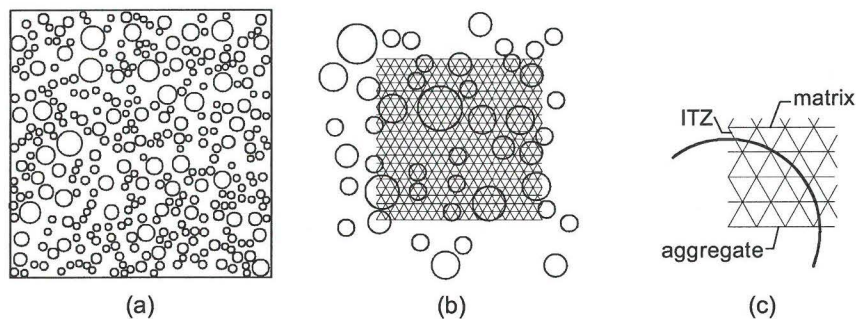


Figure 2.11. (a) Generated grain structure; (b) projection of triangular lattice; (c) definition of aggregate, ITZ and matrix beams [Schlangen<sup>1993</sup>].

Schlangen<sup>1993</sup> hypothesized that smaller particles included in the generated grain structure could enhance the ductility of the structural response. Arslan<sup>1996</sup> and Lilliu & Van Mier<sup>2003</sup> pointed out that several factors enhance the ductility of the structural response:

- Smaller particles included in the generated grain structure
- Including voids in the generated grain structure
- Taking into account the true three-dimensional nature of cracking

Based on these observations, it seems legitimate to conclude that the ductility of the structural response of plain concrete structures failing in mode I is the result of brittle microcrack phenomena at various lower scale levels.

A drawback of using regular lattices in mode I crack studies is that a certain amount of anisotropy is introduced due to the orientation of the lattice beams. Consequently, the material behaviour and crack patterns can be expected to depend on the orientation of the lattice [Schlangen & Garboczi<sup>1997</sup>]. To reduce any influence of mesh orientation, random lattices can be used [Vervuurt<sup>1997</sup>; Van Mier & Vervuurt<sup>1997</sup>]. The adoption of a fracture criterion based on the average stress

<sup>2</sup> Beam lattices as a numerical technique in theoretical physics were first used by Hermann et al<sup>1989</sup>.

state in the nodes reduces also the dependency on mesh orientation [Schlangen & Garboczi<sup>1997</sup>].

Although lattice modelling with beam removal upon cracking seems a promising tool for studying mode I or mixed mode crack phenomena, their use is highly debatable for mode II crack studies. The removal of lattice beams upon cracking is only legitimate if the crack opens and *remains* open during further loading. This is not the case for concrete loaded in (multiaxial) compression. Although cracking in compression might *initiate* in mode I, crack closure and force transfer through closed cracks are essential during the formation of the final failure mode in uniaxial and particularly in multiaxial compression.

### 2.2.2.2 Assemblages of spheres or disks

The structure of the concrete material may also be modelled as an irregular assemblage of rigid spheres or disks (resembling the coarse aggregate grains), locally bonded together by elastic contact layers. Initially, this method was used for simulating the failure process of non-cohesive granular soils [Cundall & Strack<sup>1979</sup>]. The rigid spheres or disks are allowed to translate and rotate. Normal deformation and shear deformation is allowed in the contact layers. Slip within the contact layers is most often modelled by assigning a Mohr-Coulomb type slip criterion to the contacts.

The approach may be extended to the analysis of cohesive granular materials by including cohesive strength of the contact layers. In conformance with the classical Mohr-Coulomb slip theory non-zero cohesion may be introduced [van Baars<sup>1996</sup>]. After loss of cohesive strength, the contact layers are still capable of transferring compressive stresses and the effects of internal friction are still accounted for. Conceptually, the approach may therefore capture mode I as well as mode II cracking.

Of course, other contact laws may be assigned as well. Zhong & Chang<sup>1999</sup> applied a contact law based on internal progressive microcracking in the contact layer according to the LFM theory. Acceptable results were obtained for concrete loaded in uniaxial tension and uniaxial compression. Biaxial compression tests were also simulated with the 2D model. However, its validity for such stress states can be questioned, since the 2D model only allows for crack formation with in-plane normals to the crack plane, while the normals to the crack planes in biaxial experiments typically point out-of-plane (see figure 2.12).

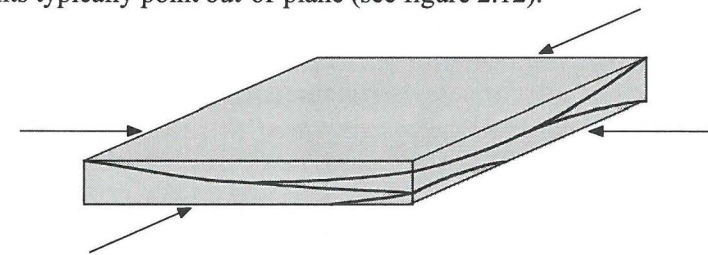


Figure 2.12. Typical crack planes (with normals pointing out-of-plane) in a biaxial compression test.

Unlike the lattice approach, the modelling consisting of locally bonded rigid spheres or disks is not easy to extend to allow for cracking through the aggregate grains. In tension or uniaxial compression substantial cracking through the aggregate grains only is observed in lightweight or high strength concrete, not in normal strength concrete. However, in multiaxial compression substantial aggregate cracking is observed in normal strength concrete [Van Geel<sup>1998</sup>].

### 2.2.3 Continuum solid mechanics

Within the framework of continuum solid mechanics, cracking is treated not as discontinuities in the displacement field, but the crack displacements are distributed over the surrounding continuum. As opposed to *discrete* cracking this concept is often referred to as *smearred* cracking.

A distinction is made in the modelling of *diffuse* cracking prior to peak load, in which the crack strains are the crack displacements divided by the crack spacing, and *localised* cracking after peak load where the term crack spacing loses its meaning (see figure 2.13).

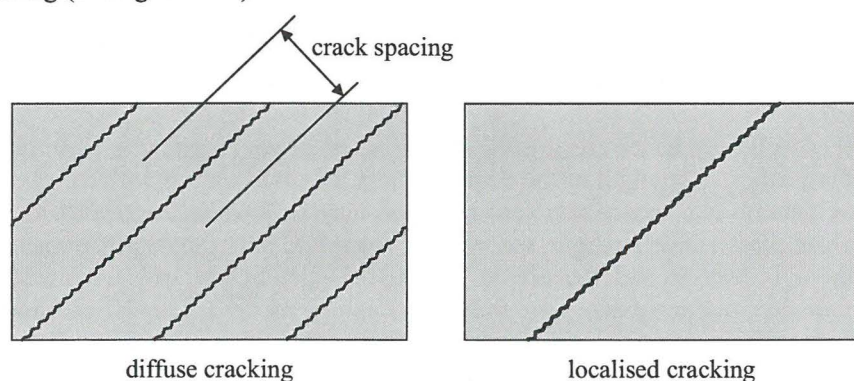


Figure 2.13. Diffuse cracking versus localised cracking.

#### 2.2.3.1 Diffuse cracking in continuum solid mechanics

The overall non-linear material behaviour of concrete in the pre-peak region of the loading diagram due to diffuse cracking is usually modelled within the framework of the theory of elasto-plasticity or/and the theory of continuum damage mechanics.

##### 2.2.3.1.1 Elasto-plasticity

The basics of the classical theory of elasto-plasticity are explained in chapter 1. Although the theory is originally developed for metals, some distinct features may also be applicable to concrete behaviour. From a macroscopic point of view concrete also displays substantial non-linear stress-strain behaviour and significant plastic strain upon unloading. Although for concrete it is more appropriate to use the term “irreversible” strain, instead of plastic strain [Chen & Han<sup>1988</sup>]. The non-linearity due to the heterogeneous nature of the concrete composite is usually accounted for by defining strengthening laws based on internal state parameters and expanding stress-state bounding surfaces until the ultimate strength surface (figures

2.3 & 2.4) is reached. Realistic volumetric strain curves as depicted in figure 2.6 may be achieved by variation of the dilatancy angle, which governs the direction of (non-associated) plastic flow. Examples of this modelling approach can be found in Vermeer & de Borst<sup>1984</sup>, Faruque & Chang<sup>1986</sup>, Lin et al<sup>1987</sup>, Ohtani & Chen<sup>1988</sup>, Pramono & Willam<sup>1989</sup>, Zaman et al<sup>1993</sup>, Etse & Willam<sup>1994</sup>, Meyer et al<sup>1994</sup>. The theory of elasto-plasticity may be formulated in strain space as well. The concept of a *stress*-state bounding surface then is replaced by an equivalent *strain*-state bounding surface. Examples of such strain-space based elasto-plasticity models are described in Mizuno & Hatanaka<sup>1992</sup> and Pekau et al<sup>1992</sup>.

##### 2.2.3.1.2 Continuum damage mechanics

The theory of continuum damage mechanics is based on degradation of stiffness due to microcracking. The stiffness of concrete usually decreases with increasing strain. This sort of behaviour is considered to be the result of decreasing ‘contact’ area during loading due to the nucleation and growth of open microcracks.

An ideal material model, for which all non-linear behaviour originates from stiffness degradation due to microcracking, was proposed by Dougill<sup>1976</sup> and called a “progressively fracturing solid” (see figure 2.14.b).

Mathematically, the formulation is closely related to elasto-plasticity [Carol et al<sup>1994</sup>]. Strains may be split in elastic strains and *degrading* strains. A loading function (or stress/strain-state bounding surface) distinguishes elastic loading from loading where changes in stiffness occur. A strengthening/softening law based on internal state parameter(s) governs the evolution of the loading function. Yet, the designation of a ‘flow’ rule (direction of degrading strains) is not sufficient to define the evolution of the degradation model. A degradation rule for the secant stiffness (or compliance) tensor itself is needed.

The stiffness degradation may directly be defined in terms of the evolution of the secant stiffness tensor itself. However, for a three-dimensional state of stress this involves evolution laws for 21 independent components of the (symmetric) 6x6 secant stiffness tensor. Alternatively, it is reasonable to assume a reduced set of variables that fully characterize the internal state of microcracking or *damage* in the material, for which simple evolution laws can be postulated. In this case, the secant stiffness tensor is the product of the original stiffness tensor with the damage-effect tensor, representing the internal state of damage. In its most simple case this damage-effect tensor reduces to a single scalar and the stiffness tensor is obtained as

$$\mathbf{S} = (1 - \omega)\mathbf{S}^0$$

In which  $\omega$  ( $0 \leq \omega \leq 1$ ) is the damage effect parameter,  $\mathbf{S}^0$  is the elastic stiffness tensor and  $\mathbf{S}$  is the secant stiffness tensor.

The internal state of microcracking may be determined considering the microstructure of concrete. Analytical solutions for the effective (mean) elastic moduli – based on the microstructure of concrete – exist for idealized crack problems, e.g. for randomly distributed flat (not interacting) cracks in a homogeneous solid [Budiansky & O’Connell<sup>1976</sup>].

The evolution of damage is the process of nucleation of new microcracks and growth of existing microcracks. The energy consumed on nucleation and growth of microcracks should balance the (strain)energy available from the intact continuum. Consequently, the process of stable (diffuse) microcracking depends on the stress state and the heterogeneity (presence of crack arrestors, like aggregates) of the concrete.

Estimation of the cracking process is only correct when crack interaction is considered (including potential crack closure) and the effect of crack arrestors. Amongst others, such a micromechanical damage model was proposed by Ju & Lee<sup>1991</sup> and Lee & Ju<sup>1991</sup>. Yet, since the experimental determination of the precise statistics of microcracks is not possible, the only identifiable and measurable continuum damage parameter is the macroscopic effective stiffness [Krajcinovic<sup>2000</sup>].

Using the macroscopic experimental observation of reduced stiffness, the evolution of damage can be calculated by tracking the movement of the loading function in its approach towards the bounding surface of ultimate strength [Baluch et al<sup>2003</sup>]. The loading function may be formulated in stress space [e.g. Voyiadjis & Abu-Lebdeh<sup>1993</sup>], strain space [e.g. Løland<sup>1980</sup>; Krajcinovic & Fonseka<sup>1981</sup>; Mazars & Lemaitre<sup>1985</sup>] or in terms of free energy (energy that can be recovered upon unloading, i.e. elastic strain energy – corresponding to the current secant stiffness – that is available for further microcracking) [e.g. Baluch et al<sup>2003</sup>]. A set of experiments, selected a priori, may be simulated easily with accurate results.

Yet, in order to have some predictive potential, such models – based on the technique of inverse modelling – also should incorporate essential physics of microcracking, such as crack closure, crack interaction and internal friction.

#### 2.2.3.1.3 Coupling of elasto-plasticity and continuum damage mechanics

Figure 2.14.c shows a material exhibiting both plastic deformation and stiffness degradation. This type of behaviour is apparent in the loading diagrams of concrete loaded in cyclic compression. A theory of elasto-plasticity coupled with continuum damage mechanics, called plastic-fracturing theory, was first proposed by Bažant & Kim<sup>1979</sup>.

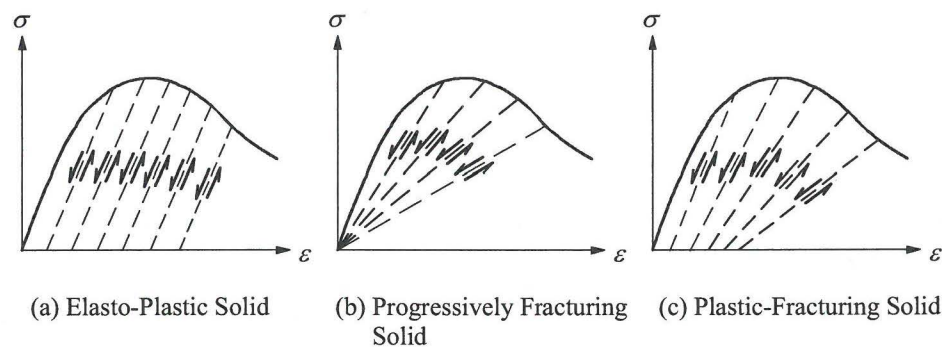


Figure 2.14. Typical material behaviours [Chen & Han<sup>1988</sup>].

The formulation of Bažant & Kim encounters some difficulties in the definition of the loading criterion because the plasticity criterion is specified in stress space while the damage criterion is specified in strain space. To avoid this problem, subsequent models have been formulated entirely in stress space [Yazdani & Schreyer<sup>1990</sup>; Abu-Lebdeh & Voyiadjis<sup>1993</sup>] or in strain space [Han & Chen<sup>1986</sup>; Stevens & Liu<sup>1992</sup>]. While continuum damage mechanics normally deals with decreasing stiffness in order to ensure positive energy dissipation during loading, the combination with elasto-plasticity also allows for treatment of stiffening effects. Stiffening as a result of volumetric compaction during triaxial compressive loading in the high confinement region is captured in this way by Burlion et al<sup>1998</sup>.

#### 2.2.3.1.4 Heterogeneity

Within the framework of continuum solid mechanics, the heterogeneity of the concrete composite is mostly accounted for by incorporating implicitly the most striking consequence of heterogeneity, i.e. the non-linearity of the material behaviour. This is accomplished by defining evolution laws for the stress/strain-state bounding surface in elasto-plasticity and loading functions in continuum damage mechanics.

Heterogeneity may also be implemented directly. Stochastic approaches can be found in elasto-plasticity [Fafitis & Shah<sup>1986</sup>] as well as in continuum damage models [Mazars & Lemaitre<sup>1985</sup>; Breyse<sup>1990</sup>; Carmeliet & Hens<sup>1994</sup>]. Instead of assigning stochastic properties to certain material parameters, the heterogeneity of the concrete composite may also be accounted for by modelling concrete as a two-phase composite of large aggregate grains embedded in a mortar matrix. As mentioned in section 2.2.1.2 most of these models allow discrete cracking at the ITZ between aggregate and mortar matrix. Cracking through the mortar matrix, on the other hand, often is allowed for through a continuum approach [Roelfstra et al<sup>1989</sup>; Stankowski<sup>1990, 1992</sup>].

#### 2.2.3.1.5 Isotropy/anisotropy

Under the assumption that pre-load (shrinkage) cracks are orientated randomly, concrete may be regarded as an isotropic material prior to loading. Unlike shrinkage cracks, stress/strain-induced cracks during loading generally do have a certain preferred direction that causes a certain degree of anisotropy. The modelling approaches of 2.2.1 and 2.2.2 incorporate this effect naturally because the orientation of the crack is fixed in the finite element mesh.

Continuum solid modelling does not incorporate stress/strain-induced anisotropy straightforwardly. Within the framework of elasto-plasticity, isotropic rules for strengthening/softening may be replaced by kinematic (or mixed) rules, i.e. the stress-state bounding surface does not expand/shrink symmetrically around the hydrostatic axis, but (also) translates in a direction dependent on the current state of stress [Chen & Han<sup>1988</sup>]. As for continuum damage mechanics, a scalar-valued damage effect parameter only is capable of 'memorizing' the extent of microcracking. Retaining also the direction of cracking would inevitably imply the



designation of additional internal state parameters, usually by replacing the damage-effect *scalar* by a higher order damage-effect *tensor*.

A physically appealing approach to account for stress-induced anisotropy is the geometric consideration of weak (continuous) planes. The normal and tangential stresses in such a plane are the resolved components of the macroscopic stress state. According to the first model in this category, the Fixed (smeared) Crack model, mode I cracking is initiated in a plane perpendicular to the maximum tensile stress, when the principal stress exceeds the uniaxial tensile strength of the continuum. Upon further loading a sudden stress drop [Rashid<sup>1968</sup>] or a strain softening law, analogous to the fictitious crack model, is applied for the tensile stress normal to the fixed (weak) plane. As no secondary cracking is allowed for in this concept, stresses may arise exceeding the tensile strength significantly upon rotation of the stress state. Various approaches were formulated in extending this concept to cope realistically with rotating stress states also. In the Rotating Crack model [Cope et al<sup>1980</sup>] the crack plane rotates so as to remain perpendicular to the maximum principal stress. Stress-induced anisotropy is however lost in this concept. Stress-induced anisotropy is retained in the Multiple Fixed Crack model [De Borst & Nauta<sup>1985</sup>; Rots<sup>1988</sup>]. In this concept, the formation of secondary fixed crack(s) is allowed for when the principal stress has rotated beyond a certain threshold angle. The statically constrained Microplane model [Carol & Prat<sup>1990</sup>] and the Adaptive Fixed Crack model [Weihe et al<sup>1998</sup>] are extensions of the Multiple Fixed Crack model in the sense that they conceptually also allow for mode II or mixed mode crack initiation and that the latter allows initiation of secondary cracks, whenever the stress state in *any* plane exceeds the cracking criterion.

The above 'weak plane' models aim at reproducing concrete behaviour with continuous planes of fracture. The material behaviour due to distributed microcracking is better reproduced by the Microplane model with a kinematic constraint [Bažant & Oh<sup>1985</sup>; Bažant & Prat<sup>1988</sup>]. In this concept, the strains at the (weak) micro-planes are the resolved components of the total macroscopic strain state. For each plane a constitutive law is applied, resulting in new normal and tangential micro-stresses. The macroscopic stress tensor is established through integration over the fixed set of microplanes in an energetically consistent manner. In a more recent version of the Microplane model [Ožbolt et al<sup>2001</sup>] the kinematic constraint has somewhat been released to account for the loss of continuity of the strain field for dominant tensile loads, i.e. continuous planes of fracture due to mode I cracking.

### 2.2.3.2 Localisation of deformations in continuum solid mechanics

As outlined in the previous section, besides pre-peak also post-peak non-linear material behaviour may be incorporated in a continuum mechanics based model by assigning a strain-softening law. However, unlike pre-peak strengthening, post-peak softening exhibits a strong dependence on the size of the finite elements. This is best explained by considering a one-dimensional strain-softening bar as depicted in figure 2.15. This bar may be divided in 5 or 15 (constant strain) elements. Under the assumption that the shaded elements are slightly weaker than the other elements,

softening will occur in these elements while the other elements are unloading. This kind of behaviour is similar to the localisation of deformations, as observed in experiments in the post-peak region.

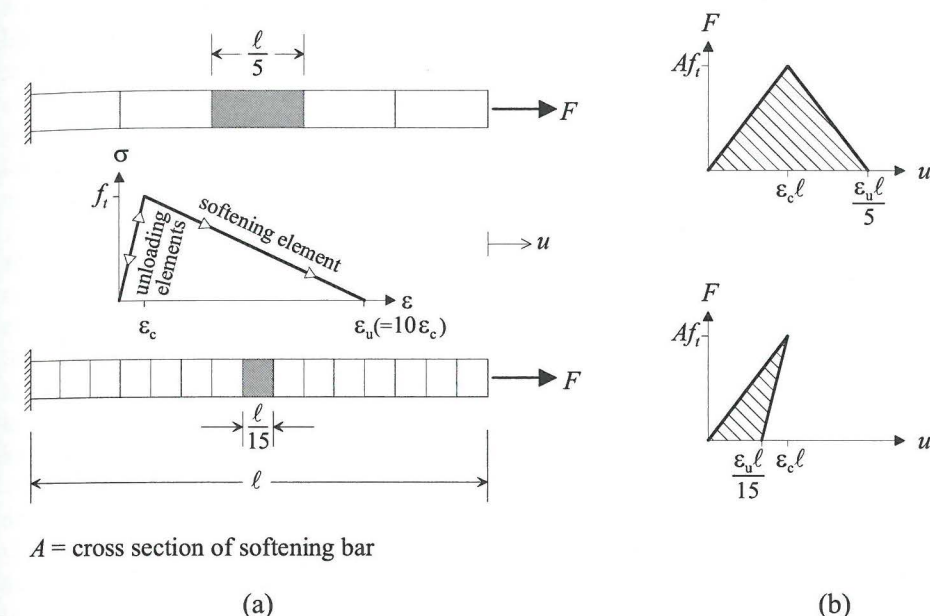


Figure 2.15. (a) Strain-softening bar and stress-strain softening law.

(b) Load displacement curves for two different element sizes.

Comparing the overall load-deformation curves (figure 2.15.b), a striking difference is found between the bars with 5 elements and 15 elements. The hatched area represents the total dissipated energy. It follows that the energy dissipation and brittleness of the bar are highly dependent on element size. More than that, the dissipated energy vanishes completely when the element size approaches to zero.

Some kind of regularization technique is obviously required. Assuming that localisation always occurs in one element, conservation of energy dissipation is satisfied by considering the fracture energy as a material property, as proposed in the Crack Band model of Bažant & Oh<sup>1983</sup>. In this model, the fracture process zone is treated as a non-sharp-edged crack band of *constant* width  $w_c$  governed by a strain softening relation as depicted in figure 2.15.a. The inelastic (fracture) strain is integrated over the crack band width resulting in constant energy dissipation *provided that* the finite element width  $h$  equals the crack band width  $w_c$ . This theory is quite equivalent to the Fictitious Crack Model (section 2.2.1.2). The fracture energy  $G_F$  corresponds now to the area under the stress-strain curve multiplied by the width of the crack band  $w_c$ . To allow for finite element sizes different from the crack band width, energy dissipation is conserved by enforcing the condition that the fracture energy in one element equals the fracture energy of the crack band, i.e.  $G_F$  corresponds to the area under the stress-strain curve multiplied by the width of

the finite element  $h$ . Obviously, this requires  $f_i$  or  $\epsilon_u$  in figure 2.15.a to be reformulated as effective material parameters dependent on the finite element width  $h$ .

Although computationally very efficient, a drawback of the Crack Band model is that it may lead to spurious stress locking when the localisation band is not aligned with the mesh, i.e. when the crack band propagates through the mesh in a zig-zag manner. As it leaves the width of the localisation band unspecified, it also is impossible to determine how the fracture process zone width could vary during fracture growth. Theoretically, a more elegant approach is to introduce additional terms (or localisation limiters) in the continuum description representing the changes in the microstructure occurring during failure processes.

Frequently applied in combination with the theory of continuum damage mechanics is the *nonlocal* theory [Pijaudier-Cabot & Bažant<sup>1987</sup>; Ožbolt & Bažant<sup>1996</sup>]. This concept deviates from the idea that the residual stress beyond peak load is exclusively a function of the inelastic strain in the material point itself. Instead, it postulates that the residual stress also depends on the inelastic strain in adjacent material points. Practically, this implies that the internal damage state in a material point is based on an average of the strain field in a neighbourhood of this material point.

Alternatively, the gradient approach introduces spatial derivatives of the inelastic strain (or internal state parameters dependent on the inelastic strain). In the early model of Schreyer & Chen<sup>1986</sup> first order derivatives were used. Later, it was recognized [Mühlhaus & Aifantis<sup>1991</sup>; De Borst et al<sup>1992</sup>] that second order spatial derivatives better characterize the geometric nature of a localisation band.

Less worked-out alternatives are the Cosserat extension of classical continua [Mühlhaus<sup>1986</sup>, De Borst<sup>1991</sup>] and introduction of strain-rate dependency [Needleman<sup>1988</sup>; Sluys & De Borst<sup>1991</sup>]. The Cosserat theory introduces rotational degrees of freedom in the continuum description, based on the observation of distinct particle rotation in localised shear bands of non-cohesive granular materials [Bardet & Proubet<sup>1992</sup>].

The above extensions of the classical continuum theory all have in common that a certain internal length scale is introduced, which in fact regularizes the localisation process. From a computationally point of view, a major drawback of these approaches is the fact that in order to capture the localisation band properly, very small finite elements need to be foreseen at and near the localisation band. This implies that either a very fine mesh has to be generated at the start of the analysis, or that a sophisticated adaptive remeshing procedure has to be applied during the analysis.

A promising development is the formulation of models that allow the introduction of displacement jumps in the conventional finite elements to reproduce the geometric nature of localised cracking [Klisinski et al<sup>1991</sup>; Larsson et al<sup>1999</sup>; Wells et al<sup>2002</sup>]. The crack path does not have to be known a priori and since the localised crack is situated in one finite element, these concepts allow the utilisation of coarse finite element meshes. Of course, attention should be paid to the continuity of the crack path across the finite element boundaries.

## CHAPTER 3

### FUNDAMENTALS OF CONCRETE LOADED IN MULTIAXIAL COMPRESSION

Research regarding the mechanical behaviour of concrete loaded in multiaxial compression is usually limited to a study of macroscopic quantities like overall stress-strain curves and localised macroscopic cracking. The basic physics/mechanics accounting for the specific characteristics of these macroscopic quantities are yet not very well understood. Due to the infinite number of potential triaxial loading cases, experimental test programs only can cover a very limited range of loading paths in the 3D stress (strain) space. Consequently, the applicability of numerical models – merely based on such test programs and developed without sufficient knowledge of the basic physics/mechanics underlying the observed macroscopic features – is not wider than its starting-basis i.e. restricted to the limited range of loading cases as carried out in the particular experimental test program.

Development of a numerical model, being more generally applicable, therefore, should incorporate a sound knowledge of the basic physics/mechanics of concrete loaded in multiaxial compression. Here, it will be demonstrated that a classification of the observed physical/mechanical phenomena in experimental tests according to the frame as shown in figure 3.1, yields such a solid understanding of the significance of these phenomena, their interaction and the basic physics/mechanics underlying them.

	Stage I	Stage II	Stage III	Stage IV
Level 1	<i>Mechanical behaviour</i>			
Level 2	<i>of concrete</i>			
Level 3	<i>loaded in multiaxial compression</i>			

Figure 3.1. Frame for classifying concrete mechanical behaviour.

The frame of figure 3.1 distinguishes on the one hand three different scale levels of observation. These scale levels are explained in section 3.1. On the other hand a distinction is made between four typical stages in multiaxial compression tests. These typical stages are explained in section 3.2. This division is chosen because the macroscopically observed mechanical behaviour at each stage is typically characteristic. Furthermore, the consideration of multiple scale levels at each stage is essential. The complex macroscopic mechanical behaviour at each stage proves to be directly related to basic mechanisms taking place at lower scale levels. As a result, the generated classification provides a solid base for numerical modelling to

be valid and applicable much wider than the mere range of experimental tests carried out.

### 3.1 Scale levels

Mechanical phenomena, such as cracking, may be observed at different scale levels during experimental testing of concrete. These separate observations often provide a direct link between global stress-strain curves and the formation and growth of micro- and macrocracks. With this in mind Wittmann<sup>1987</sup> proposed, on the basis of common practice in material science, a practical subdivision into three scale levels:

- Micro level
- Meso level
- Macro level

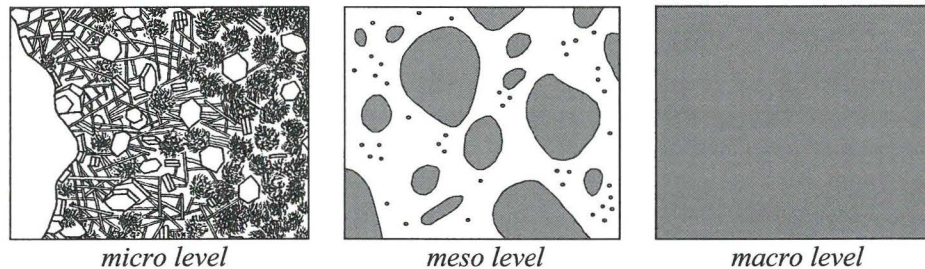


Figure 3.2. Scale levels for concrete.

#### 3.1.1 Micro level

At this level the microstructure and the mechanical properties of the hardened cement paste are considered. These properties and the porosity of the microstructure are strongly affected by the interaction of the cement with water.

The microstructure of the hardened cement paste in concrete is far from homogeneous. The most striking aspect in this respect is the existence of an interfacial transition zone (ITZ) between the aggregate grains and the bulk cement paste. Many researchers have reported the existence of this zone in normal strength Portland cement concrete and the concept is widely accepted.

The microstructure of the ITZ differs considerably from that of the surrounding bulk cement paste [Larbi<sup>1991</sup>; de Rooij<sup>1996,2000</sup>]. Figure 3.3 shows schematically the microstructural features of the ITZ and the surrounding bulk cement paste. At the surface of the aggregate grains a contact layer of about 2-3  $\mu\text{m}$  thickness exists, consisting mainly of calcium hydroxide (CH) crystals. Adjacent to this layer a thin film of calcium-silicate-hydrates (C-S-H) exists in the form of short fibres. On the other side of the contact layer a very porous zone exists. In this zone large panel-shaped CH-crystals and clusters of ettringite needles often are found. The CH-crystals in the ITZ have a preferential orientation perpendicular to the aggregate surface. This preferred orientation of the CH-crystals vanishes in the bulk cement paste microstructure.

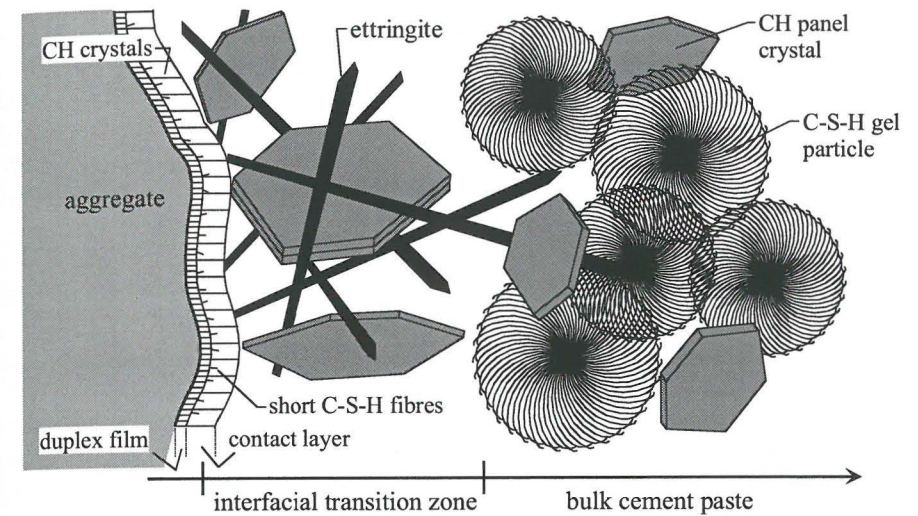


Figure 3.3. Diagrammatic representation of the ITZ and bulk cement paste in concrete [de Rooij<sup>1996</sup>].

There is no clear evidence which mechanism(s) cause(s) the formation of the ITZ. The most reported mechanisms, however, are 'micro-bleeding', introducing an excess of water at the aggregate surface, and the 'wall effect', resulting in an inefficient packing of cement grains against the aggregate surface. Only recently, another phenomenon has been formulated as a possible cause for the formation of the ITZ [de Rooij<sup>1996</sup>]. This phenomenon, called syneresis, is the tendency of a gel to shrink spontaneously under the expulsion of pore liquid. If the cement paste is seen as a gel, this phenomenon could also occur in fresh concrete. The water is then being pressed out of the cement paste and accumulates around the aggregate grains, also resulting in water excess at the aggregate - cement paste interface.

Concerning the mechanical properties of the cement paste, a distinction is made between two types of potential failure, i.e. (1) mode I / mixed mode microcracking inducing volumetric dilation and (2) pore collapse of the cement paste microstructure inducing volumetric contraction.

As already pointed out in section 2.1.2, the ITZ between the aggregate grain and the bulk cement paste can be considered as the weakest link in normal strength concrete. The density of pre-existing mode I / mixed mode microcracks in this zone is higher than in the bulk cement paste. These microcracks tend to run along the contact layer and along the cleavage (weak) planes of the calcium hydroxide (CH) crystals.

Potential pore collapse of the microstructure in the high compressive loading regime is strongly related to the porosity of the material. At the micro level, the cement paste has a distinct porous structure. Figure 3.4 shows results of pore size measurements of cement paste and mortar obtained with the aid of a mercury intrusion porosimeter [Larbi<sup>1991</sup>]. It appears that the pore structure of plain cement paste ( $a/c = 0$ ) contains mainly pores with a radius between 0.01 and 0.07  $\mu\text{m}$ .

Figure 3.4 also shows that an increase in sand-cement ratio from 0 to 2 is accompanied by an increase of total porosity of about 60% of which the increase of larger pores ( $r > 0.1 \mu\text{m}$ ) contribute to a large extent. This effect is likely to be the result of the formation of highly porous ITZs around the sand particles.

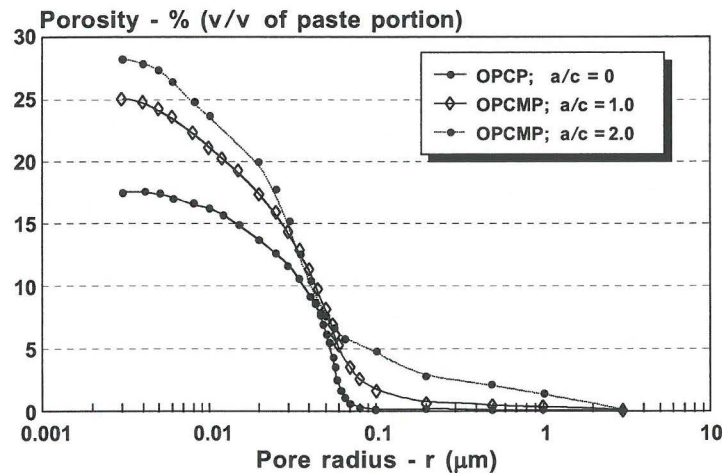


Figure 3.4. Cumulative pore size distribution of mortars plotted as volume percentage of cement paste portion in mortar ( $w/c = 0,40$ ; age = 100 days;  $a/c = \text{aggregate(sand)-cement ratio}$ ) [Larbi<sup>1991</sup>].

Studies using Scanning Electron Microscopy (SEM) combined with image analysis of backscattered electron (BSE) images frequently have reported higher proportions of larger pores ( $r > 0.1 \mu\text{m}$ ) in the ITZ than in the bulk cement paste [Scrivener & Nemati<sup>1996</sup>; Scrivener<sup>1999</sup>]. These studies also indicate that the characteristics of the microstructure of the ITZ more properly are described in terms of gradients of microstructure perpendicular to the aggregate grain. The thickness of the ITZ may be appointed as the distance between aggregate grain and bulk cement paste (see figure 3.3) over which the microstructure significantly differs from that of the bulk cement paste. However, as elucidated by Diamond & Huang<sup>2001</sup>, it should be realised that the ITZ is highly heterogeneous itself and large variations in properties are found along the surface of the aggregate grains.

Quantification of the dimensional proportions and the total porosity of bulk cement paste and ITZ is a difficult task considering the heterogeneity of the material. The thickness of the ITZ depends on the type of aggregate and cement used, the water-cement ( $w/c$ ) ratio of the mix, the age of the composite and the method used to estimate it. The reported thickness of the ITZs, which occupy 30 to 50 % of the total volume of cement paste, usually ranges from 25 to 100  $\mu\text{m}$  with a typical thickness of 50  $\mu\text{m}$  [Larbi<sup>1991</sup>].

With respect to the porosity of the ITZ, SEM studies have reported pore contents (of pores with radius  $> 0,1 \mu\text{m}$ ) up to 30% within a few  $\mu\text{m}$  proximity of the aggregates, while the porosity of the bulk cement paste is in the range of 5-15%. Based on

mercury intrusion porosimetry experimental data and on an analysis of percolation through a 3D mortar model, Bourdette et al<sup>1995</sup> computed the ITZ porosity and bulk cement paste porosity with pore radii down to 0,003  $\mu\text{m}$ . This study revealed ITZ porosity up to 50% (mean value over an assumed constant thickness of 30  $\mu\text{m}$ ) and a bulk cement paste porosity of about 20%. It is further noticed that the ITZ porosity decreases during the maturation of the material, presumably due to ongoing deposition of calcium hydroxide and hydration of anhydrous cement grains. With regard to the quantification of total porosity it should further be noted that the 'total' porosity as extracted from mercury intrusion porosimetry experimental data represents a lower bound of the actual total porosity, because only the *interconnected* pores with a radius larger than 0,003  $\mu\text{m}$  are recorded.

### 3.1.2 Meso level

At the meso level, the heterogeneous structure of concrete – a composite of aggregate grains, hardened cement paste, large pores and pre-existing cracks – is taken into account. At this level the ITZs between the aggregate grains and the bulk cement paste are schematised as homogeneous (weak) layers around the aggregate grains with constant thickness.

The mechanical behaviour of the composite at this level is determined by the mechanical properties of the individual constituents, i.e. the aggregate grains, the bulk cement paste and the ITZs.

#### 3.1.2.1 Mechanical properties of the constituents

Natural aggregates are quite heterogeneous themselves; their mechanical properties can only be specified within a range. A typical value of Young's modulus of strong and dense aggregates such as river gravel – used in most mixes of normal strength concrete in practise – is about 60.000 MPa [Hirsch<sup>1962</sup>, Wittmann et al<sup>1993</sup>]. The order of magnitude of the strength of river gravel may be compared to the strength of granite, which is characterised by a Young's modulus of 70.000-80.000 MPa and a compressive strength of about 180 MPa [Alexander<sup>1993</sup>, Caliskan et al<sup>2002</sup>].

The mechanical properties of plain cement paste (without aggregates) are strongly influenced by the type of cement, the age at testing (degree of hydration), the water-cement ( $w/c$ ) ratio, curing and the test setup. With this in mind, the stiffness and strength of cement paste out of ordinary Portland cement (age: 28 days or more,  $w/c$  ratio: 0,3-0,5) are typically within the ranges given in table 3.1.

Table 3.1 Stiffness and strength of plain cement paste

	Reported experimental data [MPa]
Young's modulus	15.000 – 25.000 <sup>(3,4)</sup>
Compressive strength	50 – 100 <sup>(1,2,3)</sup>
Direct tensile strength	3,5 – 4,0 <sup>(1)</sup>
Flexural tensile strength	9 – 12 <sup>(2)</sup>

<sup>1)</sup> Hsu & Slate<sup>1963</sup>, <sup>2)</sup> Alexander et al<sup>1968</sup>, <sup>3)</sup> Bažant et al<sup>1986</sup>

<sup>4)</sup> Hirsch<sup>1962</sup>, Wittmann et al<sup>1993</sup>, Alexander<sup>1993</sup>, Yang<sup>1998</sup>

The mechanical properties of the ITZ are obviously influenced by the properties of the aggregates (type, roughness, size) and the cement paste (type, age, w/c ratio) as well as the treatment of the concrete mix during manufacturing (vibration, curing). Van Mier & Vervuurt<sup>1999</sup> reviewed the issues regarding modelling and testing of the mechanical properties. They distinguished two strategies by which the properties of the ITZ may be determined. The first one involves scaling up of the ITZ to obtain specimens in which a macroscopic test is feasible to measure the properties of the ITZ. In these tests, composite specimens are prepared in which the cement paste is cast against a rock surface, which is usually polished. The second strategy is based on the concept of inverse modelling and involves testing of real concrete and simulation of the test by an appropriate numerical meso-level model. Knowing the properties of the aggregates and the bulk cement paste, the properties of the ITZ are calibrated so that the simulation corresponds to the experimental observations [e.g. Vervuurt<sup>1997</sup>].

The scaling up strategy provides direct test data. However, the prepared specimens are not similar to the ITZ as existent in real concrete. It is remarked that differences in surface texture and size of the aggregates and differences in the manufacturing process will undoubtedly affect the structure of the ITZ. The limitation of the inverse modelling strategy is that it relies heavily on the assumptions regarding the correctness of the simulation model used.

In view of the above drawbacks on measuring mechanical properties of the ITZ, no quantitative results are reported here on the stiffness and strength of this zone. There exists, however, consensus among researchers, that – in normal strength concrete with strong and dense aggregates – the strength and stiffness of the ITZ are less than those of the surrounding bulk cement paste.

### 3.1.2.2 Mechanical behaviour of the composite

As explained in the preceding section, the aggregate grains are much stiffer than the surrounding cement paste in normal strength concrete. As a result these grains will act as stress concentrators during initial loading. The internal forces will mainly be transferred between the aggregate grains by the shortest connection through the cement paste, resulting in a highly heterogeneous stress state. Dantu<sup>1957</sup> and (later on) Swamy<sup>1971</sup> already observed such highly heterogeneous stress states performing uniaxial compressive tests on sliced concrete specimens using a reflective photoelastic technique.

The heterogeneity of the stress state during initial loading is further enlarged by the presence of pre-existing cracks and large pores. As stated in section 2.2.1.1, large stress concentrations are found around voids and near crack tips in a homogeneous material. Although the increase in stress level is far less pronounced for a heterogeneous material – like concrete – than predicted by LEFM, the local stress level near voids and initial cracks can differ considerably from the overall stress level.

The occurrence of tensile splitting cracks in uniaxial compression tests with little lateral boundary restraint (section 2.1.2.1) has frequently been attributed to the heterogeneity of the stress state [Reinhardt<sup>1977</sup>; Murakami & Ohtani<sup>2000</sup>]. Due to the

concentration of compressive forces between stiff aggregate grains (see figure 3.5), tensile stresses often arise even when the overall stress field is compressive.

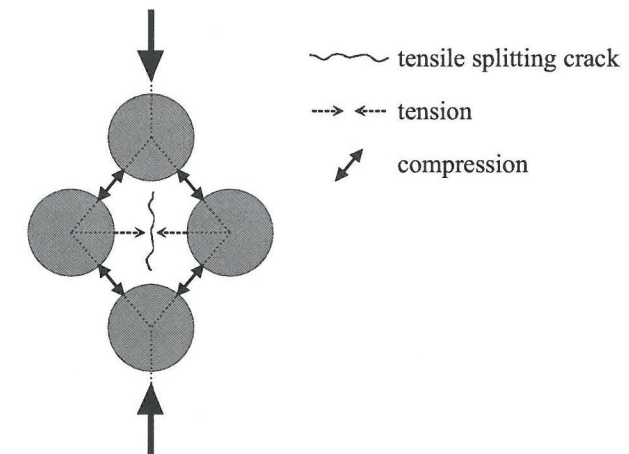


Figure 3.5. Force transfer between aggregate grains in concrete.

Horii & Nemat-Nasser<sup>1985</sup> suggested another potential cause of tensile splitting failure (section 2.1.2.1) by considering the heterogeneity of the stress field due to pre-existing cracks. By analysing an idealized brittle material with pre-existing inclined flaws loaded in compression, they showed that the local stress state at the tips of the pre-existing flaws encourage the formation of tensile splitting cracks. It was also shown that, with a suitable distribution of the pre-existing flaws, these ‘wing’-shaped cracks joined together forming a complete failure pattern.

These studies demonstrate clearly the existence of tensile stresses in a uniaxial compressive (overall) stress field when the heterogeneity of the material is taken into account. Along with the sensitivity of concrete regarding mode I crack formation this may easily lead to the formation of tensile splitting cracks. Nevertheless, a complete failure pattern is only formed when the initiated splitting cracks grow in an inclined direction to pass through the compressive strut in figure 3.5 or, in the case of pre-existing inclined cracks, when sliding along these pre-existing cracks occurs. As pointed out also in section 2.1.2.1, in combination with tensile splitting also sliding along (newly formed or pre-existing) inclined cracks is necessary for complete failure of the specimen, implying that internal friction is a determinative factor in uniaxial compressive failure.

To illustrate the formation of the – experimentally observed – tortuous crack patterns of combined mode I / mode II cracks in uniaxial compression, a generic representation of crack growth in a heterogeneous material such as concrete is explained below.

In figure 3.6 a pre-existing or newly formed mode II crack is considered. This crack is inclined with respect to the direction of the (compressive) principal stress  $\sigma_3$ . Crack growth is prevented when the crack tip meets an aggregate grain because the

strength of the aggregate grain is much higher than the strength of the surrounding cement paste. In such a case, three possible mechanisms for crack growth exist:

1. Through the aggregate grain
2. Around the aggregate grain (compressive side)
3. Around the aggregate grain (tensile side)

Considering the presence of local tensile stresses near the crack tip in uniaxial compression and the sensitivity of concrete regarding mode I crack formation, mechanism 3 will generally occur.

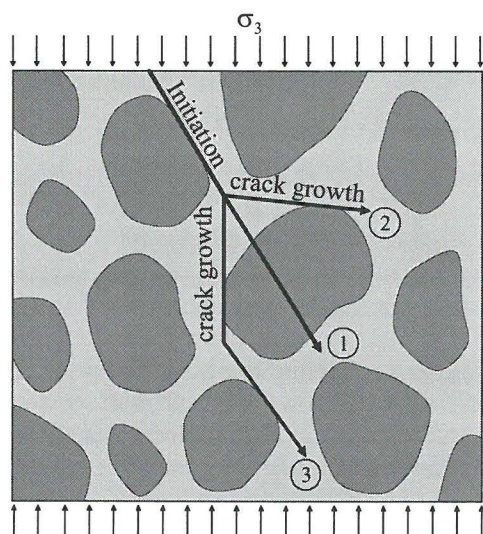


Figure 3.6. Mechanisms for crack growth in concrete.

While tensile splitting is abundant in *uniaxial* compression, concrete specimens failed in *multiaxial* compression show hardly any tensile splitting cracks. Instead, very pronounced inclined mode II cracking is observed, often passing straight through the aggregate grains [Van Geel<sup>1998</sup>]. Obviously, in these tests mechanism 1 prevails.

The absence of large tensile splitting cracks in multiaxial compression is often explained by pointing out that the confining stresses suppress the development of local tensile stresses induced by the heterogeneity of the concrete composite. However, this does not fully explain the absence of large tensile splitting cracks in multiaxial compression because close examination of the inclined crack bands does reveal the presence of *small* tensile splitting cracks along the inclined crack bands. Apparently, small-scale tensile splitting takes place but these cracks remain stable and limited in length. This kind of cracking may be viewed upon as *secondary* cracking, because – at ultimate failure – a *primary* continuous mode II crack is formed (see figure 3.7).

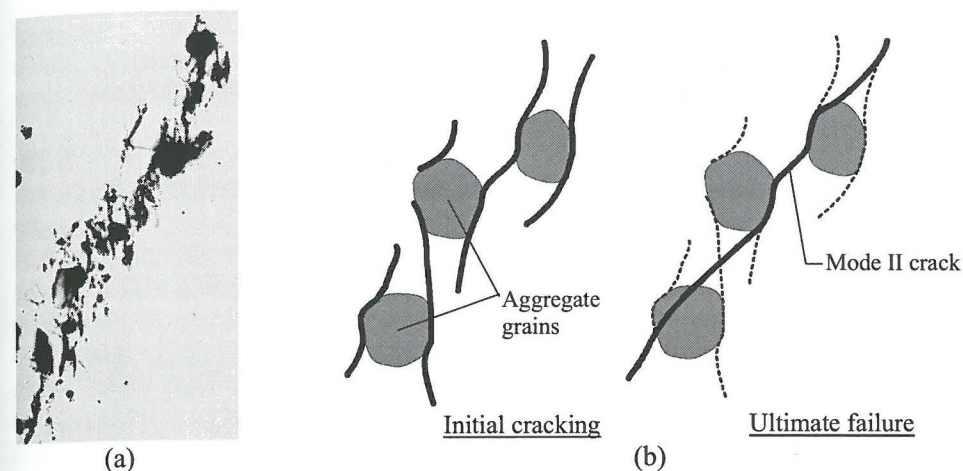


Figure 3.7. (a) UV-photograph showing small-scale tensile splitting along a mode II crack in a plane strain multiaxial compression test [Van Geel<sup>1998</sup>]. (b) Schematic representation of cracking mechanism [see also Van Mier & Vonk<sup>1991</sup>].

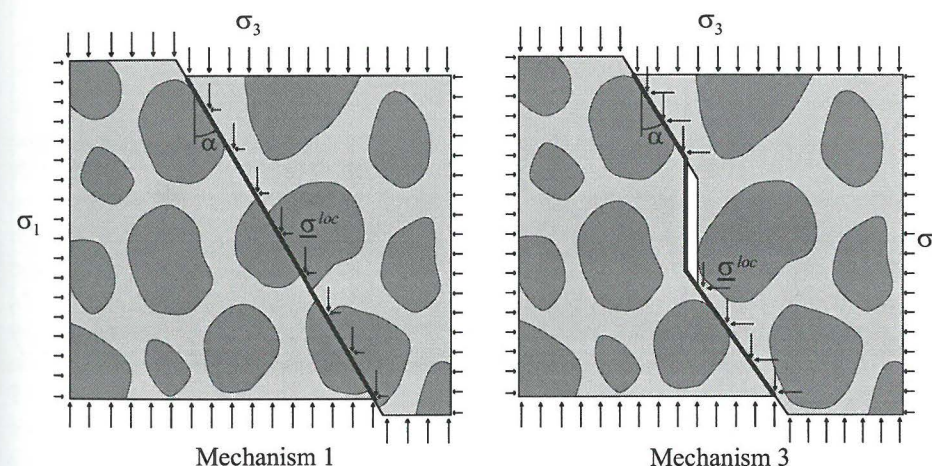


Figure 3.8. Local crack stresses in multiaxial compression.

An explanation for the formation of continuous mode II cracks at ultimate failure in multiaxial compression, can be found considering figure 3.8. It shows that when the crack is not straight (mechanisms 2 & 3), the contact area of the crack will be reduced upon sliding. Consequently, both the axial and the lateral loading will be transferred through a considerably reduced contact area of the crack. It turns out that for mechanism 3 the local crack stresses in the main loading direction (vertical axis) are equal to those for mechanism 1. However, the local crack stresses in the minor loading direction are much greater (more compressive) for mechanism 3 than

for mechanism 1. As the strength of concrete is highly sensitive to the presence of lateral confinement (section 2.1.1.1.2), the local stress state of mechanism 1 is much more favourable for crack growth in multiaxial compression than the local stress state of mechanism 3.

Another aspect of concrete failure – best explained on the meso level – is the observed shape of the descending branch of the loading curve during mode I crack growth in tensile tests, which is best typified by a steep part just beyond ultimate strength followed by a long shallow tail (figure 3.9). Whereas the (initial) steep part of the descending branch may be ascribed to opening of small isolated (ITZ) cracks in the fracture process zone, the shallow long tail of the descending branch has to be attributed to the formation of so-called *crack interface grain bridges* during the development of a continuous crack profile through the specimen [Van Mier<sup>1992</sup>]. In this process, two overlapping crack tips approach each other, but coalescence seems prohibited due to the presence of the stiff aggregate grains in the crack path. In this way ‘bridges’ are created between the overlapping cracks with rather low (flexural) stiffness.

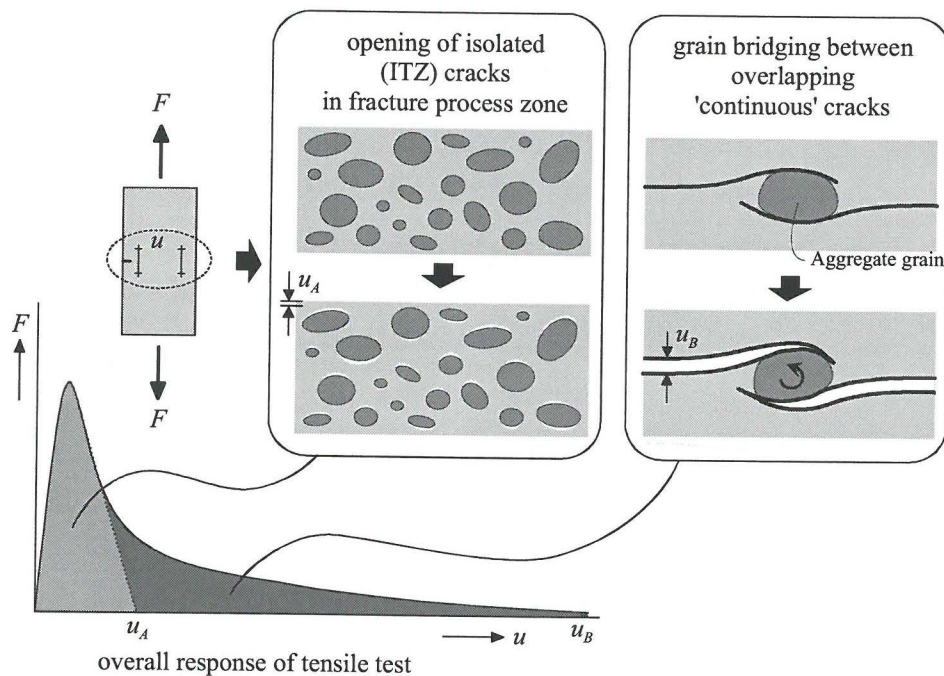


Figure 3.9. Meso-mechanical behaviour of concrete loaded in tension.

Overlapping cracks are also observed in compression. Stroeven<sup>1973</sup> reported already arrays of (micro) splitting cracks transforming in a continuous shear crack during subsequent loading in uniaxial compression and, as shown in figure 3.7, these overlapping splitting cracks exist also in multiaxial compression. Clearly, the existence of these arrays of small splitting cracks decreases the stiffness of the

structure to some extent. However, considering the small length of the splitting cracks, ductility induced by the formation of crack interface bridges between overlapping crack tips will be very limited in multiaxial compression.

### 3.1.3 Macro level

At the macro level concrete is considered a homogeneous material. Mechanical properties, such as uniaxial compressive or tensile strength, can be measured directly in standard tests at this level. The measured mechanical properties in these tests are not only dependent on the concrete mix, but also on the age at loading, moisture content, temperature, loading rate and test setup. When the strengths for different concrete mixes are compared, these other influencing factors should be the same or at least similar, which clearly indicates the need for standard, well-documented test procedures.

With respect to the mechanical behaviour of multiaxially loaded concrete, an immense number of potential loading combinations and loading histories arises. Though the availability of well-documented test data is important here also, this is not sufficient to reveal all essential aspects of the mechanical behaviour of concrete loaded in multiaxial compression. In contrast with uniaxial compression, individual testing for every potential loading path in 3D stress space is unfeasible for multiaxial compression, so trends in mechanical behaviour have to be identified and thoroughly analysed in order to be able to extrapolate them to other loading paths.

In chapter 2.1 a survey of experimental recordings at the macroscopic level has been given. From these macroscopic recordings, trends regarding ultimate strength and the shape of the  $\sigma$ - $\epsilon$  curves can already be qualified. The shape of the triaxial strength envelope is found to be convex, highly sensitive to lateral confinement and open ended, i.e. no failure is found for high hydrostatic compression. Overall loading curves of concrete loaded in multiaxial compression show large pre-peak non-linearity and characteristic points on the curve of volumetric strain may be identified. Furthermore, a distinct shift from uniformly distributed deformations in the pre-peak region to highly localised deformations (macrocracks) in the post-peak region (figure 3.10) is common for concrete loaded in multiaxial compression.

The macroscopically observed mechanical behaviour of concrete must be interpreted in terms of mechanisms acting at lower scale levels, i.e. the meso and the micro level. Coupling with these lower levels will certainly produce valuable information on the identification and quantification of trends observed at the macro level. In the next section of this chapter special attention is given to crack growth at the meso level. Much of the mechanical behaviour of normal strength concrete can be explained by its heterogeneous structure at this level. In some cases, however, an analysis at the meso level does not suffice. In these cases a further step back to the micro level is necessary in order to understand the observed macroscopic behaviour.

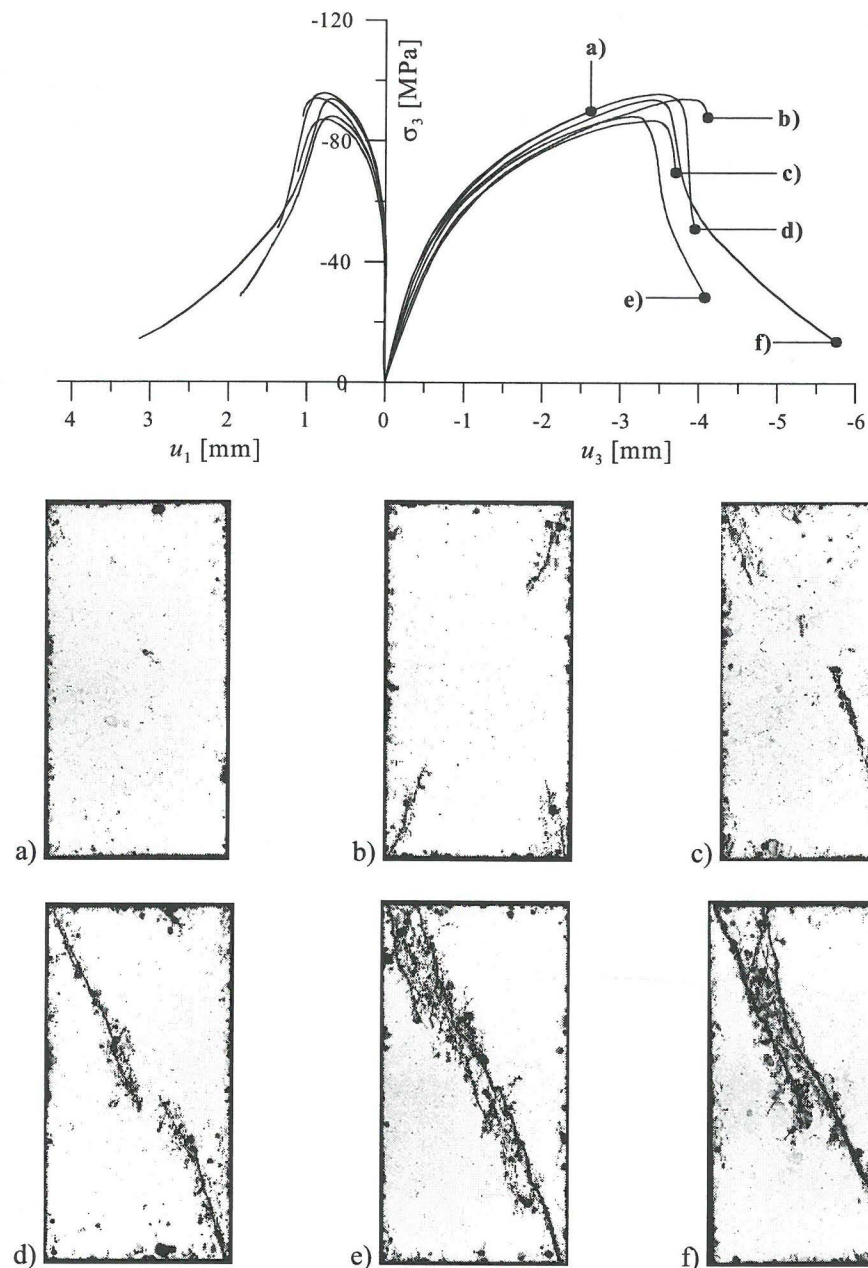


Figure 3.10. Evolution of macrocracks in multiaxial compression [Van Geel<sup>1998</sup>].

### 3.2 Stages in crack formation

This section describes concrete mechanical behaviour at several stages of multiaxial compressive loading. A subdivision into four stages is made with each stage having its own specific (macroscopic) mechanical behaviour. Figure 3.11 shows the load-deformation curve of a typical multiaxial compression test (plane strain test:  $\varepsilon_2 = 0$ ;  $\sigma_1 = 0.15 \sigma_3$  [Van Geel<sup>1998</sup>]). The stages, as indicated in figure 3.11, are entitled:

- I. Linear elastic stage
- II. Non-linear strengthening stage
- III. Around peak stress
- IV. Softening stage

The transitions between these stages are not as abrupt as indicated in figure 3.11. In fact, the transition from one stage to the other develops very gradually.

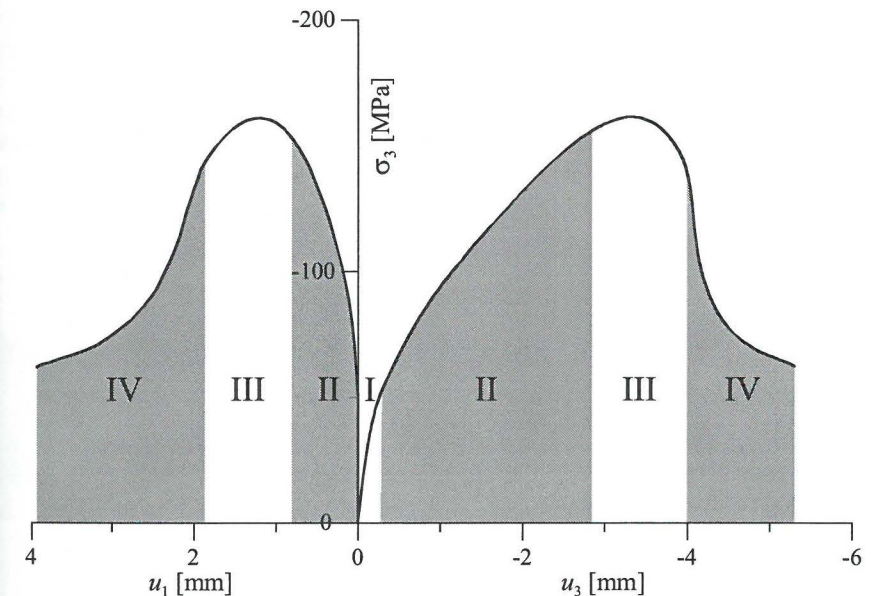


Figure 3.11. Stages in typical multiaxial compressive loading.

#### 3.2.1 Linear elastic stage (I)

During this stage, the increase in damage due to (micro) cracking is very small. As a result, the observed mechanical behaviour can be fairly well described by applying the classical theory of linear elasticity. The elastic properties of the concrete composite depend on the elastic properties of the separate components (aggregate grains and cement paste), the compaction of the concrete mixture during casting and the amount of pre-existing (ITZ) cracks.

As stated in section 2.1.2.1, normal strength concrete contains a significant number of pre-existing cracks, i.e. cracks existing prior to the application of external loads.



Although a significant number of such ITZ cracks exist prior to loading, the growth of these pre-existing ITZ cracks and the formation of new ITZ cracks during initial loading is negligible, thus producing the nearly linear stage I of the load-deformation curve.

### 3.2.2 Non-linear strengthening stage (II)

According to macroscopic observations, the non-linear strengthening stage in a multi-axial compression test is characterised by a decrease of the slope in the loading diagram coupled with *non-elastic* volume compaction. The development of non-elastic volumetric strain (total volumetric strain minus elastic volumetric strain) during the typical multi-axial compression test of figure 3.11 is displayed in figure 3.12.

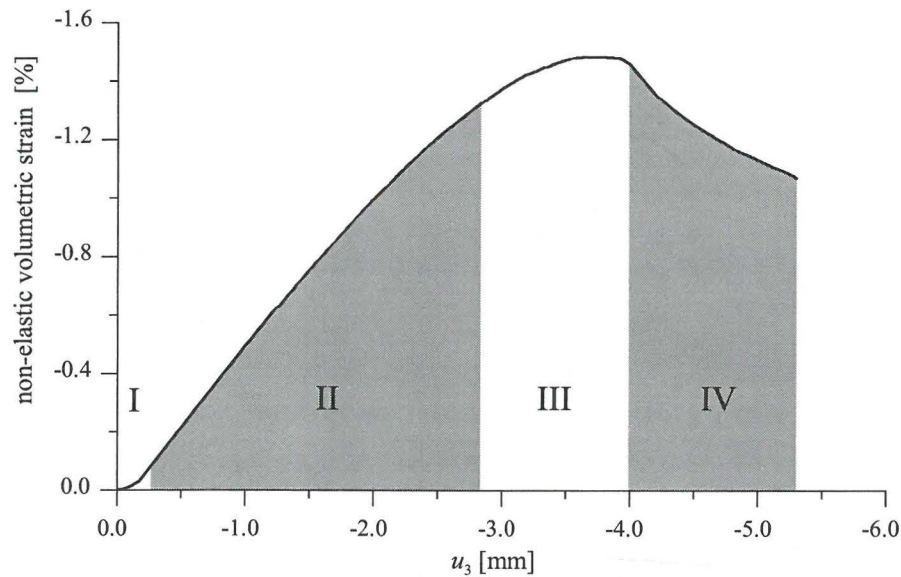


Figure 3.12. Non-elastic volumetric strain in a multi-axial compression test.

As the ITZ is the weakest link in normal strength concrete, it may be expected that the displayed macroscopic behaviour is a result of isolated crack formation in the ITZ. This assumption is supported by visual recordings of specimens loaded up to stage II in multi-axial compression. Up to this stage no (macroscopic) cracking occurs that can be seen with the naked eye. Moreover, no evident damage was visualised by Van Geel<sup>1998</sup> using a vacuum impregnation technique (figure 3.10.a). With this technique, specimens are impregnated with a fluorescent epoxy resin, which fills cracks in contact with the outer specimen surfaces. After hardening of the resin, the specimens are sawn into slices. By photographing these slices using ultraviolet light, internal cracks can be recorded. In this way only continuous crack patterns can be visualised, isolated microscopic or mesoscopic cracks remain invisible. As no continuous cracks could be visualised at stage II, the apparent

non-linear behaviour is indeed most probably due to isolated crack formation in the ITZs.

Nevertheless, the issue of the true nature of isolated crack formation in the ITZs remains. Basic crack behaviour like mesoscopic mode II or mode I failure along the ITZ results in an increase of non-elastic volumetric strain. Therefore, the displayed macroscopic behaviour must be caused primarily by another phenomenon. Consideration of the ITZ at the micro level reveals such a potential cause of the displayed macroscopic behaviour. In section 3.1.1 it was explained that the porosity of the ITZ is very high and substantially higher than the porosity of the surrounding bulk cement paste and the non-porous aggregate grains. Due to its high porosity, pore collapse of the ITZ microstructure is likely to occur in multi-axial compressive stress states, which may greatly account for the non-elastic compaction observed at stage II.

Pore collapse only occurs in highly porous materials. During pore collapse the porosity of the ITZ decreases. At a certain level of low porosity, further pore collapse of the ITZ does not occur anymore and an increase of stiffness is the result. Bazant et al<sup>1986</sup> already observed this stiffening effect, by carrying out confined compression tests on small cylindrical specimens loaded up to 2068 MPa. They found indeed that after an initial decrease, the slope of the loading diagram continuously increases.

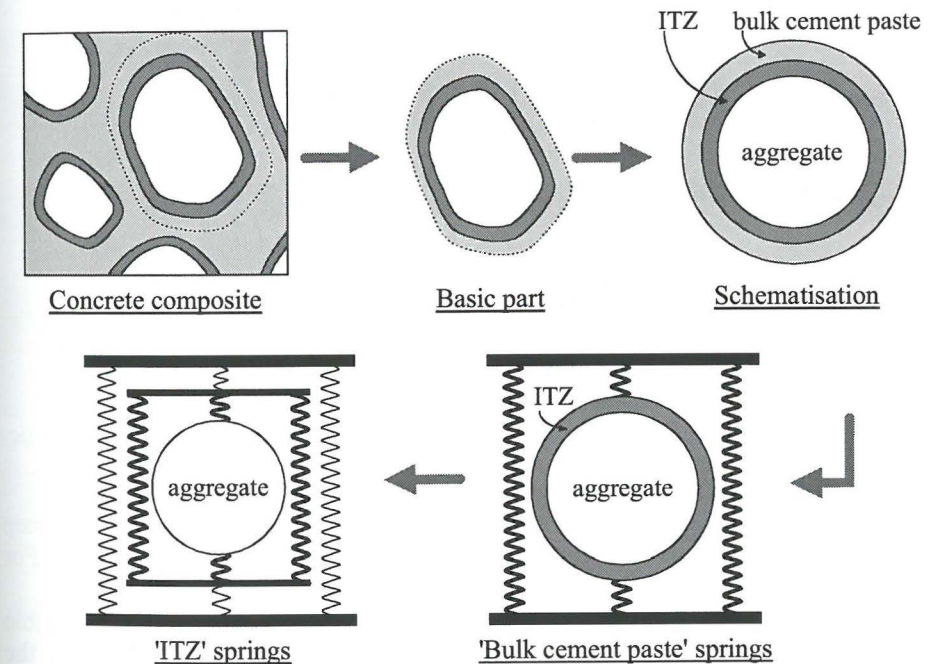


Figure 3.13. Mesoscopic 'spring' representation of concrete composite.

Though limited pore collapse may also occur within the bulk cement paste, it is assumed that only isolated crack formation in the ITZ around the aggregate grains occurs, and consequently, that the (macroscopic) strains at stage II are more or less uniformly distributed. Accordingly, the concrete composite at the meso level may be regarded as a system of springs connected in parallel and in series as shown in figure 3.13.

Due to cracking (pore collapse within the ITZ, mode I/II failure along the ITZ) the 'ITZ' springs include irreversible deformations during stage II, while the parallel connected 'bulk cement paste' springs retain their initial elastic behaviour. This combination of springs causes a branch with a positive inclination – yet considerably less than at the elastic stage – in the loading diagram.

The mesoscopic spring representation is also a useful tool for interpreting the characteristic unloading/reloading behaviour at stage II. Figure 3.14 shows the LVDT measurements for a cyclic plane strain multi-axial compression test performed by van Mier at Eindhoven University of Technology.

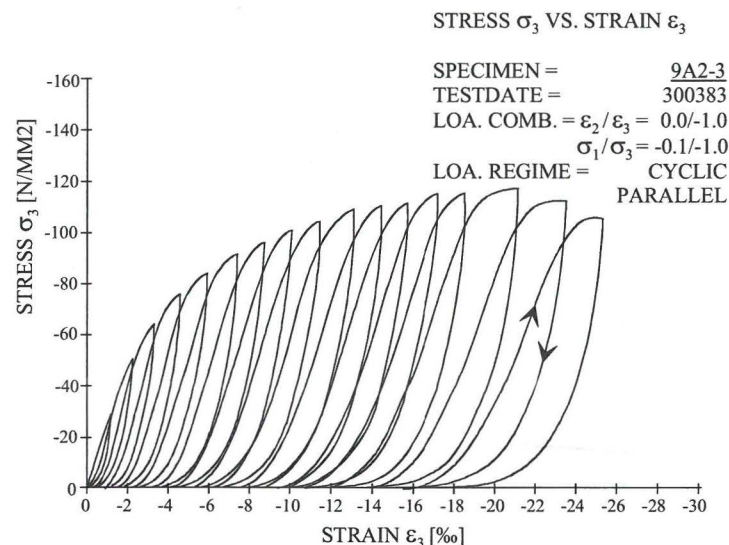


Figure 3.14. Loading diagram of the main loading axis in a typical cyclic multi-axial compression test [Van Mier<sup>1984</sup>].

According to figure 3.14 the unloading curve is characterised by an initial steep slope, which decreases considerably when a zero stress state is approached. For reloading, the opposite happens.

The analogy with the mesoscopic spring representation, with irreversible deformations in the ITZ at stage II, is straightforward. At initial unloading the stresses in the entire spring system decrease according to initial elastic stiffness until the stresses in the ITZ – and consequently in the, in series connected, aggregate grains – become zero. At this point the stresses in the parallel-connected

'bulk cement paste' springs are not zero, because there are no irreversible deformations in these components. At further unloading the ITZ opens with no further decrease of stress, as no tensile stresses can be transferred across the crushed ITZ. Further decrease of stresses therefore will occur at the parallel-connected 'bulk cement paste' springs only, which results in a rather flat unloading branch (see figure 3.15). For reloading the opposite occurs. At first, stresses are solely built up at the parallel-connected bulk cement paste springs until the gaps at the ITZs are closed again. From then on, reloading of the entire system takes place and initial elastic stiffness is recovered.

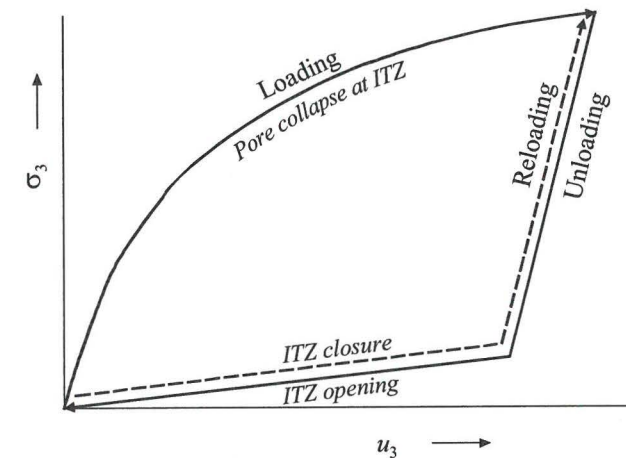


Figure 3.15. Load cycle according to the mesoscopic spring representation.

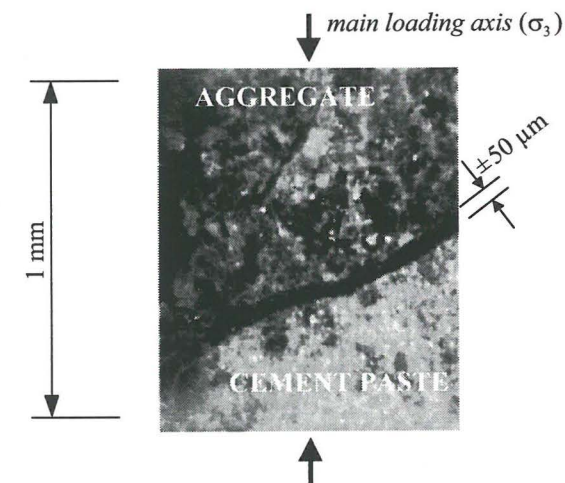


Figure 3.16. Microscopic photograph of an ITZ after loading up to stage II and subsequent unloading [Van Geel & Bongers<sup>1997</sup>].

According to the assumed mechanical behaviour as outlined above, gaps at the ITZs (perpendicular to the main compressive loading direction) should be present after unloading a specimen previously loaded up to stage II in multiaxial compression. With this in mind Van Geel & Bongers<sup>1997</sup> analysed the damage at the ITZs after unloading of specimens previously loaded up to stage II, using microscopic photography. Unlike the vacuum impregnation technique discussed before, this technique enables to visualise isolated cracks also. These microscopic photographs showed indeed clear gaps – up to 50  $\mu\text{m}$  – at the ITZs perpendicular to the main loading direction (black layer in figure 3.16). It should be noted that the recorded gaps at the ITZs are not likely due to micro-bleeding beneath the coarse aggregate grains in the fresh cement paste, as the casting direction does not coincide with the main loading direction but with the out-of-plane direction of figure 3.16.

### 3.2.3 Around peak stress (III)

At the macro level, stage III is characterised by reaching the ultimate strength and the early start of macroscopic (mode II) cracks. A clear picture of the start of macroscopic cracking at this stage is given in figure 3.10.b. At the meso level this means that the isolated cracks at the ITZs – already present at stage II – become interconnected through the bulk cement paste. This crack joining mechanism results in a non-elastic increase of the concrete volume. A gradual shift is therefore taking place with respect to the gradient of the volumetric strain curve (see figure 3.12): from volumetric compaction to (incrementally) volumetric dilation.

The ultimate strength in multiaxial compression in the first place is dependent on the concrete mix and the extent of confining pressure. Furthermore, the ultimate strength may be dependent on the loading path in 3-dimensional stress space, prior to reaching the ultimate strength envelope at a certain specific stress point. If such path dependency exists, ultimate strength envelopes such as depicted in section 2.1.1.1 are valid only for those loading paths – followed in the test series – on the basis of which the strength envelopes are constructed.

Path dependency of tensile strength might be expected when multiaxial compressive loading at stage II precedes the execution of a uniaxial tensile test. As isolated mesoscopic cracking at the ITZs takes place at stage II of multiaxial compression, the local capacity for tensile force transfer across these mesoscopic cracks decreases. Consequently, the overall capacity for tensile force transfer will decrease as well. The existence of such a path dependency of tensile strength was clearly demonstrated by Lin et al<sup>2002</sup>.

Based on the experimental observation that tensile splitting is abundant in uniaxial compression, similar effects are expected in the case of uniaxial compression. Van Geel<sup>1998</sup> investigated such an influence of multiaxial preloading on the ultimate strength in uniaxial compression. These results are displayed in figure 3.17. It appears that for uniaxial compression the ultimate strength clearly decreases with increasing multiaxial compressive preloading.

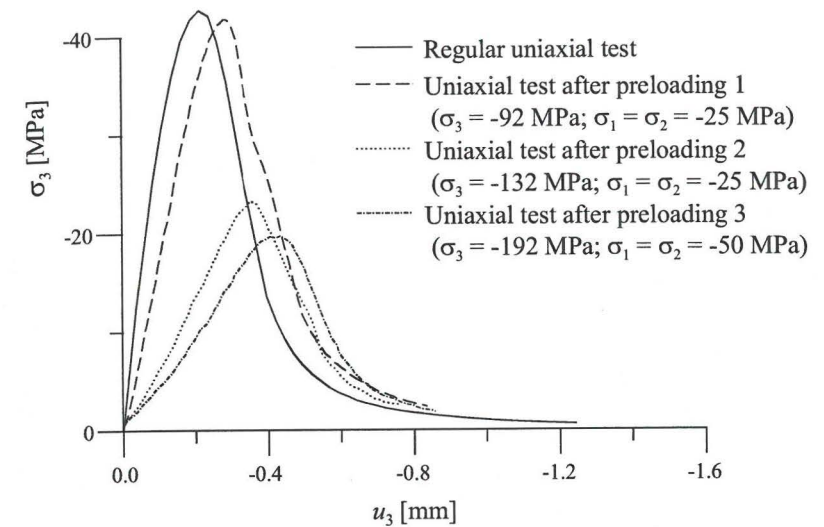


Figure 3.17. Ultimate strength in uniaxial compression with and without multiaxial compressive preloading [Van Geel<sup>1998</sup>].

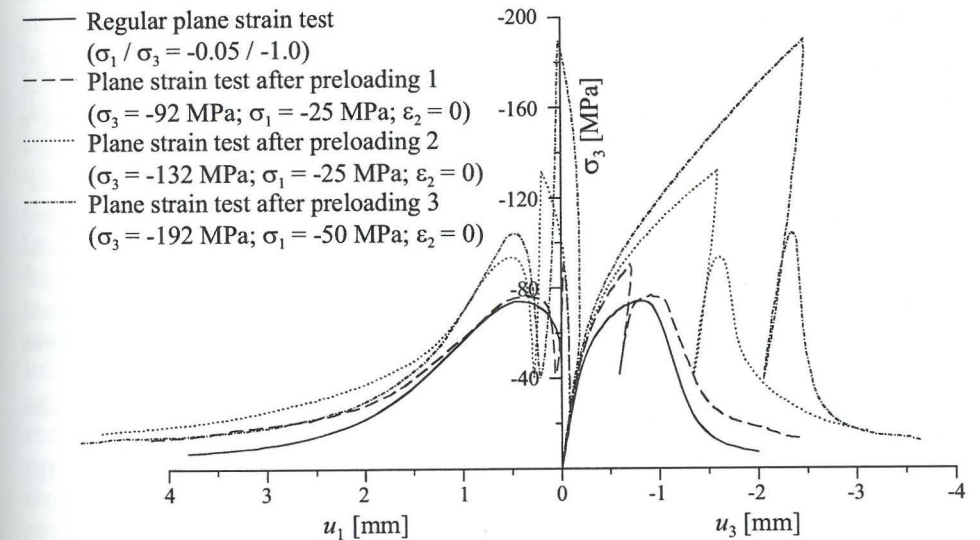


Figure 3.18. Ultimate strength in multiaxial compression with and without multiaxial compressive preloading [Van Geel<sup>1998</sup>].

When multiaxial compressive preloading is followed by a *multiaxial* compressive test, inconsistent test results are reported in literature. As stated in section 2.1.1.2, tests performed by Gerstle et al<sup>1978</sup>, Smith et al<sup>1989</sup> and Imran & Pantazopoulou<sup>1996</sup> showed no evidence for path-dependency on the triaxial strength of concrete. On the

other hand, Kotsovos<sup>1979</sup> actually found the strength results somewhat dependent on the maximum achieved hydrostatic stress level during different loading paths.

As the loading path variations in the pre-peak regime of the above test series were rather small, Van Geel<sup>1998</sup> investigated this phenomenon experimentally by testing several concrete cubes with substantial differences in multiaxial compressive preloading. After preloading, each specimen was loaded up to failure according to a multiaxial proportional loading path, the same for all tests (plain strain configuration with  $\sigma_1 / \sigma_3 = -0.05/-1.0$ ). All preloadings did not exceed stage II, so cracking was mainly restricted to the ITZ. Figure 3.18 shows the results of these multiaxial compression tests with and without preloading. A strong path-dependency is observed. Moreover, while the *uniaxial* compressive strength *decreases* upon high preloading with high confinement (figure 3.17), it appears that the *multiaxial* compressive strength *increases* upon similar preloadings.

This phenomenon of strength increase upon high multiaxial compressive preloading with high confinement may be explained by considering the process of mesoscopic crack growth. As was stated in section 3.1.2.2, initial macroscopic cracking in multiaxial compression is characterised by the growth of ITZ cracks around the aggregate grains and the growth of these cracks through the bulk cement paste, according to mechanism 3 (see figure 3.6). Crack growth according to this mechanism leads to the concentration of forces in the ‘contact area’ of the crack (figure 3.8). Considering the fact that the strength of concrete is highly dependent on the presence of lateral confinement, the local stress state at the contact area of the crack – with increasing confinement upon further crack growth – becomes invariably less favourable for crack growth according to mechanism 3. Hence, a strengthening mechanism is induced. This mechanism of crack growth proceeds – *with invariably increasing load* – until the crack grows fully around the ‘locked’ aggregate grain, or until failure through the aggregate grain occurs. Note that strengthening due to aggregate interlock, as described above, can only be supposed for brittle heterogeneous materials with strong inclusions, such as normal strength concrete, loaded in multiaxial compression. Accordingly, the influence of lateral confinement on strength will be substantially larger for the highly heterogeneous concrete composite than for its – more homogeneous – separate components.

The extent of strengthening due to aggregate interlock, and consequently, the influence on strength of lateral confinement, depends on three factors:

- The strength of the aggregate grains related to the strength of the ITZ and the bulk cement paste.
- The size of the aggregate grains
- The distance between the aggregate grains

These factors are properties of the concrete mix. However, the distance between the aggregate grains depends not only on the mesostructure of the concrete mix *prior to* loading, but may change also *during* loading. As indicated in figure 3.19, ‘contact areas’ of a potential macroscopic crack – defined as those areas where the opposite crack faces remain in contact during a sliding displacement – are situated at those locations where the local crack angle  $\alpha$  is maximum. These locations correspond to

the regions where massive compressive pore collapse within the ITZs has occurred at stage II.

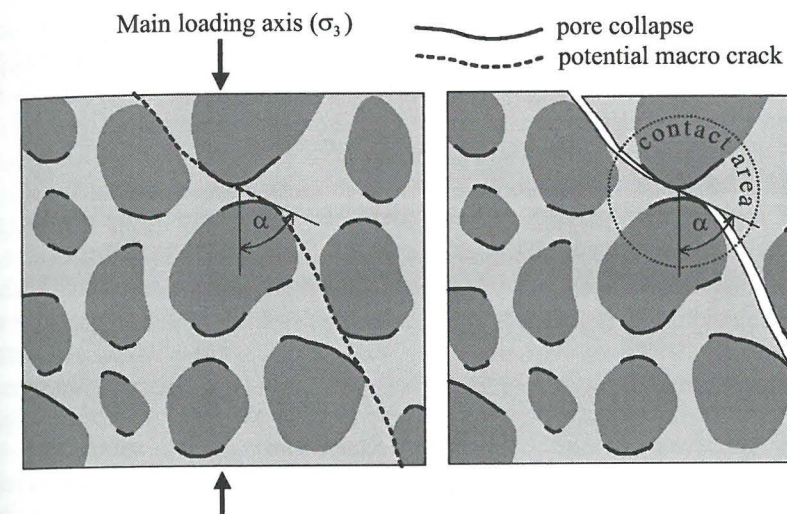


Figure 3.19. Designation of ‘contact areas’ along the crack path of a potential macro crack coinciding with regions of compressive pore collapse.

Obviously, pore collapse within the ITZs at stage II reduces the distance between the aggregate grains at those locations where the crack faces remain actually in contact during a subsequent sliding displacement, inducing an increase of the maximum local crack angle  $\alpha$ . Consequently, concentration of forces at the contact area results in a local stress state with a higher level of confinement ratio ( $\sigma_1^{loc} / \sigma_3^{loc}$ ), which is less favourable for crack growth.

In this way, the occurrence of massive pore collapse at stage II from a preloading consequently may result indeed in a higher ultimate strength in multiaxial compression. It should be noted that the observed increase of multiaxial strength is limited to those cases where the macroscopic cracks mainly curve around the aggregate grains. Generally, this is observed for specimens loaded in multiaxial compression with low confinement. Macroscopic cracks in specimens loaded in multiaxial compression with high confinement show much more cracking straight through the aggregate grains. Apparently, in the region of high confinement the strength of the concrete is dominated by the strength of the aggregate grains and no substantial effect of preloading on multiaxial compressive strength is expected here. Having this in mind, the test results of Taliencio et al<sup>1999</sup> may better be understood. They performed a series of creep tests on concrete cylinders. After loading these cylinders in a triaxial cell to a certain hydrostatic stress level, the specimens were loaded along the deviatoric plane towards the compressive meridian. At 90 % of the deviatoric strength, the stress level was sustained for a maximum period of about 5 days. After this period the specimens were reloaded to failure along the deviatoric

planes at various hydrostatic stress levels. For the reloading tests in the region of low confinement, a distinct increase of deviatoric strength with respect to the virgin loading (without sustained triaxial stresses) was found. However, the increase of deviatoric strength reduced for the reloading tests at higher hydrostatic stress levels (high confinement region). Assuming that deformations due to pore collapse increase in time upon sustained loading, these results appear consistent with the results of Van Geel.

### 3.2.4 Softening stage (IV)

At stage IV, decrease of strength and evolution of large macroscopic cracks (see figure 3.10.c-f) are observed at the macro level. The mechanical behaviour is determined by increasing deformations in the localised macroscopic cracks while the continuum in between these macroscopic cracks unloads. These phenomena are clearly shown in figure 3.20. This figure shows a plane strain multiaxial compression test ( $\sigma_1/\sigma_3 = -0.05/-1.0$ ). In this particular test, not only the overall stress-deformation behaviour was measured (LVDT's), but also the stress-deformation behaviour of the continuum (strain gauges). By subtracting the averaged continuum stress-deformation behaviour from the overall stress-deformation behaviour, the averaged stress-deformation behaviour of the localised macroscopic crack was obtained.

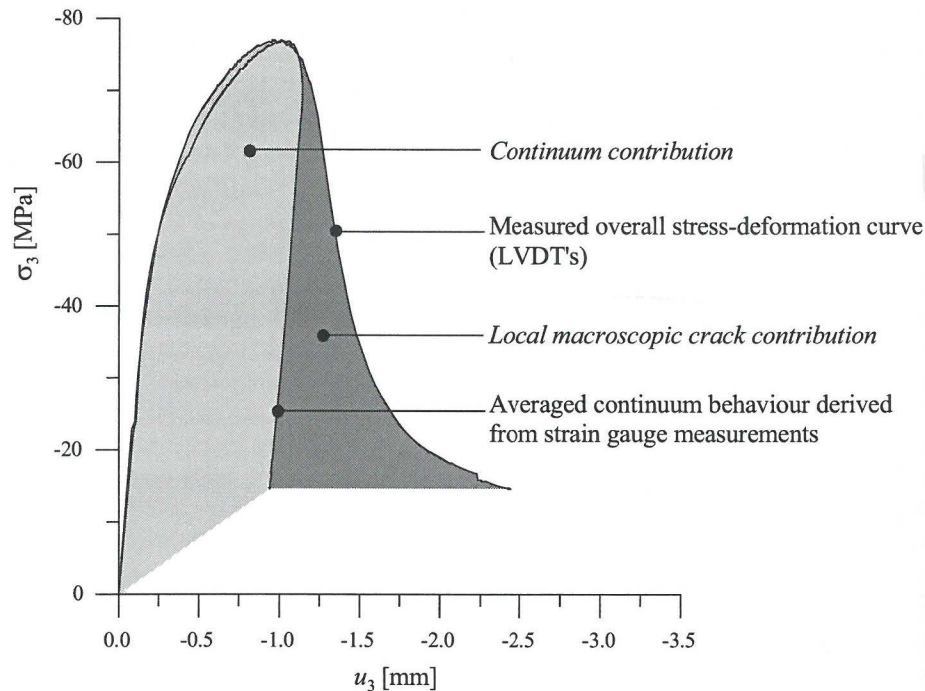


Figure 3.20. Continuum versus local behaviour [Van Geel<sup>1998</sup>].

Hence, during stage IV the deformations are localised in macroscopic cracks. In section 1.1 it was already mentioned that localisation of deformations leads to a strong dependence of the load-deformation response on the geometry and boundary conditions of the concrete structure at hand. As a result, the load-deformation behaviour at stage IV cannot be evaluated apart from the geometry and boundary conditions of the structure/specimen.

With identical geometry and boundary conditions and concrete mix, the shape of the overall  $\sigma-u$  curves still may differ considerably depending on loading path and the extent of confining pressure. The development of volumetric deformation as depicted in figure 2.6 in chapter 2 shows the influence of the extent of confining pressure. It appears that – at the softening stage IV – the incremental dilation of the specimen (with respect to the volume at peak stress) is much more for low confining pressures than for high confining pressures. The observed magnitude of difference in dilation cannot be ascribed to the continuum behaviour of the specimens because the unloading branches of the continuum parts differ only slightly. Hence, the differences in dilation arise from the differences in mechanical behaviour of the macroscopic cracks.

A variety of researchers have proposed models to describe the mechanical behaviour of a fully-grown – shear loaded – crack in concrete. Although a good agreement with experimental data is accomplished, empirical models such as the ‘rough crack model’ of Bažant & Gambarova<sup>1980</sup>, provide little insight in the mechanics of the problem. More insight is provided by the so-called physical models, which consider the geometrical structure of a fully-grown crack at the meso level [Fardis & Buyukozturk<sup>1979</sup>; Walraven<sup>1980</sup>; Li et al<sup>1989</sup>; Divakar & Fafitis<sup>1992</sup>]. In these models, overall roughness of a crack is regarded as a superposition of ‘mesoscopic roughness’, i.e. the roughness of a tortuous crack around interlocking aggregate grains discernible at the meso level (figure 3.21), and ‘microscopic roughness’, i.e. the roughness of the cement paste (bulk or ITZ) along the tortuous mesoscopic crack discernible at the micro level only. When a crack – as shown in figure 3.21 – is loaded in shear, sliding will occur. Because interlocking grains block this sliding deformation, contact points between the aggregate grains and the cement paste will be formed. Upon further sliding forces build up at these contact points until either:

- The upper part overrides the interlocking aggregate grain of the lower part. In this case the local shear force at the contact point exceeds the resisting frictional force. This resisting frictional force is determined by the extent of microscopic roughness and the magnitude of the local normal compressive force at the contact point.
- The cement paste crushes at the contact point.
- The interlocking aggregate grain fractures.

Which mechanism prevails in a particular situation depends on the properties of the concrete mix (local contact angle at the contact point, strength of the aggregate grains and the cement paste) and the compressive stress normal to the global direction of the macroscopic crack. This means that for very high confining pressures crushing of the cement paste or fracturing of the aggregate grains will

prevail, whereas for very low confining pressures overriding prevails. As the 'overriding' mechanism is the only mechanism causing substantial crack dilation, macroscopic observation of decreasing crack dilation signifies increasing confining pressures.

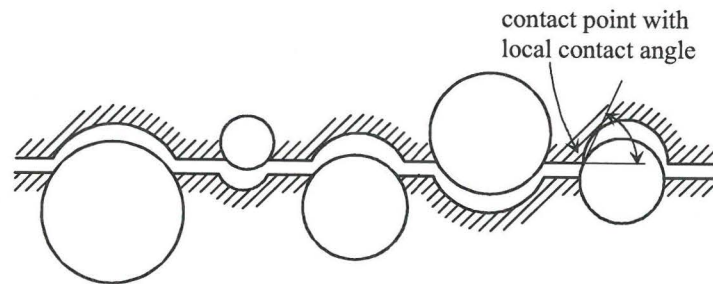


Figure 3.21. Tortuous crack due to aggregate interlock [Walraven<sup>1980</sup>].

At stage IV, the shape of the descending branch in the loading diagram of the main loading axis is highly dependent on the loading path also. Figure 3.22 shows the loading diagrams of three plane strain compression tests, each with a different loading path, but with identical test setup and concrete mix. It appears that the 'ductility' of the softening branch increases when the direction of the loading path becomes more perpendicular to the (schematic) bounding envelope of ultimate strength.

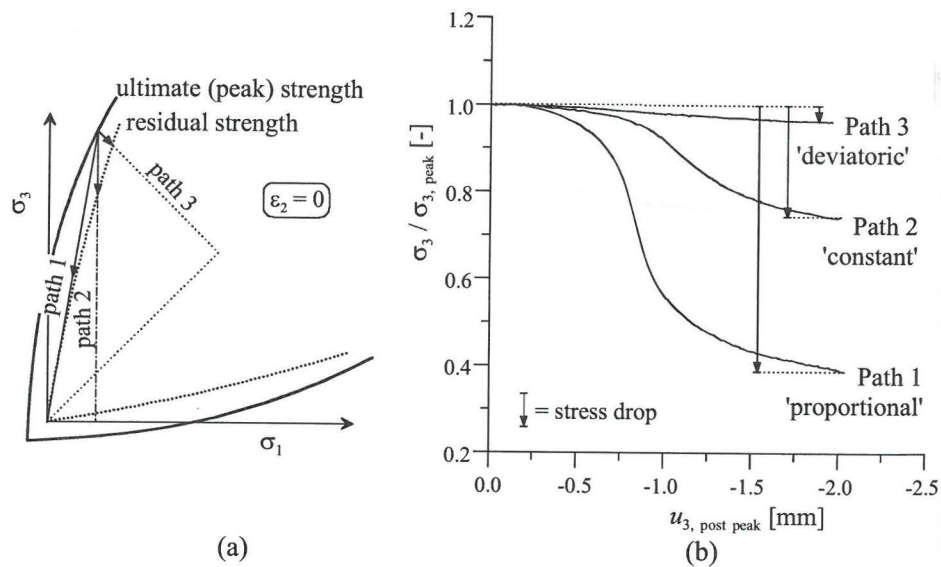


Figure 3.22. Softening branches (b) of multiaxial plane strain compression tests (a). (Proportional path:  $\sigma_1 / \sigma_3 = -0.15 / -1.0$ ).

For these tests, (schematic) bounding envelopes of ultimate and residual strength are constructed in figure 3.22.a. It can be seen that loading beyond ultimate strength along a 'deviatoric' stress path (perpendicular to the plane strain 'hydrostatic' axis) towards the envelope of residual strength leads to a small stress drop only, while a proportional stress path leads to a very large stress drop beyond ultimate strength. The residual strength in multiaxial compression tests is mainly determined by the capacity of transfer of shear forces across the fully-grown mode II cracks at large sliding displacements. At these large sliding displacements, no intact continuum junctions between the opposite crack faces exist anymore. The residual capacity of shear force transfer at large sliding displacements exclusively is based on internal friction. Worded differently, transfer of shear forces at large sliding displacements is possible due to aggregate interlock (mesoscopic roughness) and microscopic roughness of the crack only, provided that compressive forces exist normal to the crack.

The gradual transition from ultimate to residual strength in multiaxial compression coincides with the growth of macroscopic cracks with increasing crack opening, as shown in figure 3.10.c-f. Although not visualised in figure 3.10, it should be emphasized that the concrete parts not divided by visible macroscopic cracks are heavily damaged also due to mesoscopic cracking at stage II and III.

Basically, the (gradual) diminishing capacity of shear force transfer across the growing macroscopic cracks at stage IV can be explained by two phenomena:

- Loss of cohesive strength, i.e. fracture of 'intact' concrete parts along the path of growing macroscopic cracks.
- Decreasing frictional resistance against sliding due to decreasing roughness of the macroscopic crack.

The first phenomenon causes highly brittle behaviour and produces a brittle softening branch as observed in tensile tests [Van Mier<sup>1992</sup>]. The softening branch in multiaxial compression tests is much more ductile. It seems therefore that the softening branch in these tests is mainly a result of decreasing frictional resistance against sliding. The loss of cohesive strength mainly occurs during the strengthening mechanisms involving mesoscopic cracking at stage II and III, discussed previously.

As stated above, sliding along a macroscopic crack may involve several (mesoscopic) mechanisms: overriding, crushing of cement paste and aggregate fracture. In fact, all these mechanisms potentially may cause a reduction of roughness. During overriding, the local contact angle decreases at the contact areas of the crack, reducing mesoscopic roughness. Due to polishing of the contact area, also a reduction of microscopic roughness may be expected. Provided that aggregate fracture and/or cement paste crushing occur only at those aggregate grains with highest local contact angle, these mechanisms also may lead to a reduction of mesoscopic roughness, as overriding along the remaining part of the crack takes place at contact areas with lower local contact angles.

Shortly, sliding along macroscopic cracks at stage IV involves a reduction of roughness, which is caused by a complex interaction of mechanisms acting at lower scale levels in the presence of compressive stresses normal to the crack direction.

## CHAPTER 4

### NUMERICAL MODELLING AT THE MESO LEVEL

At a lower scale level than the macro level, concrete is a heterogeneous material. However, even at the macro level, it is nowadays well-known that numerical modelling can only be done properly if the specific properties of the meso- and microstructure of concrete are taken into account. The need for a localization limiter, i.e. an internal length scale as a measure of material heterogeneity in strain softening problems is here illustrative<sup>1</sup>.

There are two fundamental ways of taking into account the heterogeneous meso- and microstructure of concrete:

- Explicit consideration of the geometrical features of the heterogeneous meso- or microstructure, e.g. by generating meso- or microscopic meshes in Finite Element computations.
- Implicit consideration of the heterogeneous meso- and microstructure in the macroscopic constitutive (and possibly kinematic) equations.

For structural engineering purposes, explicit consideration of the *microstructure* of concrete involves, even in a 2D representation, great computational effort. Therefore, the heterogeneous microstructure is generally accounted for in an implicit way. Examples of models with explicit consideration of the *mesostructure* are given in section 2.2. Such models allow typical mesomechanical features – like crack interface bridging and aggregate interlock – to be reproduced by applying rather simple constitutive laws for the separate phases.

Implicit consideration of the heterogeneous meso- and microstructure in the macroscopic constitutive (and possibly kinematic) equations is common practice in models based on continuum solid mechanics (section 2.2.3). Most of these models focus on the behaviour of concrete in tension. Extension of these constitutive models to simulate tensile, compressive as well as multiaxial compressive experiments often leads to complex formulations. Generally, this complexity leads to rather abstract considerations of the mesostructure of concrete and a clear physical meaning of material properties related to the mesostructure is often lacking.

In this chapter, a method is pursued with both explicit and implicit consideration of the mesostructure of concrete. The proposed model will be entitled ‘mesoscopic model’. This mesoscopic model is restricted to two dimensions (plane strain, plane stress). Although this restriction is quite severe when simulating concrete behaviour in general, it will be shown that quite reasonable results are obtained for simulations of uniaxial, biaxial (plane stress) and plane strain tensile or compressive experiments.

---

<sup>1</sup> See section 2.2.3.2

## 4.1 Computational environment

The computations are carried out using the computer code UDEC (Universal Distinct Element Code, Itasca Consulting Group<sup>1993</sup>). At Eindhoven University of Technology, Vonk<sup>1992</sup> also used this code in a previous Ph.D study on the present topic. By using the same computer code, basic elements of this research could be transferred easily to the present study.

UDEC is based on the Distinct Element Method developed by Cundall<sup>1971</sup> and is mainly characterized by:

1. A division of structures into blocks and contacts between these blocks
2. Allowance of large displacements and rotations between blocks
3. Automatic recognition of new contacts as the calculation progresses
4. An explicit dynamic solution procedure

### 4.1.1 Division into blocks and contacts

In UDEC, a structure is split up into blocks by creating a continuous pattern of interfaces through the structure (see figure 4.1). The generated blocks may have any polygonal shape and represent the material volume of the structure.

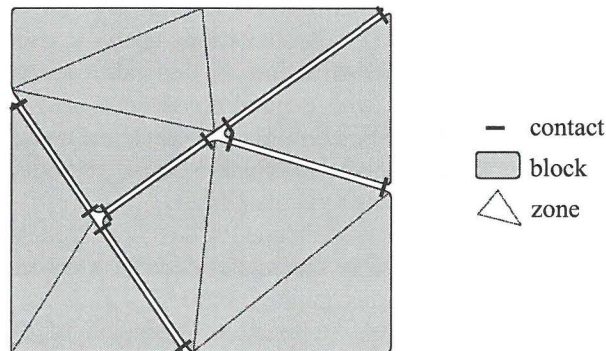


Figure 4.1. UDEC system of blocks (zones) and contacts.

The blocks may be rigid, simply deformable or fully deformable. In the latter case a mesh of finite elements is generated, dividing the block in triangular constant strain elements (called zones in UDEC).

If the corner of a block/zone (nearly) touches another block, a contact is created. Creation of these contacts may occur prior to the calculation but also during the calculation.

### 4.1.2 Explicit finite difference solution scheme

UDEC uses a dynamic explicit finite difference solution scheme, based on Newton's second law of motion and on the assumption that during one calculation cycle (time step) the influence of an incremental load or displacement on one element travels *not* further than its neighbouring elements. The velocities and accelerations are assumed to be constant within a single time step.

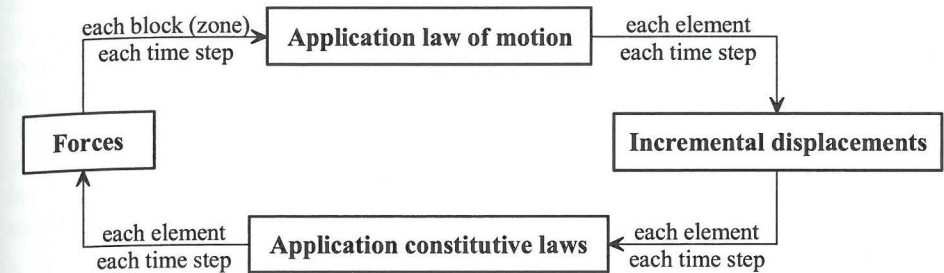


Figure 4.2. Basic calculation cycle for the Distinct Element Method.

Figure 4.2 shows the basic calculation cycle in UDEC. Each time step the law of motion is applied to each block (or zone) and the constitutive laws are applied to each element (blocks (zones) and contacts).

Figure 4.3 shows a one-dimensional illustration of the calculation procedure in case of rigid blocks. At time  $t = 0$  a force  $F$  is applied to block 1. Application of the law of motion results in an acceleration  $\ddot{u} = F/m$  of block 1. At the end of the time step  $\Delta t$  this results in a displacement increment  $\Delta u$  ( $\Delta u = \dot{u}\Delta t = \frac{1}{2}\ddot{u}\Delta t^2$ ). Now the constitutive law for the contacts (assumed: elastic springs with stiffness  $k$ ) is applied. According to this constitutive law the reaction forces in the springs are  $\Delta F = k\Delta u$ . In the next time step the law of motion for block 1 and block 2 is solved, again taking these reaction forces into account.

In this way, boundary information is transmitted through the structure. This explicit step-by-step solution scheme is only valid, however, in case of very small time steps. The critical time step is calculated by UDEC based on the speed of propagation of information through the structure.

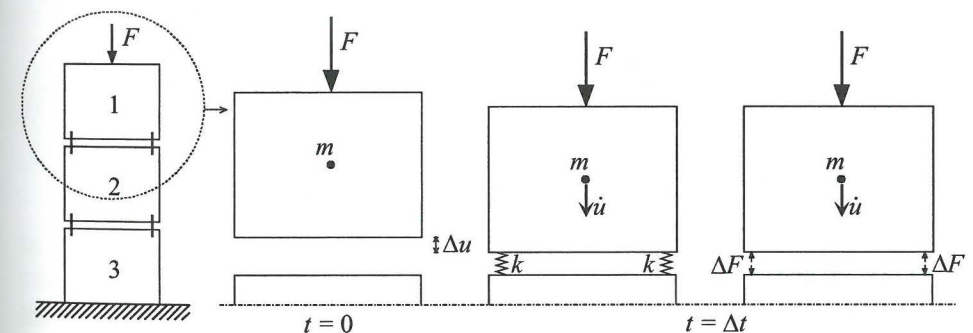


Figure 4.3. Illustrative example of the calculation procedure of UDEC (redrawn from Vonk<sup>1992</sup>).

Though the solution scheme of UDEC is dynamic, quasistatic problems can also be solved. In this case the equations of motion are damped to reach a force equilibrium state as quickly as possible [Cundall<sup>1982</sup>].



Due to the small time step needed in explicit methods in order to obtain numerical stability, these methods are – compared to implicit methods – not very effective if the structural behaviour is rather linear. However the method becomes competitive for highly non-linear problems and when there are changes in the connectivity of the elements.

A major advantage with respect to the development of non-linear constitutive models is that – due to the very small time step in the explicit method – the internal state variables may be assumed constant during the time step. This usually implies great simplifications in the constitutive equations.

## 4.2 Mesh generation

For the generation of Finite Element meshes, resembling the mesostructure of concrete, a 2D mesh generation code has been written at Eindhoven University of Technology. This mesh generation code is adapted from a method used by Vonk<sup>1992</sup> and is documented extensively in Bongers<sup>1998a</sup>.

The generation procedure aims at generating a mesh of coarse aggregate grains randomly positioned in a matrix of mortar. First, a regular pattern of hexagonal shaped aggregate grains is generated (see figure 4.4). Subsequently this pattern is deformed in such a way that the generated grain structure resembles well the irregular distribution of the coarse aggregate grains in a cross section of a real concrete structure (see figure 4.5).

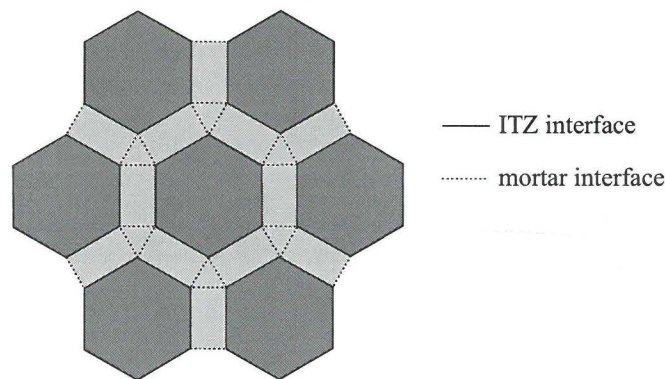


Figure 4.4. Regular pattern of aggregate grains in a mortar matrix.

In the earlier work of Vonk<sup>1992</sup>, an analogous technique was adopted with potential discrete cracks being already explicitly present in the initial mesh in the form of interfaces. Two types of interfaces were distinguished:

- ITZ interfaces, positioned around the coarse aggregate grains and representing the ITZ
- mortar interfaces, connecting the ITZ interfaces in a logical and systematic manner

As a result, interface patterns like the one in figure 4.6, were created.

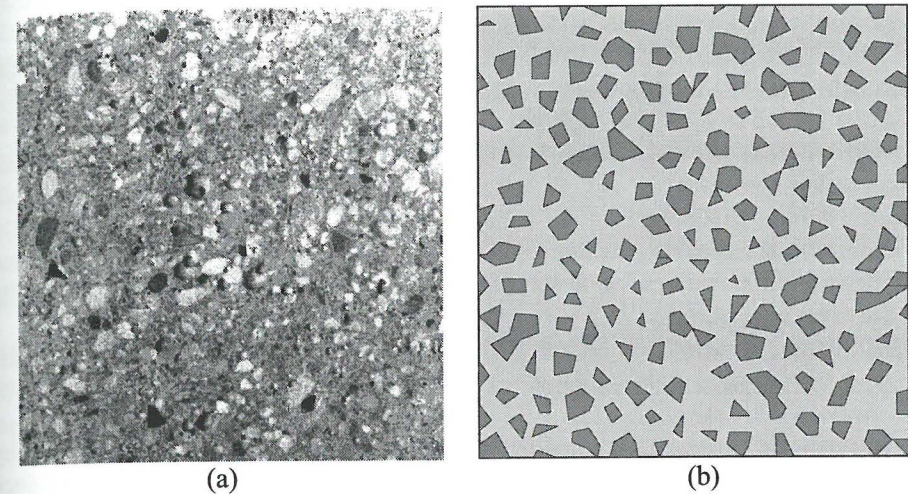


Figure 4.5. (a) Cross section of a concrete cube (casted by Van Geel<sup>1998</sup>). (b) Example of generated pattern of coarse aggregate grains.

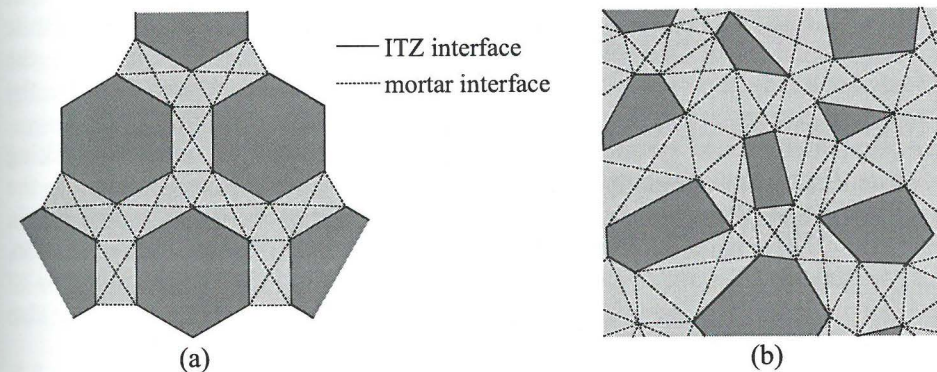


Figure 4.6. (a) Basic interface pattern and (b) randomly disturbed interface pattern [Vonk<sup>1992</sup>].

In the work of Vonk<sup>1992</sup> all potential cracking was restricted to these interfaces, the continuum remained linear elastic. Although this discrete crack approach fits very well within the computational strategy of UDEC, it has some major drawbacks:

- The direction of potential cracks through the mortar is fixed a priori
- Cracking through the aggregate grains is not possible

It depends on the properties of the concrete composite (maximum aggregate size) and the type of loading whether these drawbacks are significant or not. Failure of concrete loaded in tension or in uniaxial compression is characterized by very tortuous crack patterns through the ITZ and bulk cement paste. In these cases the drawbacks mentioned above are not very significant. In triaxial compression

however, failure of concrete is generally characterized by rather straight cracks frequently running through the aggregate grains. As a result of the above drawbacks, the procedure used by Vonk is not capable of reproducing these straight cracks. In general, this leads to a significant overestimation of the strength of a structure loaded in triaxial compression.

As the purpose of this work is to simulate concrete behaviour in triaxial compression, cracking in any direction and through any phase of the concrete material should be allowed for. This may be accomplished by (see also section 2.2):

- Adopting a remeshing technique during the analysis, i.e. insertion of interface elements (discrete cracks) at the onset of cracking in a direction determined by the cracking criterion.
- Allowing the introduction of arbitrarily located displacement jumps at the boundary of conventional finite elements to reproduce the geometric nature of localised cracking.
- Incorporating the effects of cracking through a continuum element by distributing the crack *displacements* over a certain volume in order to produce crack *strains* and preserve the original continuity of the problem formulation (smeared cracking approach).

The first two methods model cracks by introducing displacement discontinuities in the displacement field, which obviously approaches the geometric nature of cracking the most. Yet, the third method is much easier to implement in Finite Element calculations. Despite its limitations – as outlined in section 2.2.3.2 – the smeared cracking approach is therefore adopted and that in its simplest form, i.e. the crack deformations are uniformly distributed over the element width.

For parallel-connected systems, the combination of smeared and discrete cracking leads to displacement incompatibility. This is displayed in figure 4.7. Though the structure is loaded in pure tension, it will only fail if the interfaces 2 and 3 fail in pure shear. For a material like concrete, which is stronger in shear than in tension, the combination of smeared and discrete cracking will result in an overestimation of the failure load. This overestimation will be even more pronounced when also lateral compressive loading is present.

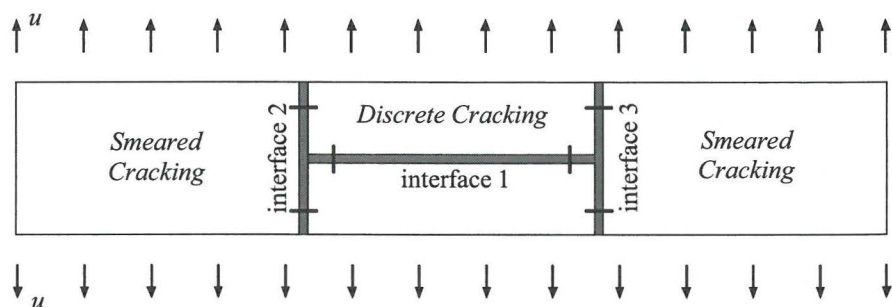


Figure 4.7. Displacement incompatibility for a combination of smeared and discrete cracking.

As the combination of discrete and smeared cracking ends in non-realistic mechanical behaviour for (partly) parallel-connected systems, the present model allows only for smeared cracking. This implies that the ITZ and mortar interfaces (as shown in figure 4.4) do not represent any potential cracks, like they did in the work of Vonk. These interfaces now only divide the structure into (convex) blocks of mortar and coarse aggregates in order to create a realistic heterogeneous material representation.

### 4.3 Constitutive theory (Stage I & II)

The development of a fundamental constitutive theory, which introduces the effects of cracking in the stress-strain relations of the continuum elements (mortar, coarse aggregate grains) of the mesh, is basically divided into two parts:

- A constitutive theory describing the effects of *micro*-cracking, i.e. isolated micro-cracking within the ITZ.
- A constitutive theory describing the effects of *meso*-cracking, i.e. the formation of continuous cracks through ITZ, bulk cement paste and possibly aggregate grains.

The distinction between micro- and meso-cracking is made because of the eminent difference in the scale of heterogeneity involved. At the meso level, the scale of heterogeneity of undamaged concrete is determined by the size of the aggregate grains. The size of micro-cracks within the ITZ does not exceed the size of the aggregate grains. As a result, this type of cracking does not affect the scale of heterogeneity of undamaged concrete.

Meso-cracking, on the other hand, affects the scale of heterogeneity of undamaged concrete considerably. The meso-cracks run along many aggregate grains, the scale of heterogeneity is hence entirely determined by the size of these cracks.

The constitutive theory for meso-cracking (at stage III and IV) is treated in chapter 5. The constitutive theory for micro-cracking is treated in this section.

#### 4.3.1 The concept of a Representative Volume Element (RVE)

The mesh layout consists of two phases, the coarse aggregate grains and the mortar matrix. The mortar is a homogenisation of the heterogeneous mesostructure of fine aggregate grains, bulk cement paste and ITZ.

The averaging method used to establish this homogenisation of the heterogeneous mesostructure of fine aggregate grains, bulk cement paste and ITZ is based on the concept of a Representative Volume Element (RVE). The term RVE was first put forward by Hill<sup>1963</sup>. As continuum mechanics deals with idealized materials consisting of material points and material neighbourhoods, it assumes that the material distribution, the stresses and the strains are essentially uniform in the direct neighbourhood of the material points. However, at the lower (meso and micro) scale levels these quantities are, in general, not uniform at all. For such a heterogeneous micro(meso)structure, an RVE at a material point of a continuum mass is a material

volume that is statistically representative of the infinitesimal material neighbourhood of that material point. To be representative, the RVE should, for randomly ordered meso- or microstructures, include a very large number of such meso- or microheterogeneities. If the material has a periodic meso- or microstructure, the RVE can be reduced to one unit cell.

In recent years, the RVE approach has among others been used by Chang<sup>1993</sup> for granular materials, by Onck et al<sup>1997</sup> for polycrystalline metals and by Smit<sup>1998</sup> for heterogeneous polymers. They used either an RVE of many microheterogeneities (Chang) or a unit cell for – assumed – periodic microstructures (Onck, Smit). In all cases the boundary conditions of the macroscopic element are applied to the RVE. Subsequently, using the Finite Element Method, the response of the RVE is calculated. This response is assumed to be representative of the whole macroscopic element. In this way, computer time is reduced considerably compared to Finite Element computations of the entire microstructure.

Although the main objective of the RVE-approach is to gain computer time, the accuracy of the method should also be considered carefully. In this respect, the fundamentals on which an RVE should be based are provided by Nemat-Nasser and Hori<sup>1993</sup>:

*'Perhaps one of the most vital decisions that the analyst makes is the definition of the RVE. An optimum choice would be one that includes the most dominant features that have first-order influence on the overall properties of interest and, at the same time, yields the simplest model.'*

Consequently, the dominant features having a first-order influence on the mechanical behaviour of concrete in multiaxial compression have to be established. These features have been explained in chapter 3. Delimiting our analysis to the stages I and II, the most dominant features are the elastic properties of the concrete composite (depending on the volume ratio's and the elastic properties of the separate components) and isolated crack formation in the ITZ. Taking the basic part of the concrete volume of figure 3.13 as an RVE in the form of a unit cell, then these most dominant features can be accounted for.

The circular-shaped schematised unit cell as displayed in figure 3.13 produces isotropic behaviour. This corresponds with the initial behaviour of real concrete that – except for the influence of the casting direction – is more or less isotropic. Disregarding the influence of the casting direction, the initial isotropy of the concrete volume is thus accounted for by the circular-shaped unit cell. Although an assembly of circular shaped unit cells cannot fill the volume completely, this is not considered an essential drawback. The adopted circular-shaped RVE for the concrete mesostructure is not a unit cell in the sense that an assembly of such identical cells fills the material volume, but merely a representative shape of an assembly of irregularly shaped and sized cells.

The circular cylinder displayed in figure 4.8 is hence the most simple model that accounts for the dominant features of concrete in multiaxial compression at stage I and II and is therefore taken as the RVE for normal strength concrete.

With respect to the meshes described in section 4.2, the dimensions of the RVE for the coarse aggregate grains are given by

$$R_1 = \sqrt{\frac{A_{agg}}{\pi}}$$

$R_2 - R_1$  = average thickness of ITZ around coarse aggregate grains

$R_3 - R_2$  = average thickness of bulk cement paste around coarse aggregate grains

with

$A_{agg}$  = area of the block representing a coarse aggregate grain

The dimensions of the RVE for each mortar continuum element are determined by the properties of the concrete mix (except for the coarse aggregate grains), i.e. the average radius of the fine aggregate grains and the volume ratio of fine aggregate grains, bulk cement paste and ITZ.

$R_1$  = average radius of fine aggregate grains

$$\frac{R_2^2 - R_1^2}{R_1^2} = \frac{V_{ITZ}}{V_{agg}^{fine}}$$

$$\frac{R_3^2 - R_2^2}{R_1^2} = \frac{V_{bulk}}{V_{agg}^{fine}}$$

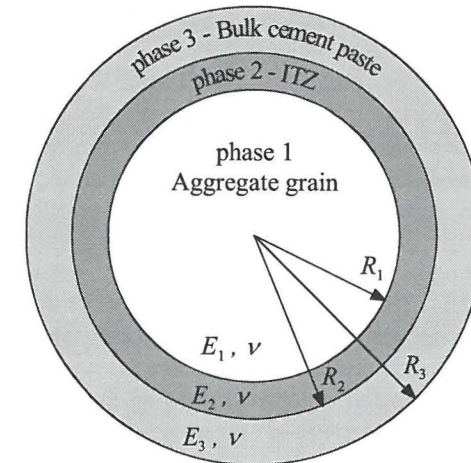


Figure 4.8. RVE for normal strength concrete.

#### 4.3.2 RVE calculation scheme

Within the basic calculation cycle of UDEC (figure 4.2), the RVE-concept is used only within the procedure "application constitutive laws". For each continuum element UDEC provides macro-strain increments  $\Delta \epsilon^m$  and the initial macro-stress state  $\sigma^{0,m}$  – according to the global  $(x,y,z)$  coordinate system – as input for the constitutive laws (index  $m$  for macro). As output UDEC requests the final macro-

stress state  $\underline{\sigma}^{1,m}$ . Figure 4.9 shows the RVE calculation scheme, which includes the effects of ITZ cracking and provides the requested final macro-stress state  $\underline{\sigma}^{1,m}$ .

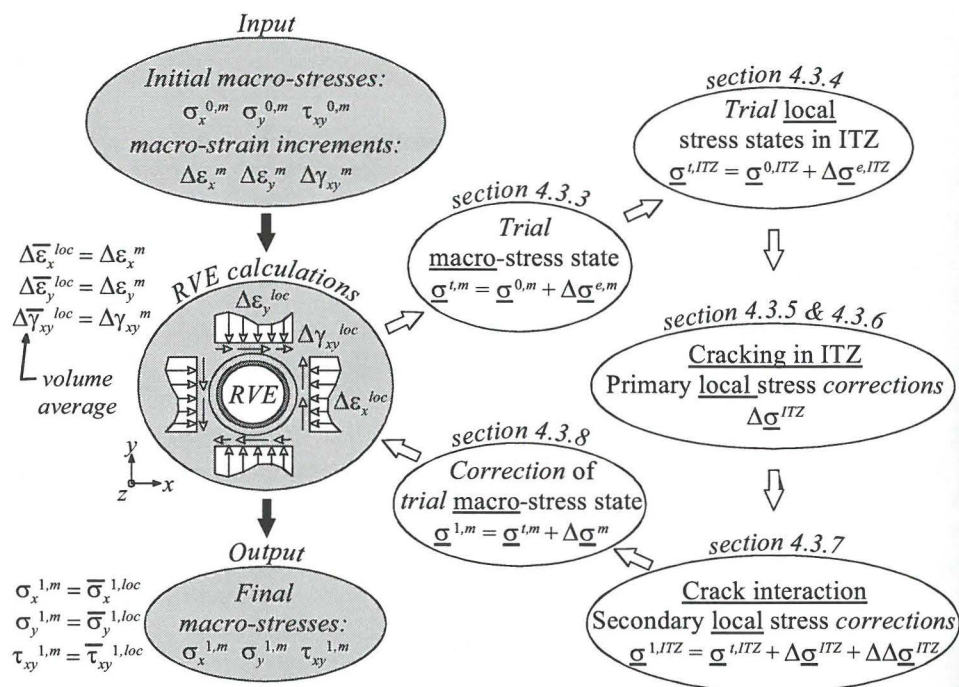


Figure 4.9. Overview of RVE calculation scheme.

The RVE is loaded by the macro-strain increments  $\Delta \epsilon^m$  provided by UDEC. From the definition of the RVE, the stresses and displacements at the outer boundary of the RVE must resemble the (uniform) macro-stress and displacement fields at the material point considered. As outlined in appendix A, these conditions can only be satisfied approximately along the outer boundary of the RVE. Worded differently, the local distributions of both incremental stresses and displacements at the outer boundary of the RVE can resemble the uniform macroscopic distributions only in an average sense.

Generally, two bounds for the distribution of outer-boundary stresses and displacements may be indicated [Nemat-Nasser & Hori<sup>1993</sup>]. The first bound refers to the case that the distribution of outer-boundary 'strain' increments  $\Delta \epsilon^{loc}$  (outer-boundary displacements divided by the width of the RVE at a specific point on the outer boundary) equals the uniform distribution of the macro-strain increments. These conditions of constraint will be referred to as *macro-strain* conditions of constraint. The second bound refers to the case that the distribution of stress increments at the outer boundary of the RVE is uniform. These uniform stress conditions of constraint will be referred to as *macro-stress* conditions of constraint.

For linear elastic material behaviour, these bounds for the distribution of outer-boundary stresses and displacements are given in appendix A. In this case and with the given macro-strain increments  $\Delta \epsilon^m$ , the true distribution of local incremental displacements at the outer boundary of the RVE may vary between the elastic macro-strain and the macro-stress distribution. When the material behaviour changes from elastic to elasto-plastic at stage II, the distribution of outer-boundary displacements may somewhat change. However, as the RVE is also *representative* at this stage, the distribution of outer-boundary displacements still has to resemble approximately the uniform macroscopic displacement field. It seems therefore legitimate to apply in this case the same procedure to determine the distribution of local outer-boundary incremental displacements as applied in the case of linear elastic material behaviour.

The mechanical response of the RVE upon the imposed conditions of constraint may be computed by means of finite (or distinct) element computations. In the present approach, however, the response is computed analytically. In this way, again a considerable gain in computation time is accomplished. The procedure pursued is indicated in figure 4.9 and is explained below.

According to the selected distribution of outer-boundary incremental displacements, a *trial* macro-stress state is computed by adding *elastic* macro-stress increments to the initial macro-stress state. To this end, *effective* elastic moduli for the RVE are determined in section 4.3.3, establishing a linear relationship between the macro-strain increments and the elastic macro-stress increments.

At stage I and II, cracking is restricted to the ITZ. Hence, the *local* stresses within this zone have to be checked upon a certain cracking criterion. To this end, a stress-based cracking criterion is developed in section 4.3.6. To check whether the *local* stress state at certain places in the ITZ violates this cracking criterion, *local* trial stress states are computed in an adequate number of points within the ITZ by adding elastic *local* stress increments to the initial *local* stress states (section 4.3.4). If a local trial stress state violates the cracking criterion, the local stress state in that point is corrected. These 'primary' stress corrections do not take into account any crack interaction effects. Such crack interaction effects are allowed for after calculation of all primary stress corrections within the ITZ. This results in secondary (minor) corrections of the local ITZ stress states (section 4.3.7).

Based on the computed stress corrections in the ITZ, section 4.3.5 shows how the local internal state variables (crack displacements) in the ITZ are computed and how the local stress corrections in the ITZ affect the stress state at the outer boundary of the RVE. Based on the obtained distribution of stress corrections at the outer boundary, the correction of the trial (elastic) macro-stress state is determined in section 4.3.8.

#### 4.3.3 Effective elastic moduli for the RVE

In literature, a wide range of models is presented for the determination of effective elastic properties of heterogeneous materials. The earliest and simplest models were based on the assumption that the material (in this case concrete) consists of two

phases: aggregate grains and cement paste. These early models involved simple mixing rules such as a volume-average of the stiffnesses [Voigt<sup>1889</sup>] or a volume-average of the compliances [Reuss<sup>1929</sup>]. Among others Hirsch<sup>1962</sup> suggested empirical expressions for the estimation of Young's modulus of mortar or concrete. More sophisticated models consider the cement paste as the connecting phase with disconnected ellipsoidal aggregate inclusions as the second phase. A review of these models is given by Nemat-Nasser and Hori<sup>1993</sup>.

More recently, models incorporate the influence of the ITZ. In these models a three-phase composite consisting of spherical aggregate grains, bulk cement paste and ITZ is modelled. Some of these models only use estimates of average stress and displacement field solutions [Yang<sup>1998</sup>, Lutz et al<sup>1997</sup>]. Other models are based on exact analytical solutions of the stress and displacement fields for distinct loading cases. Ramesh et al<sup>1996</sup> analysed the stress and displacement fields for an assembly of three composite spheres with a common centre embedded in an infinite equivalent homogeneous solid under hydrostatic and shear loading at infinity. This resulted in a rather simple solution for the overall bulk modulus whereas the solution for the overall shear modulus is very complicated. Zhao & Chen<sup>1996,1998</sup> analysed a 2D (plane stress) assemblage of two aligned and co-centred composite cylinders of circular cross sections embedded in an infinite solid of cement paste subjected to a uniaxial tensile stress at infinity (figure 4.10).

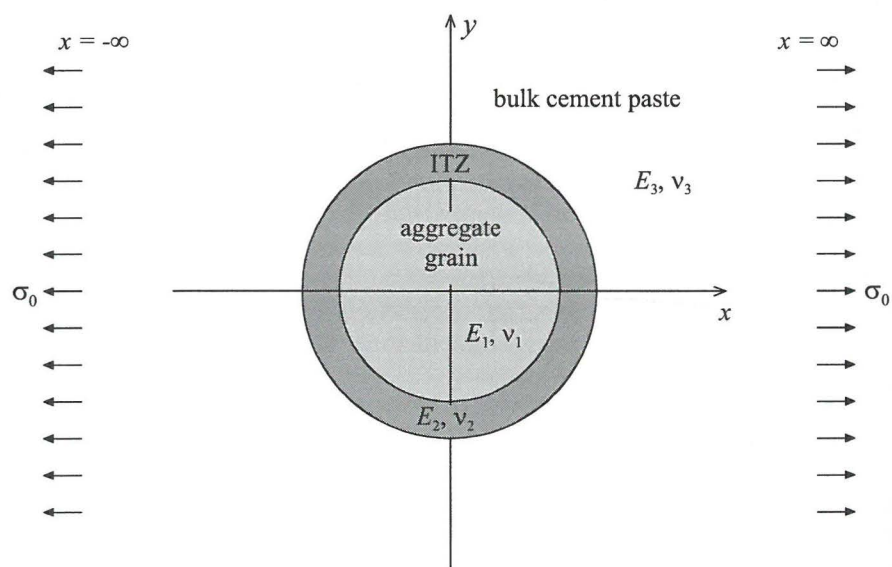


Figure 4.10. Model of microstructure of concrete [Zhao & Chen<sup>1996</sup>].

As the present RVE calculation scheme not only requires the effective elastic moduli but also the true stress distribution in the ITZ, a method is pursued resembling Zhao & Chen<sup>1996,1998</sup>. Yet instead of embedding the composite cylinders

of aggregate and ITZ in an infinite solid of cement paste, the stress/displacement fields are solved analytically for the RVE as displayed in figure 4.8 for two elementary stress-strain states. This method yields linear equations for the effective elastic moduli and exact stress/displacement fields in the ITZ for the considered stress-strain states (see appendix A). In section 4.3.4 it is shown that the elastic stress/displacement distribution in the ITZ for an arbitrary stress-strain state may be computed by a linear combination of the elementary stress-strain states considered in appendix A.

The expressions for the effective elastic moduli, derived in appendix A, are a function of the individual elastic moduli ( $E, \nu$ ) and the radii  $R_1, R_2$  and  $R_3$ . These expressions assume different Young's moduli, yet Poisson's ratio is equal for all phases. This assumption simplifies the expressions for the global moduli considerably and, whereas information about Young's modulus of the separate phases is scarce, little to nothing is known about Poisson's ratio of the separate phases.

With the given expressions for the in-plane effective elastic moduli ( $\bar{E}_{r\theta}, \bar{\nu}_{r\theta}$ ) and the out-of-plane effective Young's modulus  $\bar{E}_z$ , the in-plane macro-stresses and macro-strains in the global, Cartesian coordinate system ( $x, y, z$ ) are related to one another through

$$\begin{bmatrix} \Delta\sigma_x^{e,m} \\ \Delta\sigma_y^{e,m} \\ \Delta\tau_{xy}^{e,m} \end{bmatrix} = \begin{bmatrix} \bar{K} + \bar{G} & \bar{K} - \bar{G} & 0 \\ \bar{K} - \bar{G} & \bar{K} + \bar{G} & 0 \\ 0 & 0 & \bar{G} \end{bmatrix} \begin{bmatrix} \Delta\varepsilon_x^m \\ \Delta\varepsilon_y^m \\ \Delta\gamma_{xy}^m \end{bmatrix} \quad (4.1)$$

with

$$\bar{K} = \frac{\bar{E}_{r\theta}}{2 \left( 1 - \bar{\nu}_{r\theta} - 2\nu^2 \frac{\bar{E}_{r\theta}}{\bar{E}_z} \right)} \quad \text{and} \quad \bar{G} = \frac{\bar{E}_{r\theta}}{2(1 + \bar{\nu}_{r\theta})}$$

#### 4.3.4 Elastic stress distribution in the ITZ

Computations involving the RVE-approach not only cover the elastic behaviour (stage I) of the material, but also isolated crack formation in the ITZ at stage II. Isolated crack formation occurs when the ITZ stresses reach a certain critical value (see section 4.3.6).

To check whether the ITZ stresses reach a critical value, 'trial' stress states in the ITZ are computed by adding elastic stress increments to the initial stress states. Obviously, this procedure requires the distribution of elastic stress increments in the ITZ. In appendix A, exact solutions for this distribution of stress increments are given for two elementary stress-strain states (figure 4.11) in cylindrical coordinates. Furthermore, a distinction is made between a macrostress approach (uniform stress

boundary conditions) and a macrostrain approach (uniform displacement boundary conditions).

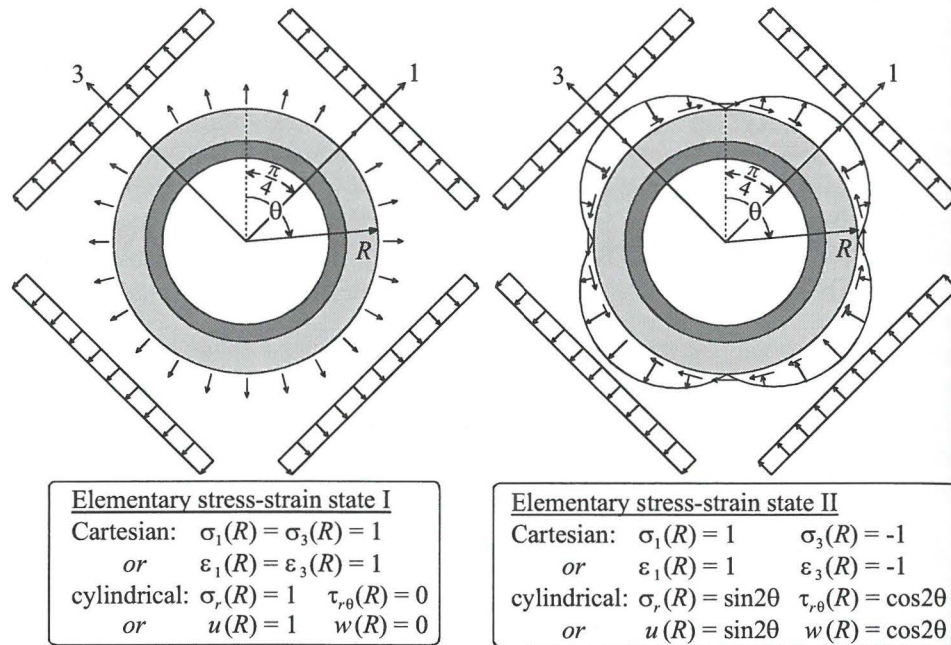


Figure 4.11. Elementary stress-strain states in cylindrical and Cartesian coordinates.

Converting the two elementary stress-strain states from cylindrical  $(r, \theta)$ -coordinates to Cartesian coordinates according to the principal 1,3-axes, results in simple, uniform distributions for these states. Furthermore it appears that any uniform macroscopic stress-strain state can be written as a linear combination of these two elementary states.

Figure 4.12 shows the conversion from the cylindrical coordinate system to the Cartesian  $(1,2,3)$ -coordinate system oriented according to the principal directions, with the 2-axis in the out-of-plane direction.

For elementary stress-strain state I ( $\tau_{r\theta} = 0$ ) this results in the following expressions:

macrostress approach:

$$F_1 = F_r \cos\left(\frac{\pi}{4} - \theta\right)$$

$$F_3 = F_r \sin\left(\frac{\pi}{4} - \theta\right)$$

macrostrain approach:

$$u_1 = u(R) \cos\left(\frac{\pi}{4} - \theta\right)$$

$$u_3 = u(R) \sin\left(\frac{\pi}{4} - \theta\right)$$

$$\sigma_1^m = \frac{F_1}{\cos\left(\frac{\pi}{4} - \theta\right) R d\theta} = \sigma_r = 1$$

$$\sigma_3^m = \frac{F_3}{\sin\left(\frac{\pi}{4} - \theta\right) R d\theta} = \sigma_r = 1$$

$$\varepsilon_1^m = \frac{u_1}{\cos\left(\frac{\pi}{4} - \theta\right) R} = \frac{u(R)}{R} = \frac{1}{R}$$

$$\varepsilon_3^m = \frac{u_3}{\sin\left(\frac{\pi}{4} - \theta\right) R} = \frac{u(R)}{R} = \frac{1}{R}$$

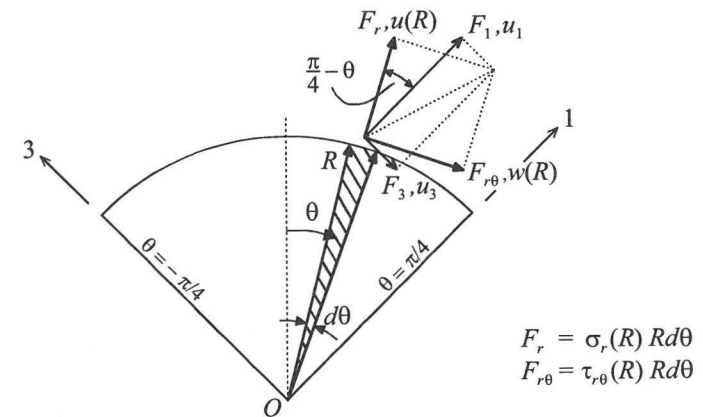


Figure 4.12. Conversion from cylindrical to Cartesian coordinates.

For elementary stress-strain state II (macrostress) the expressions for the principal macro-stresses are:

$$F_1 = \left( \sin 2\theta \cos\left(\frac{\pi}{4} - \theta\right) + \cos 2\theta \sin\left(\frac{\pi}{4} - \theta\right) \right) R d\theta$$

$$F_3 = \left( \sin 2\theta \sin\left(\frac{\pi}{4} - \theta\right) - \cos 2\theta \cos\left(\frac{\pi}{4} - \theta\right) \right) R d\theta$$

$$\sigma_1^m = \frac{F_1}{\cos\left(\frac{\pi}{4} - \theta\right) R d\theta} = \sin 2\theta + \cos 2\theta \tan\left(\frac{\pi}{4} - \theta\right)$$

$$\sigma_3^m = \frac{F_3}{\sin\left(\frac{\pi}{4} - \theta\right) R d\theta} = \sin 2\theta - \frac{\cos 2\theta}{\tan\left(\frac{\pi}{4} - \theta\right)}$$

With

$$\tan\left(\frac{\pi}{4} - \theta\right) = \frac{1 - \sin 2\theta}{\cos 2\theta}$$

$$\frac{1}{\tan\left(\frac{\pi}{4} - \theta\right)} = \frac{1 + \sin 2\theta}{\cos 2\theta}$$

this results in the following expressions for the principal macro-stresses

$$\sigma_1^m = 1$$

$$\sigma_3^m = -1$$

Likewise, it can be derived that the elementary state II implies uniform macro-strains in Cartesian 1,3-coordinates when the macrostrain approach is pursued.

$$\varepsilon_1^m = \frac{1}{R}$$

$$\varepsilon_3^m = -\frac{1}{R}$$

To derive elastic ITZ stress increments  $\Delta\sigma^{e,ITZ}$  in an arbitrary part of the ITZ – of which the location is specified by the angle  $\theta$  – it is convenient to define a Cartesian coordinate system  $(n,t,z)$  with the  $n$ -axis coinciding with the  $r$ -axis at the above angle  $\theta$  (see figure 4.13). According to such a rotated  $(n,t,z)$  coordinate system, any vector of uniformly distributed elastic stress (or strain) increments at the outer boundary of the RVE can be written as a linear combination of the two elementary states above.

$$\text{macrostress approach: } \begin{bmatrix} \Delta\sigma_n^{e,m}(\theta) \\ \Delta\sigma_t^{e,m}(\theta) \\ \Delta\tau_{nt}^{e,m}(\theta) \end{bmatrix} = p^I \begin{bmatrix} 1 \\ 1 \\ 0 \end{bmatrix} + p^{II} \begin{bmatrix} \sin 2\theta \\ -\sin 2\theta \\ \cos 2\theta \end{bmatrix} \quad (4.2)$$

(I)                      (II)

$$\text{macrostrain approach: } \begin{bmatrix} \Delta\varepsilon_n^m(\theta) \\ \Delta\varepsilon_t^m(\theta) \\ \frac{1}{2}\Delta\gamma_{nt}^m(\theta) \end{bmatrix} = \varepsilon^I \begin{bmatrix} 1 \\ 1 \\ 0 \end{bmatrix} + \varepsilon^{II} \begin{bmatrix} \sin 2\theta \\ -\sin 2\theta \\ \cos 2\theta \end{bmatrix} \quad (4.3)$$

(I)                      (II)

Figure 4.13 is a graphical representation of equation (4.2). The centre of Mohr's stress circle is determined by state I (multiplied by  $p^I$ ). The radius is determined by the multiplication factor  $p^{II}$  of state II and, finally, the arbitrarily oriented stress state  $[\Delta\sigma_n^{e,m}(\theta), \Delta\sigma_t^{e,m}(\theta), \Delta\tau_{nt}^{e,m}(\theta)]^T$  is determined by the angle  $2\theta$ .

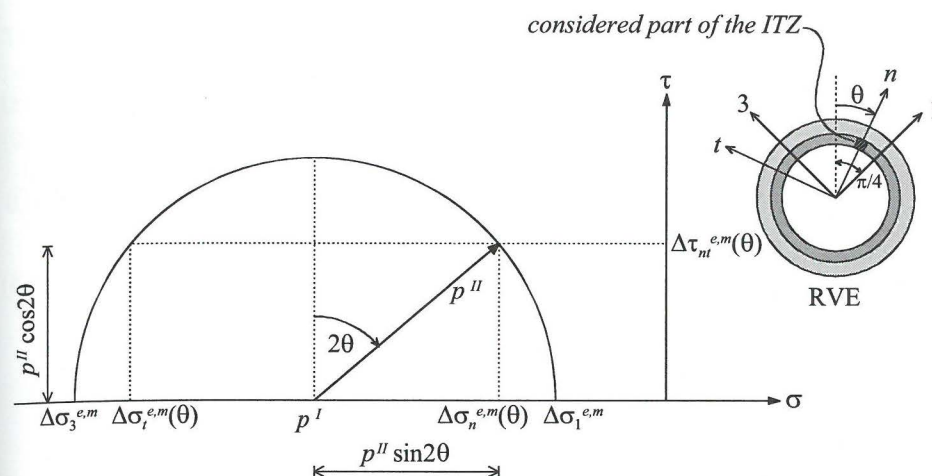


Figure 4.13. Linear combination of elementary stress-strain states I and II.

According to the macrostress approach the quantities  $p^I$ ,  $p^{II} \sin 2\theta$  and  $p^{II} \cos 2\theta$  are derived from the macro-stress increments  $[\Delta\sigma_n^{e,m}, \Delta\sigma_t^{e,m}, \Delta\tau_{nt}^{e,m}]^T$  at angle  $\theta$  using equation (4.2).

$$\begin{aligned} p^I &= \frac{1}{2} \left( \Delta\sigma_n^{e,m}(\theta) + \Delta\sigma_t^{e,m}(\theta) \right) \\ p^{II} \sin 2\theta &= \frac{1}{2} \left( \Delta\sigma_n^{e,m}(\theta) - \Delta\sigma_t^{e,m}(\theta) \right) \\ p^{II} \cos 2\theta &= \Delta\tau_{nt}^{e,m}(\theta) \end{aligned} \quad (4.4)$$

With equation (4.1) these quantities may also be derived from the macro-strain increments  $[\Delta\varepsilon_n^m, \Delta\varepsilon_t^m, \Delta\gamma_{nt}^m]^T$  at angle  $\theta$

$$\begin{aligned} p^I &= \bar{K} \left( \Delta\varepsilon_n^m(\theta) + \Delta\varepsilon_t^m(\theta) \right) \\ p^{II} \sin 2\theta &= \bar{G} \left( \Delta\varepsilon_n^m(\theta) - \Delta\varepsilon_t^m(\theta) \right) \\ p^{II} \cos 2\theta &= \bar{G} \Delta\gamma_{nt}^m(\theta) \end{aligned} \quad (4.5)$$

Following the macrostrain approach the quantities  $\varepsilon^I$ ,  $\varepsilon^{II} \sin 2\theta$  and  $\varepsilon^{II} \cos 2\theta$  are derived directly from the macro-strain increments using equation (4.3).

$$\begin{aligned} \varepsilon^I &= \frac{1}{2} \left( \Delta\varepsilon_n^m(\theta) + \Delta\varepsilon_t^m(\theta) \right) \\ \varepsilon^{II} \sin 2\theta &= \frac{1}{2} \left( \Delta\varepsilon_n^m(\theta) - \Delta\varepsilon_t^m(\theta) \right) \\ \varepsilon^{II} \cos 2\theta &= \frac{1}{2} \Delta\gamma_{nt}^m(\theta) \end{aligned} \quad (4.6)$$

The elastic stresses in the ITZ for the elementary states I and II are given by equations (A.11), (A.19) and (A.27) in appendix A ( $j = 2$ ). A linear combination of these elementary states yields the following expressions for the elastic stress increments, in cylindrical coordinates, at the centreline ( $R_0 = \frac{1}{2}(R_1 + R_2)$ ) of an arbitrary part of the ITZ at angle  $\theta$ :

$$\begin{array}{l} \text{macrostress} \\ \text{approach:} \end{array} \left\{ \begin{array}{l} \Delta\sigma_r^{e,ITZ}(\theta) = \lambda_r^I p^I + \lambda_r^II p^II \sin 2\theta \\ \Delta\sigma_\theta^{e,ITZ}(\theta) = \lambda_\theta^I p^I - \lambda_\theta^II p^II \sin 2\theta \\ \Delta\tau_{r\theta}^{e,ITZ}(\theta) = \lambda_{r\theta}^II p^II \cos 2\theta \end{array} \right. \quad (4.7)$$

$$\begin{array}{l} \text{macrostrain} \\ \text{approach:} \end{array} \left\{ \begin{array}{l} \Delta\sigma_r^{e,ITZ}(\theta) = 2\lambda_r^I \bar{K} \varepsilon^I + 2\lambda_r^II \lambda_0^II \bar{G} \varepsilon^II \sin 2\theta \\ \Delta\sigma_\theta^{e,ITZ}(\theta) = 2\lambda_\theta^I \bar{K} \varepsilon^I - 2\lambda_\theta^II \lambda_0^II \bar{G} \varepsilon^II \sin 2\theta \\ \Delta\tau_{r\theta}^{e,ITZ}(\theta) = 2\lambda_{r\theta}^II \lambda_0^II \bar{G} \varepsilon^II \cos 2\theta \end{array} \right. \quad (4.8)$$

with

$$\lambda_r^I = \frac{A_2}{R_0^2} + 2C_2$$

$$\lambda_\theta^I = -\frac{A_2}{R_0^2} + 2C_2$$

$(A_2, C_2 \rightarrow$   
Appendix A:  
-Section A.2.2)

$$\left. \begin{array}{l} \lambda_0^II = \frac{1}{-3A_3 R_3^2 - 2B_3 - \frac{D_3}{R_3^2}} \\ \lambda_r^II = -2B_2 - \frac{6C_2}{R_0^4} - \frac{4D_2}{R_0^2} \\ \lambda_\theta^II = -12A_2 R_0^2 - 2B_2 - \frac{6C_2}{R_0^4} \\ \lambda_{r\theta}^II = -6A_2 R_0^2 - 2B_2 + \frac{6C_2}{R_0^4} + \frac{2D_2}{R_0^2} \end{array} \right\} \begin{array}{l} (A_2, B_2, C_2, D_2, A_3, B_3, C_3, D_3 \rightarrow \\ \text{Appendix A:} \\ \text{-Section A.3.1.2: macrostress} \\ \text{-Section A.3.2.1: macrostrain} \end{array}$$

From (4.5), (4.6), (4.7) and (4.8) a linear relation is established between the  $(n, t, z)$  macro-strain increments and the elastic stress increments at the centreline of an arbitrary part of the ITZ at angle  $\theta$ .

$$\begin{bmatrix} \Delta\sigma_r^{e,ITZ}(\theta) \\ \Delta\sigma_\theta^{e,ITZ}(\theta) \\ \Delta\tau_{r\theta}^{e,ITZ}(\theta) \end{bmatrix} = \begin{bmatrix} \lambda_r^I \bar{K} + \lambda_r^II \lambda_0^II \bar{G} & \lambda_r^I \bar{K} - \lambda_r^II \lambda_0^II \bar{G} & 0 \\ \lambda_\theta^I \bar{K} - \lambda_\theta^II \lambda_0^II \bar{G} & \lambda_\theta^I \bar{K} + \lambda_\theta^II \lambda_0^II \bar{G} & 0 \\ 0 & 0 & \lambda_{r\theta}^II \lambda_0^II \bar{G} \end{bmatrix} \begin{bmatrix} \Delta\varepsilon_n^m(\theta) \\ \Delta\varepsilon_t^m(\theta) \\ \Delta\gamma_{nt}^m(\theta) \end{bmatrix} \quad (4.9)$$

According to equation (4.9), elastic stress increments can be computed in any point along the centreline of the ITZ. Nevertheless – to avoid excessive computations later on – the number of points along the centreline of the ITZ is limited to 12 (see figure 4.14). Due to the centre-symmetry of the RVE and its boundary conditions, this limits the directions  $\theta_i^*$  to be considered to 6 ( $i = 1, \dots, 6$ ). It is assumed that this discretization of the RVE results in sufficiently accurate results.

To avoid any dependency of the results on the orientation of the RVE, the angle  $\theta_1^*$  (with respect to the global  $y$ -axis) is chosen differently for every finite element in the structure to be analysed. In fact, a random distribution is applied in the range  $(0 \dots \pi/6)$ . Correspondingly, the directions of the remaining ITZs are given by

$$\theta_i^* = \theta_1^* + (i-1) \frac{\pi}{6} \quad (i = 2, \dots, 6)$$

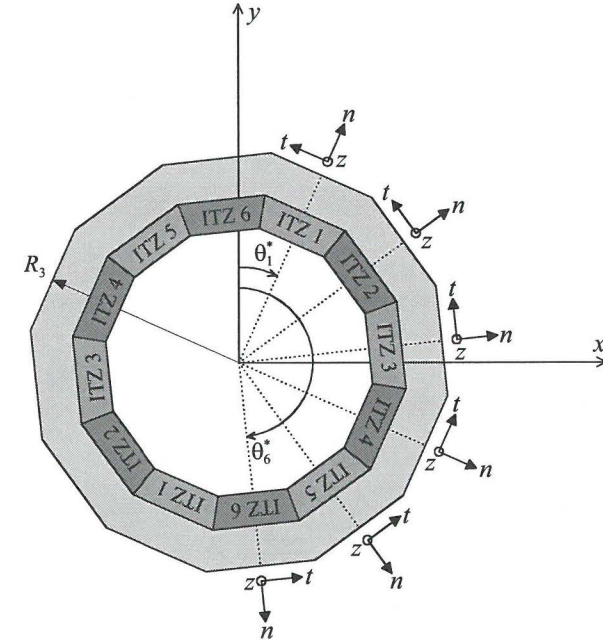


Figure 4.14. Discretization of RVE into 12 parts.

According to the proposed discretization into 6 directions, equation (4.9) turns into

$$\begin{bmatrix} \Delta\sigma_r^{e,ITZ}(\theta_i^*) \\ \Delta\sigma_\theta^{e,ITZ}(\theta_i^*) \\ \Delta\tau_{r\theta}^{e,ITZ}(\theta_i^*) \end{bmatrix} = \begin{bmatrix} \lambda_r^I \bar{K} + \lambda_r^II \lambda_0^II \bar{G} & \lambda_r^I \bar{K} - \lambda_r^II \lambda_0^II \bar{G} & 0 \\ \lambda_\theta^I \bar{K} - \lambda_\theta^II \lambda_0^II \bar{G} & \lambda_\theta^I \bar{K} + \lambda_\theta^II \lambda_0^II \bar{G} & 0 \\ 0 & 0 & \lambda_{r\theta}^II \lambda_0^II \bar{G} \end{bmatrix} \begin{bmatrix} \Delta\varepsilon_n^m(\theta_i^*) \\ \Delta\varepsilon_t^m(\theta_i^*) \\ \Delta\gamma_{nt}^m(\theta_i^*) \end{bmatrix}$$

$$(i = 1, \dots, 6)$$



#### 4.3.5 Treatment of non-linear behaviour in the ITZ

The trial stress state  $\underline{\sigma}^{t,ITZ}$  in each part of the ITZ – of which the location is specified by angle  $\theta_i^*$  – is computed according to

$$\underline{\sigma}^{t,ITZ}(\theta_i^*) = \underline{\sigma}^{0,ITZ}(\theta_i^*) + \Delta\underline{\sigma}^{e,ITZ}(\theta_i^*)$$

When this trial stress state violates a certain cracking criterion, the stress state is corrected to a final stress state  $\underline{\sigma}^{l,ITZ}$  in that particular part of the ITZ.

$$\underline{\sigma}^{l,ITZ}(\theta_i^*) = \underline{\sigma}^{t,ITZ}(\theta_i^*) + \Delta\underline{\sigma}^{ITZ}(\theta_i^*)$$

This non-linear behaviour in parts of the ITZ leads to the local stress correction vector  $\Delta\underline{\sigma}^{ITZ}(\theta_i^*)$  at  $R_0$ , as well as the local incremental crack displacements  $\Delta\underline{u}^{cr}(\theta_i^*)$  at  $R_0$  and the local correction of the stress state  $\Delta\underline{\sigma}(\theta_i^*, R_3)$  at the outer boundary  $R_3$  of pie-shaped parts of the RVE, as shown in figure 4.15.<sup>2</sup>

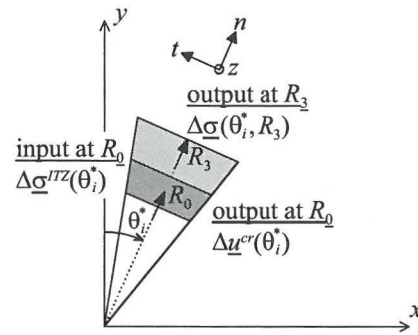


Figure 4.15. Pie-shaped part of the RVE.

To determine the local quantities  $\Delta\underline{u}^{cr}(\theta_i^*)$  and  $\Delta\underline{\sigma}(\theta_i^*, R_3)$ , a method is pursued based on similar elementary stress-strain states as considered in section 4.3.4 (macrostress approach). However, instead of imposing a macroscopic stress state  $\underline{\sigma}^m [\sigma_n^m, \sigma_t^m, \tau_{nt}^m]^T$  as a condition of constraint, a ‘displacement discontinuity’ is introduced at the centreline  $R_0$  of the ITZ (ITZ crack). At the location of this displacement discontinuity, the local ITZ stress correction vector  $\Delta\underline{\sigma}^{ITZ}(\theta_i^*)$  is imposed as a static condition of constraint. The relative incremental (crack) displacements at the centreline  $R_0$  of the ITZ are still unknown. During cracking within the ITZ the imposed macro-strain state  $\underline{\epsilon}^m$  remains intact, i.e. at the outer boundary  $R_3$  zero-displacements apply as a kinematic condition of constraint.

<sup>2</sup> The overall correction of the trial stress state at the outer boundary  $R_3$  ( $\Delta\underline{\sigma}^m$ , see figure 4.9) is determined by averaging all local stress correction vectors  $\Delta\underline{\sigma}(\theta_i^*, R_3)$ . This operation is performed in sections 4.3.7 and 4.3.8.

Unlike the macroscopic stress state  $\underline{\sigma}^m$ , the combination of arbitrary local stress correction vectors along the ITZ ( $\theta_1^*, \dots, \theta_6^*$ ) generally not represents a global uniform stress state in Cartesian coordinates. Hence, an analytical solution of the stress/displacement field is not available. A suitable approximation of the solution however may be found when it is hypothesized that the local incremental crack displacements  $\Delta\underline{u}^{cr}(\theta_i^*)$  and the local stress corrections  $\Delta\underline{\sigma}(\theta_i^*, R_3)$  at the outer boundary of the RVE for a particular pie-shaped part with direction  $\theta_i^*$  are primarily determined by the local stress corrections  $\Delta\underline{\sigma}^{ITZ}(\theta_i^*)$  in the ITZ of the same pie-shaped part. In this way, analytical solutions of global stress/displacement fields can be used to determine the local quantities  $\Delta\underline{u}^{cr}(\theta_i^*)$  and  $\Delta\underline{\sigma}(\theta_i^*, R_3)$  in each individual pie-shaped part of the RVE.

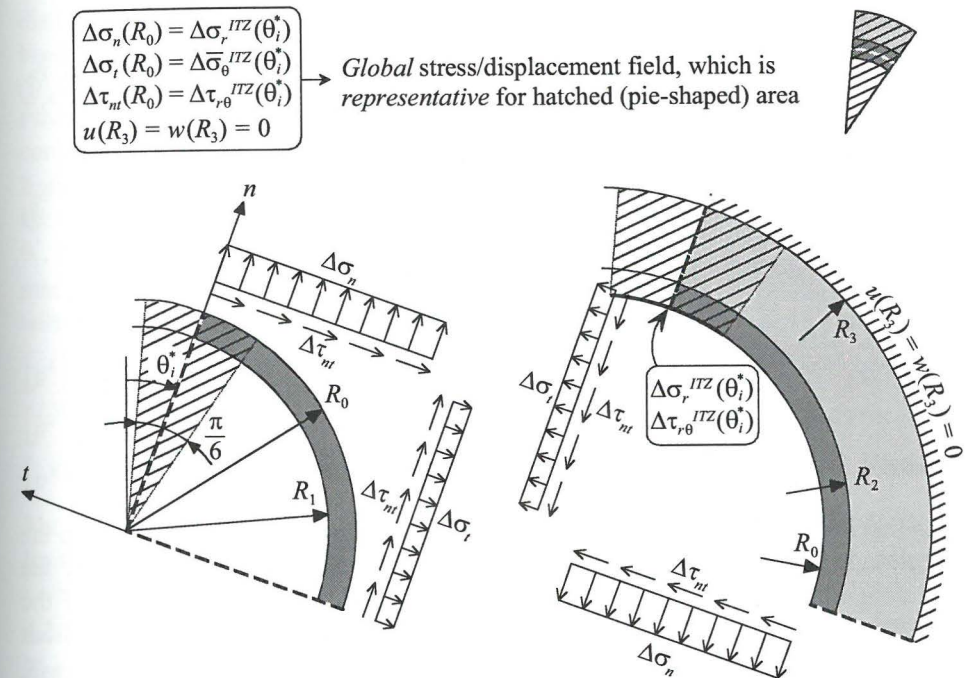


Figure 4.16. Global stress/displacement field representative of local stress/displacement field at angle  $\theta_i^*$  ( $1/4$  of RVE is drawn).

On the basis of this hypothesis, the local incremental crack displacements at  $R_0$  and the local stress corrections at the outer boundary  $R_3$  of each pie-shaped part can be found by imposing (1) the local ITZ stress correction  $\Delta\underline{\sigma}_r^{ITZ}(\theta_i^*)$  as an internal normal stress condition of constraint for the entire RVE in the direction normal to the considered part of the ITZ ( $n$ -axis in figure 4.16) and (2) the local ITZ stress correction  $\Delta\underline{\tau}_{r\theta}^{ITZ}(\theta_i^*)$  as an internal shear stress condition of constraint for the entire

RVE in the direction tangential to the considered part of the ITZ ( $t$ -axis in figure 4.16)<sup>3</sup>.

The minor influence of the stress corrections along the ITZ in the rest of the RVE is allowed for by calculating an averaged normal stress correction  $\Delta\bar{\sigma}_0^{ITZ}(\theta_1^*)$  in the direction tangential to the considered part of the ITZ ( $t$ -axis in figure 4.16) and imposing this averaged stress component as an internal normal stress condition of constraint in  $t$ -direction. In this way, the global stress/displacement field in the  $(n, t, z)$  Cartesian coordinate system as shown in figure 4.16 is *representative* of the local stress/displacement field in the pie-shaped part at angle  $\theta_1^*$ .

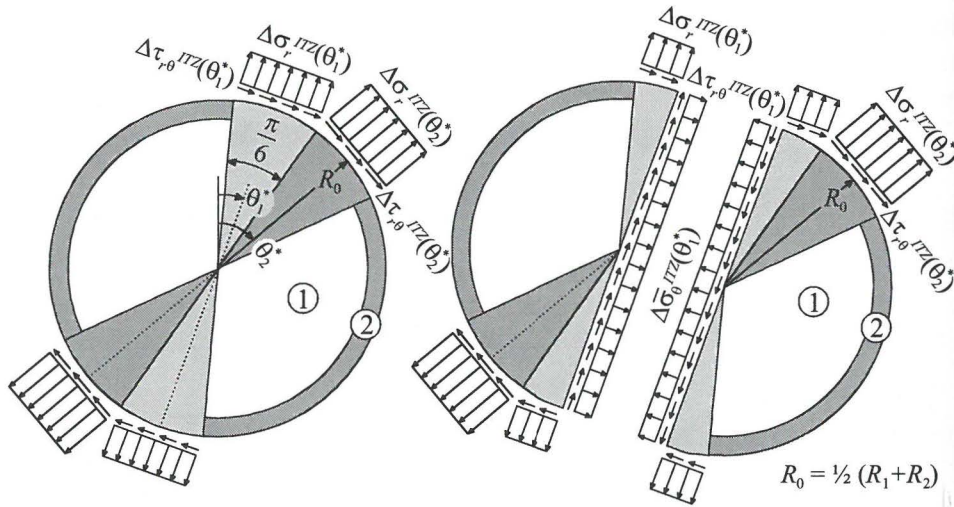


Figure 4.17. Average normal stress in tangential direction  $\Delta\bar{\sigma}_0^{ITZ}(\theta_1^*)$ .

This leaves the calculation of the (volume) averaged normal stress correction in the direction tangential to the considered pie-shaped part of the ITZ. In figure 4.17 the representative stress/displacement field is considered of a pie-shaped part of the RVE with orientation  $\theta_1^*$ . In this figure non-linear ITZ behaviour occurs, apart from the non-linear behaviour at  $\theta_1^*$ , only in one other part of the ITZ (at  $\theta_2^*$ ). In this case, the averaged normal stress correction in tangential direction at  $\theta_1^*$  is given by<sup>4</sup>

$$\Delta\bar{\sigma}_0^{ITZ}(\theta_1^*) = \frac{(\Delta\sigma_r^{ITZ}(\theta_2^*)\sin(\theta_2^* - \theta_1^*) - \Delta\tau_{r0}^{ITZ}(\theta_2^*)\cos(\theta_2^* - \theta_1^*))\frac{\pi}{6}R_0^2\sin(\theta_2^* - \theta_1^*)}{\frac{1}{2}\pi R_0^2}$$

If non-linear behaviour occurs in an arbitrary number of parts along the ITZ (other than the non-linear behaviour at  $\theta_1^*$ ), the expression becomes

<sup>3</sup> The hypothesis includes centre-symmetry of the non-linear behaviour in the ITZ.

<sup>4</sup> see also appendix A, section A.3.2.2

$$\Delta\bar{\sigma}_0^{ITZ}(\theta_1^*) = \sum_{k=2}^6 \frac{(\Delta\sigma_r^{ITZ}(\theta_k^*)\sin(\theta_k^* - \theta_1^*) - \Delta\tau_{r0}^{ITZ}(\theta_k^*)\cos(\theta_k^* - \theta_1^*))\frac{\pi}{6}R_0^2\sin(\theta_k^* - \theta_1^*)}{\frac{1}{2}\pi R_0^2}$$

Recapitulating, a *representative* (global) stress/displacement field is assigned to *each* pie-shaped part of the RVE at angle  $\theta_i^*$  ( $i = 1, \dots, 6$ ). This stress/displacement field is based primarily on the local ITZ stress correction  $\Delta\sigma^{ITZ}(\theta_i^*)$  and secondarily on an average of all other local ITZ stress corrections. By using the analytical solution of this representative stress/displacement field, local crack displacements  $\Delta u^{cr}(\theta_i^*)$  at  $R_0$  and the local correction of the stress state  $\Delta\sigma(\theta_i^*, R_3)$  at the outer boundary of the pie-shaped part at hand may be determined.

As this procedure is repeated for all pie-shaped parts of the RVE ( $\theta_1^*, \dots, \theta_6^*$ ), the distributions of both crack displacements (at  $R_0$ ) and stress corrections at the outer boundary  $R_3$  are generated along the entire circumference of the RVE.

Finally, the stress-strain state according to the representative static condition of constraint [ $\Delta\sigma_n = \Delta\sigma_r^{ITZ}(\theta_i^*)$ ,  $\Delta\sigma_t = \Delta\bar{\sigma}_0^{ITZ}(\theta_i^*)$ ,  $\Delta\tau_{nt} = \Delta\tau_{r0}^{ITZ}(\theta_i^*)$ ] can be written as a linear combination of two similar elementary stress-strain states as considered in section 4.3.4 (equation (4.2)) for each pie-shaped part of the RVE located at angle  $\theta_i^*$ . However, the quantities  $p^I$ ,  $p^{II}\sin 2\theta$  and  $p^{II}\cos 2\theta$  now are not derived from the macro-stress increments but from the ITZ stress corrections at angle  $\theta_i^*$  (compare with equation (4.4)).

$$\left. \begin{aligned} [p^I]_i &= \frac{1}{2}(\Delta\sigma_r^{ITZ}(\theta_i^*) + \Delta\bar{\sigma}_0^{ITZ}(\theta_i^*)) \\ [p^{II}\sin 2\theta]_i &= \frac{1}{2}(\Delta\sigma_r^{ITZ}(\theta_i^*) - \Delta\bar{\sigma}_0^{ITZ}(\theta_i^*)) \\ [p^{II}\cos 2\theta]_i &= \Delta\tau_{r0}^{ITZ}(\theta_i^*) \end{aligned} \right\} i = 1, \dots, 6 \quad (4.10)$$

The computation of crack displacements (at  $R_0$ ) and outer-boundary stresses (at  $R_3$ ) for these two elementary states is carried out below.

#### 4.3.5.1 Elementary state I - Stress/displacement field

The precise location of cracking within the ITZ is not necessarily the location where the elastic ITZ stresses are computed ( $R_0$ ). However, as the variation of elastic ITZ stresses over the thickness of the ITZ is very small, the stresses at the centreline of the ITZ are considered to be representative of the stress state within the entire ITZ. Likewise, the problem with respect to the location of cracking is simplified considerably by assuming the stress correction vector  $\Delta\sigma^{ITZ}$  and the elasto-plastic strains to be uniform over the thickness of the ITZ. According to this assumption the location of cracking does not have any influence on the computation of crack displacements and outer-boundary stresses. Accordingly, the ITZ stress correction vector is the same at both sides of the ITZ. With these static conditions of constraint and zero boundary displacements at the outer boundary of the RVE ( $R_3$ ), the stress/displacement fields of the RVE can be computed.

For elementary state I, the general elastic stress/displacement field of all phases of the RVE in cylindrical coordinates is described by equation (A.8) of appendix A.

$$\begin{aligned}\sigma_r &= \frac{A}{r^2} + 2C \\ \sigma_\theta &= -\frac{A}{r^2} + 2C\end{aligned}\quad (4.11)$$

$$\begin{aligned}\varepsilon_\theta &= \frac{1+\nu}{E} \left( -\frac{A}{r^2} + 2C(1-2\nu) \right) \\ u &= \frac{1+\nu}{E} \left( -\frac{A}{r} + 2Cr(1-2\nu) \right)\end{aligned}\quad (4.12)$$

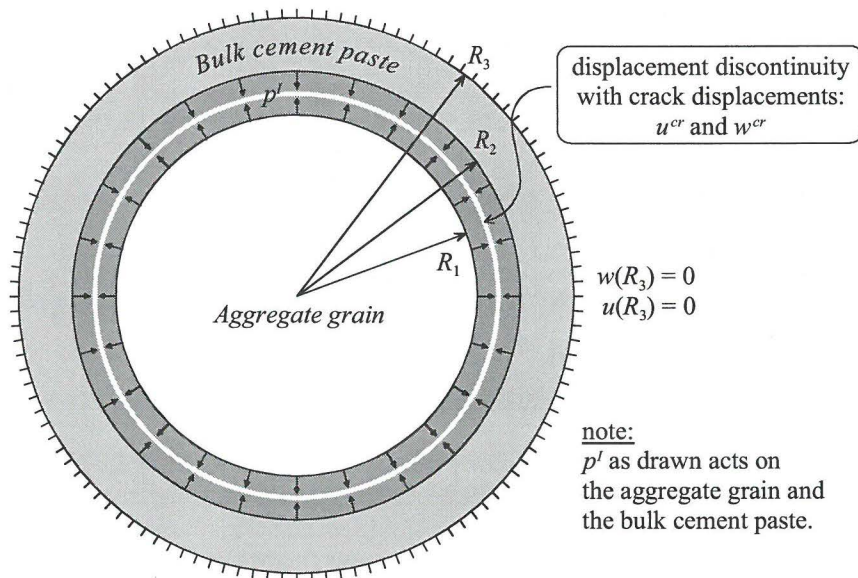


Figure 4.18. Conditions of constraint for elementary state I.

Applying the following conditions of constraint solves the constants of integration of the stress/displacement field in the aggregate grain

$$\begin{cases} \sigma_r(R_1) = p' \\ \sigma_r(0) \neq \infty \end{cases}$$

From this it follows that  $A=0$  and  $C = \frac{1}{2}p'$ , which results in the following expressions for the normal strain in tangential direction and the normal displacement at  $R_1$

$$\begin{aligned}\varepsilon_\theta(R_1) &= \lambda'_{\varepsilon\theta,1} p' & \left( \lambda'_{\varepsilon\theta,1} &= \frac{1+\nu}{E_{agg}} (1-2\nu) \right) \\ u(R_1) &= \lambda'_{u,1} p' & \left( \lambda'_{u,1} &= \frac{1+\nu}{E_{agg}} (1-2\nu) R_1 \right)\end{aligned}$$

Applying the following conditions of constraint solves the constants of integration of the stress/displacement field in the bulk cement paste

$$\begin{cases} \sigma_r(R_2) = p' \\ u(R_3) = 0 \end{cases} \rightarrow A = \frac{R_2^2 R_3^2 (1-2\nu)}{R_3^2 (1-2\nu) + R_2^2} p' \quad 2C = \frac{R_2^2}{R_3^2 (1-2\nu) + R_2^2} p'$$

For elementary state I, this results in the following expressions for the outer-boundary normal stress, the normal strain in tangential direction at  $R_2$  and the normal displacement at  $R_2$

$$\begin{aligned}\sigma_r(R_3) &= \lambda'_{\sigma r} p' & \left( \lambda'_{\sigma r} &= \frac{2R_2^2 (1-\nu)}{R_3^2 (1-2\nu) + R_2^2} \right) \\ \varepsilon_\theta(R_2) &= \lambda'_{\varepsilon\theta,2} p' & \left( \lambda'_{\varepsilon\theta,2} &= \frac{1+\nu}{E_{bulk}} \left( \frac{(1-2\nu)(R_2^2 - R_3^2)}{R_3^2 (1-2\nu) + R_2^2} \right) \right) \\ u(R_2) &= \lambda'_{u,2} p' & \left( \lambda'_{u,2} &= \frac{1+\nu}{E_{bulk}} \left( \frac{R_2 (1-2\nu)(R_2^2 - R_3^2)}{R_3^2 (1-2\nu) + R_2^2} \right) \right)\end{aligned}$$

The ITZ stresses and strains are assumed to be uniform over the ITZ. This is an approximation, so the equations (4.11) and (4.12) do not apply here. However, the (uniform) normal radial strain and the normal tangential stress/strain in the ITZ can be computed using the following simplified conditions of constraint

$$\begin{cases} \varepsilon_\theta^{ITZ} = \frac{1}{2} (\varepsilon_\theta(R_1) + \varepsilon_\theta(R_2)) = \lambda'_{\varepsilon\theta} p' & \left( \lambda'_{\varepsilon\theta} = \frac{1}{2} (\lambda'_{\varepsilon\theta,1} + \lambda'_{\varepsilon\theta,2}) \right) \\ \sigma_r^{ITZ} = p' \end{cases}$$

One additional condition of constraint is required to complete the boundary value problem. This condition of constraint depends on whether a plastic normal strain component in tangential direction is present or not. When no plastic normal strain component exists, the elastic normal strain component equals the total normal strain component in tangential direction.

$$\varepsilon_\theta^{p,ITZ} = 0 \rightarrow \varepsilon_\theta^{e,ITZ} = \varepsilon_\theta^{ITZ}$$

Applying the equations of Hooke's law for plane strain (Appendix A: equation (A.7)) yields for this case

$$\begin{aligned}\varepsilon_r^{ITZ} &= \lambda_{er}^I p^I & \left( \lambda_{er}^I &= \frac{1}{1-\nu} \left( \frac{(1+\nu)(1-2\nu)}{E_{ITZ}} - \nu \lambda_{e\theta}^I \right) \right) \\ \varepsilon_\theta^{ITZ} &= \lambda_{e\theta}^I p^I & \left( \lambda_{e\theta}^I &= \frac{1}{1-\nu} \left( \frac{E_{ITZ} \lambda_{e\theta}^I}{1+\nu} + \nu \right) \right)\end{aligned}$$

With zero  $\varepsilon_\theta^{p,ITZ}$ , the crack displacements are given by

$$\begin{aligned}u^{cr} &= u(R_2) - u(R_1) - \varepsilon_r^{ITZ} (R_2 - R_1) = \lambda_u^I p^I & \left( \lambda_u^I &= \lambda_{u,2}^I - \lambda_{u,1}^I - \lambda_{er}^I (R_2 - R_1) \right) \\ w^{cr} &= 0\end{aligned}$$

When a plastic normal strain component in tangential direction is present, the (given) normal stress in tangential direction is imposed as a condition of constraint.

$$\varepsilon_\theta^{p,ITZ} \neq 0 \rightarrow \sigma_\theta^{ITZ} \text{ is given}$$

Applying Hooke's law in this case yields

$$\begin{aligned}u^{cr} &= (\lambda_u^I - \lambda_{e\theta}^I \lambda_{u,\sigma\theta}) p^I + \lambda_{u,\sigma\theta} \sigma_\theta^{ITZ} & \left( \lambda_{u,\sigma\theta} &= \frac{-\nu(1+\nu)}{E_{ITZ}} (R_2 - R_1) \right) \\ \varepsilon_\theta^{p,ITZ} &= (-\lambda_{e\theta}^I \lambda_{e\theta,\sigma\theta}) p^I + \lambda_{e\theta,\sigma\theta} \sigma_\theta^{ITZ} & \left( \lambda_{e\theta,\sigma\theta} &= \frac{(1-\nu)(1+\nu)}{E_{ITZ}} \right) \\ w^{cr} &= 0\end{aligned}$$

#### 4.3.5.2 Elementary state II - Stress/displacement field

For elementary state II the general elastic stress field of all phases of the RVE in cylindrical coordinates is described by equation (A.14) of appendix A.

$$\begin{aligned}\sigma_r &= \left( -2B - \frac{6C}{r^4} - \frac{4D}{r^2} \right) \sin 2\theta \\ \sigma_\theta &= \left( 12Ar^2 + 2B + \frac{6C}{r^4} \right) \sin 2\theta \\ \tau_{r\theta} &= \left( -6Ar^2 - 2B + \frac{6C}{r^4} + \frac{2D}{r^2} \right) \cos 2\theta\end{aligned}$$

The displacement field is described by equation (A.15) of appendix A.

$$\begin{aligned}u &= \frac{(1+\nu)\sin 2\theta}{E} \left( -4\nu Ar^3 - 2Br + \frac{2C}{r^3} + \frac{4(1-\nu)D}{r} \right) \\ w &= \frac{(1+\nu)\cos 2\theta}{E} \left( -6Ar^3(1-\frac{2}{3}\nu) - 2Br - \frac{2C}{r^3} + \frac{(2-4\nu)D}{r} \right)\end{aligned}$$

The conditions of constraint for this loading case are indicated in figure 4.19.

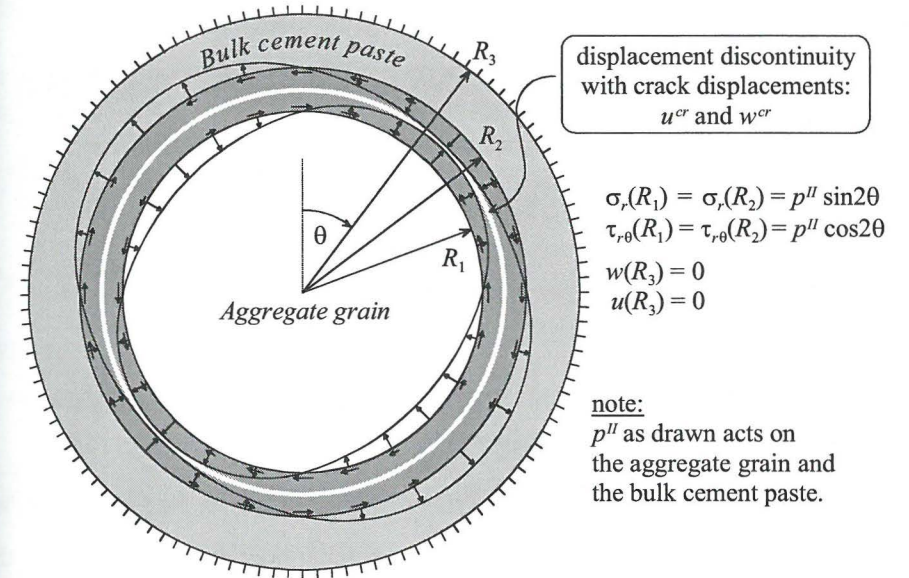


Figure 4.19. Conditions of constraint for elementary state II.

Applying the following conditions of constraint solves the constants of integration of the equations describing the stress and displacement field of the aggregate grain

$$\begin{cases} \sigma_r(R_1) = p^II \sin 2\theta \\ \tau_{r\theta}(R_1) = p^II \cos 2\theta \\ \sigma_r(0) \neq \infty \\ \tau_{r\theta}(0) \neq \infty \end{cases}$$

From this it follows that  $A=C=D=0$  and  $B = -\frac{1}{2}p^II$ , which results in the following expressions for the displacements and the normal strain in tangential direction at  $R_1$

$$u(R_1) = \lambda_{u,1}^II p^II \sin 2\theta \quad \left( \lambda_{u,1}^II = \frac{(1+\nu)R_1}{E_{agg}} \right)$$

$$w(R_1) = \lambda_{w,1}'' p'' \cos 2\theta \quad \left( \lambda_{w,1}'' = \frac{(1+\nu)R_1}{E_{agg}} \right)$$

$$\varepsilon_\theta(R_1) = \lambda_{\varepsilon\theta,1}'' p'' \sin 2\theta \quad \left( \lambda_{\varepsilon\theta,1}'' = \frac{-(1+\nu)}{E_{agg}} \right)$$

The conditions of constraint for the bulk cement paste are

$$\begin{cases} \sigma_r(R_2) = p'' \sin 2\theta \\ \tau_{r\theta}(R_2) = p'' \cos 2\theta \\ u(R_3) = w(R_3) = 0 \end{cases}$$

$$\rightarrow A = \frac{(1-\alpha_1)}{R_2^2 \alpha_3} p'' \quad B = \frac{-\alpha_2}{2\alpha_3} p'' \quad C = \frac{R_2^4}{2\alpha_3} p'' \quad D = \frac{-R_2^2 \alpha_1}{\alpha_3} p''$$

$$\alpha_0 = (R_2^4 + R_3^4(3-4\nu))R_3^2$$

$$\alpha_1 = \frac{R_2^6 + R_3^6(3-4\nu)}{\alpha_0}$$

$$\alpha_2 = \frac{3R_2^2 R_3^2 (R_3^2 - R_2^2)}{\alpha_0} + \alpha_1(3-4\nu) \frac{R_2^2}{R_3^2}$$

$$\alpha_3 = \alpha_2 - 3 + 4\alpha_1$$

This yields the following expressions for the outer-boundary stresses and the displacements and normal strain in tangential direction at  $R_2$

$$\sigma_r(R_3) = \lambda_{\sigma r}'' p'' \sin 2\theta \quad \left( \lambda_{\sigma r}'' = \frac{\alpha_2}{\alpha_3} - \frac{3R_2^4}{\alpha_3 R_3^4} + \frac{4\alpha_1 R_2^2}{\alpha_3 R_3^2} \right)$$

$$\tau_{r\theta}(R_3) = \lambda_{\tau}'' p'' \cos 2\theta \quad \left( \lambda_{\tau}'' = \frac{-6(1-\alpha_1)R_3^2}{\alpha_3 R_2^2} + \frac{\alpha_2}{\alpha_3} + \frac{3R_2^4}{\alpha_3 R_3^4} - \frac{2\alpha_1 R_2^2}{\alpha_3 R_3^2} \right)$$

$$u(R_2) = \lambda_{u,2}'' p'' \sin 2\theta \quad \left( \lambda_{u,2}'' = \frac{1+\nu}{E_{bulk}} \left( \frac{\alpha_2 + 1 - 4\nu - 4\alpha_1(1-2\nu)}{\alpha_3} \right) R_2 \right)$$

$$w(R_2) = \lambda_{w,2}'' p'' \cos 2\theta \quad \left( \lambda_{w,2}'' = \frac{1+\nu}{E_{bulk}} \left( \frac{\alpha_3 - 4(1-\nu)}{\alpha_3} \right) R_2 \right)$$

$$\varepsilon_\theta(R_2) = \lambda_{\varepsilon\theta,2}'' p'' \sin 2\theta \quad \left( \lambda_{\varepsilon\theta,2}'' = \frac{1+\nu}{E_{bulk}} \left( \frac{-\alpha_3 + 4(1-\nu)(3-2\alpha_1)}{\alpha_3} \right) \right)$$

The elastic stress-strain field of the ITZ (uniform over  $r$ ) is given by

$$\begin{cases} \sigma_r^{ITZ} = p'' \sin 2\theta \\ \tau_{r\theta}^{ITZ} = p'' \cos 2\theta \\ \gamma_{r\theta}^{ITZ} = \lambda_{\gamma}'' p'' \cos 2\theta \\ \varepsilon_\theta^{ITZ} = \frac{1}{2} (\varepsilon_\theta(R_1) + \varepsilon_\theta(R_2)) = \lambda_{\varepsilon\theta}'' p'' \sin 2\theta \end{cases} \quad \left( \lambda_{\gamma}'' = \frac{1+\nu}{E_{ITZ}} \right)$$

$$\left( \lambda_{\varepsilon\theta}'' = \frac{1}{2} (\lambda_{\varepsilon\theta,1}'' + \lambda_{\varepsilon\theta,2}'') \right)$$

In case no plastic normal strain component in tangential direction is present ( $\varepsilon_\theta^{e,ITZ} = \varepsilon_\theta^{ITZ}$ ), applying Hooke's law for plane strain yields

$$\varepsilon_r^{ITZ} = \lambda_{\varepsilon r}'' p'' \sin 2\theta \quad \left( \lambda_{\varepsilon r}'' = \frac{1}{1-\nu} \left( \frac{(1+\nu)(1-2\nu)}{E_{ITZ}} - \nu \lambda_{\varepsilon\theta}'' \right) \right)$$

$$\sigma_\theta^{ITZ} = \lambda_{\sigma\theta}'' p'' \sin 2\theta \quad \left( \lambda_{\sigma\theta}'' = \frac{1}{1-\nu} \left( \frac{E_{ITZ} \lambda_{\varepsilon\theta}''}{1+\nu} + \nu \right) \right)$$

With zero  $\varepsilon_\theta^{p,ITZ}$ , the expressions for the crack displacements are

$$u^{cr} = u(R_2) - u(R_1) - \varepsilon_r^{ITZ} (R_2 - R_1)$$

$$= \lambda_{u,2}'' p'' \sin 2\theta \quad \left( \lambda_{u,2}'' = \lambda_{u,2}'' - \lambda_{u,1}'' - \lambda_{\varepsilon r}'' (R_2 - R_1) \right)$$

$$w^{cr} = w(R_2) - w(R_1) - \gamma_{r\theta}^{ITZ} (R_2 - R_1)$$

$$= \lambda_{w,2}'' p'' \cos 2\theta \quad \left( \lambda_{w,2}'' = \lambda_{w,2}'' - \lambda_{w,1}'' - \lambda_{\gamma}'' (R_2 - R_1) \right)$$

When a plastic normal strain component in tangential direction is present, the normal stress in tangential direction  $\sigma_\theta^{ITZ}$  is imposed as a condition of constraint. Application of Hooke's law for plane strain gives

$$u^{cr} = (\lambda_{u,2}'' - \lambda_{\sigma\theta}'' \lambda_{u,\sigma\theta}) p'' \sin 2\theta + \lambda_{u,\sigma\theta} \sigma_\theta^{ITZ}$$

$$\varepsilon_\theta^{p,ITZ} = (-\lambda_{\sigma\theta}'' \lambda_{\varepsilon\theta,\sigma\theta}) p'' \sin 2\theta + \lambda_{\varepsilon\theta,\sigma\theta} \sigma_\theta^{ITZ}$$

$$w^{cr} = \lambda_{w,2}'' p'' \cos 2\theta$$

#### 4.3.5.3 Stress/displacement fields for arbitrary ITZ stress correction vectors

For any angle  $\theta_i^*$ , the local stress correction vector at the outer-boundary of the RVE  $[\Delta\sigma_r(\theta_i^*, R_3), \Delta\tau_{r\theta}(\theta_i^*, R_3)]^T$  and the local incremental crack displacements at the centreline  $R_0$  of the ITZ  $[\Delta u^{cr}(\theta_i^*), \Delta w^{cr}(\theta_i^*)]^T$  can be computed for an arbitrary ITZ stress correction vector  $[\Delta\sigma_r^{ITZ}(\theta_i^*), \Delta\tau_{r\theta}^{ITZ}(\theta_i^*), \Delta\bar{\sigma}_\theta^{ITZ}(\theta_i^*)]^T$  by inserting equations (4.10) in the stress-strain-displacement expressions of the two elementary stress-strain states derived in the preceding sections 4.3.5.1 and 4.3.5.2. The following expressions for these quantities are achieved in this way.

$$\text{at } R_3 \begin{cases} \Delta\sigma_r(\theta_i^*, R_3) = \left( \frac{\lambda_{\sigma r}^I + \lambda_{\sigma r}^{II}}{2} \right) \Delta\sigma_r^{ITZ}(\theta_i^*) + \left( \frac{\lambda_{\sigma r}^I - \lambda_{\sigma r}^{II}}{2} \right) \Delta\bar{\sigma}_\theta^{ITZ}(\theta_i^*) \\ \Delta\tau_{r\theta}(\theta_i^*, R_3) = \lambda_{\tau}^{II} \Delta\tau_{r\theta}^{ITZ}(\theta_i^*) \end{cases} \quad (4.13)$$

In case no plastic normal strain component in tangential direction is present:

$$\text{in ITZ} \begin{cases} \Delta u^{cr}(\theta_i^*) = \left( \frac{\lambda_u^I + \lambda_u^{II}}{2} \right) \Delta\sigma_r^{ITZ}(\theta_i^*) + \left( \frac{\lambda_u^I - \lambda_u^{II}}{2} \right) \Delta\bar{\sigma}_\theta^{ITZ}(\theta_i^*) \\ \Delta w^{cr}(\theta_i^*) = \lambda_w^{II} \Delta\tau_{r\theta}^{ITZ}(\theta_i^*) \\ \Delta\sigma_\theta^{ITZ}(\theta_i^*) = \left( \frac{\lambda_{\sigma\theta}^I + \lambda_{\sigma\theta}^{II}}{2} \right) \Delta\sigma_r^{ITZ}(\theta_i^*) + \left( \frac{\lambda_{\sigma\theta}^I - \lambda_{\sigma\theta}^{II}}{2} \right) \Delta\bar{\sigma}_\theta^{ITZ}(\theta_i^*) \end{cases} \quad (4.14)$$

$$\left( \begin{array}{l} \Delta\sigma_\theta^{ITZ}(\theta_i^*) = \text{local ITZ normal stress correction in tangential direction} \\ \Delta\bar{\sigma}_\theta^{ITZ}(\theta_i^*) = \text{global (averaged) ITZ normal stress correction in tangential direction} \end{array} \right)$$

In case a plastic normal strain component in tangential direction is present, the local normal stress correction in tangential direction  $\Delta\sigma_\theta^{ITZ}(\theta_i^*)$  is taken as an additional condition of constraint. The expressions then become

$$\text{in ITZ} \begin{cases} \Delta u^{cr}(\theta_i^*) = \left( \frac{\lambda_u^I + \lambda_u^{II}}{2} - \frac{\lambda_{\sigma\theta}^I + \lambda_{\sigma\theta}^{II}}{2} \lambda_{u,\sigma\theta} \right) \Delta\sigma_r^{ITZ}(\theta_i^*) + \\ \quad + \left( \frac{\lambda_u^I - \lambda_u^{II}}{2} - \frac{\lambda_{\sigma\theta}^I - \lambda_{\sigma\theta}^{II}}{2} \lambda_{u,\sigma\theta} \right) \Delta\bar{\sigma}_\theta^{ITZ}(\theta_i^*) + \lambda_{u,\sigma\theta} \Delta\sigma_\theta^{ITZ}(\theta_i^*) \\ \Delta w^{cr}(\theta_i^*) = \lambda_w^{II} \Delta\tau_{r\theta}^{ITZ}(\theta_i^*) \\ \Delta\varepsilon_\theta^{p,ITZ}(\theta_i^*) = \left( -\frac{\lambda_{\sigma\theta}^I + \lambda_{\sigma\theta}^{II}}{2} \lambda_{\varepsilon\theta,\sigma\theta} \right) \Delta\sigma_r^{ITZ}(\theta_i^*) + \\ \quad + \left( -\frac{\lambda_{\sigma\theta}^I - \lambda_{\sigma\theta}^{II}}{2} \lambda_{\varepsilon\theta,\sigma\theta} \right) \Delta\bar{\sigma}_\theta^{ITZ}(\theta_i^*) + \lambda_{\varepsilon\theta,\sigma\theta} \Delta\sigma_\theta^{ITZ}(\theta_i^*) \end{cases} \quad (4.16)$$

#### 4.3.6 Constitutive model for ITZ non-linear behaviour

In section 4.3.5 an ITZ stress correction vector  $\Delta\sigma^{ITZ}(\theta_i^*)$  is introduced which is added to the 'trial' stress state  $\underline{\sigma}^{t,ITZ}(\theta_i^*)$  in case this trial stress state violates a certain cracking criterion. Based on this ITZ stress correction vector a framework is expounded that establishes linear relationships between, on the one hand, the local ITZ stress correction vector and, on the other hand, the local outer-boundary stress

correction and the local incremental crack displacements at the centreline of the ITZ at angle  $\theta_i^*$ .

In this section a constitutive model is presented that provides the local ITZ stress correction vector in an arbitrary part of the ITZ at angle  $\theta_i^*$ , for several types of cracking in the ITZ. In chapter 3 is outlined that the macroscopic observed mechanical features at stage II of concrete in multiaxial compression can be explained by *isolated* crack formation in the ITZ, such as (microscopic) pore collapse possibly in combination with mesoscopic mode II or mode I cracking along the ITZ. These types of cracking all are incorporated in this constitutive model for ITZ non-linear material behaviour.

The constitutive model is formulated according to the principles of classical elasto-plasticity. If the elastic stress state in the ITZ falls outside the stress-state bounding surface, "yielding" is detected and the elastic (trial) stress state is put back onto the bounding surface. Expansion and/or shrinkage of the bounding surface is governed by the introduction of internal state parameters.

As the constitutive model is incorporated in the explicit solution procedure of the computer code UDEC, return mapping of the trial stress state onto the bounding surface may also occur explicitly, i.e. the assumption is made that the internal state parameters remain constant during the entire time step and are only updated at the beginning of each time step. Consequently, the shape and position of the stress-state bounding surface remains unaltered during one small time step.

#### 4.3.6.1 Mesoscopic mode I and mode II cracking along the ITZ

Mesoscopic mode I and mode II cracking along the ITZ are captured by bounding the ITZ normal stresses in radial direction ( $\sigma_r$ ) and the shear stresses in tangential direction ( $\tau_{r\theta}$ ) by a linear Mohr-Coulomb type bounding surface (see figure 4.20), allowing mesoscopic interfacial cracking along the tangential  $\theta^*$ -direction of the ITZ. The stress-state bounding surface is determined by two parameters, the friction angle  $\phi$  and the tensile strength  $f_t$ .

Tensile (linear) softening is incorporated in the model by introducing a dependency between the parameter  $f_t$  and the loading history through the internal state parameter  $\kappa_1$ . The friction angle  $\phi$  probably also depends on the loading history. Experimental observations by Alexander<sup>1971</sup> show that at first slip the friction angle increases to some extent and decreases to a stationary level as slip proceeds. The observed variation of  $\phi$  however is small and, therefore, will have only a minor influence on the global behaviour of the RVE. As this influence is small and the model only aims at reproducing the most salient mechanical behaviour, the potential dependency of  $\phi$  on the loading history is disregarded.

Mathematically, the stress-state bounding surface for mesoscopic mode I and mode II cracking along the ITZ is expressed as

$$f_t(\underline{\sigma}^{ITZ}, \kappa_1) = |\tau_{r\theta}^{ITZ}| - (f_t(\kappa_1) - \sigma_r^{ITZ}) \tan \phi = 0$$

The internal state parameter  $\kappa_1$  depends on the incremental crack opening  $\Delta u^{cr}$  and crack sliding  $\Delta w^{cr}$  displacements by

$$\Delta\kappa_1 = \sqrt{(\Delta u^{cr})^2 + (\Delta w^{cr})^2}$$

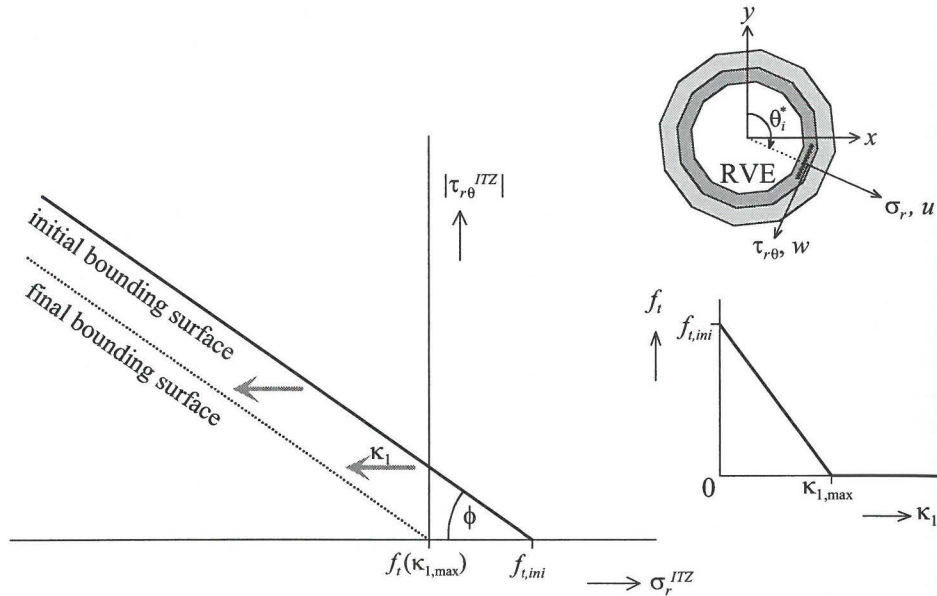


Figure 4.20. Mohr-Coulomb stress-state bounding surface with tensile softening.

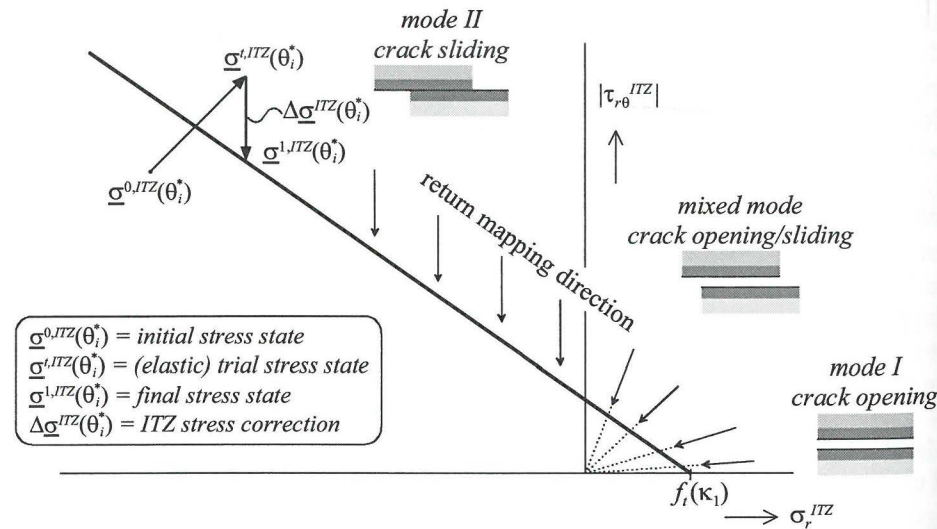


Figure 4.21. Return mapping of the (elastic) trial stress state.

The direction of return mapping of the trial stress state onto the bounding surface is determined by the direction of plastic flow, i.e. the ratio between incremental crack opening and crack sliding displacements. During mesoscopic mode I or mode II cracking along the ITZ no irreversible (plastic) normal strain component in tangential direction is present ( $\epsilon_{\theta}^{p,ITZ} = 0$ ), so the crack displacements are given by equation (4.14) in section 4.3.5.3. According to this equation, there is a linear one-to-one relation between the decrease of shear stress  $\Delta\tau_{r\theta}^{ITZ}$  and incremental crack sliding displacement  $\Delta w^{cr}$ , as well as a linear one-to-one relation between the decrease of normal stress  $\Delta\sigma_r^{ITZ}$  and incremental crack opening displacement  $\Delta u^{cr}$ . In the compressive region ( $\sigma_r^{ITZ} < 0$ ), pure mode II cracking is assumed with no dilatancy. In the tensile region ( $\sigma_r^{ITZ} > 0$ ), mixed mode cracking occurs depending on the ratio between shear and normal tensile stress. The accompanying direction of return mapping is indicated in figure 4.21.

#### 4.3.6.2 Pore collapse

As the thin contact layer between the aggregate grain and the rest of the ITZ (figure 3.3 in section 3.1.1) is considered to be the weakest layer of the ITZ, mesoscopic mode I/II cracking is likely to occur along this layer. Because this layer is also the most porous one, compressive collapse of the pore structure of the ITZ will initiate here also. However, when pore collapse proceeds and the porosity in this layer decreases, the phenomenon of pore collapse will extend over the entire thickness of the ITZ.

Microcracks involving pore collapse are not restricted to run along the tangential  $\theta^*$ -direction of the ITZ, but may run in any direction. This phenomenon is a distributed process and a continuum approach is therefore adopted.

It is assumed that the stress-state bounding surface of the ITZ continuum resembles a straight Mohr-Coulomb bounding surface determined by two parameters, the cohesion ( $c_{pc}$ ) and the friction angle ( $\phi_{pc}$ ). When the local stress state – as indicated by Mohr’s stress circle in figure 4.22 – violates this cracking criterion, the stress state represented by point *A* on Mohr’s stress circle has to be put back onto the bounding surface.

The mathematical formulation of the stress-state bounding surface for pore collapse follows from the comparison between the radius of Mohr’s stress circle  $r_M$  and the distance of  $C_M$  perpendicular to the bounding surface as drawn in figure 4.22.

$$f_2(\underline{\sigma}^{ITZ}) = r_M(\underline{\sigma}^{ITZ}) - \sin \phi_{pc} \left( \frac{c_{pc}}{\tan \phi_{pc}} - C_M(\underline{\sigma}^{ITZ}) \right) = 0$$

with

$$C_M(\underline{\sigma}^{ITZ}) = \frac{\sigma_r^{ITZ} + \sigma_{\theta}^{ITZ}}{2}$$

$$r_M(\underline{\sigma}^{ITZ}) = \sqrt{\frac{1}{4}(\sigma_r^{ITZ} - \sigma_{\theta}^{ITZ})^2 + (\tau_{r\theta}^{ITZ})^2}$$

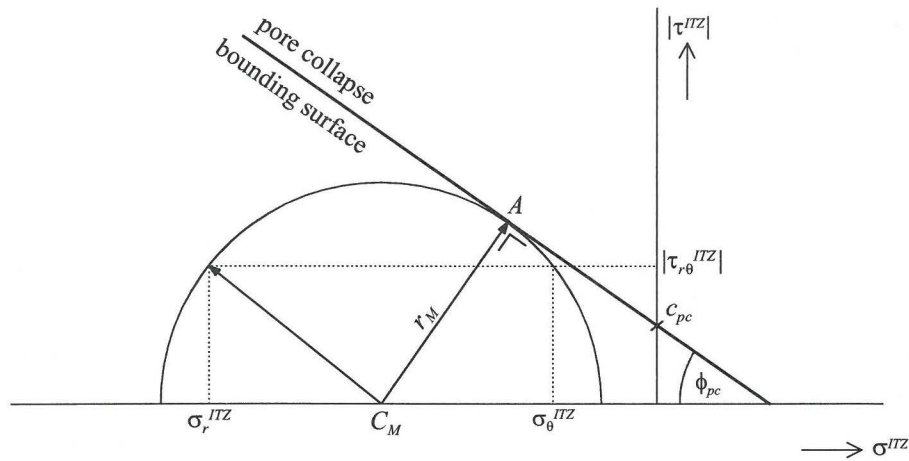


Figure 4.22. Mohr's stress circle touching bounding surface for pore collapse.

As stated before, compressive collapse of the pore structure of the ITZ initiates in the thin, most porous, contact layer between the aggregate grain and the rest of the ITZ. When pore collapse proceeds, this type of failure will extend to the – less porous and hence stronger – outer layers of the ITZ. This implies that the resistance to subsequent pore collapse will increase during the process of pore collapse until the porosity has decreased to such a level that further pore collapse does not occur anymore. This happens in the present model when the plastic volumetric compaction  $\kappa_2$  reaches a critical value  $\kappa_{2,max}$ . Beyond this critical level, the stress state in the ITZ is no longer bounded by a bounding surface for pore collapse.

The strengthening effect during pore collapse may be allowed for by introducing cohesive and/or frictional strengthening, i.e. introducing a dependency between the parameters of the Mohr-Coulomb bounding surface,  $c_{pc}$  and/or  $\phi_{pc}$ , and the plastic volumetric compaction  $\kappa_2$ . Such a strengthening law cannot be derived unambiguously, since the only obvious requirement for this law is that  $c_{pc}$  and/or  $\phi_{pc}$  should increase during pore collapse. An appropriate strengthening law may however be obtained by comparing model simulations at stage II with (macroscopic) test results. In this way, satisfactory agreement with test results was achieved applying a strengthening law including only cohesive strengthening according to the following relationship:

$$c_{pc}(\kappa_2) = c_{pc,ini} + (c_{pc,end} - c_{pc,ini}) \sqrt[4]{\frac{\kappa_2}{\kappa_{2,max}}}$$

$\kappa_{2,max}$  = plastic volumetric compaction at maximum pore closure

$c_{pc,ini}$  = cohesion at zero pore closure

$c_{pc,end}$  = cohesion at maximum pore closure

The incremental plastic volumetric compaction is given by the sum of plastic normal strains in the ITZ. (The expressions for  $\Delta u^{cr}$  and  $\Delta \varepsilon_{\theta}^{p,ITZ}$  are given by equation (4.16) and (4.17) in section 4.3.5.3)

$$\Delta \kappa_2 = \Delta \varepsilon_r^{p,ITZ} + \Delta \varepsilon_{\theta}^{p,ITZ} = \frac{\Delta u^{cr}}{R_2 - R_1} + \Delta \varepsilon_{\theta}^{p,ITZ}$$

The final expression for the stress-state bounding surface for pore collapse is given below and is graphically illustrated by figure 4.23.

$$f_2(\underline{\sigma}^{ITZ}, \kappa_2) = r_M(\underline{\sigma}^{ITZ}) - \sin \phi_{pc} \left( \frac{c_{pc}(\kappa_2)}{\tan \phi_{pc}} - C_M(\underline{\sigma}^{ITZ}) \right) = 0$$

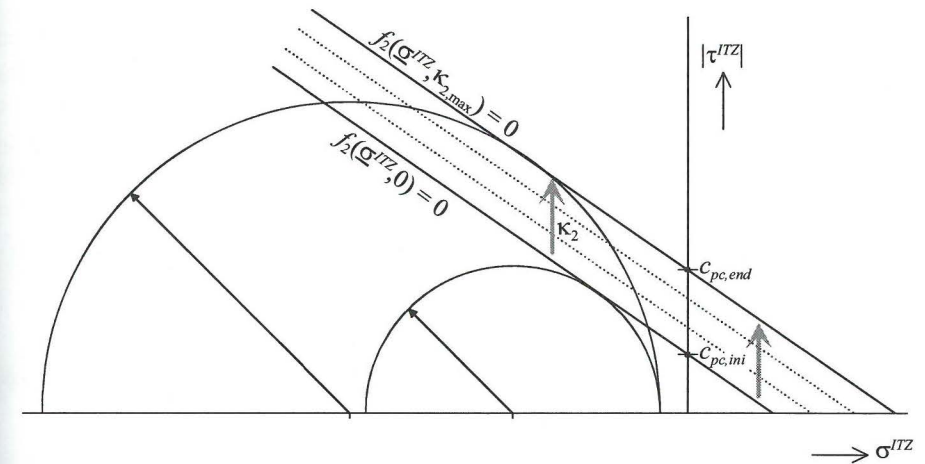


Figure 4.23. Expansion of bounding surface for pore collapse due to a decrease of porosity.

The direction of return mapping of the trial stress state onto the bounding surface is determined by the direction of plastic flow. To this end a dilatancy angle for compressive pore collapse  $\psi_{pc}$  is introduced. According to the classical theory of elasto-plasticity, the relations between the principal plastic strain increments and  $\psi_{pc}$  are

$$\begin{bmatrix} \Delta \varepsilon_1^{p,ITZ} \\ \Delta \varepsilon_3^{p,ITZ} \end{bmatrix} = \Delta \vartheta_{\varepsilon} \begin{bmatrix} \frac{1}{2}(1 + \sin \psi_{pc}) \\ -\frac{1}{2}(1 - \sin \psi_{pc}) \end{bmatrix} \quad (4.18)$$

with

$\Delta \varepsilon_1^{p,ITZ}$  = maximum principal plastic strain increment

$\Delta \varepsilon_3^{p,ITZ}$  = minimum principal plastic strain increment

$\Delta \vartheta_{\varepsilon}$  = plastic multiplier



The principal plastic strain increments are linked to the plastic strain increments in  $r$ - and  $\theta^*$ -direction by

$$\Delta \varepsilon_1^{p,ITZ} = \frac{1}{2} \left( \Delta \varepsilon_r^{p,ITZ} + \Delta \varepsilon_\theta^{p,ITZ} + \sqrt{(\Delta \varepsilon_r^{p,ITZ} - \Delta \varepsilon_\theta^{p,ITZ})^2 + (\Delta \gamma_{r\theta}^{p,ITZ})^2} \right)$$

$$\Delta \varepsilon_3^{p,ITZ} = \frac{1}{2} \left( \Delta \varepsilon_r^{p,ITZ} + \Delta \varepsilon_\theta^{p,ITZ} - \sqrt{(\Delta \varepsilon_r^{p,ITZ} - \Delta \varepsilon_\theta^{p,ITZ})^2 + (\Delta \gamma_{r\theta}^{p,ITZ})^2} \right)$$

with

$$\Delta \varepsilon_r^{p,ITZ} = \frac{\Delta u^{cr}}{R_2 - R_1} \quad \text{and} \quad \Delta \gamma_{r\theta}^{p,ITZ} = \frac{\Delta w^{cr}}{R_2 - R_1}$$

The expressions for  $\Delta \varepsilon_\theta^{p,ITZ}$ ,  $\Delta u^{cr}$  and  $\Delta w^{cr}$  at angle  $\theta_i^*$  are given by equation (4.16) and (4.17) in section 4.3.5.3. The (minor) influence of  $\Delta \bar{\sigma}_\theta^{ITZ}$ , however, is not taken into account because this stress component is calculated as an average of the stress correction vectors along the entire ITZ. As the present constitutive law will be applied locally for a single small part of the ITZ at a certain angle  $\theta_i^*$ , the value of  $\Delta \bar{\sigma}_\theta^{ITZ}$  is not known a priori. After application of the constitutive law for all parts of the ITZ, the influence of  $\Delta \bar{\sigma}_\theta^{ITZ}$  however will be allowed for (section 4.3.7).

Disregarding the influence of  $\Delta \bar{\sigma}_\theta^{ITZ}$ , the plastic strain increments in  $r$ - and  $\theta^*$ -direction are linked to the local ITZ stress corrections by

$$\begin{bmatrix} \Delta \varepsilon_r^{p,ITZ} \\ \Delta \varepsilon_\theta^{p,ITZ} \\ \Delta \gamma_{r\theta}^{p,ITZ} \end{bmatrix} = \begin{bmatrix} \lambda_{er,cr} & \lambda_{er,\sigma\theta} & 0 \\ \lambda_{e\theta,cr} & \lambda_{e\theta,\sigma\theta} & 0 \\ 0 & 0 & \lambda_\gamma \end{bmatrix} \begin{bmatrix} \Delta \sigma_r^{ITZ} \\ \Delta \sigma_\theta^{ITZ} \\ \Delta \tau_{r\theta}^{ITZ} \end{bmatrix} \quad (4.19)$$

with

$$\lambda_{er,cr} = \frac{1}{R_2 - R_1} \left( \frac{\lambda_u^I + \lambda_u^{II}}{2} - \frac{\lambda_{\sigma\theta}^I + \lambda_{\sigma\theta}^{II}}{2} \lambda_{u,\sigma\theta} \right)$$

$$\lambda_{e\theta,cr} = -\frac{\lambda_{\sigma\theta}^I + \lambda_{\sigma\theta}^{II}}{2} \lambda_{e\theta,\sigma\theta}$$

$$\lambda_{er,\sigma\theta} = \frac{\lambda_{u,\sigma\theta}}{R_2 - R_1}$$

$$\lambda_\gamma = \frac{\lambda_w^{II}}{R_2 - R_1}$$

In conformance with the theory of classical elasto-plasticity, the principal plastic strain increments due to compressive pore collapse coincide with the principal ITZ stresses, i.e. the axes of principal ITZ stresses do not rotate during return mapping. Accordingly, a stress point  $(\sigma_R, 0)$  can be indicated towards which the corrections of

all stress points on Mohr's stress circle do point (see figure 4.24). The components of the stress correction vector herewith are interrelated as follows

$$\frac{\Delta \sigma_\theta^{ITZ}}{\Delta \tau_{r\theta}^{ITZ}} = \frac{\sigma_\theta^{i,ITZ} - \sigma_R}{\tau_{r\theta}^{i,ITZ}}$$

$$\frac{\Delta \sigma_r^{ITZ}}{\Delta \tau_{r\theta}^{ITZ}} = \frac{\sigma_r^{i,ITZ} - \sigma_R}{\tau_{r\theta}^{i,ITZ}}$$

Substituting these expressions into equation (4.18) results in a quadratic equation in  $\sigma_R$ .

$$\sin \psi_{pc} \sqrt{(\alpha_2 - \sigma_R \alpha_4)^2 + \alpha_5^2} = \alpha_1 - \sigma_R \alpha_3 \quad (4.20)$$

with

$$\alpha_1 = (\lambda_{er,cr} + \lambda_{e\theta,cr}) \sigma_r^{i,ITZ} + (\lambda_{er,\sigma\theta} + \lambda_{e\theta,\sigma\theta}) \sigma_\theta^{i,ITZ}$$

$$\alpha_2 = (\lambda_{er,cr} - \lambda_{e\theta,cr}) \sigma_r^{i,ITZ} + (\lambda_{er,\sigma\theta} - \lambda_{e\theta,\sigma\theta}) \sigma_\theta^{i,ITZ}$$

$$\alpha_3 = \lambda_{er,cr} + \lambda_{e\theta,cr} + \lambda_{er,\sigma\theta} + \lambda_{e\theta,\sigma\theta}$$

$$\alpha_4 = \lambda_{er,cr} - \lambda_{e\theta,cr} + \lambda_{er,\sigma\theta} - \lambda_{e\theta,\sigma\theta}$$

$$\alpha_5 = \lambda_\gamma \tau_{r\theta}^{i,ITZ}$$

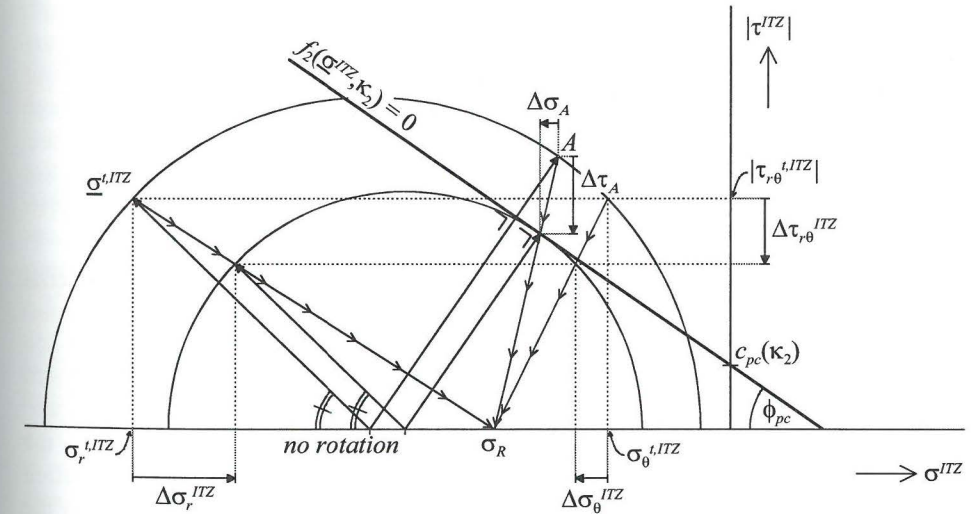


Figure 4.24. Return mapping with no rotation of axes of principal stress.

Raising equation (4.20) to the square yields the following potential solutions

$$\sigma_R = \frac{\alpha_2 \alpha_4 \sin^2 \psi_{pc} - \alpha_1 \alpha_3 \pm \sin \psi_{pc} \sqrt{Det}}{\alpha_4^2 \sin^2 \psi_{pc} - \alpha_3^2}$$

with

$$Det = (\alpha_2 \alpha_3 - \alpha_1 \alpha_4)^2 + \alpha_5^2 (\alpha_3^2 - \alpha_4^2 \sin^2 \psi_{pc})$$

It appears that for physically acceptable values assigned to the elastic properties of the RVE, the determinant  $Det$  is always positive ( $|\alpha_3| > |\alpha_4|$ ). In this way, two solutions for  $\sigma_R$  are generated. The correct solution for  $\sigma_R$  is that solution satisfying equation (4.20), and in case both solutions satisfy equation (4.20), that solution which produces the largest amount of plastic work<sup>5</sup>

$$\Delta W^p = \sigma_r^{i,ITZ} \Delta \varepsilon_r^{p,ITZ}(\sigma_R) + \sigma_\theta^{i,ITZ} \Delta \varepsilon_\theta^{p,ITZ}(\sigma_R) = \max$$

Having determined the location of  $\sigma_R$ , the ‘trial’ elastic stress state can be put back onto the stress-state bounding surface. Return mapping of stress point  $A$  gives

$$\frac{\Delta \tau_A}{\tau_A} = \frac{\Delta \sigma_A}{\sigma_A - \sigma_R} \quad \wedge \quad \Delta \tau_A + \Delta \sigma_A \tan \phi_{pc} = c_{pc}(\kappa_2) - \sigma_A \tan \phi_{pc} - \tau_A$$

$$\rightarrow \frac{\Delta \tau_A}{\tau_A} = \frac{c_{pc}(\kappa_2) - \sigma_A \tan \phi_{pc} - \tau_A}{\tau_A + (\sigma_A - \sigma_R) \tan \phi_{pc}}$$

with

$$\sigma_A = C_M(\underline{\sigma}^{i,ITZ}) + r_M(\underline{\sigma}^{i,ITZ}) \sin \phi_{pc}$$

$$\tau_A = r_M(\underline{\sigma}^{i,ITZ}) \cos \phi_{pc}$$

Finally, the ITZ stress correction vector in  $r, \theta^*$ -coordinates is given by

$$\begin{bmatrix} \Delta \sigma_r^{ITZ} \\ \Delta \sigma_\theta^{ITZ} \\ \Delta \tau_{r\theta}^{ITZ} \end{bmatrix} = \frac{\Delta \tau_A}{\tau_A} \begin{bmatrix} \sigma_r^{i,ITZ} - \sigma_R \\ \sigma_\theta^{i,ITZ} - \sigma_R \\ \tau_{r\theta}^{i,ITZ} \end{bmatrix}$$

By introducing the dilatancy angle for pore collapse  $\psi_{pc}$ , an additional material parameter is introduced that may influence the strengthening (or softening) behaviour of the RVE loaded in multiaxial compression. This becomes clear when compressive pore collapse is considered upon loading consisting of imposed deformations in radial and tangential direction, e.g. a (compressive) loading path<sup>6</sup> with  $\varepsilon_\theta = -0.1 \varepsilon_r$ . Such a loading path will induce strengthening behaviour when the ratio between the plastic strain in  $\theta^*$ -direction and the plastic strain in  $r$ -direction  $\varepsilon_\theta^p / \varepsilon_r^p$  is more (positive) than  $-0.1$ . On the other hand, softening occurs when the ratio is less than  $-0.1$ . Evidently, for each loading path of imposed deformations a critical value  $\psi_{crit}$  can be indicated upon which the material behaviour changes from strengthening to softening. This is illustrated in figure 4.25.

<sup>5</sup> The plastic work in shear is equal for both solutions of  $\sigma_R$

<sup>6</sup> In this example Poisson’s ratio is more than 0.1 ( $\nu > 0.1$ ). Hence, a loading path with  $\varepsilon_\theta = -0.1 \varepsilon_r$  is multiaxial compressive in the elastic region ( $\sigma_\theta < 0$ ).

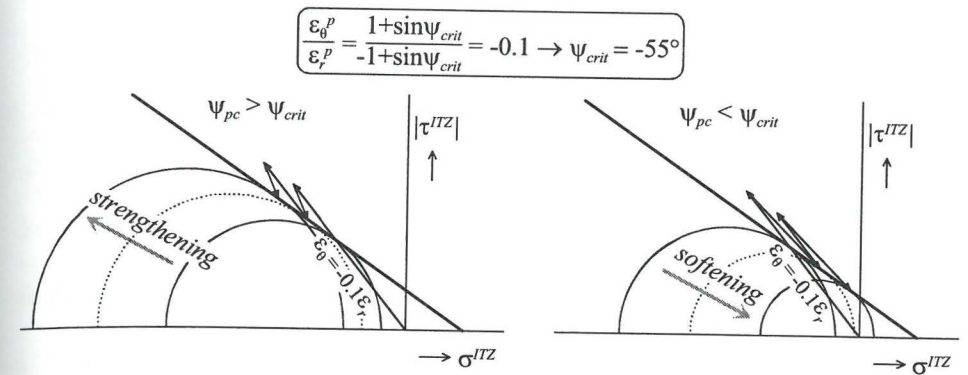


Figure 4.25. Strengthening in case  $\psi_{pc} > \psi_{crit}$  and softening in case  $\psi_{pc} < \psi_{crit}$ .

#### 4.3.6.3 Mesoscopic cracking along the ITZ or microscopic pore collapse?

The stress state in the ITZ is bounded by two bounding surfaces concerning the cracking criteria as described in the preceding sections. If the trial stress state in the ITZ violates only one of these two failure criteria, the stress state is put back onto that particular bounding surface. However, when the ITZ trial stress state violates both cracking criteria, it is not evident which procedure should be pursued.

This problem is usually tackled by determining intersection point(s) of the bounding surfaces in stress space and defining the right bounding surface at either side of the intersection point(s). Obviously, this procedure can only be applied when both bounding surfaces are formulated in *the same* stress space. The bounding surfaces concerning the cracking criteria as described in the preceding sections, however, are *not* formulated in the same stress space. While the criterion of microscopic pore collapse is formulated in a ‘continuum’ stress space (in which Mohr’s stress circle resembles the stress state in all planes with arbitrary orientation), the criterion of mesoscopic cracking along the ITZ is formulated in a ‘single plane’ stress space for a specific plane running along the tangential  $\theta^*$ -direction (in which the stress state resembles a single point).

The problem is solved when the linear Mohr-Coulomb bounding surface for pore collapse is transferred from the ‘continuum’ stress space to the ‘single plane’ stress space  $(\sigma_r, \tau_{r\theta})$ . After this transfer, the normal stress component in tangential  $\theta^*$ -direction  $\sigma_\theta$  is not considered anymore, i.e. the stress vector is reduced from three to only two components:  $\sigma_r$  and  $\tau_{r\theta}$ . To account for the influence of  $\sigma_\theta$  on the shape of the bounding surface in the case of pore collapse, this stress component is introduced as an additional internal state parameter in the ‘single plane’ stress space  $(\sigma_r, \tau_{r\theta})$ .

When the linear bounding surface for pore collapse is transferred from the ‘continuum’ stress space to the ‘single plane’ stress space  $(\sigma_r, \tau_{r\theta})$ , the shape changes into an ellipse.

$$f_2(\underline{\sigma}^{ITZ}, \kappa_2, \sigma_\theta^{ITZ}) = |\tau_{r\theta}^{ITZ}| - \sqrt{\sin^2 \phi_{pc} \left( \frac{c_{pc}(\kappa_2)}{\tan \phi_{pc}} - \sigma_\theta^{ITZ} - \frac{1}{2}(\sigma_r^{ITZ} - \sigma_\theta^{ITZ}) \right)^2 - \frac{1}{4}(\sigma_r^{ITZ} - \sigma_\theta^{ITZ})^2} = 0$$

with

$$\underline{\sigma}^{ITZ} = \begin{bmatrix} \sigma_r^{ITZ} \\ \tau_{r\theta}^{ITZ} \end{bmatrix}$$

For several values of  $\sigma_\theta^{ITZ}$ , this elliptic bounding surface is drawn in figure 4.26.

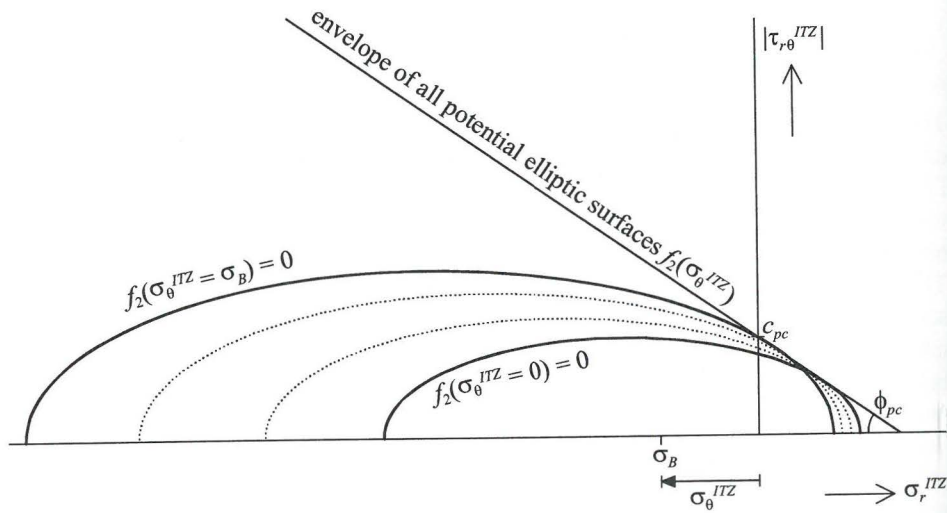


Figure 4.26. Bounding surfaces for pore collapse in the  $(\sigma_r, \tau_{r\theta})$  stress-space for several values of  $\sigma_\theta^{ITZ}$ .

The stress coordinates of the intersection point(s)  $I$  of the bounding surfaces for mesoscopic cracking along the ITZ and microscopic pore collapse are found by solving the following set of equations.

$$\begin{aligned} f_1(\underline{\sigma}^{ITZ}, \kappa_1) &= 0 \\ f_2(\underline{\sigma}^{ITZ}, \kappa_2, \sigma_\theta^{ITZ}) &= 0 \end{aligned}$$

The potential solutions of the resulting quadratic equation in  $\sigma_r^{ITZ}$  are

$$\sigma_r^{ITZ}(I) = \sigma_\theta^{ITZ} + \frac{2f_1^* \tan^2 \phi - c_{pc}^* \sin \phi_{pc} \pm \sqrt{Det}}{2 \tan^2 \phi + \frac{1}{2} \cos^2 \phi_{pc}}$$

with

$$Det = \left( 4c_{pc}^* (c_{pc}^* - f_1^* \sin \phi_{pc}) - (f_1^* \cos \phi_{pc})^2 \right) \tan^2 \phi + (c_{pc}^*)^2$$

$$f_1^* = f_1(\kappa_1) - \sigma_\theta^{ITZ}$$

$$c_{pc}^* = c_{pc}(\kappa_2) \cos \phi_{pc} - \sigma_\theta^{ITZ} \sin \phi_{pc}$$

Zero, one or two solutions exist for the point of intersection, depending on the value of the determinant  $Det$  and the sign of  $\tau_{r\theta}^{ITZ}(I)$ . These potential solutions are illustrated graphically in figure 4.27.

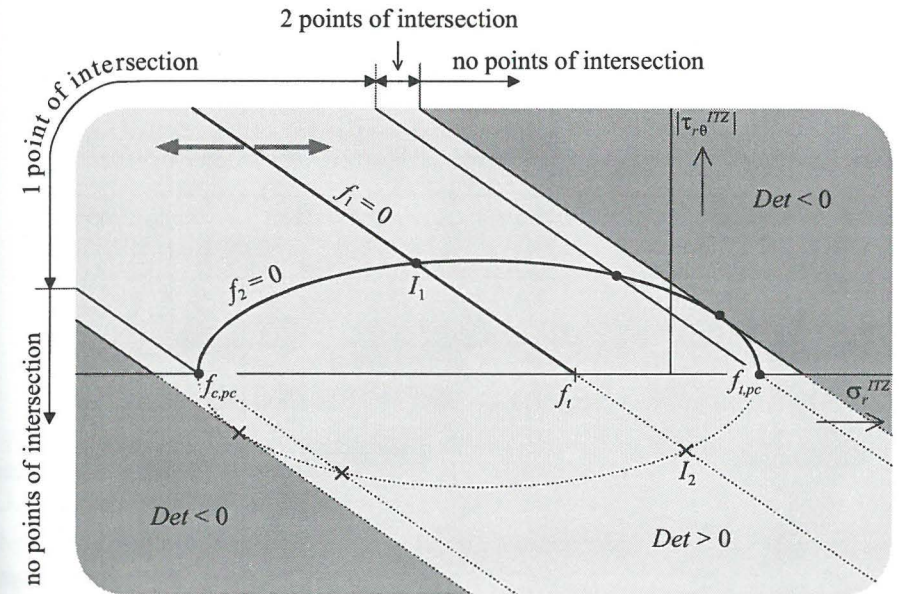


Figure 4.27. Potential intersection points of stress-state bounding surfaces.

Depending on the 'trial' stress state  $\underline{\sigma}^{ITZ}$  and the solution of the intersection point(s), the diagram displayed in figure 4.28 shows which cracking criterion should be applied. This procedure might not be very accurate for 'trial' stress states in the direct neighbourhood of the point of intersection. In those cases, the final stress state  $\underline{\sigma}^{ITZ}$  might fall outside the stress-state bounding surface that was not taken into account. However, as this error will be corrected during the next time step and the time steps are very small, the accuracy of the presented procedure suffices. Generally  $f_{c,pc} < f_t < f_{l,pc}$ , so mesoscopic cracking along the ITZ prevails in the tensile and low compressive regime, while microscopic pore collapse is predominant in the high compressive regime. This results in an overall stress-state bounding surface as depicted in figure 4.29.

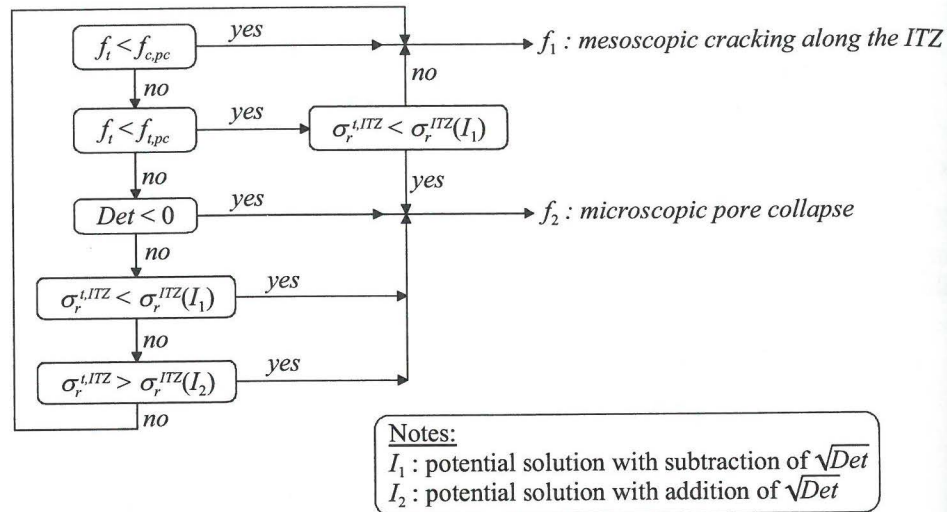


Figure 4.28. Flow chart for the determination of the ‘true’ cracking criterion.

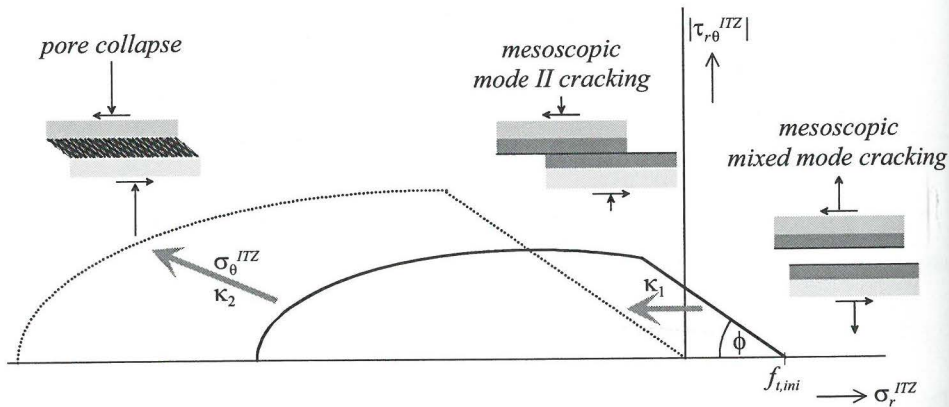


Figure 4.29. Overall stress-state bounding surface.

4.3.6.4 Crack closure

During an unloading/reloading cycle in a multiaxial compression test, potential crack closure of open mode I cracks loaded in compression is essential. Crack modelling according to the theory of classical elasto-plasticity does not capture this phenomenon sufficiently. Therefore, the classical theory is extended allowing crack closure without built-up of compressive forces.

During tensile loading the (plastic) Crack Opening Displacement  $COD^7$  is recorded. When the loading reverses from tensile to compressive, the constitutive model allows no compressive force transfer between the crack faces if the  $COD$  is positive. Consequently, no compressive forces will arise during crack closure while the  $COD$  decreases to zero. When the crack is fully closed ( $COD = 0$ ), compressive forces will build up again as in the classical theory of elasto-plasticity (figure 4.30).

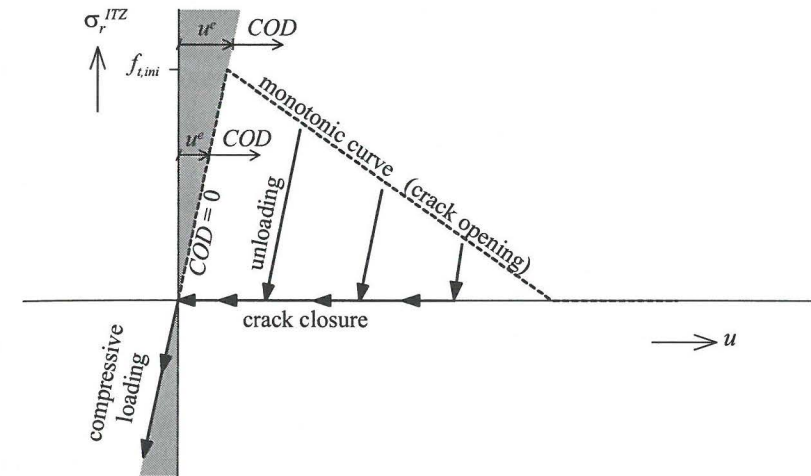


Figure 4.30. Crack opening/closure during load cycles in radial direction.

4.3.7 Crack interaction effects

The computation of local ITZ stress correction vectors  $\Delta \underline{\sigma}^{ITZ}(\theta_i^*)$ , as explained in the preceding section, does not include any crack interaction effects. Each local ITZ stress correction vector at a certain angle  $\theta_i^*$  is computed assuming no plasticity in any other part of the ITZ.

According to the equations derived in section 4.3.5.3, the incremental crack opening displacement  $\Delta u^{cr}(\theta_i^*)$  (or  $\Delta \epsilon_r^{p,ITZ}(\theta_i^*)$ ) and – in the case of microscopic pore collapse – the local plastic normal strain in tangential direction  $\Delta \epsilon_\theta^{p,ITZ}(\theta_i^*)$ , also depend on the averaged normal stress correction  $\Delta \bar{\sigma}_\theta^{ITZ}(\theta_i^*)$  in the tangential  $\theta^*$ -direction of the considered part of the ITZ. After computation of the primary ITZ stress correction vectors  $\Delta \underline{\sigma}^{ITZ}(\theta_i^*)$  in all parts around the RVE,  $\Delta \bar{\sigma}_\theta^{ITZ}(\theta_i^*)$  can be calculated for each specific part. The influence of this averaged stress component is then allowed for by computing additional secondary ITZ stress corrections  $\Delta \Delta \sigma_r^{ITZ}(\theta_i^*)$  and  $\Delta \Delta \sigma_\theta^{ITZ}(\theta_i^*)$ , with this averaged stress component and the computed incremental crack displacements (or plastic ITZ strains) as conditions of constraint. In case of mesoscopic cracking along the ITZ, these secondary ITZ stress corrections are

<sup>7</sup> The  $COD$  equals exclusively the radial crack displacement  $u^{cr}$  during mesoscopic mode I cracking along the ITZ. Potential (negative) radial crack displacement during pore collapse is not taken into account.

$$\begin{aligned}\Delta\Delta\sigma_r^{ITZ}(\theta_i^*) &= -\left(\frac{\lambda_u^I - \lambda_u^{II}}{\lambda_u^I + \lambda_u^{II}}\right)\Delta\bar{\sigma}_\theta^{ITZ}(\theta_i^*) \\ \Delta\Delta\sigma_\theta^{ITZ}(\theta_i^*) &= \left(\frac{\lambda_{\sigma\theta}^I + \lambda_{\sigma\theta}^{II}}{2}\right)\Delta\Delta\sigma_r^{ITZ}(\theta_i^*) + \left(\frac{\lambda_{\sigma\theta}^I - \lambda_{\sigma\theta}^{II}}{2}\right)\Delta\bar{\sigma}_\theta^{ITZ}(\theta_i^*)\end{aligned}\quad (4.21)$$

In case of microscopic pore collapse, the interrelation between the plastic normal strains and the *primary* ITZ normal stress corrections is given by equation (4.19). Considering (4.16) and (4.17), the interrelation between the (zero) *secondary* plastic normal strain increments and the *secondary* ITZ normal stress corrections becomes

$$\begin{bmatrix} 0 \\ 0 \end{bmatrix} = \begin{bmatrix} \lambda_{\varepsilon r, \sigma r} & \lambda_{\varepsilon r, \sigma\theta} & \lambda_{\varepsilon\theta, \sigma\theta} \\ \lambda_{\varepsilon\theta, \sigma r} & \lambda_{\varepsilon\theta, \sigma\theta} & \lambda_{\varepsilon\theta, \sigma\theta} \end{bmatrix} \begin{bmatrix} \Delta\Delta\sigma_r^{ITZ}(\theta_i^*) \\ \Delta\Delta\sigma_\theta^{ITZ}(\theta_i^*) \\ \Delta\bar{\sigma}_\theta^{ITZ}(\theta_i^*) \end{bmatrix}$$

with

$$\begin{aligned}\lambda_{\varepsilon r, \sigma\theta} &= \frac{1}{R_2 - R_1} \left( \frac{\lambda_u^I - \lambda_u^{II}}{2} - \frac{\lambda_{\sigma\theta}^I - \lambda_{\sigma\theta}^{II}}{2} \lambda_{u, \sigma\theta} \right) \\ \lambda_{\varepsilon\theta, \sigma\theta} &= -\frac{\lambda_{\sigma\theta}^I - \lambda_{\sigma\theta}^{II}}{2} \lambda_{\varepsilon\theta, \sigma\theta}\end{aligned}$$

Solving this set of equations yields identical expressions for the *secondary* ITZ stress corrections as given in equation (4.21). Obviously, in case of zero *secondary* plastic strains – i.e. elastic material behaviour – no distinction exists between the two crack mechanisms.

Crack interaction effects also exist for the shear component of the ITZ stress correction vectors. Generally, the corrected ITZ shear stresses are not in equilibrium. In fact, a state of equilibrium is only reached if the addition of all shear stress correction vectors equals zero (figure 4.31).

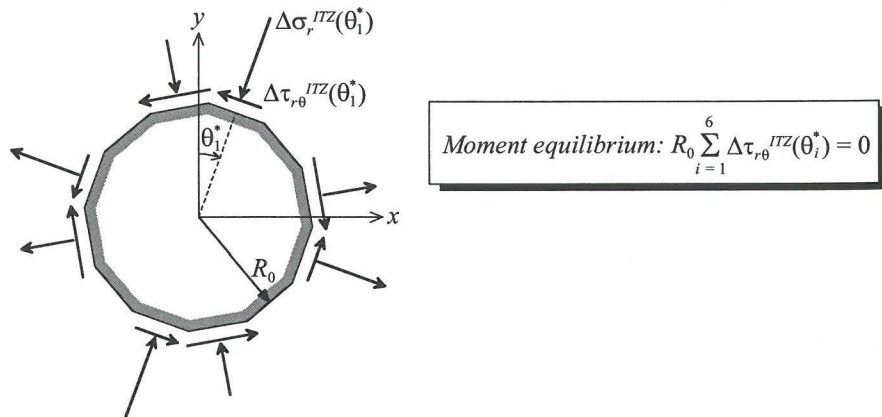


Figure 4.31. Moment equilibrium in case of non-linear ITZ behaviour.

In case the *primary* shear stress correction vectors  $\Delta\tau_{r\theta}^{ITZ}(\theta_i^*)$  are not in equilibrium, the core of the RVE rotates within the outer layer of the RVE until a state of equilibrium is reached. As a result, a *secondary* ITZ shear stress correction  $\Delta\Delta\tau_{r\theta}^{ITZ}$ , equal for all parts of the ITZ, is computed

$$\Delta\Delta\tau_{r\theta}^{ITZ} = -\frac{1}{6} \sum_{i=1}^6 \Delta\tau_{r\theta}^{ITZ}(\theta_i^*)$$

Finally, the final stress state is obtained – for each part of the ITZ at angle  $\theta_i^*$  – after applying both *primary* and *secondary* stress corrections

$$\underline{\sigma}^{i, ITZ}(\theta_i^*) = \underline{\sigma}^{i, ITZ}(\theta_i^*) + \Delta\underline{\sigma}^{ITZ}(\theta_i^*) + \Delta\Delta\underline{\sigma}^{ITZ}(\theta_i^*)$$

If cracking in the ITZ occurs, the *primary* ITZ stress corrections put the ‘trial’ stress state back onto the appropriate bounding surface. The addition of the *secondary* ITZ stress corrections causes the final ITZ stress state to deviate from this bounding surface. The algorithm therefore remains stable only when the *secondary* stress corrections remain small compared to the *primary* stress corrections. The numerical simulations with the model (section 4.4) show that this is indeed the case.

#### 4.3.8 Correction of trial macro stress state

For each part of the ITZ at a specific angle  $\theta_i^*$ , the local stress corrections at the outer boundary of the RVE are determined with equation (4.13). Including the secondary stress corrections in the ITZs they now read

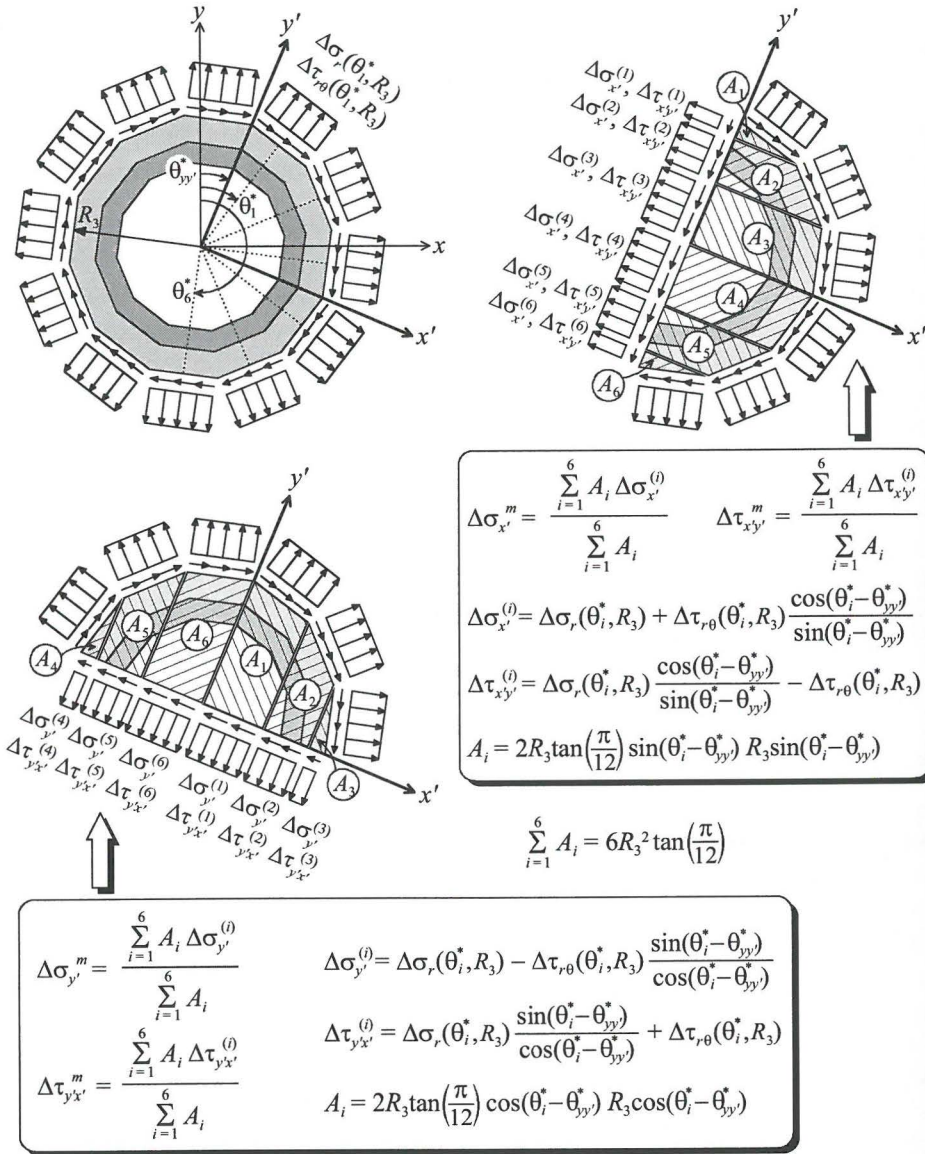
$$\begin{aligned}\Delta\sigma_r(\theta_i^*, R_3) &= \left(\frac{\lambda_{\sigma r}^I + \lambda_{\sigma r}^{II}}{2}\right) \left(\Delta\sigma_r^{ITZ}(\theta_i^*) + \Delta\Delta\sigma_r^{ITZ}(\theta_i^*)\right) + \left(\frac{\lambda_{\sigma r}^I - \lambda_{\sigma r}^{II}}{2}\right) \Delta\bar{\sigma}_\theta^{ITZ}(\theta_i^*) \\ \Delta\tau_{r\theta}(\theta_i^*, R_3) &= \lambda_{\tau}^{II} \left(\Delta\tau_{r\theta}^{ITZ}(\theta_i^*) + \Delta\Delta\tau_{r\theta}^{ITZ}(\theta_i^*)\right)\end{aligned}$$

Based on these *local* stress corrections at the outer boundary of the RVE, the correction of the trial *macro*-stress vector is determined by computing the volume average of these local stresses according to a rotated Cartesian  $(x', y', z)$ -coordinate system (with the  $y'$ -axis aligned with  $\theta_{yy'}^* = \theta_1^* - \pi/12$ ). This procedure is indicated in figure 4.32.

Further evaluation of the expressions for the  $(x', y', z)$  macro-stress corrections, as shown in figure 4.32, results in

$$\begin{aligned}\Delta\sigma_{x'}^m &= \frac{1}{3} \sum_{i=1}^6 \left( \Delta\sigma_r(\theta_i^*, R_3) \sin^2(\theta_i^* - \theta_{yy'}^*) + \Delta\tau_{r\theta}(\theta_i^*, R_3) \sin(\theta_i^* - \theta_{yy'}^*) \cos(\theta_i^* - \theta_{yy'}^*) \right) \\ \Delta\sigma_{y'}^m &= \frac{1}{3} \sum_{i=1}^6 \left( \Delta\sigma_r(\theta_i^*, R_3) \cos^2(\theta_i^* - \theta_{yy'}^*) - \Delta\tau_{r\theta}(\theta_i^*, R_3) \sin(\theta_i^* - \theta_{yy'}^*) \cos(\theta_i^* - \theta_{yy'}^*) \right) \\ \Delta\tau_{x'y'}^m &= \frac{1}{3} \sum_{i=1}^6 \left( \Delta\sigma_r(\theta_i^*, R_3) \sin(\theta_i^* - \theta_{yy'}^*) \cos(\theta_i^* - \theta_{yy'}^*) - \Delta\tau_{r\theta}(\theta_i^*, R_3) \sin^2(\theta_i^* - \theta_{yy'}^*) \right)\end{aligned}$$

$$\Delta\tau_{y'x'}^m = \frac{1}{3} \sum_{i=1}^6 \left( \Delta\sigma_r(\theta_i^*, R_3) \sin(\theta_i^* - \theta_{yy}^*) \cos(\theta_i^* - \theta_{yy}^*) + \Delta\tau_{r\theta}(\theta_i^*, R_3) \cos^2(\theta_i^* - \theta_{yy}^*) \right)$$



note:  $A_i$  = area of part  $i$

Figure 4.32. Determination of macro-stress corrections in the rotated  $(x', y', z)$ -coordinate system.

In appendix B is outlined that when the ITZ shear stress corrections (and consequently the outer boundary shear stress corrections) are in moment equilibrium, the volume averaged macroscopic shear stresses  $\Delta\tau_{x'y'}^m$  and  $\Delta\tau_{y'x'}^m$  are equal to each other. As the ITZ shear corrections are forced to be in equilibrium from the addition of the secondary ITZ shear stress corrections, the above macroscopic shear stresses are identical.

$$\Delta\tau_{x'y'}^m = \Delta\tau_{y'x'}^m$$

Finally, the results obtained in the rotated  $(x', y', z)$ -coordinate system have to be rotated back to the global  $(x, y, z)$ -coordinate system using the transformation law

$$\begin{bmatrix} \Delta\sigma_x^m \\ \Delta\sigma_y^m \\ \Delta\tau_{xy}^m \end{bmatrix} = \begin{bmatrix} \cos^2\theta_{yy}^* & \sin^2\theta_{yy}^* & -2\cos\theta_{yy}^* \sin\theta_{yy}^* \\ \sin^2\theta_{yy}^* & \cos^2\theta_{yy}^* & 2\cos\theta_{yy}^* \sin\theta_{yy}^* \\ \cos\theta_{yy}^* \sin\theta_{yy}^* & -\cos\theta_{yy}^* \sin\theta_{yy}^* & \cos^2\theta_{yy}^* - \sin^2\theta_{yy}^* \end{bmatrix} \begin{bmatrix} \Delta\sigma_{x'}^m \\ \Delta\sigma_{y'}^m \\ \Delta\tau_{x'y'}^m \end{bmatrix}$$

Adding these macro-stress corrections to the trial macro-stress state, the new macro-stress state according to the non-rotated  $(x, y, z)$ -coordinate system is given by

$$\begin{bmatrix} \sigma_x^{1,m} \\ \sigma_y^{1,m} \\ \tau_{xy}^{1,m} \end{bmatrix} = \begin{bmatrix} \sigma_x^{t,m} \\ \sigma_y^{t,m} \\ \tau_{xy}^{t,m} \end{bmatrix} + \begin{bmatrix} \Delta\sigma_x^m \\ \Delta\sigma_y^m \\ \Delta\tau_{xy}^m \end{bmatrix}$$

#### 4.4 Performance of the numerical model

The performance of the numerical model at stage I and II is illustrated by simulations of a series of multi-axial plane-strain compression tests performed by Van Geel<sup>1998</sup> at Eindhoven University of Technology. These proportional tests, with 5%, 10%, 15%, 25% and 50% ratio between lateral and axial boundary forces, are performed on cubic specimens of  $100 \times 100 \times 100 \text{ mm}^3$ . The test set-up is displayed in figure 4.33.

The tests are carried out with uniform boundary displacement of the loading platens. To reduce frictional forces at the boundary of the concrete specimen, the experiments of Van Geel are carried out with teflon layers between the loading platens and the specimen. These teflon layers are modelled by adding interface elements with low frictional restraint ( $\tan\phi = 0.012$ ) [Vonk<sup>1992</sup>] between the loading platens and the specimen.

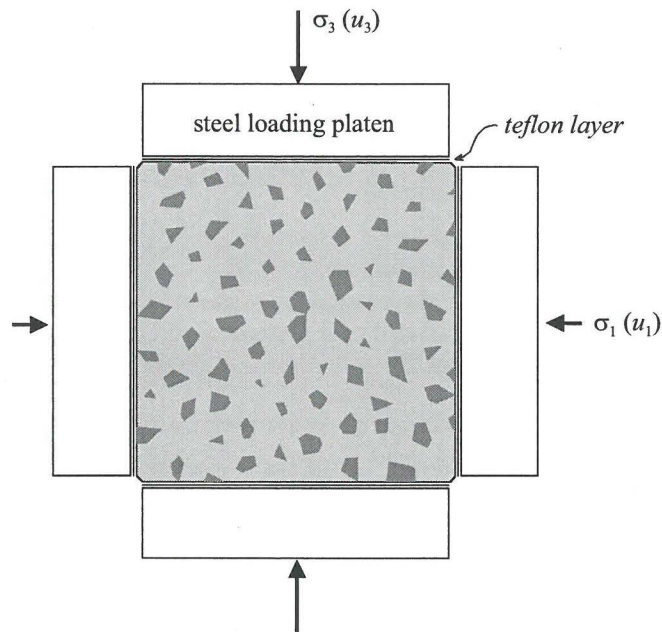


Figure 4.33. Test set-up.

The mesoscopic mesh for the concrete specimen is generated according to the procedure explained in section 4.2. Mesh generation is carried out in such a way that the grain pattern of a cross-section of the concrete cubes used by Van Geel is reproduced approximately, at least for the largest fraction of aggregate grains. The weight percentages of the concrete constituents, used by Van Geel, are listed in table 4.1.

Table 4.1. Weight percentages of concrete constituents [Van Geel<sup>1998</sup>].

C o n s t i t u e n t s		Normal Strength Concrete
PC Cement Type B		15.8 %
Max. aggregate size (Rounded river gravel)		8 mm
Size distribution	5-8 mm	17.0 %
	3-5 mm	5.7 %
	2-4 mm	15.3 %
	1-2 mm	11.5 %
	0.5-1 mm	11.5 %
	0.2-0.63 mm quartz sand	9.8 %
Water		8.1 %

The total mass of the (wet) concrete cube is about 2.5 kg. The aggregate mass percentage is 76.1 %. This means that the total mass of the aggregate is about 1.9 kg. With a density of the aggregates equal to 2800 kg/m<sup>3</sup> (estimate), the total volume of the aggregate fraction equals: 1.9/2800 ≈ 0.00068 m<sup>3</sup>.

To come to a representative cross section of a concrete cube with a certain grain distribution, a method is adopted presented by Walraven<sup>1980,1981</sup>. The method computes the total area of an arbitrary fraction of circular-shaped grains in a representative cross section out of a sphere-shaped grain distribution according to the Fuller grading-curve. As the grain distribution of Van Geel resembles the Fuller grading-curve quite well [Bongers<sup>1997, 1998a</sup>], application of the method is permitted here. According to this method, the probability that an arbitrary point in a representative cross section is located within an intersection circle with diameter  $D < D_0$  is given by

$$P_c(D < D_0) = p_k \left( 1.072 \sqrt{\frac{D_0}{D_{\max}}} - 0.0535 \left( \frac{D_0}{D_{\max}} \right)^4 - \dots \right. \\ \left. \dots - 0.0115 \left( \frac{D_0}{D_{\max}} \right)^6 - 0.0045 \left( \frac{D_0}{D_{\max}} \right)^8 - 0.0025 \left( \frac{D_0}{D_{\max}} \right)^{10} \right)$$

with

$p_k$  = ratio between the total volume of the aggregates and the concrete volume

$D_{\max}$  = diameter of the largest aggregate grain

Application of this function, with  $p_k = 0.68$  and  $D_{\max} = 8$  mm., results in the grain distribution of a representative cross section as shown in table 4.2.

Table 4.2. Grain distribution of a representative cross section of the concrete cubes casted by Van Geel.

$D_0$ [mm]	$D_{0,prev.}$ [mm]	$P_c$ ( $D < D_0$ )	$P_c$ ( $D_{0,prev.} < D < D_0$ )	Fraction ( $D_{0,prev.} < D < D_0$ ) in a cross section of 100 x 100 mm <sup>2</sup> [mm <sup>2</sup> ]
2	0	0.3643	0.3643	3643 (0.3643 x 100 x 100)
3	2	0.4457	0.0814	814 (0.0814 x 100 x 100)
5	3	0.5702	0.1245	1245 (0.1245 x 100 x 100)
8	5	0.6800	0.1098	1098 (0.1098 x 100 x 100)

The grain distribution in the generated mesh is listed in table 4.3. Comparison of the grain distributions of both the generated mesh and the representative cross section of the tested concrete cubes learns that most of the largest fraction is incorporated explicitly in the generated mesh. The remaining part of the aggregate grains will be accounted for implicitly by choosing properly the RVE-dimensions of the finest fraction.

Table 4.3. Area of grain fractions in the generated mesh.

	computed area in generated mesh [ mm <sup>2</sup> ]
<b>Total of aggregate grains</b>	1400
<b>Fraction 8-16 mm</b>	0
<b>Fraction 5-8 mm</b>	839
<b>Fraction 3-5 mm</b>	492
<b>Fraction 2-3 mm</b>	63
<b>Fraction 0-2 mm</b>	6

The RVE-dimensions of the explicit coarse aggregate grains are calculated according to section 4.3.1. The average thickness of the ITZ around these grains and the average thickness of the bulk cement paste layer are both estimated equal to 150  $\mu\text{m}$ . The total cross sectional area of the ITZ layers  $A_{ITZ}^{coarse}$  and the bulk cement paste layers  $A_{bulk}^{coarse}$  around the explicit coarse aggregate grains is interrelated by considering the average diameter of these grains

$$\bar{D}_{agg}^{coarse} = \frac{839 \cdot 6.5 + 492 \cdot 4 + 63 \cdot 2.5 + 6}{1400} = 5.42 \text{ mm.}$$

Average RVE-dimensions for explicit coarse aggregate grains:

$$\begin{aligned} R_1^{coarse} &= 2.71 \text{ mm.} \quad (t_{ITZ} = 150 \mu\text{m}) \\ R_2^{coarse} &= 2.86 \text{ mm.} \quad (t_{bulk} = 150 \mu\text{m}) \\ R_3^{coarse} &= 3.01 \text{ mm.} \end{aligned}$$

$$A_{ITZ}^{coarse} = \frac{(R_2^{coarse})^2 - (R_1^{coarse})^2}{(R_1^{coarse})^2} \cdot 1400 = 159 \text{ mm}^2$$

$$A_{bulk}^{coarse} = \frac{(R_3^{coarse})^2 - (R_2^{coarse})^2}{(R_1^{coarse})^2} \cdot 1400 = 168 \text{ mm}^2$$

The average diameter of the fine aggregate grains (mortar) is calculated by averaging the remainder of the aggregate grain fractions.

$$\begin{aligned} \bar{D}_{agg}^{fine} &= \frac{(1098 - 839) \cdot 6.5 + (1245 - 492) \cdot 4 + (814 - 63) \cdot 2.5 + (3643 - 6)}{6800 - 1400} \\ &= 1.89 \text{ mm.} \end{aligned}$$

It is assumed that the ITZs occupy 40 % of the total volume of cement paste (see section 3.1.1). This implies that the ITZs occupy 1280 mm<sup>2</sup> and the bulk cement paste occupies 1920 mm<sup>2</sup> of the total cross sectional area of cement paste (10000 - 6800 = 3200 mm<sup>2</sup>). After subtraction of the ITZ and bulk cement paste cross sectional areas around the explicit coarse aggregate grains, the cross sectional areas of the ITZ and bulk cement paste around the fine aggregate grains are

$$A_{ITZ}^{fine} = A_{ITZ} - A_{ITZ}^{coarse} = 1280 - 159 = 1121 \text{ mm}^2$$

$$A_{bulk}^{fine} = A_{bulk} - A_{bulk}^{coarse} = 1920 - 168 = 1752 \text{ mm}^2$$

The RVE-dimensions for the fine aggregate grains (mortar) are determined by the cross sectional areas of the separate components

$$\frac{(R_2^{fine})^2 - (R_1^{fine})^2}{(R_1^{fine})^2} = \frac{A_{ITZ}^{fine}}{A_{agg}^{fine}}$$

$$\frac{(R_3^{fine})^2 - (R_2^{fine})^2}{(R_1^{fine})^2} = \frac{A_{bulk}^{fine}}{A_{agg}^{fine}}$$

With  $A_{agg}^{fine} = A_{agg} - A_{agg}^{coarse} = 6800 - 1400 = 5400 \text{ mm}^2$ , this results in the following RVE-dimensions for the fine aggregate grains (mortar)

$$\begin{aligned} R_1^{fine} &= 0.945 \text{ mm.} \quad (t_{ITZ} = 93 \mu\text{m}) \\ R_2^{fine} &= 1.038 \text{ mm.} \quad (t_{bulk} = 131 \mu\text{m}) \\ R_3^{fine} &= 1.169 \text{ mm.} \end{aligned}$$

The thickness of the ITZ layer of the RVE (both for the coarse aggregate grains and the mortar) may seem somewhat too large considering the statements about this zone in section 3.1.1. However, the cross sectional thickness of this layer does not resemble the 3-dimensional thickness of the layer perpendicular to the aggregate grain (see figure 4.34). The current 2-dimensional RVE can be interpreted as a representative cross section of a spherical 3-dimensional RVE. According to figure 4.34 this apparently yields a larger thickness of the ITZ layer in a 2D-configuration than in a 3D-configuration.

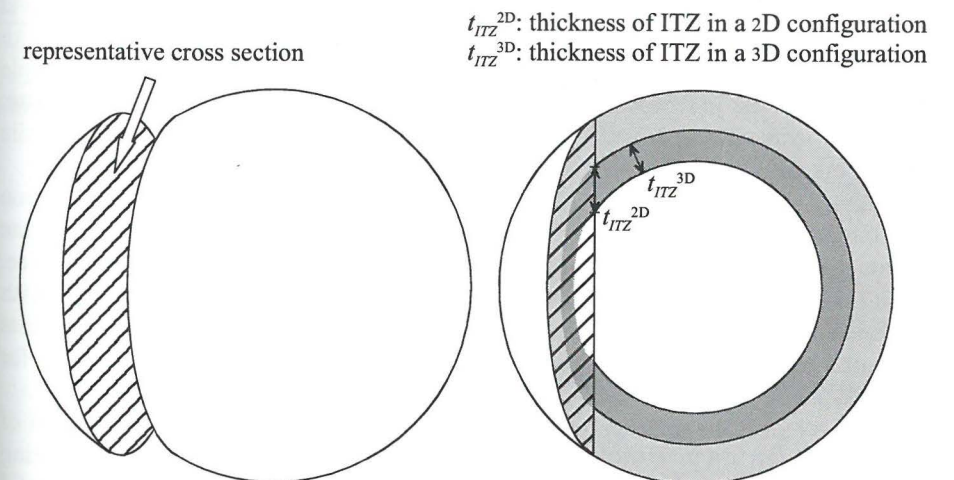


Figure 4.34. Thickness of the ITZ layer in 2D and in 3D.



Based on the properties of the concrete mix, used by Van Geel, the dimensions of the RVEs for the fine aggregate grains (mortar) and the explicit coarse aggregate grains are fixed. This leaves only the determination of the material properties of the separate phases. The material properties used in the simulations are listed in table 4.4.

Young's modulus of the aggregate grains and the bulk cement paste are averages from experimental data listed in section 3.1.2.1. Poisson's ratio and Young's modulus of the ITZ are determined according to an inverse modelling strategy, i.e. a best fit of the overall elastic moduli (computed according to appendix A) with the experimental data of Van Geel is achieved by variation of these properties.

Table 4.4. Input parameters.

Distribution of outer boundary displacements of the RVE			
$\frac{1}{2}$ macro-stress + $\frac{1}{2}$ macro-strain			
RVE-dimensions		Elastic properties	
Fine agg. / mortar	Coarse aggregates (2 - 8 mm)	Fine agg. / mortar	Coarse aggregates (2 - 8 mm)
$R_1 = 0.945$ mm.	-	$E_{agg} = 70000$ MPa	$E_{agg} = 65000$ MPa
$R_2 = 1.038$ mm.	$R_2 - R_1 = 0.150$ mm.	$E_{ITZ} = 10000$ MPa	$E_{ITZ} = 10000$ MPa
$R_3 = 1.169$ mm.	$R_3 - R_2 = 0.150$ mm.	$E_{bulk} = 18000$ MPa	$E_{bulk} = 18000$ MPa
		$\nu = 0.12$	$\nu = 0.12$
Mode I/II cracking along the ITZ		Pore collapse in ITZ	
$\phi = 25^\circ$		$\phi_{pc} = 0^\circ$	
$f_{t,ini} = 4$ MPa		$c_{pc,ini} = 15$ MPa	
$\kappa_{1,max} = 0.005$ mm.		$\kappa_{2,max} = 30$ %	
		$\psi_{pc} = -60^\circ$	
		$c_{pc,end} = 40.5$ MPa	

Experimental data on the material properties for mesoscopic mode I/II cracking along the ITZ is scarce. The friction angle  $\phi = 25^\circ$  resembles the stationary level after first slip reported by Alexander<sup>1971</sup> (see section 4.3.6.1). In conformity with the remarks regarding the tensile strength of the ITZ in section 3.1.2.1, the tensile strength  $f_{t,ini}$  of the ITZ is less than those values reported for the bulk cement paste. According to results obtained by Schlangen<sup>1993</sup> softening properties of the tensile strength are assumed to be very brittle.

Regarding the phenomenon of microscopic pore collapse, there is some experimental data available on the porosity of the ITZ layer. Based on this data (see section 3.1.1), maximum volumetric compaction of 30 % seems a proper choice. The remaining listed values are obtained by inverse modelling, i.e. a best fit with the observed macroscopic behaviour at stage II of the plane strain compression tests performed by Van Geel is achieved by variation of these material parameters for pore collapse.

The computed results are displayed in figure 4.35, along with experimental data of Van Geel. From these results it is clear that the model is capable of simulating macroscopic characteristics, such as initial elastic behaviour at stage I and strengthening behaviour and non-elastic volume compaction at stage II, quite well

for a large range of lateral confinement. The capability of the model to simulate the characteristic phenomenon of non-elastic volume compaction at stage II is also shown in figure 4.36. The experimental data of Van Geel is reproduced quite well, although the deviations become quite substantial for those tests with low confinement ( $\beta = 0.05, 0.10, 0.15$ ) way before ultimate strength is reached. This seems to indicate that the transition between stage II (volumetric contraction) and stage III (volumetric dilation) develops very gradually.

Although the agreement with the experimental data of Van Geel is very close for the axial loading diagram, the computed lateral deformations differ somewhat more from the experimental data. The fact is that, for the low confinement tests, the lateral deformations are slightly overestimated at initial non-linearity. This indicates that, at this stage, mesoscopic mode I/II cracking along the ITZ (those parts with radius  $R_0$  pointing approximately in lateral direction) is more pronounced in the simulations than in the experiments. This corresponds with experimental observations from Alexander<sup>1971</sup> as explained in section 4.3.6.1. According to these observations, the friction angle  $\phi$  for mesoscopic mode II cracking is at first slip somewhat higher than its final stationary value. As the present model uses the final stationary value also at first slip, an overestimation of lateral deformation will be the result. However, as stated in section 4.3.6.1, the influence on the macroscopic behaviour is small and is therefore not included in the numerical model.

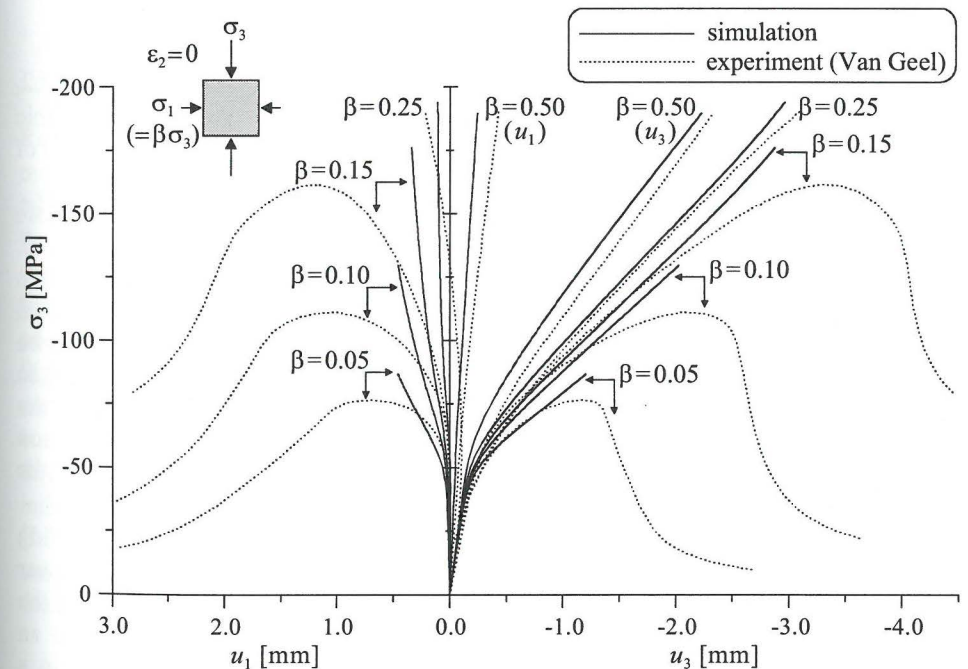


Figure 4.35. Model simulations of a test series of concrete loaded proportionally in multiaxial plane-strain compression.

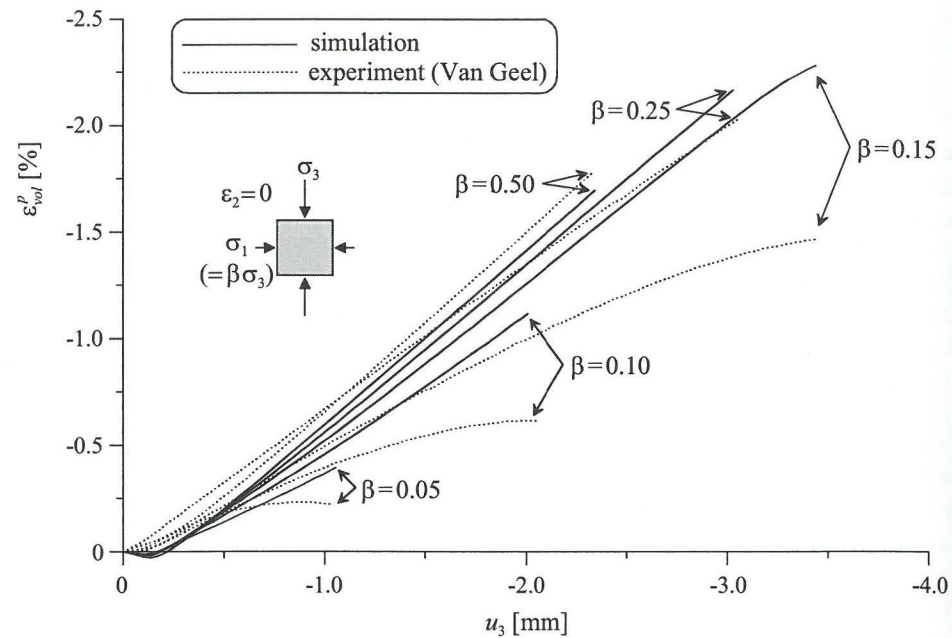


Figure 4.36. Non-elastic volume compaction at stage II.

Apart from these macroscopic characteristics, discussed in sections 3.2.1 and 3.2.2, also the unloading/reloading behaviour is mentioned as a typical macroscopic feature of concrete loaded in multiaxial compression at stage II. The performance of the model for such loading conditions is displayed in figure 4.37.

The unloading/reloading curves in figure 4.37 are quite realistic compared to those found by Van Mier (figure 3.14). Nevertheless, two differences may be pointed out. First of all, the model computations indicate that if unloading would be continued to a zero stress state, this would imply much more ‘unloading’ deformation than displayed by the experimental curves in figure 3.14. This discrepancy can be explained by the model assumption that potential cracking at stage II is limited to the ITZ. Still, as stated in the preceding section, substantial deviations between the simulations and the tests with low confinement indicate a very gradual transition between stage II and stage III. Ergo, (limited) cracking is likely to occur also in the bulk cement paste, long before ultimate strength is reached.

The second difference, pointed out with regard to the observed unloading/reloading behaviour, is that initial reloading according to the model takes place with a lower stiffness than initial reloading according to the experiment. Due to the fact that the model does not allow any compressive force transfer between crack faces in an open crack, open ITZ cracks are immediately closed at reloading, resulting in a lower initial reloading stiffness. Due to the irregular shape of the crack faces of ITZ mode I cracks, limited compressive force transfer through open cracks is likely to occur in the experiments, thus producing an initially more steep reloading branch.

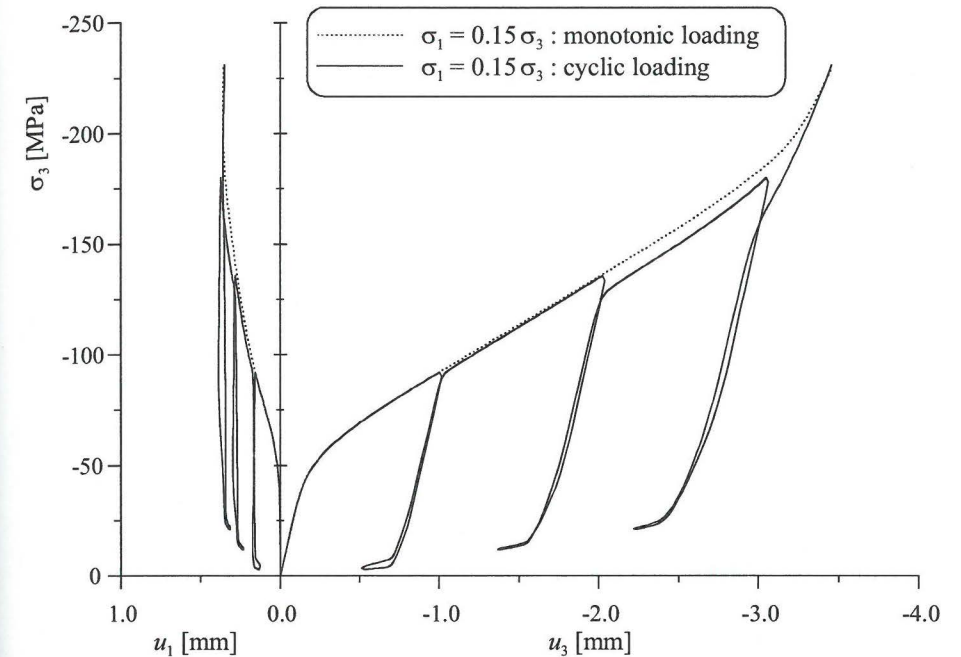


Figure 4.37. Model simulations for cyclic and monotonic loading.

Regarding the lack of mesoscopic experimental data for the determination of the numerical values of the input parameters for pore collapse ( $\phi_{pc}, c_{pc}, \psi_{pc}$ ) as listed in table 4.4, a parameter study is carried out on these parameters. Figure 4.38 shows the influence of a variation of  $\phi_{pc}$  on the macroscopic stress-displacement curves of three proportional tests ( $\beta = 0.05, 0.10$  and  $0.15$ ). For the simulations with  $\phi_{pc} = 15^\circ$ , the value of  $c_{pc, end}$  is also adjusted just in order to obtain a close match with at least one of the experimental tests ( $\beta = 0.05$ ).

Figures 4.39 and 4.40 show the influence of a variation of  $\psi_{pc}$  on the macroscopic curves of the three proportional tests. For  $\psi_{pc} = -50^\circ$  (figure 4.39) the value of  $c_{pc, end}$  is set equal to the value of  $c_{pc, ini}$ . Accordingly, no strengthening mechanism exists due to expansion of the pore collapse bounding surface. In this way, it is clearly indicated that a high (less negative) value of  $\psi_{pc}$  involves a too steep branch at stage II of the axial loading diagram. On the other hand, figure 4.40 shows that for a low value of  $\psi_{pc}$  ( $-80^\circ$ ) the degree of inclination of the ascending branch at stage II of the axial loading diagram becomes too low.

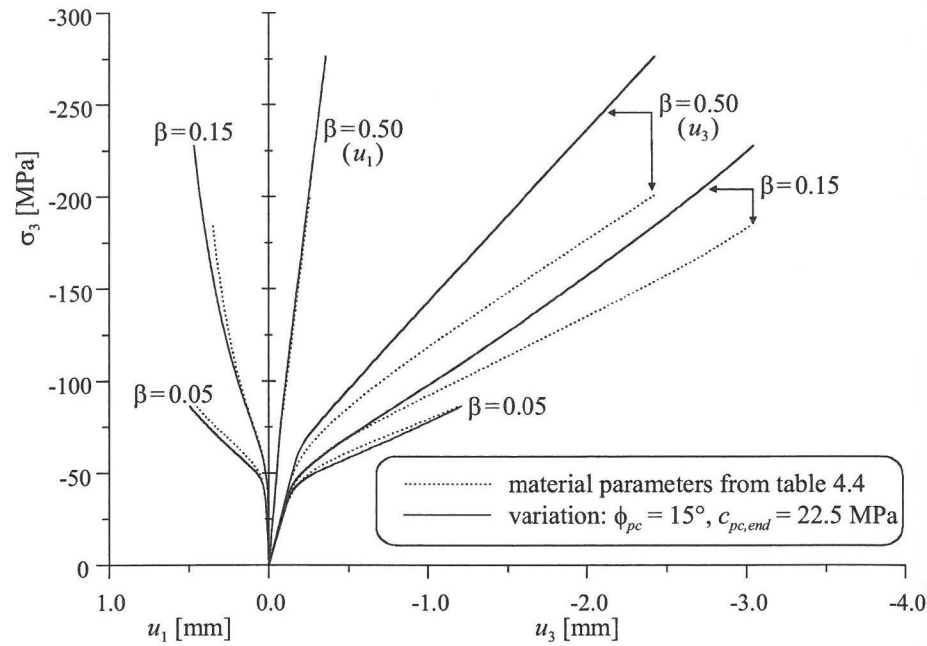


Figure 4.38. Variation of  $\phi_{pc}$  and  $c_{pc,end}$ .

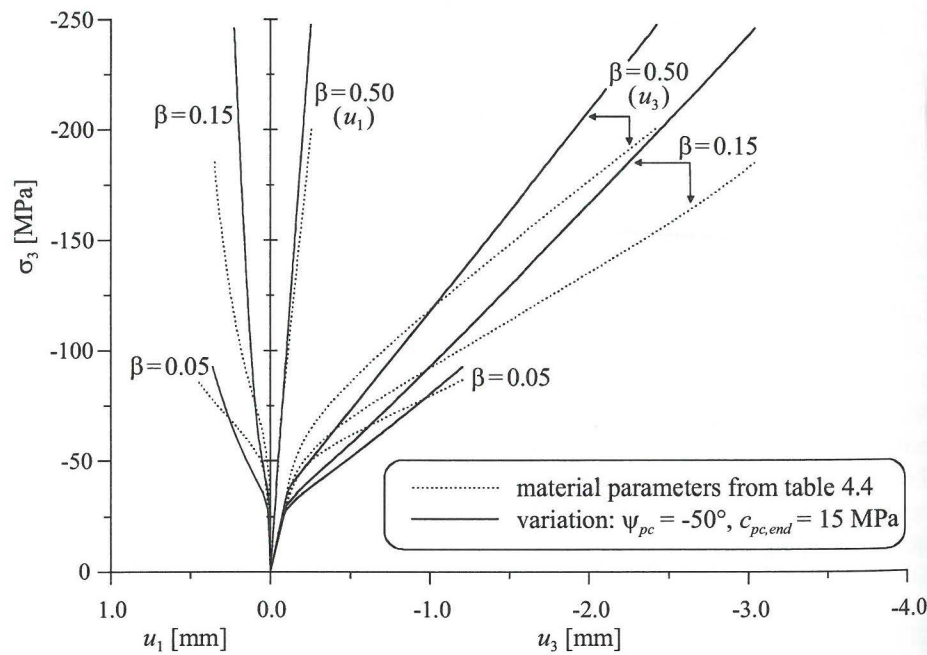


Figure 4.39. Variation of  $\psi_{pc}$  (high value) and  $c_{pc,end}$ .

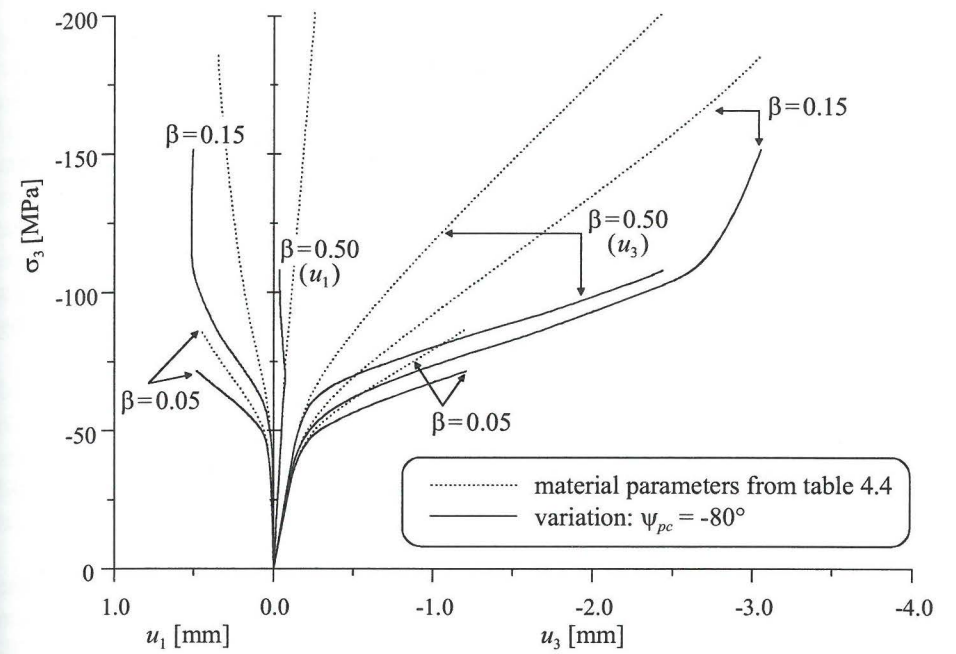


Figure 4.40. Variation of  $\psi_{pc}$  (low value).

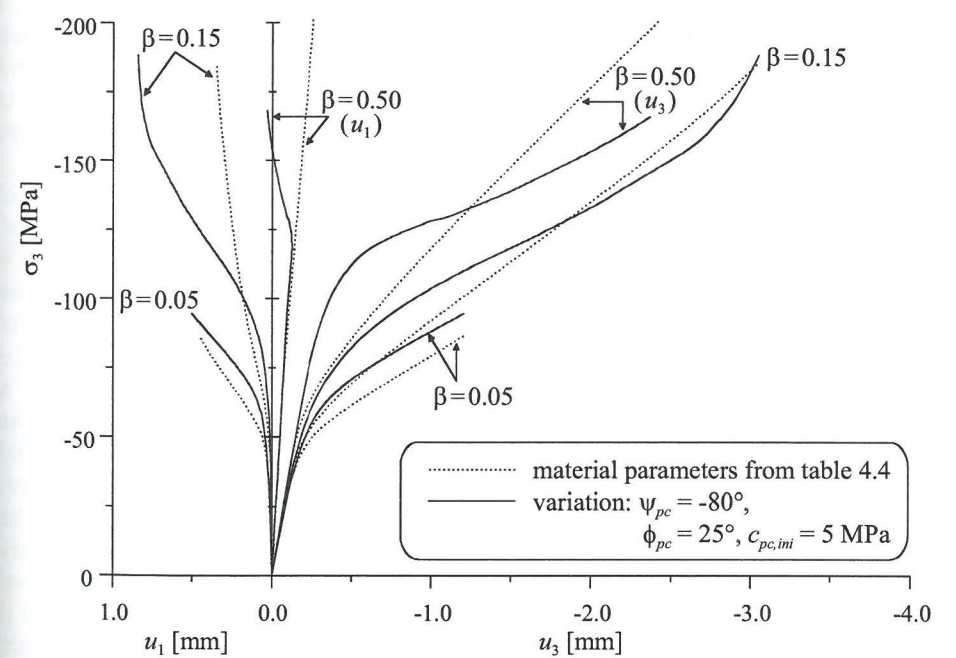


Figure 4.41. Variation of  $\psi_{pc}$  (low value),  $\phi_{pc}$  and  $c_{pc,ini}$ .

As a low dilation angle  $\psi_{pc}$  involves a low degree of inclination of the loading branch at stage II and a high friction angle  $\phi_{pc}$  as well as a large expansion of the pore collapse bounding surface ( $c_{pc,end} - c_{pc,ini}$ ) involve a high degree of inclination of the loading branch at stage II, it is investigated whether such a combination of material parameters also results in a good correspondence with experimental data (like the simulations with material parameters from table 4.4). Figure 4.41 shows the computed results for such a combination of material parameters. From these results it appears that a high friction angle and a large expansion of the failure surface for pore collapse mainly induce a shift of the loading branch at stage II to a higher (more compressive) stress level. However, the inclination of the loading branch at stage II is hardly affected.

With regard to the parameter study of the phenomenon of pore collapse, displayed in the figures 4.38 to 4.41, it appears that the dilatancy angle  $\psi_{pc}$  and the friction angle  $\phi_{pc}$  are dominant parameters describing the shape of the loading curves qualitatively. Having determined the values of these parameters, the initial- and end-values of the cohesion  $c_{pc}$  can be chosen so that close quantitative agreement with experimental results is obtained.

Besides the lack of mesoscopic experimental data for the numerical values of the input parameters for pore collapse, there is also no mesoscopic experimental data about the true distribution of displacements at the outer boundary of the RVE. Therefore, a parameter study is also carried out for this parameter. The influence of this parameter is best demonstrated by cyclic test simulations. Figure 4.42 shows the results of a simulation of a proportional ( $\beta = 0.15$ ) cyclic test for a distribution of outer-boundary displacements according to the macro-stress approach, whereas figure 4.43 shows the results for a ratio of 75% macro-strain displacements and 25% macro-stress displacements. Simulations with outer-boundary displacements distributed completely according to the macro-strain approach did not produce stable material behaviour, and therefore, are omitted from this analysis.

The most striking difference between figures 4.42 and 4.43 concerns the model behaviour at the final stage of unloading. It turns out that for '100% macrostress' boundary displacements, the transition point between the initial – high stiffness – branch of the unloading curve and the final – low stiffness – branch of the unloading curve is located at a higher (more compressive) stress level than for '25% macrostress/75% macrostrain' boundary displacements. Furthermore, the lateral deformations in the latter case increase exorbitantly at final unloading, a phenomenon which is not observed in the experiments of Van Mier. Based on these distinct features at the final stage of unloading, comparison between experimental data and computed model simulations indicates that the distribution of outer-boundary displacements according to table 4.4 is a proper choice. A remark must be made, however, that the model assumes the same distribution of outer-boundary displacements throughout the entire simulation. Although this is a proper assumption in case of linear elastic material behaviour, it is questionable whether it still holds when the material behaviour of the RVE becomes elasto-plastic. As there is no data available on this aspect, further research on this topic is required.

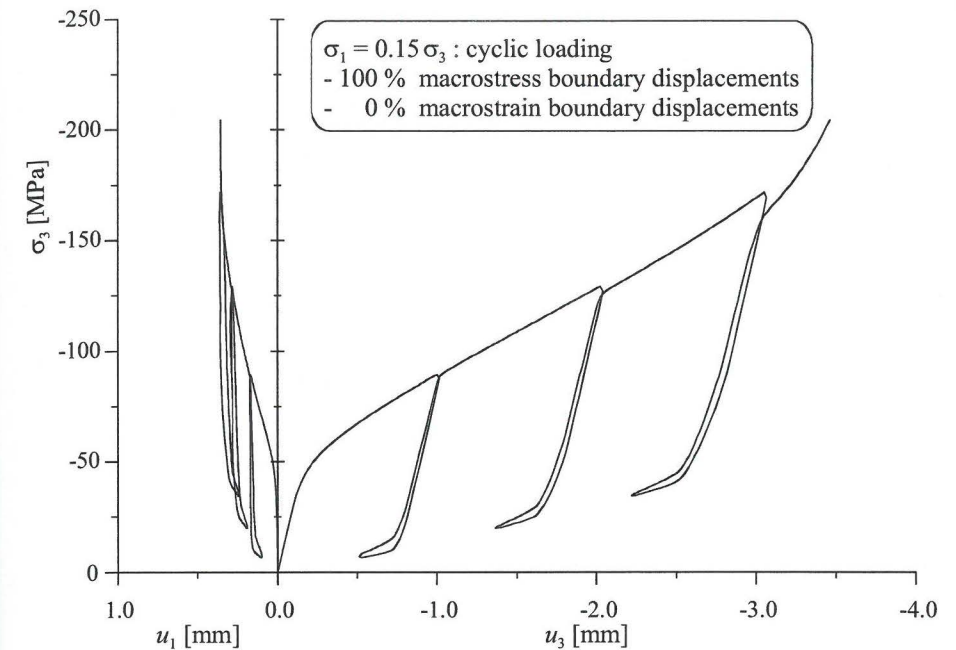


Figure 4.42. Variation of RVE boundary displacements (1).

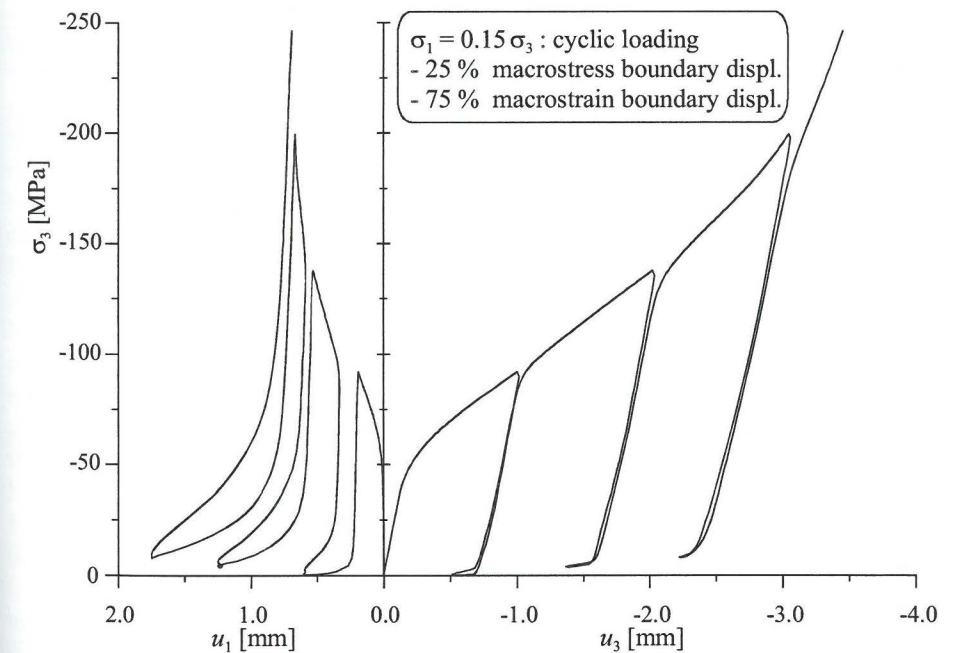


Figure 4.43. Variation of RVE boundary displacements (2).

## CHAPTER 5

### NUMERICAL MODELLING OF STAGE III AND IV BEHAVIOUR

In chapter 3, stage III is characterised by reaching the ultimate strength and the onset of mesoscopic cracking, i.e. crack propagation is taking place in the bulk cement paste starting from the ITZ cracks originated at stage II. At stage IV, these mesoscopic cracks localise into large macroscopic cracks, forming a failure pattern. In section 4.3, a clear distinction is drawn between micro-cracking at stage II and meso/macro-cracking at stage III and IV. This distinction is based on the eminent difference in the scale of heterogeneity involved. Whereas the scale of heterogeneity for micro-cracking is determined by the size of the aggregate grains, the scale of heterogeneity for meso- or macro-cracking is determined by the size of the cracks, running along a few (meso-cracking) or many (macro-cracking) aggregate grains. This implies that for meso- and macro-cracking the RVE of figure 4.8 is not applicable anymore.

#### 5.1 RVE for meso- and macro-cracking

As it is stated in section 3.2.3, a strengthening mechanism exists during meso-cracking at stage III as a result of a redistribution of stresses along the curved crack. Growth of a newly formed mesoscopic crack around an ‘interlocking’ aggregate grain will in this case only occur at a higher stress-level. Yet, before reaching this higher stress-level, additional meso-cracking will take place parallel to the first mesoscopic crack until also these cracks meet an ‘interlocking’ aggregate grain. In brief, due to the strengthening mechanism induced by aggregate interlock, a distributed pattern of parallel mesoscopic cracks will arise at stage III of concrete loaded in multiaxial compression.

At stage IV, the stresses at the interlocked aggregate grains have reached a critical level. At this level, mesoscopic cracks will grow either around the aggregate grains or through the aggregate grains. In either case the capability of transferring stresses across the crack will decrease during further crack growth. During this *softening* process the mesoscopic cracks will localise into large macroscopic cracks forming a failure pattern.

For a distributed pattern of parallel mesoscopic cracks a unit cell may be defined as indicated in figure 5.1.b. The crack spacing  $d$  between the mesoscopic cracks determines the size of the unit cell. In this case, the crack spacing is equal to the (average) size of the aggregate grains. For a localised macroscopic crack, a similar unit cell may be defined as indicated in figure 5.1.c. In this case the crack displacements of only one localised crack are, according to the smeared cracking approach, uniformly distributed over the width of the finite element. Consequently,

taking the thickness  $d$  of the unit cell for macroscopic cracking equal to the width of the finite element, is an appropriate choice.

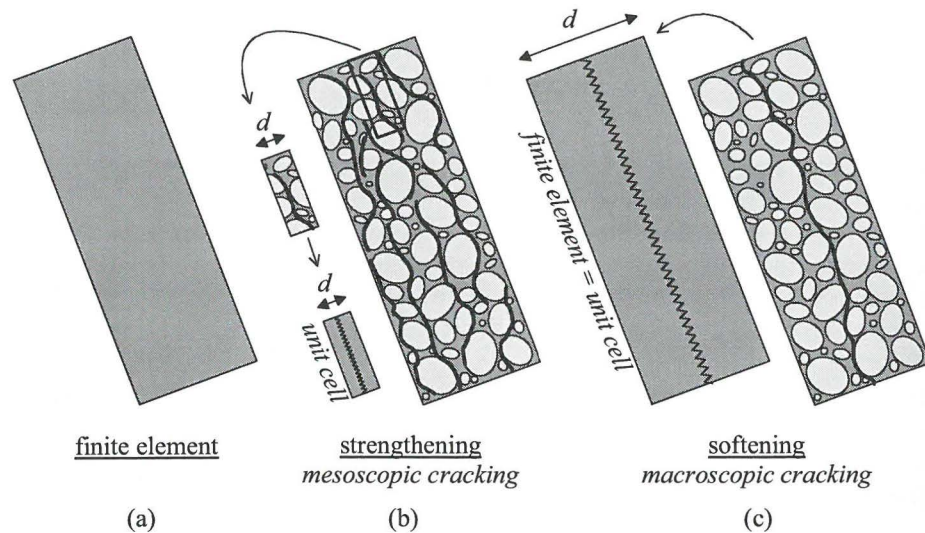


Figure 5.1. Unit cell for (b) mesoscopic and (c) macroscopic cracking.

## 5.2 Incorporation in main calculation scheme

The RVE-calculations for stage III and IV behaviour are incorporated in the main calculation scheme of figure 4.9. This results in the extended calculation scheme as displayed in figure 5.2.

Within the second RVE-concept ( $RVE_2$  for stage III and IV behaviour), the heterogeneous concrete material around the potential meso/macro-crack is homogenised into an isotropic material displaying linear elastic behaviour. The elastic moduli for such a homogenised material are given by  $\bar{K}$  and  $\bar{G}$  in section 4.3.3. With these effective elastic moduli and the macro-strain increments (provided by UDEC), the  $RVE_2$  elastic macro-stress increments  $\Delta\sigma^{e,m}$  are determined according to equation (4.1) in section 4.3.3 and added to the initial stress state  $\sigma^{0,m}$ . The stress state along the potential crack corresponds to the stress state given by a point on Mohr's stress circle in that particular direction (see section 1.2.1). This elastic stress state is treated as a trial stress state<sup>1</sup> and it is checked whether this trial stress state violates a certain cracking criterion. If so, cracking occurs and a stress correction vector  $\Delta\sigma$  is added to the trial stress state, producing a new – corrected – stress state that does not violate the cracking criterion anymore.

Based on this stress correction vector, the plastic part of the macro-strain increments is computed (smeared crack displacements) and subtracted from the total macro-

<sup>1</sup> Generally, *only* macroscopic stress/strain fields are considered in stage III/IV  $RVE_2$  computations. Therefore, the index  $m$  (to indicate macroscopic stress/strain fields) is omitted. In the occasional event of local stress/strain states, the index  $loc$  will be added.

strain increments. Finally, this results in a new vector of elastic macro-strain increments, which, together with the unaltered initial macro-stress state  $\sigma^{0,m}$ , serves as input for the stage I/II  $RVE_1$  calculations.

According to the calculation scheme of figure 5.2, the occurrence of meso/macro-cracking ( $RVE_2$ ) is checked before the occurrence of micro-cracking ( $RVE_1$ ). In this way, potential meso/macro-cracking – which produces lower material strength than micro-cracking – will always prevail. This agrees with the fact that, in case of several potential failure mechanisms, nature always chooses for the one having the lowest strength. Nevertheless, the sequence of checking will be of minor importance in the case of computations with very small loading steps. In fact, reversing the checking sequence for various UDEC-calculations with the present model, did not have any noticeable effect on the results.

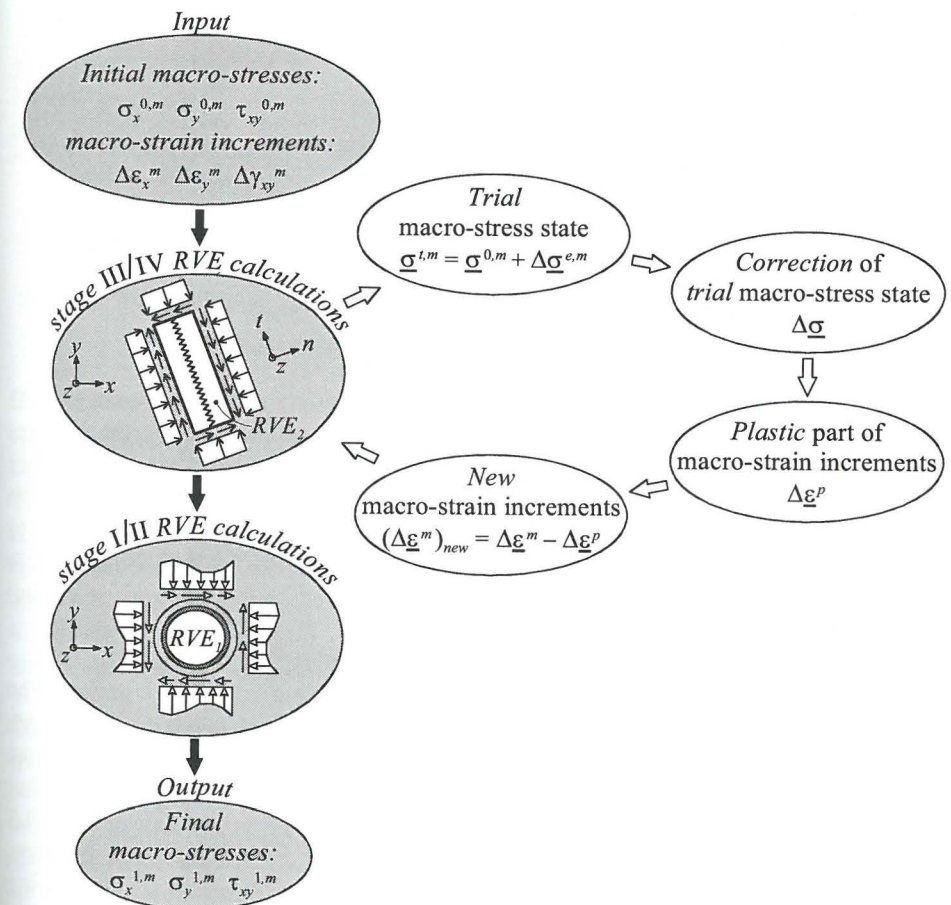


Figure 5.2. Main calculation scheme extended with  $RVE_2$  calculations.

### 5.3 Crack initiation criterion

For a concrete material, a mesoscopic or macroscopic mode II crack may arise according to three basic mesoscopic mechanisms (section 3.2.4): overriding, aggregate fracture and cement paste crushing (figure 5.3). Overriding involves the initiation of a curved crack running solely through the cement paste, while aggregate fracture involves the initiation of a straight crack through both the aggregate grains and the cement paste. In normal strength concretes, with strong aggregates embedded in a matrix of (porous) cement paste, cement paste crushing postpones fracture of the aggregates while still a straight crack (with zero crack dilatancy) is initiated. As both aggregate fracture and cement paste crushing involve the initiation of a straight crack, both mechanisms will be represented by only one crack initiation criterion.

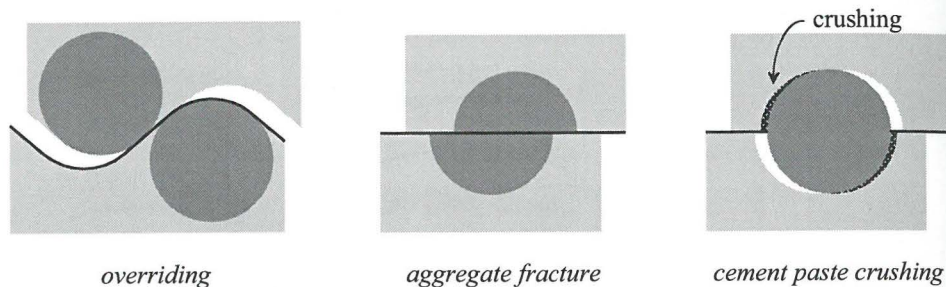


Figure 5.3. Basic mesoscopic cracking mechanisms.

Whether a mesoscopic or macroscopic crack is actually initiated depends on the global stress state in the RVE. To check this stress state upon cracking, the concept of a stress-state bounding surface is employed. The bounding surfaces applied here for concrete crack initiation are based on the classical Mohr-Coulomb formulation for mode II cracking (see section 1.2.4). Appropriate bounding surfaces representing the initiation criterion of a straight crack running through cement paste only<sup>2</sup> as well as a straight crack incorporating also aggregate fracture and/or cement paste crushing are given in section 5.3.1.

In normally compacted concretes, a crack – running through cement paste only – cannot be straight, but has to curve around interlocking aggregate grains. The curvature of such a crack can be characterised by a material property  $\Delta\alpha$ , which represents the *maximum* local deviation angle of the curved crack with respect to the global crack direction. Based on this material property, a stress-state bounding surface is derived in section 5.3.2 for initiation of a curved crack. In section 5.3.3 the individual bounding surfaces are combined to one overall bounding surface, accounting for the initiation of cracks with an *arbitrary* mixture of curved cracking through cement paste, aggregate fracture and cement paste crushing.

<sup>2</sup> Potential cracking mechanism in concretes with a diluted distribution of aggregate grains

#### 5.3.1 Straight crack running through cement paste or aggregate grains

The – Mohr-Coulomb type – bounding surfaces applied for initiation of straight cracks running through cement paste only (dilute distribution of aggregate grains) and straight cracks in normally compacted concretes (aggregate fracture / cement paste crushing) are displayed in figure 5.4.

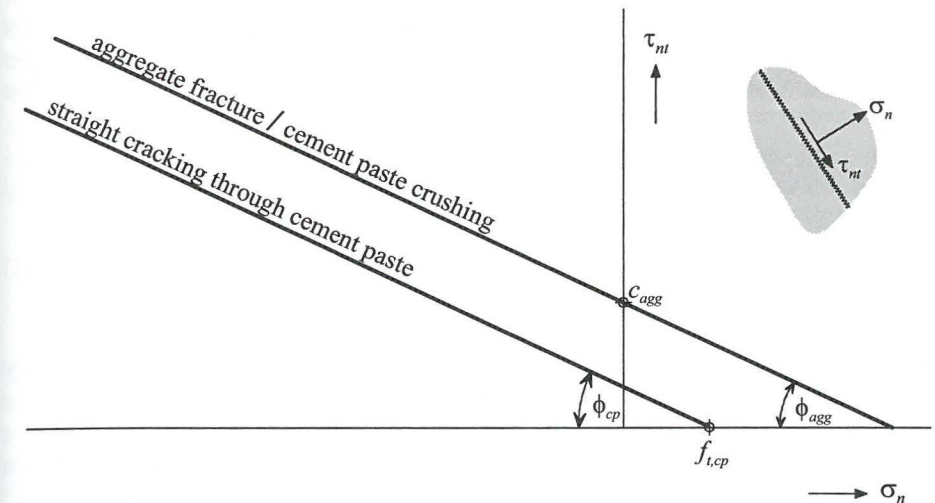


Figure 5.4. Stress-state bounding surfaces representing initiation criteria of straight cracks.

Each bounding surface is defined by two parameters, the friction angle  $\phi_{cp}$  and tensile strength  $f_{t,cp}$  for cracking through cement paste and the friction angle  $\phi_{agg}$  and cohesion  $c_{agg}$  for aggregate fracture/cement paste crushing.

The friction angle of a straight crack (at the meso-level) depends on the micro-roughness of the crack. As a straight crack through cement paste will mostly run through the weakest zone of the cement paste, i.e. the thin contact layer between the aggregate grain and the rest of the ITZ, the friction angle of a straight meso- or macroscopic crack through cement paste will not deviate much from the friction angle  $\phi$  for mesoscopic cracking along the ITZ at stage II as discussed in section 4.3.6.1.

Observation of cracks through the aggregate grains in the experiments of Van Geel indicate that these cracks have very smooth surfaces, comparable with the (smooth) outer surface of an intact aggregate grain. Taking furthermore into consideration that the friction angle for mesoscopic cracking along the ITZ at stage II is mainly determined by the smooth outer surface of the aggregate grain, it is acceptable to assume that also the friction angle of a straight crack through an aggregate grain will not deviate much from the friction angle for mesoscopic cracking along the ITZ at stage II.

The mechanism of cement paste crushing is essentially identical to the mechanism of pore collapse as explained in section 4.3.6.2. Best fit with experimental test data (section 4.4) was obtained for  $\phi_{pc} = 0$ , i.e. with no influence of confinement on the maximum shear strength. To obtain the overall strength of the straight crack, the crushing (cohesive) strength must be added to the strength of the straight part of the crack through cement paste (as drawn in figure 5.3). This implies that the *friction angle* is only determined by the straight part of the crack through cement paste. The influence of potential cement paste crushing is allowed for only by the *cohesion*  $c_{agg}$ , which is either the aggregate cohesive strength or the crushing cohesive strength of the cement paste, whichever is the lowest.

For reasons of simplicity, small deviations between the friction angles are neglected in the present model. Therefore, the friction angles of the crack types as discussed above are assumed to be equal.

$$\phi_{cp} = \phi_{agg} = \phi \text{ (stage II)} \quad (5.1)$$

### 5.3.2 Curved crack running through cement paste

According to figure 5.4, a straight crack runs preferably through cement paste only instead of crossing (stronger) aggregate grains either by aggregate fracture or cement paste crushing. At least, if interlocking aggregate grains do not prevent the formation of such a straight crack, as in the case of normally compacted concrete. In such concrete the crack has to curve around the interlocking aggregate grains.

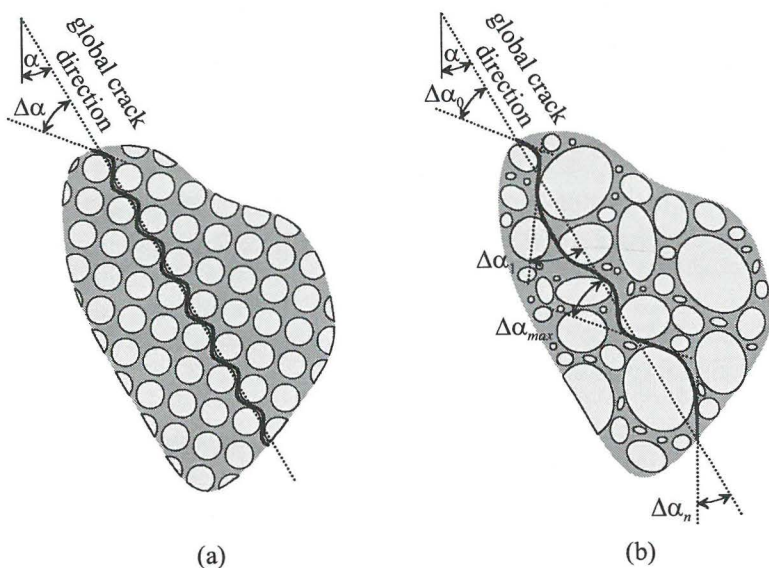


Figure 5.5. Deviation angle of a regularly (a) and irregularly (b) curved crack.

The curvature of the crack at the meso-level introduces an additional roughness to the crack, which may be characterised by a *maximum* mesoscopic deviation angle  $\Delta\alpha$  (figure 5.5). In case of a regularly curved crack, as shown in figure 5.5.a, the

crack is fully characterised by  $\Delta\alpha$ . Cracks in concrete, however, are highly irregular and in that case, in addition to the maximum deviation angle  $\Delta\alpha$ , also the irregularity of the crack must be quantified to characterise the crack completely.

Slip along a *regularly* curved crack will only occur when the crack is fully developed, that is when the stress state has reached the initiation criterion of a straight crack through cement paste in the crack directions ranging from  $\alpha - \Delta\alpha$  to  $\alpha + \Delta\alpha$ . This criterion is graphically illustrated in figure 5.6 for the initiation of a curved mode II crack along a plane making an angle  $\alpha$  with the minimum (most compressive) principal stress direction. According to this procedure, a new stress-state bounding surface may be identified representing the initiation criterion of a regularly curved mode II crack through cement paste with a global crack angle  $\alpha$  and a deviation angle  $\Delta\alpha$ .

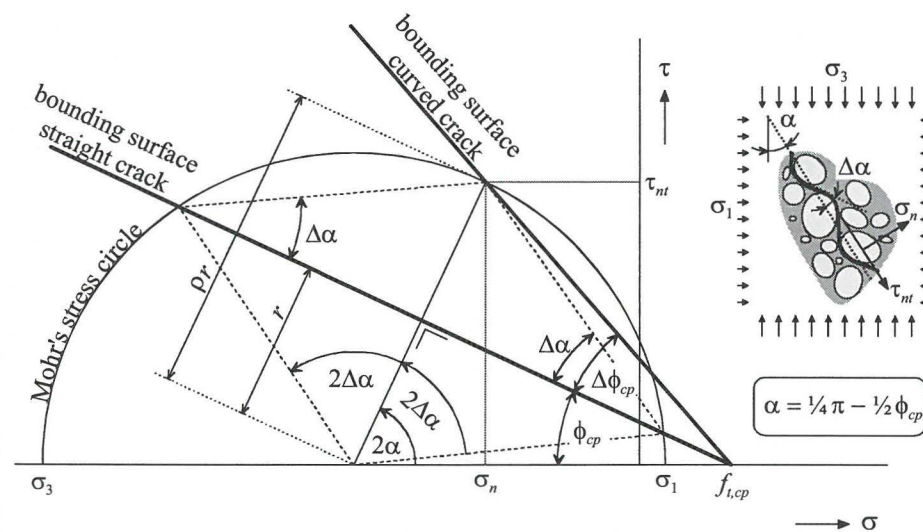


Figure 5.6. Stress-state bounding surface for initiation of a regularly curved mode II crack through cement paste.

The new stress-state bounding surface for initiation of a regularly curved mode II crack is characterised by an increase of the friction angle with  $\Delta\phi_{cp}$ . According to figure 5.6 this increase of the friction angle is determined by the magnitude of the overlap of Mohr's stress circle with regard to the bounding surface for a straight crack through cement paste.

$$(\rho - 1)r = r \tan(2\Delta\alpha) \tan \Delta\alpha$$

$$\rho = \frac{1 + \tan^2 \Delta\alpha}{1 - \tan^2 \Delta\alpha}$$

$$\tan \Delta\phi_{cp} = (\rho - 1) \tan \phi_{cp} \quad (5.2)$$



From figure 5.6 it can be seen that when the deviation angle  $\Delta\alpha$  equals the global crack angle  $\alpha$ ,  $\Delta\phi_{cp}$  equals  $\alpha$  too and Mohr's stress circle passes through the tensile strength  $f_{t,cp}$ . In this case, the deviation angle at the right-hand side of the global crack direction  $\alpha$  ( $\Delta\alpha_r$  in figure 5.7) is no longer limited by the bounding surface. As a result, initiation of a crack is still possible for the same stress state, even when  $\Delta\alpha$  exceeds  $\alpha$ . In this case, a mixed mode crack will be formed such that the addition of the left- and right-hand deviation angles ( $\Delta\alpha_l + \Delta\alpha_r$ ) still equals the material property  $2\Delta\alpha$  (see figure 5.7). Hence, the bounding surface for mode II crack initiation does not expand when  $\Delta\alpha$  is increased beyond  $\alpha$ . In other words,  $\Delta\phi_{cp}$  is bounded by a maximum value

$$\Delta\phi_{cp}^{\max} = \alpha \tag{5.3}$$

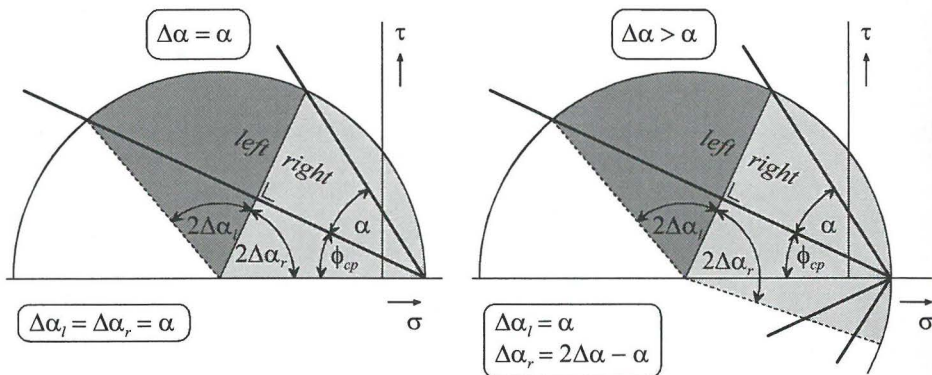


Figure 5.7. Cracking criterion when  $\Delta\alpha$  exceeds the global crack angle  $\alpha$ .

The direction of the bounding surface according to the maximum friction angle, as defined in equation (5.3), coincides with the direction of the stress path of uniaxial compression in stress space (figure 5.8). This specific stress path appears to be a special stress path, not only with respect to crack initiation, but also with respect to the mechanical behaviour of the crack after initiation. This will be discussed further in section 5.4.

To find the stress-state bounding surface for initiation of an irregularly curved crack, a similar approach is adopted as for initiation of a regularly curved crack. In this case the crack is subdivided into parts, each having a different deviation angle  $\Delta\alpha_i$ . For each part, a local bounding surface is determined according to equations (5.2) and (5.3). A global bounding surface is derived next by averaging these local bounding surfaces.

To illustrate this procedure, a number of bounding surfaces is drawn in figure 5.9, each belonging to a different part with a different local deviation angle  $\Delta\alpha_i$  of an irregularly curved crack. As the bounding surface for a regularly curved crack is defined by a maximum overlap of Mohr's stress circle with respect to the bounding

surface of a straight crack, it seems logical to average the overlap  $\rho$  for an irregularly crack in order to come to an equivalent bounding surface – with an equivalent overlap  $\bar{\rho}$  – for the entire crack (see figure 5.9).

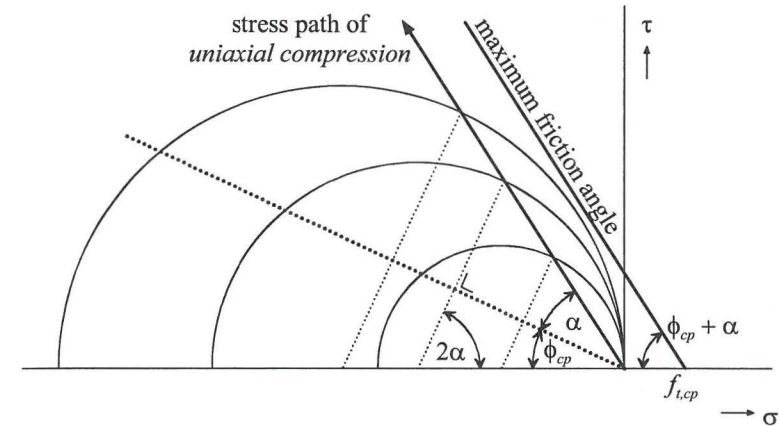


Figure 5.8. Maximum friction angle and stress path of uniaxial compression.

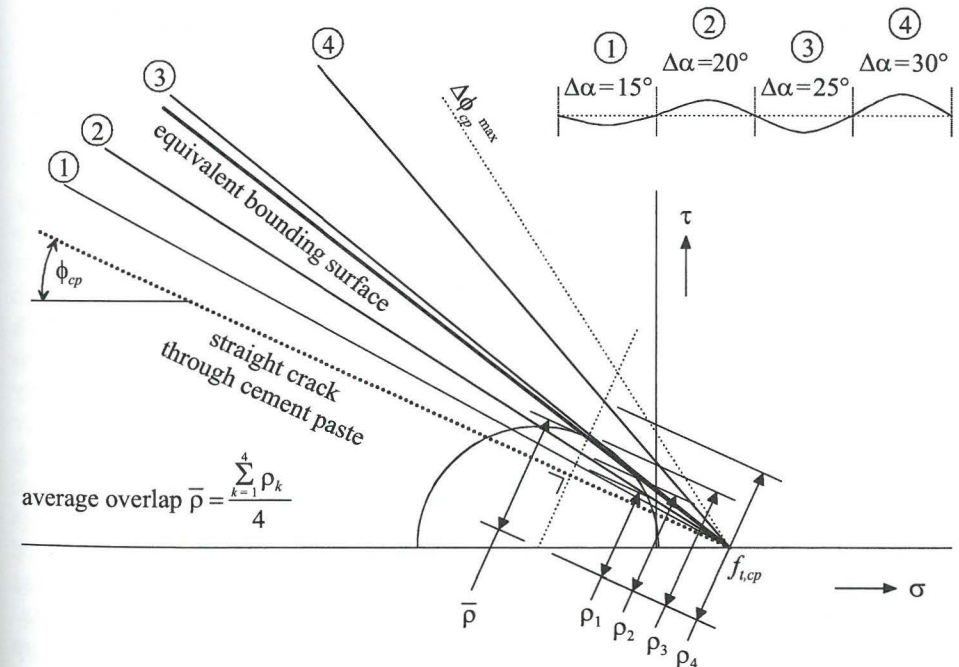


Figure 5.9. Equivalent bounding surface for initiation of an irregularly curved mode II crack.

### 5.3.3 Overall bounding surface

To account for both straight mode II cracking crossing aggregate grains and curved cracking through cement paste, the bounding surface of figure 5.4 and the equivalent bounding surface of figure 5.9 are combined to one bilinear overall bounding surface (see figure 5.10).

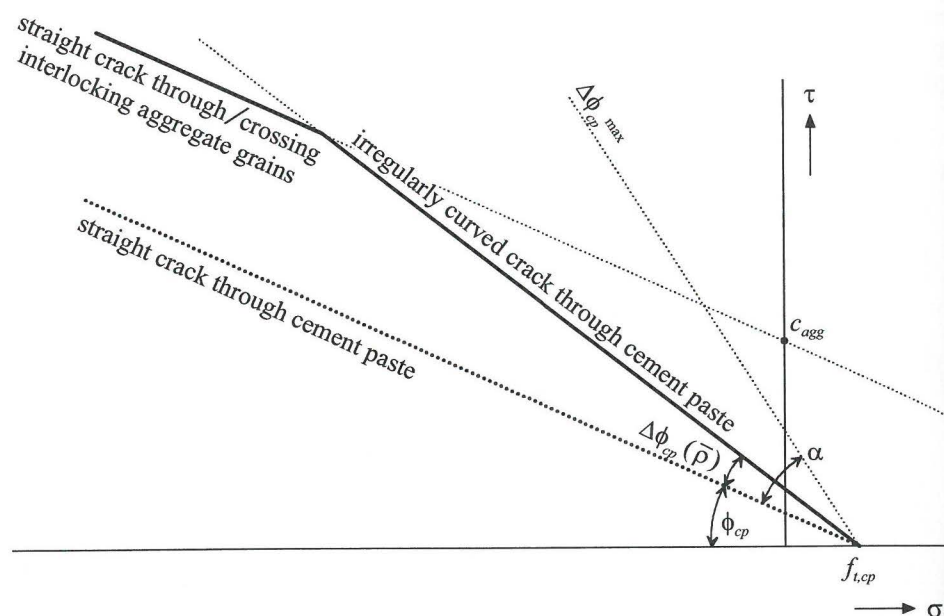


Figure 5.10. Construction of a bilinear overall bounding surface for mode II crack initiation.

The sharp corner of such an overall bounding surface indicates a sudden transition from a curved crack running through cement paste around the aggregate grains to a completely straight crack through or crossing all interlocking aggregate grains (aggregate fracture or cement paste crushing). Such a sudden transition is not likely to occur. The bounding surface of figure 5.10 is based on averaging the local *linear* bounding surfaces of an irregularly curved crack through cement paste only. With respect to the construction of an overall bounding surface it is, however, more realistic to average the 'local' *bilinear* bounding surfaces instead. This procedure is shown in figure 5.11. In this figure a potential irregularly curved crack is considered with local deviation angles ranging from 15° to 30°. The bilinear bounding surfaces for crack initiation in each local part of the crack (part 1 to 4) are drawn in stress-space. The overall bounding surface representing the initiation criterion of the entire crack may now be established as a curved surface, through continuously averaging the overlap  $\rho$  along the bounding surface representing the initiation criterion of a straight crack through cement paste.

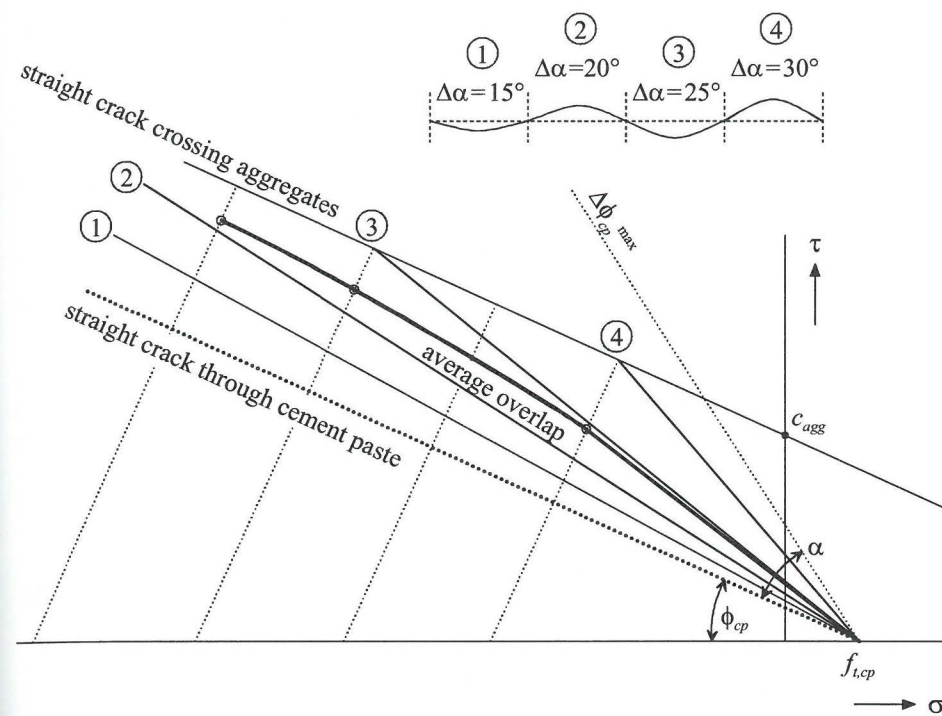


Figure 5.11. Construction of overall bounding surface for mode II crack initiation by averaging 'local' bilinear bounding surfaces.

The curvilinear shape of the overall stress-state bounding surface as derived in figure 5.11 is not very convenient for computational purposes. Therefore, the curvilinear shape of figure 5.11 is approximated by a mathematical more convenient shape.

The proposed shape consists of a linear part as well as a part of a circle (see figure 5.12). The proposed simplified overall bounding surface is determined by two material parameters, the maximum deviation angle  $\Delta\alpha$  – which determines  $\Delta\phi_{cp}$  according to equation (5.2) and (5.3) – and the position of the linear part relative to the stress-state bounding surfaces for initiation of a straight crack through cement paste only and a straight crack crossing interlocking aggregate grains. This relative distance depends on the irregularity of the crack and decreases with increasing irregularity of the crack.

For ordinary types of concrete mixes, the irregularity of a potential curved crack through cement paste will not vary much. Therefore, a fixed value is assigned to this material property. According to figure 5.12, the relative distance is 2/3. This value is also applied for the computations performed with the model at hand (section 5.7) and provides acceptable results. Moreover, the observed macroscopic mechanical behaviour is influenced only moderately upon variation of this parameter (section 5.7.6).

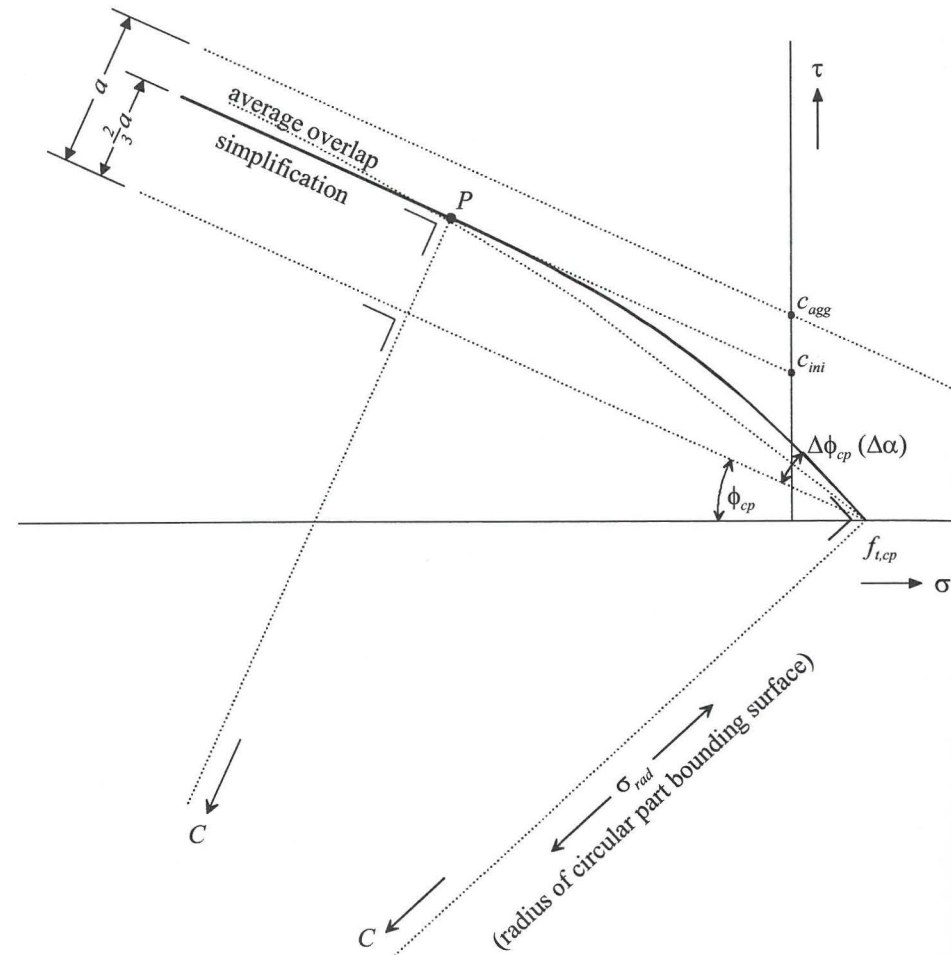


Figure 5.12. Simplification of overall stress-state bounding surface.

Applying the value of 2/3, the linear part of the simplified overall bounding surface for mode II crack initiation is characterised by the friction angle  $\phi_{cp}$  and the cohesion  $c_{ini}$ .

$$c_{ini} = \frac{2}{3}c_{agg} + \frac{1}{3}f_{t,cp} \tan \phi_{cp} \quad (5.4)$$

The coordinates of the point of contact  $P$  between the circular part of the bounding surface and the linear part of the bounding surface are

$$\sigma_P = \frac{c_{ini} - f_{t,cp} \tan(\phi_{cp} + \frac{1}{2} \Delta \phi_{cp})}{\tan \phi_{cp} - \tan(\phi_{cp} + \frac{1}{2} \Delta \phi_{cp})}$$

$$\tau_P = c_{ini} - \sigma_P \tan \phi_{cp}$$

The coordinates of the centre of the circular part of the bounding surface are

$$\sigma_C = \frac{(\tau_P \tan \phi_{cp} - \sigma_P) \tan(\phi_{cp} + \Delta \phi_{cp}) + f_{t,cp} \tan \phi_{cp}}{\tan \phi_{cp} - \tan(\phi_{cp} + \Delta \phi_{cp})}$$

$$\tau_C = \frac{\sigma_C - f_{t,cp}}{\tan(\phi_{cp} + \Delta \phi_{cp})}$$

### 5.3.4 Potential crack directions

Mode II cracking is triggered when the stresses in the potential global crack direction  $\alpha$  reach the stress-state bounding surface as established in the preceding section. Referring to figure 1.13 (section 1.2.4), two other potential crack directions are also indicated with respect to the present cracking criterion in figure 5.13.

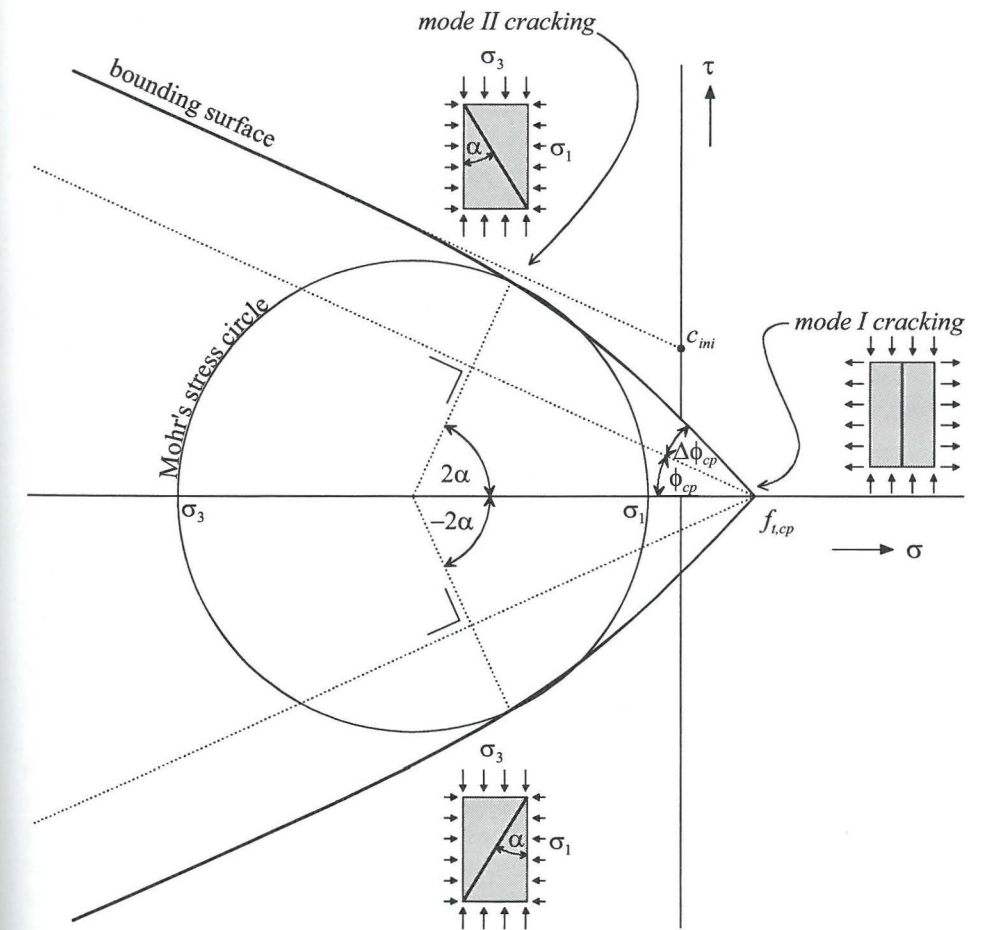


Figure 5.13. Potential crack directions for mode I and mode II crack initiation.

Mode I cracking is triggered when the maximum principal stress  $\sigma_1$  exceeds the tensile strength  $f_{t,cp}$ . However, due to the restriction – given in equation (5.3) – for the maximum friction angle, mode II cracking always occurs before the tensile strength is reached. So, when the tensile strength is set equal for all potential crack directions – as it is drawn in figure 5.13 – mode I cracking will never occur. Due to the heterogeneous structure of concrete, however, the tensile strength is not equal for the different crack directions. For that matter, the maximum deviation angle  $\Delta\alpha$  may also be different for different crack directions. Taking the heterogeneity into account, mode I as well as mode II cracking ( $\alpha$  or  $-\alpha$ ) may occur depending on the stress state and the local distribution of material strength properties.

### 5.3.5 Material parameters

The stress-state bounding surface from the foregoing is characterised by four material parameters:

1. Cohesive strength of a straight crack crossing interlocking aggregates  $c_{agg}$
2. Tensile strength of the cement paste  $f_{t,cp}$
3. Friction angle of a straight crack  $\phi_{cp}$  ( $= \phi_{agg} = \phi$  (stage II) )
4. Maximum deviation angle for curved cracking around the aggregate grains  $\Delta\alpha$

The friction angle of a straight crack depends on the type of aggregate. The cohesive strength of a straight crack crossing interlocking aggregate grains depends on the cohesive strength of the aggregates (aggregate fracture), but also on the (cohesive) strength of the cement paste (cement paste crushing). The tensile strength of the cement paste depends on the tensile strength of both the bulk cement paste and the ITZ. The maximum deviation angle for curved cracking around the aggregate grains depends on the degree of compaction.

During stage II both the tensile strength of the ITZ and the degree of compaction are affected by progressive pore collapse and mode I/II cracking along the ITZ. This implies that mesoscopic/macroscopic crack initiation also depends on the amount of cracking during stage II, in conformance with the observed path-dependency upon high multiaxial compressive preloading as outlined in section 3.2.3.

#### Maximum deviation angle

During compaction of the fresh concrete mix the distance between the aggregate grains decreases, resulting in a larger maximum deviation angle of a potential curved crack around the aggregate grains. So, prior to loading, the maximum deviation angle  $\Delta\alpha_0$  is a property of the concrete mix.

During stage II, the distance between the aggregate grains decreases further as a result of pore collapse at the ITZ. This causes an increase of the maximum deviation angle. To quantify this phenomenon, the RVE<sub>1</sub> – adopted for describing stage II behaviour – is displayed in figure 5.14. As a result of pore collapse, the shape of the RVE<sub>1</sub> changes from circular to oval. According to figure 5.14, the increase of the deviation angle  $\Delta\Delta\alpha$  is related to the impression  $u^{cr}$  caused by pore collapse.

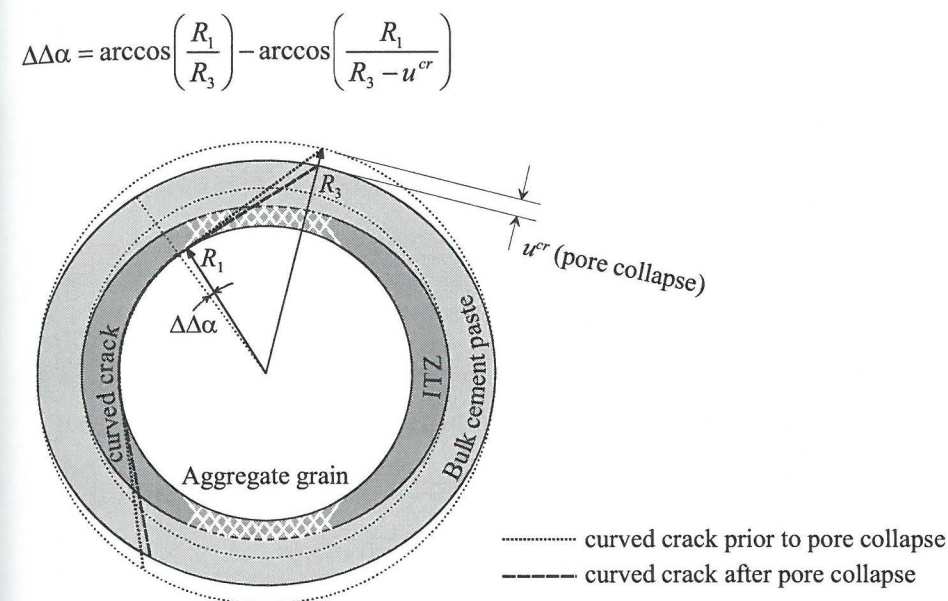


Figure 5.14. Increase of deviation angle due to pore collapse at stage II.

By adding the increase of the deviation angle to the maximum deviation angle of the virgin concrete, the total maximum deviation angle at the onset of potential mesoscopic or macroscopic cracking, is obtained.

$$\Delta\alpha = \Delta\alpha_0 + \Delta\Delta\alpha \quad (5.5)$$

#### Tensile strength of the cement paste

A curved crack through cement paste runs partly through the ITZ and partly through the bulk cement paste. The relative part running through the ITZ can be estimated by considering again the RVE<sub>1</sub> (see figure 5.15). According to this figure, the relative ITZ part of a curved crack is

$$\frac{\ell_{ITZ}}{\ell_{tot}} = \frac{R_1\Delta\alpha + \sqrt{R_2^2 - R_1^2}}{R_1\Delta\alpha + \sqrt{R_3^2 - R_1^2}}$$

Based on the above equation, the relative ITZ length depends on the maximum deviation angle  $\Delta\alpha$ . As the maximum deviation angle is dependent on the extent of pore collapse in the ITZ at stage II, the relative ITZ length is also dependent on the extent of ITZ pore collapse at stage II. However, more important is the fact that the tensile strength of the ITZ  $f_{t,ITZ}$  reduces substantially due to cracking in the ITZ at stage II.

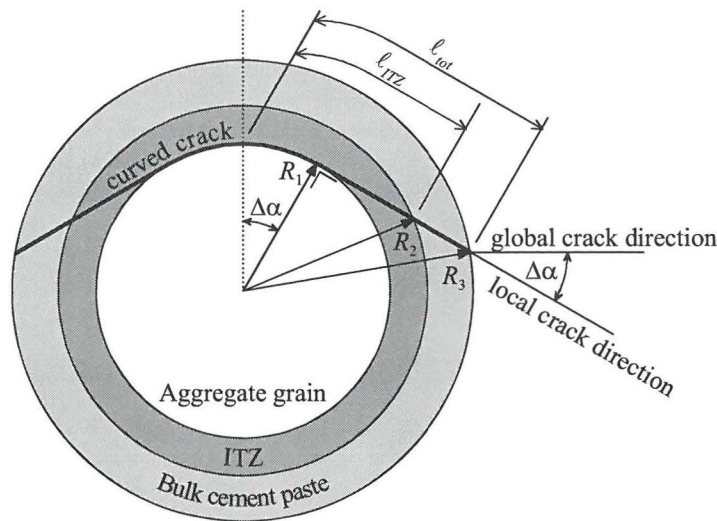


Figure 5.15. Relative ITZ length of a curved crack.

The tensile strength of the entire curved crack through cement paste is determined by averaging the tensile strength of the ITZ and the bulk cement paste according to their relative lengths.

$$f_{t,cp} = \left( \frac{\ell_{ITZ}}{\ell_{tot}} \right) f_{t,ITZ} + \left( 1 - \frac{\ell_{ITZ}}{\ell_{tot}} \right) f_{t,bulk} \quad (5.6)$$

The tensile strength of the ITZ  $f_{t,ITZ}$  in this equation is the average of the actual (reduced) tensile strengths of those parts of the ITZ located along the curved crack. Determination of the average tensile strength  $f_{t,cp}$  according to the procedure outlined above applies for mode II crack initiation. For mode I crack initiation a somewhat different approach is adopted. The *global* mode I crack is subdivided into three *local* crack parts having each a different *local* stress state. At first, *local* crack initiation criteria are established for the *local* stress state. Subsequently, a *global* crack initiation criterion is achieved by averaging both the local stress states and the local crack initiation criteria.

According to figure 5.16, a *global* mode I crack consists of *local* mode I crack parts as well as *local* mode II crack parts. It appears from figure 5.17 that the local mode II crack parts through the ITZ and through the bulk cement paste are initiated – along a deviation angle  $\Delta\alpha^{mode I}$  – before the local maximum principal stress reaches the tensile strength of, respectively, the ITZ and the bulk cement paste. As indicated in figure 5.17, the initiation of a *local* mode II crack may be captured by introducing an equivalent tensile strength. This means that *local* mode II cracking is initiated when the *local* maximum principal stress reaches the equivalent tensile strength.

$$f_{t,ITZ}^{eq} = C_M + (f_{t,ITZ} - C_M) \sin \phi_{cp} \quad (f_{t,ITZ}^{eq} \geq 0)$$

$$f_{t,bulk}^{eq} = C_M + (f_{t,bulk} - C_M) \sin \phi_{cp} \quad (f_{t,bulk}^{eq} \geq 0)$$

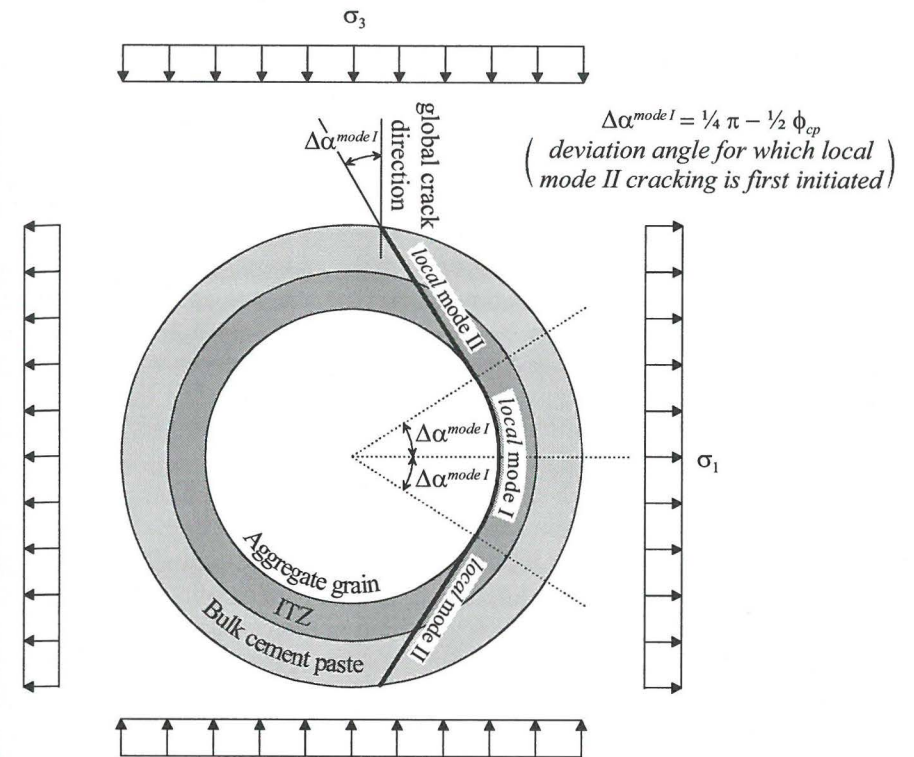


Figure 5.16. Local crack modes for global mode I cracking.

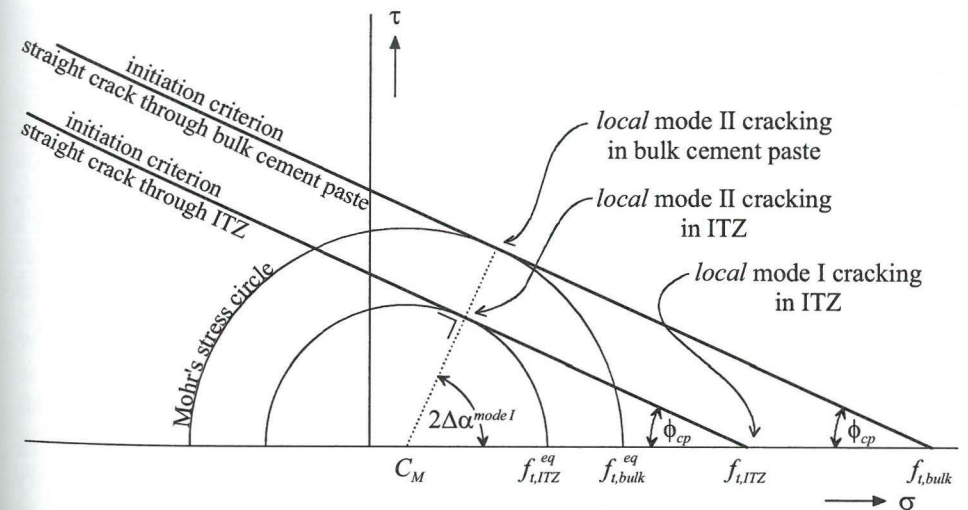


Figure 5.17. Equivalent tensile strength for local mode II cracking.

Global mode I crack initiation is triggered when the *global* maximum principal stress  $\sigma_1$  exceeds an averaged (effective) tensile strength of the entire crack  $f_{t,cp}^{mode I}$ .

$$f_{t,cp}^{mode I} = \left( \frac{\ell_{ITZ}}{\ell_{tot}} \right) \frac{1}{2} (f_{t,ITZ} + f_{t,ITZ}^{eq}) + \left( 1 - \frac{\ell_{ITZ}}{\ell_{tot}} \right) f_{t,bulk}^{eq} \quad (5.7)$$

This equation holds the assumption that cracking through the bulk cement paste initiates locally in mode II and that cracking through the ITZ initiates half in mode I and half in mode II. In fact, the relative amount of local mode I and mode II cracking through the ITZ depends on the size of the aggregate grain and the thickness of the ITZ layer as can be concluded from figure 5.16. However, the relative amount of local mode I and mode II cracking also depends largely on the true shape of the aggregate grains. Since this has not been taken into account in figure 5.16 and to avoid a seeming accuracy, both tensile strengths of the ITZ are simply averaged in equation (5.7).

Except for a stress state in which  $\sigma_1$  equals  $\sigma_3$ , the tensile strength for global mode I cracking is lower than the tensile strength for global mode II cracking. In stress space, this could be visualised by introducing a linear bounding surface that bounds the maximum principal stress.

$$\sigma_1 \leq f_{t,cp}^{mode I}$$

In other words, a tension cut-off criterion is introduced which resembles the classical Rankine bounding surface for mode I cracking (section 1.2.4).

## 5.4 Mechanical behaviour of a crack after initiation

In section 5.3 criteria are introduced for mesoscopic crack initiation in mode I as well as mode II. In this section, the model will be extended so as to incorporate also the behaviour of the crack after initiation. The important phenomena going along with this transition are analysed in the following: (5.4.1) behaviour of the crack upon rotation of the stress state, (5.4.2) the direction of plastic flow, or, the relation between crack sliding and opening displacements in relation to the stress state, (5.4.3) potential mode I crack closure, (5.4.4) implications due to a change from a rather homogeneous stress state prior to crack initiation to a very heterogeneous stress state after crack initiation and initial crack sliding and (5.4.5) material softening during subsequent crack deformations.

### 5.4.1 Rotation of the stress state after crack initiation

According to figure 5.13, a crack may be initiated along three potential crack directions. These crack directions are determined completely by the momentary stress state. After initiation, however, this stress state may rotate. In standard smeared crack analyses, three basic concepts are distinguished to deal with such a

rotated stress state after crack initiation. These concepts are discussed shortly in section 2.2.3.1.5 and more elaborately in Rots<sup>1988</sup>.

The most prominent feature of the first concept, the fixed smeared crack concept, is that after crack initiation the crack orientation remains fixed throughout the entire cracking process. This implies that when the stress state rotates after initiation, crack shear stresses will built up. However, after mode I crack initiation not only the normal stiffness of the smeared crack will decrease, but also the shear stiffness. Within the standard fixed smeared crack concept, this is generally included by introducing a shear retention factor.

An extension of the fixed smeared crack concept is the fixed multi-directional smeared crack concept. Within this concept multiple cracks in a limited number of fixed directions may be initiated. When the stress state rotates significantly, new mode I cracks will arise as soon as the tensile normal stress exceeds the tensile strength in a new fixed direction.

The rotating smeared crack concept can be conceived as the limiting case of the fixed multi-directional smeared crack concept for an unlimited number of directions. In this case, the crack orientation co-rotates with the axes of principal stress. Consequently, there is no need to reduce the smeared crack shear stiffness after crack initiation. Due to the co-axiality of principal stresses and crack orientation, the crack remains in mode I and no crack shear stresses will develop. In the rotating smeared crack concept no history of crack directions is kept in memory, all damage accumulated in the past is transferred to the new crack direction.

Although these concepts (fixed, multi-directional and rotated smeared cracking) were intended only for mode I crack initiation in a model formulated according to the theory of continuum damage mechanics, the same basic principles can also be applied for mode I *and* mode II crack initiation in the model at hand formulated according to the theory of elasto-plasticity.

For curved mode I fracture, in which crack sliding displacements are apparently present after initiation, Rots<sup>1988</sup> concluded that the fixed smeared crack concept with significant shear stiffness after initiation, produces far too stiff behaviour. Only the fixed smeared cracks with (almost) no shear stiffness and the rotating smeared cracks produced acceptable results. Based on these findings and because it results in a very simple model, the rotating smeared crack concept is adopted in the model at hand. By adopting the rotating smeared crack concept, checking the stress state upon mode I or mode II cracking *after* initiation can simply take place at the same stress points on Mohr's stress circle as outlined in section 5.3 *before* initiation.

Of course, the rotating smeared crack concept will produce less accurate results when the stress state rotates considerably after a lot of damage has been accumulated in the crack. In that case, the rotating crack concept will transfer all damage to the new preferential crack direction. In reality, this transfer of damage is unlikely to occur, and consequently, the bearing power of the structure will be underestimated. However, strongly rotating stress states are very exceptional in the field of structural engineering. Furthermore, eminent damage will always localise into a small zone of finite elements as a result of material softening. After a considerable rotation of the stress state, the preferential direction of such a

localisation zone will not coincide with the localisation zone already present in the mesh. Consequently, the influence of potential non-realistic damage transfer is limited to only the areas of intersection of existing and new localisation zones. Ergo, in the exceptional event of a strongly rotating stress state after considerable damage accumulation, the influence of potential non-realistic damage transfer will be limited to small isolated areas and will always lead to a safe approximation of the bearing power of the structure.

Only one exception on applying the rotating smeared crack concept is made. If a crack has opened in mode I (figure 5.18.a), then no shear stress will be transferred across the crack during subsequent crack sliding until the crack faces are again in contact, i.e. the crack is closed (figure 5.18.b). Consequently, the stress state cannot rotate as long as the crack remains open.

The inability of a stress state to rotate in case of an open crack is accounted for by adopting the fixed smeared crack concept with no shear capacity for as long as a (mode I) crack is open. At initiation, the direction of such a crack is stored in memory and subsequent opening and sliding crack displacements are only possible normal to and along the direction of the stored crack. As no shear stresses can be transferred across the stored open crack, rotation of the stress state is not possible until the crack closes. For such a closed crack, the rotating smeared crack concept is adopted and rotation of the stress state is again allowed for.

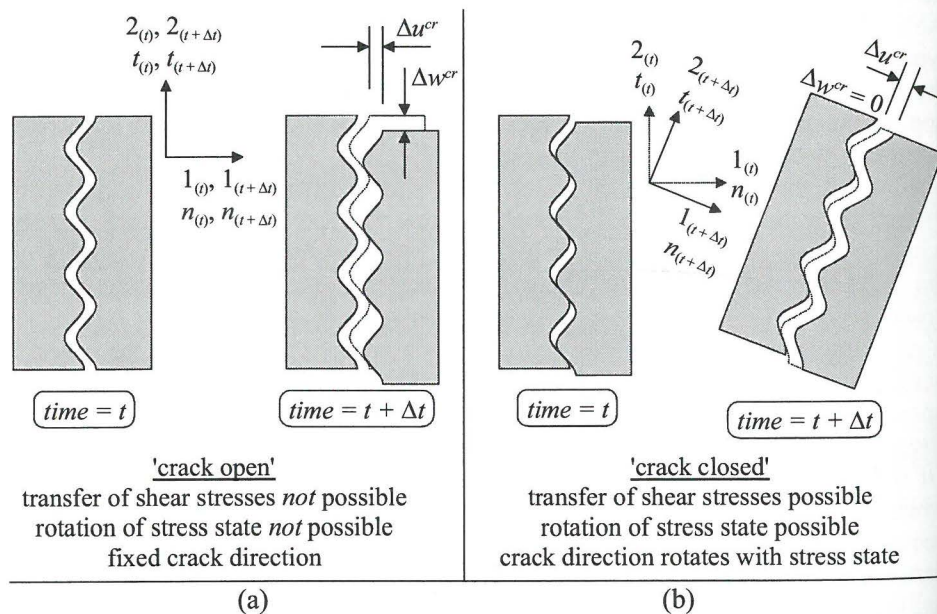


Figure 5.18. Rotation of the elastic (trial) stress state. Crack orientation before and after time step  $\Delta t$  in case of an open and a closed mode I crack.

#### 5.4.2 Plastic crack deformations and return mapping of trial stress state

When the *trial* stress state  $\underline{\sigma}^t$  violates the bounding surface for crack initiation, cracking takes place and the stress state is put back onto the bounding surface. The direction of return mapping depends on the direction of plastic flow, which is different for mode I and mode II cracking.

##### Mode II cracking

According to the theory of elasto-plasticity described in section 1.2.3, the direction of plastic flow is governed by the dilatancy angle  $\psi$  according to

$$\Delta \varepsilon_{vol}^p = \Delta \gamma_{max}^p \sin \psi$$

The dilatancy angle in this equation is strongly correlated with the maximum deviation angle  $\Delta \alpha$ , which was put forward in section 5.3 to represent the mesoscopic roughness of a curved crack running through cement paste. Yet – as indicated in figure 5.11 – a mode II crack does not only curve around interlocking aggregate grains, but also crosses interlocking aggregate grains by either aggregate fracture or cement paste crushing (with  $\psi = 0$ ). The amount of aggregate fracture and/or cement paste crushing depends on the location of the macroscopic stress state in stress space and may substantially reduce crack dilatancy, hence

$$\psi \leq \Delta \alpha \quad (5.8)$$

The elastic relation between the macro-stresses and the macro-strains is given by equation (4.1) in section 4.3.3. Applying this equation, return mapping of the trial stress state yields

$$\begin{aligned} \Delta C_M &= \bar{K} \Delta \varepsilon_{vol}^p = \bar{K} \Delta \gamma_{max}^p \sin \psi \\ \Delta r_M &= \bar{G} \Delta \gamma_{max}^p \end{aligned} \quad (5.9)$$

The direction of return mapping is determined by the angle  $\phi_{cp} + \delta$  in figure 5.19. According to this figure, the angle of return mapping is given by

$$\tan(\phi_{cp} + \delta) = \frac{\Delta C_M + \Delta r_M \sin \phi_{cp}}{\Delta r_M \cos \phi_{cp}} = \frac{\bar{K} \sin \psi}{\bar{G} \cos \phi_{cp}} + \tan \phi_{cp}$$

The correction of the trial stress state ( $\Delta C_M, \Delta r_M$ ) can be determined by intersecting the direction of return mapping with the overall bounding surface.

In case the direction of return mapping intersects the linear part of the bounding surface, the final stress state ( $\sigma_n^1, \tau_{nt}^1$ ) is

$$\tau_{nt}^1 = \frac{c_{ini} - (\sigma_n^t - \tau_{nt}^t \tan(\phi_{cp} + \delta)) \tan \phi_{cp}}{1 + \tan(\phi_{cp} + \delta) \tan \phi_{cp}}$$

$$\sigma_n^1 = \frac{c_{ini} - \tau_{nt}^1}{\tan \phi_{cp}}$$

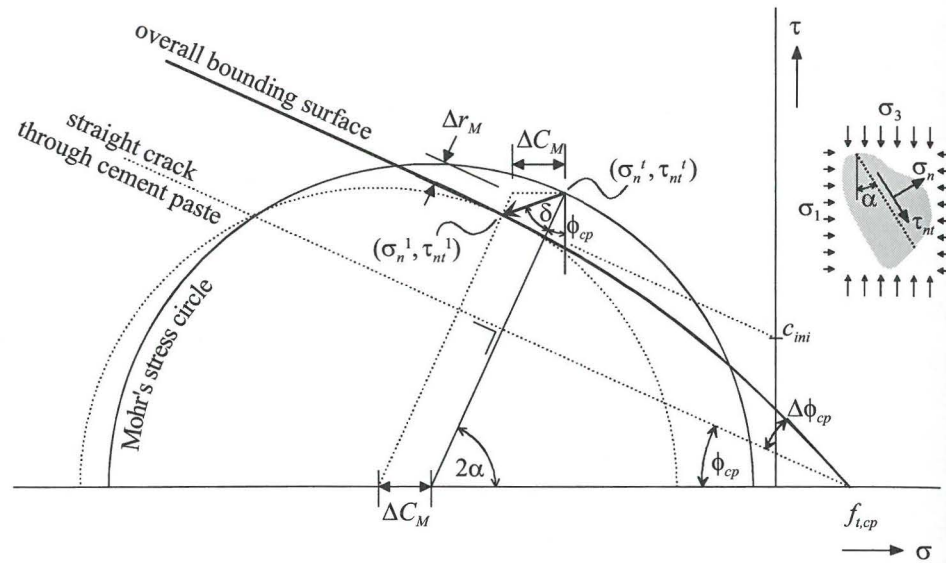


Figure 5.19. Return mapping of trial stress state in case of mode II cracking.

In case the direction of return mapping intersects the circular part of the bounding surface, the final stress state follows from figure 5.20.

$$\begin{bmatrix} \sigma_n^1 \\ \tau_{nt}^1 \end{bmatrix} = \begin{bmatrix} \sigma_c \\ \tau_c \end{bmatrix} + \sigma_{rad} \begin{bmatrix} \cos(\xi - \phi_{cp} - \delta) \\ \sin(\xi - \phi_{cp} - \delta) \end{bmatrix}$$

The corrections of the radius and centre of Mohr's stress circle are

$$\Delta r_M = \frac{\tau_{nt}^t - \tau_{nt}^1}{\cos \phi_{cp}}$$

$$\Delta C_M = \sigma_n^t - \sigma_n^1 - (\tau_{nt}^t - \tau_{nt}^1) \tan \phi_{cp}$$

According to equation (5.9), the plastic volumetric strain increment and the incremental maximum plastic shear deformation are given by

$$\Delta \varepsilon_{vol}^p = \frac{\Delta C_M}{\bar{K}} = \frac{\sigma_n^t - \sigma_n^1 - (\tau_{nt}^t - \tau_{nt}^1) \tan \phi_{cp}}{\bar{K}}$$

$$\Delta \gamma_{max}^p = \frac{\Delta r_M}{\bar{G}} = \frac{\tau_{nt}^t - \tau_{nt}^1}{\bar{G} \cos \phi_{cp}}$$

Using equation (1.6) and (1.7), the incremental plastic crack strains in  $(n,t)$ -coordinates finally become (note that  $\Delta \varepsilon_{t'}^p = 0$ )

$$\Delta \varepsilon_n^p = \frac{\sigma_n^t - \sigma_n^1 - (\tau_{nt}^t - \tau_{nt}^1) \tan \phi_{cp}}{\bar{K}} \quad (5.10)$$

$$\Delta \gamma_{nt}^p = \frac{(\tau_{nt}^t - \tau_{nt}^1) \cos \psi}{\bar{G} \cos \phi_{cp}}$$

The incremental crack displacements are obtained by multiplying the crack strains with the unit cell width  $d$  (see figure 5.1).

$$\begin{aligned} \Delta u^{cr} &= d \Delta \varepsilon_n^p \\ \Delta w^{cr} &= d \Delta \gamma_{nt}^p \end{aligned} \quad (5.11)$$

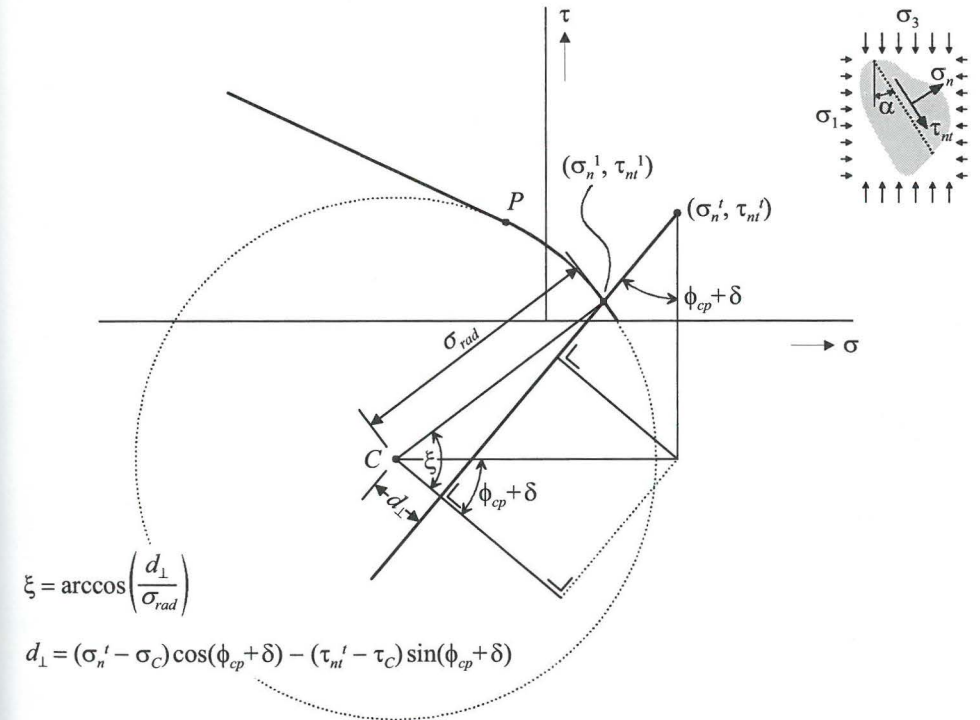


Figure 5.20. Return mapping to circular part of bounding surface.

#### Mode I cracking

As discussed in the preceding section, the fixed smeared crack concept is applied for open mode I cracks, whereas the rotating smeared crack concept is applied for mode I cracks that are closed. In the latter case, return mapping of the trial stress state simply consists of mapping the maximum principal stress back to the tensile strength.

In case of an open crack the crack direction is fixed and – based on the strain increments – the trial stress state is calculated with respect to this direction. In



contrast to the rotating crack concept, the shear component of the trial stress state is not necessarily equal to zero for the fixed crack concept. The open crack is not able to transfer shear stresses and only limited normal tensile stresses, so the trial stress state in the fixed crack direction is mapped back to the linear bounding surface ( $\sigma_n \leq f_{t,cp}^{mode I} \wedge \tau_{nt} = 0$ ) as depicted in figure 5.21(a).

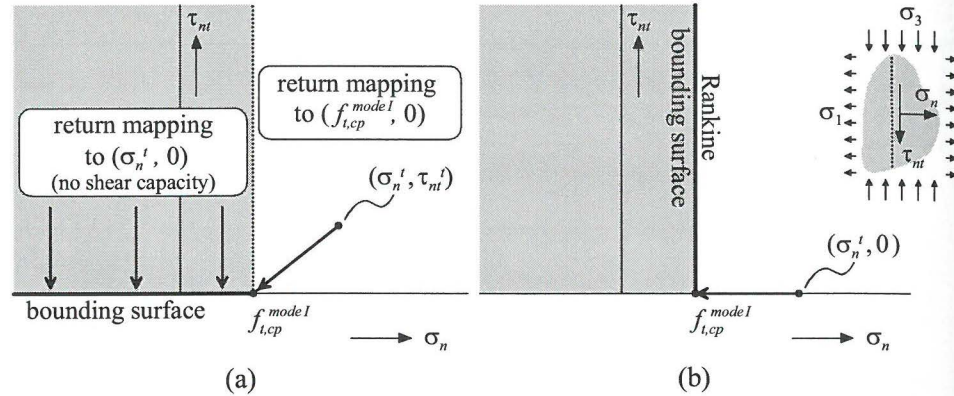


Figure 5.21. Return mapping of the trial stress state in case of mode I cracking.  
(a) Open 'fixed' crack and (b) closed 'rotating' crack.

The incremental plastic normal strain is both for the fixed smeared crack concept and the rotating smeared crack concept equal to

$$\Delta \varepsilon_n^p = \frac{\sigma_n^t - f_{t,cp}^{mode I}}{\bar{K} + \bar{G}} \quad (5.12)$$

The incremental plastic shear strain is zero for the rotating smeared crack concept. For an open fixed crack the incremental shear strain is given by

$$\Delta \gamma_{nt}^p = \frac{\tau_{nt}^t}{\bar{G}} \quad (5.13)$$

Just as for mode II cracking, the incremental crack displacements are obtained by multiplying the crack strains with the unit cell width  $d$ .

$$\begin{aligned} \Delta u^{cr} &= d \Delta \varepsilon_n^p \\ \Delta w^{cr} &= d \Delta \gamma_{nt}^p \end{aligned} \quad (5.14)$$

To determine whether a mode I crack is open or closed, the crack opening displacement  $COD$  of the mode I crack has to be calculated and stored into memory. When no crack sliding occurs, the increment of the  $COD$  equals the incremental normal crack displacement  $\Delta u^{cr}$ , otherwise<sup>3</sup>

<sup>3</sup> Mode I cracking incorporates no aggregate fracture or cement paste crushing, so  $\psi$  equals  $\Delta \alpha$ .

$$\Delta COD = \Delta u^{cr} - |\Delta w^{cr}| \tan \Delta \alpha \quad (5.15)$$

For mode I as well as mode II cracking, the corrected stress state  $\underline{\sigma}^1$  in  $(n,t,z)$ -coordinates is finally computed as

$$\begin{bmatrix} \sigma_n^1 \\ \sigma_t^1 \\ \tau_{nt}^1 \end{bmatrix} = \begin{bmatrix} \sigma_n^t \\ \sigma_t^t \\ \tau_{nt}^t \end{bmatrix} - \begin{bmatrix} \bar{K} + \bar{G} & \bar{K} - \bar{G} & 0 \\ \bar{K} - \bar{G} & \bar{K} + \bar{G} & 0 \\ 0 & 0 & \bar{G} \end{bmatrix} \begin{bmatrix} \Delta \varepsilon_n^p \\ 0 \\ \Delta \gamma_{nt}^p \end{bmatrix} \quad (5.16)$$

### 5.4.3 Mode I crack closure

According to the theory of classical elasto-plasticity, plastic deformations are not reversible. Consequently, closure of open mode I cracks in compression is not incorporated so far. To account for proper crack closure behaviour, the fixed smeared crack concept is extended with a crack closure criterion.

According to the proposed fixed smeared crack concept, the crack direction is fixed as soon as a mode I crack opens. This concept is now extended by shrinking the stress-state bounding surface for that crack direction to the line-segment displayed in figure 5.22 ( $0 \leq \sigma_n \leq f_{t,cp}^{mode I} \wedge \tau_{nt} = 0$ ), immediately after crack opening. Consequently, an open mode I crack is not able to transfer any shear or normal compressive forces (or normal tensile force beyond the tensile strength of the crack). When the trial crack normal stress  $\sigma_n^t$  changes from tensile to compressive, crack closure will take place without building up compressive forces. Crack closure will continue as long as the trial stress state remains compressive, until the crack is completely closed ( $COD$  is zero). From then on, the rotating crack concept is adopted, the bounding surface of figure 5.21(b) is restored and compressive force transfer is again allowed for.

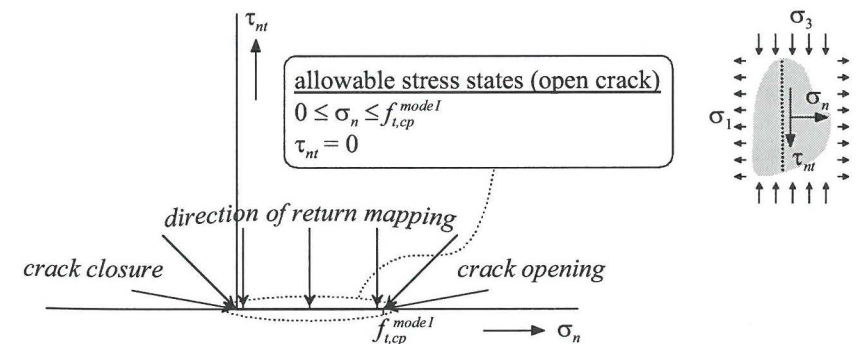


Figure 5.22. Return mapping of trial crack stresses (open mode I crack).

#### 5.4.4 Implications due to redistribution of local stresses around the crack after initial (mode II) sliding

As a result of the tortuous surface of a crack through cement paste at the meso-level (characterised by the maximum deviation angle  $\Delta\alpha$ ), sliding along such a crack in mode II will give rise to a highly heterogeneous stress state in the vicinity of the crack. The implications of this phenomenon are outlined in this section. In the first place, the distribution of local stresses in the vicinity of the crack, after initial sliding along a curved crack *and* after complete de-bonding between the opposite crack faces, is approximated. Due to this (first order or *primary*) redistribution of local stresses, the (macroscopic) stress-state bounding surface for curved cracking through cement paste changes. The new shape of this bounding surface after initial sliding and de-bonding is derived in section 5.4.4.1.

In section 5.4.4.2, the plastic deformations during initial crack sliding are considered. This leads to the quantification of the amount of ‘initial’ crack sliding, during which the process of (primary) redistribution of local stresses takes place. Then, in section 5.4.4.3, straight cracking across interlocking aggregate grains is introduced. This results in the formulation of an overall bounding surface, accounting for both curved cracking through cement paste and straight cracking across interlocking aggregate grains, for stress states after initial crack sliding and after de-bonding.

The transition of the overall bounding surface from crack initiation to the state after initial crack sliding and de-bonding incorporates two aspects:

- Loss of tensile strength. The softening law for the tensile strength is treated in section 5.4.5.1. In this section, it is sufficient to state that such a softening law exists.
- Material strengthening during initial crack sliding.

In section 5.4.4.4, these two phenomena are decoupled and, as a result, a consistent material strengthening law during initial crack sliding is formulated.

##### 5.4.4.1 Bounding surface of a curved crack through cement paste after initial sliding and after de-bonding between the opposite crack faces

During initial crack sliding and de-bonding, the stress state in the vicinity of the crack changes from rather homogeneous to highly heterogeneous. To illustrate the essence of this process of local stress redistribution, a regular sawtooth-shaped crack is considered. Figure 5.23.a shows such a crack of which, due to crack sliding, certain parts are unloading while other parts are loaded extra. This redistribution of local stresses continues until the unloading crack parts are stress free, and consequently, the load is fully concentrated at the remaining parts of the crack. An elementary crack part is considered in figure 5.23.b. Although the actual distribution of the local stresses will be quite non-uniform, an averaged uniform distribution as depicted in figure 5.23.b is satisfactory to illustrate the essentials of local stress redistribution in multiaxial compression.

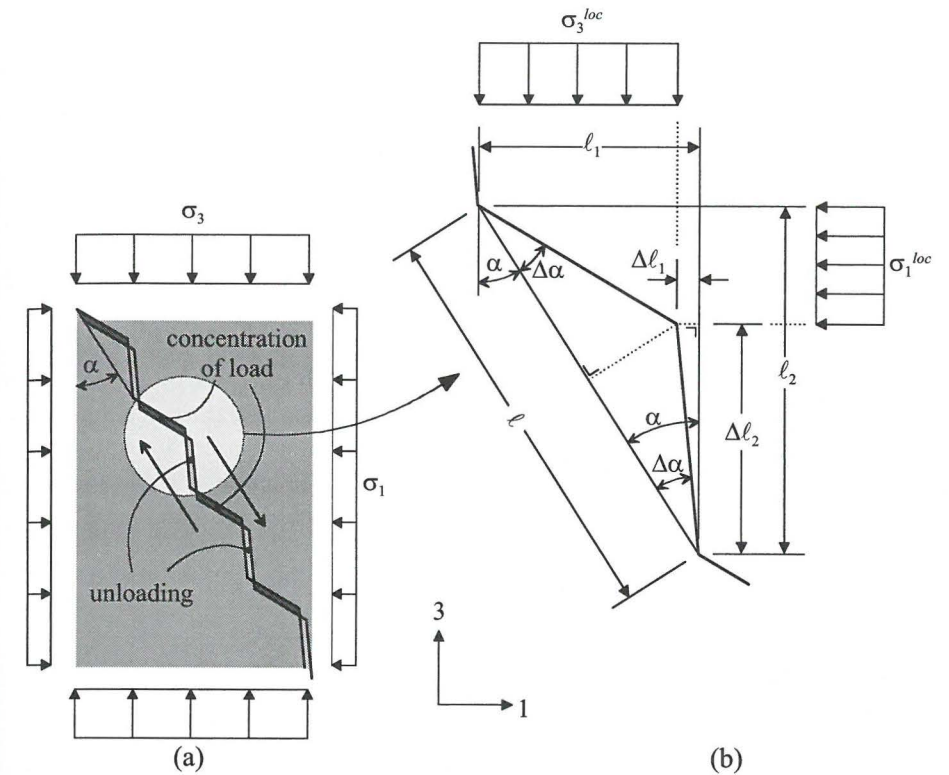


Figure 5.23. Redistribution of local stresses near a mode II crack.

The crack sliding displacement during the process of local stress redistribution is very small and therefore negligible with respect to the size of the sawtooth  $\ell$ . According to figure 5.23.b the concentrated local stresses ( $\sigma_1^{loc}, \sigma_3^{loc}$ ) at the vicinity of the crack can thus be related to the macroscopic stress state ( $\sigma_1, \sigma_3$ ) – at an adequate distance from the crack – as follows

$$\sigma_1 = \frac{\ell_2 - \Delta\ell_2}{\ell_2} \sigma_1^{loc} \quad (5.17)$$

$$\sigma_3 = \frac{\ell_1 - \Delta\ell_1}{\ell_1} \sigma_3^{loc} \quad (5.18)$$

The lengths introduced in the equations above are

$$\ell_1 = \ell \sin \alpha$$

$$\ell_2 = \ell \cos \alpha$$

$$\Delta\ell_1 = \frac{\ell}{2 \cos \Delta\alpha} \sin(\alpha - \Delta\alpha) = \frac{\ell(\sin \alpha \cos \Delta\alpha - \cos \alpha \sin \Delta\alpha)}{2 \cos \Delta\alpha}$$

$$\Delta \ell_2 = \frac{\ell}{2 \cos \Delta \alpha} \cos(\alpha - \Delta \alpha) = \frac{\ell (\cos \alpha \cos \Delta \alpha + \sin \alpha \sin \Delta \alpha)}{2 \cos \Delta \alpha}$$

Entering these expressions for the lengths in the equations (5.17) and (5.18) results in the following relations between the macroscopic and local stresses.

$$\sigma_1 = \left( \frac{1}{2} - \frac{1}{2} \tan \alpha \tan \Delta \alpha \right) \sigma_1^{loc} \quad (5.19)$$

$$\sigma_3 = \left( \frac{1}{2} + \frac{1}{2} \frac{\tan \Delta \alpha}{\tan \alpha} \right) \sigma_3^{loc} \quad (5.20)$$

The state after complete de-bonding is considered ( $f_{t,cp} = 0$ ), so only the combination of shear and normal compressive loading can be transferred across the crack. The question is now by which surface the *macroscopic* stress state ( $\sigma_1, \sigma_3$ ) is bounded when the *local* concentrated stress state in the direction  $\alpha + \Delta \alpha$  is situated on the bounding surface for a straight crack through cement paste (see figure 5.24).

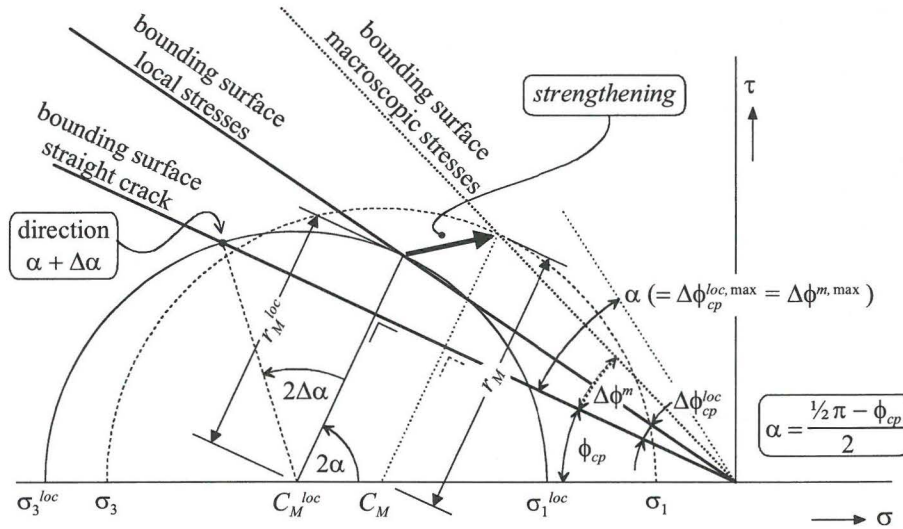


Figure 5.24. Rotation of bounding surface due to local concentration of loading.

The relation between the centre and the radius of Mohr's stress circle for the concentrated local stress state, is according to section 5.3.2

$$r_M^{loc} = -\rho^{loc} C_M^{loc} \sin \phi_{cp} \quad (f_{t,cp} = 0) \quad (5.21)$$

with

$$\rho^{loc} = \frac{1 + \tan^2 \Delta \alpha}{1 - \tan^2 \Delta \alpha} \quad (5.22)$$

The expressions for the centre and the radius of Mohr's stress circle for the macroscopic stress state  $C_M$  and  $r_M$ , result from equation (5.19) and (5.20)

$$C_M + r_M = \left( \frac{1}{2} - \frac{1}{2} \tan \alpha \tan \Delta \alpha \right) (C_M^{loc} + r_M^{loc})$$

$$C_M - r_M = \left( \frac{1}{2} + \frac{1}{2} \frac{\tan \Delta \alpha}{\tan \alpha} \right) (C_M^{loc} - r_M^{loc})$$

Insertion of equation (5.21) and further elaboration gives

$$C_M = \frac{1}{2} C_M^{loc} (\delta_1 + \delta_2)$$

$$r_M = \frac{1}{2} C_M^{loc} (\delta_2 - \delta_1)$$

with

$$\delta_1 = (1 + \rho^{loc} \sin \phi_{cp}) \left( \frac{1}{2} + \frac{1}{2} \frac{\tan \Delta \alpha}{\tan \alpha} \right)$$

$$\delta_2 = (1 - \rho^{loc} \sin \phi_{cp}) \left( \frac{1}{2} - \frac{1}{2} \tan \alpha \tan \Delta \alpha \right)$$

The increase of the friction angle with respect to the macroscopic stress state is derived from equation (5.2)

$$\tan \Delta \phi^m = (\rho^m - 1) \tan \phi_{cp} \quad (5.23)$$

with (according to figure 5.24)

$$\rho^m = \frac{r_M}{-C_M \sin \phi_{cp}} = \frac{\delta_1 - \delta_2}{(\delta_1 + \delta_2) \sin \phi_{cp}}$$

Inserting the expressions for  $\delta_1$  and  $\delta_2$  gives

$$\rho^m = \frac{2\rho^{loc} \sin \phi_{cp} + \tan \Delta \alpha \left( \frac{1}{\tan \alpha} + \tan \alpha + \rho^{loc} \sin \phi_{cp} \left( \frac{1}{\tan \alpha} - \tan \alpha \right) \right)}{\left( 2 + \tan \Delta \alpha \left( \frac{1}{\tan \alpha} - \tan \alpha + \rho^{loc} \sin \phi_{cp} \left( \frac{1}{\tan \alpha} + \tan \alpha \right) \right) \right) \sin \phi_{cp}} \quad (5.24)$$

This expression contains the variables  $\alpha$  as well as  $\phi_{cp}$ , which are related via

$$\alpha = \frac{\frac{1}{2} \pi - \phi_{cp}}{2}$$

The following expressions can then be derived according to ordinary goniometry

$$\frac{1}{\tan \alpha} + \tan \alpha = \frac{2}{\cos \phi_{cp}}$$

$$\frac{1}{\tan \alpha} - \tan \alpha = 2 \tan \phi_{cp}$$

This result greatly simplifies the expression for  $\rho^m$  given in equation (5.24)

$$\rho^m = \frac{\rho^{loc} + \tan \Delta\alpha \left( \frac{1}{\cos \phi_{cp} \sin \phi_{cp}} + \rho^{loc} \tan \phi_{cp} \right)}{1 + (1 + \rho^{loc}) \tan \Delta\alpha \tan \phi_{cp}} \quad (5.25)$$

Inserting (5.25) in (5.23) gives after rewriting

$$\tan \Delta\phi^m = \frac{(\rho^{loc} - 1) \tan \phi_{cp} + \tan \Delta\alpha}{1 + (1 + \rho^{loc}) \tan \Delta\alpha \tan \phi_{cp}}$$

Inserting equation (5.22) leads to

$$\tan \Delta\phi^m = \frac{\left( \frac{2 \tan^2 \Delta\alpha}{1 - \tan^2 \Delta\alpha} \right) \tan \phi_{cp} + \tan \Delta\alpha}{1 + \left( \frac{2}{1 - \tan^2 \Delta\alpha} \right) \tan \Delta\alpha \tan \phi_{cp}} = \tan \Delta\alpha$$

Hence,

$$\Delta\phi^m = \Delta\alpha \quad (\Delta\alpha \leq \alpha) \quad (5.26)$$

Due to local stress concentration, the bounding surface thus rotates during initial cracking. It follows from the equations (5.26) and (5.2) that this rotation induces a strengthening mechanism as long as  $\Delta\alpha$  does not exceed the global crack angle  $\alpha$ . According to figure 5.7, the stress point at the local crack angle  $\alpha + \Delta\alpha$  on Mohr's stress circle does not change for a deviation angle larger than  $\alpha$ . Consequently, equation (5.3) also holds in the case of local stress concentration.

$$\Delta\phi^m = \alpha \quad (\Delta\alpha > \alpha) \quad (5.27)$$

The foregoing is valid for a regular sawtooth-shaped crack. Yet, for an irregularly curved crack through cement paste (as drawn in figure 5.5.b), a similar approach can be applied. In this case, concentration of loading takes place at the location where the local deviation angle is highest. Such concentration of loading is shown in figure 5.25. The model for a regular sawtooth-shaped crack applies for parts A1 and A2 in this figure. Parts B and C are also unloaded. The average crack angle of these unloading parts equals the global crack angle  $\alpha$ . Consequently, the local stress state in part A1 grows proportionally with ongoing unloading of parts B and C, travelling along the bounding surface for the local stress state (see figure 5.26).

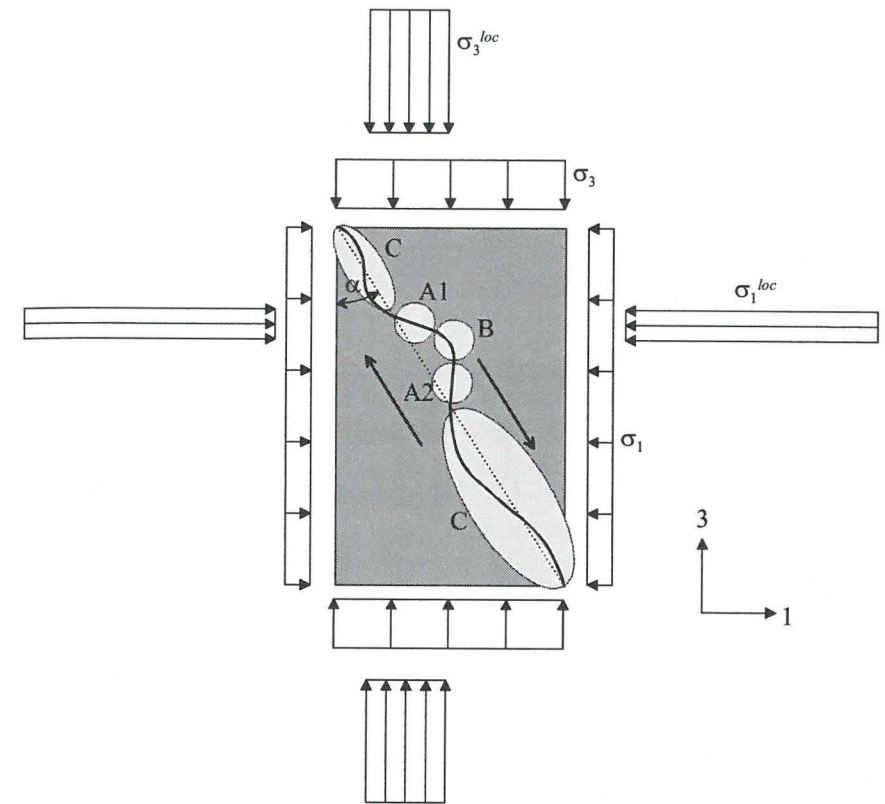


Figure 5.25. Local concentration of loading near an irregularly curved crack.

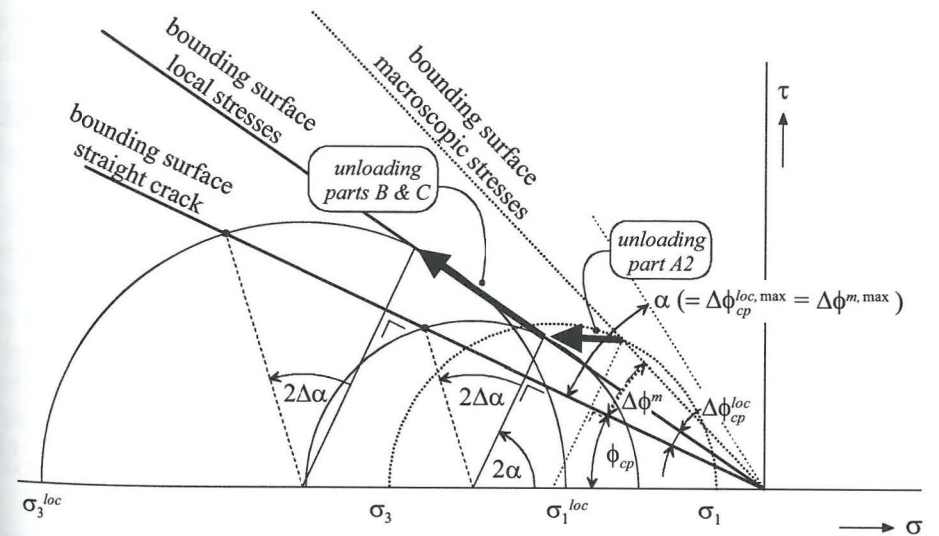


Figure 5.26. Local stress state in A1 due to unloading of parts A2, B and C.

As the local stress state in part A1 remains located on the bounding surface for the local stress state, unloading of part B and C does not affect the position of the bounding surface for the *macroscopic* stress state. As a result, the position of the (macroscopic) stress-state bounding surface is determined by equations (5.26) and (5.27) with  $\Delta\alpha$  being the *maximum* deviation angle.

#### 5.4.4.2 Plastic deformations during initial crack sliding

Stress redistribution during initial sliding induces a strengthening mechanism. According to section 5.1, mesoscopic cracking takes place in this case and a unit cell must be considered with a width  $d$  equal to the average size of the aggregate grains. Mesoscopic cracking will proceed until no substantial redistribution of stresses takes place anymore. This brings up the question when the point of no further substantial stress redistribution will be reached. To this end, crack dilatancy during initial crack sliding is considered.

As outlined in section 5.4.2, crack dilatancy depends on the location of the macroscopic stress state in stress space. Generally, this means that overriding will not occur along the maximum deviation angle  $\Delta\alpha$ . On the contrary, potential aggregate fracture (and/or cement paste crushing) takes place at those locations where the local crack deviation angle is highest (see figure 5.11). Ergo, for a certain macroscopic stress state, the dilatancy angle equals the maximum local deviation angle – denoted as  $\Delta\alpha_\psi$  – at which overriding still occurs. In accordance with equation (5.8), this implies

$$\Delta\alpha_\psi(\sigma^t) \leq \Delta\alpha$$

The actual value of  $\Delta\alpha_\psi$  will be discussed more in detail in section 5.4.5.2. For the present purpose, it is sufficient to recognise that such a *reduced* deviation angle can be appointed for each arbitrary macroscopic stress state. In the following, the plastic deformations during initial crack sliding will be quantified at that part of the crack where overriding takes place along  $\Delta\alpha_\psi$ . To this end, a regular sawtooth-shaped crack – with deviation angle equal to  $\Delta\alpha_\psi$  – is considered in figure 5.27.

During initial crack sliding, the continuum around crack part A2 (with direction  $\alpha - \Delta\alpha_\psi$ ) unloads while the continuum around crack part A1 (direction  $\alpha + \Delta\alpha_\psi$ ) is loaded extra. During this process, unloading of the continuum will fill the gap at  $\alpha - \Delta\alpha_\psi$  that would arise if cracking took place with no redistribution of stresses at all (see figure 5.27). The process of *primary* stress redistribution ends when crack part A2 is unloaded completely. At this point, a gap arises at crack part A2 and the crack starts to dilate. *During* the process of primary stress redistribution, no gap exists and when the macroscopic stress state remains unaltered, the total volume of the material does not change.

$$\varepsilon_{vol}^1 - \varepsilon_{vol}^0 = 0$$

with

$\varepsilon_{vol}^1$  : volumetric strain at crack opening (end of primary stress redistribution)

$\varepsilon_{vol}^0$  : volumetric strain at crack initiation

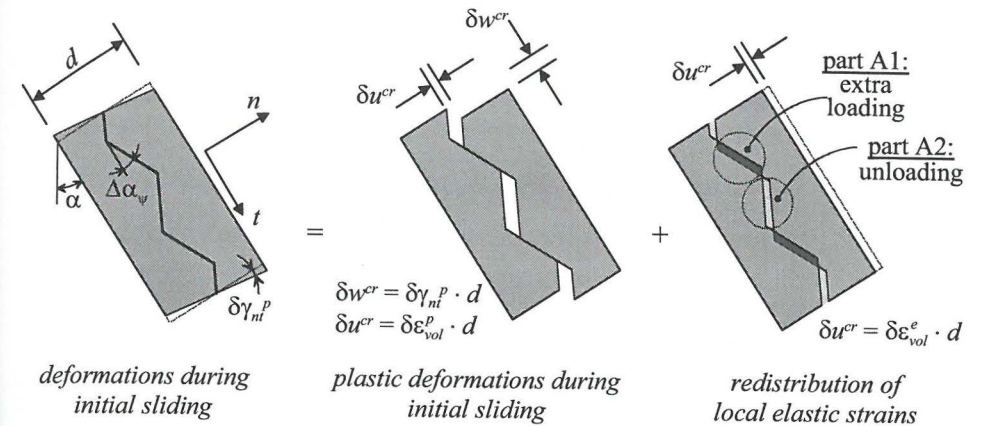


Figure 5.27. Deformations during initial sliding.

In case of a regular sawtooth-shaped crack, the dilatancy angle  $\psi$  remains constant during initial sliding and equals the reduced deviation angle  $\Delta\alpha_\psi$ . Disregarding the elastic volume change due to primary local stress redistribution and applying the theory of elasto-plasticity (as described in section 1.2.3), the volume around crack part A1 increases according to

$$\delta\varepsilon_{vol}^p = \varepsilon_{vol}^{p,1} - \varepsilon_{vol}^{p,0} = \left| \delta\gamma_{nt}^p \right| \tan \Delta\alpha_\psi$$

with

$$\delta\gamma_{nt}^p = \gamma_{nt}^{p,1} - \gamma_{nt}^{p,0}$$

$$\varepsilon_{vol}^{p,0} = \gamma_{nt}^{p,0} = 0$$

The maximum (negative) increase of stresses around crack part A1 during primary stress redistribution can be derived from equation (5.19) and (5.20)

$$\delta\sigma_1^{loc} = \sigma_1^{loc} - \sigma_1 = \left( \frac{1 + \tan \alpha \tan \Delta\alpha_\psi}{1 - \tan \alpha \tan \Delta\alpha_\psi} \right) \sigma_1$$

$$\delta\sigma_3^{loc} = \sigma_3^{loc} - \sigma_3 = \left( \frac{\tan \alpha - \tan \Delta\alpha_\psi}{\tan \alpha + \tan \Delta\alpha_\psi} \right) \sigma_3$$

This results in the following decrease of elastic volumetric strain

$$\begin{aligned} \delta \varepsilon_{vol}^e &= \varepsilon_{vol}^{e,1} - \varepsilon_{vol}^{e,0} = \frac{\delta \sigma_1^{loc} + \delta \sigma_2^{loc}}{2\bar{K}} = \\ &= \frac{\left( \frac{1 + \tan \alpha \tan \Delta \alpha_\psi}{1 - \tan \alpha \tan \Delta \alpha_\psi} \right) \sigma_1 + \left( \frac{\tan \alpha - \tan \Delta \alpha_\psi}{\tan \alpha + \tan \Delta \alpha_\psi} \right) \sigma_3}{2\bar{K}} \end{aligned}$$

During the primary stress redistribution process, the total volumetric strain is zero. Hence, we have

$$\delta \varepsilon_{vol}^e + \delta \varepsilon_{vol}^p = 0 \quad \text{or} \quad (\varepsilon_{vol}^{e,1} - \varepsilon_{vol}^{e,0}) + \varepsilon_{vol}^{p,1} = 0$$

As a result, the absolute value of the plastic shear strain at crack opening has the following value

$$\gamma_{nt}^{p,1} = -\frac{\varepsilon_{vol}^{e,1} - \varepsilon_{vol}^{e,0}}{\tan \Delta \alpha_\psi} = -\frac{\left( \frac{1 + \tan \alpha \tan \Delta \alpha_\psi}{1 - \tan \alpha \tan \Delta \alpha_\psi} \right) \sigma_1 + \left( \frac{\tan \alpha - \tan \Delta \alpha_\psi}{\tan \alpha + \tan \Delta \alpha_\psi} \right) \sigma_3}{2\bar{K} \tan \Delta \alpha_\psi}$$

In case of a regular sawtooth-shaped crack, the total volumetric strain remains zero during initial mesoscopic mode II cracking until the (absolute value of the) plastic shear strain reaches the value  $\gamma_{nt}^{p,1}$ . From that moment on no primary redistribution of stresses takes place anymore and the volume increase is solely plastic.

$$\dot{\varepsilon}_{vol}^p = \left| \dot{\gamma}_{nt}^p \right| \tan \Delta \alpha_\psi \quad \left( \left| \dot{\gamma}_{nt}^p \right| > \left| \dot{\gamma}_{nt}^{p,1} \right| \right)$$

The above is valid for a regular sawtooth-shaped crack. In case of an irregularly curved crack through cement paste, as depicted in figure 5.25, a somewhat different approach must be pursued. In this case, immediately after crack initiation, crack sliding will occur with zero dilatancy. At this stage, the crack is merely an assembly of sawteeth heaving each a different local deviation angle. For all these separate sawteeth, the regular sawtooth-shaped crack model applies (crack parts A2 unload; crack parts A1 are loaded extra). Yet, due to the heterogeneous structure of the mesoscopic crack and the heterogeneity of the stress state, certain isolated crack parts will be unloaded completely very soon after crack initiation. At that moment, the crack already slightly starts to dilate. During further sliding, more and more crack parts are unloaded completely and crack dilation becomes more and more pronounced.

Capturing this phenomenon in a model based on the theory of elasto-plasticity, the development of the dilatancy angle  $\psi$  will gradually change from zero to maximum dilatancy, instead of displaying a sudden jump at  $\gamma_{nt}^{p,1}$  (see figure 5.28).

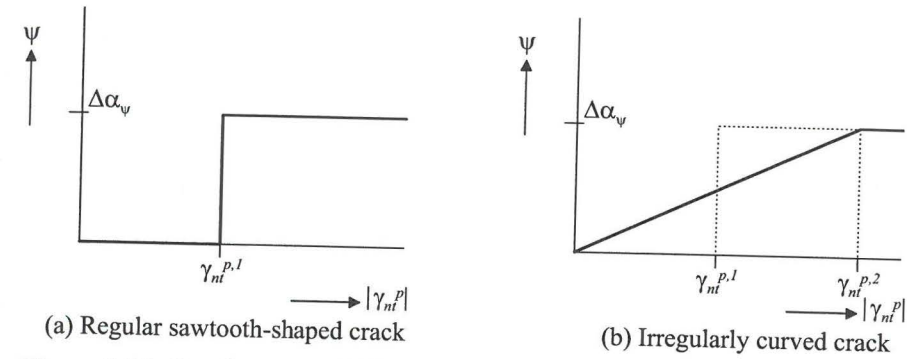


Figure 5.28. Development of dilatancy angle during mesoscopic cracking.

It is hypothesised that the *primary* stress redistribution process during initial sliding, in case of an irregularly curved crack with a gradually increasing dilatancy angle, ends when the local stresses at crack part A2 ( $\alpha - \Delta \alpha_\psi$ ) are transferred to crack part A1 ( $\alpha + \Delta \alpha_\psi$ ), with  $\Delta \alpha_\psi$  being the *maximum* local deviation angle of that part of the crack that irregularly curves through the cement paste. The plastic shear strain  $\gamma_{nt}^{p,2}$ , defining the end of initial sliding, is in this case determined by the conditions

$$\int_0^{\gamma_{nt}^{p,2}} \tan \psi d\gamma_{nt}^p = \varepsilon_{vol}^{e,2} - \varepsilon_{vol}^{e,0} + \varepsilon_{vol}^{p,2} - \varepsilon_{vol}^{p,0} = \varepsilon_{vol}^{e,2} - \varepsilon_{vol}^{e,0} + \gamma_{nt}^{p,2} \tan \Delta \alpha_\psi \quad (5.28)$$

$$\varepsilon_{vol}^{e,2} - \varepsilon_{vol}^{e,0} = \varepsilon_{vol}^{e,1} - \varepsilon_{vol}^{e,0} = -\gamma_{nt}^{p,1} \tan \Delta \alpha_\psi$$

The latter condition accounts for the fact that the total amount of elastic volumetric strain redistribution does not change when applying a different evolution law for  $\psi$ . If a linearly increasing evolution law is applied for the angle of dilatancy  $\psi$  (as drawn in figure 5.28.b), then applying condition (5.28) gives

$$\int_0^{\gamma_{nt}^{p,2}} \tan \left( \frac{\gamma_{nt}^p}{\gamma_{nt}^{p,2}} \Delta \alpha_\psi \right) d\gamma_{nt}^p = -\gamma_{nt}^{p,1} \tan \Delta \alpha_\psi + \gamma_{nt}^{p,2} \tan \Delta \alpha_\psi$$

or

$$\gamma_{nt}^{p,2} = \frac{\Delta \alpha_\psi \tan \Delta \alpha_\psi}{\ln |\cos \Delta \alpha_\psi| + \Delta \alpha_\psi \tan \Delta \alpha_\psi} \gamma_{nt}^{p,1}$$

For numerical computations this relation might be approximated by

$$\gamma_{nt}^{p,2} = \frac{2 \sin \Delta \alpha_\psi}{\Delta \alpha_\psi} \gamma_{nt}^{p,1} \quad (5.29)$$

For small deviation angles the error induced by the above approximation is negligible. Moreover, the error is still very small for very large deviation angles. For instance, the error for a deviation angle equal to  $40^\circ$  is still smaller than 1%.

#### 5.4.4.3 Extension to combined curved and straight cracking

So far, only the consequences of primary stress redistribution during initial sliding have been illustrated for an irregularly curved crack through cement paste with zero tensile strength. In this section, the model will be extended to incorporate also potential crack sliding along a straight crack crossing interlocking aggregate grains (aggregate fracture and/or cement paste crushing).

The direction of such a straight crack is equal to the global crack angle  $\alpha$  ( $\phi_{agg} = \phi_{cp}$ , section 5.3.1). In other words, the maximum local deviation angle equals zero for aggregate fracture and/or cement paste crushing. For such a crack, the phenomenon of local stress redistribution does not exist. Consequently, the bounding surface for initiation of a straight crack crossing aggregates is not affected during initial sliding. Having established the expression for the stress-state bounding surface of an irregularly curved crack running through cement paste as well as the expression for the stress-state bounding surface of a completely straight crack crossing all aggregate grains, the overall bounding surface for irregularly curved cracking through cement paste *and* straight cracking across the aggregate grains (after initial sliding and de-bonding between the opposite crack faces) is derived next.

In section 5.4.4.1, it is explained that during primary stress redistribution, the load concentrates in the vicinity of the *maximum* deviation angle  $\Delta\alpha$ . As a result, the local stress state changes according to figure 5.26. In this, the change of the local stress state at crack part A1 – due to unloading of crack part A2 – is solely determined by the magnitude of the maximum deviation angle  $\Delta\alpha$ . Yet, the change of the local stress state at crack part A1 – due to unloading of crack parts B and C – depends on the relative length of crack part A (A1 & A2) with respect to the entire crack length. For a regular sawtooth-shaped crack, the relative length equals 1 while, for a very irregularly curved crack, the relative length will be close to zero. The change of the local stress state at crack part A1 due to unloading of crack parts B and C thus depends on the irregularity of the crack, which is – as stated in section 5.3.3 – implicitly taken as a fixed material property.

Due to unloading of crack parts B and C during initial sliding, the local stress state at A1 reaches the bounding surface for aggregate crack initiation before the macroscopic stress state reaches this bounding surface. Consequently, the *overall* (macroscopic) stress-state bounding surface – for combined curved and straight cracking – deviates further and further from the straight bounding surface for curved cracking through cement paste, when approaching the bounding surface for straight crack initiation. The result is a gradual transition between the stress-state bounding surface for curved cracking through cement paste (after initial sliding and de-bonding between the opposite crack faces) and the stress-state bounding surface for straight crack initiation across interlocking aggregate grains.

With respect to this transition, two bounding conditions may be formulated. First of all, for macroscopic stress states close to zero, the local stress state at A1 will not reach the bounding surface for straight crack initiation after unloading of crack parts B and C. Therefore, at the origin of stress space  $(\sigma, \tau) = (0, 0)$ , the friction angle of the overall stress-state bounding surface equals the friction angle of a curved crack

through cement paste. Secondly, the strengthening mechanism during initial sliding exists for all deviation angles less than  $\alpha$ . Consequently, the overall bounding surface – after initial sliding and de-bonding between the opposite crack faces – must be located in stress space above the overall bounding surface for crack initiation.

Based on these considerations, a circular transition is applied as drawn in figure 5.29. According to this figure, the overall bounding surface – after initial sliding and de-bonding between the opposite crack faces – is completely determined by the existing material parameters: the maximum deviation angle  $\Delta\alpha$ , which equals  $\Delta\phi^m$  according to equation (5.26) with a maximum of  $\alpha$ , the friction angle  $\phi_{cp}$  ( $= \phi_{agg}$ ) and the cohesive strength  $c_{agg}$  of a straight crack crossing interlocking aggregates.

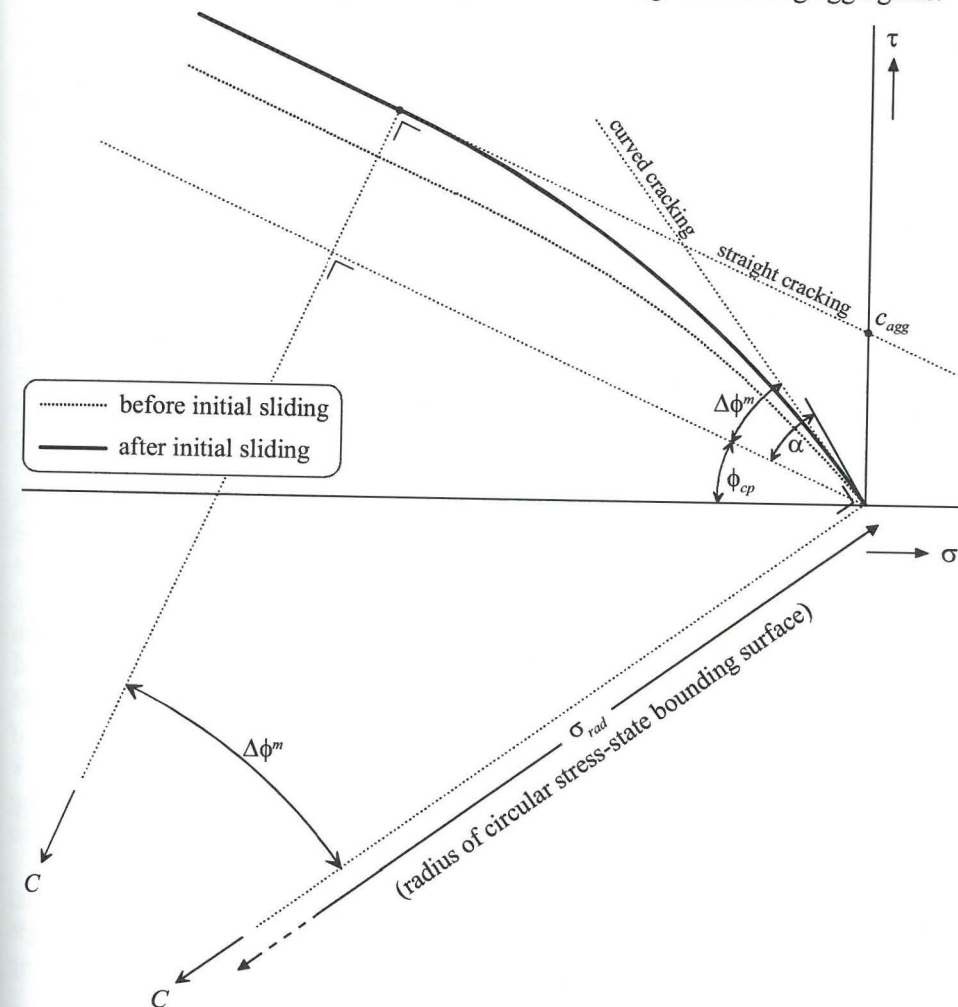


Figure 5.29. Overall stress-state bounding surface (mode II cracking) after initial sliding and de-bonding between the opposite crack faces.

By choosing resembling mathematical representations for the stress-state bounding surfaces *before* and *after* initial sliding, representing the change of shape of the bounding surface during initial sliding is simply a matter of assigning ascending functions to the increase of the friction angle  $\Delta\phi$  and the cohesion  $c$  (in case  $f_{i,cp}$  is zero).

$$\Delta\phi(\gamma_{nt}^p) = \Delta\phi_{cp} + \frac{|\gamma_{nt}^p|}{\gamma_{nt}^{p,2}} (\Delta\phi^m - \Delta\phi_{cp}) \quad (5.30)$$

$$c(\gamma_{nt}^p) = c_{ini} + \frac{|\gamma_{nt}^p|}{\gamma_{nt}^{p,2}} (c_{agg} - c_{ini}) \quad (5.31)$$

According to these functions, no difference exists between the stress-state bounding surfaces after initial sliding of a crack with  $\Delta\alpha = \alpha$  and a crack with  $\Delta\alpha > \alpha$ , because – according to equations (5.3) and (5.27) – the increase of the friction angle ( $\Delta\phi_{cp}$  as well as  $\Delta\phi^m$ ) is bounded to the maximum value  $\alpha$ . Considering a regularly curved crack, the local deviation angle  $\Delta\alpha$  is the same along the entire crack. In that case, the shape of the bounding surface does indeed not change if  $\Delta\alpha$  exceeds the global crack angle  $\alpha$  (the shape is the bilinear bounding surface of figure 5.10 with  $\Delta\phi_{cp}$  equal to  $\alpha$ ). However, in the present model an irregularly curved crack is considered. Local deviation angles smaller than  $\alpha$  are present along such a crack, even when the maximum deviation angle is larger than  $\alpha$ . Due to the presence of these local crack parts (B and C), the length of crack part A is always less than the total crack length and, consequently, the overall bounding surface comprises a curvilinear transition between the bounding surfaces of a straight crack crossing interlocking aggregate grains and a curved crack running through cement paste. As this curvilinear transitional part of the bounding surface is governed by the amount of local crack parts with a local deviation angle less than  $\alpha$ , this part of the bounding surface is still affected when the maximum deviation angle of the entire crack exceeds the global crack angle  $\alpha$ .

It is reasonable to assume that an irregularly curved crack, with a maximum deviation angle substantially higher than  $\alpha$ , will include less crack parts – with local deviation angles smaller than  $\alpha$  – than a crack with a maximum deviation angle equal to  $\alpha$ . This results in a diminishing size of the curvilinear transitional part of the bounding surface when the maximum deviation angle of the entire crack increases beyond  $\alpha$ . Ultimately, the curvilinear transitional part of the bounding surface will vanish completely when the maximum deviation angle becomes so large that even the smallest local deviation angle exceeds the global crack angle  $\alpha$ . This phenomenon is introduced in the present model by introducing an additional linear part to the overall bounding surface in case the maximum deviation angle exceeds the global crack angle  $\alpha$ . Figure 5.30 shows examples of the corresponding overall stress-state bounding surface when  $\Delta\alpha$  is smaller or larger than  $\alpha$ .

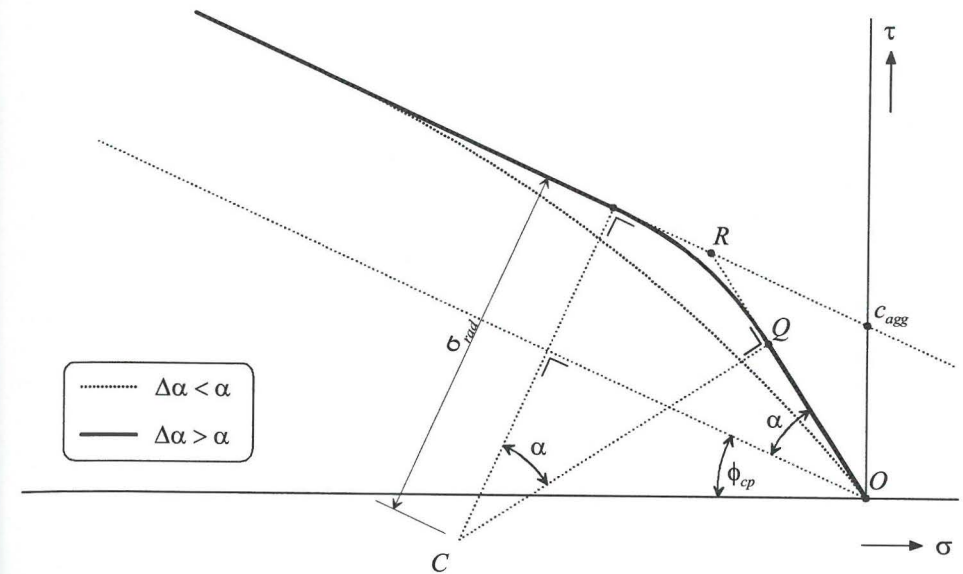


Figure 5.30. Stress-state bounding surface: introduction of linear part  $OQ$  when  $\Delta\alpha$  exceeds the global crack angle  $\alpha$ .

The length of  $\overline{OQ}$  depends both on the maximum deviation angle  $\Delta\alpha$  and the irregularity of the crack (distribution of local deviation angle along the crack). The irregularity of the crack is not specified explicitly, but is implicitly taken into account in the model.

When the maximum deviation angle  $\Delta\alpha$  exceeds the global crack angle  $\alpha$ , the shape of the stress-state bounding surface does not change in the vicinity of the origin  $O$ , i.e.  $\Delta\phi_{cp} = \Delta\phi^m = \alpha$ . The stress-state bounding surface only expands away from the origin  $O$  through equation (5.31) and through a gradual increase of the length of  $\overline{OQ}$  during initial sliding until the final state as displayed in figure 5.30 is reached. Simulations (section 5.7) with the model show good results when the following expression is applied.

$$\begin{aligned} \Delta\alpha < \alpha: & \quad \lambda_{rel}(\gamma_{nt}^p) = 0 \\ \alpha < \Delta\alpha \leq \frac{1}{4}\pi: & \quad \lambda_{rel}(\gamma_{nt}^p) = \left( \frac{\Delta\alpha - \alpha}{\frac{1}{4}\pi - \alpha} \right) \frac{|\gamma_{nt}^p|}{\gamma_{nt}^{p,2}} \end{aligned} \quad (5.32)$$

$$\text{with } \lambda_{rel}(\gamma_{nt}^p) = \frac{|\overline{OQ}(\gamma_{nt}^p)|}{|\overline{OR}|}$$



#### 5.4.4.4 Decoupling ‘material strengthening during initial crack sliding’ and ‘material softening as a result of de-bonding’

Equation (5.26) applies when the opposite crack faces are de-bonded completely. In reality, this condition will be satisfied when crack sliding proceeds and – due to accumulating damage – the tensile strength reduces to zero (modelling of this process of material softening is treated in section 5.4.5). Consequently, the stress-state bounding surface displayed in figure 5.29 (or 5.30) can be regarded as a limit case (*after* initial sliding and *after* the opposite crack faces are de-bonded completely). Additionally, the stress-state bounding surface displayed in figure 5.12 is also a limit case (at crack initiation and *before* any crack sliding or de-bonding). These limit case stress-state bounding surfaces are shown in figure 5.31.

In-between these limit cases, the stress-state bounding surface transforms gradually from the initial state (dotted line in figure 5.31) into the final state (solid line in figure 5.31). This leaves the issue of the transformation procedure. Because primary local stress redistribution during initial sliding and (gradual) de-bonding between the opposite crack faces do not necessarily occur simultaneously, these phenomena will be decoupled and treated separately. Transformation of the stress-state bounding surface due to only primary local stress redistribution (material strengthening) is treated in this section; transformation due to gradual de-bonding between the opposite crack faces (tensile softening) is treated in section 5.4.5.

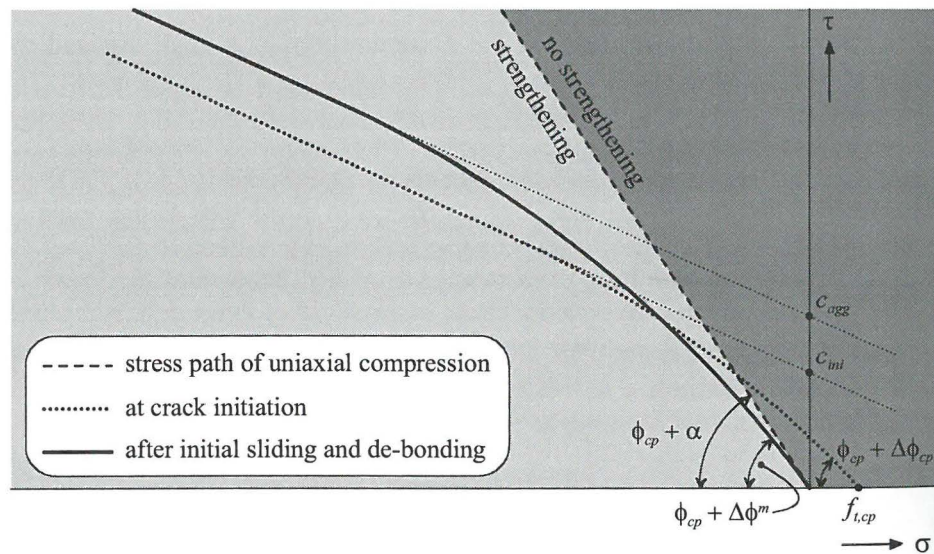


Figure 5.31. Bounding surfaces for two limit cases.

The phenomenon of strengthening due to primary stress redistribution only takes place in multiaxial compression, i.e. when the maximum principal stress is compressive. In the limiting case of uniaxial compression ( $\sigma_1 = 0$ ), the local lateral stress  $\sigma_1^{loc}$  at crack part A1 (figure 5.25) remains zero during initial sliding. Hence,

the local stress state at A1 does not rotate in stress space during initial sliding and, consequently, no material strengthening occurs. In the case of lateral tension ( $\sigma_1 > 0$ ), concentration of lateral forces would result in high lateral tensile stresses at crack part A1. These high tensile stresses cannot be transferred due to a limited tensile strength. Consequently, no concentration of lateral forces takes place in this case and no material strengthening occurs.

In figure 5.31, the stress space is divided by the stress path of uniaxial compression, characterised by the angle  $\phi_{cp} + \alpha$ . If the stress point on Mohr's stress circle (macroscopic stress state) according to the global crack direction  $\alpha$  (or  $-\alpha$ ) is located at the right of this line, the maximum principal stress is positive (tensile). Conversely, when this stress point is located at the left of this line, the maximum principal stress is negative (compressive).

Hence, with respect to material strengthening, only the part of the stress-state bounding surface at the left of the dividing line is relevant.

The intersection point  $S$  of the initial stress-state bounding surface and the stress path of uniaxial compression (see figure 5.32) is a special point. This point is the most left point on the bounding surface that is not affected by primary local stress redistribution. As a consequence, the expanding part of the bounding surface (due to primary local stress redistribution) always has to start from point  $S$  and this point acts therefore as a rotation point during initial sliding (see figure 5.33). A practical way to model this transformation process is to introduce a *fictitious tensile strength*  $f_{t,fc}$  for the determination of the material parameters of the expanding bounding surface according to the equations (5.30), (5.31) and (5.32). According to this approach,  $c_{ini}$ ,  $OQ$  and  $OR$  are based on a fictitious tensile strength  $f_{t,fc}$  so as to force the bounding surface to pass through point  $S$ .

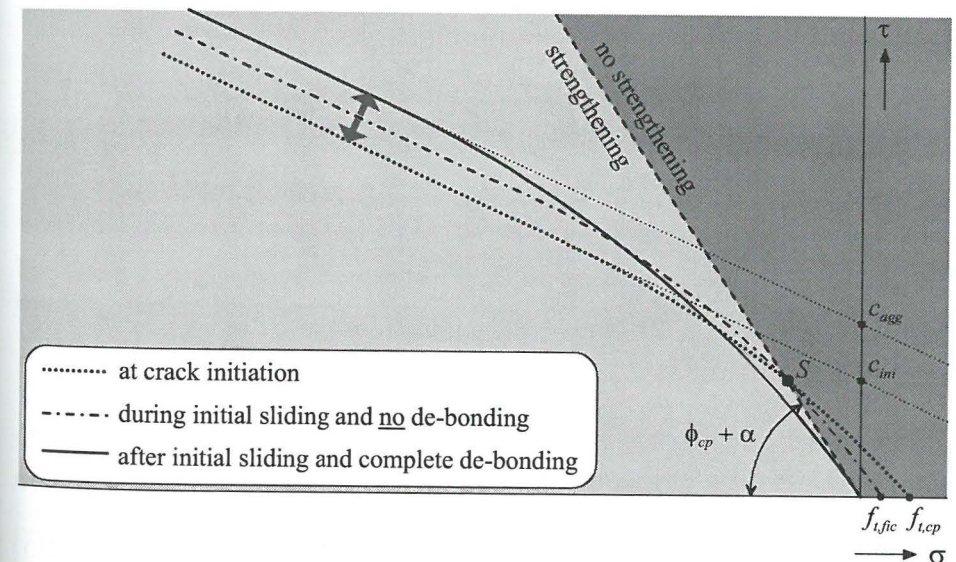


Figure 5.32. Identification of fictitious tensile strength  $f_{t,fc}$ .



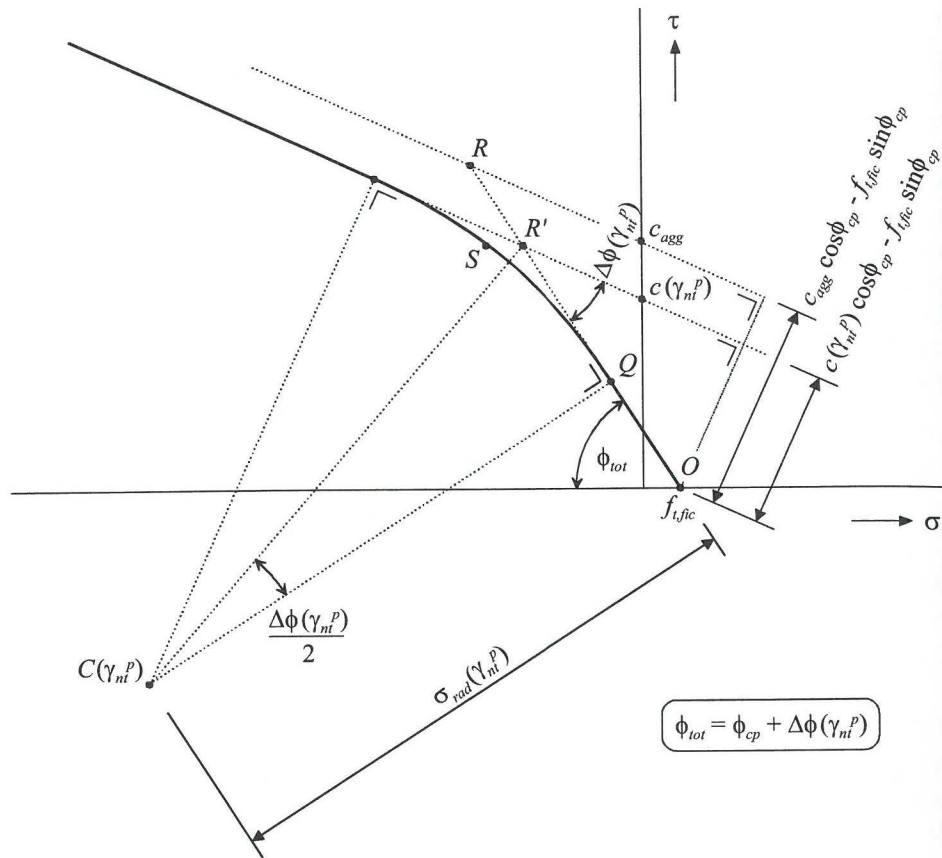


Figure 5.34. Determination of fictitious tensile strength  $f_{t, fic}$  at an arbitrary stage  $\gamma_{nt}^P$  of initial sliding.

The expressions for the centre and the radius of the circular part of the stress-state bounding surface are linearly dependent on – the only unknown –  $f_{t, fic}$ . The equation of this circle reads

$$(\sigma - \sigma_C(\gamma_{nt}^P))^2 + (\tau - \tau_C(\gamma_{nt}^P))^2 = (\sigma_{rad}(\gamma_{nt}^P))^2$$

The rotation point  $S$  lies on this circle too<sup>4</sup>, hence

$$(\sigma_S - \sigma_C(\gamma_{nt}^P))^2 + (\tau_S - \tau_C(\gamma_{nt}^P))^2 = (\sigma_{rad}(\gamma_{nt}^P))^2$$

Inserting the above  $\sigma_C(\gamma_{nt}^P)$ ,  $\tau_C(\gamma_{nt}^P)$  and  $\sigma_{rad}(\gamma_{nt}^P)$ , results in a quadratic equation for  $f_{t, fic}$

$$a \cdot (f_{t, fic})^2 + b \cdot f_{t, fic} + c = 0$$

<sup>4</sup> The coordinates of stress point  $S$  ( $\sigma_S$ ,  $\tau_S$ ) are based on  $\sigma_C(0)$ ,  $\tau_C(0)$  and  $\sigma_{rad}(0)$ . For these quantities: see figure 5.12 and consecutive formulas.

with

$$a = 1 + B_2^2 + 2B_2 \cos \phi_{tot} + 2B_1 \sin \phi_{tot}$$

$$b = -2(\sigma_S + A_2 B_2 + (B_2 \sigma_S + A_2 + B_1 \tau_S) \cos \phi_{tot} + (B_1 \sigma_S + A_1 - B_2 \tau_S) \sin \phi_{tot})$$

$$c = \sigma_S^2 + \tau_S^2 + A_2^2 + 2(A_2 \sigma_S + A_1 \tau_S) \cos \phi_{tot} + 2(A_1 \sigma_S - A_2 \tau_S) \sin \phi_{tot}$$

$$A_1 = \frac{c(\gamma_{nt}^P) - \lambda_{rel}(\gamma_{nt}^P) c_{agg}}{1 - \cos \Delta\phi(\gamma_{nt}^P)} \cos \phi_{cp}$$

$$B_1 = \frac{1 - \lambda_{rel}(\gamma_{nt}^P)}{1 - \cos \Delta\phi(\gamma_{nt}^P)} \sin \phi_{cp}$$

$$A_2 = \frac{\lambda_{rel}(\gamma_{nt}^P)}{\sin \Delta\phi(\gamma_{nt}^P)} c_{agg} \cos \phi_{cp}$$

$$B_2 = \frac{\lambda_{rel}(\gamma_{nt}^P)}{\sin \Delta\phi(\gamma_{nt}^P)} \sin \phi_{cp}$$

The right solution of this quadratic equation is

$$f_{t, fic} = \frac{-b - \sqrt{b^2 - 4ac}}{2a} \quad (5.33)$$

#### 5.4.5 Introduction of softening behaviour

According to the terminology regarding shrinkage of a stress-state bounding surface, described in section 1.2.4, three kinds of softening may be distinguished: frictional, cohesive and tensile softening. By adopting softening laws for certain material parameters (as discussed in section 5.3.5), these three kinds of softening behaviour may be introduced.

The introduction of tensile softening is crucial for describing the decrease of material strength during mode I cracking in tensile tests. Therefore, tensile softening is accounted for by adopting a softening law for the tensile strength  $f_{t, cp}$ . As outlined in section 3.2.4, the reduction of load bearing capacity at stage IV (softening stage) in multiaxial compression tests (mode II failure) may be ascribed to:

- Fracture of ‘intact’ concrete parts along the crack path of the growing cracks, i.e. fracture of the cement paste (decrease of  $f_{t, cp}$ , i.e. tensile softening) or fracture of interlocking aggregate grains (decrease of  $c_{agg}$ , i.e. cohesive softening).
- Reduction of mesoscopic roughness, i.e. reduction of maximum crack deviation angle  $\Delta\alpha$  due to overriding of interlocking aggregate grains along a mode II crack (figure 5.35), aggregate fracture and/or crushing of the cement paste.
- Reduction of microscopic roughness, i.e. reduction of the friction angle of a straight crack running through cement paste or aggregate grains due to polishing during crack sliding (reduction of  $\phi_{cp}$ ,  $\phi_{agg}$  and/or  $\phi$  (stage II))

Reduction of mesoscopic as well as microscopic roughness may both account for frictional softening. As outlined in section 4.3.6.1, experimental observations by Alexander<sup>1971</sup> on the extent of polishing of the aggregate-cement interface during crack sliding, show only a small reduction of the microscopic roughness. In line with the assumption that the differences between the *initial* microscopic roughness of a crack running either through the ITZ, through the bulk cement paste or through an aggregate grain are small (section 5.3.1;  $\phi_{cp} = \phi_{agg} = \phi(\text{stage II})$ ), also the differences in *reduction* of the microscopic roughness during crack sliding are assumed to be small. Ergo, to avoid unnecessary complexity of the model, reduction of the microscopic roughness is disregarded and frictional softening is only accounted for by applying a softening law for the mesoscopic roughness, i.e. the maximum deviation angle  $\Delta\alpha$ .

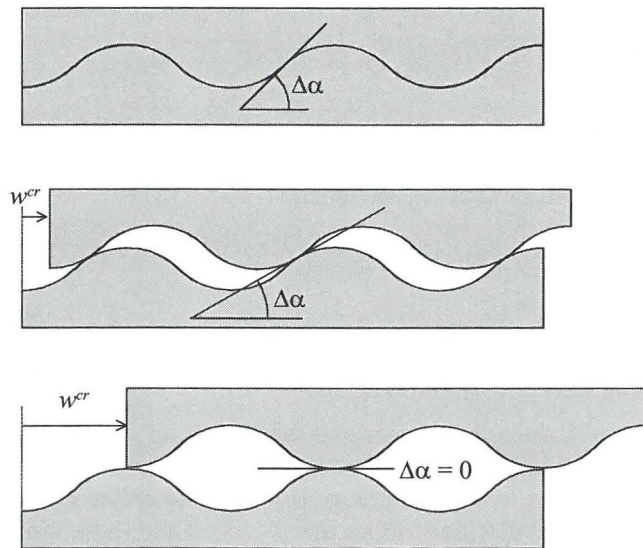


Figure 5.35. Decrease of maximum deviation angle due to overriding.

#### 5.4.5.1 Tensile softening

In section 5.3.5, the tensile strength of the cement paste is determined for mode I ( $f_{t,cp}^{mode I}$ ) as well as mode II ( $f_{t,cp}$ ) crack initiation. During subsequent crack opening (or sliding), more and more bonds between the opposite crack faces will break and the capacity of the crack to transfer tensile forces gradually diminishes.

Introducing a softening law for the tensile strength can quite easily incorporate such characteristics. For mode I cracking, softening laws have been proposed by many researchers (see for instance figure 2.10 [Hillerborg et al<sup>1976</sup>]). With respect to the formulation of a softening law, two essential criteria are pointed out:

- As a decrease of strength leads to localisation of deformations, a softening law should be based on fracture energy rather than on (smeared) crack strains. Otherwise, the results would inevitably become mesh dependent (section 2.2.3.2).
- As outlined in section 3.1.2.2, the shape of the descending branch of the loading curve during mode I crack growth in tensile tests is best typified by a steep part just beyond ultimate strength followed by a long shallow tail. The (initial) steep part of the descending branch is ascribed to opening of small isolated (bond) cracks in the fracture process zone, whereas the shallow long tail of the descending branch is attributed to the formation of *crack interface grain bridges* during the development of a continuous crack profile through the specimen [Van Mier<sup>1992</sup>].

This type of softening behaviour is well accounted for by applying a bilinear softening law, which leads to good results in case of mode I cracking [Rots et al<sup>1985,1989</sup>; Roelfstra & Sadouki<sup>1986</sup>; Carpinteri et al<sup>1989</sup>; Cotterell et al<sup>1992</sup>; Guinea et al<sup>1994</sup>].

According to these criteria, a bilinear tensile softening law is adopted for mode I cracking (see figure 5.36). To account for a constant dissipation of fracture energy irrespective of the size of the finite elements, the internal state parameter governing tensile softening  $\kappa_1$  is based on (smeared) crack strains multiplied by the width of the localisation zone, i.e. the crack displacements.

$$\Delta\kappa_1 = \sqrt{(\Delta u^{cr})^2 + (\Delta w^{cr})^2} \quad (5.34)$$

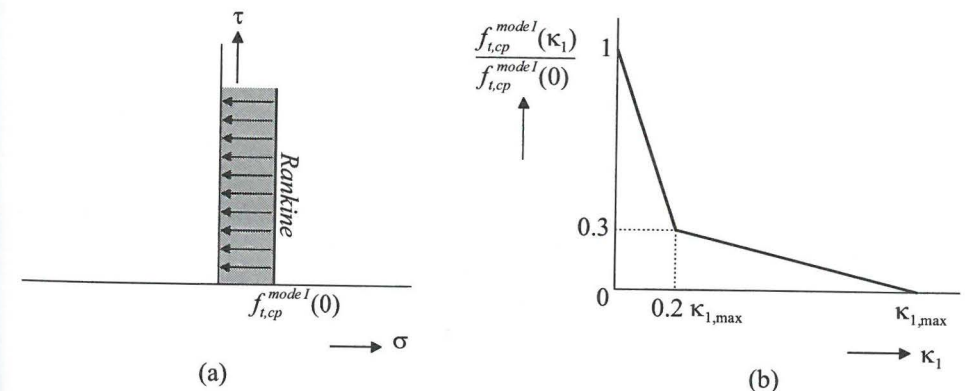


Figure 5.36. (a) Shrinkage of Rankine stress-state bounding surface during mode I cracking and (b) bilinear tensile softening law.

With respect to tensile softening during mode II cracking in multiaxial (or uniaxial) compression, little is reported in literature. The same tensile softening law as for mode I cracking is adopted for the mode II tensile strength  $f_{t,cp}$  because of two reasons:

- The descending branch of a loading curve in a multiaxial compression test does not show such a steep part just beyond ultimate strength as it is observed in

tensile tests (section 3.2.4). Ergo, a sudden decrease of bond strength between the opposite faces of a growing macrocrack (tensile softening) does not result in a sudden decrease of overall strength. As outlined in section 5.4.4, material (tensile) softening goes along with material strengthening during initial sliding of a mode II crack. Such material strengthening is only present for multiaxial compressive stress states and evidently, given the ductility observed in multiaxial compression tests on normal strength concrete, predominates the sudden decrease of bond strength at crack initiation. Note that substantial material strengthening during initial sliding is only expected for *rough* mode II cracks (see figure 5.37). Evidently, the maximum deviation angle at crack initiation is relatively large in normal strength concrete.

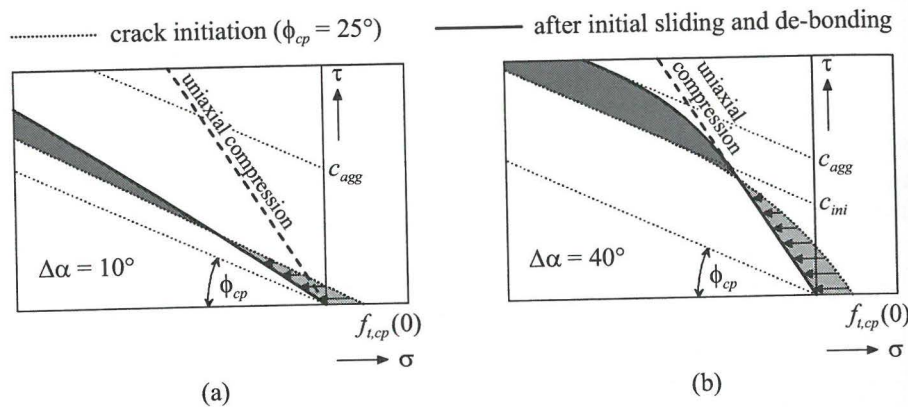


Figure 5.37. Material strengthening / tensile softening in case of (a) a small and (b) a large maximum deviation angle  $\Delta\alpha$ .

Due to the large roughness of mode II cracks in normal strength concrete, the influence of tensile softening does not extend into the multiaxial compressive regime in stress space. Consequently, the formulation of the tensile softening law does not have a large impact on the softening branch of normal strength concrete loaded in multiaxial (or uniaxial) compression. In this respect, it is justifiable to simply adopt the same tensile softening law as for mode I cracking.

- In section 3.1.2.2 it is pointed out that arrays of small overlapping (splitting) cracks are also observed along mode II cracks in concrete specimens loaded in uniaxial and multiaxial compression. Like in mode I, the stiffness of the structure decreases to some extent due to these arrays of small overlapping cracks. Hence, a bilinear tensile softening law also applies during mode II cracking.

#### 5.4.5.2 Cohesive and frictional softening

As outlined in section 3.2.4 and figure 5.3, sliding along a macroscopic mode II crack may involve several (mesoscopic) mechanisms: overriding, crushing of

cement paste and aggregate fracture. As explained further in this section, all these mechanisms involve a reduction of roughness (frictional softening) and/or a reduction of cohesive bond between the opposite crack faces of the potential mode II crack (cohesive softening).

To account for cohesive as well as frictional softening during mode II cracking, softening laws – based on the crack sliding displacement  $|w^{cr}|$  as an internal state parameter – are incorporated for the aggregate cohesion  $c_{agg}$  and the maximum crack deviation angle  $\Delta\alpha$ . In this way, the stress-state bounding surface for mode II cracking shrinks during stage IV (softening stage) from a bounding surface of ultimate strength to a bounding surface of residual strength (crack with no bond strength and only microscopic roughness) as indicated in figure 5.38. Basically, this transition of the stress-state bounding surface resembles the transition from ultimate to residual strength as indicated in figure 3.22.

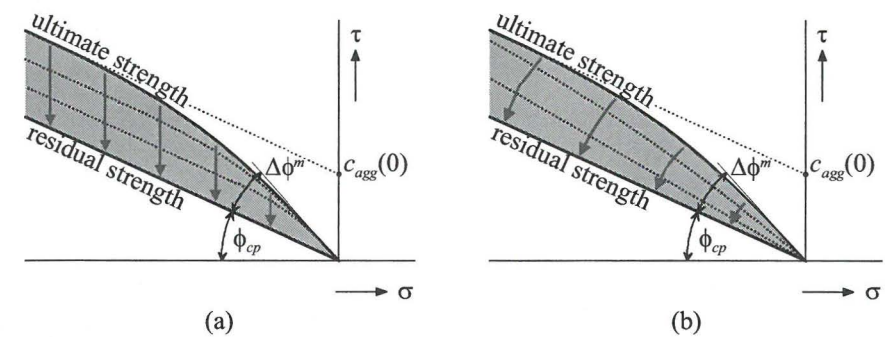


Figure 5.38. (a) Cohesive softening and (b) frictional softening.

With respect to macroscopic mode II crack sliding during stage IV in multiaxial compression, a distinction can be made between two elementary mechanisms:

1. Sliding along a curved crack around the aggregate grains
  2. Sliding along a straight crack through or crossing interlocking aggregate grains
- With respect to the basic mesoscopic cracking mechanisms as displayed in figure 5.3, it is obvious that elementary mechanism 1 (curved cracking) involves overriding while elementary mechanism 2 (straight cracking) involves aggregate fracture. As indicated in figure 5.3, cement paste crushing postpones the formation of a crack through the aggregate grains. In other words, some ductility is introduced during sliding along a straight mode II crack.

Cement paste crushing only occurs in highly compressed *porous* zones. At stage IV, most of the *internal* pores of the cement paste are already closed due to extensive pore collapse during stage II (non-linear strengthening stage). So, to allow for cement paste crushing, open space in the vicinity of the potential 'crushing zone' needs to be created during the process of macroscopic mode II crack sliding itself. Although crushing of the cement paste during sliding along a straight crack creates some open space (see figure 5.3), much more open space is created (available for

deposit of cementitious material during cement paste crushing) when the crack dilates a little bit due to overriding at another location along the macro-crack. Overriding along a curved crack is the only mechanism producing substantial crack dilatancy. Figure 2.6 shows that crack dilatancy (volumetric expansion) is high for low levels of confinement, while it decreases drastically for high levels of confinement in triaxial compression tests. From this it can be concluded that elementary mechanism 1 (overriding along a curved crack) is predominant in uniaxial compression and triaxial compression with low confinement, while elementary mechanism 2 (aggregate fracture and cement paste crushing along a straight crack) is predominant in triaxial compression with high confinement. These areas in stress space are indicated in figure 5.39. For stress states in-between, cracking according to both elementary mechanisms occurs.

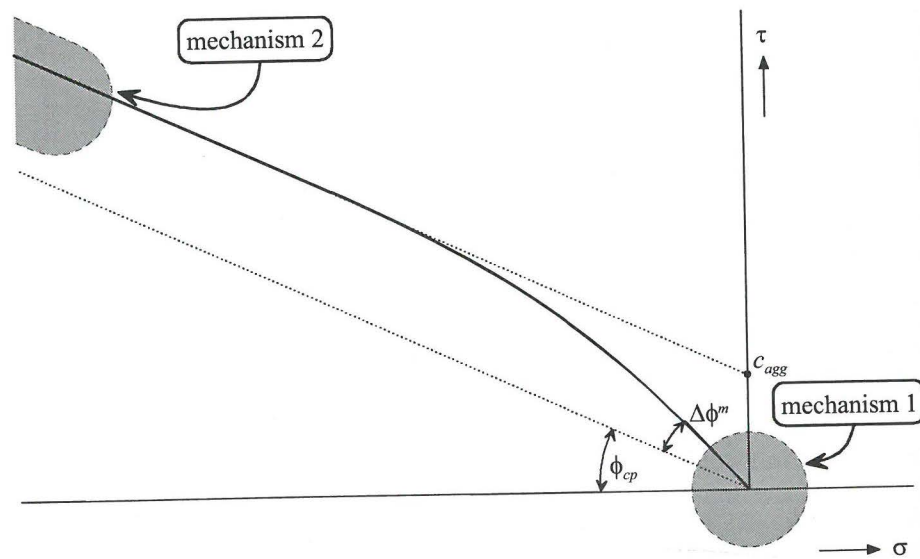


Figure 5.39. Areas in stress space with predominance of elementary mechanism 1 and 2.

#### Elementary mechanism 1: Overriding along a curved crack

Mode II crack sliding according to (exclusively) mechanism 1 takes place when the stress state is located in stress space in the low compressive region as indicated in figure 5.39. Figure 5.35 shows such mode II crack sliding along a regularly curved crack. It appears that after a certain amount of sliding, the value of  $\Delta\alpha$  has decreased to zero. In case of a regularly curved crack, the magnitude of the crack sliding displacement  $w^{cr}$  – for which  $\Delta\alpha$  has decreased to zero – is of the order of magnitude of the diameter of the aggregate grains ( $w^{cr} = O(R_3)$ ).

Besides frictional softening (decrease of  $\Delta\alpha$ ), mode II crack sliding according to mechanism 1 induces also cohesive softening (decrease of  $c_{agg}$ ). This is illustrated in figure 5.40.b by considering a crack, for which – after a certain amount of

“mechanism 1” crack sliding – the (low confinement) stress state changes to a stress state with high confinement. As a result, the crack sliding mechanism changes also from mechanism 1 to mechanism 2 and either a straight crack (dotted line) develops through the aggregates or the cement paste crushes at the (local) contact areas of the dilated crack. At this point, the strength of the potential “mechanism 2” crack is lower than in the original situation (before “mechanism 1” sliding), because *both* the potential crack area through the aggregates is reduced *and* the local contact areas are reduced. In other words, mode II crack sliding according to mechanism 1 also underlies material softening for stress states with high confinement. The reduction of the aggregate crack area / cement paste crushing area of a potential “mechanism 2” straight crack is allowed for by introducing a softening law for  $c_{agg}$ . As indicated in figure 5.40, this softening law is similar to the softening law of  $\Delta\alpha$ , because after the same amount of “mechanism 1” sliding ( $w^{cr} = 2R_3$ ), both  $\Delta\alpha$  and  $c_{agg}$  have decreased to zero.

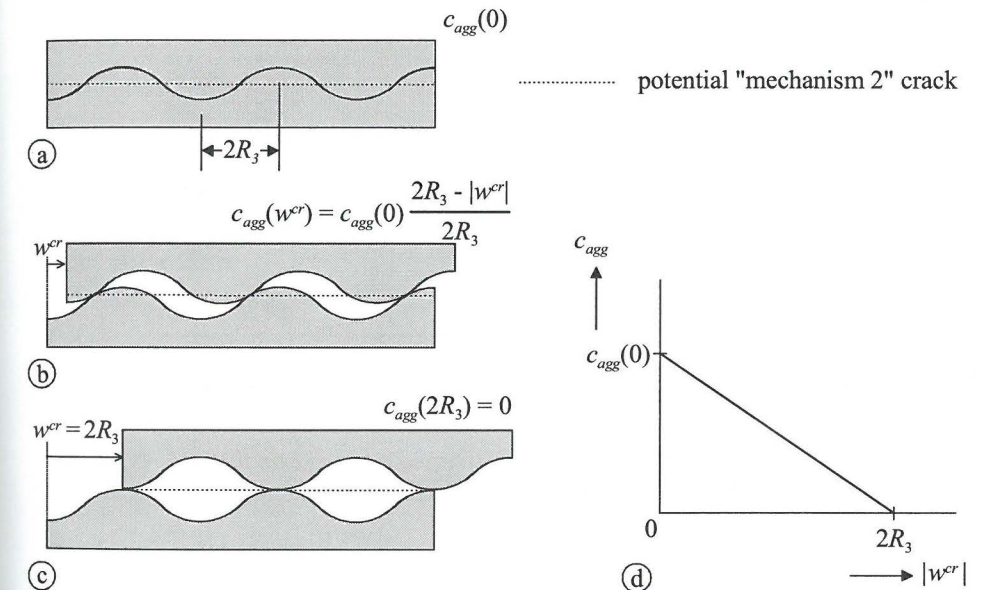


Figure 5.40. Cohesive softening during overriding along a regularly curved crack.

Based on the foregoing, both cohesive and frictional softening are introduced in the model when mode II crack sliding takes place along a curved crack through cement paste (mechanism 1). In case of a regularly curved crack, the end of the softening process is reached when the sliding displacement reaches a value of the order of magnitude of the diameter of the RVE<sub>1</sub>. This applies for both the cohesive and the frictional softening process during mode II crack sliding according to mechanism 1. The shape of the softening curve depends on the true shape of the curved crack, which in turn is dependent on the mutual positions of the aggregate grains. In the

absence of relevant data, a 'simple' linear shape of the softening curve for both cohesive and frictional softening has been chosen as indicated in figure 5.40.d. The above applies for a regularly curved crack. The structure of real concrete is, however, highly heterogeneous, and consequently, mode II macro cracking according to mechanism 1 results in a very irregularly curved crack shape. Such a crack curves around aggregate grains of different size. For such a heterogeneous structure, the diameter of the RVE<sub>1</sub> is only an average of the distribution of the actual grain sizes.

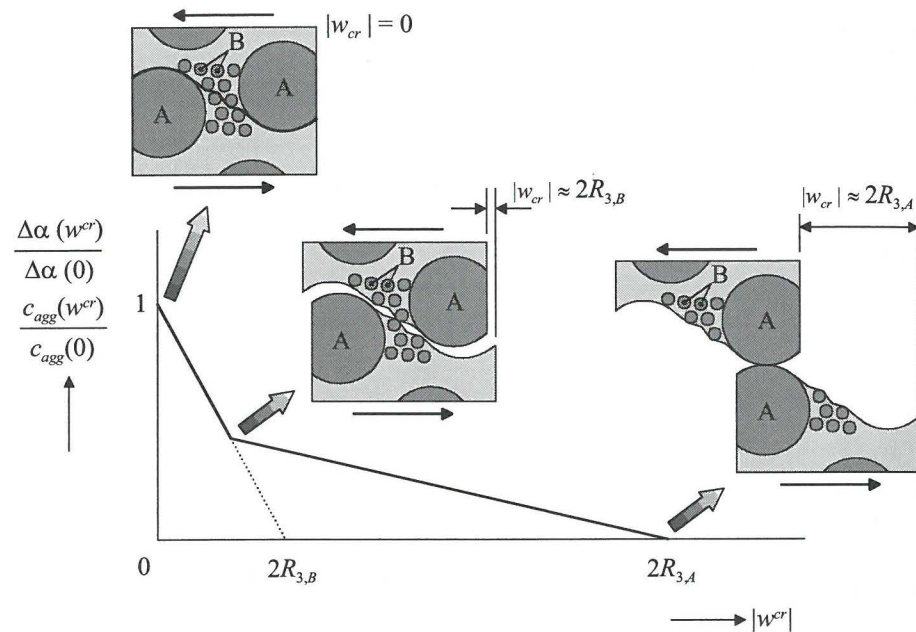


Figure 5.41. Softening diagram in case of overriding along an irregularly curved crack around aggregate grains of two different sizes.

Figure 5.41 shows an irregularly curved crack, curving around aggregate grains of two different sizes. Two meso-scale sub-levels may be indicated in this case: the sub-level of the large aggregate grains *A* and the sub-level of the fine aggregate grains *B* surrounding the large aggregate grains. It shows that the roughness due to the fine aggregate grains may be superimposed on the roughness due to the large aggregate grains (just as the microscopic roughness is superimposed on the mesoscopic roughness). In this configuration, both  $\Delta\alpha$  and  $c_{agg}$  decrease rapidly during initial sliding along the fine aggregate grains while simultaneously the crack dilates with  $\Delta\alpha$  linearly decreasing from  $\Delta\alpha_{large} + \Delta\alpha_{fine}$  to  $\Delta\alpha_{large}$  with increasing crack sliding up to a sliding displacement of the order of magnitude of the diameter of the *fine* aggregate grains  $2R_{3,B}$ . During further sliding, the dilation of the crack is much more determined by the roughness on the sub-level of the large aggregate

grains. In the course of this process, both  $\Delta\alpha$  and  $c_{agg}$  decrease slowly to zero with increasing crack sliding up to a sliding displacement of the order of magnitude of the diameter of the *large* aggregate grains  $2R_{3,A}$ . This kind of behaviour is well accounted for by adopting a bilinear overall softening diagram as displayed in figure 5.41.

The main implications, due to an irregular crack shape along different sizes of aggregate grains, are accounted for by introducing a heterogeneity parameter  $\eta$ . This parameter characterises the maximum aggregate grain size divided by the average aggregate grain size along the macrocrack.

$$\eta = \frac{D_{agg}^{max}}{D_{agg}} > 1$$

With the heterogeneity parameter  $\eta$ , a bilinear softening law – similar to the one as displayed in figure 5.41 – may be formulated for different ratios between the maximum and average size of the aggregate grains.

$$\begin{aligned} \Delta\alpha(w^{cr}) &= \Delta\alpha(0) \left(1 - \frac{\eta|w^{cr}|}{2R_3}\right) & : |w^{cr}| \leq 2R_3 \left(\frac{\eta - \eta^2}{1 - \eta^3}\right) \\ \Delta\alpha(w^{cr}) &= \frac{\Delta\alpha(0)}{\eta} \left(1 - \frac{|w^{cr}|}{2\eta R_3}\right) & : |w^{cr}| > 2R_3 \left(\frac{\eta - \eta^2}{1 - \eta^3}\right) \end{aligned} \quad (5.35)$$

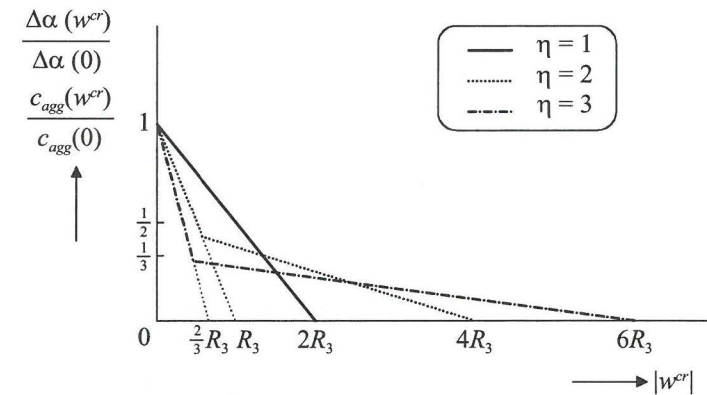


Figure 5.42. Influence of  $\eta$  on the shape of the softening diagram.

To show the influence of the heterogeneity parameter  $\eta$  on the shape of the softening diagram, equation (5.35) is graphically represented in figure 5.42 for three values of  $\eta$ <sup>5</sup>.

<sup>5</sup> The softening law for the cohesion  $c_{agg}$  is simply achieved by replacing  $\Delta\alpha$  in equation (5.35) by  $c_{agg}$ .

*Elementary mechanism 2: Sliding along a straight crack with no dilation (aggregate fracture and cement paste crushing)*

Sliding along a straight crack involves fracture of the aggregate grains. Consequently, more brittle material behaviour is expected than in the case of elementary mechanism 1 (overriding along a curved crack). Nevertheless, some ductility may be introduced during sliding along a straight mode II crack due to cement paste crushing, which postpones the formation of a crack through the aggregate grains<sup>6</sup> (figure 5.3).

In this case, linear softening is incorporated by introducing a material softening parameter  $w_{\max}^{cr}$ , defining the crack sliding displacement for which the cohesive strength  $c_{agg}$  has decreased to zero (see figure 5.43).

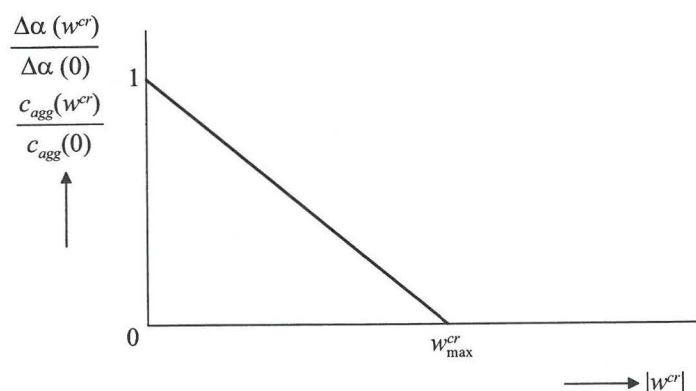


Figure 5.43. Softening diagram for crack sliding according to mechanism 2

Linear softening for the aggregate cohesion is introduced to model progressive fracture of the aggregate grains. Within a heterogeneous material, such as concrete, the stresses will concentrate in the regions with highest stiffness. In reality, these are the regions with the highest grade of compaction. Due to these higher stress levels, cement paste crushing and (subsequent) aggregate fracture occur first in these regions. Further crack sliding leads to cement paste crushing and aggregate fracture in less compacted regions and so on.

During progressive fracture of the aggregate grains, also the maximum deviation angle  $\Delta\alpha$  decreases to zero. Local failure of an aggregate grain sets the local deviation angle to zero. This occurs in the region with the highest grade of compaction, i.e. where the local deviation angle is highest. Consequently, the maximum deviation angle  $\Delta\alpha$  diminishes simultaneously with the aggregate cohesion  $c_{agg}$ .

<sup>6</sup> The crushing strength of the cement paste is assumed to be less than the strength of the aggregate grains.

*Combined crack sliding according to mechanism 1 as well as mechanism 2*

Generally, crack sliding according to both mechanism 1 and mechanism 2 will occur along the macroscopic crack. The ratio between them depends on the location of the macroscopic stress state in stress space during crack sliding (see figure 5.39). To determine the ratio between both mechanisms for an arbitrary stress state, an equivalent fictitious regularly curved crack through cement paste is introduced for the actual stress state at a certain state of crack sliding. The stress-state bounding surface for such an equivalent fictitious curved crack is displayed in figure 5.44<sup>7</sup>.

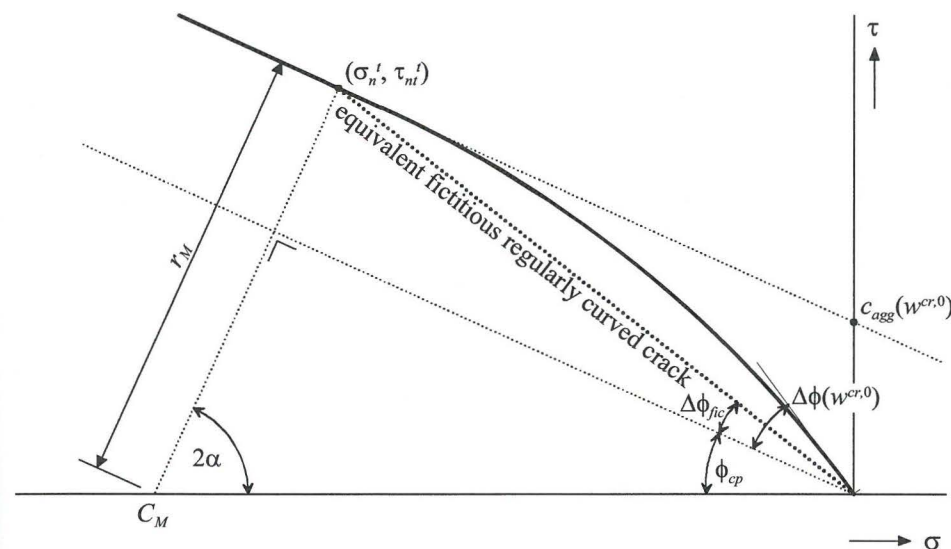


Figure 5.44. Identification of the stress-state bounding surface of an equivalent fictitious regularly curved crack through cement paste.

For both the actual crack and the equivalent fictitious crack the stress-state bounding surface travels through the actual macroscopic stress state at the initial state of crack sliding  $w^{cr,0}$  (at beginning of loading (time) step), which practically resembles the trial stress state  $\underline{\sigma}^t$  ( $\sigma_n^t, \tau_{nt}^t$ ) in the case of very small loading steps. Based on intended equivalence in crack dilatancy of both cracks, it is hypothesized that for the same state of stress, the reduced “overriding” local deviation angle  $\Delta\alpha_{\psi}(\underline{\sigma}^t, w^{cr,0})$  of the actual crack equals the (constant) deviation angle  $\Delta\alpha_{fic}$  of the fictitious crack.

As outlined in section 5.4.4.2, overriding (mechanism 1) generally not occurs along the maximum deviation angle  $\Delta\alpha$ , but along a reduced deviation angle  $\Delta\alpha_{\psi}$ . At those locations where the local crack deviation angle exceeds  $\Delta\alpha_{\psi}$ , crack sliding according to mechanism 2 occurs (aggregate fracture and/or cement paste crushing). For the actual crack, a linear distribution of the local crack deviation

<sup>7</sup> The tensile strength  $f_{i,cr}$  is assumed zero in figure 5.44. This simplifies the procedure considerably, while only a small error is made in the determination of  $\Delta\phi_{fic}$ .



angle with respect to the crack length is assumed (figure 5.45). According to this assumption, the ratio of mechanism 1 crack sliding during the crack sliding increment  $\Delta w^{cr}$  is simply derived as<sup>8</sup>.

$$\lambda_{mech1} = \frac{\ell_{mech1}}{\ell_{crack}} = \frac{[\Delta\alpha_{\psi}(\underline{\sigma}^t, w^{cr,0}); \alpha]_{\min}}{[\Delta\alpha(w^{cr,0}); \alpha]_{\min}} = \frac{[\Delta\alpha_{fic}; \alpha]_{\min}}{[\Delta\alpha(w^{cr,0}); \alpha]_{\min}} \quad (5.36)$$

with

$\lambda_{mech1}$  = relative crack length – at crack sliding  $w^{cr,0}$  – with crack sliding increment according to mechanism 1 ( $0 < \lambda_{mech1} < 1$ )

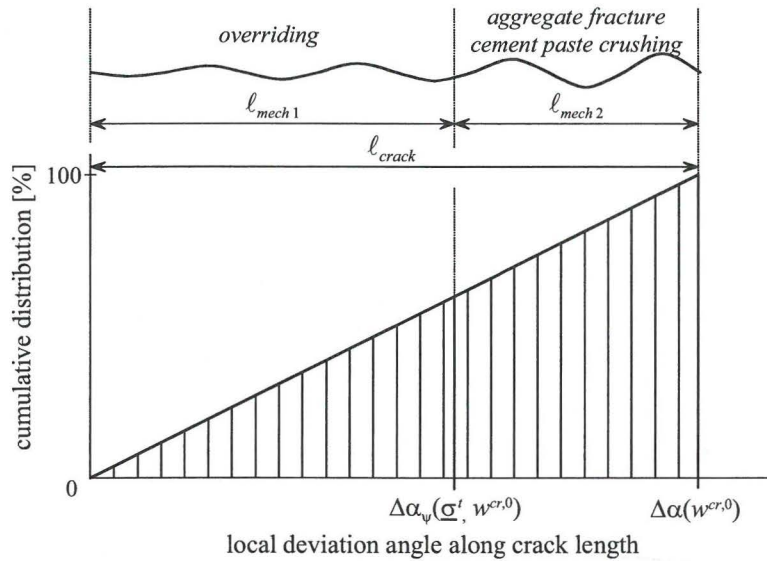


Figure 5.45. Cumulative distribution of local deviation angle along the crack length.

As the relation between  $\Delta\alpha$  and  $\Delta\phi$  of the actual crack changes during initial crack sliding (equations (5.2) and (5.26)), also the relation between  $\Delta\alpha_{fic}$  and  $\Delta\phi_{fic}$  of the equivalent fictitious crack changes during initial crack sliding.

At crack initiation, the equivalent deviation angle  $\Delta\alpha_{fic,1}$  is related to  $\Delta\phi_{fic}$  according to equation (5.2).

$$\tan(\Delta\phi_{fic}) = \frac{2 \tan^2(\Delta\alpha_{fic,1})}{1 - \tan^2(\Delta\alpha_{fic,1})} \tan \phi_{cp} = \frac{1 - \cos(2\Delta\alpha_{fic,1})}{\cos(2\Delta\alpha_{fic,1})} \tan \phi_{cp}$$

<sup>8</sup> In consequence of equations (5.3) and (5.27), both  $\Delta\alpha_{fic}$  and  $\Delta\alpha(w^{cr,0})$  in equation (5.36) are limited to the global crack angle  $\alpha$ .

or

$$\Delta\alpha_{fic,1} = \frac{1}{2} \arccos \left( \frac{\tan \phi_{cp}}{\tan(\Delta\phi_{fic}) + \tan \phi_{cp}} \right)$$

After initial crack sliding, the equivalent deviation angle  $\Delta\alpha_{fic,2}$  is related to  $\Delta\phi_{fic}$  according to equation (5.26).

$$\Delta\alpha_{fic,2} = \Delta\phi_{fic}$$

During initial crack sliding,  $\Delta\alpha_{fic}$  changes linearly from  $\Delta\alpha_{fic,1}$  to  $\Delta\alpha_{fic,2}$  (equation (5.30)). This leads to the following general relation between  $\Delta\alpha_{fic}$  and  $\Delta\phi_{fic}$ .

$$|\gamma_{nt}^p| < \gamma_{nt}^{p,2} : \quad \Delta\alpha_{fic} = \Delta\alpha_{fic,1} \frac{\gamma_{nt}^{p,2} - |\gamma_{nt}^p|}{\gamma_{nt}^{p,2}} + \Delta\alpha_{fic,2} \frac{|\gamma_{nt}^p|}{\gamma_{nt}^{p,2}} \quad (5.37)$$

$$|\gamma_{nt}^p| \geq \gamma_{nt}^{p,2} : \quad \Delta\alpha_{fic} = \Delta\alpha_{fic,2}$$

With  $\Delta\alpha_{fic}$  from equation (5.37) during a crack sliding increment  $\Delta w^{cr}$ , the *momentary* value of  $\lambda_{mech1}$  during that crack sliding increment can be determined according to equation (5.36).

In this equation,  $\Delta\alpha(w^{cr,0})$  is the maximum deviation angle – at the initial state of crack sliding  $w^{cr,0}$  – according to the *combi*-frictional softening law for combined mechanism 1 and mechanism 2 crack sliding. This *combi*-frictional softening law – as well as the *combi*-cohesive softening law – depends on the *average* value of  $\lambda_{mech1}$  during the formation history of the macrocrack<sup>9</sup>

$$\Delta\alpha(w^{cr,0}) = \bar{\lambda}_{mech1} [\Delta\alpha(w^{cr,0})]_{MECH1} + (1 - \bar{\lambda}_{mech1}) [\Delta\alpha(w^{cr,0})]_{MECH2} \quad (5.38)$$

$$c_{agg}(w^{cr,0}) = \bar{\lambda}_{mech1} [c_{agg}(w^{cr,0})]_{MECH1} + (1 - \bar{\lambda}_{mech1}) [c_{agg}(w^{cr,0})]_{MECH2}$$

with

$$\bar{\lambda}_{mech1} = \frac{1}{|w^{cr,0}|} \int_0^{w^{cr,0}} \lambda_{mech1} dw^{cr} \quad (\text{formation history of the macrocrack: } 0 \dots w^{cr,0})$$

$$[\Delta\alpha(w^{cr,0})]_{MECH1}; [c_{agg}(w^{cr,0})]_{MECH1} \quad \text{softening law according to equation (5.35)}$$

$$[\Delta\alpha(w^{cr,0})]_{MECH2}; [c_{agg}(w^{cr,0})]_{MECH2} \quad \text{softening law according to figure 5.43}$$

With the derivation of the *combi*-frictional/cohesive softening laws, an additional internal state parameter  $\bar{\lambda}_{mech1}$  is introduced to quantify the relative *average* contribution of mechanism 1 and 2 crack sliding during the formation history of macrocracking.

<sup>9</sup> The average value of  $\lambda_{mech1}$  is based on the formation *history* of the macrocrack, so *without* the contribution of  $\lambda_{mech1}$  for the *current* sliding increment  $\Delta w^{cr}$  as computed in equation (5.36).

## 5.5 Localisation of deformations and smeared crack analysis

At stage IV (softening stage), deformations localise in a few macrocracks while the continuum unloads (see section 3.2.4). To model such localised deformations, the concept of smeared cracking is adopted, i.e. the crack displacements are distributed over the width of *one* finite element.

As outlined in section 2.2.3.2, a drawback of the smeared cracking approach is that it may lead to spurious stress locking (as a fundamental consequence of finite element displacement compatibility) when the finite elements are not aligned with the crack path. With respect to mode I cracking, adopting the rotating crack concept partly remedies this shortcoming [Rots<sup>1988</sup>]. However, adoption of the rotating crack concept is not likely to improve significantly the softening characteristics of a localised mode II crack when the finite elements are not aligned with the crack path. In such case of non-alignment, the mode II crack band is likely to extend over more than one finite element.

As outlined in section 4.2, the model computations are based on finite element meshes that are generated in a random way. The finite elements are consequently not aligned with the crack path of a potential mode II crack. Hence, the crack band is likely to extend over more than one finite element and the smeared crack results will invariably exhibit too little overall softening. This drawback of the smeared cracking approach with respect to mode II cracking may be remedied simply by implementing a more brittle softening law. Obviously, such a brittle softening law is not a true material property and results will be dependent on the geometry of the finite element mesh, i.e. the existence of preferential crack directions that are aligned with the finite element mesh.

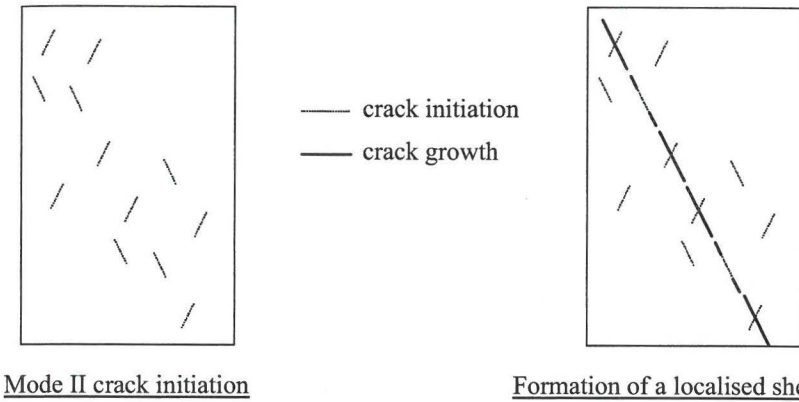
Nevertheless, because of the randomness of the finite element mesh, no preferential direction of a potential mode II crack exists. In such case, the *combination* of a (too) brittle softening law with a random finite element mesh may actually be qualified as a true material property. Because the smeared cracking approach is based on the size of the finite elements, the results are independent of the *size* of the finite elements, and, because the random finite element mesh inhabits no preferential crack direction, the results are also independent of the *orientation* of the (random) mesh.

So, with the smeared cracking approach in combination with a random finite element mesh, localised mode II cracking will result in the formation of a crack band extending over multiple finite elements, irrespective of *size* and *orientation* of the finite elements. As the crack band extends over multiple finite elements while the material parameters  $w_{\max}^{cr}$  and  $\eta$  (as defined in section 5.4.5.2) are based on a crack band width resembling the width of only one single finite element, realistic softening behaviour can only be realised by implementing a more brittle softening law (reduced value of  $w_{\max}^{cr}$  and increased value of  $\eta$ ).

Apart from the issue of the alignment of the finite element mesh with a potential mode II macrocrack in smeared crack analysis, there is also the issue of the alignment of the actual macrocrack itself. This issue is treated in the next section.

### 5.5.1 Alignment of macroscopic cracks

According to the present model formulation, mode II cracking may occur in two directions (crack angle  $\alpha$  or  $-\alpha$ ). Initially, isolated cracking will occur along the (locally) weakest direction, which depends on the loading history. However, when the cracks start forming a localised shear band, mode II crack growth should only occur along the direction of the localised shear band (see figure 5.46).



Mode II crack initiation

Formation of a localised shear band

Figure 5.46. Mode II crack initiation and crack growth during the formation of a localised shear band.

Upon failure of a concrete structure, a localised shear band will develop in a zone where – on the global level of the structure – the average strength is smallest. Propagation of an isolated – not aligned – mode II crack within such a localisation zone is prevented because such a crack is arrested at both crack tips by stronger, intact material outside the localisation zone. Such crack arrest does not take place for cracks aligned with the localisation zone. So, in the actual concrete structure, cracks naturally propagate in the direction of the localisation zone.

When the crack displacements are smeared out according to the principle of smeared cracking, the distinction between aligned crack displacements and not aligned crack displacements becomes however less transparent. To illustrate this, smeared crack displacements for cracking along  $\alpha$  are compared with smeared crack displacements for cracking along  $-\alpha$ .

Transformation of smeared crack displacements – or plastic crack strains ( $\varepsilon_n^p, \gamma_m^p$ ) – from the first potential crack direction ( $-\alpha$ ) to the second potential crack direction ( $+\alpha$ ) yields ( $\varepsilon_t^p[-\alpha] = 0$ , no plastic strains in crack direction)

$$\begin{aligned} \varepsilon_n^p[+\alpha] &= \varepsilon_n^p[-\alpha] \cos^2 2\alpha + \gamma_m^p[-\alpha] \cos 2\alpha \sin 2\alpha \\ \varepsilon_t^p[+\alpha] &= \varepsilon_n^p[-\alpha] \sin^2 2\alpha - \gamma_m^p[-\alpha] \cos 2\alpha \sin 2\alpha \\ \gamma_m^p[+\alpha] &= -2\varepsilon_n^p[-\alpha] \cos 2\alpha \sin 2\alpha + \gamma_m^p[-\alpha] (\cos^2 2\alpha - \sin^2 2\alpha) \end{aligned} \quad (5.39)$$

When an associated flow rule is adopted, i.e.  $\psi = \phi_{cp}$ , the following relation between the normal and shear crack strain is established (see section 1.2.3).

$$\epsilon_n^p [-\alpha] = \gamma_{nt}^p [-\alpha] \tan \phi_{cp} \tag{5.40}$$

According to figure 5.6 the crack angle  $\alpha$  and the friction angle of a straight crack through cement paste  $\phi_{cp}$  are interrelated by

$$\tan \phi_{cp} = \frac{1}{\tan 2\alpha} \tag{5.41}$$

Inserting equation (5.40) and (5.41) into equation (5.39) results in the following plastic crack strains according to the local coordinate system of the second potential crack direction.

$$\epsilon_n^p [+ \alpha] = \epsilon_n^p [-\alpha]$$

$$\epsilon_t^p [+ \alpha] = 0$$

$$\gamma_{nt}^p [+ \alpha] = -\gamma_{nt}^p [-\alpha]$$

For associated flow, this means that mode II cracking in the first potential crack direction exactly yields the same plastic strains as mode II cracking in the second potential crack direction (see figure 5.47).

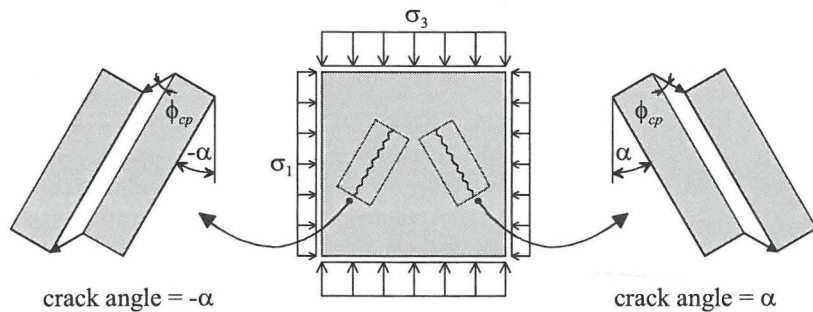


Figure 5.47. Mode II cracking according to two potential crack directions in case of associated flow ( $\psi = \phi_{cp}$ ).

Because of the similarity of plastic strains, crack arrest of not aligned mode II cracks will not take place in a natural way in case the smeared cracking principle is adopted in combination with an associated flow rule. Furthermore, if a non-associated flow rule is adopted with only a small difference between the dilatancy angle  $\psi$  and the friction angle of a straight crack through cement paste  $\phi_{cp}$ , plastic straining will almost be similar and crack arrest of not aligned mode II cracks will not occur either.

However, although the plastic strains are (almost) the same during mode II cracking along the first or second potential crack direction, there is a distinct difference in the

orientation of the finite element. This is indicated in figure 5.48. During the formation of a localisation band in the direction  $\alpha$ , together with the evolution of plastic strains ( $\gamma_{nt}^p [+ \alpha]$ ,  $\epsilon_n^p [+ \alpha]$ ) the element rotates in a clockwise direction. Conversely, when a localisation band evolves in the direction  $-\alpha$ , the element rotates in a counter clockwise direction.

In conclusion, a clockwise rotation of the finite element during loading clearly indicates the formation of a localisation band in the direction  $\alpha$ , while a counter clockwise rotation of the finite element indicates the formation of a localisation band in the direction  $-\alpha$ . So, provided that no large rotation of the whole structure takes place during loading, the direction of a potential localisation band ( $\alpha$  or  $-\alpha$ ) can be traced easily by considering the angle of rotation of the finite element.

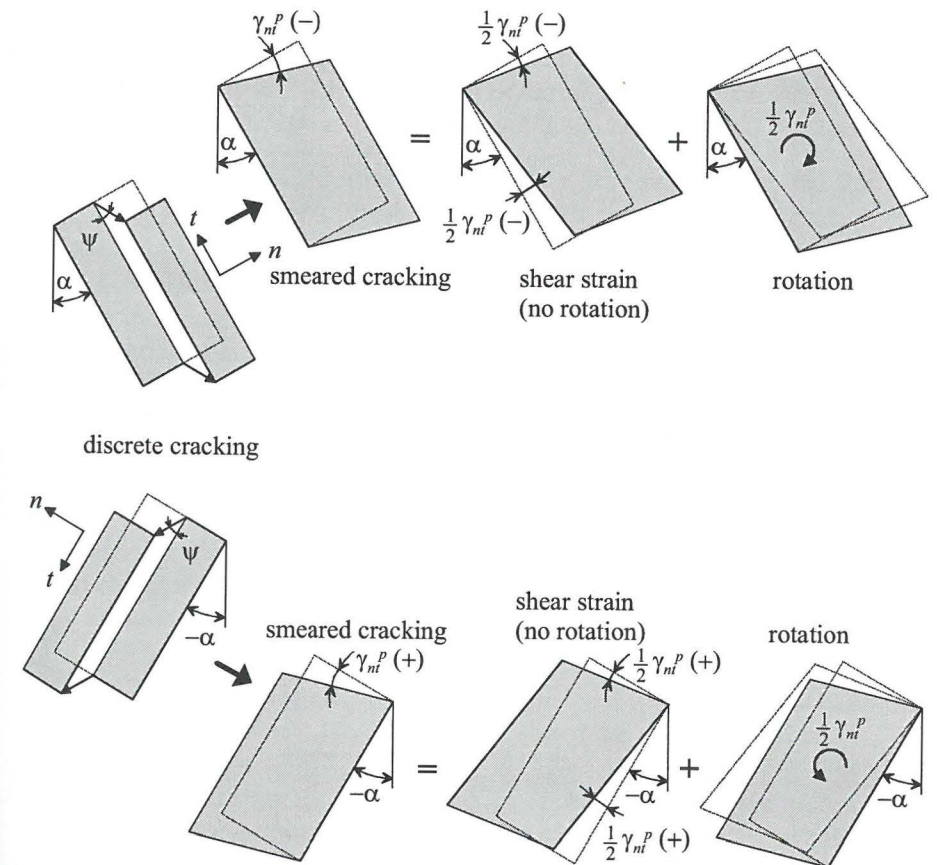


Figure 5.48. Rotation of finite element during localisation.

The phenomenon of localisation of deformations only takes place in the case of material softening. In section 5.4.4 it is outlined that during initial sliding

( $|\gamma_{nt}^p| < \gamma_{nt}^{p,2}$ ) the material strengthens if the stress state is located in the light grey area of figure 5.31. Although some material strength parameters also slightly decrease during initial sliding as a result of the softening mechanisms as discussed in section 5.4.5, it is hypothesized that the amount of strengthening will always exceed the amount of softening as long as the stress state is located in the light grey area of figure 5.31 and  $|\gamma_{nt}^p| < \gamma_{nt}^{p,2}$ . Hence, a check on the formation of a localisation band is only required when  $|\gamma_{nt}^p| > \gamma_{nt}^{p,2}$ , or when the stress state is located in the dark grey area of figure 5.31.

The rotation  $ROT$  of the finite element is regarded negative when it is in a clockwise direction and positive when it is in a counter clockwise direction. The plastic shear strain  $\gamma_{nt}^p$  is regarded negative when cracking occurs along  $\alpha$  and positive when cracking occurs along  $-\alpha$ . According to this sign convention, a negative rotation ( $ROT < 0$ ) indicates the formation of a localisation band along  $\alpha$ . In this case, only cracking along  $\alpha$  has to be considered. Conversely, if the rotation is positive ( $ROT > 0$ ), only cracking along  $-\alpha$  has to be considered.

Taking into consideration the condition of crack alignment in the case of material softening, not only the trial stress state  $\underline{\sigma}^t$  is computed based on the node displacements of the finite element (figure 5.2), but also the rotation  $ROT^t$  of the finite element. This rotation is considered to be a *trial* rotation, because part of it ( $\frac{1}{2}\Delta\gamma_{nt}^p$ ) may be due to the smearing out of the potential crack displacements. In analogy with the theory of plasticity, the latter part is named the *plastic* part of the rotation. To obtain the true (or final) rotation of the material continuum within the finite element, the plastic part has to be subtracted from the trial rotation. This procedure is illustrated in figure 5.49.

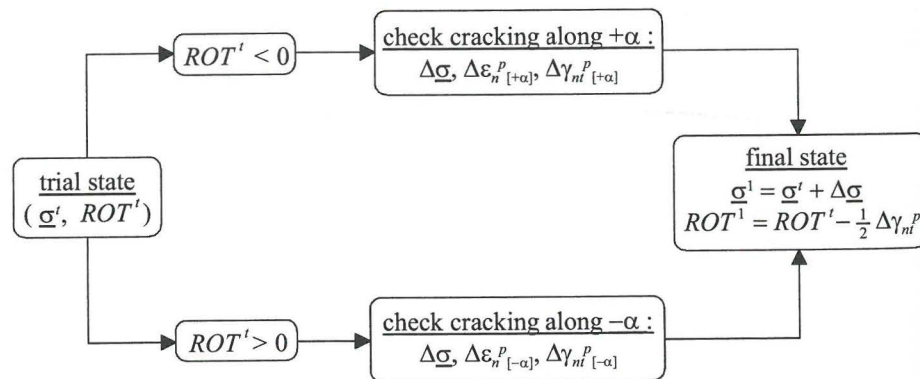


Figure 5.49. Computing procedure in case of material softening.

## 5.6 Overview of computational procedure

In sections 5.3, 5.4 and 5.5, the essential aspects with regard to mesoscopic/macroscopic cracking at stage III/IV are outlined. In this section, these essential aspects are brought together into a consistent computational procedure applicable within the main calculation scheme as depicted in figure 5.2. This computational procedure is listed at the end of this section.

Mesoscopic/macroscopic cracking at stage III/IV is checked for three potential crack directions (see figure 5.13). Crack stresses in each potential crack are obtained by rotating the stress state according to the *global*  $(x,y,z)$  coordinate system to the *local*  $(n,t,z)$  coordinate system of the crack. To distinguish specific crack quantities of each potential crack, such as crack stresses and internal state parameters, the crack angle (with respect to the maximum principal stress direction) is put between square brackets (subscript) behind the quantity.

In accordance with figure 5.2, a trial  $(x,y,z)$  stress state  $\underline{\sigma}^t$  is computed based on the initial  $(x,y,z)$  stress state  $\underline{\sigma}^{0,m}$  and the  $(x,y,z)$  macro-strain increments  $\Delta\underline{\varepsilon}^m$ , provided by UDEC. To allow for mode II crack alignment (section 5.5.1), also the (incremental) rotation of the element is considered. Subsequently, the trial stress state is checked upon mode I cracking (crack angle 0) and mode II cracking (crack angle  $+\alpha$  or  $-\alpha$ ). To this end, stress-state bounding surfaces are constructed for both mode I and mode II cracking, based on the initial value (at the beginning of the calculation cycle or time step) of the internal state parameters.

If the trial *crack* stress state  $\underline{\sigma}^t_{[0]}$  violates the mode I cracking criterion,  $\underline{\sigma}^t_{[0]}$  is put back onto the stress-state bounding surface for mode I cracking. The  $(x,y,z)$  plastic strain vector  $\Delta\underline{\varepsilon}^{p(\text{mode I})}$  is computed from the correction of the trial crack stress state and, finally, the internal state parameters for the mode I crack –  $\kappa_{1[0]}$  and  $COD_{[0]}$  – are updated.

The *final* stress state after checking of mode I cracking  $\underline{\sigma}^1_{[0]}$  is treated as a *trial* stress state for checking mode II cracking. Depending on the sign of the trial rotation of the element  $ROT^t$ , mode II cracking is checked along a crack angle  $+\alpha$  or  $-\alpha$ . If the trial crack stress state  $\underline{\sigma}^t_{[\pm\alpha]}$  violates the mode II cracking criterion,  $\underline{\sigma}^t_{[\pm\alpha]}$  is put back onto the stress-state bounding surface for mode II cracking, the  $(x,y,z)$  plastic strain vector  $\Delta\underline{\varepsilon}^{p(\text{mode II})}$  is computed and the internal state parameters for the mode II crack –  $\kappa_{1[\pm\alpha]}$ ,  $w^{cr}_{[\pm\alpha]}$ ,  $\bar{\lambda}_{mech1[\pm\alpha]}$  and the element rotation  $ROT$  – are updated.

In conformance with the main calculation scheme in figure 5.2, the plastic part of the  $(x,y,z)$  macro-strain increments due to mode I and/or mode II cracking at stage III/IV are subtracted from the  $(x,y,z)$  macro-strain increments  $\Delta\underline{\varepsilon}^m$  as provided by UDEC. Together with the initial  $(x,y,z)$  stress vector  $\underline{\sigma}^{0,m}$ , this newly obtained vector of  $(x,y,z)$  macro-strain increments ( $\Delta\underline{\varepsilon}^m = \Delta\underline{\varepsilon}^m - \Delta\underline{\varepsilon}^{p(\text{mode I})} - \Delta\underline{\varepsilon}^{p(\text{mode II})}$ ) serves as input for the stage I/II RVE<sub>1</sub> calculations.

**COMPUTATIONAL PROCEDURE  
FOR MESOSCOPIC/MACROSCOPIC CRACKING AT STAGE III/IV**

INPUT	
<u>Initial (x,y,z) stress-state / (x,y,z) strain increments and element rotation</u>	
$\underline{\sigma}^{0,m}; \Delta \underline{\epsilon}^m; \Delta ROT$	
<u>Initial value of internal state parameters</u>	
$ROT^0$	
$COD^0_{[0]}$	(mode I cracking)
$w^{cr,0}_{[\pm\alpha]}; \bar{\lambda}_{mech1}^0_{[\pm\alpha]}$	(mode II cracking)
$\kappa_1^0_{[0;\pm\alpha]}$	(mode I/II cracking)
<u>Material parameters</u>	
$\phi_{cp}, f_{t,bulk}, \Delta\alpha_0, c_{agg}$	
Softening laws: $f_{t,cp}(\kappa_1); \Delta\alpha(w^{cr}); c_{agg}(w^{cr})$	



TRIAL (x,y,z) STRESS-STATE AND ELEMENT ROTATION (elastic increments)	
$\underline{\sigma}^t = \underline{\sigma}^{0,m} + \Delta \underline{\sigma}^{e,m}$ (see chapter 4, equation (4.1))	
$ROT^t = ROT^0 + \Delta ROT$	



CHECK MODE I CRACKING	
<u>(Trial) crack stresses in mode I crack</u>	
$\begin{bmatrix} \sigma_{n[0]}^t \\ \sigma_{t[0]}^t \\ \tau_{nt[0]}^t \end{bmatrix} = \begin{bmatrix} \cos^2 \theta_{[0]}^{**} & \sin^2 \theta_{[0]}^{**} & 2 \cos \theta_{[0]}^{**} \sin \theta_{[0]}^{**} \\ \sin^2 \theta_{[0]}^{**} & \cos^2 \theta_{[0]}^{**} & -2 \cos \theta_{[0]}^{**} \sin \theta_{[0]}^{**} \\ -\cos \theta_{[0]}^{**} \sin \theta_{[0]}^{**} & \cos \theta_{[0]}^{**} \sin \theta_{[0]}^{**} & \cos^2 \theta_{[0]}^{**} - \sin^2 \theta_{[0]}^{**} \end{bmatrix} \begin{bmatrix} \sigma_x^t \\ \sigma_y^t \\ \tau_{xy}^t \end{bmatrix}$	
( $\theta_{[0]}^{**}$ = angle between the x-axis and the maximum principal stress direction)	
<u>Actual value of material parameters (construction of stress-state bounding surface)</u>	
$f_{t,cp}^{mode I}(0)$ according to equation (5.7)	
Apply tensile softening law (figure 5.36.b) $\rightarrow f_{t,cp}^{mode I} = f_{t,cp}^{mode I}(\kappa_1^0_{[0]})$	
<u>Return mapping of trial stress state to stress-state bounding surface</u>	
$\sigma_{n[0]}^t > f_{t,cp}^{mode I} \rightarrow$ Return mapping of $\underline{\sigma}^t_{[0]}$ according to figure 5.21	
$COD^0_{[0]} > 0 \rightarrow$ Return mapping of $\underline{\sigma}^t_{[0]}$ according to figure 5.22	
<u>Increments of plastic strains / crack displacements</u>	
$\Delta \underline{\epsilon}^p$ according to equations (5.12) and (5.13)	
$\Delta u^{cr}, \Delta w^{cr}$ according to equations (5.14) (d according to figure 5.1.c)	

(...continuing from previous page)

Plastic part of strain increments in (x,y,z) coordinate system

$$\begin{bmatrix} \Delta \epsilon_x^{p(mode I)} \\ \Delta \epsilon_y^{p(mode I)} \\ \Delta \gamma_{xy}^{p(mode I)} \end{bmatrix} = \begin{bmatrix} \cos^2 \theta_{[0]}^{**} & \sin^2 \theta_{[0]}^{**} & -2 \cos \theta_{[0]}^{**} \sin \theta_{[0]}^{**} \\ \sin^2 \theta_{[0]}^{**} & \cos^2 \theta_{[0]}^{**} & 2 \cos \theta_{[0]}^{**} \sin \theta_{[0]}^{**} \\ \cos \theta_{[0]}^{**} \sin \theta_{[0]}^{**} & -\cos \theta_{[0]}^{**} \sin \theta_{[0]}^{**} & \cos^2 \theta_{[0]}^{**} - \sin^2 \theta_{[0]}^{**} \end{bmatrix} \begin{bmatrix} \Delta \epsilon_n^p \\ \Delta \epsilon_t^p \\ \Delta \gamma_{nt}^p \end{bmatrix}$$

Final stress state

$$\underline{\sigma}^1_{[0]} \text{ according to equation (5.16)}$$

Update internal state parameters

$$\begin{aligned} \kappa_1^1_{[0]} &= \kappa_1^0_{[0]} + \Delta \kappa_1 & (\Delta \kappa_1 \text{ according to equation (5.34)}) \\ COD^1_{[0]} &= COD^0_{[0]} + \Delta COD & (\Delta COD \text{ according to equation (5.15)}) \end{aligned}$$



CHECK MODE II CRACKING	
<u>Choice of (potential) crack direction (+α or -α)</u>	
Crack direction according to figure 5.49	
<u>(Trial) crack stresses in mode II crack</u>	
$\begin{bmatrix} \sigma_{n[\pm\alpha]}^t \\ \sigma_{t[\pm\alpha]}^t \\ \tau_{nt[\pm\alpha]}^t \end{bmatrix} = \begin{bmatrix} \cos^2(\pm\alpha) & \sin^2(\pm\alpha) & 2 \cos(\pm\alpha) \sin(\pm\alpha) \\ \sin^2(\pm\alpha) & \cos^2(\pm\alpha) & -2 \cos(\pm\alpha) \sin(\pm\alpha) \\ -\cos(\pm\alpha) \sin(\pm\alpha) & \cos(\pm\alpha) \sin(\pm\alpha) & \cos^2(\pm\alpha) - \sin^2(\pm\alpha) \end{bmatrix} \begin{bmatrix} \sigma_{n[0]}^t \\ \sigma_{t[0]}^t \\ \tau_{nt[0]}^t \end{bmatrix}$	
<u>Actual value of material parameters</u>	
$\Delta\alpha(0)$ according to equation (5.5)	
$f_{t,cp}(0)$ according to equation (5.6)	
Apply tensile softening law (figure 5.36.b) $\rightarrow f_{t,cp} = f_{t,cp}(\kappa_1^0_{[\pm\alpha]})$	
Apply combi-cohesive/frictional softening laws (equation (5.38)):	
<ul style="list-style-type: none"> <li>▪ <math>\Delta\alpha = \Delta\alpha(w^{cr,0}_{[\pm\alpha]}, \bar{\lambda}_{mech1}^0_{[\pm\alpha]})</math></li> <li>▪ <math>c_{agg} = c_{agg}(w^{cr,0}_{[\pm\alpha]}, \bar{\lambda}_{mech1}^0_{[\pm\alpha]})</math></li> </ul>	
<u>Construction of stress-state bounding surface</u>	
$\Delta\phi_{cp}$ and $\Delta\phi^m$ according to equations (5.2), (5.3), (5.26) and (5.27)	
$\Delta\phi(\gamma_{nt}^p), c(\gamma_{nt}^p)$ and $\lambda_{rel}(\gamma_{nt}^p)$ according to equations (5.30), (5.31) and (5.32) with:	
<ul style="list-style-type: none"> <li>▪ <math>\gamma_{nt}^p = \frac{w^{cr,0}_{[\pm\alpha]}}{d}</math> (d according to figure 5.1.b)</li> <li>▪ <math>\gamma_{nt}^{p,2}</math> and <math>\Delta\alpha_{\psi}</math> according to equations (5.29) and (5.37) (This implies a (simple) numerical iterative solution procedure)</li> <li>▪ <math>c_{ini}</math> according to equation (5.4)</li> </ul>	
$f_{t,fc}$ according to equation (5.33)	

(...continuing from previous page)

### Return mapping of trial stress state to stress-state bounding surface

Dilatancy angle  $\psi$  according to figure 5.28.b

If  $\underline{\sigma}'_{[\pm\alpha]}$  violates the mode II cracking criterion

→ return mapping according to figure 5.19 or figure 5.20.

### Increments of plastic strains / crack displacements

$\Delta \underline{\epsilon}^p$  according to equation (5.10)

Material *strengthening* or *softening*?

- $|\gamma_{nt}^p| < \gamma_{nt}^{p,2}$  and  $\underline{\sigma}'_{[\pm\alpha]}$  is located in the light grey area of figure 5.31  
→ material *strengthening*
- $|\gamma_{nt}^p| \geq \gamma_{nt}^{p,2}$  or  $\underline{\sigma}'_{[\pm\alpha]}$  is located in the dark grey area of figure 5.31  
→ material *softening*

$\Delta u^{cr}, \Delta w^{cr}$  according to equations (5.11)

- Material *strengthening* →  $d$  according to figure 5.1.b
- Material *softening* →  $d$  according to figure 5.1.c

### Plastic part of strain increments in global (x,y,z) coordinate system

$$\begin{bmatrix} \Delta \epsilon_x^{p(\text{mode II})} \\ \Delta \epsilon_y^{p(\text{mode II})} \\ \Delta \gamma_{xy}^{p(\text{mode II})} \end{bmatrix} = \begin{bmatrix} \cos^2 \theta_{[\pm\alpha]}^{**} & \sin^2 \theta_{[\pm\alpha]}^{**} & -2 \cos \theta_{[\pm\alpha]}^{**} \sin \theta_{[\pm\alpha]}^{**} \\ \sin^2 \theta_{[\pm\alpha]}^{**} & \cos^2 \theta_{[\pm\alpha]}^{**} & 2 \cos \theta_{[\pm\alpha]}^{**} \sin \theta_{[\pm\alpha]}^{**} \\ \cos \theta_{[\pm\alpha]}^{**} \sin \theta_{[\pm\alpha]}^{**} & -\cos \theta_{[\pm\alpha]}^{**} \sin \theta_{[\pm\alpha]}^{**} & \cos^2 \theta_{[\pm\alpha]}^{**} - \sin^2 \theta_{[\pm\alpha]}^{**} \end{bmatrix} \begin{bmatrix} \Delta \epsilon_n^p \\ \Delta \epsilon_t^p \\ \Delta \gamma_{nt}^p \end{bmatrix}$$

with

$$\theta_{[\pm\alpha]}^{**} = \theta_{[0]}^{**} \pm \alpha$$

### Update internal state parameters

$$\kappa_{1[\pm\alpha]}^1 = \kappa_{1[\pm\alpha]}^0 + \Delta \kappa_1 \quad (\Delta \kappa_1 \text{ according to equation (5.34)})$$

$$w_{[\pm\alpha]}^{cr,1} = w_{[\pm\alpha]}^{cr,0} + \Delta w^{cr}$$

$$\bar{\lambda}_{mech1[\pm\alpha]}^1 = \frac{\bar{\lambda}_{mech1[\pm\alpha]}^0 \cdot w_{[\pm\alpha]}^{cr,0} + \lambda_{mech1} \cdot \Delta w^{cr}}{w_{[\pm\alpha]}^{cr,1}} \quad (\lambda_{mech1} \text{ according to equation (5.36)})$$

$$ROT_{[\pm\alpha]}^1 = ROT_{[\pm\alpha]}^t - \frac{1}{2} \Delta \gamma_{nt}^p$$

### OUTPUT

#### New (x,y,z) strain increments (input for stage I/II calculations)

$$\Delta \underline{\epsilon}^m = \Delta \underline{\epsilon}^m - \Delta \underline{\epsilon}^{p(\text{mode I})} - \Delta \underline{\epsilon}^{p(\text{mode II})}$$

#### Final value of internal state parameters

$$ROT^1$$

$$COD_{[0]}^1 \quad (\text{mode I cracking})$$

$$w_{[\pm\alpha]}^{cr,1}; \bar{\lambda}_{mech1[\pm\alpha]}^1 \quad (\text{mode II cracking})$$

$$\kappa_{1[0;\pm\alpha]}^1 \quad (\text{mode I/II cracking})$$

## 5.7 Performance of the numerical model

### 5.7.1 Mesh design

The simulations – including stage III/IV behaviour – are carried out according to the test set-up given in figure 5.50.a. This test set-up is basically the same as used for the stage I/II in section 4.4 (figure 4.33), except for the size of the loading platens. In this series of simulations of the experimental test program performed by Van Geel<sup>1998</sup>, the width of the loading platens is 90 mm instead of the actual width of 97 mm as applied in the experiments of Van Geel.

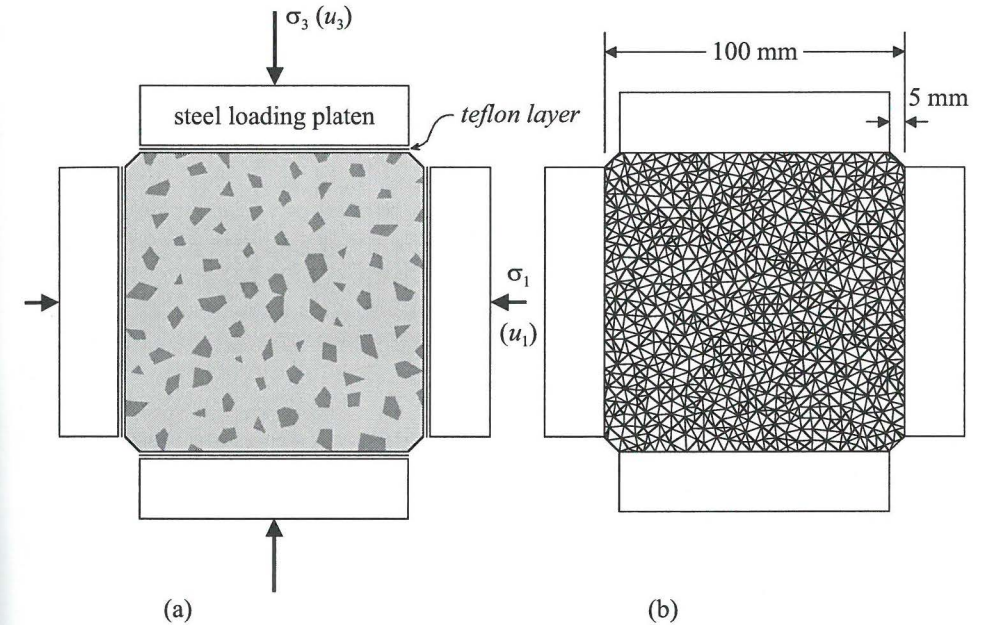


Figure 5.50. (a) Test set-up and (b) mesh of finite elements (zones in UDEC).

The dimensions of the loading platens are reduced, because potential *localised cracking* in macroscopic (mode II) cracks is modelled by *smearred* cracking. In the experiments, only a slight distance between the loading platens provides sufficient space for a mode II crack (with displacement discontinuity) to develop in the corners of the specimen. To prevent (partly) blocking of the development of the localisation zone, the gap between the loading platens should at least resemble the width of *one* finite element when the displacement discontinuity is modelled by a smeared crack.

However, as outlined in section 5.5, in combination with a random finite element mesh, localised mode II cracking will result in the formation of a localisation zone extending over multiple finite elements. Hence, to allow the development of such a localisation zone, the minimum gap between the loading platens should be at least a few finite elements (zones in UDEC) wide (see figure 5.50.b).

### 5.7.2 Discussion of material properties

Numerical simulations of the test series performed by Van Geel, as demonstrated in the following sections, cover the whole loading curve of concrete loaded in multiaxial compression from stage I up to and including stage IV. The material properties herein of the stage I/II constitutive model are listed in table 4.4 and discussed in section 4.4. In this section, the additional material properties of the stage III/IV constitutive model are discussed. These material properties, as used in the simulations, are listed in table 5.1.

Table 5.1. Material properties (stage III/IV constitutive model).

Mode I cracking		Mode II cracking	
Fine agg. / mortar	Coarse aggregates (2 - 8 mm)	Fine agg. / mortar	Coarse aggregates (2 - 8 mm)
$f_{t,bulk} = 8 \text{ MPa}$	$f_{t,bulk} = 8 \text{ MPa}$	$\phi_{cp} = 25^\circ$	$\phi_{cp} = 25^\circ$
$\kappa_{1,max} = 0.05 \text{ mm.}$	$\kappa_{1,max} = 0.05 \text{ mm.}$	$\Delta\alpha_0 = 34.6^\circ$	$\Delta\alpha_0 = 37^\circ$
		$c_{agg} = 30 \text{ MPa}$	$c_{agg} = 37 \text{ MPa}$
		$\eta = 2$	$\eta = 1$
		$w_{max}^{cr} = 0.15 \text{ mm.}$	$w_{max}^{cr} = 0.15 \text{ mm.}$

Mode I cracking is mostly determined by two material properties, the tensile strength of the bulk cement paste<sup>10</sup>  $f_{t,bulk}$  and the softening law of the tensile strength, which is established by  $\kappa_{1,max}$ . The displayed values of these material properties are obtained by inverse modelling of a uniaxial tensile test (see section 5.7.3). The value of  $f_{t,bulk}$  may be compared to the direct or flexural tensile strength of plain cement paste as found in literature (table 3.1). Taking into consideration the large scatter in these test results, a value of 8 MPa is an adequate choice.

In accordance with equation (5.1), the friction angle  $\phi_{cp}$  is equal to the friction angle  $\phi$  for cracking along the ITZ at stage II. The crack deviation angle of the virgin concrete  $\Delta\alpha_0$  and the aggregate/cement paste crushing cohesive strength  $c_{agg}$  are fine-tuned by inverse modelling of strength results in a series of multiaxial compressive tests (section 5.7.3). A magnitude of  $\Delta\alpha_0$  in the order of  $35^\circ$  is realistic, considering the degree of compaction of the concrete (according to section 4.4, the volume of the aggregate fraction is about 68% of the total concrete volume) and reviewing the heterogeneous structure of a true concrete cross section (see figure 4.5(a)).

The uniaxial compressive strength of the aggregates (estimated at 180 MPa in section 3.1.2.1) gives an indication whether  $c_{agg}$  represents the aggregate cohesive strength or the cement paste crushing cohesive strength. Assuming a straight Mohr-

<sup>10</sup> According to equation (5.6), the overall tensile strength  $f_{t,cp}$  is also determined by the tensile strength of the ITZ  $f_{t,ITZ}$ , which is a material property of the stage I/II constitutive model.

Coulomb strength envelope (with  $\phi_{agg} = 25^\circ$ ), the uniaxial compressive strength  $f_{c,agg}$  and  $c_{agg}$  are interrelated through

$$c_{agg} \cos \phi_{agg} = \frac{1}{2} f_{c,agg} (1 - \sin \phi_{agg})$$

With  $\phi_{agg} = 25^\circ$  and  $f_{c,agg} = 180 \text{ MPa}$ , this results in a value of 57 MPa for the aggregate cohesive strength. From this, it seems that  $c_{agg}$  in the model is more determined by the crushing strength of the cement paste, than the strength of the aggregate grains. This conclusion is also supported when the differences in strength between test-results of normal strength and high strength concrete are analysed in the experiments of Van Geel<sup>1998</sup>. For these different concrete mixtures, only the structure of the cement paste changes, the type of aggregate (rounded river gravel) is the same for both mixtures. Despite the use of the same type of aggregate, not only the uniaxial strength increases for the high strength concrete, but also the multiaxial compressive strength increases enormously (even in multiaxial compression tests with high confining pressures). This increase in multiaxial compressive strength can only be attributed to the improved (less porous) structure of the cement paste, thus increasing the crushing strength of the cement paste and *not* the aggregate cohesive strength.

As outlined in section 5.5, the cohesive/frictional softening laws for mode II cracking have to be quite brittle in combination with a random finite element mesh. Due to the influence of the randomness of the mesh, the softening parameters  $\eta$  and  $w_{max}^{cr}$  can only be assessed indirectly. Therefore, the cohesive/frictional softening parameters  $\eta$  and  $w_{max}^{cr}$  are obtained by inverse modelling of the slope of the softening branch of the multiaxial compressive test ( $\beta = 0.10$ ) as shown in figure 5.51. Obviously, the appropriateness of this approach can only be demonstrated by the results of *other* test simulations with respect to stage IV behaviour (these are given in sections 5.7.3 – 5.7.5). In line with the above, the chosen values of  $\eta$  and  $w_{max}^{cr}$  are discussed here only qualitatively. For the coarse aggregates (only a single grain),  $\eta$  equals 1. The heterogeneity of the mortar with respect to grain sizes is accounted for by a larger value:  $\eta = 2$ . With respect to  $w_{max}^{cr}$  the dominance of cement paste crushing is emphasised to account for a relatively large degree of ductility.

### 5.7.3 Simulations of proportional tests

Figure 5.51 shows the results of the model simulations of a test series performed by Van Geel<sup>1998</sup> with concrete cubes loaded proportionally in multiaxial plane-strain compression. This figure is similar to figure 4.35, but now with stage III and IV behaviour included in the simulations<sup>11</sup>.

<sup>11</sup> Test simulations with very high lateral confinement ( $\beta = 0.25$  and  $\beta = 0.5$ ) are omitted because these experiments/simulations did not show any stage III/IV behaviour.

With regard to both the axial loading curves and lateral deflections, the experimental data of Van Geel is reproduced quite well by the model simulations. Having in mind that each loading configuration in the experimental test program consists of only one experiment, small deviations between experiments and simulations must be expected as a certain scatter in experimental test results is inevitable.

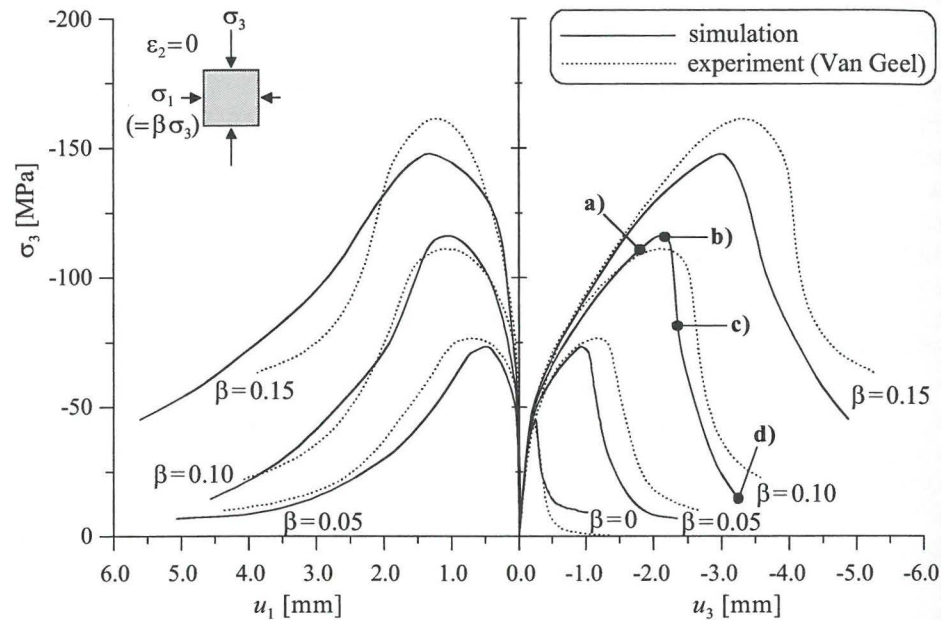


Figure 5.51. Model simulations of a test series of concrete loaded proportionally in multiaxial plane-strain compression.

As stated in section 3.1.3, the deformational behaviour of concrete loaded in multiaxial compression is characterised by a distinct shift from uniformly distributed deformations in the pre-peak region to highly localised deformations (macrocracks) in the post-peak region. To illustrate the model performance in this respect, the evolution of macrocracks is indicated in figure 5.52 for a simulation of a typical multiaxial compressive test with  $\beta = 0.10$  (the loading phases a, b, c and d are indicated in the axial loading curve of figure 5.51). In this figure, thicker lines at the centre of the finite elements indicate the crack sliding displacements. The orientation of the lines corresponds with the orientation of the crack and the (relative) length of the lines corresponds with the magnitude of the sliding displacement.

The final failure pattern of the simulation (figure 5.52.d) corresponds well with the experimentally observed V-shaped crack pattern at failure as depicted in figure 5.53. The evolution of macrocracks in the simulation may be compared to the

experimental results of figure 3.10. Although multiaxial compressive testing of concrete cubes and prisms results in different final failure patterns, the essence of the process – a distinct shift from uniformly distributed deformations in the pre-peak region to highly localised deformations in the post-peak region – is clearly demonstrated in the simulation.

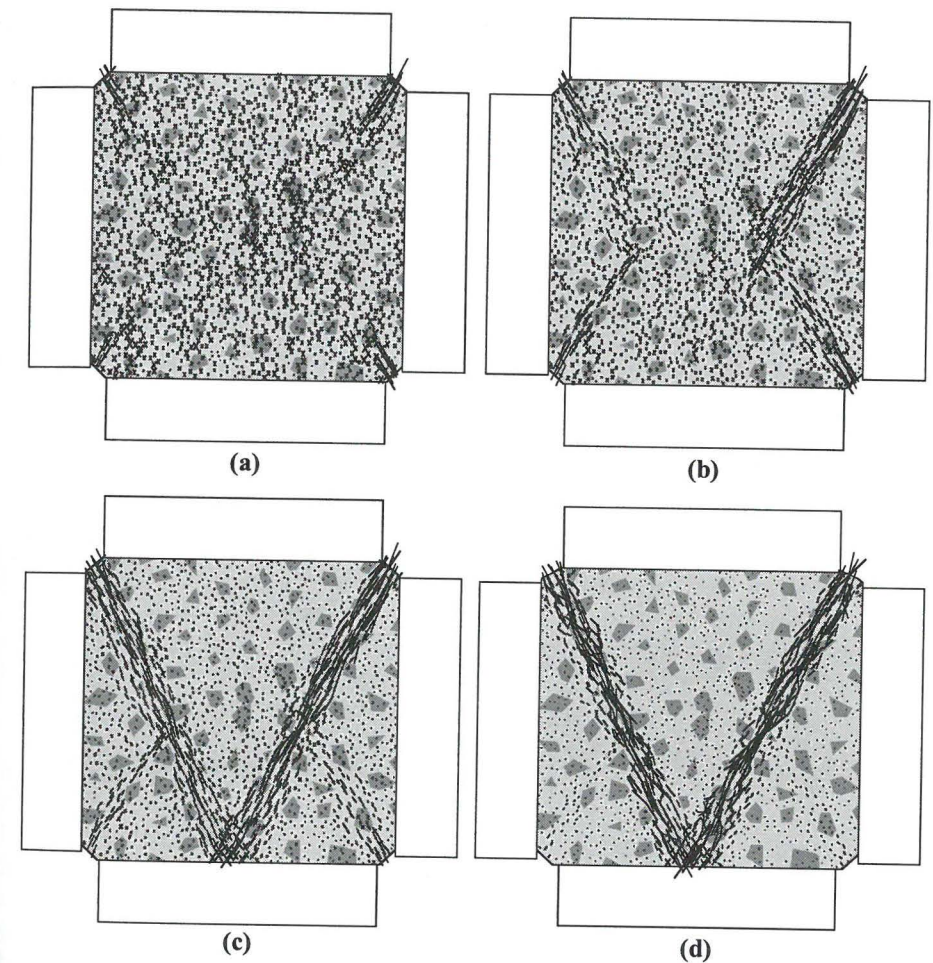


Figure 5.52. Evolution of macrocracks in simulation of multiaxial compressive test ( $\beta = 0.10$ )



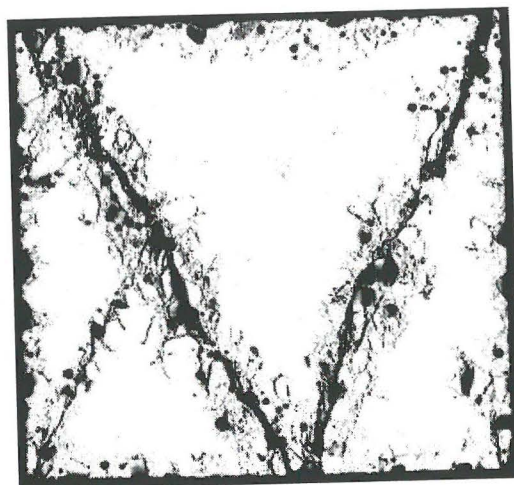


Figure 5.53. Ultraviolet photograph of the failure pattern of a 100 mm cube loaded in multiaxial plane strain compression ( $\beta = 0.10$ ) [Van Geel<sup>1998</sup>]

Figure 5.54 shows the failure patterns (at the end of the simulations) for all loading configurations ( $\beta=0; 0.05; 0.10; 0.15$ ). It shows that all simulations of the multiaxial compression tests show the same V-shaped crack pattern at failure. This is in correspondence with the experiments.

With respect to the simulation of the uniaxial compression test ( $\beta=0$ ), some remarks have to be made. First of all, the length of the lines at the centre of the finite elements – in figure 5.54.a – do not correspond with the magnitude of the crack sliding displacement, but with the internal state parameter  $\kappa_1$ , which incorporates both crack sliding and crack opening displacements (equation (5.34)). This distinction is made in order to visualise not only mode II cracking, but also potential mode I cracking (tensile splitting), which is reported frequently to affect the crack pattern at failure in uniaxial compression.

With the visualisation of the internal state parameter  $\kappa_1$ , figure 5.54.a shows that tensile splitting cracks are indeed present in the simulation. However, tensile splitting in the simulation is less abundant than observed in the uniaxial compression tests of Van Geel. In fact, this observation supports the model assumption that the stress path of uniaxial compression is highly critical with respect to lateral stresses (compressive or tensile). In section 2.1.2.1, it is already stated that much controversy exist about the degree of mode I (axial splitting) and mode II (inclined shear) cracking in uniaxial compression tests. Apparently, some lateral compression (or tension) is easily introduced at the specimen-loading platen interface. Although the frictional restraint of the interface used in the experiments of van Geel (teflon sheet with some grease added) is accounted for in the simulations by assigning a low frictional restraint ( $\tan\phi = 0.012$ ) to this interface, this is only a rough estimate of the actual behaviour of the interface.

Another explanation for the observed differences in the degree of tensile splitting may originate from the 2D nature of the numerical model. Unlike the 2D nature of the V-shaped failure pattern observed in multiaxial plane-strain compression tests, the nature of the failure pattern in uniaxial compression is highly 3D. This aspect is not taken into account by the 2D model simulations. Due to this 3D-effect, interfering mode II cracks are more likely to produce additional mode I cracking.

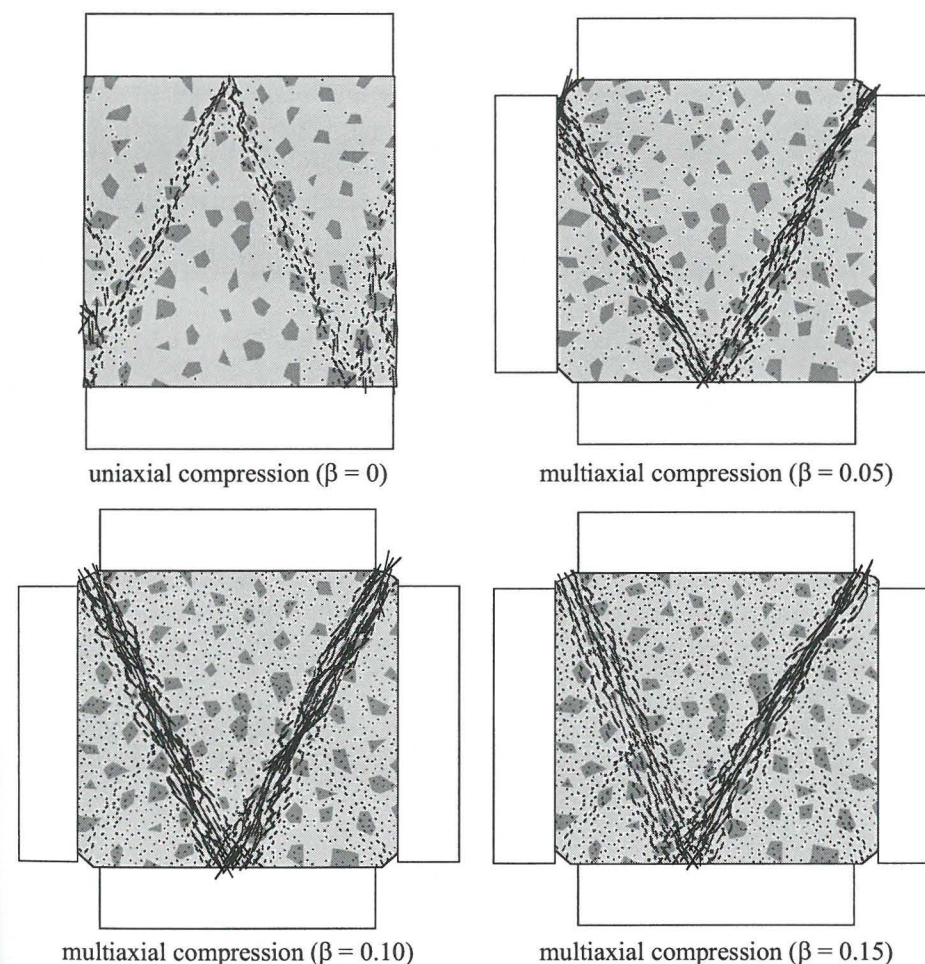


Figure 5.54. Failure patterns at the end of the simulations.

To illustrate the model's ability to simulate concrete structural behaviour in a wide range of loading configurations, also a uniaxial tensile test is simulated. The test set-up (figure 5.55) is taken from the test set-up as used by Van Geel<sup>1998</sup>. A notch of 5 mm width is sawn at middle height of a 100 mm concrete cube. The remaining cross-section at the notch is  $57 \times 57 \text{ mm}^2$ .

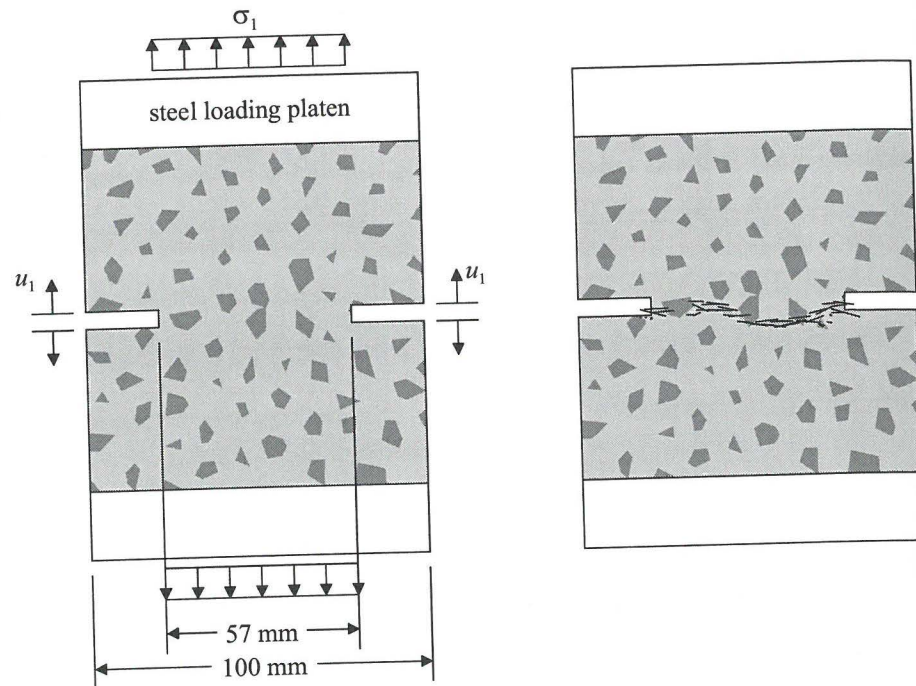


Figure 5.55. Uniaxial tensile test: test set-up and final failure pattern.

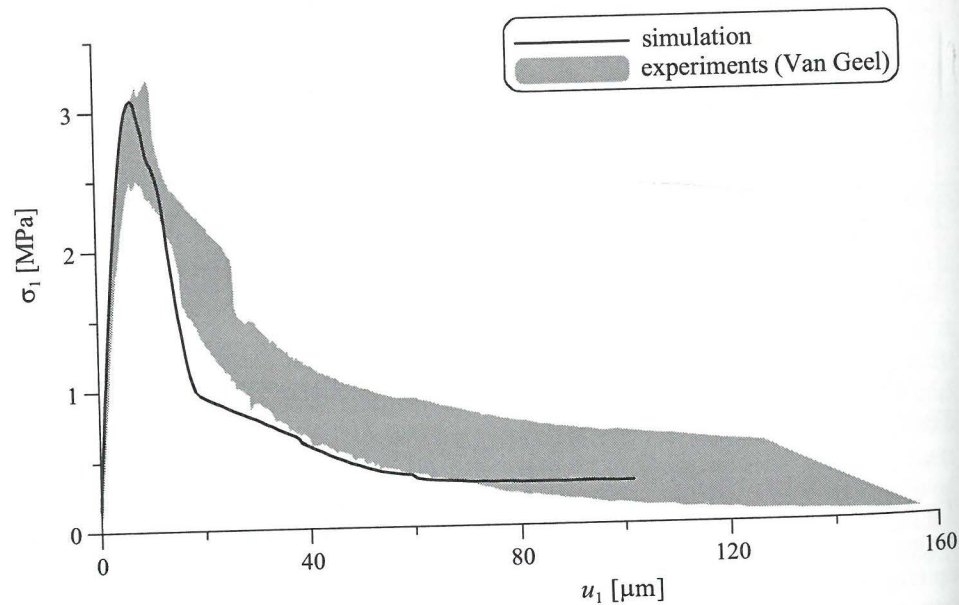


Figure 5.56. Uniaxial tensile test: Loading curve.

With  $\kappa_1$  visualised, figure 5.55 (right part) shows a typical mode I failure pattern. It is noticed that the width of the crack band in mode I is substantially smaller than in mode II. Apparently, adopting the rotating crack concept in mode I indeed (partly) remedies spurious stress locking when the finite elements are not aligned with the crack path (see section 5.5).

The shaded area in figure 5.56 denotes the range of the experimental test results of Van Geel<sup>1998</sup>. The loading curve obtained in the simulation shows acceptable agreement with these experiments. The result shows a slight underestimation of the ductility of the structural response. This also might be explained by the 2D nature of the numerical model. As pointed out by Lilliu & Van Mier<sup>2003</sup>, taking into account the true three-dimensional nature of cracking in model simulations substantially enhances the ductility of the structural response in mode I testing (section 2.2.2.1).

#### 5.7.4 Influence of loading path in stress space

At stage IV, the shape of the descending branch in the loading diagram (with the main loading axis) is highly dependent on the loading path in stress space. In section 3.2.4, it is outlined that the ductility of the softening branch increases when the direction of the loading path inclines towards a 90 degrees angle with the (schematic) stress-state bounding surface of ultimate strength. In this way, the model results in figure 5.57 correspond well with the experimental test results as indicated in figure 3.22.

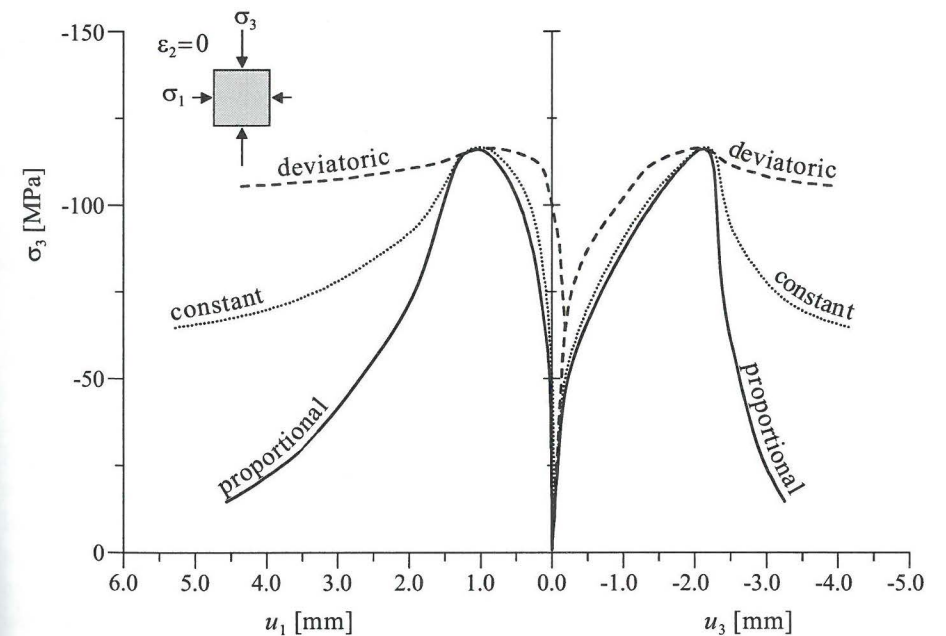


Figure 5.57. Influence of loading path: model simulations with proportional ( $\beta = 0.10$ ), constant and deviatoric loading paths.

Evidently, the combination of tensile, cohesive and frictional softening – as implemented in the model – captures properly the experimentally observed shift from the stress-state bounding surface of ultimate strength to the stress-state bounding surface of residual strength in multiaxial compression.

Another important issue regarding loading path dependency is its potential influence on ultimate strength. In section 3.2.3, figures 3.17 and 3.18 illustrate such loading path dependency observed in the experiments of Van Geel. Comparison between the simulations (figures 5.58 and 5.59) and the experiments of Van Geel demonstrates that in the experiments as well as in the simulations a strong path-dependency is observed. In both cases, the *uniaxial* compressive strength *decreases* upon high preloading with high confinement<sup>12</sup> (figures 3.17 and 5.58), while the *multiaxial* compressive strength *increases* upon similar pre-loadings. Evidently, weakening due to accumulated damage at the ITZ at stage II is dominant in the *uniaxial* compressive loading regime, while strengthening due to pore collapse (compaction) is dominant in the *multiaxial* compressive loading regime. In addition, note that not only the loading path dependency on the ultimate strength is simulated well, but also the reduction of stiffness in the uniaxial compression tests and the reduction of ductility in the multiaxial compression tests upon high compressive pre-loading.

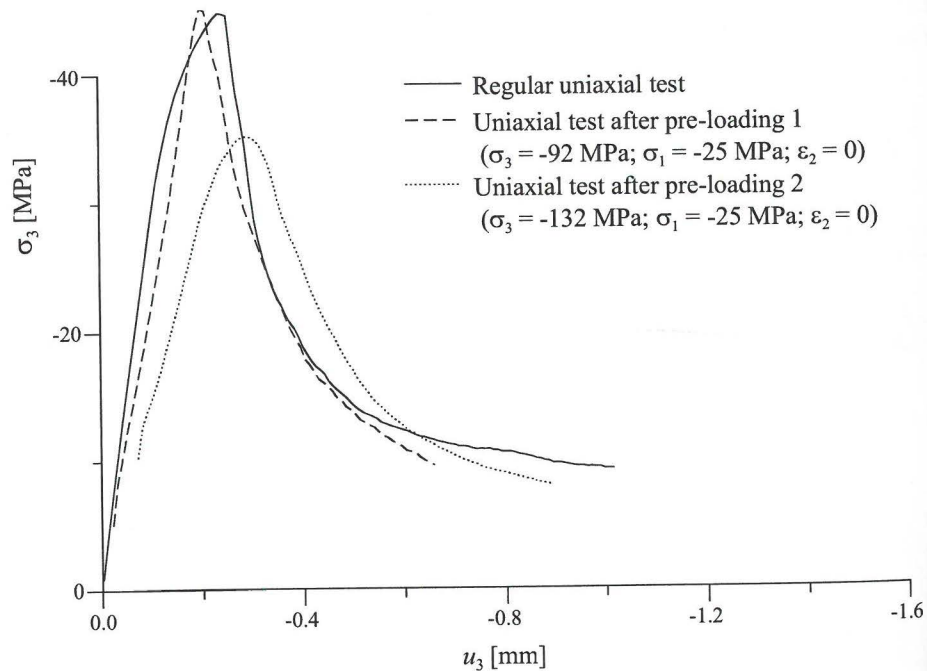


Figure 5.58. Simulations of uniaxial compressive tests with multiaxial pre-loading.

<sup>12</sup> Due to the 2D-formulation of the model, the multiaxial compressive pre-loadings of the uniaxial compression test simulations are slightly different from the experiments.

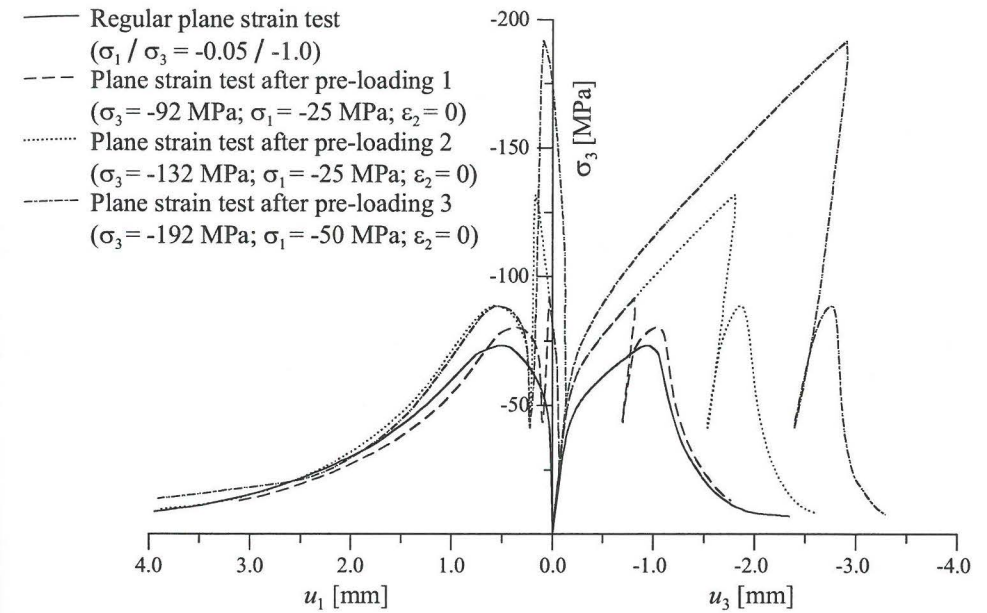


Figure 5.59. Simulations of proportional tests ( $\beta = 0.05$ ) with multiaxial pre-loading.

In addition to the loading path dependency tests above (with *multiaxial* compressive pre-loading), Van Geel<sup>1998</sup> also carried out some multiaxial compressive experiments with *uniaxial* compressive pre-loading. Results of these experiments are illustrated in figure 5.60. Two different uniaxial compressive pre-loadings are applied; pre-loading 1 ends right after peak stress, while pre-loading 2 extends considerably into the post-peak regime. It shows that the multiaxial plane strain compression test with  $\beta = 0.05$  is hardly affected by uniaxial compressive pre-loading 1, while the ultimate strength of the multiaxial plane strain compression test with  $\beta = 0.15$  reduces only slightly when uniaxial compressive pre-loading 2 is applied. Evidently, accumulating (macroscopic) damage inflicted in the post-peak regime of a uniaxial compression test has no significant influence on the ultimate strength in a multiaxial plane strain compression test.

Figure 5.61 shows the loading curves obtained in the model simulations of the same multiaxial compressive test series with and without uniaxial compressive pre-loadings similar to those applied by Van Geel. The model simulations show the same tendency as the experiments; the simulation with  $\beta = 0.05$  is hardly affected by uniaxial compressive pre-loading 1, while the ultimate strength of the simulation with  $\beta = 0.15$  reduces only slightly when uniaxial compressive pre-loading 2 is applied.

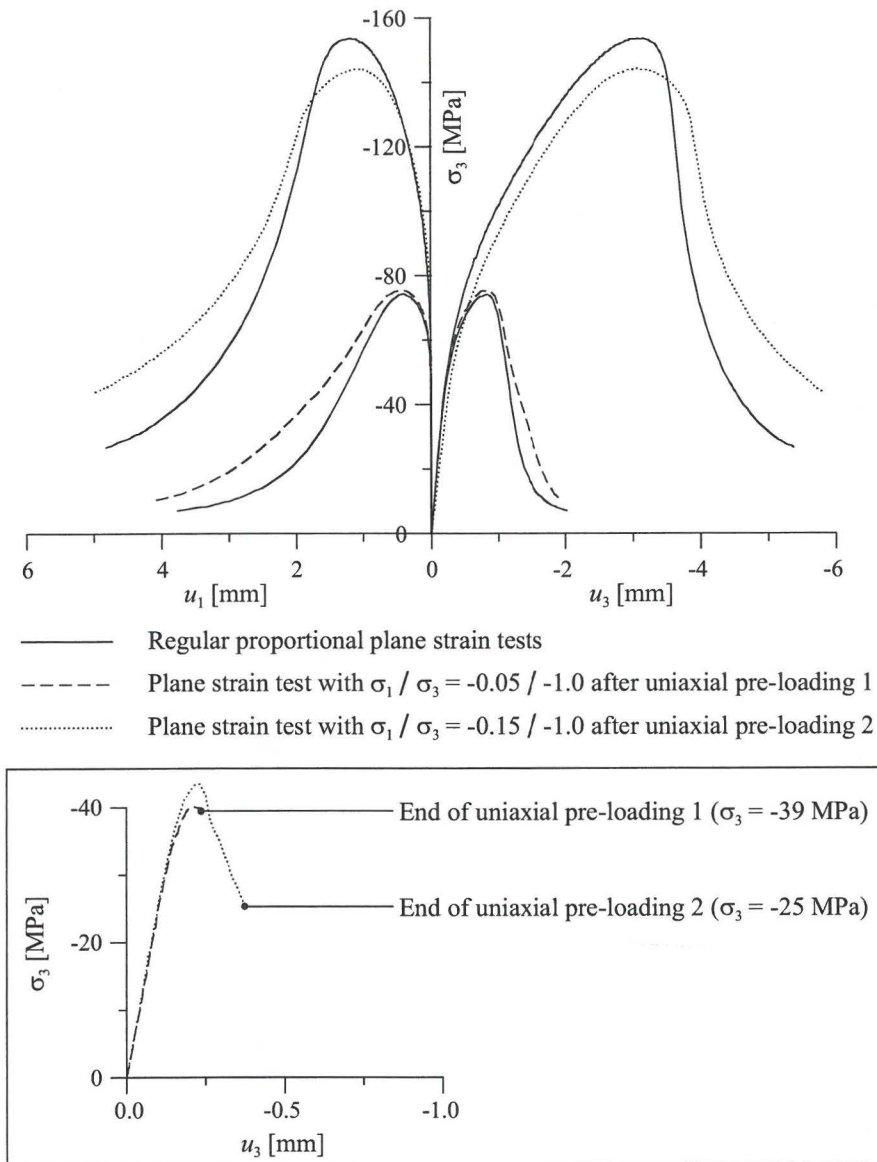


Figure 5.60. Plane strain tests after uniaxial compressive pre-loading [Van Geel<sup>1998</sup>].

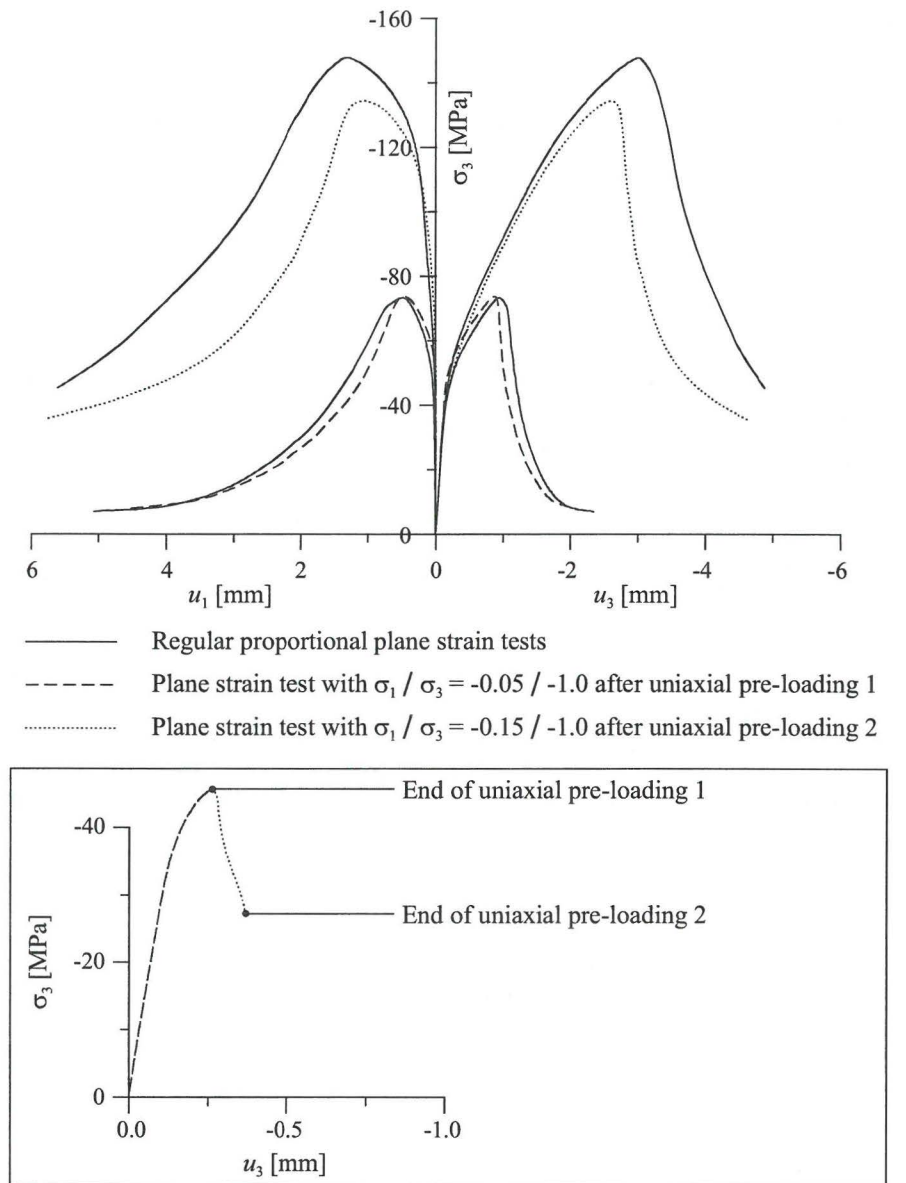


Figure 5.61. Simulations of plane strain tests with uniaxial compressive pre-loading.

**5.7.5 Influence of boundary conditions**

In section 1.1, a distinction has been made between ‘continuum’ material behaviour – specifying the concrete behaviour at the loading stage *before* reaching the ultimate load-bearing capacity – and *structural behaviour*, which specifies best the concrete

behaviour at the loading stage *after* reaching the ultimate load-bearing capacity. After initiation of the macroscopic cracks at stage III, the concrete specimen can no longer be regarded as a continuum. Instead, the specimen becomes a structure consisting of uncracked elements divided by local fracture planes. The observed behaviour of such a structure during testing is a structural response rather than a material characteristic. The load application system (boundary conditions) is in fact part of this structure and the observed structural response at stage III and IV will be influenced by these boundary conditions.

In this respect, it is generally known that frictional stresses between loading platens and specimen boundaries seriously affect the structural response of a concrete cube loaded in uniaxial compression. Dry steel loading platens, as used in standard uniaxial compression tests, introduce large frictional stresses at the specimen boundaries. These large frictional stresses prevent the specimen to deform laterally and consequently result in a considerable increase of ultimate strength and ductility. Figure 5.62 shows model simulations of uniaxial compression tests with loading platens of different frictional restraint. The frictional restraint of the (polished) dry steel loading platens is – in the simulations – accounted for by assigning a rather high frictional restraint ( $\tan\phi = 0.13$  [Vonk<sup>1992</sup>]) to the interface elements between the loading platens and the specimen.

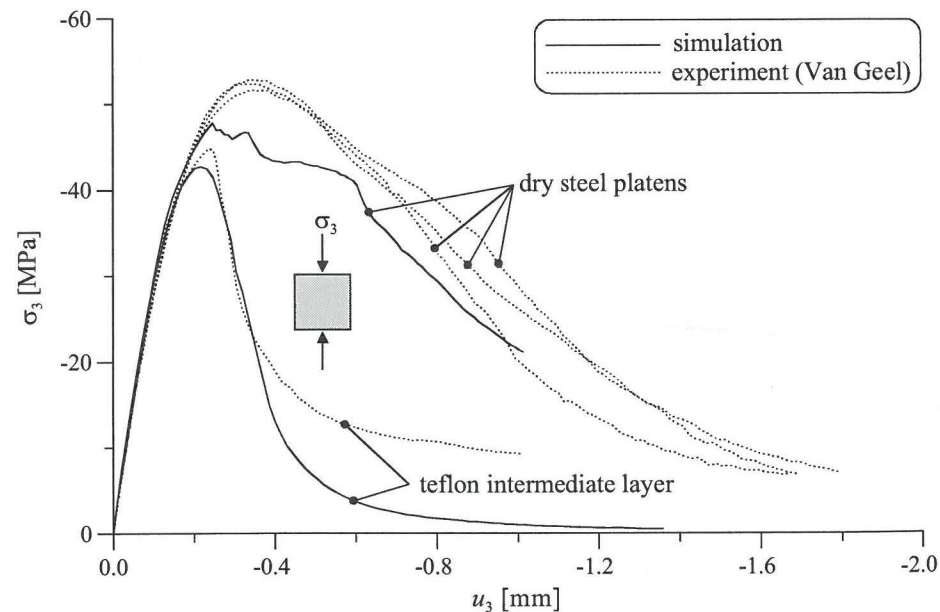


Figure 5.62. Influence of boundary friction on the loading curve of concrete loaded in uniaxial compression.

The results in figure 5.62 demonstrate that the model simulations show the same tendency as the experiments of Van Geel; ultimate strength and ductility increase

substantially with increasing frictional boundary restraint. Although the simulations match the experiments quite well, the raise in ultimate strength in the simulations with dry steel loading platens is lower than in the experiments. This might be due to the assignment of a constant friction angle to the interface between the dry steel loading platen and the specimen. The value of  $\tan\phi = 0.13$  is taken from friction measurements performed by Vonk<sup>1992</sup> after 1.5 mm of sliding between the loading platen and the concrete specimen. In this work, it was also recognised that the friction angle at initial sliding tends to exceed the value of 0.13 substantially, which – if incorporated in the simulation – certainly would have affected the ultimate strength.

In the experimental research, Van Geel<sup>1998</sup> also investigated the influence of the geometrical layout of the loading platens. It was observed that in multiaxial compressive experiments, with standard layout of the loading platens as illustrated in figure 5.50, macroscopic cracks initiate consistently at the specimen corners (see figure 3.10). With cubic specimens such onset of macroscopic cracking ends in a typical V-shaped failure mode as illustrated in figure 5.53.

Two reasons might be appointed to explain the consistent onset of macroscopic cracks at the specimen corners. First of all, stresses may concentrate at the corner of the specimen – being a geometrical singularity – at stage I / II, which could create a local stress state more susceptible to the initiation of a macroscopic crack. The second reason relates to the geometrical layout of the loading platens. To avoid contact between the loading platens and the transfer of forces via these platens instead of via the concrete specimen, the loading platens are smaller than the cross-sectional area of the specimen. This implies that everywhere along the boundary of the specimen local displacement jumps perpendicular to the boundary are prevented by the steel loading platens *except* at the specimen corners. Ergo, the corners of the specimen are the only locations at the specimen boundary where mode II cracking is not obstructed by the steel loading platens.

From proportional multiaxial plane strain compressive experiments ( $\beta = 0.15$ ) carried out with different geometrical layout of the loading platens (figure 5.63; right part), the second reason proves to be most important. Macroscopic cracks initiate consistently at those locations where mode II crack displacements are not obstructed by the steel loading platens.

As illustrated in figure 5.63 (left part), the influence of the geometrical layout of the loading platens is confirmed by the model simulations<sup>13</sup>. Nevertheless, some striking differences are found with respect to the degree of localisation (configuration (b) and the left branch of the V-shaped crack in configuration (a)) and the inclination of the mode II cracks (configuration (c)). These differences, which manifest themselves also in the loading curves (figure 5.64), most probably originate from the limitations of the smeared cracking method adopted to regularize localisation of deformations in combination with a randomised finite element mesh, as explained in section 5.5.

<sup>13</sup> To prevent (partly) blocking of the development of a mode II localisation zone, the gap between the loading platens is enlarged in all model simulations (see also section 5.7.1)

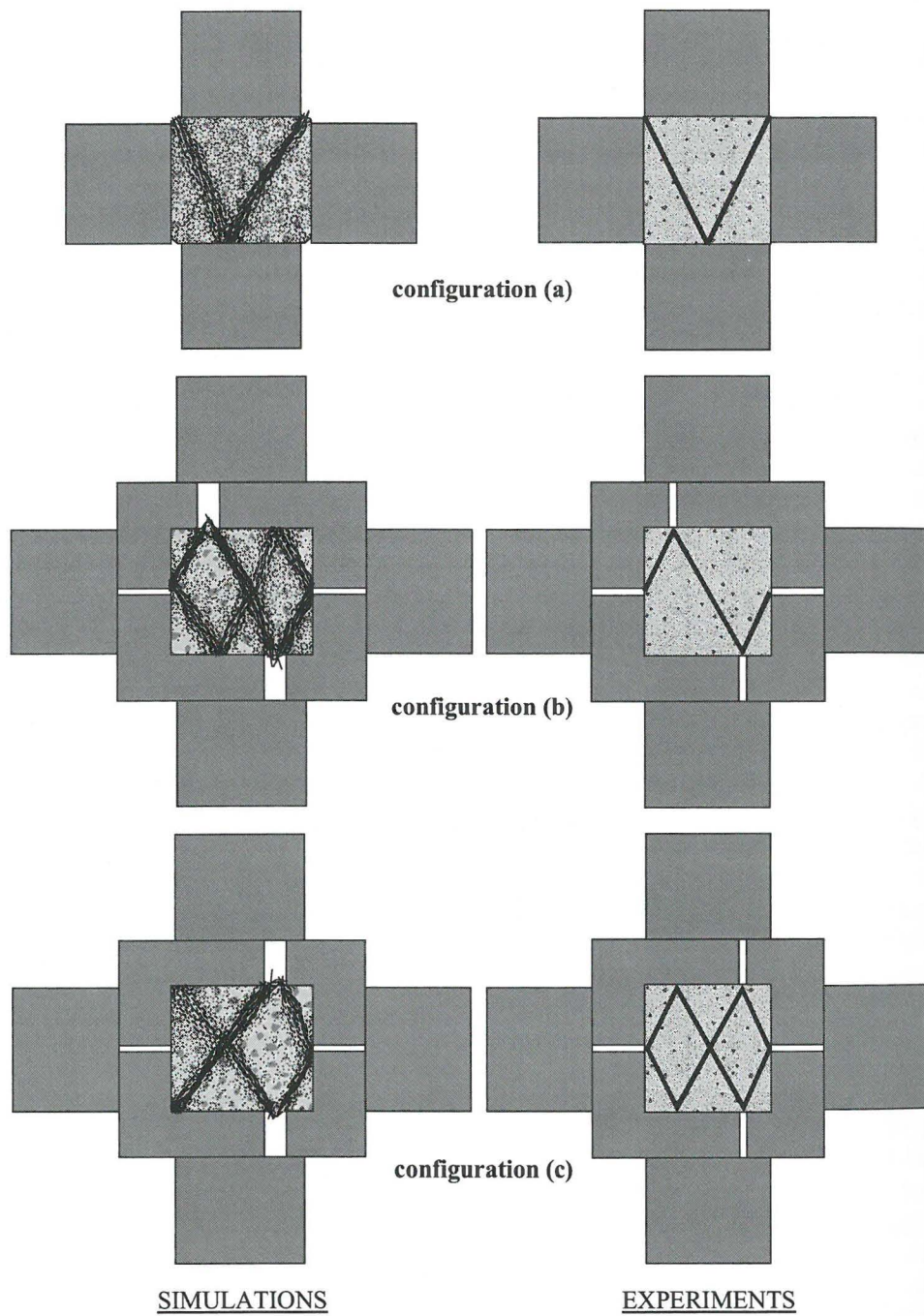


Figure 5.63. Failure patterns in simulations and experiments [Van Geel<sup>1998</sup>] with different configurations of loading platens.

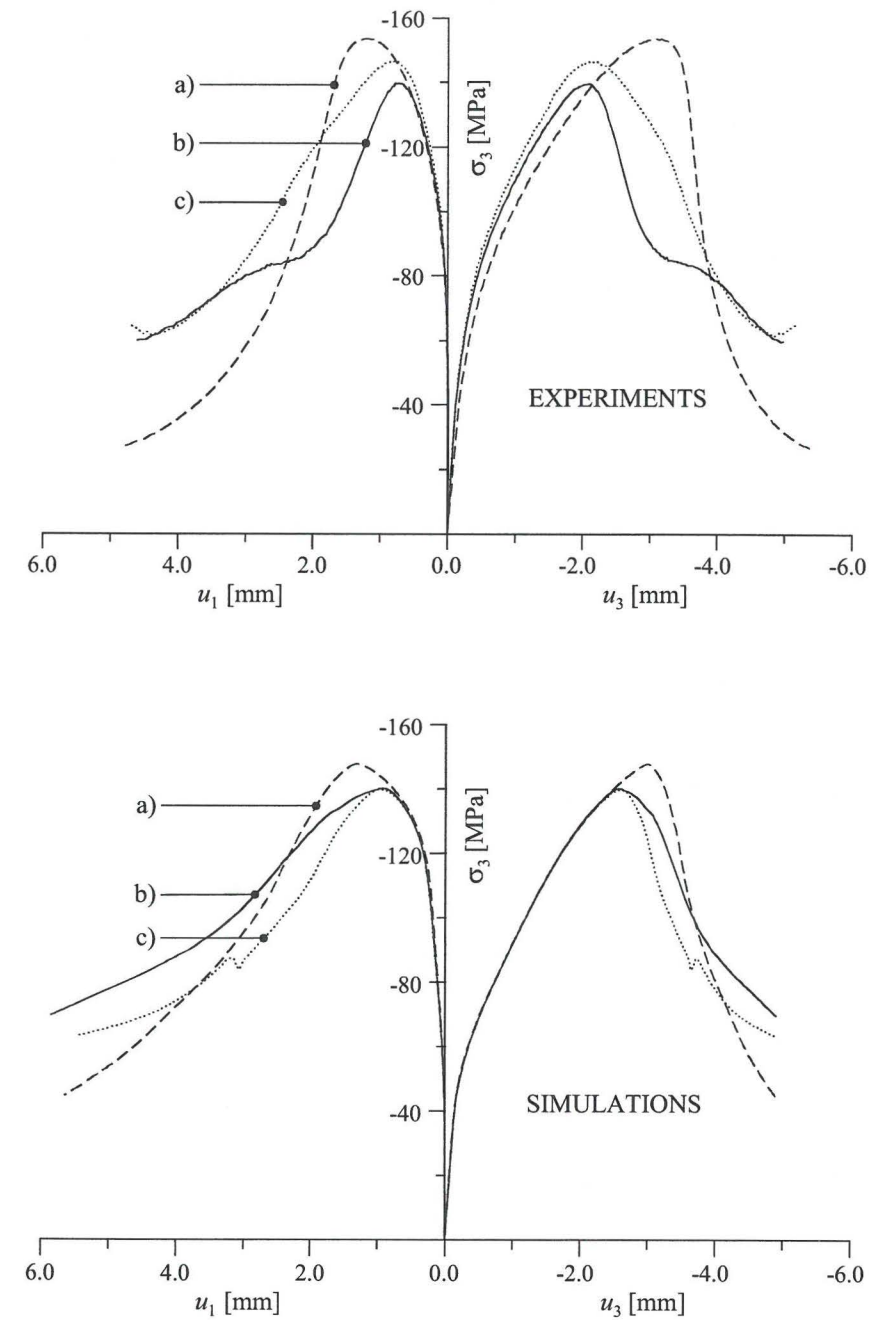


Figure 5.64. Influence of different configurations of loading platens on the loading curve of concrete loaded proportionally ( $\beta = 0.15$ ) in multiaxial plane-strain compression.

5.7.6 Parameter study

To show the influence of the stage III/IV model parameters (listed in table 5.1), a parameter study is performed. The influence of variation of the model parameters is illustrated for three proportional plane strain tests with different levels of confinement, i.e. a uniaxial compression test ( $\beta = 0$ ) and two proportional multiaxial plane strain compression tests ( $\beta = 0.05$  and  $\beta = 0.15$ ). The test set-up of these simulations is shown in figure 5.50.

In this parameter study, only the model parameters for mode II cracking are considered (figures 5.65 through 5.69). For the model parameters of mode I cracking ( $f_{t,bulk}$  and  $\kappa_{1,max}$ ) the results of the uniaxial tensile test as displayed in figures 5.55 and 5.56 are largely determinative. The parameter  $\phi_{cp}$  is not included in the parameter study because this value is – by definition – equal to the friction angle of mesoscopic cracking along the ITZ at stage II (equation (5.1)).

In section 5.3.3, the parameter  $c_{ini}$  has been introduced, which sets the relative distance between the linear part of the stress-state bounding surfaces for initiation of a straight crack through cement paste only and a straight crack crossing interlocking aggregate grains. This relative distance depends on the irregularity of the crack, which has been assumed to be the same for ordinary types of concrete mixes. According to equation (5.4), a fixed value has been assigned to  $c_{ini}$ . The influence of this model assumption is also studied in this section (figure 5.65).

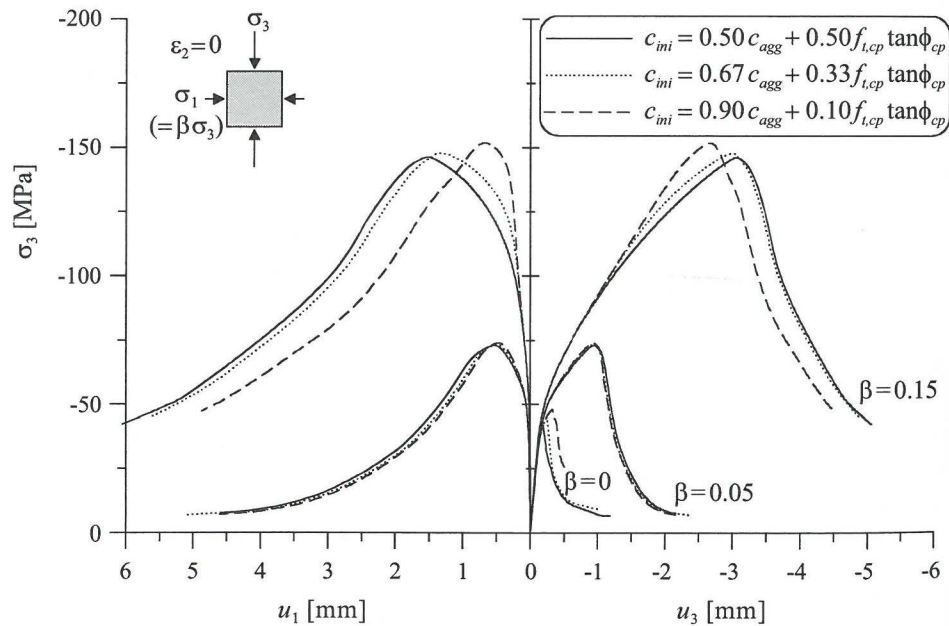


Figure 5.65. Variation of  $c_{ini}$ .

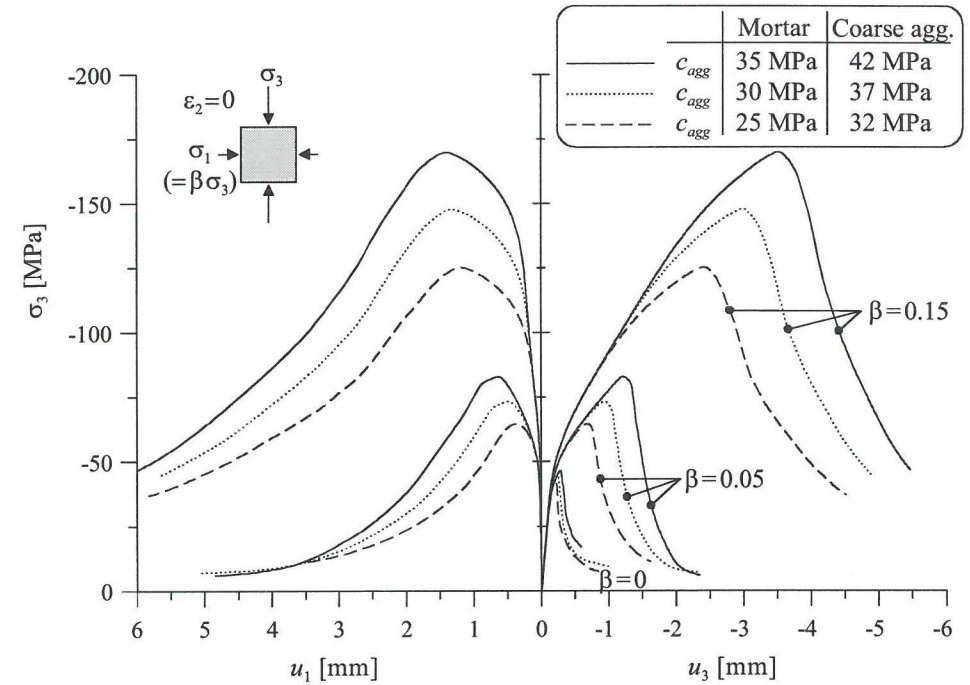


Figure 5.66. Variation of  $c_{agg}$ .

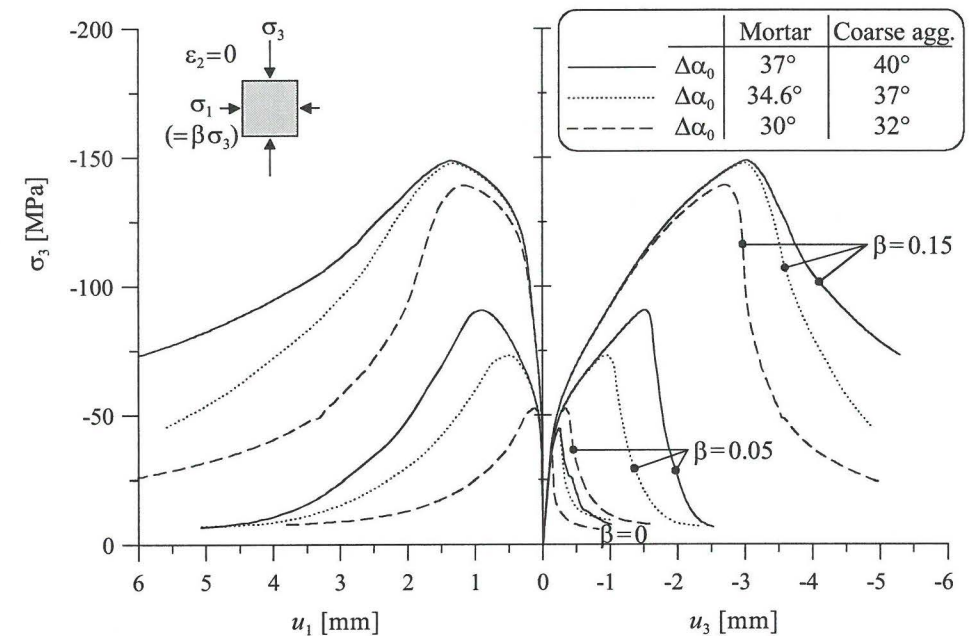
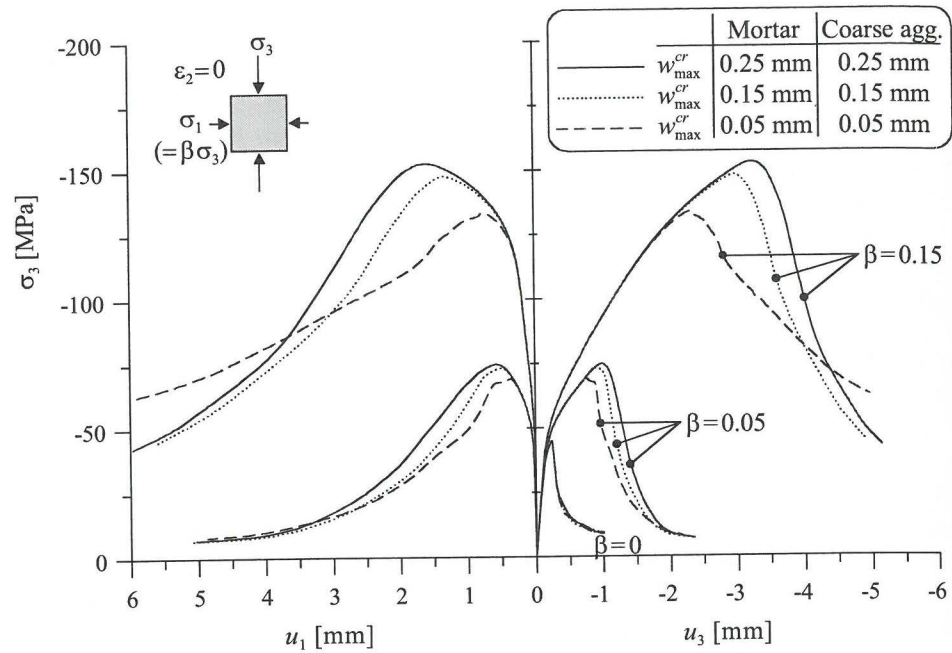
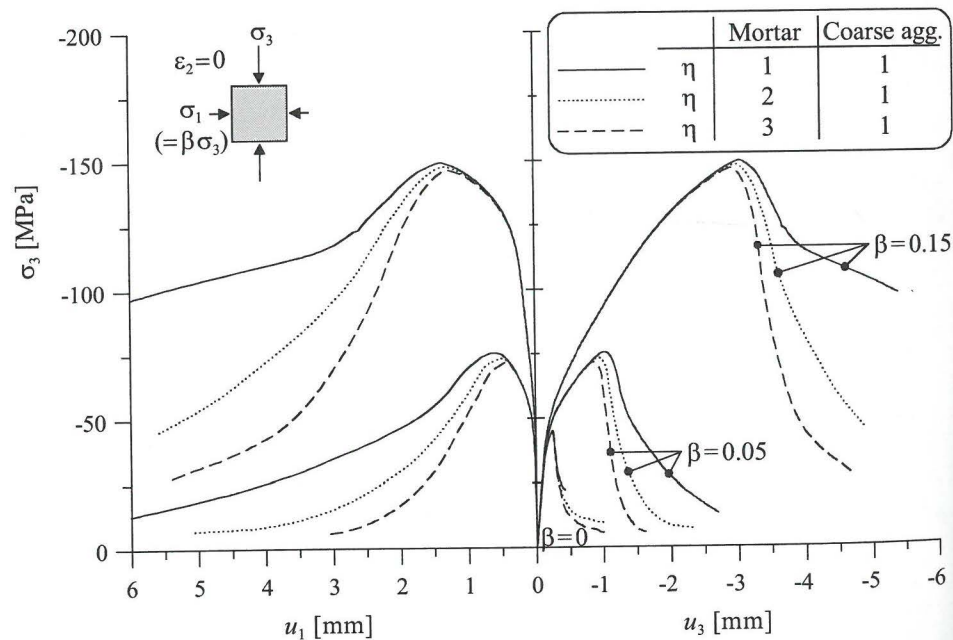


Figure 5.67. Variation of  $\Delta\alpha_0$ .

Figure 5.68. Variation of  $w_{\max}^{cr}$ .Figure 5.69. Variation of  $\eta$ .

The results in figure 5.65 confirm the assumption in section 5.3.3 that the macroscopic mechanical behaviour is only moderately influenced upon variation of the (implicit) model parameter  $c_{ini}$ . A noticeable effect at stage III is only observed for multiaxial compressive testing with high confinement ( $\beta = 0.15$ ) when  $c_{ini}$  approaches  $c_{agg}$ .

The model parameters  $c_{agg}$  and  $\Delta\alpha_0$  both determine the shape of the overall stress-state bounding surface of ultimate strength in the multiaxial compressive regime in stress space. This bounding surface is – in the low compressive regime – mainly determined by the value of  $\Delta\alpha_0$ , while the linear part in the high compressive region is solely determined by  $c_{agg}$ . This is reflected in the loading curves of the simulations displayed in figures 5.66 and 5.67; the ultimate strength of the multiaxial compressive test with high confinement ( $\beta = 0.15$ ) is mainly influenced by variation of  $c_{agg}$ , while the ultimate strength in uniaxial compression and multiaxial compression with low confinement ( $\beta = 0.05$ ) is more influenced by variation of  $\Delta\alpha_0$ .

Figures 5.68 and 5.69 show the influence of the softening parameters  $w_{\max}^{cr}$  and  $\eta$  on the loading curves. While  $\eta$  clearly determines the slope of the softening curve (stage IV) of the multiaxial compression tests, the brittleness induced by a low value of  $w_{\max}^{cr}$  is apparently so high that it reduces the ultimate strength rather than the slope of the softening curve. Because the relative amount of macro cracking according to elementary mechanism 2 (aggregate fracture and/or cement paste crushing; see section 5.4.5.2) increases with increasing confinement, this influence of  $w_{\max}^{cr}$  appears best in the multiaxial compression test with  $\beta = 0.15$ .

Even though the brittleness induced by a low value of  $w_{\max}^{cr}$  reduces the ultimate strength, the (negative) slope of the softening branch of the loading curve does not increase. This seeming contradiction can be explained by the model theory outlined in section 5.4.5.2. In multiaxial compression tests with high confinement, the relative amount of macro cracking according to elementary mechanism 2 (aggregate fracture and/or cement paste crushing) is quite large *at the initiation of macro cracking*. However, *during further crack sliding* overriding along a curved crack (elementary mechanism 1) becomes more and more important because the roughness of the crack  $\Delta\alpha(w^{cr})$  decreases while the *reduced deviation angle*  $\Delta\alpha_{\psi}$  hardly changes in a proportional test (equation (5.36)). Ergo, a low value of  $w_{\max}^{cr}$  causes the roughness of the crack  $\Delta\alpha(w^{cr})$  to decrease rapidly during stage III, while later on – at stage IV – the dominant crack sliding mechanism changes to the (more ductile) elementary mechanism 1 (overriding along a curved crack).

Unlike the softening branches of the loading curves of the multiaxial compression tests, the slope of the softening curve in uniaxial compression is hardly affected by either  $w_{\max}^{cr}$  or  $\eta$ . This is not surprisingly, since – after tensile softening – the maximum slope of the overall stress-state bounding surface at the origin of stress space is limited to the stress-path of uniaxial compression (equations (5.3) and (5.27)). Unlike concrete in multiaxial compression, the softening curve of concrete



in uniaxial compression is much more influenced by its tensile softening properties (see figures 5.31 and 5.37.b).

### 5.7.7 Discussion of results

The results of the model simulations show a great applicability of the model in 3D stress space. Good agreement with experimental results is demonstrated over the full range of uniaxial tension, uniaxial compression up to multiaxial compression with high lateral confining pressures. The correspondence with experimental results not only concerns the similarity of the loading curve of the main loading axis, but also essential features like lateral deformations, crack growth and crack patterns at failure. Variations in boundary conditions (section 5.7.5) and in (pre- and post-peak) loading paths in stress space (section 5.7.4) – both in the model simulations and the experiments – also have similar effects on the structural response of the concrete specimen.

Furthermore, the model is based on a clear physical theory by taking into account the structure of concrete at the macro, meso and micro scale level. In conformance with the statements in section 3.1.3, trends in mechanical behaviour of concrete loaded in multiaxial compression are identified and thoroughly analysed. In this sense, the model answers to the main objective of this thesis as formulated in section 1.1:

*“The numerical model developed aimed from the beginning at simulating the experimental test program as close as possible, but also at predicting the true mechanical response of an arbitrary 2D structure subjected to an arbitrary loading path. From this point of view, it is essential that convincing physical explanations – versus empirical formulations – should be found for the observed phenomena.”*

Although the overall performance of the model satisfies the objectives of this thesis, correspondence with the experiments may still be enhanced in some areas. In particular, the transition between stage II and stage III behaviour incorporates an interesting phenomenon. When the loading curves in the main loading direction at stage III of the various multiaxial compression tests are analysed, two contradictory tendencies are observed:

- The rounding of the loading curves of the model simulations of the proportional multiaxial compression tests ( $\beta = 0.05; 0.10; 0.15$ ) around peak stress is consistently *too sharp* compared to the experiments (figure 5.51).
- The rounding of the loading curves around peak stress of the proportional multiaxial compression tests ( $\beta = 0.05$ ) *after pre-loading* with high confinement is *not* too sharp compared to the experiments, rather the opposite (figures 3.18 & 5.59: pre-loadings 2 and 3).

According to the model theory in section 5.4.4, the rounding of the loading curve around peak stress is determined by the process of local stress redistribution along the (macro) crack during initial crack sliding. Actually, the rounding of the loading curve around peak stress is determined by the plastic deformations during this process of local stress redistribution. According to equation (5.29), these plastic deformations are determined only by the macroscopic (trial) stress state  $\underline{\sigma}^t$ . This

implies that – due to the increase of ultimate strength – the plastic deformations around peak stress in the model simulations of the proportional multiaxial compression test ( $\beta = 0.05$ ) *after pre-loading* with high confinement are even larger than in the ordinary proportional test with  $\beta = 0.05$ . This is in contradiction with the experimental observations.

This seeming contradiction ensues from the assumption of linear elastic behaviour of the continuum during local stress redistribution at stage III, i.e. potential pore collapse at the ITZ during local stress redistribution is not taken into account in the stage III/IV ( $RVE_2$ ) model computations. During local stress redistribution, the load concentrates at those regions where the local deviation angle of the crack is highest. These are exactly the regions where pore collapse takes place at stage II. This implies that when the load concentrates in these regions during stage III, substantial pore collapse will take place. However, as the model does not transfer this redistribution of local stresses to the  $RVE_1$  (only *global* unloading is considered as a result of plastic straining at stage III/IV), the occurrence of substantial pore collapse at stage III is not provided for by the model.

The above implies that the model *consistently* underestimates the plastic deformations at stage III. At least, when stage III behaviour is preceded by stage II behaviour. When stage III behaviour is preceded by stage I behaviour – as in the case of the proportional multiaxial compression tests ( $\beta = 0.05$ ) *after pre-loading* with high confinement – the local stress state at the compressed ITZs is not likely to violate the pore collapse cracking criterion. Due to the pre-loading with high confinement, the critical stress level for pore collapse is raised considerably and – consequently – the material behaviour of the continuum stays linear elastic, even after substantial concentration of loading.

## CHAPTER 6

### TOWARDS NUMERICAL MODELLING AT THE MACRO LEVEL

The mesoscopic model – as outlined in chapter 4 and 5 – is a useful tool for *small-scale* studies on structures subjected to multiaxial stress states, such as junctions of concrete members and introduction zones of concentrated loads (external loads, internal loads that may arise in anchorage zones of steel reinforcing bars, pre-tensioning wires/strands or post-tensioning tendons). For *large-scale* studies, the mesoscopic model is not practical. Successful application of the model in large-scale studies requires at least (1) a simplification of mesh generation and (2) the introduction of larger finite elements.

Basically, complex mesh generation and the restriction of small finite element sizes are a result of modelling the mesoscopic structure of concrete explicitly. In order to simplify mesh generation, explicit modelling of the coarse aggregate grains (section 4.4) may be omitted. In this way, only one homogeneous phase is generated with all aggregate grain fractions incorporated in the dimensions of the RVE<sub>1</sub>. This simplifies mesh generation considerably although the generation of a *randomised* mesh is still required because the softening properties of the concrete material are based on such randomness (section 5.5).

When the coarse aggregate grains are not modelled explicitly, the maximum size of the finite elements is no longer related to the size of the coarse aggregate grains. Consequently, the finite element size may be based on the *macroscopic* structure of concrete instead of its *mesoscopic* structure. Consistent with common practice, this enables the generation of rather coarse meshes with – where needed – local mesh refinement. Particular attention must be paid to those areas exhibiting (potential) macroscopic crack growth in mode II. The finite element size in such areas has to be in proportion to the size of the (potential) macrocracks so as to enable the formation of crack bands through multiple finite elements in a randomised mesh<sup>1</sup>.

#### 6.1 Implicit modelling of the coarse aggregate grains

Without explicit modelling of the coarse aggregate grains, the RVE<sub>1</sub> and RVE<sub>2</sub> approaches are still applicable. To allow for similar material behaviour as in the mesoscopic layout, two aspects have to be considered carefully:

---

<sup>1</sup> By adopting the *smearred crack approach*, the constitutive model is based on crack *displacements* (or fracture energy) instead of crack *strains*. Consequently, the softening branch of the loading curve is not influenced substantially by the size of the finite elements within the crack band. Still, crack bands in mode II must extend over *multiple* finite elements in a randomised mesh because the (mode II) softening properties of the concrete material are based on such mesh configurations (section 5.5).

1. The coarse aggregate grains have to be incorporated in the dimensions of the RVE<sub>1</sub>.
2. Heterogeneity, introduced by explicit modelling of stronger and stiffer coarse aggregate grains, has to be accounted for in a different way.

### 6.1.1 Dimensions of the RVE<sub>1</sub>

In a macroscopic layout, also the coarse aggregate grains are modelled implicitly. Consequently, *all* aggregate grain fractions (table 4.2) are taken into account for the determination of the dimensions of the RVE<sub>1</sub>. This results in the following average diameter of the aggregate grains.

$$\bar{D}_{agg} = \frac{1098 \cdot 6.5 + 1245 \cdot 4 + 814 \cdot 2.5 + 3643 \cdot 1}{6800} = 2.62 \text{ mm.}$$

With the ITZs occupying 40 % of the total volume of cement paste (see section 3.1.1), the ITZs occupy 1280 mm<sup>2</sup> and the bulk cement paste occupies 1920 mm<sup>2</sup> of the total cross sectional area of cement paste (10000 – 6800 = 3200 mm<sup>2</sup>). The RVE<sub>1</sub>-dimensions are determined by the cross sectional areas of the separate components

$$\begin{aligned} \frac{R_2^2 - R_1^2}{R_1^2} = \frac{A_{ITZ}}{A_{agg}} = \frac{1280}{6800} & \rightarrow R_1 = 1.310 \text{ mm.} \\ \frac{R_3^2 - R_2^2}{R_1^2} = \frac{A_{bulk}}{A_{agg}} = \frac{1920}{6800} & \rightarrow R_2 = 1.428 \text{ mm.} \\ & R_3 = 1.589 \text{ mm.} \end{aligned}$$

### 6.1.2 Alternative way of introducing heterogeneity

The mesoscopic model, as described in chapter 4 and 5, takes into account the effects of the heterogeneous mesostructure of concrete in two ways:

- *Implicitly*: The geometry of the RVE<sub>1</sub> is derived from the heterogeneous mesostructure of concrete; the crack initiation criterion for meso-/macro-cracking (section 5.3) is based on the heterogeneous mesostructure of concrete; a strengthening mechanism during initial crack sliding is introduced in the constitutive model (section 5.4.4), which is based on the mesoscopic geometry of a crack curving (irregularly) around interlocking aggregate grains; softening laws are introduced (section 5.4.5), which are also derived from basic crack mechanisms in the heterogeneous mesostructure of concrete.
- *Explicitly*: The coarse aggregate grains – with different stiffness and strength – are modelled explicitly in the finite element mesh.

Given the relatively small differences in stiffness and strength between the mortar phase (fine aggregate grains) and the coarse aggregate grains (tables 4.4 and 5.1), the extra mesoscopic heterogeneity induced by *explicit* modelling of the coarse

aggregate grains in the finite element mesh seems of secondary importance compared with the *implicit* consideration of the heterogeneous mesostructure of concrete. Nevertheless, it is tried to approximate the performance of the mesoscopic model as close as possible in the macroscopic layout. Therefore, the extra heterogeneity of the mesoscopic model is accounted for by employing a stochastic approach instead, which still allows for varying material stiffness and strength throughout the concrete structure. By randomly distributing material stiffness and strength throughout the structure instead of explicitly modelling coarse aggregate grains, (random) mesh generation is simplified considerably.

As outlined in section 2.2.1.2, stochastic modelling requires the size of the (finite) mesh elements to be sufficiently small with respect to the size of the structure to be analysed, so that the probabilistic analysis performed on the scale of the mesh elements is still representative of the true heterogeneous mesostructure of the concrete. In the present context, this is not a serious drawback, as mesh refinement is required anyway to allow mode II crack bands at stage III and IV to extend over multiple finite elements.

To allow for varying material stiffness and strength throughout the concrete structure, three material properties are selected for stochastic modelling:

- The radius of the aggregate grains  $R_1$ : in this way, material *stiffness* is varied throughout the structure.
- The maximum deviation angle  $\Delta\alpha_0$ : in this way, material *strength* in the *low compressive* region is varied throughout the structure.
- The cohesive strength  $c_{agg}$ : in this way, material *strength* in the *high compressive* region is varied throughout the structure.

Variation of material stiffness may be realized either by variation of the RVE<sub>1</sub> dimensions ( $R_1, R_2, R_3$ ) or by variation of the Young's moduli of the separate phases ( $E_{agg}, E_{ITZ}, E_{bulk}$ ). Given the wide range in diameter of the aggregate grains in the concrete mix, variation of the RVE<sub>1</sub> dimensions seems the most natural approach. Although it seems logical to vary the diameter of the aggregate grains according to the true grain distribution of a representative cross section of the concrete cubes as given in table 4.2, this would have *no* effect on the effective stiffness of the RVE<sub>1</sub> when the *ratios*  $R_2/R_1$  and  $R_3/R_1$  are kept constant. In fact, *only* the ratios of the radii determine the effective stiffness, the absolute value of the aggregate grain diameter is no part in this at all. Such a variation of the ratios  $R_2/R_1$  and  $R_3/R_1$ , can simply be realised by varying the radius of the aggregate grain  $R_1$  and keeping the thickness of the ITZ-layer  $R_2 - R_1$  and the thickness of the bulk cement paste layer  $R_3 - R_2$  constant. It is emphasised that in this sense, *no* evident correlation exists between the true grain distribution and the variation of  $R_1$ .

In the mesoscopic layout, the mode I cracking parameters in table 5.1 are the same for both the coarse and the fine aggregate grains (mortar). Mode I strength variation manifests itself here in the differences in RVE<sub>1</sub> dimensions between the coarse and fine aggregate grains. According to equation (5.7) in section 5.3.5, the dimensions of the RVE<sub>1</sub> determine the length of the 'ITZ-part' of the mode I crack and with that

also the *global* mode I tensile strength. In the macroscopic layout, a similar effect is accomplished by the variation of the ratios  $R_2/R_1$  and  $R_3/R_1$  as outlined above.

With respect to mode II cracking, the material properties  $\Delta\alpha_0$ ,  $c_{agg}$  and  $\eta$  are varied in the mesoscopic layout. With respect to  $\Delta\alpha_0$  and  $c_{agg}$ , therefore a similar variation is adopted in the macroscopic layout. As illustrated in the figures 5.66 and 5.67, ultimate *strength* in both the *low compressive* region and the *high compressive* region is varied throughout the structure. Variation of  $\eta$  affects the strength along large macrocracks during crack sliding at stage IV. Such *local* redistribution of strength is not likely to affect substantially the *global* behaviour of the macrocrack. Therefore, stochastic variation of this parameter is not introduced in the macroscopic layout.

A normal distribution with mean value  $\mu$  and standard deviation  $\sigma$  is assigned to the stochastic material properties  $\Delta\alpha_0$  and  $c_{agg}$ . Having in mind that with the variation of  $R_1$  merely a variation of the ratios  $R_2/R_1$  and  $R_3/R_1$  is intended, also a normal distribution is assigned to  $R_1$ . A practical way, to generate random digits from such a normal distribution, is to use the random generator of a computer in combination with Monte Carlo Simulation [Kohlas<sup>1972</sup>]. Such a random generator generates a series of random digits  $x_{ij}$  from a uniform (or rectangular) distribution on the interval  $0 < x < 1$ . With this series of random digits  $x_{ij}$ , a series of random digits  $y_j$  is generated according to

$$y_j = \frac{\left( \sum_{i=1}^n x_{ij} \right) - \frac{1}{2}n}{\sqrt{\frac{n}{12}}} \quad j = 1, 2, \dots$$

With a sufficient number  $n$  of random digits  $x_{ij}$ , the generated series of random digits  $y_j$  will be normally distributed with mean value  $\mu = 0$  and standard deviation  $\sigma = 1$ . According to Kohlas<sup>1972</sup>, a number  $n \geq 10$  already produces a satisfactory approximation of the normal distribution. For computational convenience often a number  $n = 12$  is chosen, which results in

$$y_j = \left( \sum_{i=1}^{12} x_{ij} \right) - 6 \quad j = 1, 2, \dots$$

Finally, a series of random digits  $z_j$  from a normal distribution with mean value  $\mu$  and standard deviation  $\sigma$  is generated according to

$$z_j = \mu + \sigma y_j$$

## 6.2 Performance of the model

The test set-up for the test simulations in the macroscopic layout is equal to the test set-up of the mesoscopic model in figure 5.50 (with absence of the coarse aggregate grains) and is displayed in figure 6.1. In view of the small size of the specimen and the need to apply small finite elements to allow the formation of crack bands in the corners of the specimen (between the loading platens), the (randomised) finite element mesh is simply copied from the mesoscopic model.

Notwithstanding the fact that the potency of 'simplified mesh generation' and 'introduction of larger finite elements' is not expressed in this *small-scale* study, it must be emphasised that the omission of the coarse aggregate grains offers great opportunities in *large-scale* studies. Since the elaborate procedure of identifying groups of adjacent finite elements as 'coarse aggregate grains' has become redundant, also simple (standard) random mesh generators may be used, possibly in combination with standard mesh refinement techniques.

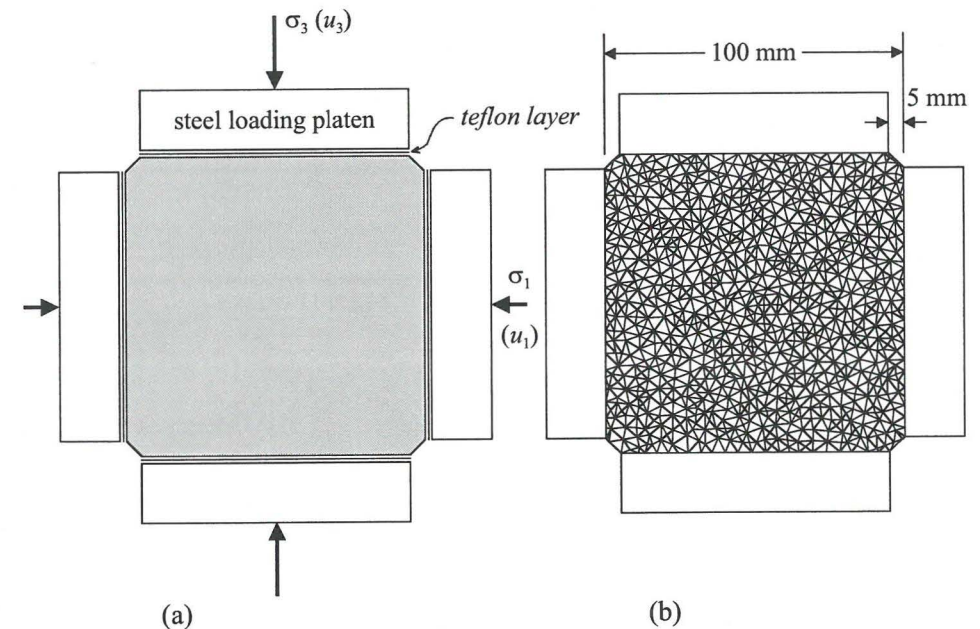


Figure 6.1. (a) Test set-up and (b) mesh of finite elements.

The material properties for the stage I/II and the stage III/IV constitutive model are listed in tables 6.1 and 6.2. Comparing the numerical values of the material properties in tables 6.1 and 6.2 with those in the mesoscopic layout (tables 4.4 and 5.1), only small differences are observed. Obviously, the material properties of the (overall) concrete in the macroscopic layout are a certain average between the

material properties of the mortar and the material properties of the coarse aggregate grains in the mesoscopic layout.

Table 6.1. Material properties (stage I/II constitutive model).

Distribution of outer boundary displacements of the RVE	
$\frac{1}{2}$ macro-stress + $\frac{1}{2}$ macro-strain	
RVE-dimensions [mm]	Elastic properties
$R_1 : \mu = 1.310$	$E_{agg} = 70000 \text{ MPa}$
$\sigma = 0.2 \mu$	$E_{ITZ} = 10000 \text{ MPa}$
$R_2 = R_1 + 0.118$	$E_{bulk} = 18000 \text{ MPa}$
$R_3 = R_2 + 0.161$	$\nu = 0.12$
Mode I/II cracking along the ITZ	Pore collapse in ITZ
$\phi = 25^\circ$	$\phi_{pc} = 0^\circ$
$f_{t,ini} = 4 \text{ MPa}$	$c_{pc,ini} = 15 \text{ MPa}$
$\kappa_{1,max} = 0.005 \text{ mm.}$	$c_{pc,end} = 40.5 \text{ MPa}$
	$\kappa_{2,max} = 30 \%$
	$\psi_{pc} = -60^\circ$

Table 6.2. Material properties (stage III/IV constitutive model).

Mode I cracking	Mode II cracking
$f_{t,bulk} = 8 \text{ MPa}$	$\phi_{cp} = 25^\circ$
$\kappa_{1,max} = 0.05 \text{ mm.}$	$\eta = 2$
	$w_{max}^{cr} = 0.15 \text{ mm.}$
	$\Delta\alpha_0 : \mu = 35.5^\circ$
	$\sigma = 0.05 \mu$
	$c_{agg} : \mu = 32 \text{ MPa}$
	$\sigma = 0.05 \mu$

In the macroscopic layout, only the proportional tests (see section 5.7.3) are simulated with the model. As the basics of the model in the macroscopic layout are similar to those of the mesoscopic model, it is assumed that this test series suffices to illustrate the performance of the model in the macroscopic layout.

### 6.2.1 Simulations of proportional tests

Figure 6.2 shows the results of the model simulations – in the macroscopic layout – of the test series performed by Van Geel<sup>1998</sup> with concrete cubes loaded proportionally in multiaxial plane-strain compression. Clearly, the correspondence with the experimental data of Van Geel is very similar to the results of the mesoscopic model (figure 5.51).

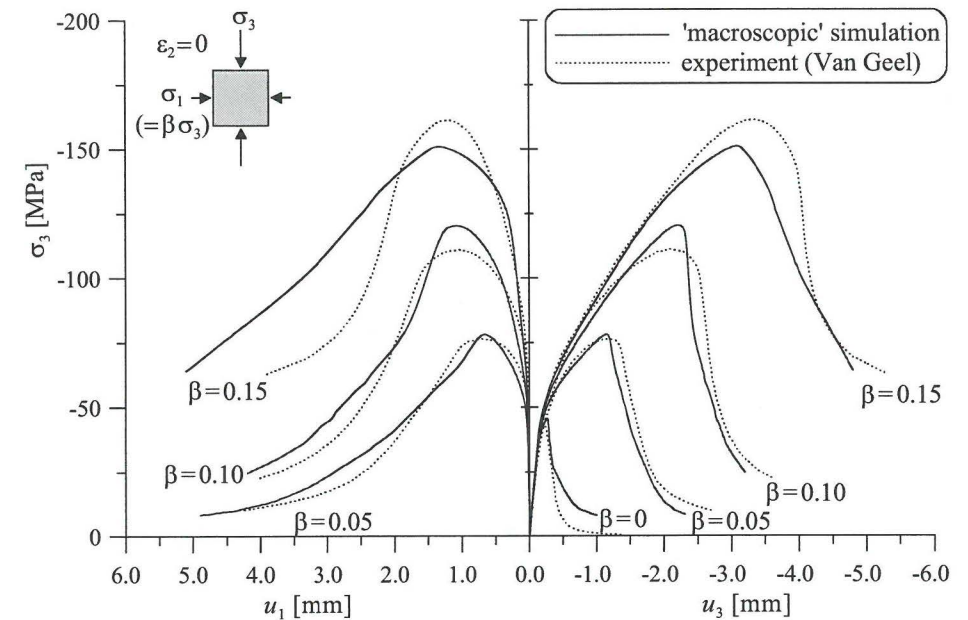


Figure 6.2. Model simulations of a test series of concrete loaded proportionally in multiaxial plane-strain compression.

Not only the loading curves, but also the final failure patterns of the model simulations in the macroscopic layout are very similar to the final failure patterns obtained with the mesoscopic model (figure 5.54) and in close agreement with the (V-shaped) crack patterns at failure observed in the experiments. Figure 6.3 shows the failure patterns (at the end of the simulations) for all loading configurations ( $\beta = 0; 0.05; 0.10; 0.15$ ) in the macroscopic layout. Figures 6.3 and 5.54 also show the apparent arbitrariness of the orientation of the V-shaped crack pattern (upright or upside down). While the orientation of the V-shaped crack pattern is upright in the simulations with the mesoscopic model (configurations  $\beta = 0.05$  and  $\beta = 0.10$  in figure 5.54), the orientation for the same loading configurations is reversed in the macroscopic layout.

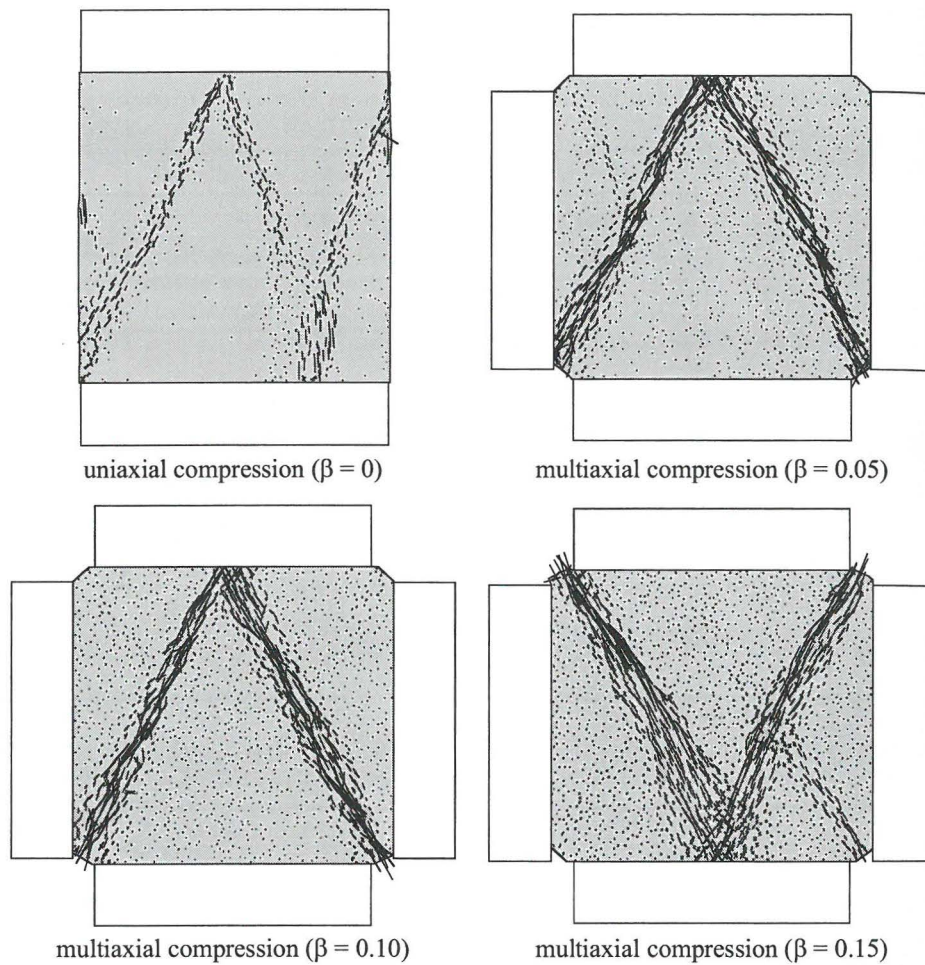


Figure 6.3. Failure patterns of the simulations in the macroscopic layout.

To complete the comparison of the model in the macroscopic layout with the mesoscopic model, also the uniaxial tensile test is simulated in the macroscopic layout (figures 6.4 and 6.5). The test set-up in figure 6.4 is identical to the test set-up in figure 5.55 (simulation with mesoscopic model). It is shown that, also in the macroscopic layout, experimental test results of Van Geel are reproduced well with the model. Furthermore, very little difference is observed between the results of the simulations in the mesoscopic and the macroscopic layout.

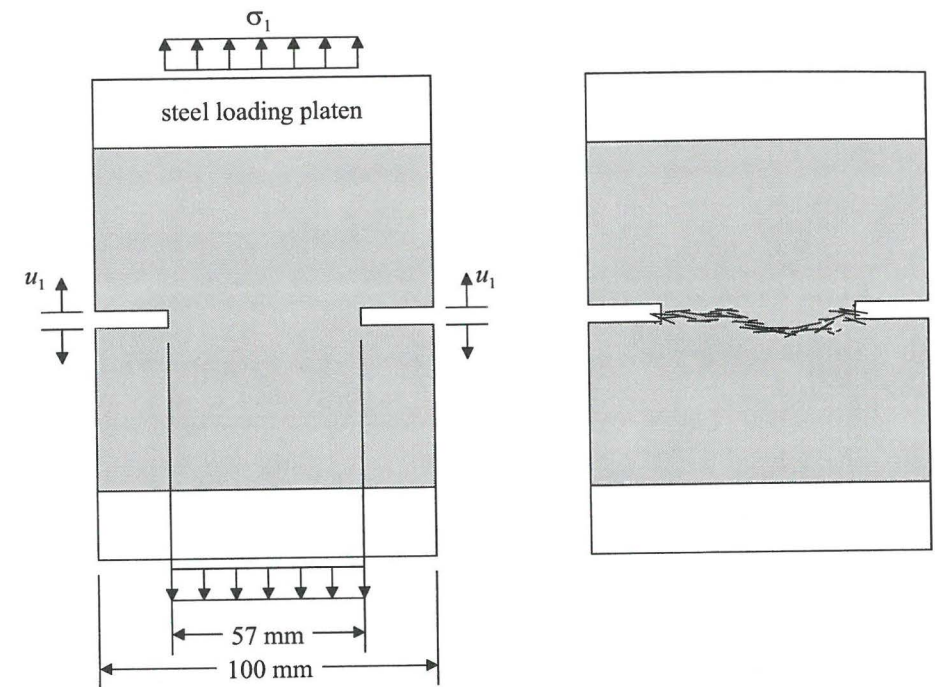


Figure 6.4. Uniaxial tensile test: test set-up and final failure pattern.

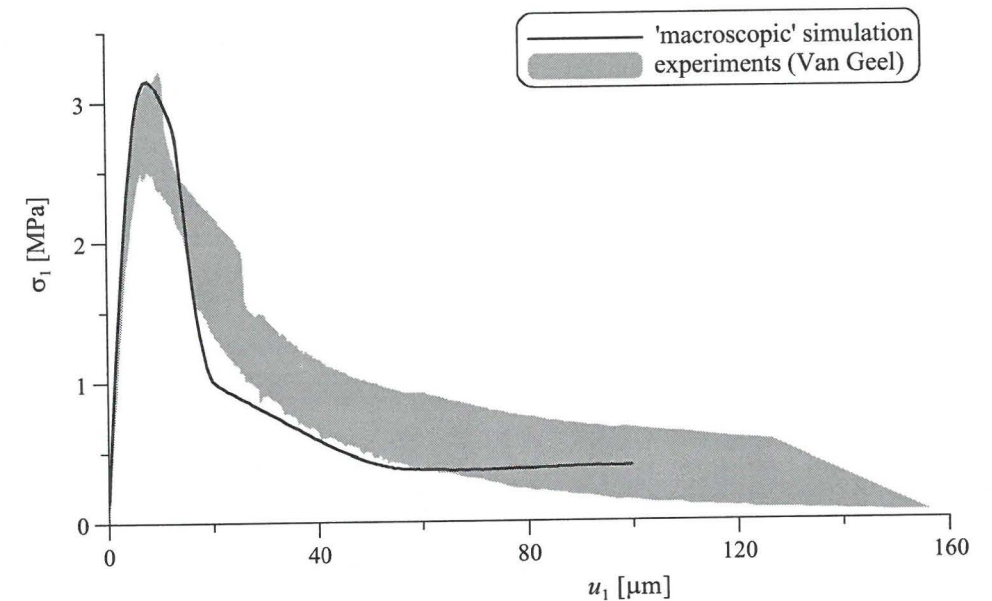


Figure 6.5. Uniaxial tensile test: Loading curve.

As illustrated in this section, the differences between model performance in the mesoscopic and the macroscopic layout are negligible. Although only demonstrated for the proportional test series, it may be concluded that stochastic modelling as proposed in section 6.1 is a proper alternative for the introduction of heterogeneity by explicit incorporation of the coarse aggregate grains in the finite element mesh.

## CHAPTER 7

### CONCLUSIONS & RECOMMENDATIONS

#### 7.1 General conclusions

The main objective of this research (set in chapter 1) is achieved, i.e. a 2D numerical model is developed, which is capable of providing accurate predictions of the mechanical response of multiaxial compressive tests in a 2D test lay-out. This is demonstrated by a wide range of accurate numerical simulations of multiaxial compressive tests from the extensive experimental test program performed by Van Geel<sup>1998</sup>, which was carried out in close cooperation with the present numerical research.

Key element in the development of the numerical model is the subdivision of mechanical concrete behaviour in three different scales of observation and four typical stages (see chapter 3). Such a subdivision proves to be very practical to analyse the basic mechanics of the concrete material when loaded in multiaxial compression.

Convincing physical explanations are found for the macroscopic mechanical behaviour of concrete, observed during multiaxial compressive testing, by considering relevant processes occurring at lower scale levels. This resulted in the evolution of constitutive laws based on these lower level processes, which prove to be adequate to simulate the macroscopic behaviour of concrete loaded in multiaxial compression as observed in experimental tests (sections 4.4 and 5.7.7).

With the formulation of constitutive laws, based on convincing physical explanations (versus empirical formulations), together with adequate performance demonstrated for a wide range of tests in the multiaxial loading regime, the numerical model complies with two essential conditions for predicting the true mechanical response of an *arbitrary* 2D structure subjected to an *arbitrary* loading path.

#### 7.2 General recommendations

Clearly, the mechanical behaviour of (parts of) concrete structures subjected to an arbitrary loading path in 3D stress space are best simulated by appropriate 3D numerical models capable of handling arbitrary stresses and strains in 3D stress/strain space. Therefore, it is recommended to extend the present 2D formulation of the model to three dimensions. To this end, no serious difficulties are expected for the extension of the RVE<sub>2</sub> approach to three dimensions. This part of the model (stage III/IV) is exclusively based on the *maximum* and *minimum principal* stresses. So, the formation of a 2D-crack plane in a 3D-solid is basically

similar to the present 2D formulation (line crack in a 2D-plane). With respect to the RVE<sub>1</sub> approach, extension of the model to three dimensions requires extra investigations. To this end, the cylindrical shaped RVE has to be replaced by a multi-layered sphere. Although a *linear elastic* analytic solution of the stress/strain field exists for such a spherical RVE when uniform macro-stress (or macro-strain) boundary conditions (Cartesian coordinate system) are applied [Rutten<sup>2003</sup>], introducing proper *non-linear* ITZ material behaviour still remains a challenging issue.

As outlined in chapter 6, the mesoscopic model is not well-suited for *large-scale* studies on structures subjected to multiaxial stress states. To speed up such computations, chapter 6 presents an alternative approach. Yet, as already indicated by the title of this chapter “*Towards numerical modelling at the macro level*”, important steps still have to be taken to come to a computing method suitable for large-scale application in engineering practice. Most important herein is the numerical treatment of localisation of deformations. Even though the combination of smeared cracking and a random mesh with rather small finite elements suffices for small-scale analyses, the problem of localisation of deformations might be dealt with more elegantly through the utilisation of models that allow the introduction of displacement jumps in conventional finite elements, in order to reproduce the geometric nature of localised cracking as described in section 2.2.3.2.

### 7.3 Conclusions/recommendations regarding stage I/II

The basics of the pre-peak mechanical behaviour of concrete loaded in multiaxial compression (stage I and II), i.e. initial linear elasticity, non-elastic strengthening, non-elastic volume compaction and characteristic unloading/reloading cycles are simulated very well by the model. Hence, the simple RVE<sub>1</sub>-representation of normal strength concrete is well capable of capturing basic macroscopic mechanical behaviour when – at the lower scale levels – material non-linearity (cracking) is introduced that is based solely on simple Mohr-Coulomb type stress-state bounding surfaces.

Although the overall performance of the RVE<sub>1</sub> model is satisfactory, further research is recommended on the following topics:

- *True distribution of RVE outer-boundary displacements.* In chapter 4, two bounds are indicated for this distribution. These bounds are entitled ‘macrostrain’ and ‘macrostress’ boundaries. The model assumes a distribution of ‘50% macrostrain/50% macrostress’ outer-boundary displacements, which is constant throughout the entire simulation. As outlined in section 4.4, this seems a proper assumption in case of linear elastic material behaviour. However, it is questionable whether this still holds when the material behaviour of the RVE<sub>1</sub> changes to elasto-plastic. It is recommended that valuable information in this should be gained through comparison with a small-scale meso-mechanical FEM model that incorporates explicit modelling of spherical aggregates and ITZs, as well as ITZ non-linearity.

- *Treatment of non-linear material behaviour in the ITZ.* The approach chosen in section 4.3 gives only an approximation of the true solution of the RVE<sub>1</sub> stress/displacement field. Due to the local crack criteria formulated in this approach, crack displacements are – in theory – allowed to develop considerable jumps along the ITZ. It could be argued whether the occurrence of such jumps is physically admissible. Ergo, it is worthwhile to consider alternative approaches also.

For example, the incremental crack displacements along the ITZ could be enforced to be continuous in the form:

$$\Delta u^{cr}(\theta) = L' + L'' \sin 2\theta, \Delta w^{cr}(\theta) = L'' \cos 2\theta$$

For such (inner) boundary conditions, an analytical solution of the stress/displacement fields of the RVE<sub>1</sub> can be found. The above boundary conditions could be referred to as *macrostrain* inner boundary conditions. Analogous with the application of *outer* boundary conditions, the *inner* boundary conditions could also be formulated as *macrostress* boundary conditions:

$$\Delta \sigma_r^{ITZ}(\theta) = p' + p'' \sin 2\theta, \Delta \tau_{r\theta}^{ITZ}(\theta) = p'' \cos 2\theta$$

Of course, in case of pore collapse, analogous continuity of the plastic normal strain along the ITZ  $\epsilon_0^{p,ITZ}(\theta)$  (or stress  $\Delta \sigma_0^{ITZ}(\theta)$ ) should be enforced also.

As a result, no storage of local stress states and local internal state variables is required, only storage of the global vectors. Conversely, simple local crack criteria do not suffice anymore. Instead, more complicated *global* crack criteria have to be derived from the local crack criteria as outlined in this thesis.

- *Pore collapse in the bulk cement paste.* The RVE<sub>1</sub> model allows no pore collapse in the bulk cement paste. Yet, in the high compressive region, limited pore collapse is likely to occur also in the bulk cement paste. Incorporation of this phenomenon is expected to improve model performance, especially with respect to the simulation of realistic ‘unloading’ deformations when unloading continues to a zero stress state.
- *Stiffness during crack closure.* As outlined in section 4.4, improvement of model performance regarding unloading/reloading behaviour is expected by ascribing (limited) stiffness to a closing crack.

### 7.4 Conclusions/recommendations regarding stage III/IV

Also in these regimes (stage III ‘around peak stress’ and stage IV ‘softening stage’), the model performance is adequate in simulating the basics of the mechanical behaviour of concrete loaded in multiaxial compression, i.e. prediction of ultimate strength, onset and growth of macroscopic cracks, gradual shift from volumetric compaction to volumetric dilation, path dependency of both ultimate strength and shape of the softening curve and strong dependence on actually applied boundary conditions. Hence, also the RVE<sub>2</sub>-representation of normal strength concrete is well capable of capturing basic macroscopic mechanical behaviour when – at the lower



scale levels – material non-linearity (cracking) is introduced that is based solely on simple Mohr-Coulomb type stress-state bounding surfaces.

With respect to the RVE<sub>2</sub>-representation, further research is recommended on two topics:

- *Transition between stage II and stage III behaviour.* As stated in section 5.7.7, contradictory tendencies are observed with respect to the rounding of axial loading curves at ultimate strength in different tests. This seeming contradiction ensues from the assumption of linear elastic material behaviour of the continuum during local stress redistribution at stage III. Ergo, potential pore collapse at the ITZ during local stress redistribution is not taken into account in the stage III/IV RVE<sub>2</sub> model computations. To improve the model performance with respect to this issue, it is recommended to analyse the mutual interference of RVE<sub>1</sub> and RVE<sub>2</sub> material behaviour during local stress redistribution at stage III.

- *'True' softening laws for  $\eta$  and  $w_{\max}^{cr}$ .* The cohesive/frictional softening laws have to be quite brittle in combination with a random finite element mesh to allow for proper softening behaviour (see section 5.5). Such softening laws reflect no 'true' material behaviour, irrespective of mesh geometry. To identify 'true' softening laws for  $\eta$  and  $w_{\max}^{cr}$ , it is recommended to perform additional studies in which two separate analyses are carried out.

The first analysis, with a random mesh, is carried out just to identify the orientation of macrocracks. This result is used in the second analysis, i.e. an analysis is performed with alignment of the finite element mesh with potential macrocracks. Such a finite element mesh allows the development of localisation bands in mode II within the width of one finite element without the occurrence of spurious stress locking. Based on these analyses with mesh alignment, 'true' softening laws may be determined by inverse modelling techniques. Undoubtedly, such studies will reveal that crushing of cement paste (ductile mechanism) will predominate aggregate fracture (brittle mechanism) more than assumed in this research.

Although the derivation of 'true' softening laws has little meaning in the present concept of the model (with smeared cracking in a randomised mesh), implementation of such 'true' softening laws is essential when the numerical treatment of localisation of deformations is dealt with more elegantly as proposed in section 7.2.

## REFERENCES

- ABU-LEBDEH, T.M., VOYIADJIS, G.Z. (1993). Plasticity-damage model for concrete under cyclic multiaxial loading. *Journal of Engineering Mechanics, ASCE*, 119(7), pp. 1465-1484.
- AHMAD, S.H., SHAH, S.P. (1982). Complete triaxial stress-strain curves for concrete. *Journal of the Structural Division, ASCE*, 108(ST4), pp. 728-742.
- ALEXANDER, K.M., WARDLAW, J., GILBERT, D.J. (1968). Aggregate-cement bond, cement paste strength and the strength of concrete. *The Structure of Concrete and its Behaviour under Load* (eds. A.E. Brooks & K. Newman); Proceedings of an International Conference, London, pp. 59-81.
- ALEXANDER, K.M. (1971). The mechanism of shear failure at the steel-cement and aggregate-cement interface. *Structure, Solid Mechanics and Engineering Design, Part I* (ed. M. Te'eni); Proc. of the Southampton Civil Engineering Materials Conference, Southampton, U.K., pp. 317-326.
- ALEXANDER, M.G. (1993). Two experimental techniques for studying the effects of the interfacial zone between cement paste and rock. *Cement and Concrete Research*, 23(3), pp. 567-575
- ARSLAN, A., SCHLANGEN, E., VAN MIER, J.G.M. (1996). Effect of model fracture law and porosity on tensile softening of concrete. *Fracture Mechanics of Concrete Structures, Volume I* (ed. F.H. Wittmann); Proc. of the 2nd International Conference (FraMCoS-2), Zürich, Switzerland, pp. 45-54.
- BALUCH, M.H., AL-GADHIB, A.H., KHAN, A.R., SHAALAN, A. (2003). CDM model for residual strength of concrete under cyclic compression. *Cement & Concrete Composites*, 25, pp. 503-512.
- BARDET, J.P., PROUBET, J. (1992). Shear-band analysis in idealized granular material. *Journal of Engineering Mechanics, ASCE*, 118(2), pp. 397-415.
- BARENBLATT, G.I. (1962). The mathematical theory of equilibrium cracks in brittle fracture. *Advances in Applied Mechanics*, 7, pp. 55-129.
- BAŽANT, Z.P., KIM, S.-S. (1979). Plastic-fracturing theory for concrete. *Journal of the Engineering Mechanics Division, ASCE*, 105(EM3), pp. 407-428 (with errata in 106).
- BAŽANT, Z.P., GAMBAROVA, P. (1980). Rough cracks in reinforced concrete. *Journal of the Structural Division, ASCE*, 106(ST4), pp. 819-842.
- BAŽANT, Z.P., OH, B.H. (1983). Crack band theory for fracture of concrete. *Materials and Structures, RILEM*, 16(93), pp. 155-177.
- BAŽANT, Z.P. (1984). Size effect in blunt fracture: concrete, rock, metal. *Journal of Engineering Mechanics, ASCE*, 110(4), pp. 518-535.
- BAŽANT, Z.P., OH, B.H. (1985). Microplane model for progressive fracture of concrete and rock. *Journal of Engineering Mechanics, ASCE*, 111(4), pp. 559-582.
- BAŽANT, Z.P., BISHOP, F.C., CHANG, T.P. (1986). Confined compression tests of cement paste and concrete up to 300 ksi. *ACI Journal*, 83(July-August), pp. 553-560.
- BAŽANT, Z.P., PRAT, P.C. (1988). Microplane model for brittle-plastic material: I. Theory and II. Verification. *Journal of Engineering Mechanics, ASCE*, 114(10), pp. 1672-1702.
- BAŽANT, Z.P., TABBARA, M.R., KAZEMI, M.T., PIJAUDIER-CABOT, G. (1990). Random particle model for fracture of aggregate or fiber composites. *Journal of Engineering Mechanics, ASCE*, 116(8), pp. 1686-1705.

- BAŽANT, Z.P., OŽBOLT, J., ELIGEHAUSEN, R. (1994). Fracture size effect: Review of evidence for concrete structures. *Journal of Structural Engineering, ASCE*, 120(8), pp. 2377-2398.
- BERGUES, J., TERRIEN, M. (1982). Study of concrete's cracking under multiaxial stresses. *Advances in Fracture Research* (eds. D. Francois et al); Proceedings of the 5<sup>th</sup> International Conference on Fracture (ICF 5), Cannes, France, pp. 2253-2260.
- BERTACCHI, P., BELLOTTI, R. (1972). Experimental research on deformation and failure of concrete under triaxial loads. *Deformation and the Rupture of Solids Subjected to Multiaxial Stresses - part I: 'Concrete', paper I/3*; Proceedings of the International RILEM Symposium, Cannes, France, pp. 37-52.
- BITTENCOURT, T.N., WAWRZYNEK, P.A., INGRAFFEA, A.R., SOUSA, J.L. (1996). Quasi-automatic simulation of crack propagation for 2D LEFM problems. *Engineering Fracture Mechanics*, 55(2), pp. 321-334.
- BONGERS, J.P.W., VAN GEEL, H.J.G.M. (1997). Numerical meso scale simulations of multiaxially loaded concrete. *Advances in Fracture Research, Vol. 2* (eds. B.L. Karihaloo, Y.W. Mai, M.I. Ripley & R.O. Ritchie); Proc. ICF9 congress, Sydney, Australia, pp. 949-956.
- BONGERS, J.P.W. (1998<sup>a</sup>). 2D Mesh generator for concrete composites. *TUE/BKO-98.18*, Eindhoven University of Technology, Eindhoven, The Netherlands.
- BOURDETTE, B., RINGOT, E., OLLIVIER, J.P. (1995). Modelling of the transition zone porosity. *Cement and Concrete Research*, 25(4), pp. 741-751
- BREYSSE, D. (1990). Probabilistic formulation of damage-evolution law of cementitious composites. *Journal of Engineering Mechanics, ASCE*, 116(7), pp. 1489-1510.
- BROEK, D. (1986). *Elementary engineering fracture mechanics*. Martinus Nijhoff Publishers, The Hague.
- BUDIANSKY, B., O'CONNELL, R.J. (1976). Elastic moduli of a cracked solid. *International Journal of Solids and Structures*, 12, pp. 81-97.
- BURLION, N., GATUNGT, F., DAUDEVILLE, L., PIAUDIER-CABOT, G. (1998). Modelling of materials with voids: A mixed damage and plasticity approach for compaction and tension problems. *Computational Modelling of Concrete Structures, Vol. 1* (eds. R. de Borst, N. Bicanic, H. Mang & G. Meschke); Proceedings International EURO-C Conference, Badgastein, Austria, pp. 209-217.
- BURT, N.J., DOUGILL, J.W. (1977). Progressive failure in a model heterogeneous medium. *Journal of the Engineering Mechanics Division, ASCE*, 103(EM3), pp. 365-376.
- BÜYÜKÖZTÜRK, O., LEE K.-M. (1993). Assessment of interfacial fracture toughness in concrete composites. *Cement & Concrete Composites*, 15, pp. 143-151.
- CALISKAN, S., KARIHALOO, B.L., BARR, B.I.G. (2002). Study of rock-mortar interfaces. Part I: surface roughness of rock aggregates and microstructural characteristics of interface. *Magazine of Concrete Research*, 54(6), pp. 449-461.
- CARMELIET, J., HENS, H. (1994). Probabilistic nonlocal model for continua with random field properties. *Journal of Engineering Mechanics, ASCE*, 120(10), pp. 2013-2027.
- CAROL, I., PRAT, P.C. (1990). A statically constrained microplane model for the smeared analysis of concrete cracking. *Computer Aided Analysis and Design of Concrete Structures* (eds. N. Bicanic & H.A. Mang); Proceedings of 2nd International SCI-C Conference, Zell am See, Austria, pp. 919-930.
- CAROL, I., RIZZI, E., WILLAM, K. (1994). A unified theory of elastic degradation and damage based on a loading surface. *International Journal of Solids and Structures*, 31(20), pp. 2835-2865.

- CARPINTERI, A., COLOMBO, G., FERRARA, G., GIUSEPPE, G. (1989). Numerical simulation of concrete fracture through a bilinear softening stress-crack opening displacement law. *Fracture of Concrete and Rock* (eds. S.P. Shah & S.E. Swartz); Proc. of SEM/RILEM International Conference, Houston, Texas, USA, pp. 131-141.
- CHANG, C.S. (1993). Micromechanical modeling of deformation and failure for granulates with frictional contacts. *Mechanics of Materials*, 16, pp. 13-24.
- CHEN, W.F., HAN, D.J. (1988). *Plasticity for structural engineers*. Springer-Verlag, New York.
- COPE, R.J., RAO, P.V., CLARK, L.A., NORRIS, P. (1980). Modelling of reinforced concrete behaviour for finite element analysis of bridge slabs. *Numerical Methods for Non-Linear Problems, Vol. 1* (eds. C. Taylor, E. Hinton, D.R.J. Owen); Proceedings of the International Conference, Swansea, U.K., pp. 457-470.
- COTTERELL, B., PARAMASIVAM, P., LAM, K.Y. (1992). Modelling the fracture of cementitious materials. *Materials and Structures, RILEM*, 25, pp. 14-20.
- CUNDALL, P.A. (1971). A computer model for simulating progressive large scale movements in blocky rock systems. *Rock Fracture, Vol. 1*; Proc. of the Symposium of the International Society for Rock Mechanics, Nancy, France, Paper No. II-8.
- CUNDALL, P.A., STRACK, O.D.L. (1979). A discrete numerical model for granular assemblies. *Géotechnique*, 29(1), pp. 47-65.
- CUNDALL, P.A. (1982). Adaptive density-scaling for time-explicit calculations. *Numerical Methods in Geomechanics, Vol. 1* (ed. Z. Eisenstein); Proc. of the 4<sup>th</sup> International Conference, Edmonton, Canada, pp. 23-26.
- DANTU, P. (1957). I – Étude des contraintes dans les milieux hétérogènes application au béton; II – Utilisation des réseaux pour l'étude des déformations. *Publication No. 57-6*, Laboratoire central des ponts et chaussées, Paris, France.
- DARWIN, D., DEWEY, G.R. (1989). Image analysis of microcracks. *Cracking and Damage: Strain Localization and Size Effect* (eds. J. Mazars & Z.P. Bažant); Proceedings of the France-U.S. Workshop, Cachan, France, pp. 65-75.
- DE BORST, R., NAUTA, P. (1985). Non-orthogonal cracks in a smeared finite element model. *Engineering Computations*, 2(1), pp. 35-46.
- DE BORST, R. (1991). Simulation of strain localization: A reappraisal of the Cosserat continuum. *Engineering Computations*, 8, pp. 317-332.
- DE BORST, R., MÜHLHAUS, H.B., PAMIN, J. (1992). A gradient continuum model for mode-I fracture in concrete and rock. *Fracture Mechanics of Concrete Structures* (ed. Z.P. Bažant); Proc. of the 1<sup>st</sup> International FraMCoS1 Conference, Breckenridge, Colorado, pp. 251-259.
- DE ROOIJ, M.R. (1996). What is abstract can not be concrete. *Stevin report 25.1-96.01*, Delft University of Technology, Delft, The Netherlands.
- DE ROOIJ, M.R. (2000). *Syneresis in cement paste systems*, PhD thesis, Delft University of Technology, Delft, The Netherlands.
- DIAMOND, S., HUANG, J. (2001). The ITZ in concrete - a different view based on image analysis and SEM observations. *Cement & Concrete Composites*, 23, pp. 179-188.
- DIVAKAR, M.P., FAFITIS, A. (1992). Micromechanics-based constitutive model for interface shear. *Journal of Engineering Mechanics, ASCE*, 118(7), pp. 1317-1337.
- DOUGILL, J.W. (1976). On stable progressively fracturing solids. *ZAMP: Zeitschrift fuer Angewandte Mathematik und Physik (Journal of Applied Mathematics and Physics)*, 27(4), pp. 423-437.

- DUGDALE, D.S. (1960). Yielding of steel sheets containing slits. *Journal of the Mechanics and Physics of Solids*, 8, pp. 100-104.
- ERDOGAN, F., SIH, G.C. (1963). On the crack extension in plates under plane loading and transverse shear. *Journal of Basic Engineering, ASME*, 85, pp. 519-527.
- ETSE, G., WILLAM, K. (1994). Fracture energy formulation for inelastic behavior of plain concrete. *Journal of Engineering Mechanics, ASCE*, 120(9), pp. 1983-2011.
- FAFITIS, A., SHAH, S.P. (1986). Constitutive model for biaxial cyclic loading of concrete. *Journal of Engineering Mechanics, ASCE*, 112(8), pp. 760-775.
- FAN, S.-C., WANG, F. (2002). A new strength criterion for concrete. *ACI Structural Journal*, 99(3), pp. 317-326.
- FARDIS, M.N., BÜYÜKÖZTÜRK, O. (1979). Shear transfer model for reinforced concrete. *Journal of the Engineering Mechanics Division, ASCE*, 105(EM2), pp. 255-275.
- FARUQUE, M.O., CHANG, C.J. (1986). New cap model for failure and yielding of pressure-sensitive materials. *Journal of Engineering Mechanics, ASCE*, 112(10), pp. 1041-1053.
- GÁLVEZ, J.C., CERVENKA, J., CENDON, D.A., SAOUMA, V. (2002). A discrete crack approach to normal/shear cracking of concrete. *Cement and Concrete Research*, 32, pp. 1567-1585.
- GERSTLE, K.H., LINSE, D.L., BERTACCHI, P., KOTSOVOS, M.D., KO, H.-Y., NEWMAN, J.B., ROSSI, P., SCHICKERT, G., TAYLOR, M.A., TRAINA, L.A., ZIMMERMAN, R.M., BELLOTTI, R. (1978). Strength of concrete under multiaxial stress states. *Concrete and Concrete Structures* (ed. B. Bresler); Proceedings of the Douglas McHenry International Symposium, Mexico City, SP 55-5, ACI, Detroit, pp. 103-131.
- GRIFFITH, A.A. (1924). The theory of rupture. *Proceedings of the 1st International Congress for Applied Mechanics* (eds. C.B. Biezeno and J.M. Burgers), Delft, The Netherlands, pp. 55-63.
- GUINEA, G.V., PLANAS, J., ELICES, M. (1994). A general bilinear fit for the softening curve of concrete. *Materials and Structures, RILEM*, 27, pp. 99-105.
- HAN, D.J., CHEN, W.F. (1986). Strain-space plasticity formulation for hardening-softening materials with elastoplastic coupling. *International Journal of Solids and Structures*, 22(8), pp. 935-950.
- HANNANT, D.J. (1974). Nomograms for the failure of plain concrete subjected to short-term multiaxial stresses. *The Structural Engineer*, 52(5), pp. 151-165.
- HARRIS, J.R. (2002). Report on collapse of part of the Pentagon building. ISO/TC98 Meeting, Brussels, December 13, 2002.
- HERRMANN, H.J., HANSEN, H., ROUX, S. (1989). Fracture of disordered, elastic lattices in two dimensions. *Physical Review B*, 39(1), pp. 637-648.
- HILL, R. (1963). Elastic properties of reinforced solids: some theoretical principles. *Journal of the Mechanics and Physics of Solids*, 11, pp. 357-372.
- HILLERBORG, A., MODÉER, M., PETERSSON, P.-E. (1976). Analysis of crack formation and crack growth in concrete by means of fracture mechanics and finite elements. *Cement and Concrete Research*, 6(6), pp. 773-782.
- HILLERBORG, A. (1983). Analysis of one single crack. *Fracture Mechanics of Concrete* (ed. F.H. Wittmann); Developments in Civil Engineering, Vol. 7, pp. 223-249.
- HIRSCH, T.J. (1962). Modulus of elasticity of concrete affected by elastic moduli of cement paste matrix and aggregate. *ACI Journal*, 59(March), pp. 427-451.
- HOBBS, D.W. (1971). Strength of concrete under combined stress. *Cement and Concrete Research*, 1(1), pp. 41-56.

- HOEK, E., BROWN, E.T. (1980). Empirical strength criterion for rock masses. *Journal of the geotechnical engineering division*, 106(GT9), pp. 1013-1035.
- HORII, H., NEMAT-NASSER, S. (1985). Compression-induced microcrack growth in brittle solids: Axial splitting and shear failure. *Journal of Geophysical Research*, 90(B4), pp. 3105-3125.
- HSIEH, S.S., TING, E.C., CHEN, W.F. (1982). A plastic-fracture model for concrete. *International Journal of Solids and Structures*, 18(3), pp. 181-197.
- HSU, T.T.C., SLATE, F.O. (1963). Tensile bond strength between aggregate and cement paste or mortar. *ACI Journal*, 60(April), pp. 465-486.
- HSU, T.T.C., SLATE, F.O., STURMAN, G.M., WINTER, G. (1963). Microcracking of plain concrete and the shape of the stress-strain curve. *ACI Journal*, 60(February), pp. 209-223.
- IMRAN, I., PANTAZOPOULOU, S.J. (1996). Experimental study of plain concrete under triaxial stress. *ACI Materials Journal*, 93(6), pp. 589-601.
- INGLIS, C.E. (1913). Stresses in a plate due to the presence of cracks and sharp corners. *Transactions of the Institution of Naval Architects*, 55, pp. 219-230.
- INGRAFFEA, A.R., SAOUMA, V. (1985). Numerical modeling of discrete crack propagation in reinforced and plain concrete. *Fracture Mechanics of Concrete: Structural Application and Numerical Calculation* (eds. G. Sih, A. di Tomasso); Engineering Application of Fracture Mechanics, Vol. 4, pp. 171-225.
- IRWIN, G.R. (1957). Analysis of stresses and strains near the end of a crack traversing a plate. *ASME Journal of Applied Mechanics*, 24(2), pp. 361-364.
- IRWIN, G.R. (1958). Fracture. *Handbuch der Physik (Encyclopedia of Physics), Volume VI: Elasticity and Plasticity* (ed. S. Fluegge), pp. 551-590.
- ITASCA CONSULTING GROUP, INC. (1993). *UDEC (Universal Distinct Element Code) Version 2.0, Vol. I: User's Manual*, Minneapolis, Minnesota, U.S.A.
- IYENGAR, K.T.S.R., CHANDRASHEKHARA, K., KRISHNASWAMY, K.T. (1965). Strength of concrete under biaxial compression. *ACI Journal*, 62(February), pp. 239-249.
- JAMET, P., MILLARD, A., NAHAS, G. (1984). Triaxial behaviour of a micro-concrete - complete stress-strain curves for confining pressures ranging from 0 to 100 Mpa. *Concrete under Multiaxial Conditions - session 4: 'experimental results', Vol. 1;* Proceedings of RILEM-CEB Symposium, Toulouse, France, pp. 133-140.
- JU, J.W., LEE, X. (1991). Micromechanical damage models for brittle solids. I: Tensile loadings. *Journal of Engineering Mechanics, ASCE*, 117(7), pp. 1495-1514.
- KLISINSKI, M., RUNESSON, K., STURE, S. (1991). Finite element with inner softening band. *Journal of Engineering Mechanics, ASCE*, 117(3), pp. 575-587.
- KOHLAS, J. (1972). *Monte Carlo simulation in operations research* (Lecture Notes in Economics and Mathematical Systems: Vol. 63). Springer-Verlag, Berlin.
- KOTSOVOS, M.D., NEWMAN, J.B. (1977). Behaviour of concrete under multiaxial stress. *ACI Journal*, 74(September), pp. 443-446.
- KOTSOVOS, M.D. (1979). Effect of stress path on the behavior of concrete under triaxial stress states. *ACI Journal*, 76(February), pp. 213-223.
- KOTSOVOS, M.D. (1983). Effect of testing techniques on the post-ultimate behaviour of concrete in compression. *Materials and Structures, RILEM*, 16(91), pp. 3-12.
- KRAJINOVIC, D., FONSEKA, G.U. (1981). The continuous damage theory of brittle materials - Part 1: General Theory. *ASME Journal of Applied Mechanics*, 48(December), pp. 809-815.

- KRAJINOVIC, D. (2000). Damage mechanics: accomplishments, trends and needs. *International Journal of Solids and Structures*, 37, pp. 267-277.
- KRISHNASWAMY, K.T. (1968). Strength and microcracking of plain concrete under triaxial compression. *ACI Journal*, 65(October), pp. 856-862.
- KUPFER, H., HILSDORF, H.K., RUSCH, H. (1969). Behavior of concrete under biaxial stresses. *ACI Journal*, 66(August), pp. 656-666.
- KUPFER, H.B., GERSTLE, K.H. (1973). Behavior of concrete under biaxial stresses. *Journal of the Engineering Mechanics Division, ASCE*, 99(EM4), pp. 853-866.
- KWAN, A.K.H., WANG, Z.M., CHAN, H.C. (1999). Mesoscopic study of concrete II: nonlinear finite element analysis. *Computers & Structures*, 70, pp. 545-556.
- LADE, P.V. (1982). Three-parameter failure criterion for concrete. *Journal of the Engineering Mechanics Division, ASCE*, 108(EM5), pp. 850-863.
- LARBI, J.A. (1991). *The cement paste-aggregate interfacial zone in concrete*, PhD thesis, Delft University of Technology, Delft, The Netherlands.
- LARSSON, R., STEINMANN, P., RUNESSON, K. (1999). Finite element embedded localization band for finite strain plasticity based on a regularized strong discontinuity. *Mechanics of cohesive-frictional materials*, 4, pp. 171-194.
- LAUNAY, P., GACHON, H., POITEVIN, P. (1970). Déformation et résistance ultime du béton sous étreinte triaxiale. *Annales de l'Institut Technique du Bâtiment et des Travaux Publics*, 269(Mai), pp. 23-48.
- LEE, X., JU, J.W. (1991). Micromechanical damage models for brittle solids. II: Compressive loadings. *Journal of Engineering Mechanics, ASCE*, 117(7), pp. 1515-1536.
- LI, B., MAEKAWA, K., OKAMURA, H. (1989). Contact density model for stress transfer across cracks in concrete. *Journal of the Faculty of Engineering, The University of Tokyo (B)*, 40(1), pp. 9-52.
- LILLIU, G., VAN MIER, J.G.M. (2003). 3D lattice type fracture model for concrete. *Engineering Fracture Mechanics*, 70, pp. 927-941.
- LIN, F.B., BAŽANT, Z.P., CHERN, J.C., MARCHERTAS, A.H. (1987). Concrete model with normality and sequential identification. *Computers & Structures*, 26(6), pp. 1011-1025.
- LIN, G., LU, J., WANG, Z., XIAO, S. (2002). Study on the reduction of tensile strength of concrete due to triaxial compressive loading history. *Magazine of Concrete Research*, 54(2), pp. 113-124.
- LIU, T.C.Y., NILSON, A.H., SLATE, F.O. (1972). Stress-strain response and fracture of concrete in uniaxial and biaxial compression. *ACI Journal*, 69(May), pp. 291-295.
- LØLAND, K.E. (1980). Continuous damage model for load-response estimation of concrete. *Cement and Concrete Research*, 10(3), pp. 395-402.
- LUTZ, M.P., MONTEIRO, P.J.M., ZIMMERMAN, R.W. (1997). Inhomogeneous interfacial transition zone model for the bulk modulus of mortar. *Cement and Concrete Research*, 27, pp. 1113-1122.
- MAZARS, J., LEMAITRE, J. (1985). Application of continuous damage mechanics to strain and fracture behavior of concrete. *Application of Fracture Mechanics to Cementitious Composites* (ed. S.P. Shah); Proc. of the NATO Advanced Research Workshop, Evanston, Illinois, pp. 507-520.
- MENÉTREY, PH., WILLAM, K.J. (1995). Triaxial failure criterion for concrete and its generalization. *ACI Structural Journal*, 92(3), pp. 311-318.
- MEYER, R., AHRENS, H., DUDDECK, H. (1994). Material model for concrete in cracked and uncracked states. *Journal of Engineering Mechanics, ASCE*, 120(9), pp. 1877-1895.

- MILLS, L.L., ZIMMERMAN, R.M. (1970). Compressive strength of plain concrete under multiaxial loading conditions. *ACI Journal*, 67(October), pp. 802-807.
- MIZUNO, E., HATANAKA, S. (1992). Compressive softening model for concrete. *Journal of Engineering Mechanics, ASCE*, 118(8), pp. 1546-1563.
- MÜHLHAUS, H.B., (1986). Scherfugenanalyse bei granularem material im rahmen der Cosserat-theorie. *Ingenieur-Archiv*, 56, pp. 389-399.
- MÜHLHAUS, H.B., AIFANTIS, E.C. (1991). A variational principle for gradient plasticity. *International Journal of Solids and Structures*, 28(7), pp. 845-857.
- MURAKAMI, M., OHTANI, Y. (2000). Failure phenomena and determination of damaged zone of concrete in softening regime under triaxial compression. *Magazine of Concrete Research*, 52(2), pp. 137-152.
- NEEDLEMAN, A. (1988). Material rate dependence and mesh sensitivity in localization problems. *Computer Methods in Applied Mechanics and Engineering*, 67, pp. 69-85.
- NELISSEN, L.J.M. (1972). Biaxial testing of normal concrete. *Heron*, 18(1).
- NEMATI, K.M., MONTEIRO, P.J.M., SCRIVENER, K.L. (1998). Analysis of compressive stress-induced cracks in concrete. *ACI Materials Journal*, 95(5), pp. 617-630.
- NEMAT-NASSER, S., HORI, M. (1993). *Micromechanics: overall properties of heterogeneous materials* (North-Holland series in applied mathematics and mechanics, Vol 37), North-Holland, Amsterdam, The Netherlands.
- NEWMAN, J.B. (1979). Concrete under complex stress. *Developments in Concrete Technology – I* (ed. F.D. Lydon), Applied Science Publishers, London, pp. 151-219.
- OHTANI, Y., CHEN, W.F. (1988). Multiple hardening plasticity for concrete materials. *Journal of Engineering Mechanics, ASCE*, 114(11), pp. 1890-1910.
- ONCK, P., VAN DER GIESSEN, E. (1997). Microstructurally-based modelling of intergranular creep fracture using grain elements. *Mechanics of Materials*, 26, pp. 109-126.
- OŽBOLT, J., BAŽANT, Z.P. (1996). Numerical smeared fracture analysis: nonlocal microcrack interaction approach. *International Journal for Numerical Methods in Engineering*, 39, pp. 635-661.
- OŽBOLT, J., LI, Y., KOZAR, I. (2001). Microplane model for concrete with relaxed kinematic constraint. *International Journal of Solids and Structures*, 38, pp. 2683-2711.
- PEARCE, C.J., THAVALINGAM, A., LIAO, Z., BICANIC, N. (2000). Computational aspects of the discontinuous deformation analysis framework for modelling concrete fracture. *Engineering Fracture Mechanics*, 65, pp. 283-298.
- PEKAU, O.A., ZHANG, Z.X., LIU, G.T. (1992). Constitutive model for concrete in strain space. *Journal of Engineering Mechanics, ASCE*, 118(9), pp. 1907-1927.
- PETIT, C., VERGNE, A., ZHANG, X. (1996). A comparative numerical review of cracked materials. *Engineering Fracture Mechanics*, 54(3), pp. 423-439.
- PIJAUDIER-CABOT, G., BAŽANT, Z.P. (1987). Nonlocal damage theory. *Journal of Engineering Mechanics, ASCE*, 113(10), pp. 1512-1533.
- PODGORSKI, J. (1985). General failure criterion for isotropic media. *Journal of Engineering Mechanics, ASCE*, 111(2), pp. 188-201.
- PRAMONO, E., WILLAM, K. (1989). Fracture energy-based plasticity formulation of plain concrete. *Journal of Engineering Mechanics, ASCE*, 115(6), pp. 1183-1204.
- RAMESH, G., SOTELINO, E.D., CHEN, W.F. (1997). Effect of transition zone on elastic moduli of concrete materials. *Cement and Concrete Research*, 26, pp. 611-622.
- RASHID, Y.R. (1968). Ultimate strength analysis of prestressed concrete pressure vessels. *Nuclear Engineering and Design*, 7, pp. 334-344.

- REICH, R.W., CERVENKA, J., SAOUMA, V.E. (1994). MERLIN: A computational environment for 2D/3D discrete fracture analysis. *Computational Modelling of Concrete Structures, Vol. 2* (eds. H. Mang, N. Bicanic & R. de Borst); Proceedings International EURO-C Conference, Innsbruck, Austria, pp. 999-1008.
- REINHARDT, H.W. (1977). Ansprüche des konstruktors an den Beton, hinsichtlich festigkeit und verformung. *Beton*, 27(5), pp. 195-199.
- REUSS, A. (1929). Berechnung der fließgrenze von mischkristallen auf grund der plastizitätsbedingung für einkristalle. *ZAMM: Zeitschrift für Angewandte Mathematik und Mechanik*, 9(1), pp. 49-58.
- RICE, J.R. (1968). A path independent integral and the approximate analysis of strain concentration by notches and cracks. *ASME Journal of Applied Mechanics*, 35, pp. 379-386.
- RICHART, F.E., BRANDTZAEG, A., BROWN, R.L. (1928). A study of the failure of concrete under combined compressive stresses. *Engineering experiment station, Bulletin No. 185*, University of Illinois, Urbana, Illinois.
- ROBINSON, G.S. (1967). Behavior of concrete in biaxial compression. *Journal of the Structural Division, ASCE*, 93(ST1), pp. 71-86.
- ROELFSTRA, P.E., SADOUKI, H. (1986). Fracture process in numerical concrete. *Fracture Toughness and Fracture Energy of Concrete* (ed. F.H. Wittmann); Proceedings of the International Conference, Lausanne, Switzerland, pp. 105-116.
- ROELFSTRA, P.E. (1989). Simulation of strain localization processes with numerical concrete. *Cracking and Damage: Strain Localization and Size Effect* (eds. J. Mazars & Z.P. Bažant); Proceedings of the France-U.S. Workshop, Cachan, France, pp. 79-90.
- ROSSI, P., RICHER, S. (1987). Stochastic modelling of concrete cracking. *Constitutive Laws for Engineering Materials: Theory and Applications, Vol. II* (eds. C.S. Desai, E. Krempl, P.D. Kioussis, T. Kundu); Proceedings of 2nd International Conference, Tucson, Arizona, pp. 915-922.
- ROSSI, P., WU, X. (1992). Probabilistic model for material behaviour analysis and appraisalment of concrete structures. *Magazine of Concrete Research*, 44(161), pp. 271-280.
- ROTS, J.G., NAUTA, P., KUSTERS, G.M.A., BLAAUWENDRAAD, J. (1985). Smeared crack approach and fracture localization in concrete. *Heron*, 30(1), pp. 3-48.
- ROTS, J.G. (1988). *Computational modeling of concrete fracture*, PhD Thesis, Delft University of Technology, Delft, The Netherlands.
- ROTS, J.G., BORST, R. DE (1989). Analysis of concrete fracture in 'direct' tension. *International Journal of Solids and Structures*, 25(12), pp. 1381-1394.
- RUTLAND, C.A., WANG, M.L. (1997). The effects of confinement on the failure orientation in cementitious materials - experimental observations. *Cement & Concrete Composites*, 19, pp. 149-160.
- RUTTEN, H.S. (2003). *A 3D-RCE (Representative Constitutive Element) in capacity/failure modelling of granular materials, e.g. concrete*, Eindhoven University of Technology, Eindhoven, The Netherlands.
- SCHICKERT, G., WINKLER, H. (1977). Versuchsergebnisse zur Festigkeit und Verformung von Beton bei mehraxialer Druckbeanspruchung. *Deutscher Ausschuss fuer Stahlbeton*, 277, Berlin.
- SCHLANGEN, E., VAN MIER, J.G.M. (1992a). Experimental and numerical analysis of micromechanisms of fracture of cement-based composites. *Cement & Concrete Composites*, 14, pp. 105-118.

- SCHLANGEN, E., VAN MIER, J.G.M. (1992b). Simple lattice model for numerical simulation of fracture of concrete materials and structures. *Materials and Structures, RILEM*, 25, pp. 534-542.
- SCHLANGEN, E. (1993). *Experimental and numerical analysis of fracture processes in concrete*, PhD thesis, Delft University of Technology, Delft, The Netherlands.
- SCHLANGEN, E., GARBOCZI, E.J. (1997). Fracture simulations of concrete using lattice models: computational aspects. *Engineering Fracture Mechanics*, 57(2/3), pp. 319-332.
- SCHORN, H., RODE, U. (1991). Numerical simulation of crack propagation from microcracking to fracture. *Cement & Concrete Composites*, 13, pp. 87-94.
- SCHREYER, H.L., CHEN, Z. (1986). One-dimensional softening with localization. *ASME Journal of Applied Mechanics*, 53(December), pp. 791-797.
- SCRIVENER, K.L., NEMATI, K.M. (1996). The percolation of pore space in the cement paste/aggregate interfacial zone of concrete. *Cement and Concrete Research*, 26(1), pp. 35-40.
- SCRIVENER, K. (1999). Characterisation of the ITZ and its quantification by test methods. *Engineering and transport properties of the interfacial transition zone in cementitious composites* (eds. M.G. Alexander et al), RILEM, Cachan, pp. 3-17.
- SFER, D., CAROL, I., GETTU, R., ETSE, G. (2002). Study of the behavior of concrete under triaxial compression. *Journal of Engineering Mechanics, ASCE*, 128(2), pp. 156-163.
- SHAH, S.P., CHANDRA, S. (1968). Critical stress, volume change and microcracking of concrete. *ACI Journal*, 65(September), pp. 770-781.
- SIH, G.C. (1974). Strain-energy-density factor applied to mixed mode crack problems. *International Journal of Fracture*, 10(3), pp. 305-321.
- SLATE, F.O., HOVER, K.C. (1984). Microcracking in concrete. *Fracture Mechanics of Concrete: Material Characterization and Testing* (eds. A. Carpinteri and A.R. Ingraffea); Engineering Application of Fracture Mechanics: Vol. 3, pp. 137-159.
- SLUYS, L.J., DE BORST, R. (1991). Rate-dependent modelling of concrete fracture. *Heron*, 36(2), pp. 3-15.
- SMIT, R.J.M. (1993). *Toughness of heterogeneous polymeric systems – a modeling approach*, PhD thesis, Eindhoven University of Technology, Eindhoven, The Netherlands.
- SMITH, S.S., WILLAM, K.J., GERSTLE, K.H., STURE, S. (1989). Concrete over the top, or: Is there life after peak? *ACI Materials Journal*, 86(5), pp. 491-497.
- SOUSA, J.L., MARTHA, L.F., WAWRZYNEK, P.A., INGRAFFEA, A.R. (1989). Simulation of non-planar crack propagation in three-dimensional structures in concrete and rock. *Fracture of Concrete and Rock: Recent Developments* (eds. S.P. Shah, S.E. Swartz & B. Barr); Proceedings of the International Conference, Cardiff, U.K., pp. 254-264.
- STANKOWSKI, T. (1990). *Numerical simulation of progressive failure in particle composites*, PhD Thesis, University of Colorado, Boulder, Colorado, U.S.A.
- STANKOWSKI, T. (1992). Composite analysis with discrete and smeared crack concepts. *Fracture Mechanics of Concrete Structures* (ed. Z.P. Bažant); Proc. of the 1<sup>st</sup> International FraMCoSI Conference, Breckenridge, Colorado, pp. 269-274.
- STEVENS, D.J., LIU, D. (1992). Strain-based constitutive model with mixed evolution rules for concrete. *Journal of Engineering Mechanics, ASCE*, 118(6), pp. 1184-1200.
- STROEVEN, P. (1973). *Some aspects of the micromechanics of concrete*, PhD thesis, Delft University of Technology, Delft, The Netherlands.
- SUARIS, W., FERNANDO, V. (1987). Detection of crack growth in concrete from ultrasonic intensity measurements. *Materials and Structures, RILEM*, 20, pp. 214-220.

- SWAMY, N. (1971). Aggregate-matrix interaction in concrete systems. *Structure, Solid Mechanics and Engineering Design, Part 1* (ed. M. Te'eni); Proc. of the Southampton Civil Engineering Materials Conference, Southampton, U.K., pp. 301-315.
- TALIERCIO, A.L.F., BERRA, M., PANDOLFI, A. (1999). Effect of high-intensity sustained triaxial stresses on the mechanical properties of plain concrete. *Magazine of Concrete Research*, 51(6), pp. 437-447.
- TORRENTI, J.-M., DESRUES, J., ACKER, P., BOULAY, C. (1989). Application of stereophotogrammetry to the strain localization in concrete compression. *Cracking and Damage: Strain Localization and Size Effect* (eds. J. Mazars & Z.P. Bažant); Proceedings of the France-U.S. Workshop, Cachan, France, pp. 30-41.
- TRAN, T.X., DORFMANN, A., RHIE, Y.B. (1998). Micromechanical modeling of cracking and damage of concrete structures. *Computational Modelling of Concrete Structures, Vol. 1* (eds. R. de Borst, N. Bicanic, H. Mang & G. Meschke); Proceedings International EURO-C Conference, Badgastein, Austria, pp. 61-69.
- VAN BAARS, S. (1996). Discrete element modelling of granular materials. *Heron*, 41(2), pp. 139-157.
- VAN GEEL, H.J.G.M. (1995<sup>a</sup>). Concrete behaviour under compressive loading - Experimental research. Part I: Survey of literature. *Report BKO95.02*, Eindhoven University of Technology, Eindhoven, The Netherlands.
- VAN GEEL, H.J.G.M. (1995<sup>b</sup>). Concrete behaviour under compressive loading - Experimental research. Part II: Bibliography 1900-1994. *Report BKO95.02*, Eindhoven University of Technology, Eindhoven, The Netherlands.
- VAN GEEL, H.J.G.M., BONGERS, J.P.W. (1997). Failure characteristics of concrete in plane strain compression. *Advances in Fracture Research, Vol. 2* (eds. B.L. Karihaloo, Y.W. Mai, M.I. Ripley & R.O. Ritchie); Proc. ICF9 congress, Sydney, Australia, pp. 965-972.
- VAN GEEL, H.J.G.M. (1998). *Concrete behaviour in multiaxial compression: experimental research*, PhD thesis, Eindhoven University of Technology, Eindhoven, The Netherlands.
- VAN MIER, J.G.M. (1984). *Strain-softening of concrete under multiaxial loading conditions*, PhD thesis, Eindhoven University of Technology, Eindhoven, The Netherlands.
- VAN MIER, J.G.M. (1986). Multiaxial strain-softening of concrete - Part II: Load-Histories, *Materials and Structures, RILEM*, 19(111), pp. 179-199.
- VAN MIER, J.G.M., VONK, R.A. (1991). Fracture of concrete under multiaxial stress - recent developments. *Materials and structures, RILEM*, 24, pp. 61-65.
- VAN MIER, J.G.M. (1992). Scaling in tensile and compressive fracture of concrete. *Applications of fracture mechanics to reinforced concrete* (ed. A. Carpinteri); Proc. of International Workshop, Turin, Italy, pp. 95-135.
- VAN MIER, J.G.M. ET AL (1997). Strain softening of concrete loaded in uniaxial compression. Report of the round robin test carried out by RILEM TC 148-SSC: Test methods for the strain-softening response of concrete, *Materials and structures, RILEM*, 30(198), pp. 195-209.
- VAN MIER, J.G.M., VERVUURT, A. (1997). Numerical analysis of interface fracture in concrete using a lattice-type fracture model. *International Journal of Damage Mechanics*, 6(October), pp. 408-432.

- VAN MIER, J.G.M., VERVUURT, A. (1999). Test methods and modelling for determining the mechanical properties of the ITZ in concrete. *Engineering and transport properties of the interfacial transition zone in cementitious composites* (eds. M.G. Alexander et al.), RILEM, Cachan, pp. 19-52.
- VAN VLIET, M.R.A., VAN MIER, J.G.M., (1996). Experimental investigation of concrete fracture under uniaxial compression. *Mechanics of Cohesive-Frictional Materials*, 1, pp. 115-127.
- VERMEER, P.A., DE BORST, R. (1984). Non-associated plasticity for soils, concrete and rock. *Heron*, 29(3), pp. 1-64.
- VERVUURT, A. (1997). *Interface fracture in concrete*. PhD Thesis, Delft University of Technology, Delft, The Netherlands.
- VOIGT, W. (1889). Über die beziehung zwischen den beiden Elastizitätskonstanten isotroper Körper. (*Wiedemanns Annalen der Physik und Chemie*, 38, pp. 573-587.
- VONK, R.A. (1992). *Softening of concrete loaded in compression*, PhD thesis, Eindhoven University of Technology, Eindhoven, The Netherlands.
- VOYIADJIS, G.Z., ABU-LEBDEH, T.M. (1993). Damage model for concrete using bounding surface concept. *Journal of Engineering Mechanics, ASCE*, 119(9), pp. 1865-1885.
- WALRAVEN, J.C. (1980). *Aggregate interlock: A theoretical and experimental analysis*, PhD thesis, Delft University of Technology, Delft, The Netherlands.
- WANG, J., HUET, C. (1993). A numerical model for studying the influences of pre-existing microcracks and granular character on the fracture of concrete materials and structures. *Micromechanics of Concrete and Cementitious Composites* (ed. C. Huet); Proceedings of the International Conference JMX 13, Lausanne, Switzerland, pp. 229-240.
- WEIHE, S., KRÖPLIN, B., DE BORST, R. (1998). Classification of smeared crack models based on material and structural properties. *International Journal of Solids and Structures*, 35(12), pp. 1289-1308.
- WELLS, G.N., SLUYS, L.J., DE BORST, R. (2002). Simulating the propagation of displacement discontinuities in a regularized strain-softening medium. *International Journal for Numerical Methods in Engineering*, 53, pp. 1235-1256.
- WILLAM, K.J., WARNEKE, E.P. (1975). Constitutive model for the triaxial behaviour of concrete. *Concrete structures subjected to triaxial stresses*; colloquium, Bergamo, IABSE Report 19, Part III, pp. 1-30.
- WITTMANN, F.H. (1987). Structure of concrete and crack formation. *Fracture of Non-Metallic Materials* (eds. K.P. Herrmann & L.H. Larsson); Proc. of the 5<sup>th</sup> Advanced Seminar on Fracture Mechanics, Ispra, Italy, pp. 309-340.
- WITTMANN, F.H., SADOUKI, H., STEIGER, T. (1993). Experimental and numerical study of effective properties of composite materials. *Micromechanics of Concrete and Cementitious Composites* (Ed. C. Huet); Proc. of the International Conference JMX 13, Lausanne, Switzerland, pp. 59-82.
- YANG, C.C. (1998). Effect of the transition zone on the elastic moduli of mortar. *Cement and Concrete Research*, 28(5), pp. 727-736.
- YAZDANI, S., SCHREYER, H.L. (1990). Combined plasticity and damage mechanics model for plain concrete. *Journal of Engineering Mechanics, ASCE*, 116(7), pp. 1435-1450.
- ZAITSEV, Y.B., WITTMANN, F.H. (1981). Simulation of crack propagation and failure of concrete. *Materials and Structures, RILEM*, 14(83), pp. 357-365.
- ZAMAN, M., NAJJAR, Y.M., FARUQUE, M.O. (1993). Modelling of stress-strain behaviour of plain concrete using a plasticity framework. *Materials and Structures, RILEM*, 26, pp. 129-135.

- ZHAO, X.-H., CHEN, W.F. (1996). Stress analysis of a sand particle with interface in cement paste under uniaxial loading. *International Journal for Numerical and Analytical Methods in Geomechanics*, 20, pp. 275-285.
- ZHAO, X.-H., CHEN, W.F. (1998). Effective elastic moduli of concrete with interface layer. *Computers & Structures*, 66, pp. 275-288.
- ZHONG, X., CHANG, C.S. (1999). Micromechanical modeling for behavior of cementitious granular materials. *Journal of Engineering Mechanics, ASCE*, 125(11), pp. 1280-1285.

## APPENDIX A

### ELASTIC PROPERTIES OF THE RVE

The effective elastic moduli of the RVE, in terms of an effective modulus of elasticity ( $\bar{E}$ ) and Poisson's ratio ( $\bar{\nu}$ ), can be determined by considering both the heterogeneous RVE and an equivalent homogeneous solid with an overall geometry identical to that of the RVE. By applying the same boundary conditions to the heterogeneous RVE as well as the homogeneous solid, and comparing the mechanical response to these boundary conditions, the effective elastic moduli of the RVE can be determined.

Generally, the mechanical responses are not identical along the entire boundary. Only the average mechanical response of the homogeneous solid can be compared with the average mechanical response of the heterogeneous RVE. Here, two different approaches are pursued:

1. The same stress boundary conditions to the RVE and the homogeneous solid are applied and the resulting average strains or boundary displacements are compared (macrostress prescribed approach).
2. The same displacement boundary conditions are applied and the resulting average stresses are compared (macrostrain prescribed approach).

The stress and displacement fields of the RVE are computed for two elementary loading cases (plane strain). Based on these solutions the effective elastic moduli of the RVE in plane strain are computed according to the macrostress as well as the macrostrain prescribed approach.

#### A.1 General equations in cylindrical coordinates

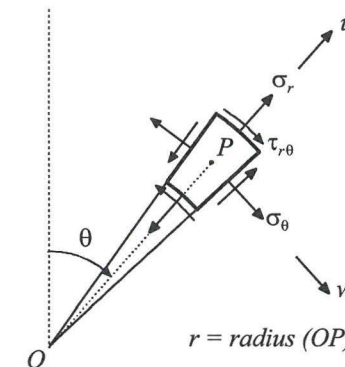


Figure A.1. Stresses and displacements in cylindrical coordinates.

According to the notations displayed in figure A.1, the partial differential equation of compatibility of two-dimensional problems becomes

$$\left(\frac{\partial^2}{\partial r^2} + \frac{1}{r} \frac{\partial}{\partial r} + \frac{1}{r^2} \frac{\partial^2}{\partial \theta^2}\right) \left(\frac{\partial^2 f}{\partial r^2} + \frac{1}{r} \frac{\partial f}{\partial r} + \frac{1}{r^2} \frac{\partial^2 f}{\partial \theta^2}\right) = 0 \quad (\text{A.1})$$

where  $f$  is the stress function as a function of  $r$  and  $\theta$ . When body forces are zero the stresses in cylindrical coordinates take the form

$$\begin{aligned} \sigma_r &= \frac{1}{r} \frac{\partial f}{\partial r} + \frac{1}{r^2} \frac{\partial^2 f}{\partial \theta^2} \\ \sigma_\theta &= \frac{\partial^2 f}{\partial r^2} \\ \tau_{r\theta} &= -\frac{\partial}{\partial r} \left( \frac{1}{r} \frac{\partial f}{\partial \theta} \right) \end{aligned} \quad (\text{A.2})$$

The strains are related to the radial displacement  $u$  and the tangential displacement  $w$  by

$$\begin{aligned} \varepsilon_r &= \frac{\partial u}{\partial r} \\ \varepsilon_\theta &= \frac{u}{r} + \frac{\partial w}{r \partial \theta} \\ \gamma_{r\theta} &= \frac{\partial u}{r \partial \theta} + \frac{\partial w}{\partial r} - \frac{w}{r} \end{aligned} \quad (\text{A.3})$$

## A.2 Elementary state I: Uniform radial boundary stress (or displacement)

In this case the stress function depends on  $r$  only and the mechanical response on the boundary of both the RVE and the homogeneous solid will take the form of a uniform radial stress distribution  $p$  (figure A.2). For convenience, a unit boundary stress ( $p = 1$ ) may be considered<sup>1</sup>.

When the stress function depends on  $r$  only, equation (A.1) becomes

$$\left(\frac{\partial^2}{\partial r^2} + \frac{1}{r} \frac{\partial}{\partial r}\right) \left(\frac{\partial^2 f}{\partial r^2} + \frac{1}{r} \frac{\partial f}{\partial r}\right) = \frac{\partial^4 f}{\partial r^4} + \frac{2}{r} \frac{\partial^3 f}{\partial r^3} - \frac{1}{r^2} \frac{\partial^2 f}{\partial r^2} + \frac{1}{r^3} \frac{\partial f}{\partial r} = 0 \quad (\text{A.4})$$

This ordinary differential equation can be reduced to a linear differential equation with constant coefficients by introducing a new variable  $t$  such that  $r = e^t$ . The general solution of equation (A.4) then becomes

$$f = A \log r + Br^2 \log r + Cr^2 + D \quad (\text{A.5})$$

<sup>1</sup> The magnitude of  $p$  is not of interest when comparing the stress/strain fields of the homogeneous and heterogeneous solids, provided that the boundary stress is equal on both solids.

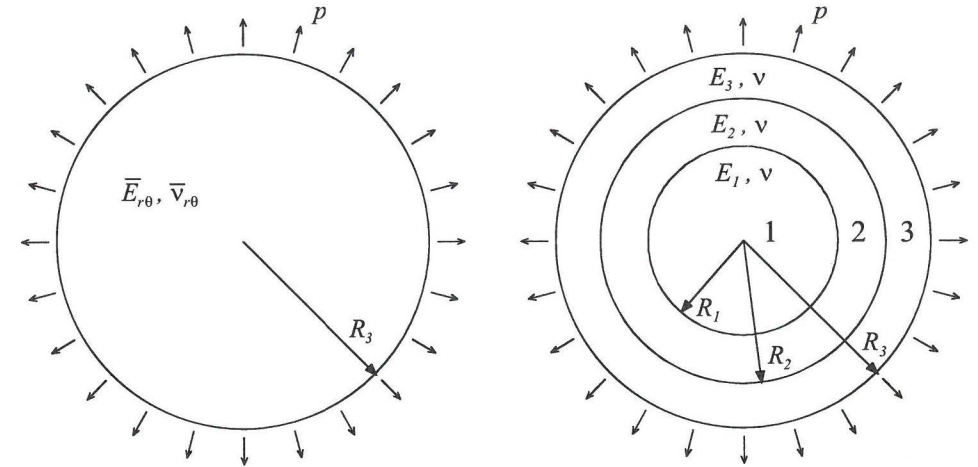


Figure A.2. Homogeneous solid and heterogeneous RVE.

For a uniform radial stress distribution, the stress components are

$$\begin{aligned} \sigma_r &= \frac{1}{r} \frac{\partial f}{\partial r} = \frac{A}{r^2} + B(1 + 2 \log r) + 2C \\ \sigma_\theta &= \frac{\partial^2 f}{\partial r^2} = -\frac{A}{r^2} + B(3 + 2 \log r) + 2C \\ \tau_{r\theta} &= 0 \end{aligned} \quad (\text{A.6})$$

Substituting now the expressions for the strain components (A.3) into the equations of Hooke's law for plane strain,

$$\begin{aligned} \varepsilon_r &= \frac{1+\nu}{E} (\sigma_r(1-\nu) - \nu\sigma_\theta) \\ \varepsilon_\theta &= \frac{1+\nu}{E} (\sigma_\theta(1-\nu) - \nu\sigma_r) \\ \gamma_{r\theta} &= \frac{1}{G} \tau_{r\theta} \end{aligned} \quad (\text{A.7})$$

the following expressions for  $u$  and  $w$  are obtained.

$$\begin{aligned} \frac{\partial u}{\partial r} = \varepsilon_r &= \frac{1+\nu}{E} \left( \frac{A}{r^2} + B(1-4\nu) + 2B(1-2\nu) \log r + 2C(1-2\nu) \right) \\ u &= \frac{1+\nu}{E} \left( -\frac{A}{r} - Br + 2Br(1-2\nu) \log r + 2C(1-2\nu)r \right) + g(\theta) \end{aligned}$$

where  $g(\theta)$  is a function of  $\theta$  only.



$$\frac{\partial w}{\partial \theta} = r \varepsilon_{\theta} - u = \frac{1+\nu}{E} \left( 4Br(1-\nu) \right) - g(\theta)$$

$$w = \frac{1+\nu}{E} \left( 4Br(1-\nu) \theta \right) - \int g(\theta) d\theta + g_1(r)$$

where  $g_1(r)$  is a function of  $r$  only. Substituting the expressions for  $u$  and  $w$  in the expression for the shear strain in equation (A.3), we find

$$\frac{1}{r} \frac{\partial g(\theta)}{\partial \theta} + \frac{\partial g_1(r)}{\partial r} + \frac{1}{r} \int g(\theta) d\theta - \frac{1}{r} g_1(r) = 0$$

from which

$$g_1(r) = Fr \quad g(\theta) = H \sin \theta + K \cos \theta$$

The constants  $F$ ,  $K$  and  $H$  can be determined from the conditions of constraint. For the loading case considered these conditions are

$$w = 0 \quad \frac{\partial w}{\partial r} = 0 \quad \text{for all } \theta$$

From this it follows that  $F = K = H = B = 0$ . The expressions for the radial and tangential stress components and the radial displacement now become

$$\begin{aligned} \sigma_r &= \frac{A}{r^2} + 2C \\ \sigma_{\theta} &= -\frac{A}{r^2} + 2C \\ u &= \frac{1+\nu}{E} \left( -\frac{A}{r} + 2Cr(1-2\nu) \right) \end{aligned} \quad (\text{A.8})$$

### A.2.1 Homogeneous solid

As the stresses cannot become infinite when  $r$  approaches to zero, the constant  $A$  in equation (A.8) equals zero. As the radial stress at the boundary equals  $p$ , the constant  $C$  is equal to  $\frac{1}{2}p$ . The expressions for the stresses and displacement herewith read

$$\begin{aligned} \sigma_r(r) &= \sigma_{\theta}(r) = p \\ u(r) &= \frac{pr(1-\bar{\nu}-2\bar{\nu}^2)}{\bar{E}} \end{aligned}$$

Making a distinction between the elastic moduli in the out-of-plane direction ( $\bar{E}_z, \bar{\nu}_{z1}, \bar{\nu}_{z2}$ ) and the elastic moduli in  $\theta$ - or  $r$ -direction, the radial and out-of-plane normal strain components are given by

$$\varepsilon_r = \frac{\sigma_r}{\bar{E}_{r\theta}} - \frac{\sigma_{\theta}}{\bar{E}_{r\theta}} \bar{\nu}_{r\theta} - \frac{\sigma_z}{\bar{E}_z} \bar{\nu}_{z1} = \frac{p(1-\bar{\nu}_{r\theta})}{\bar{E}_{r\theta}} - \frac{\sigma_z}{\bar{E}_z} \bar{\nu}_{z1}$$

$$\varepsilon_z (= 0) = \frac{\sigma_z}{\bar{E}_z} - \frac{\sigma_r + \sigma_{\theta}}{\bar{E}_{r\theta}} \bar{\nu}_{z2} \rightarrow \frac{\sigma_z}{\bar{E}_z} = \frac{2p}{\bar{E}_{r\theta}} \bar{\nu}_{z2}$$

Because Poisson's ratio is identical for all layers of the RVE, the layers do not interact when a uniform normal strain in out-of-plane direction is imposed. Consequently,  $\bar{E}_z$  and  $\bar{\nu}_{z1}$  are given by

$$\bar{E}_z = \frac{E_1 R_1^2 + E_1 (R_2 - R_1)^2 + E_1 (R_3 - R_2)^2}{R_3^2} \quad (\text{A.9})$$

$$\bar{\nu}_{z1} = \nu$$

From the set of equations above a new expression for  $u(r)$  is derived.

$$u(r) = \frac{pr(1-\bar{\nu}_{r\theta}-2\nu\bar{\nu}_{z2})}{\bar{E}_{r\theta}} \quad (\text{A.10})$$

### A.2.2 Heterogeneous RVE

For each of the three regions (1, 2 and 3) of the heterogeneous RVE (see figure A.2), different values are found for the constants  $A$  and  $C$  of the general equation of compatibility. This means that six constants are unknown:

$$A_1, C_1, A_2, C_2, A_3, C_3$$

For region 1 the same argumentation applies as for the homogeneous solid, that the stresses cannot become infinite when  $r$  approaches zero. Therefore,  $A_1$  equals zero. The other unknowns can be determined from the following conditions of constraint:

$$\begin{aligned} \sigma_r(R_3) &= p \\ \sigma_r(R_2)_3 &= \sigma_r(R_2)_2 \\ \sigma_r(R_1)_2 &= \sigma_r(R_1)_1 \\ u(R_2)_3 &= u(R_2)_2 \\ u(R_1)_2 &= u(R_1)_1 \end{aligned}$$

(Subscripts 1, 2, 3 refer to regions 1, 2 and 3 of the heterogeneous RVE)

Inserting the expressions for the radial stresses and displacements (A.8) into the above conditions of constraint yields the following system of linear equations (Poisson's ratio is assumed equal for all three regions)

$$\frac{A_3}{R_3^2} + 2C_3 = p \quad (p = 1 \text{ in solving the linear system of equations})$$

$$\frac{A_3}{R_2^2} + 2C_3 = \frac{A_2}{R_2^2} + 2C_2$$

$$\frac{A_2}{R_1^2} + 2C_2 = 2C_1 \quad (A_1 = 0)$$

$$\frac{1+\nu}{E_3} \left( -\frac{A_3}{R_2} + 2C_3 R_2 (1-2\nu) \right) = \frac{1+\nu}{E_2} \left( -\frac{A_2}{R_2} + 2C_2 R_2 (1-2\nu) \right)$$

$$\frac{1+\nu}{E_2} \left( -\frac{A_2}{R_1} + 2C_2 R_1 (1-2\nu) \right) = \frac{1+\nu}{E_1} \left( 2C_1 R_1 (1-2\nu) \right) \quad (A_1 = 0)$$

Solving this system of linear equations yields

$$C_1 = \frac{1}{2} \alpha_{01} \alpha_{02}$$

$$C_2 = \frac{\alpha_{02} (R_2^2 - \alpha_{01} R_1^2)}{2(R_2^2 - R_1^2)}$$

$$C_3 = \frac{R_3^2 - \alpha_{02} R_2^2}{2(R_3^2 - R_2^2)}$$

$$A_1 = 0$$

$$A_2 = \frac{\alpha_{02} (\alpha_{01} - 1) R_1^2 R_2^2}{R_2^2 - R_1^2}$$

$$A_3 = \frac{(\alpha_{02} - 1) R_2^2 R_3^2}{R_3^2 - R_2^2}$$

with

$$\alpha_{01} = \frac{2R_2^2}{\frac{R_2^2 - R_1^2}{1-\nu} \left( \frac{E_2}{E_1} (1-2\nu) + \nu \right) + R_2^2 + R_1^2}$$

$$\beta_{01} = \frac{(1-2\alpha_{01}) R_1^2 + R_2^2}{R_2^2 - R_1^2}$$

$$\alpha_{02} = \frac{2R_3^2}{\frac{R_3^2 - R_2^2}{1-\nu} \left( \frac{E_3}{E_2} (\beta_{01} - \nu(\beta_{01} + 1)) + \nu \right) + R_3^2 + R_2^2}$$

Inserting the above values into equation (A.8) yields the final expressions for the stress and displacement components

$$\left. \begin{aligned} \sigma_r(r) &= p \left( \frac{A_j}{r^2} + 2C_j \right) \\ \sigma_\theta(r) &= p \left( -\frac{A_j}{r^2} + 2C_j \right) \\ u(r) &= p \frac{1+\nu}{E_j} \left( -\frac{A_j}{r} + 2C_j r (1-2\nu) \right) \end{aligned} \right\} j=1,2,3 \quad (\text{A.11})$$

( $j$  refers to the regions of the heterogeneous RVE)

### A.2.3 Determination of effective elastic moduli

The effective Poisson's ratio in out-of-plane direction ( $\bar{\nu}_{z2}$ ) can be determined by comparing the average out-of-plane stress ( $\bar{\sigma}_z$ ) of the RVE and the out-of-plane stress of the homogeneous solid with effective Poisson's ratio in out-of-plane direction

$$\sigma_z = 2p \bar{\nu}_{z2} \frac{\bar{E}_z}{\bar{E}_{r\theta}} \quad (\text{Homogeneous solid})$$

$$\bar{\sigma}_z = \frac{2p\nu (\alpha_{01} \alpha_{02} R_1^2 + \alpha_{02} (R_2^2 - \alpha_{01} R_1^2) + R_3^2 - \alpha_{02} R_2^2)}{R_3^2} = 2p\nu \quad (\text{RVE})$$

It appears that in case Poisson's ratio is equal for all parts of the RVE, the effective Poisson's ratio in out-of-plane direction becomes

$$\bar{\nu}_{z2} = \nu \frac{\bar{E}_{r\theta}}{\bar{E}_z} \quad (\text{A.12})$$

(With  $\bar{E}_z$  according to equation (A.9).)

Substitution of equation (A.12) in (A.10) results in the following expression for the radial displacement at the boundary of the homogeneous solid

$$u(R_3) = p R_3 \left( \frac{1 - \bar{\nu}_{r\theta}}{\bar{E}_{r\theta}} - \frac{2\nu^2}{\bar{E}_z} \right) \quad (\text{Homogeneous solid})$$

The radial displacement at the boundary of the RVE is given by equation (A.11) with  $A_j = A_3$  and  $C_j = C_3$

$$u(R_3) = p R_3 \frac{1+\nu}{E_3} \left( (1-\nu) \frac{R_2^2 (1-2\alpha_{02}) + R_3^2}{R_3^2 - R_2^2} - \nu \right) \quad (\text{RVE})$$

Comparing the radial displacement at the boundary of the homogeneous solid with the radial displacement at the boundary of the RVE leads to one linear relation between the effective in-plane elastic moduli ( $\bar{E}_{r\theta}, \bar{\nu}_{r\theta}$ ).

$$\frac{1 - \bar{\nu}_{r\theta}}{\bar{E}_{r\theta}} = \frac{2\nu^2}{\bar{E}_z} + \frac{1 + \nu}{E_3} \left( (1 - \nu) \frac{R_2^2(1 - 2\alpha_{02}) + R_3^2}{R_3^2 - R_2^2} - \nu \right) \quad (\text{A.13})$$

### A.3 Elementary state II: Sine curved radial boundary stress

For elementary state I, the mechanical response of the homogeneous solid and the heterogeneous RVE are identical along the entire boundary. Consequently, the macrostress and macrostrain prescribed solutions are identical for this elementary state. This is not the case for the elementary state II considered in this section. For this loading configuration, the mechanical response of the homogeneous solid and the heterogeneous RVE can only be compared in an average sense. Hence, the macrostress and macrostrain prescribed approaches will result in different solutions. In section A.3.1 the *macrostress* prescribed solution of the stress and displacement fields are determined. Combined with the solution for elementary state I, this results in unique expressions for the effective in-plane elastic moduli. In section A.3.2 the *macrostrain* prescribed solution is combined with the solution for elementary state I. This also results in unique – *however different* – expressions for the effective in-plane elastic moduli. In section A.3.3 both results will be compared upon a set of realistic input data for normal strength concrete.

#### A.3.1 Macrostress prescribed approach

A second relation between the effective in-plane elastic moduli is arrived at when a loading configuration as displayed in figure A.3 is considered. As the macrostress prescribed approach is pursued in this section, the boundary *stresses* of the homogeneous solid and the RVE are equal. For convenience, a sine curved boundary load with maximum magnitude of  $p = 1$  may be considered.

In this case the stress function  $f$  depends on  $r$  and  $\theta$

$$f = \varphi(r) \sin 2\theta$$

The differential equation of compatibility (A.1) now becomes

$$\left( \frac{\partial^2}{\partial r^2} + \frac{1}{r} \frac{\partial}{\partial r} - \frac{4}{r^2} \right) \left( \frac{\partial^2 \varphi}{\partial r^2} + \frac{1}{r} \frac{\partial \varphi}{\partial r} - \frac{4\varphi}{r^2} \right) = \frac{\partial^4 \varphi}{\partial r^4} + \frac{2}{r} \frac{\partial^3 \varphi}{\partial r^3} - \frac{9}{r^2} \frac{\partial^2 \varphi}{\partial r^2} + \frac{9}{r^3} \frac{\partial \varphi}{\partial r} = 0$$

Solving this equation in the same way, as done for the first elementary state, the following general solution for the stress function  $f$  is found

$$f = \left( Ar^4 + Br^2 + \frac{C}{r^2} + D \right) \sin 2\theta$$

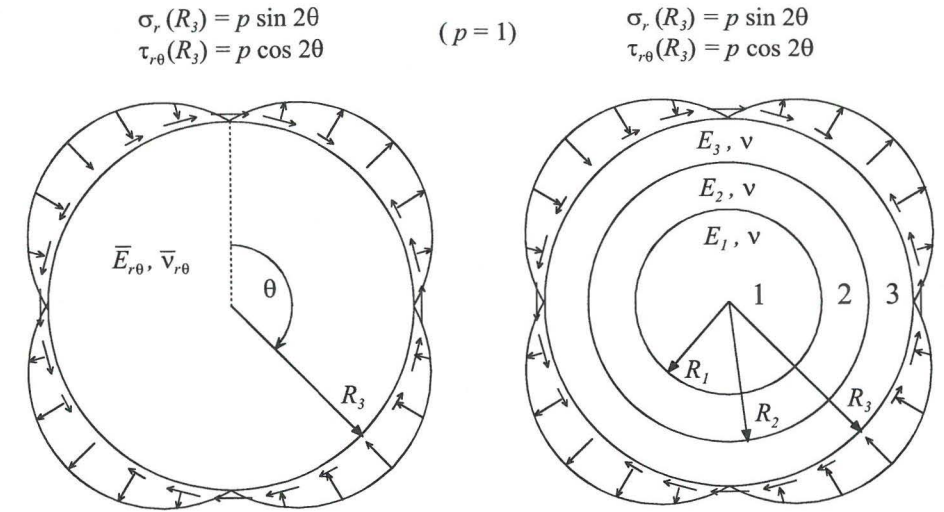


Figure A.3. Sine curved boundary load for homogeneous solid and heterogeneous RVE (macrostress prescribed).

The stress components are

$$\begin{aligned} \sigma_r &= \frac{1}{r} \frac{\partial f}{\partial r} + \frac{1}{r^2} \frac{\partial^2 f}{\partial \theta^2} = \left( -2B - \frac{6C}{r^4} - \frac{4D}{r^2} \right) \sin 2\theta \\ \sigma_\theta &= \frac{\partial^2 f}{\partial r^2} = \left( 12Ar^2 + 2B + \frac{6C}{r^4} \right) \sin 2\theta \\ \tau_{r\theta} &= -\frac{\partial}{\partial r} \left( \frac{1}{r} \frac{\partial f}{\partial \theta} \right) = \left( -6Ar^2 - 2B + \frac{6C}{r^4} + \frac{2D}{r^2} \right) \cos 2\theta \end{aligned} \quad (\text{A.14})$$

Applying Hooke's law for plane strain (A.7), the following expressions for the radial and tangential displacements are found

$$\begin{aligned} \frac{\partial u}{\partial r} = \epsilon_r &= \frac{(1 + \nu) \sin 2\theta}{E} \left( -12\nu Ar^2 - 2B - \frac{6C}{r^4} - \frac{4D(1 - \nu)}{r^2} \right) \\ u &= \frac{(1 + \nu) \sin 2\theta}{E} \left( -4\nu Ar^3 - 2Br + \frac{2C}{r^3} + \frac{4(1 - \nu)D}{r} \right) + g(\theta) \\ \frac{\partial w}{\partial \theta} = r\epsilon_\theta - u &= \frac{(1 + \nu) \sin 2\theta}{E} \left( 12Ar^3(1 - \frac{2}{3}\nu) + 4Br + \frac{4C}{r^3} - \frac{4D(1 - 2\nu)}{r} \right) - g(\theta) \\ w &= \frac{(1 + \nu) \cos 2\theta}{E} \left( -6Ar^3(1 - \frac{2}{3}\nu) - 2Br - \frac{2C}{r^3} + \frac{2(1 - 2\nu)D}{r} \right) - \int g(\theta) d\theta + g_1(r) \end{aligned}$$

where  $g(\theta)$  is a function of  $\theta$  only and  $g_1(r)$  is a function of  $r$  only.

As the lines  $\theta = -\frac{1}{4}\pi$  and  $\theta = \frac{1}{4}\pi$  are axes of symmetry, the following conditions of constraint apply

$$w = \frac{\partial w}{\partial r} = \frac{\partial u}{\partial \theta} = 0 \quad \text{for } \theta = -\frac{1}{4}\pi \text{ and } \theta = \frac{1}{4}\pi$$

From these conditions it follows that both  $g_1(r)$  and  $g(\theta)$  are equal to zero. The expressions for the radial and tangential displacement consequently are

$$\begin{aligned} u &= \frac{(1+\nu)\sin 2\theta}{E} \left( -4\nu Ar^3 - 2Br + \frac{2C}{r^3} + \frac{4(1-\nu)D}{r} \right) \\ w &= \frac{(1+\nu)\cos 2\theta}{E} \left( -6Ar^3(1-\frac{2}{3}\nu) - 2Br - \frac{2C}{r^3} + \frac{(2-4\nu)D}{r} \right) \end{aligned} \quad (\text{A.15})$$

### A.3.1.1 Homogeneous solid

As infinite stresses are physically impossible, the constants  $C$  and  $D$  in the equations (A.14) and (A.15) are zero. The other constants can be determined from the following conditions of constraint

$$\sigma_r(R_3) = p \sin 2\theta$$

$$\tau_{r\theta}(R_3) = p \cos 2\theta$$

Inserting the expressions for the stresses (A.14) yields

$$-2B = p$$

$$-6Ar^2 - 2B = p$$

From this it can be concluded that  $B = -\frac{1}{2}p$  and  $A = 0$ . Inserting these values into (A.14) and (A.15) yields the final expressions for the stress and displacement fields.

$$\sigma_r(r, \theta) = p \sin 2\theta$$

$$\sigma_\theta(r, \theta) = -p \sin 2\theta$$

$$\tau_{r\theta}(r, \theta) = p \cos 2\theta$$

$$u(r, \theta) = \frac{p(1+\bar{\nu}_{r\theta})r \sin 2\theta}{\bar{E}_{r\theta}} \quad (\text{A.16})$$

$$w(r, \theta) = \frac{p(1+\bar{\nu}_{r\theta})r \cos 2\theta}{\bar{E}_{r\theta}}$$

### A.3.1.2 Heterogeneous RVE

For the heterogeneous RVE, twelve constants are unknown

$$A_1, B_1, C_1, D_1, A_2, B_2, C_2, D_2, A_3, B_3, C_3, D_3$$

For zero  $r$  the stresses can not become infinite, so

$$C_1 = D_1 = 0$$

The other unknowns are to be determined from the following conditions of constraint

$$\begin{aligned} \sigma_r(R_3) &= p \sin 2\theta \\ \tau_{r\theta}(R_3) &= p \cos 2\theta \\ \sigma_r(R_2)_3 &= \sigma_r(R_2)_2 \\ \tau_{r\theta}(R_2)_3 &= \tau_{r\theta}(R_2)_2 \\ u(R_2)_3 &= u(R_2)_2 \end{aligned} \quad \left. \begin{aligned} w(R_2)_3 &= w(R_2)_2 \\ \sigma_r(R_1)_2 &= \sigma_r(R_1)_1 \\ \tau_{r\theta}(R_1)_2 &= \tau_{r\theta}(R_1)_1 \\ u(R_1)_2 &= u(R_1)_1 \\ w(R_1)_2 &= w(R_1)_1 \end{aligned} \right\}$$

According to the first and the second condition of constraint the boundary stresses are equal to those of the homogeneous solid. When the expressions (A.14) and (A.15) are inserted into the above equations, the following system of linear equations is generated

$$\begin{aligned} &\left. \begin{aligned} -2B_3 - \frac{6C_3}{R_3^4} - \frac{4D_3}{R_3^2} &= p \\ -6A_3R_3^2 - 2B_3 + \frac{6C_3}{R_3^4} + \frac{2D_3}{R_3^2} &= p \end{aligned} \right\} (p = 1 \text{ in solving the linear system of equations}) \\ &-2B_3 - \frac{6C_3}{R_2^4} - \frac{4D_3}{R_2^2} = -2B_2 - \frac{6C_2}{R_2^4} - \frac{4D_2}{R_2^2} \\ &-6A_3R_2^2 - 2B_3 + \frac{6C_3}{R_2^4} + \frac{2D_3}{R_2^2} = -6A_2R_2^2 - 2B_2 + \frac{6C_2}{R_2^4} + \frac{2D_2}{R_2^2} \\ &\frac{1}{E_3} \left( -2\nu A_3R_2^2 - B_3 + \frac{C_3}{R_2^4} + \frac{2(1-\nu)D_3}{R_2^2} \right) = \frac{1}{E_2} \left( -2\nu A_2R_2^2 - B_2 + \frac{C_2}{R_2^4} + \frac{2(1-\nu)D_2}{R_2^2} \right) \\ &\frac{1}{E_3} \left( -A_3R_2^2(3-2\nu) - B_3 - \frac{C_3}{R_2^4} + \frac{(1-2\nu)D_3}{R_2^2} \right) = \\ &\quad \frac{1}{E_2} \left( -A_2R_2^2(3-2\nu) - B_2 - \frac{C_2}{R_2^4} + \frac{(1-2\nu)D_2}{R_2^2} \right) \\ &-2B_2 - \frac{6C_2}{R_1^4} - \frac{4D_2}{R_1^2} = -2B_1 \\ &-6A_2R_1^2 - 2B_2 + \frac{6C_2}{R_1^4} + \frac{2D_2}{R_1^2} = -6A_1R_1^2 - 2B_1 \\ &\frac{1}{E_2} \left( -2\nu A_2R_1^2 - B_2 + \frac{C_2}{R_1^4} + \frac{2(1-\nu)D_2}{R_1^2} \right) = \frac{1}{E_1} \left( -2\nu A_1R_1^2 - B_1 \right) \\ &\frac{1}{E_2} \left( -A_2R_1^2(3-2\nu) - B_2 - \frac{C_2}{R_1^4} + \frac{(1-2\nu)D_2}{R_1^2} \right) = \frac{1}{E_1} \left( -A_1R_1^2(3-2\nu) - B_1 \right) \end{aligned}$$

Solving this system of linear equations results in the following solution of the unknown constants in the stress and displacement fields of region 3 and 2<sup>2</sup>

$$\begin{aligned} C_3 &= \frac{\beta_5 + \beta_2 \beta_3}{2(\beta_1 \beta_3 - \beta_4)} \\ D_3 &= -2\beta_1 C_3 + \beta_2 \\ A_3 &= \frac{2C_3}{R_3^6} + \frac{D_3}{R_3^4} \\ B_3 &= -\frac{3C_3}{R_3^4} - \frac{2D_3}{R_3^2} - \frac{1}{2} \end{aligned} \quad (\text{A.17})$$

$$\begin{aligned} A_2 &= 2\Gamma_{01}C_3 + \Gamma_{11}D_3 + \Gamma_{21} \\ B_2 &= \Gamma_{02}C_3 + \frac{1}{2}\Gamma_{12}D_3 + \frac{1}{2}\Gamma_{22} \\ C_2 &= \Gamma_{03}C_3 + \frac{1}{2}\Gamma_{13}D_3 + \frac{1}{2}\Gamma_{23} \\ D_2 &= 2\Gamma_{04}C_3 + \Gamma_{14}D_3 + \Gamma_{24} \end{aligned} \quad (\text{A.18})$$

With

$$\begin{aligned} \beta_1 &= \frac{E_2 \left( \frac{\alpha_6}{R_3^6} + \frac{1}{R_2^2} \right) - E_3 \left( \Gamma_{01}\alpha_6 + \frac{\Gamma_{03}}{R_2^2} + \Gamma_{04} \right)}{E_2 \left( \frac{\alpha_6}{R_3^4} + 1 \right) - E_3 \left( \Gamma_{11}\alpha_6 + \frac{\Gamma_{13}}{R_2^2} + \Gamma_{14} \right)} \\ \beta_2 &= \frac{E_3 \left( \Gamma_{21}\alpha_6 + \frac{\Gamma_{23}}{R_2^2} + \Gamma_{24} \right)}{E_2 \left( \frac{\alpha_6}{R_3^4} + 1 \right) - E_3 \left( \Gamma_{11}\alpha_6 + \frac{\Gamma_{13}}{R_2^2} + \Gamma_{14} \right)} \\ \beta_3 &= E_2 \left( \frac{1}{R_3^2} \left( 4 - \frac{3R_2^2}{R_3^2} \right) + \alpha_7 \right) + E_3 \left( 3\Gamma_{11}R_2^2 + \Gamma_{12} - \alpha_7\Gamma_{14} \right) \\ \beta_4 &= E_2 \left( \frac{3}{R_3^4} \left( 1 - \frac{R_2^2}{R_3^2} \right) \right) + E_3 \left( 3\Gamma_{01}R_2^2 + \Gamma_{02} - \alpha_7\Gamma_{04} \right) \\ \beta_5 &= E_2 + E_3 \left( 3\Gamma_{21}R_2^2 + \Gamma_{22} - \alpha_7\Gamma_{24} \right) \end{aligned}$$

<sup>2</sup> The solution of the stress and displacement field of region 1 is not required in the scope of this thesis and is therefore omitted

$$\begin{aligned} \Gamma_{01} &= \frac{\gamma_2}{\gamma_1} & \Gamma_{11} &= \frac{\gamma_3}{\gamma_1} & \Gamma_{21} &= \frac{\alpha_0}{\gamma_1} \\ \Gamma_{04} &= \frac{1}{\alpha_0} (\alpha_1 - \Gamma_{01}(R_2^6 + \alpha_3)) & \Gamma_{14} &= \frac{1}{\alpha_0} (\alpha_2 - \Gamma_{11}(R_2^6 + \alpha_3)) & \Gamma_{24} &= -\frac{1}{\gamma_1} (R_2^6 + \alpha_3) \\ \Gamma_{02} &= \alpha_4\Gamma_{04} - 3R_1^2\Gamma_{01} & \Gamma_{12} &= \alpha_4\Gamma_{14} - 3R_1^2\Gamma_{11} & \Gamma_{22} &= \alpha_4\Gamma_{24} - 3R_1^2\Gamma_{21} \\ \Gamma_{03} &= -R_1^2\Gamma_{04} - \alpha_3\Gamma_{01} & \Gamma_{13} &= -R_1^2\Gamma_{14} - \alpha_3\Gamma_{11} & \Gamma_{23} &= -R_1^2\Gamma_{24} - \alpha_3\Gamma_{21} \\ \alpha_0 &= R_1^2 - R_2^2 & \alpha_3 &= \frac{R_1^6(3-4\nu)(E_1 - E_2)}{E_1 + E_2(3-4\nu)} & \alpha_5 &= \frac{4}{R_2^2} - \frac{3R_1^2}{R_2^4} \\ \alpha_1 &= \frac{R_2^6}{R_3^6} - 1 & \alpha_4 &= \frac{E_1(3-4\nu) + E_2}{R_1^2(E_1 - E_2)} & \alpha_6 &= (3-4\nu)R_2^4 \\ \alpha_2 &= R_2^2 \left( \frac{R_2^4}{R_3^4} - 1 \right) & & & \alpha_7 &= \frac{3-4\nu}{R_2^2} \end{aligned}$$

$$\gamma_1 = (R_2^6 + \alpha_3)(\alpha_4 + \alpha_5) + 3\alpha_0 \left( R_1^2 + \frac{\alpha_3}{R_2^4} \right)$$

$$\gamma_2 = \alpha_1(\alpha_4 + \alpha_5) + 3\alpha_0 \left( \frac{1}{R_3^4} - \frac{1}{R_2^4} \right)$$

$$\gamma_3 = \alpha_2(\alpha_4 + \alpha_5) + 4\alpha_0 \left( \frac{1}{R_3^2} - \frac{1}{R_2^2} \right)$$

Inserting the values of the integration constants into equations (A.14) and (A.15) yields the final expressions for the stress and displacement components

$$\begin{aligned} \sigma_r(r, \theta) &= p \left( -2B_j - \frac{6C_j}{r^4} - \frac{4D_j}{r^2} \right) \sin 2\theta \\ \sigma_\theta(r, \theta) &= p \left( 12A_j r^2 + 2B_j + \frac{6C_j}{r^4} \right) \sin 2\theta \\ \tau_{r\theta}(r, \theta) &= p \left( -6A_j r^2 - 2B_j + \frac{6C_j}{r^4} + \frac{2D_j}{r^2} \right) \cos 2\theta \\ u(r, \theta) &= p \frac{1+\nu}{E_j} \left( -4\nu A_j r^3 - 2B_j r + \frac{2C_j}{r^3} + \frac{4(1-\nu)D_j}{r} \right) \sin 2\theta \\ w(r, \theta) &= p \frac{1+\nu}{E_j} \left( -6A_j r^3 (1 - \frac{2}{3}\nu) - 2B_j r - \frac{2C_j}{r^3} + \frac{(2-4\nu)D_j}{r} \right) \cos 2\theta \end{aligned} \quad (\text{A.19})$$

$$j = 2, 3 \quad (A_j \dots D_j \text{ according to equations (A.17) and (A.18)})$$

### A.3.1.3 Determination of effective elastic moduli

A second relation between the in-plane elastic moduli can be determined by equating the average normal strains in the principal stress directions of the homogeneous solid and the heterogeneous RVE. The Cartesian coordinate system of principal stresses is rotated  $\pi/4$  radians with respect to the  $\theta = 0$  axis (see figure A.4). Indeed, conversion of the boundary stress state in cylindrical coordinates to Cartesian coordinates leads to a simple uniformly distributed stress state with  $\sigma_1 = p$  and  $\sigma_3 = -p$ . Given the symmetry of the problem it suffices to consider the normal average strain in only one direction of principal stress.

The average normal strain in 1-direction (see figure A.4) is equal to the average boundary displacement in 1-direction ( $\bar{u}_1$ ) divided by the average length ( $\bar{\ell}_1$ ).

$$\bar{\epsilon}_1 = \frac{\bar{u}_1}{\bar{\ell}_1} = \frac{\bar{u}_1}{\frac{1}{4}\pi R_3}$$

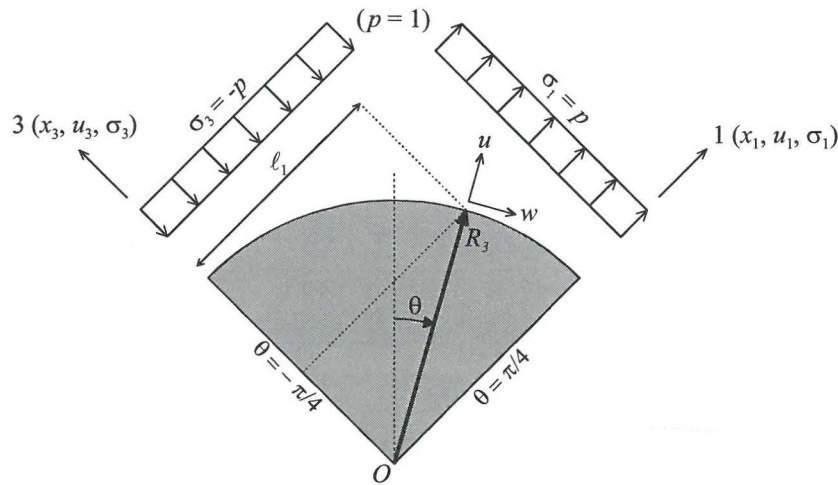


Figure A.4. Computation of average normal strain in principal stress direction.

$$\begin{aligned} \bar{u}_1 &= \frac{1}{R_3} \int_0^{R_3} u_1 dx_3 = \frac{1}{R_3} \int_{-\pi/4}^{\pi/4} \left( u(R_3) \cos\left(\frac{\pi}{4} - \theta\right) + w(R_3) \sin\left(\frac{\pi}{4} - \theta\right) \right) R_3 \cos\left(\frac{\pi}{4} - \theta\right) d\theta \\ &= \int_{-\pi/4}^{\pi/4} \left( u(R_3) \sqrt{\frac{1}{2}(1 + \sin 2\theta)} - w(R_3) \sqrt{\frac{1}{2}(1 - \sin 2\theta)} \right) \sqrt{\frac{1}{2}(1 + \sin 2\theta)} d\theta \end{aligned}$$

With  $u(R_3) = L' \sin 2\theta$  and  $w(R_3) = L'' \cos 2\theta$  this results in the following expression for the average displacement in 1-direction.

$$\begin{aligned} \bar{u}_1 &= \frac{1}{2} \int_{-\pi/4}^{\pi/4} \left( L' (\sin 2\theta + \sin^2 2\theta) + L'' \cos^2 2\theta \right) d\theta \\ &= \frac{1}{4} \left[ L' \left( \theta - \cos 2\theta - \frac{1}{2} \cos 2\theta \sin 2\theta \right) + L'' \left( \theta + \frac{1}{2} \cos 2\theta \sin 2\theta \right) \right]_{-\pi/4}^{\pi/4} \\ &= \frac{1}{8} \pi (L' + L'') \\ \bar{\epsilon}_1 &= \frac{\frac{1}{8} \pi (L' + L'')}{\frac{1}{4} \pi R_3} = \frac{L' + L''}{2R_3} \end{aligned}$$

Inserting the expressions for  $L'$  and  $L''$  for the homogeneous solid and the RVE (respectively, (A.16) and (A.19)) results in a second relation between the in-plane elastic moduli.

$$\frac{1 + \bar{\nu}_{r\theta}}{\bar{E}_{r\theta}} = \frac{1 + \nu}{E_3} \left( -3A_3 R_3^2 - 2B_3 + \frac{(3-4\nu)D_3}{R_3^2} \right) \quad (\text{A.20})$$

Having established two independent mathematical relations [(A.13) and (A.20)] between the effective in-plane Young's modulus and Poisson's ratio, the final expressions for these quantities can now be calculated

$$\begin{aligned} \bar{E}_{r\theta} &= \frac{2}{\delta_1 + \delta_2} \\ \bar{\nu}_{r\theta} &= \frac{\delta_2 - \delta_1}{\delta_1 + \delta_2} \end{aligned} \quad (\text{A.21})$$

With

$$\begin{aligned} \delta_1 &= \frac{1 + \nu}{E_3} \left( (1 - \nu) \frac{R_2^2 (1 - 2\alpha_{02}) + R_3^2}{R_3^2 - R_2^2} - \nu \right) + \frac{2\nu^2}{E_z} \\ \delta_2 &= \frac{1 + \nu}{E_3} \left( -3A_3 R_3^2 - 2B_3 + \frac{(3-4\nu)D_3}{R_3^2} \right) \end{aligned}$$

( $\bar{E}_z$  according to equation (A.9);  $A_3, B_3, C_3$  and  $D_3$  according to equation (A.17))

### A.3.2 Macrostrain prescribed approach

In this section the macrostrain prescribed approach is pursued, i.e. the boundary displacements of the homogeneous solid and the RVE are equal. This implies for the present loading configuration (elementary state II) that the boundary stresses of the RVE are not equal to the boundary stresses of the homogeneous solid (see figure A.5).

Instead of introducing the imposed displacement boundary conditions as shown in figure A.5 directly into the set of linear equations, a somewhat different approach is chosen. In order to keep the set of equations nearly similar to that obtained by the macrostress approach, the two imposed *displacement* conditions of constraint are replaced by four *equivalent* (mixed) conditions of constraint at the outer boundary.

$$\left. \begin{aligned} u(R_3) &= L \sin 2\theta \\ w(R_3) &= L \cos 2\theta \end{aligned} \right\} \begin{aligned} &\equiv \left. \begin{aligned} \sigma_r(R_3) &= p \sin 2\theta \\ \tau_{r\theta}(R_3) &= p \cos 2\theta \end{aligned} \right\} \text{homogeneous solid} \\ &\left. \begin{aligned} \sigma_r(R_3) &= p' \sin 2\theta \\ u(R_3) &= w(R_3) \tan 2\theta \end{aligned} \right\} \text{heterogeneous RVE} \end{aligned}$$

The second condition of constraint of the heterogeneous RVE relates the boundary displacements in the same way as in the case of the homogeneous solid. Hence, the boundary displacements of the homogeneous solid and the heterogeneous RVE can be set exactly the same by choosing a specific ratio between  $p$  and  $p'$ . By performing this operation in section A.3.2.2, the original conditions of constraint of equal displacements along the entire boundaries of the homogeneous solid and the heterogeneous RVE are satisfied. The required second relation between the effective in-plane elastic moduli is finally determined by comparing the average normal stresses of the homogeneous solid and the heterogeneous RVE in the direction of the principal strains.

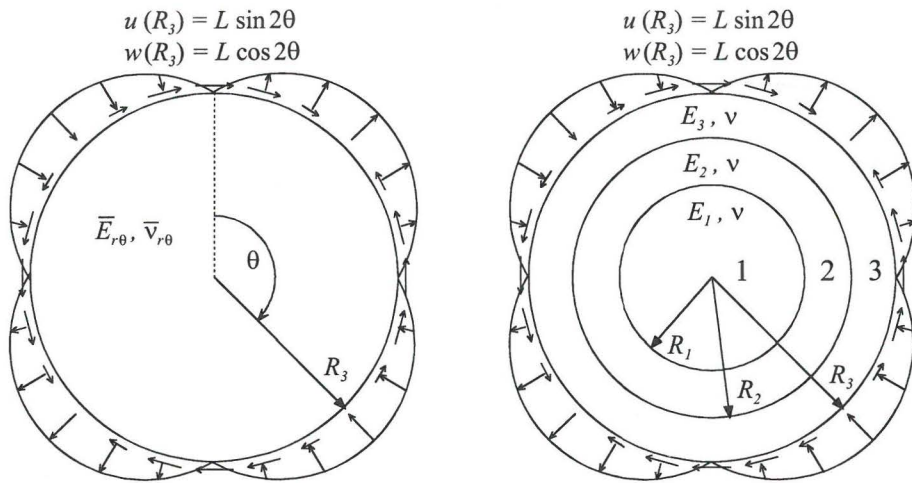


Figure A.5. Sine curved boundary displacement for homogeneous solid and heterogeneous RVE (macrostrain prescribed).

The general equations of section A.3.1 are valid for the macrostress prescribed approach as well as the macrostrain prescribed approach. This means that the expressions (A.16) for the homogeneous solid also apply for the macrostrain approach.

$$\begin{bmatrix} \sigma_r \\ \sigma_\theta \\ \tau_{r\theta} \\ u \\ w \end{bmatrix} = p \begin{bmatrix} \sin 2\theta \\ -\sin 2\theta \\ \cos 2\theta \\ \frac{(1 + \bar{\nu}_{r\theta})r \sin 2\theta}{\bar{E}_{r\theta}} \\ \frac{(1 + \bar{\nu}_{r\theta})r \cos 2\theta}{\bar{E}_{r\theta}} \end{bmatrix} \quad (\text{Homogeneous solid})$$

This leaves the determination of new expressions for the heterogeneous RVE, as these expressions change because of the introduction of *mixed* instead of pure *stress* conditions of constraint at the outer boundary.

#### A.3.2.1 Heterogeneous RVE

For the heterogeneous RVE, the first and second conditions of constraint at the outer boundary are different (conditions in section A.3.1.2)

$$\sigma_r(R_3) = p \sin 2\theta \rightarrow \sigma_r(R_3) = p' \sin 2\theta$$

$$\tau_{r\theta}(R_3) = p \cos 2\theta \rightarrow u(R_3) = w(R_3) \tan 2\theta$$

Inserting (A.14) and (A.15) into the above equations yields the following expressions

$$-2B_3 - \frac{6C_3}{r^4} - \frac{4D_3}{r^2} = p' \quad (=1 \text{ in this section})$$

$$A_3 R_3^2 (3 - 4\nu) + \frac{2C_3}{R_3^4} + \frac{D_3}{R_3^2} = 0$$

Solving the set of linear equations with this modification results in the following solution of the unknown constants in the stress and displacement fields of region 2 and 3.

$$C_3 = \frac{\beta_5 + \beta_2 \beta_3}{2(\beta_1 \beta_3 - \beta_4)}$$

$$D_3 = -2\beta_1 C_3 + \beta_2$$

$$A_3 = -\frac{2C_3}{(3 - 4\nu)R_3^6} - \frac{D_3}{(3 - 4\nu)R_3^4}$$

$$B_3 = -\frac{3C_3}{R_3^4} - \frac{2D_3}{R_3^2} - \frac{1}{2}$$

(A.22)

$$\begin{aligned}
A_2 &= 2\Gamma_{01}C_3 + \Gamma_{11}D_3 + \Gamma_{21} \\
B_2 &= \Gamma_{02}C_3 + \frac{1}{2}\Gamma_{12}D_3 + \frac{1}{2}\Gamma_{22} \\
C_2 &= \Gamma_{03}C_3 + \frac{1}{2}\Gamma_{13}D_3 + \frac{1}{2}\Gamma_{23} \\
D_2 &= 2\Gamma_{04}C_3 + \Gamma_{14}D_3 + \Gamma_{24}
\end{aligned} \tag{A.23}$$

With

$$\begin{aligned}
\beta_1 &= \frac{E_2 \left( \frac{1}{R_2^2} - \frac{R_2^4}{R_3^6} \right) - E_3 \left( \Gamma_{01}\alpha_6 + \frac{\Gamma_{03}}{R_2^2} + \Gamma_{04} \right)}{E_2 \left( 1 - \frac{R_2^4}{R_3^4} \right) - E_3 \left( \Gamma_{11}\alpha_6 + \frac{\Gamma_{13}}{R_2^2} + \Gamma_{14} \right)} \\
\beta_2 &= \frac{E_3 \left( \Gamma_{21}\alpha_6 + \frac{\Gamma_{23}}{R_2^2} + \Gamma_{24} \right)}{E_2 \left( 1 - \frac{R_2^4}{R_3^4} \right) - E_3 \left( \Gamma_{11}\alpha_6 + \frac{\Gamma_{13}}{R_2^2} + \Gamma_{14} \right)} \\
\beta_3 &= E_2 \left( \frac{1}{R_3^2} \left( \frac{3}{\alpha_7 R_3^2} + 4 \right) + \alpha_7 \right) + E_3 (3\Gamma_{11}R_2^2 + \Gamma_{12} - \alpha_7\Gamma_{14}) \\
\beta_4 &= E_2 \left( \frac{3}{R_3^4} \left( \frac{1}{\alpha_7 R_3^2} + 1 \right) \right) + E_3 (3\Gamma_{01}R_2^2 + \Gamma_{02} - \alpha_7\Gamma_{04}) \\
\beta_5 &= E_2 + E_3 (3\Gamma_{21}R_2^2 + \Gamma_{22} - \alpha_7\Gamma_{24}) \\
\alpha_1 &= -\frac{R_2^6}{(3-4\nu)R_3^6} - 1 \\
\alpha_2 &= -R_2^2 \left( \frac{R_2^4}{(3-4\nu)R_3^4} + 1 \right) \\
&\left. \begin{array}{l} \alpha_0, \alpha_3 \dots \alpha_7 \\ \gamma_1 \dots \gamma_3 \\ \Gamma_{01} \dots \Gamma_{04}, \Gamma_{11} \dots \Gamma_{14}, \Gamma_{21} \dots \Gamma_{24} \end{array} \right\} \text{the same as in macrostress approach}
\end{aligned}$$

### A.3.2.2 Determination of effective elastic moduli

For the macrostrain prescribed approach, the second relation between the in-plane elastic moduli can be determined by equating the *average* stresses and the *exact* boundary displacements of the homogeneous solid and the heterogeneous RVE. As the tangential boundary displacement relative to the radial boundary displacement is equal for both the RVE and the homogeneous solid, equating only the radial boundary displacements suffices.

$$\frac{(1+\bar{\nu}_{r\theta})}{\bar{E}_{r\theta}} p R_3 = \frac{(1+\nu)}{E_3} \left( -4\nu A_3 R_3^3 - 2B_3 R_3 + \frac{2C_3}{R_3^3} + \frac{4(1-\nu)D_3}{R_3} \right) p' \tag{A.24}$$

The boundary stresses of the homogeneous solid and heterogeneous RVE are not exactly the same, but only in an average sense. The volume average of the normal stress in 1-direction (see figure A.4) is given by

$$\begin{aligned}
\bar{\sigma}_y &= \frac{\int_0^{R_3} \sigma_1 \ell_1 dx_3}{\frac{1}{4}\pi R_3^2} = \frac{4}{\pi R_3^2} \int_{-\frac{\pi}{4}}^{\frac{\pi}{4}} \left( \sigma_r(R_3) \cos\left(\frac{\pi}{4} - \theta\right) + \tau_{r\theta}(R_3) \sin\left(\frac{\pi}{4} - \theta\right) \right) R_3^2 \cos\left(\frac{\pi}{4} - \theta\right) d\theta \\
&= \frac{4}{\pi} \int_{-\frac{\pi}{4}}^{\frac{\pi}{4}} \left( \sigma_r(R_3) \sqrt{\frac{1}{2}(1+\sin 2\theta)} - \tau_{r\theta}(R_3) \sqrt{\frac{1}{2}(1-\sin 2\theta)} \right) \sqrt{\frac{1}{2}(1+\sin 2\theta)} d\theta
\end{aligned}$$

With  $\sigma_r(R_3) = p' \sin 2\theta$  and  $\tau_{r\theta}(R_3) = p'' \cos 2\theta$  this results in the following expression for the heterogeneous RVE.

$$\begin{aligned}
\bar{\sigma}_1 &= \frac{2}{\pi} \int_{-\frac{\pi}{4}}^{\frac{\pi}{4}} \left( p' (\sin 2\theta + \sin^2 2\theta) + p'' \cos^2 2\theta \right) d\theta \\
&= \frac{1}{\pi} \left[ p' \left( \theta - \cos 2\theta - \frac{1}{2} \cos 2\theta \sin 2\theta \right) + p'' \left( \theta + \frac{1}{2} \cos 2\theta \sin 2\theta \right) \right]_{-\frac{\pi}{4}}^{\frac{\pi}{4}} \\
&= \frac{1}{2} (p' + p'')
\end{aligned}$$

For the homogeneous solid, the volume average of the normal stress in 1-direction equals  $p$ . Equating the average boundary stresses and inserting the expressions for the boundary stresses of the RVE, i.e.  $p'$  and  $p''$  (refer (A.14)), gives

$$\begin{aligned}
p &= \frac{1}{2} (p' + p'') \\
&= \left( -3A_3 R_3^2 - 2B_3 - \frac{D_3}{R_3^2} \right) p' \quad \text{or} \quad p' = \frac{p}{-3A_3 R_3^2 - 2B_3 - \frac{D_3}{R_3^2}} \tag{A.25}
\end{aligned}$$



Inserting equation (A.25) into equation (A.24) sets the required second relation between the in-plane elastic moduli

$$\frac{1 + \bar{\nu}_{r\theta}}{\bar{E}_{r\theta}} = \frac{(1 + \nu) \left( -4\nu A_3 R_3^2 - 2B_3 + \frac{2C_3}{R_3^4} + \frac{4(1-\nu)D_3}{R_3^2} \right)}{E_3 \left( -3A_3 R_3^2 - 2B_3 - \frac{D_3}{R_3^2} \right)} \quad (\text{A.26})$$

Combining equation (A.26) with equation (A.13), which applies for the macrostress approach as well as the macrostrain approach, finally sets the expressions for the effective in-plane Young's modulus and Poisson's ratio according to the macrostrain prescribed approach.

$$\bar{E}_{r\theta} = \frac{2}{\delta_1 + \delta_2}$$

$$\bar{\nu}_{r\theta} = \frac{\delta_2 - \delta_1}{\delta_1 + \delta_2}$$

With

$$\delta_1 = \frac{1 + \nu}{E_3} \left( (1 - \nu) \frac{R_2^2 (1 - 2\alpha_{02}) + R_3^2}{R_3^2 - R_2^2} - \nu \right) + \frac{2\nu^2}{\bar{E}_z}$$

$$\delta_2 = \frac{1 + \nu}{E_3} \frac{\left( -4\nu A_3 R_3^2 - 2B_3 + \frac{2C_3}{R_3^4} + \frac{4(1-\nu)D_3}{R_3^2} \right)}{\left( -3A_3 R_3^2 - 2B_3 - \frac{D_3}{R_3^2} \right)}$$

( $\bar{E}_z$  according to equation (A.9);  $A_3, B_3, C_3$  and  $D_3$  according to equation (A.22))

Inserting the values of the integration constants – (A.22) and (A.23) – into equations (A.14) and (A.15) and making use of the above deduced relation between  $p'$  and  $p$  (A.25), the expressions for the stress and displacement components now read

$$\sigma_r(r, \theta) = p \frac{\left( -2B_j - \frac{6C_j}{r^4} - \frac{4D_j}{r^2} \right)}{\left( -3A_3 R_3^2 - 2B_3 - \frac{D_3}{R_3^2} \right)} \sin 2\theta$$

$$\sigma_\theta(r, \theta) = p \frac{\left( 12A_j r^2 + 2B_j + \frac{6C_j}{r^4} \right)}{\left( -3A_3 R_3^2 - 2B_3 - \frac{D_3}{R_3^2} \right)} \sin 2\theta \quad (\text{A.27a})$$

$$\tau_{r\theta}(r, \theta) = p \frac{\left( -6A_j r^2 - 2B_j + \frac{6C_j}{r^4} + \frac{2D_j}{r^2} \right)}{\left( -3A_3 R_3^2 - 2B_3 - \frac{D_3}{R_3^2} \right)} \cos 2\theta$$

$$u(r, \theta) = p \frac{1 + \nu}{E_j} \frac{\left( -4\nu A_j r^3 - 2B_j r + \frac{2C_j}{r^3} + \frac{4(1-\nu)D_j}{r} \right)}{\left( -3A_3 R_3^2 - 2B_3 - \frac{D_3}{R_3^2} \right)} \sin 2\theta \quad (\text{A.27b})$$

$$w(r, \theta) = p \frac{1 + \nu}{E_j} \frac{\left( -6A_j r^3 (1 - \frac{2}{3}\nu) - 2B_j r - \frac{2C_j}{r^3} + \frac{(2-4\nu)D_j}{r} \right)}{\left( -3A_3 R_3^2 - 2B_3 - \frac{D_3}{R_3^2} \right)} \cos 2\theta$$

$j = 2, 3$  ( $A_j \dots D_j$  according to equations (A.22) and (A.23))

### A.3.3 Comparison of results from the macrostress and macrostrain approach

The in-plane effective elastic moduli are calculated for various combinations of aggregate, ITZ and bulk cement paste properties. This is done using both the macrostress and the macrostrain prescribed expressions for the effective elastic properties, as derived in this appendix. Table A.1 shows the results of these calculations for the RVE dimensions and elastic properties as derived in section 4.4, representing the concrete mix used in the experimental test program of Van Geel. In addition to these results, two alternatives are considered with such modifications that the effective elastic moduli resemble those of the RVE for the fine aggregate grain fraction of the concrete mix of Van Geel.

To compare the results of the macrostress and the macrostrain approach, it is convenient to use the (plane strain) bulk and shear modulus ( $\bar{K}_{r\theta}$  and  $\bar{G}_{r\theta}$ ) as elastic constants instead of  $\bar{E}_{r\theta}$  and  $\bar{\nu}_{r\theta}$ . The bulk modulus  $\bar{K}_{r\theta}$  is determined by elementary loading case I only and is therefore the same for the macrostress and the macrostrain approach. Hence, the difference between the macrostress and the macrostrain approach is entirely governed by just one constant, the shear modulus  $\bar{G}_{r\theta}$ , which is determined by elementary loading case II. In the current plane strain configuration, the bulk and shear modulus are defined as:

$$\bar{K}_{r\theta} = \frac{\bar{E}_{r\theta}}{2 \left( 1 - \bar{\nu}_{r\theta} - 2\nu^2 \frac{\bar{E}_{r\theta}}{\bar{E}_z} \right)}$$

$$\bar{G}_{r\theta} = \frac{\bar{E}_{r\theta}}{2(1 + \bar{\nu}_{r\theta})}$$

From table A.1 it appears that the deviations between the results from the macrostrain and the macrostress approach for the shear modulus are about 7%. With  $\bar{K}_{r\theta}$  being the same for the macrostress and macrostrain approach, deviations in elastic behaviour are expected to be in the range 0 – 7% (mean value of 3,5%). Hence, the effective elastic properties do not depend much on the exact distribution of the boundary loads of the RVE. This means that for linear elastic material behaviour the choice of either the macrostress or macrostrain approach makes little difference.

Table A.1. Effective elastic moduli [MPa].

	Coarse aggregates		Fine aggregates		Alternative 1		Alternative 2	
	macro-stress	macro-strain	macro-stress	macro-strain	macro-stress	macro-strain	macro-stress	macro-strain
$\bar{E}_{r\theta}$	40740	41830	32130	33550	32080	33460	32040	33310
$\bar{\nu}_{r\theta}$	0.160	0.138	0.176	0.140	0.170	0.135	0.175	0.142
$\bar{K}_{r\theta}$	24890	24890	19950	19950	19820	19820	19850	19850
$\bar{G}_{r\theta}$	17550	18380	13660	14720	13700	14750	13640	14580
$\frac{\Delta\bar{G}_{r\theta}}{\bar{G}_{r\theta}}$	4.7 %		7.8 %		7,7 %		6,9 %	

Table A.2. Input properties for table A.1.

	$R_1$ [mm]	$R_2$ [mm]	$R_3$ [mm]	$E_1$ [MPa]	$E_2$ [MPa]	$E_3$ [MPa]	$\nu$
Coarse aggregates	2.710	2.860	3.010	65000	10000	18000	0.12
Fine aggregates	0.945	1.038	1.169	70000	10000	18000	0.12
Alternative 1	0.945	1.038	1.169	61000	15000	15000	0.12
Alternative 2	0.945	0.955	1.169	70000	2000	18000	0.12

## APPENDIX B

### EQUILIBRIUM OF THE RVE

In appendix A, two elementary states of loading on the RVE are discussed. For these elementary states of loading, an analytical solution of the elastic stress/displacement field is found by solving the equations of compatibility, the constitutive equations of linear elasticity and the equations of equilibrium. Though not explicitly cited in appendix A, these elementary states of loading satisfy an essential condition, i.e. the external loading on the RVE is in a state of equilibrium. Worded differently, the RVE does not move (translate or rotate) as a rigid body acted by these external forces. A state of equilibrium for the elementary states of loading is ensured because:

1. The normal loading on the outer-boundary of the RVE is symmetrical with respect to the centre of the RVE, i.e. no residual force exists causing the RVE to translate.
2. The integral of (tangential) shear loading along the outer-boundary of the RVE is equal to zero, i.e. no residual moment exists causing the RVE to rotate.

As any loading path can be considered as a linear combination of the elementary states of loading (section 4.3.4), any linear elastic state of the RVE is in equilibrium.

This changes when material non-linearity is introduced due to cracking in the ITZ. As outlined in section 4.3.5.3, ITZ cracking induces an arbitrary distribution of stresses along the centreline of the ITZ layer. In consequence of the conditions of equilibrium, there are some limits to the arbitrariness of these stresses. The first condition of equilibrium (no translation of the RVE) is satisfied, since the normal stresses along the centreline of the ITZ are still symmetrical with respect to the centre of the RVE. The second condition of moment equilibrium is not satisfied directly, but only after introducing secondary ITZ shear stress corrections (section 4.3.7). As a result of the introduction of secondary ITZ shear stress corrections, the summation of the local shear forces  $F_{r\theta}(\theta^*)$  (see figure B.1) along the circumference of the outer-boundary at  $R_3$  is forced to be zero. Consequently, the cylindrical RVE is in moment equilibrium.

If the loading on the outer boundary of the RVE is in moment equilibrium, the macroscopic representative stress state – as determined in section 4.3.8 by averaging the forces at the outer-boundary of the RVE – should be in moment equilibrium as well, i.e.  $\tau_{xy}^m = \tau_{yx}^m$ . Hence, the condition of moment equilibrium sets requirements for the averaging procedure. In this appendix it will be outlined that the so-called volume-averaging procedure as applied throughout this thesis meets these requirements.

The summation of the local shear forces along the circumference of the outer-boundary at  $R_3$  is forced to be zero. This implies that for any set of boundary forces

$(F_r, F_{r\theta})$  in an arbitrary point (denoted by  $\theta^* = \theta_1^*$ ) of the outer-boundary of the RVE, always a shear force exists in another arbitrary point (denoted by  $\theta^* = \theta_2^*$ ) that counterbalances the shear force  $F_{r\theta}$  at  $\theta^* = \theta_1^*$ . Ergo, an arbitrary distribution of forces on the outer-boundary of the RVE, which is in moment equilibrium, may be represented as an assemblage of pairs of forces of which each single pair is in moment equilibrium.

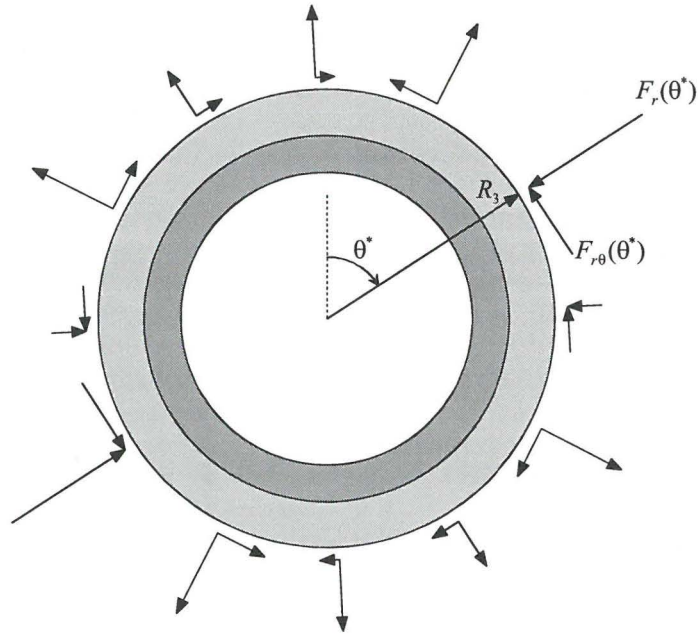


Figure B.1. RVE with arbitrary loading at the outer boundary.

Such a pair of forces is depicted in figure B.2. The contribution of such a single pair of forces to the macroscopic shear stresses  $\tau_{xy}^m$  and  $\tau_{yx}^m$  is denoted by the volume-averaged quantities  $\Delta\tau_{xy}^m$  and  $\Delta\tau_{yx}^m$ . The averaging procedure is denoted as *volume-averaging*, which means that the boundary stresses are weighted by that part of the volume they act upon<sup>1</sup>. If boundary forces are considered, the weighted volume reduces to the distance of the point of action of the force perpendicular to a cross-section through the centre of the RVE in either the global  $x$ - or  $y$ -direction, hence (see figure B.2)

$$\begin{aligned} \Delta\tau_{xy}^m &= \frac{(F_r^1 \cos\theta_1^* - F_{r\theta}^1 \sin\theta_1^*)R_3 \sin\theta_1^* + (F_r^2 \cos\theta_2^* - F_{r\theta}^2 \sin\theta_2^*)R_3 \sin\theta_2^*}{\frac{1}{2}\pi R_3^2} \\ &= \frac{2}{\pi R_3} \left( F_r^1 \cos\theta_1^* \sin\theta_1^* + F_r^2 \cos\theta_2^* \sin\theta_2^* - F_{r\theta}^1 \sin^2\theta_1^* - F_{r\theta}^2 \sin^2\theta_2^* \right) \end{aligned} \quad (\text{B.1})$$

<sup>1</sup> Equations are given in section 4.3.8 and appendix A

$$\begin{aligned} \Delta\tau_{yx}^m &= \frac{(F_r^1 \sin\theta_1^* + F_{r\theta}^1 \cos\theta_1^*)R_3 \cos\theta_1^* - (F_r^2 \sin\theta_2^* + F_{r\theta}^2 \cos\theta_2^*)(-R_3 \cos\theta_2^*)}{\frac{1}{2}\pi R_3^2} \\ &= \frac{2}{\pi R_3} \left( F_r^1 \cos\theta_1^* \sin\theta_1^* + F_r^2 \cos\theta_2^* \sin\theta_2^* + F_{r\theta}^1 \cos^2\theta_1^* + F_{r\theta}^2 \cos^2\theta_2^* \right) \end{aligned} \quad (\text{B.2})$$

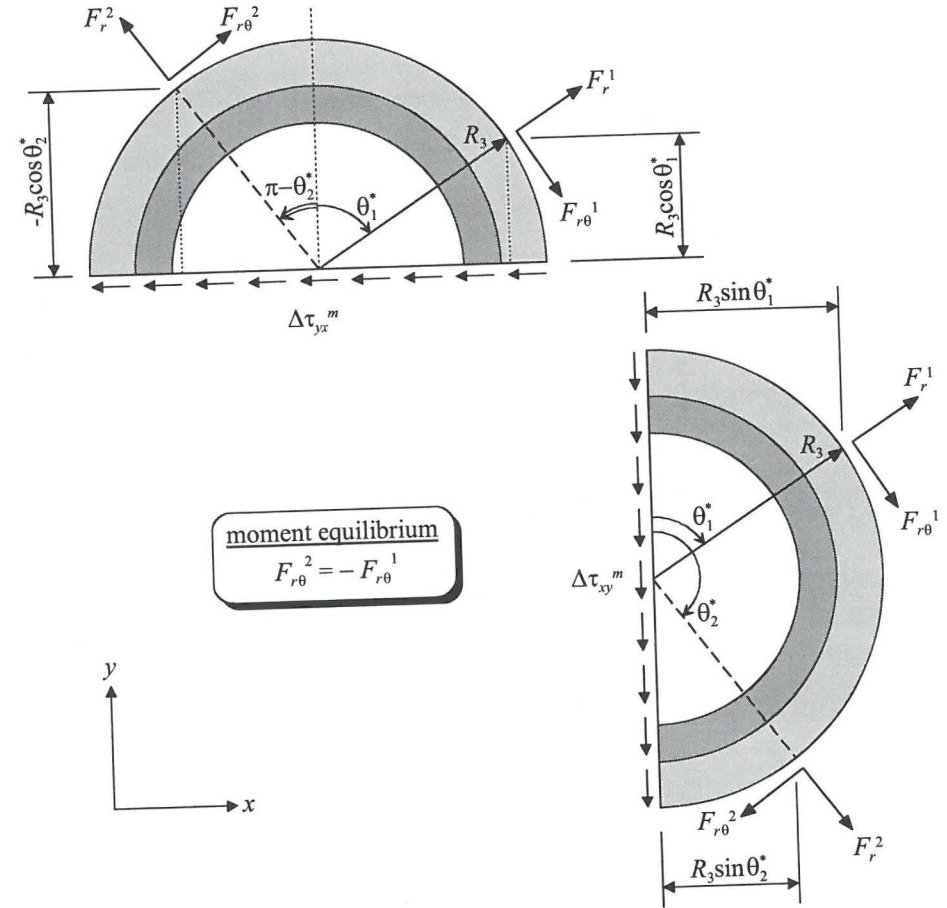


Figure B.2. Macroscopic (volume averaged) shear stresses of the RVE loaded by an arbitrary pair of balanced forces.

Introducing the equality  $F_{r\theta}^2 = -F_{r\theta}^1$  (moment equilibrium) in equation (B.1) and equation (B.2) results in

$$\Delta\tau_{xy}^m = \frac{2}{\pi R_3} \left( F_r^1 \cos\theta_1^* \sin\theta_1^* + F_r^2 \cos\theta_2^* \sin\theta_2^* - F_{r\theta}^1 (\sin^2\theta_1^* - \sin^2\theta_2^*) \right)$$

$$\begin{aligned}\Delta\tau_{yx}^m &= \frac{2}{\pi R_3} \left( F_r^1 \cos\theta_1^* \sin\theta_1^* + F_r^2 \cos\theta_2^* \sin\theta_2^* + F_{r,\theta}^1 (\cos^2\theta_1^* - \cos^2\theta_2^*) \right) \\ &= \frac{2}{\pi R_3} \left( F_r^1 \cos\theta_1^* \sin\theta_1^* + F_r^2 \cos\theta_2^* \sin\theta_2^* - F_{r,\theta}^1 (\sin^2\theta_1^* - \sin^2\theta_2^*) \right)\end{aligned}$$

Hence, the contribution of a single arbitrary pair of (balanced) forces to the macroscopic stress state is in moment equilibrium

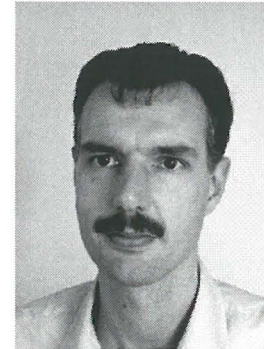
$$\Delta\tau_{yx}^m = \Delta\tau_{xy}^m \quad (\text{B.3})$$

If equation (B.3) applies for a single pair of arbitrary balanced forces, the equality between macroscopic (volume averaged) shear stresses must also apply to any assemblage of pairs of balanced forces. Hence

$$\tau_{yx}^m = \tau_{xy}^m$$

for any loading on the outer boundary of the RVE, which is in moment equilibrium.

## CURRICULUM VITAE



Hans Bongers was born on August 1, 1968 in Valkenswaard, the Netherlands. He grew up in Lieshout and attended secondary school at the Macropedius College in Gemert from 1980 until 1986.

His interest in building technology arose in 1981, helping his father building their new home on their own account. So, after passing the atheneum- $\beta$  examinations in 1986, he commenced his studies at the Faculty of Building, Architecture and Planning at the Eindhoven University of Technology. He specialised in structural design and graduated in 1992 on the subject of 'concrete behaviour loaded in multiaxial compression' under supervision of prof.dr.ir. H.S. Rutten.

Also thanks to a grant of the Netherlands Technology Foundation (STW), he was able to continue the research on 'concrete behaviour loaded in multiaxial compression' and was employed, from 1992 to 1999, as a research assistant at the Department of Structural Design of the Eindhoven University of Technology.

Since 2000, he is employed as a (senior) structural engineer at the company of Betonson in Son. He is concerned with the design of (pre-tensioned) precast concrete structures, with a growing concern to research and development in this field.

BOUWSTENEN is een publikatiereeks van de Faculteit Bouwkunde, Technische Universiteit Eindhoven. Zij presenteert resultaten van onderzoek en andere activiteiten op het vakgebied der Bouwkunde, uitgevoerd in het kader van deze Faculteit.

BOUWSTENEN zijn verkrijgbaar bij:

Publikatiewinkel 'Legenda'  
Gebouw Vertigo  
Faculteit Bouwkunde  
Technische Universiteit Eindhoven  
Postbus 513  
5600 MB Eindhoven

of telefonisch te bestellen:  
040 - 2472383  
040 - 2475832

**Kernredactie**  
MTOZ

Reeds verschenen in de serie  
BOUWSTENEN

- nr.1  
**Elan, a computer model for building energy design, theory and validation**  
M.H. de Wit  
H.H. Driessen  
R.M.M. van der Velden
- nr.2  
**Kwaliteit, keuzevrijheid en kosten Evaluatie van experiment Klarendal, Arnhem**  
drs J. Smeets  
C. le Nobel, arch. HBO  
M. Broos, J. Frenken, A. v.d. Sanden
- nr.3  
**Crooswijk van 'bijzonder' naar 'gewoon'**  
drs V. Smit  
ir K. Noort
- nr.4  
**Staal in de woningbouw**  
ir E.J.F. Delsing
- nr.5  
**Mathematical theory of stressed skin action in profiled sheeting with various edge conditions**  
ir A.W.A.M.J. v.d. Bogaard
- nr.6  
**Hoe berekenbaar en betrouwbaar is de coëfficiënt  $k$  in  $\bar{x} - k\sigma$  en  $\bar{x} - ks$ ?**  
ir K.B. Lub  
drs A.J. Bosch
- nr.7  
**Het typologisch gereedschap Een verkennende studie omtrent typologie en omtrent de aanpak typologisch onderzoek**  
J.H. Luiten arch. HBO
- nr.8  
**Informatievoorziening en beheerprocessen**  
ir A. Nauta / drs J. Smeets (red.)  
Prof. H. Fassbinder (projectleider)  
ir A. Proveniers,  
drs J.v.d. Moosdijk
- nr.9  
**Strukturering en verwerking van tijdgegevens voor de uitvoering van bouwwerken**  
ir W.F. Schaefer  
ir P.A. Erkelens
- nr.10  
**Stedebouw en de vorming van een speciale wetenschap**  
K. Doevendans
- nr.11  
**Informatica en ondersteuning van ruimtelijke besluitvorming**  
dr G.G. van der Meulen
- nr.12  
**Staal in de woningbouw, corrosiebescherming van de begane grondvloer**  
ir E.J.F. Delsing
- nr.13  
**Een thermisch model voor de berekening van staalplaatbetonvloeren onder brandomstandigheden**  
ir A.F. Hamerlinck
- nr.14  
**De wijkgedachte in Nederland Gemeenschapsstreven in een stedebouwkundige context**  
dr ir K. Doevendans  
dr R. Stolzenburg
- nr.15  
**Diaphragm effect of trapezoidally profiled steel sheets. Experimental research into the influence of force application**  
ir A.W.A.M.W. v.d. Bogaard
- nr.16  
**Versterken met spuit-ferrocement. Het mechanische gedrag van met spuit-ferrocement versterkte gewapende betonbalken**  
ir K.B. Lub  
ir M.C.G. van Wanroy
- nr.17  
**De tractaten van Jean Nicolas Louis Durand**  
ir G. van Zeyl
- nr.18  
**Wonen onder een plat dak. Drie opstellen over enkele vooronderstellingen van de stedebouw**  
dr ir K. Doevendans
- nr.19  
**Supporting decision making processes A graphical and interactive analysis of multivariate data**  
drs W. Adams
- nr.20  
**Self-help building productivity A method for improving house building by low-income groups applied to Kenya 1990-2000**  
ir P. A. Erkelens
- nr.21  
**De verdeling van woningen: een kwestie van onderhandelen**  
drs V. Smit
- nr.22  
**Flexibiliteit en kosten in het ontwerp-proces Een besluitvormingondersteunend model**  
ir M. Prins
- nr.23  
**Spontane nederzettingen begeleid Voorwaarden en criteria in Sri Lanka**  
ir P.H. Thung
- nr.24  
**Fundamentals of the design of bamboo structures**  
O. Arce-Villalobos
- nr.25  
**Concepten van de bouwkunde**  
Prof. dr ir M.F.Th. Bax (red.)  
dr ir H.M.G.J. Trum (red.)
- nr.26  
**Meaning of the site**  
Xiaodong Li
- nr.27  
**Het woonmilieu op begrip gebracht**  
Jaap Ketelaar
- nr.28  
**Urban environment in developing countries**  
editors: dr ir Peter A. Erkelens  
dr George G. van der Meulen
- nr.29  
**Stategische plannen voor de stad Onderzoek en planning in drie steden**  
Prof. dr H. Fassbinder (red.)  
ir H. Rikhof (red.)
- nr.30  
**Stedebouwkunde en stadsbestuur**  
ir Piet Beekman
- nr.31  
**De architectuur van Djenné Een onderzoek naar de historische stad**  
P.C.M. Maas
- nr.32  
**Conjoint experiments and retail planning**  
Harmen Oppewal
- nr.33  
**Strukturformen Indonesischer Bautechnik Entwicklung methodischer Grundlagen für eine 'konstruktive pattern language' in Indonesien**  
Heinz Frick
- nr.34  
**Styles of architectural designing Empirical research on working styles and personality dispositions**  
Anton P.M. van Bakel
- nr.35  
**Conjoint choice models for urban tourism planning and marketing**  
Benedict Dellaert
- nr.36  
**Stedelijke Planvorming als co-productie**  
Prof. dr H. Fassbinder (red.)

- nr 37  
**Design Research in the Netherlands**  
editors: Prof. dr R.M.Oxman,  
Prof. dr ir. M.F.Th. Bax,  
Ir H.H. Achten
- nr 38  
**Communication in the Building Industry**  
Bauke de Vries
- nr 39  
**Optimaal dimensioneren van gelaste plaatliggers**
- nr 40  
**Huisvesting en overwinning van armoede**  
dr.ir. P.H. Thung en dr.ir. P. Beekman (red.)
- nr 41  
**Urban Habitat: The environment of tomorrow**  
George G. van der Meulen,  
Peter A. Erkelens
- nr 42  
**A typology of joints**  
John C.M. Olie
- nr 43  
**Modeling constraints-based choices for leisure mobility planning**  
Marcus P. Stemerding
- nr 44  
**Activity-based travel demand modeling**  
D. Ettema
- nr 45  
**Wind-induced pressure fluctuations on building facades**  
Chris Geurts
- nr 46  
**Generic Representations**  
Henri Achten
- nr 47  
**Johann Santini Aichel**  
Dirk De Meyer
- nr 48  
**Concrete behaviour in multiaxial compression**  
Erik van Geel
- nr 49  
**Modelling site selection**  
Frank Witlox
- nr 50  
**Ecolemma model**  
Ferdinand Beetstra
- nr 51  
**Conjoint approaches to developing activity-based models**  
Donggen Wang
- nr 52  
**On the effectiveness of ventilation**  
Ad Roos
- nr 53  
**Conjoint modeling approaches for residential group preferences**  
Eric Molin
- nr 54  
**Modelling architectural design information by features**  
Jos van Leeuwen
- nr 55  
**A spatial decision support system for the planning of retail and service facilities**  
Theo Arentze
- nr 56  
**Integrated lighting system assistant**  
Ellie de Groot
- nr 57  
**Ontwerpend leren, leren ontwerpen**  
dr.ir. J.T. Boekholt
- nr 58  
**Temporal aspects of theme park choice behaviour**  
Astrid Kemperman
- nr 59  
**Ontwerp van een geïndustrialiseerde funderingswijze**  
Faas Moonen
- nr 60  
**Merlin: A decision support system for outdoor leisure planning**  
Manon van Middelkoop
- nr 61  
**The aura of modernity**  
Jos Bosman (nog niet gepubliceerd)
- nr 62  
**Urban Form and Activity-Travel Patterns**  
Daniëlle Snellen
- nr 63  
**Design Research in the Netherlands 2000**  
Henri Achten
- nr 64  
**Computer Aided Dimensional Control in Building Construction**  
Rui Wu
- nr 65  
**Beyond Sustainable Building**  
editors: Peter A. Erkelens  
Sander de Jonge  
August A.M. van Vliet  
co-editor: Ruth J.G. Verhagen
- nr 66  
**Das globalrecyclingfähige Haus**  
Hans Löfflad
- nr 67  
**Cool Schools For Hot Suburbs**  
René J. Dierkx
- nr 68  
**A Bamboo Building Design Decision Support Tool**  
Fitri Mardjono
- nr 69  
**Driving rain on building envelopes**  
Fabien van Mook
- nr 70  
**Heating Monumental Churches**  
Henk Schellen
- nr 71  
**Van Woningverhuurder naar Aanbieder van Woongenot**  
Patrick Dogge
- nr 72  
**Moisture transfer properties of coated gypsum**  
Emile Goossens
- nr 73  
**Plybamboo Wall-panels for Housing**  
Guillermo E. González-Beltrán
- nr 74  
**The Future Site-Proceedings**  
Ger Maas  
Frans van Gassel
- nr 75  
**Radon transport in Autoclaved Aerated Concrete**  
Michel van der Pal
- nr 76  
**The Reliability and Validity of Interactive Virtual Reality Computer Experiments**  
Amy Tan
- nr 77  
**Measuring Housing Preferences Using Virtual Reality And Belief Networks**  
Maciej A. Orzechowski
- nr 78  
**Computational Representations of Words and Associations in Architectural Design**  
Nicole Segers
- nr 79  
**Measuring and Predicting Adaptation in Multidimensional Activity-Travel Patterns**  
Chang-Hyeon Joh
- nr 80  
**Strategic Briefing**  
Fayez Al Hassan (nog niet gepubliceerd)
- nr 81  
**Well Being in Hospitals**  
Simona Di Cicco
- nr 82  
**Solares Bauen Implementierungs- und Umsetzungsaspekte in der Hochschulausbildung in Österreich**  
Gerhard Schuster

nr 83  
**Supporting Strategic Design of  
workplace Environments with  
Case-Based Reasoning**  
Shauna Mallory-Hill

nr 84  
**ACCEL: a Tool for Supporting Concept  
Generation in the Early Design Phase**  
Maxim Ivashkov

nr 85  
**Brick-mortar interaction in masonry  
under compression**  
Ad Vermeltfoort

nr 86  
**Zelfredzaam Wonen**  
Guus van Vliet

nr 87  
**Een ensemble met grootstedelijke  
allure**  
Jos Bosman/Hans Schippers

nr 88  
**On the Computation of Well-  
Structured Graphic Representations in  
Architectural Design**  
Henri Achten

nr 89  
**De Evolutie van een West-Afrikaanse  
Vernaculaire Architectuur**  
Wolf Schijns

nr 90  
**ROMBO tactiek**  
Christoph Maria Ravesloot

nr 91  
**External coupling between building  
energy simulation and computational  
fluid dynamics**  
Ery Djunaedy

nr 92  
**Design Research in the  
Netherlands 2005**  
Editors:  
Henri Achten  
Kees Dorst  
Pieter Jan Stappers  
Bauke de Vries

nr 93  
**Ein Modell zur baulichen Transformation**  
Jalil H.Saber Zaimian

nr 94  
**Human Lighting Demands  
Healthy Lighting in an Office  
Environment**  
Myriam Aries

nr 95  
**A Spatial Decision Support System for  
the Provision and Monitoring of Urban  
Greenspace**  
Claudia Pelizaro

nr 96  
**Leren Creëren**  
Adri Proveniers

nr 97  
**Simlandscape**  
Rob de Waard

nr 98  
**Design Team Communication**  
Ad den Otter

nr 99  
**Juri Czabanowski**

nr 100  
**Hambase**  
Martin de Wit

nr 101  
**Bron- v.d. Jagt**  
(nog niet gepubliceerd)

nr 102  
**Het Bouwkundig Contrapunt**  
Jan Francis Boelen

nr 103  
**A Framework for a Multi-Agent  
Planning Support System**  
Dick Saarloos

nr 104  
**Bracing Steel Frames with Calcium  
Silicate Element Walls**  
Bright Mweene Ng'andu

nr 105  
**Naar een nieuwe houtskeletbouw**  
F.N.G. De Medts

nr 106  
**Anatomy of Dwelling**  
Enno Wiersma  
(nog niet gepubliceerd)

nr 107  
**Healing Architecture**  
Ewa Mosiniak  
(nog niet gepubliceerd)

nr 108  
**Geborgenheid**  
drs T.E.L. van Pinxteren  
(nog niet gepubliceerd)

nr 109  
**Modelling Strategic Behaviour  
in Anticipation of Congestion**  
Qi Han

nr 110  
**Reflecties op het Woondomein**  
Fred Sanders

nr 111  
**On Assessment of Wind Comfort  
by Sand Erosion**  
Gabor Dezso

nr 112  
**Bench Heating in Monumental  
Churches**  
Dionne Limpens-Neilen

nr 113  
**RE. Architecture**  
Anna Pereira Roders

nr 114  
**Toward Applicable Green Architecture**  
Usama El Fiky

nr 115  
**Knowledge Representation Under  
Inherent Uncertainty in a Multi-Agent  
System for Land Use Planning**  
Liyang Ma

nr 116  
**Integrated Heat Air and Moisture  
Modeling and Simulation**  
Jos van Schijndel

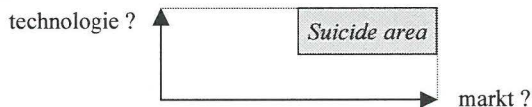


## STELLINGEN

behorende bij het proefschrift

### CONCRETE BEHAVIOUR IN MULTIAXIAL COMPRESSION – NUMERICAL MODELLING

1. Bij het modelleren van mode II scheuren in beton middels zgn. interface elementen dient ook de invloed van de tangentiële normaalspanning te worden meegenomen als additionele parameter. Dit komt voort uit het feit dat het scheuoppervlak in normale sterkte beton niet glad maar ruw is.
2. Als de resultaten van computersimulaties niet overeenkomen met de theoretische verwachtingen, dan dient men zich ook te realiseren dat over de correctheid van software, in studies waar deze software normaliter niet wordt gebruikt, grote twijfel kan bestaan.
3. Een numeriek model is als een lange ketting: zo sterk als zijn zwakste schakel en bij te grote lengte bezwijkt hij onder zijn eigen gewicht.
4. Het heeal is een verzameling van bolronde materie met een zeer losse pakking. In dit opzicht lijkt beton op het heeal, alleen dan op een ander schaalniveau en véél beter verdicht.
5. De menselijke waarneming is beperkt tot bepaalde schaalniveaus. Dientengevolge neemt de betrouwbaarheid van metingen aan het heeal sterk toe naarmate deze zich concentreren op *lokale* (aardse) eigenschappen, terwijl de betrouwbaarheid van metingen aan beton sterk toeneemt naarmate deze zich concentreren op *globale* eigenschappen.
6. ... *Helaas is (gewapend) beton een complex en eigenzinnig materiaal dat soms weigert zich te gedragen volgens de heersende regels der mechanica<sup>1</sup>...*  
Wetenschap dwingt ons tot het creëren van categorieën en regels. Beton deelt echter de menselijke eigenschap dat het zich niet altijd in een dergelijk keurslijf laat dwingen.
7. Een simpele boodschap die goed klinkt wordt vaak (te) gemakkelijk voor waar gehouden (zonder de bronnen te controleren). Beoordeel dit proefschrift daarom niet uitsluitend op de figuren met de resultaten van de computer simulaties, maar controleer ook de theoretische afleidingen die hieraan ten grondslag liggen...
8. Om een betonconstructie winstgevend te kunnen verkopen, dient de constructie – in marketing termen – te zijn voorzien van ‘toegevoegde waarde’. Aangezien de constructieve veiligheid tegenwoordig géén vanzelfsprekendheid meer is, dient de inbreng van een hoofdconstructeur dus als ‘toegevoegde waarde’ te worden gezien met een grote potentiële bijdrage aan de winstgevendheid van een project.
9. Promoveren versterkt alsook verzwakt de onderzoeker. Hoe dit experiment verloopt hangt sterk af van de proefpersoon en de randvoorwaarden. Doel van het experiment is te stoppen voordat de uiterste ‘sterkte’ wordt bereikt.
10. Het innovatiegebied waar (nog) geen duidelijke markt voor is en waar ook de technologie nog voor ontwikkeld moet worden, wordt door innovatie managers ook wel als ‘suicide area’ of ‘no-go area’ aangeduid. Het betreden van dit risicogebied is vooralsnog voorbehouden aan (optimistische) junior onderzoekers.



11. Leidraad bij zowel het stimuleren van de ontwikkeling van een (gehandicapt) kind als bij het beoefenen van de wetenschap:

Vorderingen gaan in kleine stapjes. Is de stap te groot om deze in één keer te zetten? Geef dan niet op, maar zoek steeds naar manieren om deze grote stap in kleinere (behabbare) stapjes op te delen. Het resultaat zal zich uiteindelijk in al zijn schoonheid openbaren.

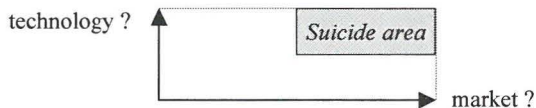
<sup>1</sup> F.J. VECCHIO (2001). Non-linear finite element analysis of reinforced concrete: at the crossroads? *Structural Concrete*, 2 (4), pp. 201-212

# PROPOSITIONS

with the PhD-thesis

## CONCRETE BEHAVIOUR IN MULTIAXIAL COMPRESSION – NUMERICAL MODELLING

1. Modelling of mode II cracks in concrete by means of so-called interface elements also should incorporate the influence of the tangential normal stress as an additional parameter. This originates from the fact that the crack surface in normal strength concrete is not smooth but rough.
  2. If the results of computer simulations do not agree with the theoretical expectations, then one should also realise that the correctness of software, in analyses outside the normal scope of the software, could be highly questionable.
  3. A numerical model is like a long chain: as strong as its weakest link and if too long it breaks under its own weight.
  4. The universe is a very loose packed system of sphere-like material. In this sense concrete resembles the universe, yet on a different scale level and much better compacted.
  5. Human perception is restricted to certain scale levels. For that reason the reliability of measurements on the universe strongly increases when these are focused on *local* (down-to-earth) properties, whereas the reliability of concrete measurements strongly increases when these are focused on *global* properties.
  6. ... *Unfortunately, (reinforced) concrete is a complex and stubborn material that sometimes refuses to act according to accepted rules of mechanics*<sup>1</sup>...
- Science forces us to create categories and rules. However, concrete shares the human characteristic of not always complying with such a straitjacket.
7. A simple pleasing statement is often (too) easy taken for truth (without verification of the sources). Therefore, do not judge this thesis only by the figures with the results of the computer simulations, but also verify the theoretical derivations underlying them...
  8. To lucratively sell a concrete structure, the structure has – in terms of marketing – to be equipped with ‘added value’. Regarding the fact that nowadays structural safety cannot be taken for granted anymore, the contribution of a senior structural engineer has to be regarded as ‘added value’ with a large potential contribution to the profit of a project.
  9. Ph.D. research strengthens as well as weakens the researcher. The way this experiment evolves strongly depends on the testee and the boundary conditions. Purpose of the experiment is to stop *before* reaching the ultimate ‘strength’.
  10. That sector of potential innovations for which a distinct market is (as yet) lacking and the technology required still has to be developed as well, is – by innovation managers – often entitled as ‘suicide area’ or ‘no-go area’. Entering this hazardous area is, as yet, reserved for (optimistic) junior researchers.



11. Guiding principle for both the education of a (disabled) child and the practice of science:

Progress is made in small steps. Is the step too large to take it in one go? Do not give up, but keep searching for ways to split this large step into smaller (manageable) steps. Eventually, the result will reveal itself in all its beauty.

---

<sup>1</sup> F.J. VECCHIO (2001). Non-linear finite element analysis of reinforced concrete: at the crossroads? *Structural Concrete*, 2 (4), pp. 201-212



## Concrete behaviour in multiaxial compression

### Numerical modelling

The research presented comprises the development of a two-dimensional (2D) numerical model, which is capable of providing reliable predictions of the mechanical response of multiaxial compressive tests on concrete specimens in a 2D test lay-out.

The model has been based on sound physical/mechanical interpretation and explanation of the complex mechanical behaviour of concrete loaded in multiaxial compression. To establish such a basis, this behaviour was subdivided in two ways. On the one side, three scale levels of perception/observation were distinguished. On the other side, a distinction was made between four typical behavioural stages in multiaxial compression tests.

The great differences in scale of heterogeneity of the concrete material between the pre-peak and the post-peak region of a multiaxial compression test could be captured well by the subdivision chosen. With respect to constitutive modelling, these differences required the formulation of two so-called 'Representative Volume Elements' (RVEs), a concept that accounts for the specific heterogeneity of concrete at the lower scale levels of observation. By choosing the geometrical shape of the RVEs rationally and with a thorough analysis of basic (crack) mechanics, straightforward 'low-scale' constitutive laws could be efficiently combined with sophisticated – physically appealing – 'high-scale' constitutive laws, applicable both in the pre-peak and post-peak region.

The 'mesoscopic model', consisting of the above RVE-formulations, is well suited for small-scale analyses of concrete structures subjected to multiaxial compression. For large-scale analyses, the mesoscopic model is less practical. To enhance the practicality and speed up computations, an adjusted approach is presented, entitled as 'macroscopic model'.

A wide range of accurate numerical simulations of multiaxial compressive tests illustrates the performance of both the mesoscopic and the macroscopic model.